Fermi National Accelerator Laboratory

FERMILAB-Conf-98/166

International Symposium on Near Beam Physics

Editors Richard A. Carrigan, Jr. and Nikolai V. Mokhov

Fermi National Accelerator Laboratory
P.O. Box 500, Batavia, Illinois 60510

June 1998

Operated by Universities Research Association Inc. under Contract No. DE-AC02-76CH03000 with the United States Department of Energy

Disclaimer

Distribution

INTERNATIONAL SYMPOSIUM
ON
NEAR BEAM PHYSICS

Fermilab, September 22-24, 1997

EDITORS
Richard A. Carrigan, Jr.
Nikolai V. Mokhov

Fermi National Accelerator Laboratory
Batavia, Illinois

June 1998

ORGANIZING COMMITTEE

M. Albrow (Fermilab)
A. Asseev (IHEP)
J. Bjorken (SLAC)
D. Carrigan (Fermilab) - co-chair
K. Ehret (DESY)
A. Hahn (Fermilab)
W. Herr (CERN)
J. Holt (Fermilab)
D. Kaplan (IIT)
P. Kasper (Fermilab)
N. Mokhov (Fermilab) - co-chair
S. Peggs (BNL)
S. Pruss (Fermilab)
M. Richardson (Fermilab) - secretariat
A. Santoro (Lafex/Cbpf Rio)
C. Sazama (Fermilab) - secretariat
W. Scandale (CERN)
M. Sullivan (SLAC)
K. Takayama (KEK)
C. Taylor (Case-Western Reserve)
F. Willeke (DESY)

Contents

INTRODUCTION

The International Symposium on Near Beam Physics was held at Fermilab September 22-24, 1997. More than sixty physicists attended including representatives from BNL, CERN, DESY, Fermilab, IHEP (Protvino), KEK, and SLAC.

The purpose of the symposium was to assay the current understanding of beam halo phenomena, accelerator techniques, and diffractive physics and other experiments that operate near beams. The emphasis was on the interplay of these subjects, not so much on experimental results. The symposium also apprised future possibilities and probed where additional work was useful to facilitate near beam operation.

The introductory presentation was given by Giorgio Matthiae (Rome). Matthiae pioneered the development of the Roman pot, one of the first devices to run near circulating beams. He noted that developments go back three decades in this field. Roman pots are now being used as adjuncts to powerful collider detectors to study hard diffraction processes. Another pioneering “in-beam” technique, the use of gas jets, was reviewed by Mario Macri from Genoa. The history of gas jets also goes back twenty-five years to E36, the first experiment to operate at Fermilab. A rich tapestry of diffractive physics issues can be attacked with these techniques. These possibilities were emphasized by Johannes Ranft of Siegen. He described a number of interesting theoretical topics that could be addressed with a near beam approach.

Michael Albrow of Fermilab reported on the recent addition of Roman pots to CDF for diffractive studies. Andrew Brandt (FNAL) described the proposed addition of Roman pots to the D0 experiment for detailed studies of hard diffraction in Run II at Fermilab. Carsten Hast, Klaus Ehret, and Michael Bieler reported on the status of HERA-B, the B-physics experiment at DESY that will exploit a wire target placed near the DESY proton beam. Bieler also discussed the HERA proton collimation system and the HERA beam diagnostic system and gave an overview of the Roman pot forward spectrometers in operation at HERA. Dan Kaplan of IIT described plans for BTEV at Fermilab where a similar possibility is being discussed. Other new possibilities included the FELIX concept at the LHC reported by Cyrus Taylor (Case-Western Reserve) and work at Fermilab proposed by Larry Jones and Michael Longo (Michigan). These approaches seek to investigate the diffractive region in more detail.

Beam dynamics issues were covered by Todd Satogata (BNL), Pat Colestock (FNAL), Weiren Chou (FNAL), and Walter Scandale (CERN). While much progress has been made, the presence of non-linearities and the difficulty of halo characterization complicate progress toward a practical understanding in this area. Some of the best information on beam halo is provided by experimental and theoretical work on collimation. Collimation studies were reported by Bernard Jeanneret (CERN), Michael Sullivan (SLAC), and Stanley Pruss and Alexandr Drozhdin of Fermilab. Michael Church briefed the symposium on the collimation system planned for the Tevatron in the coming years.

At Brookhaven’s RHIC with its heavy ion beams some of the beam dynamics and collimation issues will be particularly intriguing. Dejan Trbojevic described the collimation considerations for the machine while Sebastian White reported on the development of a new zero degree neutron calorimeter for luminosity monitoring that might also have applications at LHC.

Operating near an accelerator beam poses several difficult challenges. Mechanical stability is important. Vasily Parkhomchuk of Novosibirsk and Craig Moore of FNAL outlined some of the experience with vibration problems. Hisayasu Mitsui (Toshiba) summarized work at KEK with Ken Takayama investigating radiation damage to near beam components. Alan Hahn and Vladimir Shiltzev of Fermilab discussed instrumentation for beam monitoring.

By its nature, extraction requires operating near the accelerator beam. One of the interesting new extraction developments is the use of bent channeling crystals. Several proposals for the use of channeling extraction have appeared over the last several years. Alexey Asseev presented an overall review of the work at IHEP (Protvino) including their pioneering work on crystal extraction. Konrad

Elsener reviewed the very detailed studies of crystal extraction at CERN. Thornton Murphy summarized the recent 900 GeV Fermilab extraction experiment where luminosity-driven extraction was recently achieved. Valery Biryukov of IHEP reported on theoretical investigations of the process, noting that the efficiency can be modeled quite well.

Walter Scandale (CERN), Cyrus Taylor (Case-Western Reserve), and Nikolai Mokhov (FNAL) closed the symposium with reviews of several broad questions. They listed some of the principal concerns of experiments: halo free beams, stable orbits, luminosity measurements accurate to 2-3%, and good collimation to reduce backgrounds. Perhaps the ultimate criterion for bragging rights in the near beam field is the distance a device is from the beam in units of beam size. A survey of accelerator practice around the world showed just how close some devices operate: crystals and wire targets are positioned at 3.5 to 9 sigma, primary collimators at 5.5 to 8 sigma, and Roman pots at 8 to 15 sigma from the beam axis.

Most of the participants felt the conference was extremely successful and led to many useful discussions between accelerator experts and experimentalists. It is clear that continued interactions will result in better understanding and better performance of accelerators and improved experimental capabilities for experiments operating near beams.

The Symposium was sponsored by Fermilab with particular support from the Beams Division and the head of the Division, David Finley. Additional help was received from KEK. The organizing committee included Dick Carrigan and Nikolai Mokhov along with Michael Albrow (FNAL), Alexey Asseev (IHEP), James Bjorken (SLAC), Klaus Ehret (DESY), Alan Hahn (Fermilab), Werner Herr (CERN), Jim Holt (FNAL), Daniel Kaplan (IIT), Peter Kasper (FNAL), Steve Peggs (BNL), Stanley Pruss (FNAL), Alberto Santoro (Lafex/Cbpf Rio), Walter Scandale (CERN), Michael Sullivan (SLAC), Ken Takayama (KEK), Cyrus Taylor (Case-Western Reserve), and Ferdinand Willeke (DESY). The conference secretaries were Marion Richardson and Cynthia Sazama. The cover was provided by Angela Gonzales. Cynthia Crego and Dmitri Mokhov helped at some stages of the proceedings preparation.

I. NEAR BEAM EXPERIMENTS

Near Beam Physics – Introductory Prospect

G. Matthiae
Università di Roma II and Sezione INFN, Roma, Italy

Abstract

The near beam experiments make use of the technique invented at the CERN ISR about 25 years ago to study elastic scattering at small angles with detectors very close to the circulating beams. The technique was further developed at the SPS collider, at HERA and at the Tevatron to study diffractive processes. Applications are foreseen at RHIC and LHC.

1 NEAR BEAM PHYSICS

I wish to start with a brief overview of some recent and typical data on near beam physics. The measurement of the total cross section σ_{tot} involves observation of elastic scattering at low momentum transfer - a typical near beam experiment. The luminosity of the hadron colliders is generally not well known and therefore σ_{tot} is obtained with the *luminosity independent method* using the following formula:

$$\sigma_{tot} = \frac{16\pi}{(1+\rho^2)} \frac{(dN_{el}/dt)_{t=0}}{N_{el} + N_{inel}}$$

where $(dN_{el}/dt)_{t=0}$ is the elastic scattering rate extrapolated to t=0 and N_{inel} is the rate of the inelastic interactions. The correction due to the parameter ρ (ratio of the real to the imaginary part of the forward amplitude) is small and sufficiently well known.

A compilation of the total cross sections for proton-proton and proton-antiproton collisions in the high-energy region is shown in Fig. 1. It is evident that σ_{tot} is rising with energy but the actual rate of increase is still a matter of debate. The solid line in Fig. 1 is the result of a dispersion relation fit [1] where the high-energy dependence of σ_{tot} was described by the term $(\log s)^\gamma$. The best fit gives $\gamma = 2.2 \pm 0.3$.

The fit reproduces well the data [2] at $\sqrt{s}$ = 546 GeV while at $\sqrt{s}$ = 1.8 TeV it predicts a value of σ_{tot} which lies between the two measurements at the Tevatron. The result of E710 [3] seems to favour a $\log s$ increase while the result of CDF [4] favours the $(\log s)^2$ dependence. Cosmic ray data have large uncertainties but are consistent with the extrapolation of ref. [1].

At the energy of the LHC, $\sqrt{s} = 14$ TeV, the fit predicts $\sigma_{tot} = 109 \pm 8$ mb while extrapolating as $\log s$, one would obtain $\sigma_{tot} \simeq 95$ mb.

The $(\log s)^2$ dependence corresponds to the maximum rate of increase with energy which is theoretically allowed by the fundamental theorems [5] on the asymptotic properties of the scattering amplitude.

Another typical near beam measurement is the observation of the interference between the strong-interaction and the Coulomb amplitude which gives information on the parameter ρ. Coulomb interference takes place at so small angles that we should consider these experiments as being "*very near*" to the beam.

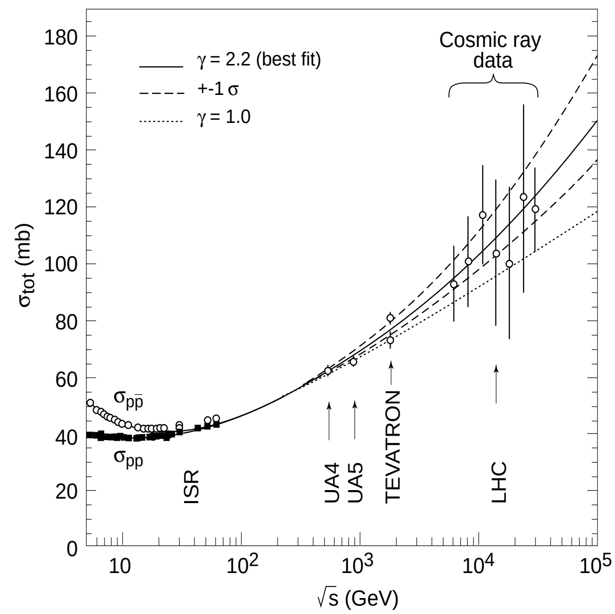

Figure 1: The total cross section for $\bar{p}p$ and pp scattering is shown together with the prediction of the dispersion relations fit of ref.[1]. The best fit (solid line) corresponds to γ =2.2. The region of uncertainty is delimited by the dashed lines. The dotted line refers to $\gamma = 1$.

A quantity useful for the understanding of the mechanism of high-energy collisions is the ratio σ_{el}/σ_{tot} which is plotted as a function of energy in Fig. 2. The Tevatron data confirm the trend already observed at the SPS collider that the ratio σ_{el}/σ_{tot} increases with energy. This observation tells us that the effective *"opacity"* of the two colliding particles increases, although slowly, with energy.

Closely related to elastic scattering is the process of single diffraction dissociation which may be regarded as a two-body reaction

$$p + p \rightarrow p + X \quad \textit{or} \quad \bar{p} + p \rightarrow \bar{p} + X$$

where one of the colliding particles is excited to a system X which then decays into stable particles.

The energy dependence of the ratio of single diffraction to the total cross section, σ_{SD}/σ_{tot}, is shown in Fig. 2 together with the ratio σ_{el}/σ_{tot}. At present energies σ_{SD} is a sizeable fraction of σ_{tot} but its relative importance is decreasing with energy.

The mass M of the diffractively produced system X may take large values in high-energy collisions. If p_0 is the beam momentum and p the momentum of the final state particle which is scattered quasi-elastically and recoils against the system X, the mass M is given by $M^2 = (1-x)\ s$ where $x = p/p_0$. High-energy data provide evidence for diffractive production up to $M^2/s \sim 0.05$. The momentum spectrum measured by CDF [6] and shown in Fig. 3

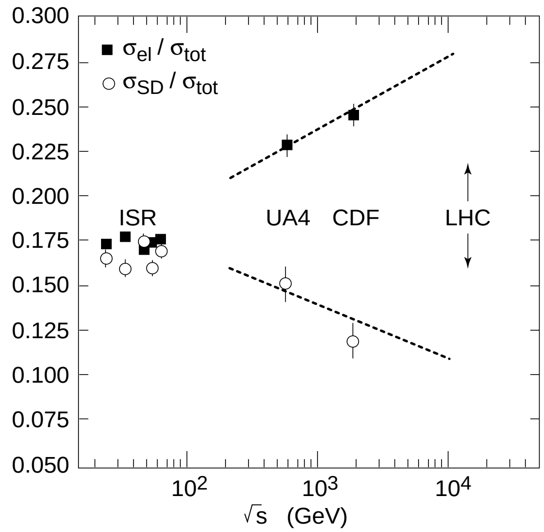

Figure 2: The ratios σ_{el}/σ_{tot} and σ_{SD}/σ_{tot} are shown as a function of energy. The ISR data on diffraction dissociation are from the CHLM collaboration [ref.7]. The lines are linear extrapolations to guide the eye.

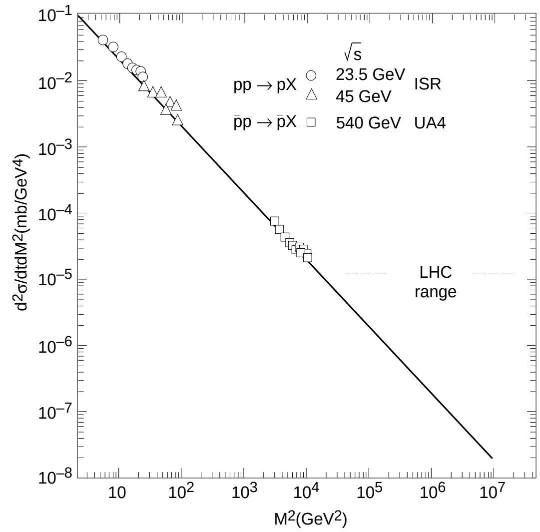

Figure 4: The mass spectrum of the diffractively produced system. The line represents the $1/M^2$ behaviour.

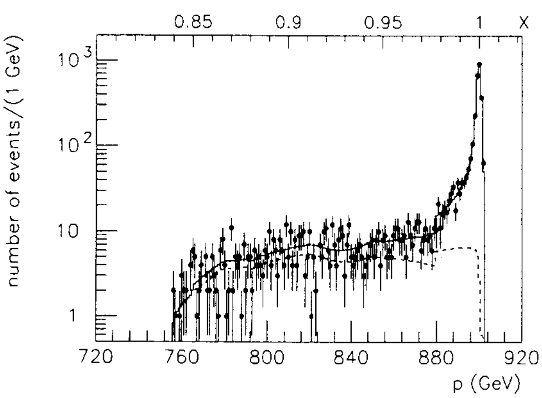

Figure 3: The momentum spectrum of the particle which is scattered quasi-elastically as observed by CDF at the Tevatron.

has a large peak at $x > 0.95$ which corresponds to diffractive production. The LHC with its very large c.m.s. energy opens new possibilities because M is as large as 3 TeV for $M^2 \sim 0.05\ s$.

The mass dependence of the production cross section was studied by several experiments. The data [7, 8] at a fixed value of the momentum transfer, $-t$ = 0.5 GeV^2, which are shown in Fig. 4, indicate that the spectrum has a $1/M^2$ behaviour as predicted by the classical theory of triple Pomeron exchange. Deviations are expected, however, in the Regge models with effective Pomeron intercept larger than one.

The region of large momentum transfer is of course of great interest both for elastic and for diffraction dissociation. At present energies the differential cross section of elastic scattering shows a diffraction-like structure which is followed by a smooth behaviour. According to a QCD model [9], at large momentum transfer the dominant mechanism is the three-gluon exchange diagram which predicts $d\sigma/dt \sim 1/t^8$. However, other models lead to different conclusions. The impact picture of ref.[10] and the Regge model of ref.[11], predict the emergence of a diffraction pattern with several dips (see Fig. 5) in contrast with the three-gluon exchange model which predicts a smooth behaviour. Measurements at the LHC will be able to clarify this issue.

Recently special attention has been devoted to the field of hard diffractive scattering which is of great interest because it reveals the Pomeron structure of the proton. The first experiment on this subject was UA8 at the SPS collider [12] which studied the production of jets in association with a diffractively scattered antiproton. Further extensive studies on this new and promising field are now being planned at the Tevatron by the CDF [13] and DØ [14] collaborations.

A more complete review of high-energy diffractive processes can be found in ref.[15].

2 NEAR BEAM TECHNIQUES

2.1 The Roman pots

The measurement of elastic scattering and diffraction dissociation at the hadron colliders requires observation of particles at very small angles (at the Tevatron typical angles are a fraction of a $mrad$). In practice this is achieved by placing the detectors into special units mounted on the vacuum chamber of the accelerator, which have become known as "Roman pots" and were first used at the CERN ISR [16].

In its retracted position the Roman pot leaves the full aperture of the vacuum chamber free for the beam, as required at the injection stage when the beam is wide. Once the final energy is reached and the circulating beams are stable, the Roman pot is moved toward the machine axis by

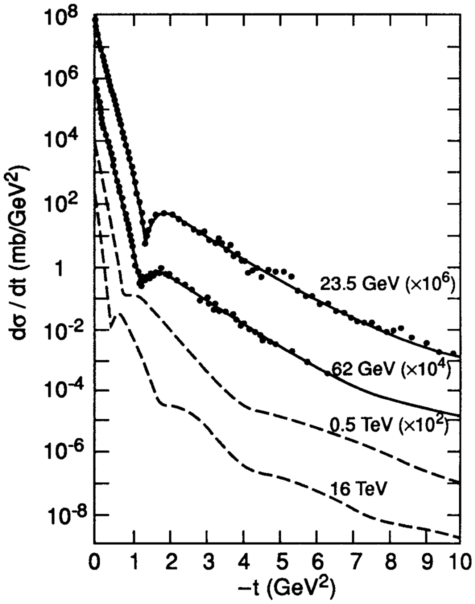

Figure 5: Proton-proton elastic scattering data are shown together with the predictions of the model of ref.[11].

Figure 6: The first Roman pot used at the ISR by the CERN-Rome collaboration. The name of the device originates from its peculiar shape. The flange which is connected to the machine vacuum chamber by a bellow is visible below the pot.

compressing the bellow, until the inner edge of the detector is at a distance of the order of one *millimeter* from the beam. There is no interference with the machine vacuum.

In Fig. 6 a picture is shown of the first Roman pot used in the small angle elastic scattering experiment of the CERN-Rome group [16] at the CERN ISR in 1970-72. The pot was about 15 cm wide. The detectors inside the Roman pots were small hodoscopes of scintillation counters.

In Fig. 7 a Roman pot designed and built at CERN but similar to those recently used in the Fermilab experiments is shown. The pot itself is about 6 cm wide with a 0.1 mm thick window which is 3 cm x 2 cm in size.

The detectors placed inside the Roman pots are so small that usually there is no problem to attain the best spatial resolution offered by available technologies.

There is, however, a specific technical problem - the need for having the detector efficient very near to the physical edge of the detector itself. In fact the detector has to be "frameless" on one side (the side which is touching the bottom window of the Roman pot, i.e. facing the beam). This is a special and really peculiar requirement of near beam experiments.

The overall mechanical structure of the Roman pot system used at the SPS collider by experiment UA4 is shown in Fig. 8 while a sketch of the detector is shown in Fig. 9. The drift chamber has a special C-shape frame with a thin window on the beam side. This allows reducing the minimum accessible scattering angle. In Fig. 9 the sense wires run horizontally and measure the vertical coordinate while a bundle of vertical scintillating fibers measure the horizontal coordinate.

In the recent experiments by the ZEUS collaboration at HERA and CDF at Fermilab, silicon detectors have been used. The detector of CDF, shown in Fig. 10, has a small drift chamber with four sense wires which induce a signal on a delay line for measuring the other coordinate. In addition there is a silicon detector with pad and strips read-out.

A new concept was recently proposed by the Fermilab collaboration E710/E811 [17]. The idea is to use a bundle of scintillating fibers oriented along the beam direction and placed inside the vacuum chamber of the machine (Fig. 11). Particles scattered at small angles travel along a fiber thus producing a large signal. The read-out is by image intensifiers.

2.2 The experimental layout

The measurement of elastic scattering is simple in principle. Both scattered particles are detected in coincidence and the elastic events are then selected by requiring collinearity. A sketch of the first elastic scattering experiment using Roman pots [16] is shown in Fig. 12. In this experiment the Roman pots (already shown in Fig. 6) were placed at about 10 m from the crossing point.

In the recent hadron colliders which have higher energy, the typical scattering angle is smaller (in fact it scales down as the inverse of the c.m.s. energy) and therefore the Roman pots have to be placed at a much larger distance from the crossing. This means that machine elements (quadrupoles and in some case also dipoles) are usually present between the crossing and the detectors.

The typical layout for elastic scattering is shown in

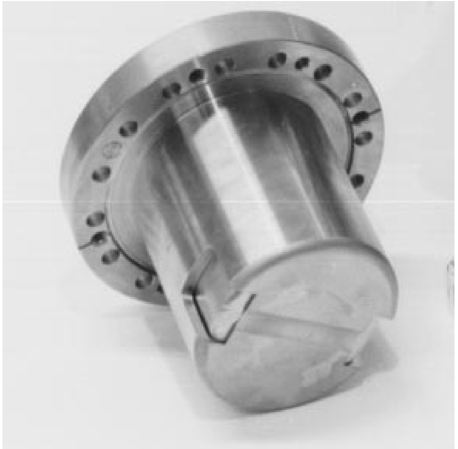

Figure 7: A modern Roman pot built at CERN. The section facing the beam is concave in shape. This allows a closer approach of the edge of the detector to the beam.

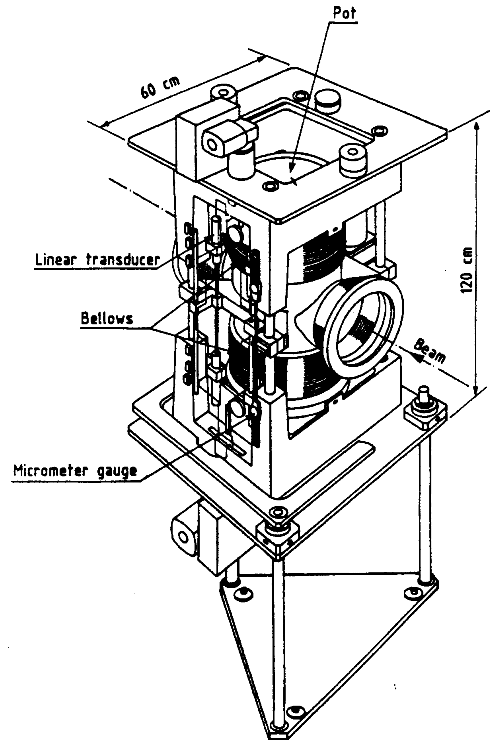

Figure 8: The Roman pot system of UA4 at the SPS collider.

Fig. 13. On each side there is a telescope of two Roman pots placed a few meters apart and therefore able to measure both the position and the direction of the scattered particles. Between the detectors and the crossing point there are magnetic elements of the machine.

The optics of the insertion is of great importance for near beam measurements. In fact hadron colliders are usually operated at high luminosity for the search of rare events. To obtain high luminosity, the transverse size of the beam at the crossing point is reduced by the focusing action of quadrupoles. As a consequence the angular divergence of the beams is correspondingly increased so that a large fraction of the particles scattered at low momentum transfer remain inside the aperture of the machine itself and are not accessible to detection.

To measure elastic scattering and diffraction dissociation at small momentum transfer, the opposite scheme is actually required. The beam size at the crossing point is made relatively large while the beam divergence becomes very small. Nearly parallel beams are normally used. This implies that the betatron function at the crossing point has to be large. The corresponding loss of luminosity is not a problem because diffractive processes have large cross sections at small momentum transfer.

The relevant parameters of the insertion are the values of the betatron function $\beta^\star$ and β_d at the crossing point and at the detector respectively. The phase advance of the betatron oscillations from the crossing to the detector is $\Delta\psi = \int ds/\beta(s)$.

The best configuration for elastic scattering [18], corresponds to the optics with *parallel-to-point* focusing from the crossing to the detectors. This is achieved when the detectors are placed at the position where the phase advance is $\Delta\psi = \pi/2$. In this case the displacement y at the detector is proportional to the scattering angle ϑ and does not depend on the actual position of the collision point :

$$y = L_{eff}\,\vartheta \quad , \quad L_{eff} = \sqrt{\beta^* \beta_d}$$

where the quantity L_{eff} represents the effective distance of the detectors from the crossing point. This arrangement has the very convenient property that measuring the particle position at the detectors allows the scattering angle to be reconstructed in a way which is unambiguous and straightforward.

The method is basically the same as the classical technique of measuring the direction of light rays by means of an optical system having a screen on the focal plane.

This scheme was used at the SPS collider [19] to measure the parameter ρ. Recently it was proposed for the proton-proton scattering experiment in preparation at RHIC [20] and by the TOTEM collaboration at LHC [18].

For the study of diffraction dissociation, one has to detect the particle which is scattered quasi-elastically and measure its momentum. One takes advantage from the fact that the sequence of magnetic elements of the machine downstream of the crossing point may actually be used as a powerful *magnetic spectrometer* to select protons (or antiprotons) with momentum close to the beam momentum.

At the SPS collider the quadrupoles located in the long straight section of the machine were used by UA4 [8] to measure the momentum of the outgoing particle with a momentum resolution of 0.6 %.

A more powerful system used by CDF [6] is shown in Fig. 14. Detectors are placed in front and behind a string of machine dipoles. The result is a very effective forward

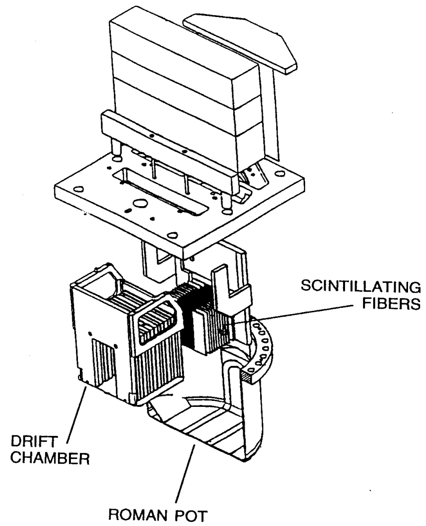

Figure 9: Exploded view of the UA4 detector with a drift chamber and scintillating fibers.

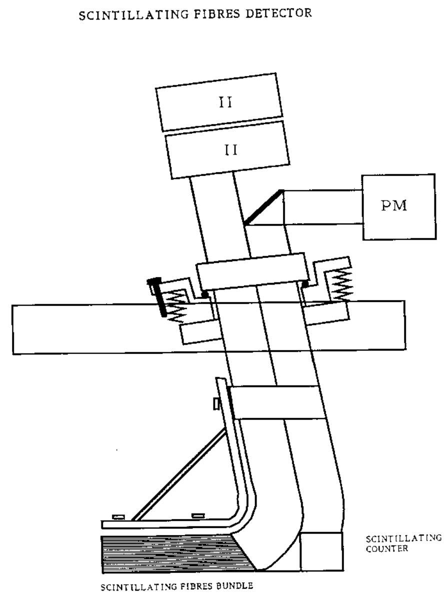

Figure 11: The new detector proposed by the E710/E811 collaboration. A bundle of scintillating fibers parallel to the beam direction is placed inside the vacuum chamber.

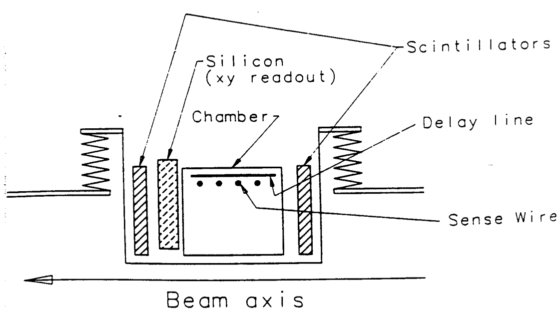

Figure 10: Sketch of the CDF detector. A small size drift chamber is used together with a silicon detector.

magnetic spectrometer with momentum resolution of about 0.1 %. A typical momentum distribution obtained with this apparatus was shown in Fig. 3.

A similar system with several Roman pot stations inserted between elements of the machine has been proposed by the FELIX collaboration [21] at LHC.

2.3 *Background and collimation*

In the near beam experiments it is generally required to move the Roman pots as close as possible to the beam. The reduction and control of the beam halo is therefore of crucial importance.

As expected, the minimum distance of approach y_{min} was found, in various experiments, to be proportional to the size of the beam at the position of the pot itself. The r.m.s. value of the beam size σ_{beam} is related to the local value of the betatron function β_d :

$$y_{min} = K\sigma_{beam} \quad , \quad \sigma_{beam} = \sqrt{\epsilon\beta_d}$$

where ϵ is the beam emittance.

The parameter K may be controlled by the system of scrapers and collimators of the machine which are adjusted to protect the detectors from being hit by the particles of the beam halo. At the SPS collider the value of K was normally found to be between 15 and 20, depending on the beam conditions. Smaller values, around 10 or 12, have been reached at the Tevatron.

At the LHC the background due to the high beam-beam interaction rate is a cause of concern for the forward detectors of large solid angle experiments but it is not relevant for the detectors inside the Roman pots because they stay far away from the crossing point where the radiation flux is not large already with low-β optics and is further reduced for medium or high-β operation.

The loss of particles around the ring may have serious consequences at the LHC because a too high radiation flux could cause quenching of the superconducting magnets of the machine. This problem has prompted a detailed study of the background which has led to the design of a sophisticated system with two-stage collimation [22, 23].

The secondary collimator will catch particles which are not removed but only scattered on the edge of the primary collimator. The primary and secondary collimators will be set at a distance from the beam axis equal to 6 σ_{beam} and 7 σ_{beam} respectively. In these conditions the maximum excursion of the halo should not exceed 10 σ_{beam} and the mechanical aperture around the LHC ring was designed accordingly.

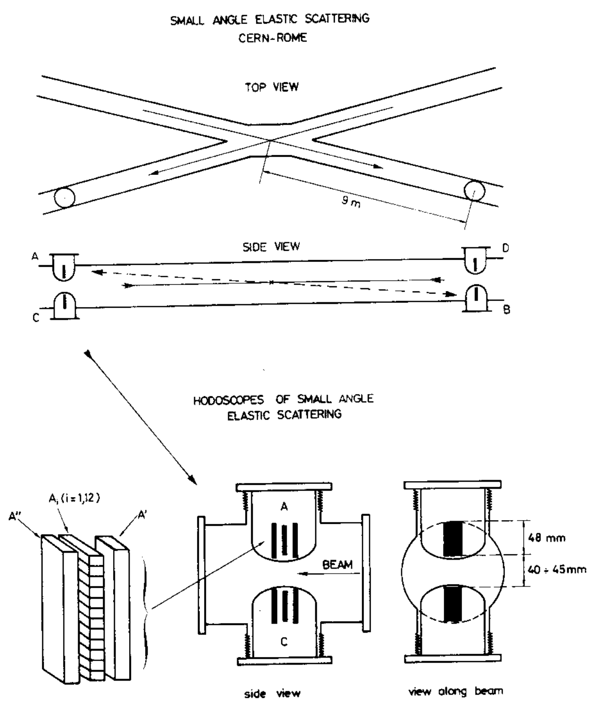

Figure 12: The first Roman pot experiment at the CERN ISR.

It is clear that near beam experiments at LHC will take advantage from the system of beam cleaning which will be implemented to prevent quenching. We may expect that Roman pots installed at the LHC could approach the beam to a distance somewhat less than 10 σ_{beam}.

3 REFERENCES

[1] C.Augier et al., Phys. Lett. B315 (1993) 503.

[2] M.Bozzo et al., Phys. Lett. 147B (1984) 392.

[3] N.A.Amos et al., Phys. Lett. 243B (1990) 158 and Phys. Rev. Lett. 68 (1992) 2433.

[4] F.Abe et al., Phys. Rev. D, 50 (1994) 5550.

[5] M.Froissart, Phys. Rev. 123 (1961) 1053 and A.Martin, Nuovo Cimento 42 (1966) 930.

[6] F.Abe et al., Phys. Rev.D50 (1994) 5535.

[7] J.C.M.Armitage et al., Nucl. Phys. B194 (1982) 365 and refs. therein.

[8] M.Bozzo et al., Phys. Lett. B136 (1984) 217.

[9] A.Donnachie and P.V.Landshoff, Z. Phys. C2 (1979) 55, and preprint DAMPT 96/66, M/C-TH 96/22.

[10] C.Bourrely, J.Soffer and T.T.Wu, Nucl. Phys. B247 (1984) 15 and Z. Phys. C37 (1988) 369.

[11] P.Desgrolard, M.Giffon and E.Predazzi, Z. Phys. C63 (1994) 241.

[12] A.Brandt et al., Phys. Lett. B297 (1992) 417.

[13] M.Albrow, Proceedings of this Conference.

[14] A.Brandt, Proceedings of this Conference.

[15] G.Matthiae, Rep. Prog. Phys. 57 (1994) 743.

[16] U.Amaldi et al., Phys. Lett. 43B (1973) 231.

[17] C. Da Via et al., Nucl. Instr. and Methods, A323 (1992) 419.

[18] The TOTEM Letter of Intent, CERN/LHCC 97-49, LHCC/I11, 1997.

[19] C.Augier et al., Phys. Lett. B316 (1993) 448.

[20] W.Guryn, Proc. of the VII Rencontres de Blois, Blois 1995, pag.419.

[21] The FELIX Letter of Intent, CERN/LHCC 97-45, LHCC/I10, 1997.

[22] *The Large Hadron Collider* - Conceptual Design CERN/AC/95-05.

[23] B.Jeanneret, Proceedings of this Conference.

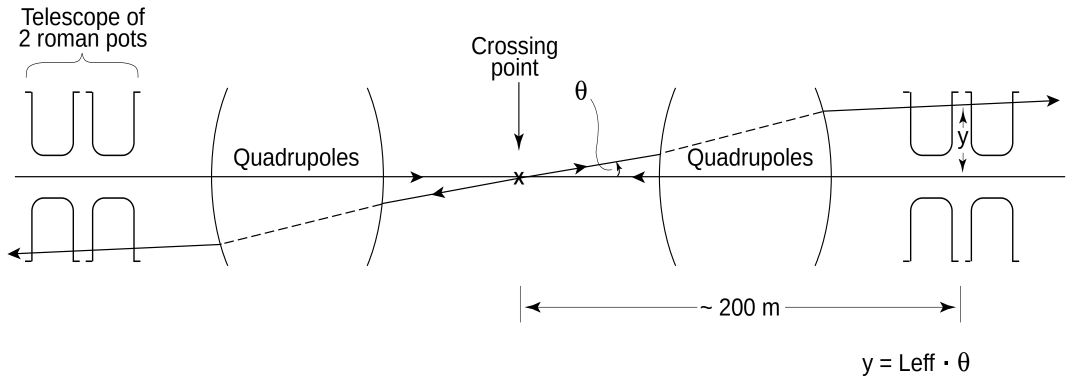

Figure 13: Typical layout for measuring elastic scattering at high-energy hadron colliders. The effective distance L_{eff} is determined by the optics of the insertion.

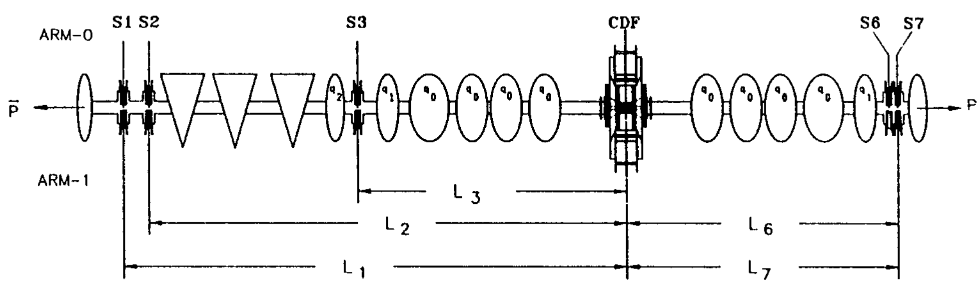

Figure 14: The forward spectrometer of the CDF experiment. Prisms and lenses represent dipoles and quadrupoles respectively. The three Roman pot stations S1, S2 and S3 located on the outgoing $\bar{p}$ arm are used for accurate measurement of the $\bar{p}$ momentum.

Hard Diffraction and Central Diffraction in Hadron–Hadron and Photon–Hadron Collisions

R. Engel[1]
University of Delaware, Bartol Research Institute, Newark, DE 19716 USA
J. Ranft[2]
FIGS and Physics Dept. Universität Siegen, D–57068 Siegen, Germany
Presented by J. Ranft

Abstract

Hadron production in single and central diffraction dissociation is studied in a model which includes soft hadron interaction as controlled by a supercritical pomeron parametrization and hard diffraction. Hard diffraction is described using leading-order QCD matrix elements together with the parton distributions for the proton, the less well known photon parton densities and a conjectured parton distribution function for the pomeron. Within this model, particle production in collisions with pomerons exhibit properties like multiple soft interactions and multiple minijets, quite similar to hadron production in non-diffractive hadronic collisions at high energies. However, important differences occur in transverse momentum jet and hadron distributions. It is shown that the model is able to describe data on single diffractive hadron production from the CERN-SPS collider and from the HERA lepton-proton collider as well as first data on central diffraction dissociation. We present also model predictions for single and central diffraction at TEVATRON.

1 INTRODUCTION

High-energy hadron production in hadron–hadron collisions and in hadronic interactions of photons is characterized by two mechanisms: (i) minijet production and (ii) soft hadronic interactions. Whereas the minijet cross section can be estimated applying the QCD-improved parton model, soft hadron production cannot be computed directly from perturbative QCD. Most models for multiparticle production being constructed in form of Monte Carlo event generators use soft and hard mechanisms. Such models are usually called minijet models if they use minijets and a simple model for the soft component of the interaction. They are called two component Dual Parton models (DPM's) if they use minijets and incorporate a evolved soft component which is derived from Regge theory, Gribov's reggeon calculus [1, 2] and Abramowski-Gribov-Kancheli (AGK) cutting rules [3] (a review is given in Ref.[4]).

Models inspired by Regge theory or the DPM describe high-mass diffractive hadron production in terms of the so-called triple-pomeron graph. According to this diffractive processes can be considered as collisions of a color neutral object, the pomeron, with hadrons, photons or other pomerons. Experimental data on diffraction support this idea showing that diffraction dissociation exhibits similar features as non-diffractive hadron production whereas the mass of the diffractively produced system corresponds to the collision energy in non-diffractive interactions [5, 6]. Clearly, the pomeron cannot be considered as an ordinary hadron. It is important to keep in mind that the pomeron is only a theoretical object providing an effective description of the important degrees of freedom of a certain sum of Feynman diagrams. Pomeron-hadron or pomeron-pomeron interactions can only be discussed in the framework of collisions of other particles like hadrons or photons. On the other hand, the striking similarities between diffractive and non-diffractive multiparticle production suggest that multiple soft and hard interactions may also play an important role in high-mass diffraction dissociation.

The DPM was already successfully applied to diffractive hadron production reactions [7, 8, 9] and even hard diffractive processes [10]. In [11] cross sections on single and central diffraction were calculated. Up to now, the minijet component in diffractive processes within the two-component DPM was obtained using a parton distribution function (PDF) for the pomeron and flux factorization. The soft component of diffractive interactions was described by two hadronic chains (cutting the triple-pomeron graph). Here we will argue, that for the description of diffraction dissociation producing hadronic systems with very large masses, such models are not enough. Also for high-mass diffractive hadron production we need multiple soft and multiple hard interactions.

2 THE MODEL

2.1 *The event generator* PHOJET

In the PHOJET model[12, 13], interactions of hadrons are described within the DPM in terms of reggeon ($\mathbb{R}$) and pomeron ($\mathbb{P}$) exchanges. The realization of the DPM with a hard and a soft component is similar to the event generator DTUJET [14, 15] for p–p and $\bar{p}$–p collisions. In the following we briefly describe the treatment of the pomeron exchange in non-diffractive interactions since the same framework is also used for the description of particle production in diffraction dissociation.

The pomeron exchange is artificially subdivided into *soft* processes and processes with at least one large momentum transfer (*hard* processes). This allows us to use the predictive power of the QCD-improved Parton Model with lowest-order QCD matrix elements [16, 17] and parton density functions. Practically, soft and hard processes are distinguished by applying a transverse momentum cutoff $p_\perp^{\rm cutoff}$ to the partons. Consequently, the pomeron is considered as a two-component object with the Born graph cross section for pomeron exchange given by the sum of hard and soft cross sections.

[1] e–mail: eng@lepton.bartol.udel.edu
[2] e–mail: Johannes.Ranft@cern.ch

2.2 *Diffractive cross section calculation*

Concerning diffraction dissociation, our approach is the following.

In order to get an effective parametrization of Born graphs describing diffraction within Gribov's reggeon calculus, we calculate the triple-, loop- and double-pomeron graphs using a renormalized pomeron intercept $\alpha_{\tilde{I\!P}} = 1 + \Delta_{\tilde{I\!P}} = 1.08$. For example, let's consider the the Born graph cross sections for high-mass diffraction dissociation in A–B scattering (for simplicity, we omit in the following expressions the pomeron signature factors; for a discussion of the couplings etc. see [11]).

High-mass single diffraction dissociation of particle A is calculated using the triple-pomeron approximation

$$\begin{aligned}\frac{d^2\sigma_{AB}^{\mathrm{TP,A}}}{dt\,dM_{\mathrm{D}}^2} &= \frac{1}{16\pi}\left(g_{BI\!P}^0\right)^2 g_{3I\!P}^0\, g_{AI\!P}^0\left(\frac{s}{s_0}\right)^{2\Delta_{\tilde{I\!P}}} \\ &\times\left(\frac{s_0}{M_{\mathrm{D}}^2}\right)^{\alpha_{\tilde{I\!P}}(0)}\exp\left\{b_{AB}^{\mathrm{SD}}\,t\right\}. \qquad (1)\end{aligned}$$

The differential cross sections for the high-mass double diffraction dissociation reads

$$\begin{aligned}\frac{d^3\sigma_{\mathrm{LP}}}{dt\,dM_{D_1}^2\,dM_{D_2}^2} &= \frac{1}{16\pi}g_{AI\!P}^0\ \left(g_{3I\!P}^0\right)^2\ g_{BI\!P}^0 \\ &\times\ \left(\frac{s}{s_0}\right)^{2\Delta_{\tilde{I\!P}}}\left(\frac{s_0}{M_{D_1}^2}\right)^{\alpha_{\tilde{I\!P}}(0)} \\ &\times\ \left(\frac{s_0}{M_{D_2}^2}\right)^{\alpha_{\tilde{I\!P}}(0)}\exp\left\{b_{AB}^{\mathrm{DD}}\,t\right\}. \qquad (2)\end{aligned}$$

Finally, we give the expression for central diffraction dissociation

$$\begin{aligned}\frac{d\sigma_{\mathrm{DP}}}{dt_1ds_1dt_2ds_2} &= \frac{1}{256\pi^2}\frac{1}{s_0}\left(g_{AI\!P}^0 g_{BI\!P}^0 g_{3I\!P}^0\right)^2 \\ &\times\ \left(\frac{s}{s_0}\right)^{\Delta_{\tilde{I\!P}}}\left(\frac{s}{s_1}\right)^{\Delta_{\tilde{I\!P}}}\left(\frac{s}{s_2}\right)^{\Delta_{\tilde{I\!P}}} \\ &\times\ \frac{1}{s_1s_2}\exp\left\{b_{\mathrm{A}}^{\mathrm{CD}}\,t_1 + b_{\mathrm{B}}^{\mathrm{CD}}\,t_2\right\}. \qquad (3)\end{aligned}$$

The experimentally observable diffractive cross sections (i.e. cross sections of rapidity gap events) are considerably smaller than the Born graph cross section given in (1), (2) and (3). The reason for this are significant shadowing contributions which are estimated by a two-channel eikonal model [14, 13].

2.3 *Particle production in diffraction dissociation*

However, not only for cross section calculations, but also for the description of particle production, shadowing effects are important. Unitarity and AGK cutting rules predict that shadowing effects are directly connected with so-called multiple interaction contributions. In the case of diffractive multiparticle production we have to consider rescattering effects in pomeron-hadron and pomeron-pomeron interactions of enhanced graphs. Whereas it was sufficient to introduce a renormalized pomeron trajectory to calculate cross sections, one needs for the calculation of particle production a model for the physical final states which correspond to the unitarity cut of such a renormalized pomeron propagator. Following Refs. [18, 19] we assume that the pomeron-pomeron coupling can be described by the formation of an intermediate hadronic system $h^\star$ where the pomerons couple to. Assuming that this intermediate hadronic system has properties similar to a pion, the n-m pomeron coupling reads [19]

$$g_{n-m} = G\prod_{i=1}^{n+m-2} g_{h^\star I\!P} \qquad (4)$$

with $g_{h^\star I\!P} = g_{\pi I\!P}$ being the pomeron-pion coupling. G is a scheme-dependent constant. Hence, pomeron-hadron and pomeron-pomeron scattering should exhibit features similar to pion-hadron and pion-pion scattering.

To introduce hard interactions in diffraction dissociation, the exchanged (renormalized) pomerons in pomeron–hadron and pomeron–pomeron scattering are again treated as two-component objects

$$a_{AI\!P}(s,\vec{B}) \approx \frac{i}{2}\,G\,\left\{1-\exp\left[-\chi_{\mathrm{S}}^{\mathrm{diff}} - \chi_{\mathrm{H}}^{\mathrm{diff}}\right]\right\} \qquad (5)$$

with the diffractive eikonal functions

$$\begin{aligned}\chi_{\mathrm{S}}^{\mathrm{diff}} &= \frac{g_{AI\!P}^0 g_{h^\star I\!P}^0 (M_D^2/s_0)^{\Delta_{I\!P}}}{8\pi b_{I\!P}(M_D^2)} \\ &\times\ \exp\left(-\frac{\vec{B}^2}{4b_{I\!P}(M_D^2)}\right) \qquad (6)\\ \chi_{\mathrm{H}}^{\mathrm{diff}} &= \frac{\sigma_{\mathrm{hard}}^{AI\!P}(M_D^2)}{8\pi b_{\mathrm{h,diff}}}\exp\left(-\frac{\vec{B}^2}{4b_{\mathrm{h,diff}}}\right). \qquad (7)\end{aligned}$$

In all calculations the pomeron PDFs proposed by Capella, Kaidalov, Merino, and Tran (CKMT) [20, 21] with a hard gluon component are used.

2.4 *Toy model with direct pomeron coupling*

To estimate the sensibility of the model results to non-factorizing coherent pomeron contributions as proposed in [32, 33], we use optionally also a toy model with a direct pomeron-quark coupling [34]. In this case, the pomeron is treated similar to a photon having a flavor independent quark coupling λ. For definiteness, the corresponding matrix elements are given

$$\begin{aligned}\left|M_{I\!Pq\to\,qg}\right|^2 &= \lambda\alpha_s\left[-\frac{8}{3}\frac{\hat{u}^2+\hat{s}^2}{\hat{s}\hat{u}}\right] \qquad (8)\\ \left|M_{I\!Pg\to\,q\bar{q}}\right|^2 &= \lambda\alpha_s\left[\frac{\hat{u}^2+\hat{t}^2}{\hat{t}\hat{u}}\right] \qquad (9)\\ \left|M_{I\!P\gamma\to\,q\bar{q}}^2\right|^2 &= \lambda\alpha_{\mathrm{em}}e_q^2\left[6\frac{\hat{u}^2+\hat{t}^2}{\hat{u}\hat{t}}\right] \qquad (10)\\ \left|M_{I\!PI\!P\to\,q\bar{q}}\right|^2 &= \lambda^2\left[6\frac{\hat{u}^2+\hat{t}^2}{\hat{u}\hat{t}}\right] \qquad (11)\end{aligned}$$

Here, α_s (α_{em}) denotes the strong (electromagnetic) coupling and $\hat{s}$, $\hat{t}$ and $\hat{u}$ are the Mandelstam variables of the partonic scattering process.

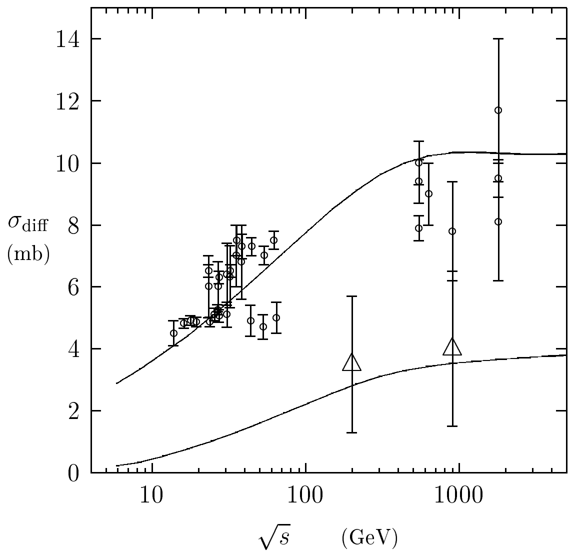

Figure 1: Single and double diffractive $p\bar{p}$ cross sections as a function of the center of mass energy $\sqrt{s}$ calculated with the model. We compare to data on single diffractive cross sections [22, 23, 24, 25, 26, 27, 28, 29, 30]. In addition, some experimental estimates for the cross section on double diffraction dissociation [26, 27] are shown.

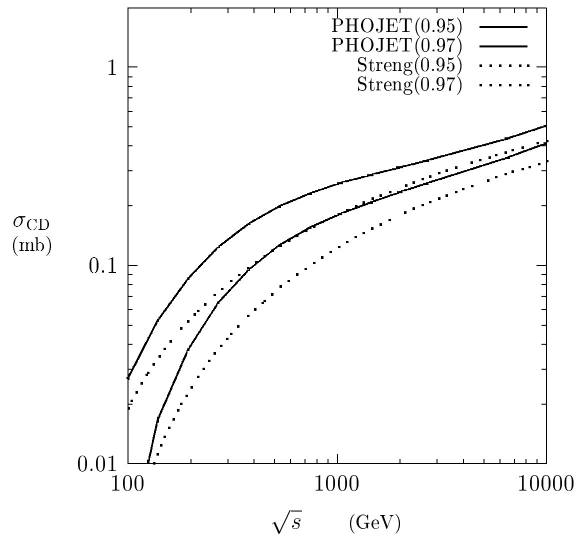

Figure 2: The energy dependence of the central diffraction cross section. We compare the cross section as obtained from PHOJET with unitarization using a supercritical pomeron with the cross section obtained by Streng [31] without unitarization and with a critical pomeron. Both cross sections are for the same two kinematic cuts: $M_{\mathrm{CD}} >$2GeV/c^2 and c = 0.95 and 0.97. The cross sections decrease with rising c.

3 COMPARISON WITH DATA

3.1 Diffractive cross sections

First we compare single diffractive cross sections according to our model in p–$\bar{p}$ collisions to data and we present the results of the model for single and double diffractive cross sections in γ–p collisions and for central diffraction cross sections in p–p collisions. Studying diffractive cross sections is not the primary concern of this paper. Results on diffractive cross sections were already presented using the DTUJET model in Refs. [14, 15] and using the present PHOJET model in Refs. [12, 11], we include updated results for these cross sections here to make the present paper self-contained.

In Fig. 1 data on single diffractive cross sections [22, 23, 24, 25, 26, 27, 28, 29, 30] are compared with our model results. It is to be noted that the data on single diffractive cross sections at collider energies are subject to large uncertainties. Nevertheless the rise of the cross section from ISR energies to the energies of the CERN and FERMILAB colliders is less steep than expected from the Born level expression from the triple pomeron formula (1). It is the eikonal unitarization procedure in the model, which suppresses the strong rise of the triple pomeron cross section in the full model. The same effect was also found by Capella et al. [35] and Gotsman et al. [36].

In Fig. 2 we compare as function of the energy the central diffraction cross sections in proton-proton collisions, which we obtain from PHOJET with the cross section obtained by Streng [31]. In PHOJET we use a supercritical pomeron with $\Delta_{\tilde{I\!P}}$ = 0.08 whereas Streng [31] uses a critical Pomeron with $\Delta_{I\!P}$ = 0. Note that also the double-pomeron cross section grows in Born approximation with s like $\sim s^{2\Delta_{I\!P}}$. This rapid increase is damped in PHOJET by the unitarization procedure. At high energies, contributions from multiple interactions become important. The rapidity gaps are filled with hadrons due to inelastic rescattering and the cross section for central diffraction gets strongly reduced. In contrast, Streng calculates only the Born term cross section. Figure 2 illustrates the differences obtained using different theoretical methods. We stress, both methods use the measured single diffractive cross sections to extract the triple-pomeron coupling.

3.2 Single diffraction in hadron-hadron collisions at collider energies

There are the following experiments which have studied hadron production in single diffraction in $p\bar{p}$ collisions at the CERN–SPS–Collider:

1. The UA–4 Collaboration [39, 6, 40] measured pseudorapidity distributions of charged hadron production for different masses of the diffractive system. We have already twice compared earlier versions of the Dual Parton Model[8, 9] to this data. New in the present model is hard diffraction and multiple chains in the diffractive hadron production, therefore we have again compared to this data and we find a very good agreement. It is evident from the data as well as from the model that multiple interactions and minijets lead to a rising rapidity plateau in pomeron–proton collisions in a simi-

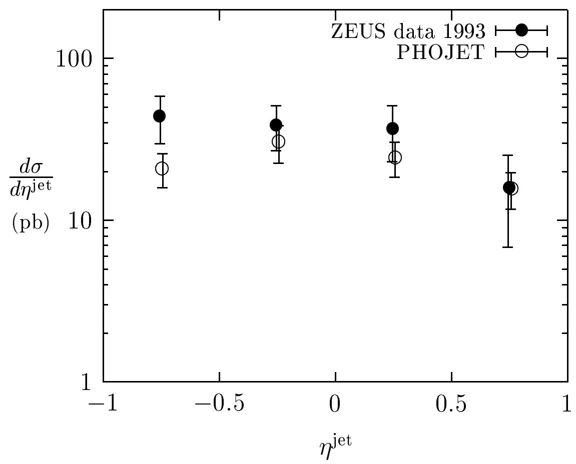

Figure 3: Differential $e-p$ cross section $d\sigma/d\eta_{\rm jet}(\eta_{max}^{had} < 1.8)$ for inclusive jet production with $E_T^{\rm jet} > 8$ GeV in the kinematic region $Q^2 \leq 4$ GeV^2 and $0.2 < y < 0.85$. We compare data from the ZEUS Collaboration [37] with PHOJET results using the same trigger as used for the ZEUS data.

lar way as observed in hadron–hadron collisions. (Unfortunately, there is not enough space here to show the Figs. of this comparison.)

2. Hard diffractive proton–antiproton interactions were investigated by the UA–8 Collaboration [41]. In this experiment the existence of a hard component of diffraction was demonstrated for the first time. Because of the importance of these findings, we compared them already in a recent paper [10] to our model and found the model to be consistent with this experiment. Therefore we will not repeat this comparison here.

3.3 Single diffraction in photoproduction

Results on single photon diffraction dissociation and in particular hard single diffraction were presented by both experiments at the HERA electron–proton collider [42, 43, 44, 37, 45, 46].

The ZEUS Collaboration[37] has presented differential and integrated jet pseudorapidity cross sections for jets with $E_T^{\rm jet} > 8$ GeV. The absolute normalization of these data is given. This allows one a more severe check of the model. In Figs. 3 we compare the differential jet pseudorapidity cross sections from ZEUS [37] to the model. The Monte Carlo events from PHOJET have been treated with the same cuts and trigger as used for the data. We find a reasonable agreement. We should, however, point out that the data include contributions from non-diffractive processes while the results from the model concern only diffractive events.

3.4 Central diffraction dissociation

Data on hard central diffraction in proton–antiproton collisions at 0.63 TeV have been published by Joyce et al. [38]. These data were obtained with the UA–1 detector at the

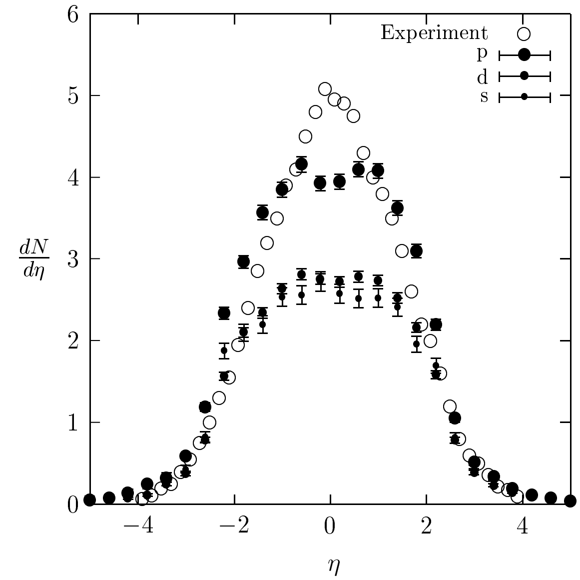

Figure 4: The pseudorapidity distribution in central diffraction as observed by the UA–1 Collaboration [38] compared with the corresponding distribution in PHOJET without direct pomeron coupling with the UA–1 trigger applied to the Monte Carlo events (p), with a direct pomeron coupling (d) and without multiple interactions (s).

CERN–SPS collider. The data are not easy to understand since they have been obtained with triggers demanding a pair of jets with $E_t > 3$ GeV or localized electromagnetic energy depositions larger than 1.2 GeV. This trigger accepts a cross section of 0.3 μb while we find in our model at this energy a total central diffraction cross section of approximately 0.3 mb (see Fig. 2). Thus the trigger of Joyce et al.[38] accepts only a tiny fraction of all central diffraction events. The most remarkable features of the data are the following:

The pseudorapidity distribution of the events accepted by the trigger reaches a maximum central plateau of around 5 per pseudorapidity unit, 30 percent higher than the non-diffractive minimum bias events at the full p–$\bar{p}$ collision energy.

We try to understand these data [38] in three versions of the model. (i) The full model without a direct pomeron coupling, (ii) the full model with a direct pomeron quark coupling, (iii) the model without multiple interactions and without a direct pomeron coupling. We use for the Monte Carlo events the same trigger requirements as described in [38].

In Fig. 4 the charged particle η distribution of the three versions of the model are compared to the data. Only the full model gives a pseudorapidity maximum comparable to the data. This is easy to understand, only in the full model we have enough multiple soft chains and multiple minijets to obtain such a large particle density. In the model with direct coupling we trigger to events with one pair of direct jets, this does not give enough particle density. Similarly in the model without multiple interactions we just get one pair of soft chains together with a minijet, also in this configuration the particle density is lower than in the full model.

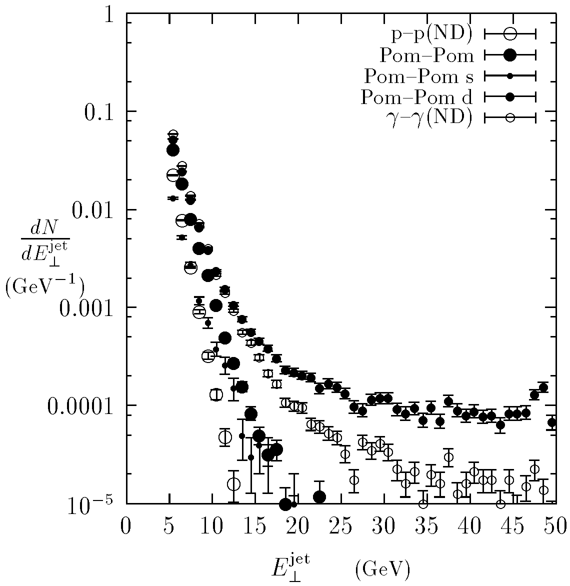

Figure 5: Jet transverse energy distributions in non-diffractive p–p and γ–γ collisions compared with the jet transverse energy distribution in central diffraction (pomeron–pomeron collisions). For the latter channel we give the distributions separately for the full model, the model without multiple interactions (s) and the model with a direct pomeron coupling (d). The distributions were generated with PHOJET, the c.m. energy / diffractive mass is 100 GeV in all cases.

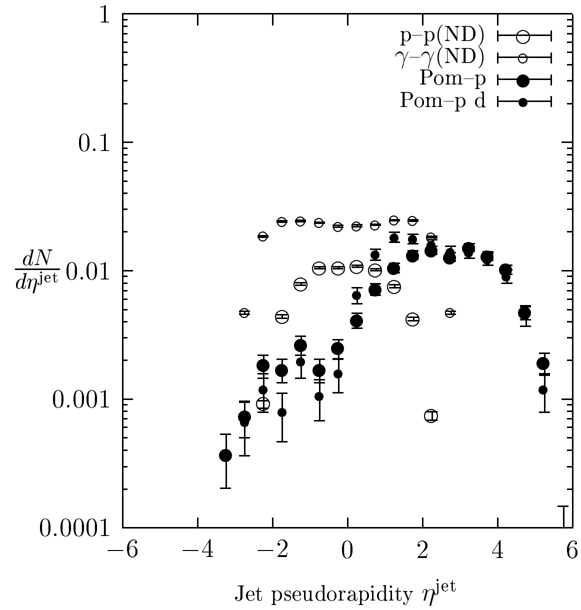

Figure 6: Jet pseudorapidity distributions in non-diffractive p–p and γ–γ collisions compared with the jet pseudorapidity distribution in single diffraction (pomeron–p scattering). The distributions were generated with PHOJET , the c.m. energy is 100 GeV in all cases, but the pseudorapidities in the collisions with pomerons given refer to the $\sqrt{s}$ = 2 TeV p–p collisions used to generate the diffractive events.

4 COMPARING HADRON PRODUCTION IN DIFFRACTIVE PROCESSES TO NON-DIFFRACTIVE PARTICLE PRODUCTION IN P–P AND γ–γ REACTIONS

In Sections II we have already pointed out, that our model for particle production in pomeron–hadron/photon collisions and pomeron–pomeron collisions has the same structure characterized by multiple soft collisions and multiple minijets like models for hadron production in hadron–hadron collisions. Therefore, again we expect the main differences in comparison to other channels in the hard component due to the differences between the pomeron and hadron structure functions and due to the existence or nonexistence of a direct pomeron–quark coupling. We will use in all comparisons here three models for $I\!P$–p, $I\!P$–γ and $I\!P$–$I\!P$ collisions:

(i) our model with multiple soft and hard collisions,

(ii) in order to see the influence of the multiple soft and hard collisions a model with only one soft or hard collision allowed and

(iii) the full model (i) assuming in addition the existence of a direct pomeron–quark coupling according to the toy–model . We present this despite the fact that we did not find in the presently existing data any feature which could only be described with such a coupling.

The differences in the parton structure functions of protons, photons and pomerons lead to quite different energy dependences of the hard cross sections. In all processes where pomerons are involved, single diffraction and central diffraction, hard processes become important already at lower energies. For pomeron–pomeron scattering at low energy the hard cross section is about a factor 100 bigger than in p–$\bar{p}$ collisions. At high energies the opposite happens, the hard cross sections in all processes where pomerons are involved rise less steep with the energy than in pure hadronic or photonic processes. The reason for this is the different low-x behavior of the parametrization of the structure functions used. However, nothing is known at present from experiment about the low-x behavior of the pomeron structure function.

In Fig. 5 we compare jet transverse energy distributions in p–p and γ–γ collisions with the ones in $I\!P$–$I\!P$ collisions. In the channels with pomerons we present again the distributions according to our full model, according to the model without multiple interactions and the model with a direct pomeron–quark coupling. In all non-diffractive collisions we have $\sqrt{s}$ = 100 GeV and the diffractive events are generated in $\sqrt{s}$ = 2 TeV collisions with $M_D = 100$ GeV. The differences in the jet transverse energy distributions between the channels are as to be expected more important than in the hadron $p_\perp$ distributions. We observe an im-

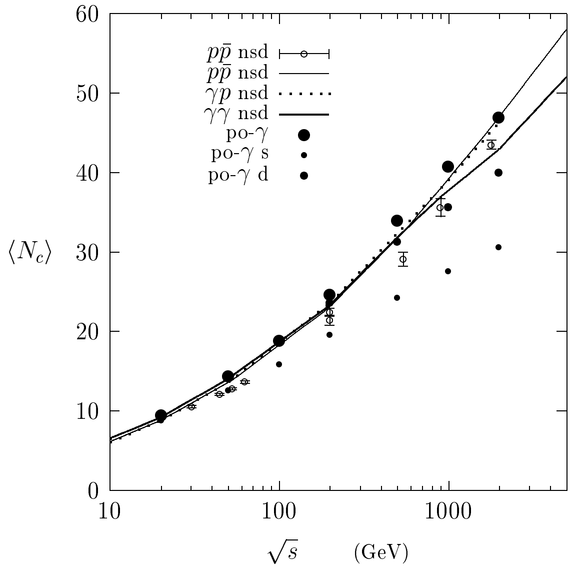

Figure 7: Average charged multiplicity as function of the c.m. energy in single diffractive collisions (pomeron–γ collisions) according to PHOJET (points) is compared to the average charged multiplicities in non single diffractive $p\bar{p}$, γp and $\gamma\gamma$ collisions, also according to PHOJET (lines) and experimental data in $p\bar{p}$ collisions.

portant reduction in the jet distributions in the model without multiple interactions. The effect of the direct pomeron coupling is as dramatic as the effect due to the direct photon coupling. The $E_\perp$ distributions in the $I\!P$–γ and $I\!P$–$I\!P$ channels extend up to the kinematic boundary. In the latter two cases as in the case of γ–γ collisions the entries at large $E_\perp$ come only from direct processes.

In Fig. 6 we compare jet pseudorapidity distributions in p–p, γ–γ and $I\!P$–p, again, all collisions at $\sqrt{s}$ = 100 GeV with the diffractive events generated in $\sqrt{s}$ = 2 TeV collisions. For the jets we observe substantial differences in the shape of the pseudorapidity distributions.

In Figs. 7 we compare the average charged multiplicity in non-diffractive $\bar{p}$–p, γ–γ and γ–p collisions according to the model as function of $\sqrt{s}$ with the charged multiplicity in the pomeron–γ diffractive channel as function of the invariant mass of the diffractive system. In the same plots we compare also to data in the case of $\bar{p}$–p collisions. We find at collision energies below say 500 GeV only small differences between the channels. However, at energies above 1 TeV the model with only one pomeron exchange (one-pomeron cut) in diffraction dissociation (labeled with s) predicts a smaller average multiplicity than observed in hadron-hadron or photon-hadron scattering.

5 SINGLE DIFFRACTION AND CENTRAL DIFFRACTION AT TEVATRON

In Figs. 8 to 15 we present some cross sections calculated using PHOJET at TEVATRON energy. The distributions are mass distributions in single and central diffraction Fig. 8, jet pseudorapidity distributions in single and central diffraction as well as in non-diffractive p–p collisions (ND) using $E_\perp$ thresholds of 5 and 15 GeV Fig.9 to 11, Jet $E_\perp$ distributions Fig.12 to 14 and the charged multiplicity as function of the diffractive mass Fig.15. In some of the distributions we give besides the full PHOJET model also the plots for a model with a small direct pomeron coupling and for a model with only single soft or hard chains pairs.

Results on diffractive jet production from the two TEVATRON Collaborations are discussed in [47, 48, 49, 50, 51], one of the results obtained by the D0 Collaboration is the ratio of double–pomeron exchange (DPE) (in the present paper we use the term *central diffraction* (CD) instead of DPE) to non–diffractive (ND) dijet events:

$$\left(\frac{\sigma(DPE)}{\sigma(ND)}\right)_{E_\perp^{\rm jet}>15GeV} \approx 10^{-6} \qquad (12)$$

PHOJET gives the following cross sections:
Non-diffractive (ND):$\sigma(ND) =$ 45.2 mb,
Single diffractive (SD):$\sigma(SD) =$ 11.2 mb,
Central diffraction (CD): $\sigma(CD) =$ 0.64 mb.

From these cross sections together with Figs. 9 to 14 we get for this and similar ratios always for $E_\perp$ larger than 15 GeV:
(CD)/(ND)$\approx 2 \times 10^{-6}$,
(SD)/(ND)$\approx 4 \times 10^{-3}$,
(CD)/(SD)$\approx 0.5 \times 10^{-3}$.

Despite the fact that no experimental acceptance has been considered for these PHOJET results it is interesting to find the (CD)/(ND) ratio so close to the D0 value given above.

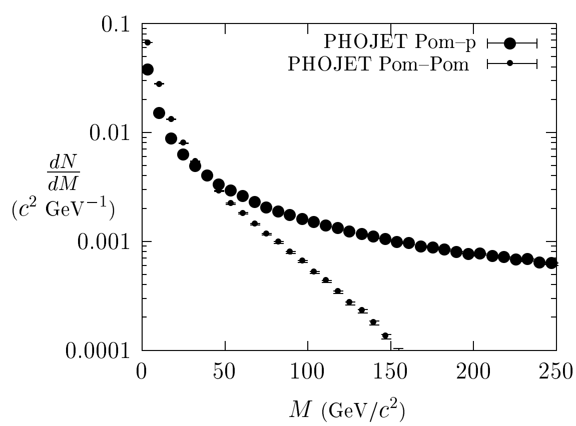

Figure 8: Distribution of the diffractive mass in single diffraction (Pomeron–proton) and central diffraction (Pomeron–Pomeron) at TEVATRON with $\sqrt{s} = 1.8$ TeV.

6 CONCLUSIONS AND SUMMARY

Multiple soft and multiple hard interactions (minijets) which we have also introduced in diffractive hadron production lead to a rise of the rapidity plateau, which agrees in

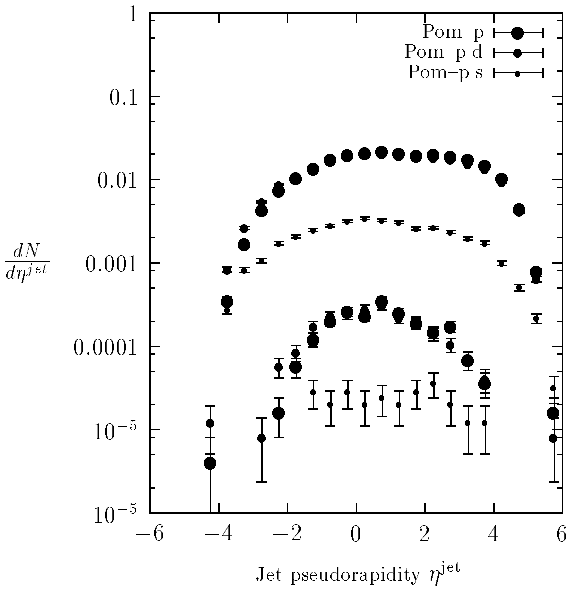

Figure 9: Pseudorapidity distribution of jets with $E_\perp$ larger than 5 GeV and 15 GeV in (one side) single diffraction (Pom–p) at TEVATRON. The upper curves with the same plotting symbol are generally for $E_\perp$ = 5 GeV, the lower curves are for $E_\perp$ = 15 GeV. We plot also the distributions (d) using a small direct Pomeron coupling ($\lambda = 0.05$) and (s) in a model where only single soft or hard chains are permitted.

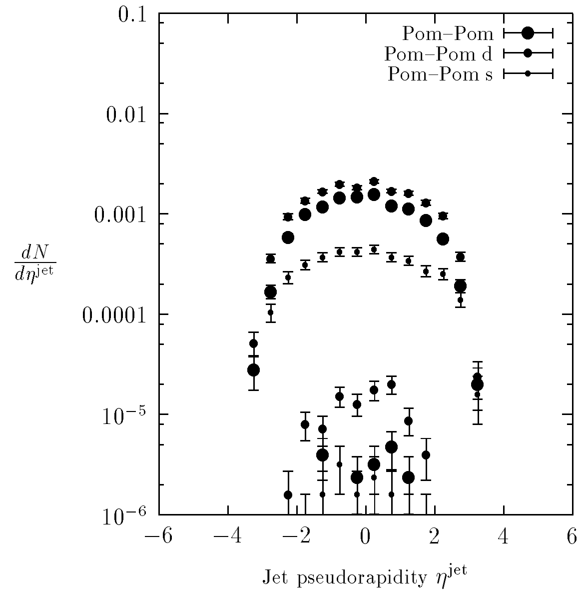

Figure 10: Pseudorapidity distribution of jets with $E_\perp$ larger than 5 GeV and 15 GeV in central diffraction (Pom–Pom) at TEVATRON. The upper curves with the same plotting symbol are for $E_\perp$ = 5 GeV, the lower curves are for $E_\perp$ = 15 GeV. We plot also the distributions (d) using a small direct Pomeron coupling ($\lambda = 0.05$) and (s) in a model where only single soft or hard chains are generated.

hadron-hadron and photon-hadron collisions very well with the rise of the plateau observed experimentally.

Minimum bias hadron production in hadron-hadron, and photon-photon collisions as well as in pomeron–hadron, pomeron–photon and pomeron–pomeron collisions of the same c.m. energy is remarkably similar. To see this, one has to restrict the comparison to inelastic events and to exclude also the diffractively produced vector mesons in reactions involving photons. The only striking differences appear in the transverse momentum distribution or distributions where the transverse momentum behavior is essential. This difference can be understood to be due to the direct photon interaction contribution and due to the photon and pomeron structure functions being considerably harder than hadronic structure functions.

Finally we would like to emphasize that measurements at TEVATRON on CD and SD would allow one to study many of the open questions: Is it possible at all to describe diffraction and hard diffraction using the triple pomeron graph? Can QCD factorization be applied to the description of hard diffraction? Does a direct pomeron–quark coupling exist? Do we have multiple soft and hard chains in diffractive particle production?

Acknowledgments
The authors are grateful to F.W. Bopp and S. Roesler for many discussions. One author (R.E.) thanks T.K. Gaisser for helpful comments and remarks. The work of R.E. is supported in part by the U.S. Department of Energy under Grant DE-FG02-91ER40626.

7 REFERENCES

[1] V. N. Gribov: Sov. Phys. JETP 26 (1968) 414

[2] V. N. Gribov and A. A. Migdal: Sov. J. Nucl. Phys. 8 (1969) 583

[3] V. A. Abramovski, V. N. Gribov and O. V. Kancheli: Sov. J. Nucl. Phys. 18 (1974) 308

[4] A. Capella, U. Sukhatme, C. I. Tan and J. Trân Thanh Vân: Phys. Rep. 236 (1994) 225

[5] K. Goulianos: Phys. Rep. 101 (1983) 169

[6] UA4 Collab.: D. Bernard et al.: Phys. Lett. B166 (1986) 459

[7] V. Innocente, A. Capella, A. V. Ramello and J. Trân Thanh Vân: Phys. Lett. B169 (1986) 285

[8] J. Ranft: Z. Phys. C33 (1987) 517

[9] S. Roesler, R. Engel and J. Ranft: Z. Phys. C59 (1993) 481

[10] R. Engel, J. Ranft and S. Roesler: Phys. Rev. D52 (1995) 1459

[11] R. Engel, M. A. Braun, C. Pajares and J. Ranft: Z. Phys. C74 (1997) 687

[12] R. Engel: Z. Phys. C66 (1995) 203

[13] R. Engel and J. Ranft: Phys. Rev. D54 (1996) 4244

[14] P. Aurenche, F. W. Bopp, A. Capella, J. Kwieciński, M. Maire, J. Ranft and J. Trân Thanh Vân: Phys. Rev. D45 (1992) 92

[15] F. W. Bopp, R. Engel, D. Pertermann and J. Ranft: Phys. Rev. D49 (1994) 3236

[16] B. L. Combridge, J. Kripfganz and J. Ranft: Phys. Lett. B70 (1977) 234

[17] D. W. Duke and J. F. Owens: Phys. Rev. D26 (1982) 1600

[18] J. L. Cardy: Nucl. Phys. B75 (1974) 413

[19] A. B. Kaidalov, L. A. Ponomarev and K. A. Ter-Martirosyan: Sov. J. Nucl. Phys. 44 (1986) 468

[20] A. Capella, A. Kaidalov, C. Merino and J. Trân Thanh Vân: Phys. Lett. B343 (1995) 403

[21] A. Capella, A. Kaidalov, C. Merino, D. Pertermann and J. Trân Thanh Vân: Phys. Rev. D53 (1996) 2309

[22] J. W. Chapmann et al.: Phys. Rev. Lett. 32 (1974) 257

[23] J. Schamberger et al.: Phys. Rev. Lett. 34 (1975) 1121

[24] CHLM Collab.: M. G. Albrow et al.: Nucl. Phys. B108 (1976) 1

[25] CHLM Collab.: J. C. M. Armitage et al.: Nucl. Phys. B194 (1982) 365

[26] UA5 Collab.: R. E. Ansorge et al.: Z. Phys. C33 (1986) 175

[27] UA1 Collab.: D. Robinson and C. E. Wulz: Calibration of the UA1 luminosity monitor, Report UA1-TN / 89-10, 1989

[28] E710 Collab.: N. A. Amos et al.: Phys. Lett. B243 (1990) 158

[29] E710 Collab.: N. A. Amos et al.: Phys. Lett. B301 (1993) 313

[30] CDF Collab.: F. Abe et al.: Phys. Rev. D50 (1994) 5535

[31] K. H. Streng: Phys. Lett. 166B (1986) 443

[32] J. Collins, L. Frankfurt and M. Strikman: Phys. Lett. B307 (1993) 161

[33] J. C. Collins, J. Huston, J. Pumplin, H. Weerts and J. J. Whitmore: Phys. Rev. D51 (1995) 3182

[34] B. Kniehl, H.-G. Kohrs and G. Kramer: Z. Phys. C65 (1995) 657

[35] A. Capella, J. Kaplan and J. Trân Thanh Vân: Nucl. Phys. B105 (1976) 333

[36] E. Gotsman, E. M. Levin and U. Maor: Phys. Lett. B353 (1995) 526

[37] ZEUS Collab.: M. Derrick et al.: Phys. Lett. B356 (1995) 129

[38] D. Joyce et al.: Phys. Rev. D48 (1993) 1943

[39] UA4 Collab.: M. Bozzo et al.: Phys. Lett. B147 (1984) 392

[40] UA4 Collab.: D. Bernard et al.: Phys. Lett. B186 (1987) 227

[41] UA8 Collab.: A. Brandt et al.: Phys. Lett. B297 (1992) 417

[42] H1 Collab.: T. Ahmed et al.: Nucl. Phys. B435 (1995) 3

[43] H1 Collab.: S. Aid et al.: Z. Phys. C69 (1995) 27

[44] ZEUS Collab.: M. Derrick et al.: Phys. Lett. B346 (1995) 399

[45] ZEUS Collab.: M. Derrick et al.: Z. Phys. C67 (1995) 227

[46] ZEUS Collab.: M. Derrick et al.: High-E_T jet cross sections in photoproduction at HERA, preprint pa02-041, to appear in Proceedings of the XXVIII International Conference on High Energy Physics, Warsaw, Poland, 1996

[47] M. Albrow: presented at this meeting, 1997

[48] A. Brandt: presented at this meeting, 1997

[49] A. Santoro: Diffractive phenomena at Tevatron, to be published in the Proceedings of the VI Conference on the Intersection of Particle and Nuclear physics, Big Sky, Montana,USA, 1997

[50] K. Goulianos: Results on Diffraction, presented at the XVII th International Conference on Physics in Collision, Bristol, UK, 1997

[51] A. Brandt: Rapidity gaps in jet events at D0, to be published in the Proceedings of the XI Topical Workshop on Proton–Antiproton Collider Physics, Albano Terme, Italy, 1996

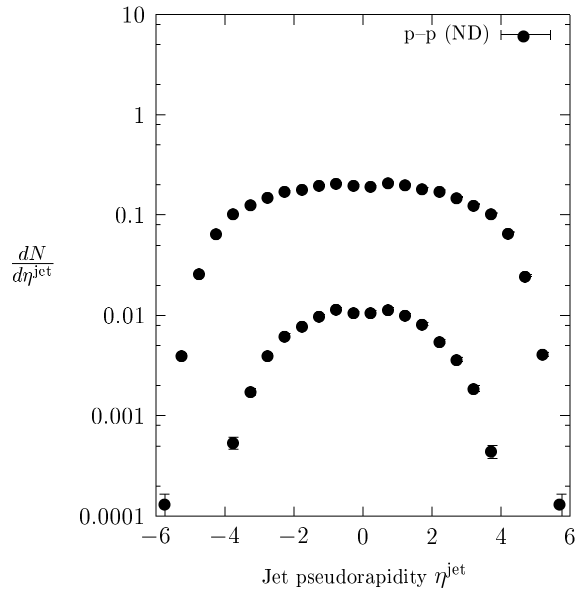

Figure 11: Pseudorapidity distribution of jets with $E_\perp$ larger than 5 GeV and 15 GeV in non-diffractive (ND) p–p collisions at TEVATRON. The upper curve is for $E_\perp$ = 5 GeV and the lower curve is for $E_\perp$ = 15 GeV.

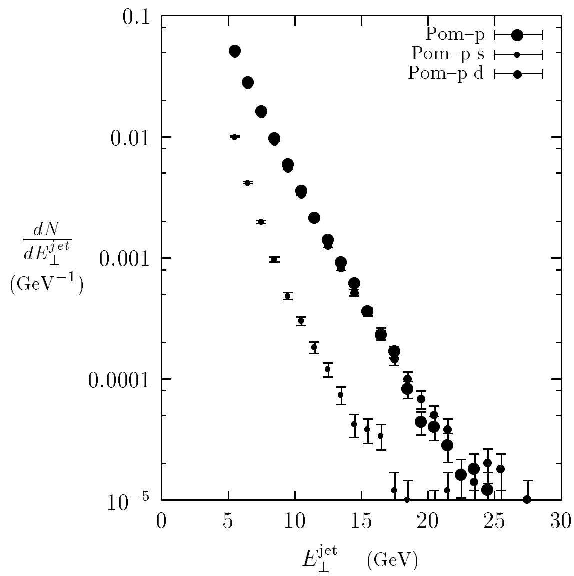

Figure 12: Transverse energy distribution of jets in (one side) single diffraction (Pom–p) at TEVATRON. We plot also the distributions (d) using a small direct Pomeron coupling ($\lambda = 0.05$) and (s) in a model where only single soft or hard chains are generated.

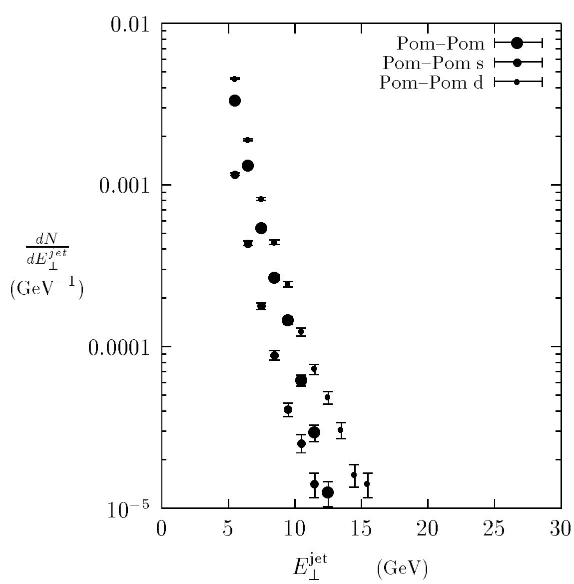

Figure 13: Transverse energy distribution of jets in central diffraction (Pom–Pom) at TEVATRON. We plot also the distributions (d) using a small direct Pomeron coupling ($\lambda = 0.05$) and (s) in a model where only single soft or hard chains are permitted.

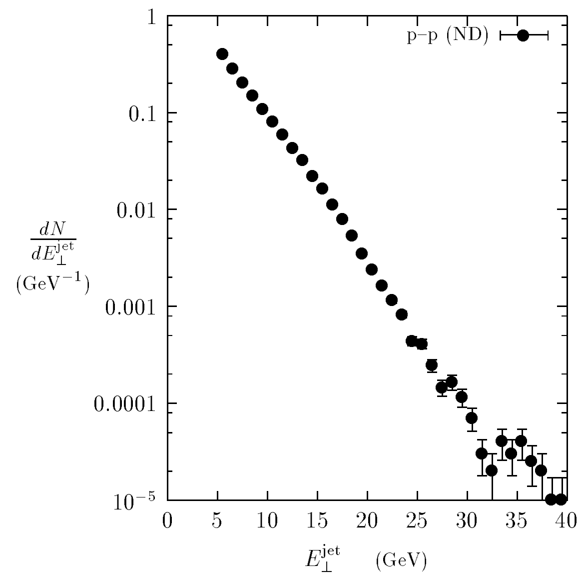

Figure 14: Transverse energy distribution of jets in non-diffractive (ND) p–p collisions at TEVATRON.

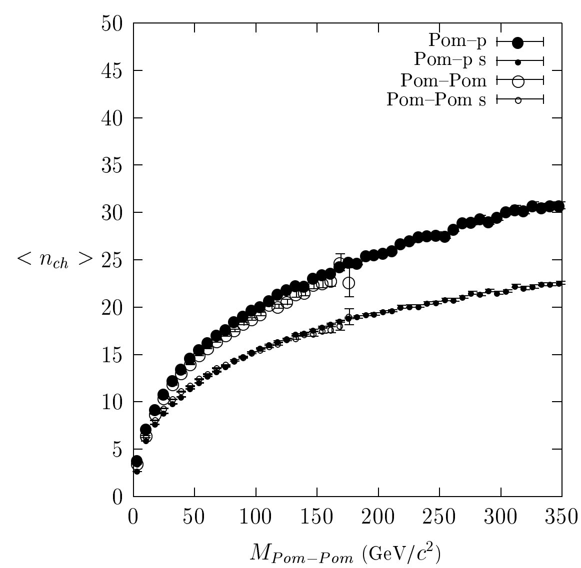

Figure 15: Charged multiplicity as function of the diffractive mass in single diffraction (Pom–p) and central diffraction (Pom–Pom) at TEVATRON. We plot also the distributions (s) in a model where only single soft or hard chains are considered.

HERA-B and its Vertex detection System

C. Hast[1]

Deutsches Elektronen-Synchrotron DESY, Notkestr. 85, D-22603 Hamburg, Germany

Abstract

HERA – B is an experiment designed primarily to study CP violation in decays of B mesons into the "gold plated" decay mode $B^0 \rightarrow J/\psi K_S^0$. The B mesons are produced in interactions of 820 GeV protons in the HERA proton beam with an Internal Wire Target in the beam halo. The physics goal and detector requirements are shortly described. Main focus is on the interplay between the Vertex Detection System and the HERA Proton machine. Some results from the 1996 and new results of the 1997 test measurements are presented. The conception of the Internal Wire Target and results of the target tests are described somewhere else in this issue.

1 INTRODUCTION

One of the outstanding problems in High Energy Physics is the origin of CP violation, a phenomenon discovered 30 years ago in decays of neutral Kaons. A decisive test of the implementation of CP violation in the standard model of electroweak interactions requires the discovery and accurate measurement of CP violation phenomena in systems heavier than Kaons. The most promising laboratory for CP violation studies are decays of neutral B mesons, where CP violating effects are expected to be large. However, the decay channels which can exhibit CP asymmetries are extremely rare, typically suppressed by four to five orders of magnitude. Experimental cuts to select clean signatures and to identify the B flavors reduce the useful rates further. An experiment will therefore require the production of very large numbers of B mesons, i.e. a machine acting as a B factory.

One possibility to produce large numbers of B mesons is offered by hadronic interactions at high energies. In this case, cross sections and therefore the rate of B events are much higher compared to e^+e^- machines; the events contain, however, a large number of particles besides the decay products of B mesons and the background of events with no B mesons produced is severe. This shifts the experimental challenge to the construction of adequate detectors and trigger systems. With increasing CM energy, the B cross section in hadronic interactions rises relative to the fraction of non-B background, so large center of mass energies are of advantage.

In reference [1] the feasibility of using the existing HERA proton ring for a B experiment was discussed for the first time. In a fixed target environment, the 820 GeV proton

[1]Now at University of California San Diego, Department of Physics, Mail Stop 0319, 9500 Gilman Drive, La Jolla, CA 92093, e-mail: Carsten.Hast@SLAC.Stanford.edu

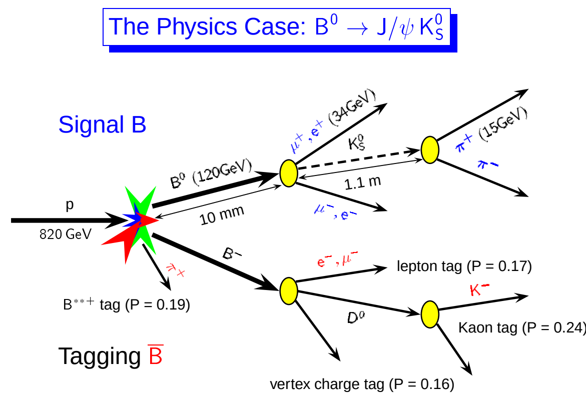

Figure 1: Decay chain of the $B^0 \rightarrow J/\psi K_S^0$ decay. The mean flight paths of the B and the K_S^0 meson are 10 mm and 1.1 m, respectively. Mean Energies are given in GeV. The tagging powers of the lepton, Kaon, vertex charge, and B^{**} tags are given as well.

beam energy leads to a center of mass energy $\sqrt{s} \approx 40$ GeV, an energy not too far above the B threshold. At this relatively low energy the background of normal inelastic interactions dominates B production by six orders of magnitude. A CP experiment therefore requires extreme event rates in the order of 30 to 50 MHz during a running period of several years. Since the maximal bunch crossing (BX) frequency of the HERA proton ring amounts to 10 MHz, several events must be produced simultaneously per BX.

The details of the HERA – B experiment and its physics goals were discussed in the Proposal [2], which was submitted in May 1994. In January 1995, a Design Report [3] was presented, which includes detailed technical solutions and time schedules for all the components of the experiment. The approval was granted in February 1995. For the time being, the collaboration comprises about 250 physicists coming from 33 institutes of 13 different countries.

2 THE HERA – B DETECTOR

The proposed HERA – B detector has been optimized for the detection of the "gold plated" decay mode $B^0 \rightarrow J/\psi K_S^0$ being displayed in Figure 1. Figure 2 shows this diagram once more now indicating the different detector components and the trigger scheme required. The HERA – B detector is a huge magnetic forward spectrometer with outer dimensions of $20 \cdot 9 \cdot 7\ \mathrm{m}^3$ (see Figure 3). The detector components and their properties are summarized in Table 1.

The main design choices are:

- Solid angle coverage from 10 mrad polar angle to about 200 mrad, corresponding to about 90 % solid-angle coverage in the center of mass system.
- Use of a single normal-conducting dipole magnet for momentum analysis, with a field integral of 2.1 Tm. Here the coils of the ARGUS Detector were reused.
- For a description of the HERA – B Target see the report of K. Ehret elsewhere in this proceedings.

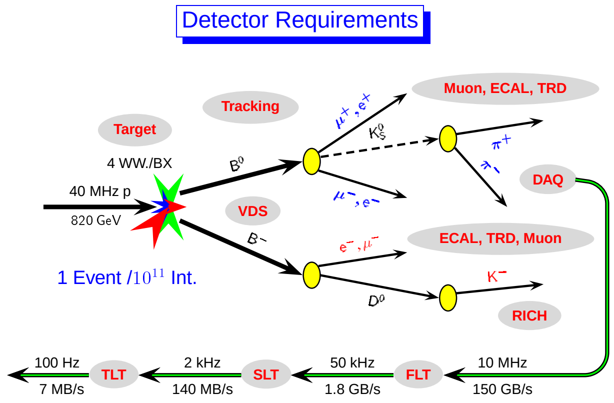

Figure 2: Detector components and trigger scheme required to detect the $B^0 \rightarrow J/\psi\, K^0_S$ decay

- A silicon vertex detector system starting at 10 mm radius from the beam with seven layers of double-sided Silicon strip detectors. The inner radius is limited by the requirement that the system has to survive radiation damage for at least one year before it can be exchanged. The silicon detectors will reconstruct the $J/\psi \rightarrow l^+ l^-$ vertex, disentangles vertices of overlaid events, and determines the impact parameters of tagging particles. In the second level trigger stage background will be suppressed.

- A main tracking system, whose granularity and technology vary with distance from the beam in order to limit the occupancy of each detector cell and yet minimize the number of channels. Below a radius of 6 cm $-$ required only for the first tracking stations $-$ Silicon strip detectors will be used, followed by microstrip gaseous detectors with Gas Electron Multiplier foils (GEM) in the intermediate region out to about 20 cm, and by honeycomb drift cells of varying radius and active length at larger distances from the beam. The tracking strategy is as follows: Pattern recognition is performed in the field free region outside the magnet. Tracks are extrapolated to the electro-magnetic calorimeter and the muon system. Here large chambers behind the RICH and in front of the calorimeter enable efficient linking of charged tracks in the spectrometer with calorimeter hits and with track segments in the muon system. Additionally these chambers provide first level trigger information.

  Found tracks are swum through the magnet to the vertex detector and are extrapolated to vertices originating from the target.

- The ring imaging Čerenkov counter as the only technology to identify a tagging Kaon with its momentum between a few GeV and about 50 GeV. C_4F_{10} is used as radiation gas. The Čerenkov angle of particles with $\beta = 1$ is $55.6\,mrad$. The light is bundled with 140 spherical mirrors and deflected to the photon detectors

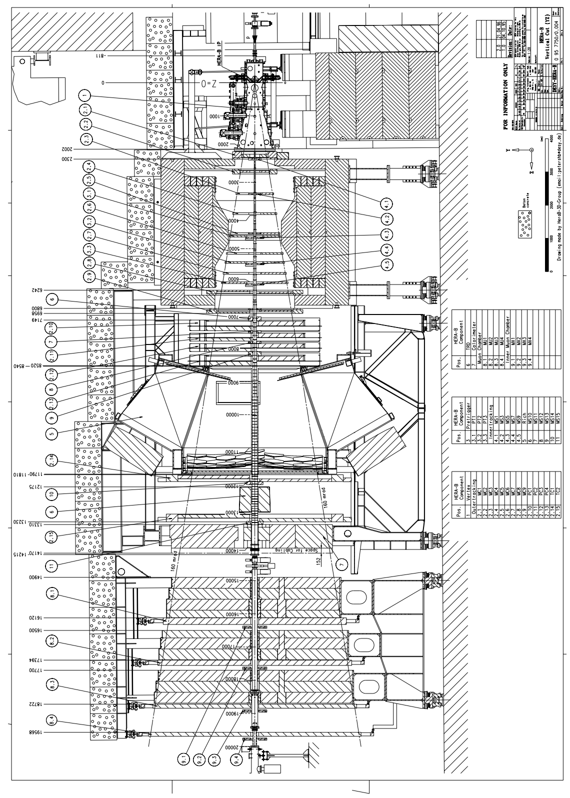

Figure 3: Vertical cut of the HERA – B detector.

by additional planar mirrors. The Hamamatsu multichannel photo-multiplier used to detect the Čerenkov photons are placed outside of the overall acceptance of 200 mrad.

- A (relatively) small transition radiation detector using a fiber radiator and straw detector cells in the very forward region, in order to improve electron identification in the congested small-angle region. The TRD is part of the pretrigger to find electron/positron candidates as first level trigger input. In the reconstruction it increases the probability to find electron or positron tags.

- The electro-magnetic Pb/Scintillator and W/Scintillator shashlic calorimeter fulfills the requirements concerning energy resolution in a cost effective fashion, and allows matched granularities with a minimal Moliére radius close to the beam. In the inner section of $1.6\,\mathrm{m} * 0.9\,\mathrm{m} 2\,\mathrm{mm}$ thick tungsten plates are used as absorber. The Moliére radius is 1.3 mm. The innermost calorimeter modules are expected to be exchanged after 1 year due to radiation damage. As the TRD the calorimeter serves as pretrigger for electron/positron candidates and the reconstruction of tagging particles.

- A conventional muon system with four chamber layers at different depths in the absorber. The information of the last two layers is used as pretrigger to find muon candidates. During the reconstruction the muon system finds tagging muons.

The total number of channels sums up to over half a million. 150 000 out of these are used as first level trigger inputs.

HERA – B has a multilevel trigger scheme (see Figure 2). The first level trigger works with the HERA bunch crossing rate of 10 MHz as input rate. In total 150 GByte of data have to be searched for lepton pairs per second. Already at this level a mass cut around the nominal J/ψ mass is introduced. The second level trigger includes SVD information to resolve decay vertices. Here a cut is introduced forcing B decay vertex candidates not to origin from one of the target wires. The 2 kHz second level trigger output rate is either transfered to a third level where a more refined track analyses is performed or directly to a large computer farm for the online reconstruction of the events. In total HERA – B aims to write 20 events per second to tape.

Detector	*Technology*	*Channels*	*Hits per BX*
Vertex detector	Si-strip	136 k	≈ 0.05
Tracker			
inner (2-6 cm)	Si-strip	40 k	≈ 0.02
inner (6-19 cm)	micro-strip gas-chamber	135 k	≈ 0.04
outer (>19 cm)	honeycomb DC	120 k	≈ 0.15
High-p_T trigger $B^0 \to \pi^+\pi^-$	gas pixel/straw	26 k	≈ 0.05
RICH Kaon iden.	C_4F_{10} radiator PMT	32 k	≈ 0.1
TRD Electron iden.	fiber radiator straw chamber	15.7 k	≈ 0.1
ECAL Electron iden.	W/Pb scint. shashlic	5.8 k	≈ 0.2
Muon system Muon iden.	gas pad + pixel prop. tubes	31.3 k	< 0.01
Total		550 k	

Table 1: Main components of the HERA – B detector including the number of readout channels and the average number of hits per bunch crossing.

3 THE HERA – B SILICON VERTEX DETECTOR

The Silicon Vertex Detector (SVD) [4] is build by the Max-Plank-Institute für Kernphysik in Heidelberg and the Max-Plank-Institute für Physik in Munich, both Germany. The acceptance is 10 – 160 mrad horizontally and 10 – 250 mrad vertically. This corresponds to 95 % of the solid angle in the center of mass system. The resolution is planned to be 20 – 30 μm transverse to the beam and 500 μm along the beam. Data from the SVD are used in the second level trigger to find lepton pair vertices displaced from the target wires. On the reconstruction level the SVD establishes the $J/\psi \to l^+l^-$ vertex and measures impact parameters of the tagging particles.

The design challanges for the SVD can be described in the following way:

- The complete Vertex Detection System, consisting out of tank, counters and targets is an integral part of the proton ring of HERA, since the proton beam centrally traverses the tank.
  - During injection a clearenc of 19 mm in radius is needed which has to be reduced to 10 mm during data taking. This leads to a radial movable counter arrangement. Therefore the usage of a solid beam tube is excluded
  - Since the proton beam's mirror currents have to be guided through the tank a movable RF shield has to be provided.
  - Inside the SVD the very high proton beam vacuum has to be mantained. Since this is impossible with inbuild silicon, carrier materials, a Binary-Ice cooling system, etc. the counters have to be wrapped. Here long thin Aluminum caps have been choosen to reduce multiple scattering. Since these caps are not stable under air preasure these covers are connected to a seconadary vacuum system.
- with a HERA – B interaction rate of 40 MHz the particle flux of $\mathcal{O}(3\times10^{14}\,\mathrm{particles/cm^2y})$ leads to a severe radiation damage in both Silicon wafers and readout chips.
- The HERA bunch crossing frequency of 10 MHz demands a deadtimeless readout and an online processing of 8 GBytes of data per second.
- General points are low mass support material to reduce multiple scattering.

In the following subsections these points are discussed in more detail and technical solutions are described.

3.1 The Secondary Vacuum System

Since the ultra high proton machine vacuum ($p < 10^{-8}\,\mathrm{mbar}$) has to be mantained inside of the VDS tank the counters were wrapped with a thin Aluminum shield. Figure 4 shows the schematic design of one Silicon station.

These Aluminum shields have a length of approximately 20 cm for the stations nearest to the target and up to 50 cm in 2 m distance to the target. To reduce multiple scattering these shields have to be as thin as possible. Two technical solutions for the production have been found: Electro erosion which turned out to be very time consuming and expensive, and galvanic deposition of Aluminum onto form

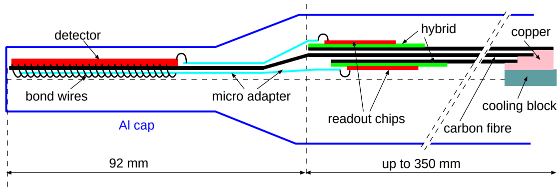

Figure 4: Schematic side view of a silicon layer. Each station consists of two layers of doublesided read out Silicon wafers. The strip directions of one layer are tilted in respect to the other by $\pm 2.5^{\circ}$ allowing a spatial track reconstruction.

pieces to a thickness of $120 - 150\,\mu\mathrm{m}$. These long thin caps are unable to stand one atmosphere of pressure. Therefore a secondary vacuum system has to be applied. Here the HERA vacuum group did a great job in designing and building a safe system. Pumping down and venting the vessel is a delicate task since the pressure difference between HERA vacuum and the secondary one has to be maintained at a level better than 1 mbar. A sudden pressure change in one of the systems would most probably end in a damage of the wire bonds which are very close to the Aluminum caps. Venting the vessel needs approximately four hours, the pump down time before HERA can start with proton injection is 48 hours. Up to now this system was operated reliably for two running periods.

3.2 The RF Shield

A technical not finally solved problem it the RF shielding between the proton beam and the Aluminum caps. In 1996 a $100\,\mu\mathrm{m}$ thin Aluminum tube with slits for the Silicon modules and many holes to reduce the amount of material which was build in. This tube worked perfect as an RF shield but provided by far too much material in terms of multiple scattering. During 1997 four $5\mu\mathrm{m}$ thick steel bands were tested, again with very good results. Late in October 1997 the RF shield was changed again to a configuration consisting out of eight CuBe wires. Here severe technical problems occurred due to heating of the wires. With a length of roughly two meters it takes only little heating to prolong the wires enough to bend into the proton beam. Two wires broke and operation of HERA was partly disabled. Here more engineering work is needed, especially since the radial movement of the RF shield was not established up to now.

Mafia calculations performed by members of the HERA crew and people from the VDS group, a RF test of a half scale model of the vertex tank at the INFN at Naples, and the operation at HERA have shown that all three solution, tube, ribbons, and wires are principally working.

3.3 Radiation Damage

HERA – B foresees an exchange of all Silicon counters once per year. But even to achieve this lifetime special measures have to be taken. The Silicon counters are operated at 8° C to reduce leakage current, noise, and reverse annealing. A special guard ring structure allows the Silicon to be biased up to more than 300 Volts.

To distribute the highest radiation damage which occures only at the very first millimeters closest to the proton beam, the 5 cm broad Silicon counters can be moved lateral by 3 cm relative to the beam to distribute the hot spot on a larger area.

Instead of using explicit radiation hard electronics the readout chips are connected through so called micro adapters to the Silicon at regions where the radiation dose is expected to be below 100 krad per year.

3.4 The Readout Chain

The readout chain consists of the so called HELIX readout chip, analog optical transmission lines from the detector to the control room, front-end driver boards (FED) for digitization and event buffer boards.

The design bandwidth of the chain is chosen such that the readout will be dead timeless for 100 kHz event rate.

The silicon detector is read out after a first level trigger has been issued for a given HERA bunch crossing. In this case the Fast Control System (FCS) sends a trigger signal, a 7-bit bunch crossing number, and a 16-bit event number to the front-end driver boards. The FEDs send the trigger with the correct latency to the readout chips.

The readout chips contain a pipeline for the analog detector signals and upon receiving a trigger mark the correct pipeline column will be read out: The 128 input channels of each HELIX chip are multiplexed to one output line and a gate is generated during which the data are valid for readout. This gate is used by the FEDs for digitization. The column management of the HELIX chips allows for continuous writing during readout.

4 RESULTS FROM THE 1996 AND 1997 RUNS

In the 1996 HERA – B test run 3 double sided Silicon layers had been mounted. Figure 5 shows one event where a track originating from a target wire and traversing all three layers could be reconstructed. An overlay of target positions measured in runs with different single target wires is shown in Figure 6. The elongated forms of the hit distributions on the wires are clearly visible. From the rms-width of the projection orthogonal to the wires the intrinsic resolution for the target wires was measured to be around 300 μm in agreement with Monte Carlo estimates for the 1996 geometry. Along the wires the width of the distributon is dominated by the width of the beam profile, which has a rms-width around 500 μm. Data from one wire with its two projections are shown in Figure 7. The gaussian profile in both views indicates that the target wires are scraping the beam in order to produce the required interaction rates. (See the report of K. Ehret elsewhere in this proceedings).

Analyzing runs with more than one target wire allowed one to determine by direct measurement the distribution of hits between different wires, thereby monitoring the performance of the target control system with respect to

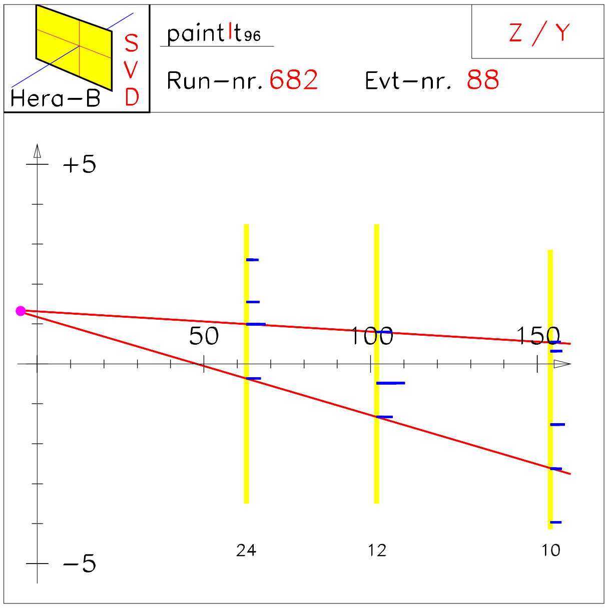

Figure 5: Display of an event with track candidates originating from a target wire and being observed in all three detector modules.

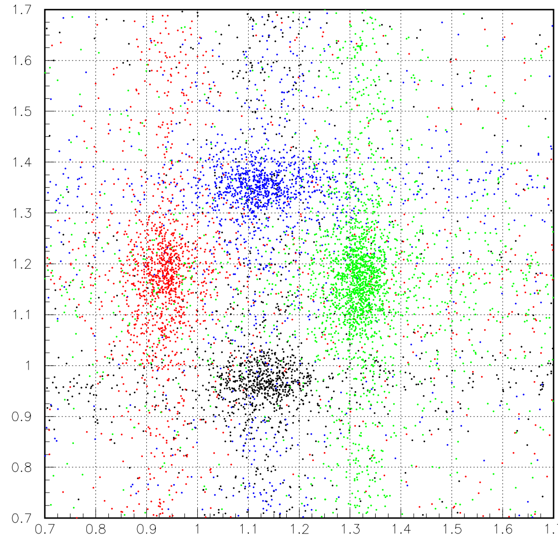

Figure 6: Overlay of data from runs with different single target wires. The transverse coordinates of track candidates from the vertex detector are plotted at the plane of the target wires. The clusters correspond to a individual wire.

equalizing the contributions from all wires.

For the 1997 run the Silicon layers and readout electronics were exchanged but the geometric setup remained the same. The main focus on this running period was to establish a common data acquisition for all sub detectors. Figure 8 shows typical measurements of different detector components: The number of interactions per bunch crossing measured in the Target Hodoscopes, number of clusters in the Silicon counters, occupancies in % for Outer Tracker (OTR), Transition Radiation Detector (TRD), and ECAL. These measurements are plotted versus the bunch number of the proton beam. Clearly the fill pattern of the machine can be seen: from -21 to -17 the last filled buckets, from -15 to -1 the empty buckets and, from 1 to 11 the first filled ones. The high occupancy for the ECAL at the first bunch crossing is due to a LED pulser which was running for calibration purposes. With these simultaneously read out data the functionality of the Fast Control System could be established (see above).

In a further step the VDS, ECAL, and DAQ groups of HERA − B were able to establish a working first level trigger. For a given bunch crossing they surched for high energy clusters in the 320 ECAL test modules. This cluster was interpreted as a single high energey electron. With this trigger the Silicon was read out. These events showed after reconstruction an excess of tracks originating from the target and traversing both, Silicon and ECAL. The magnet was switched off during these measurements. Figure 9 shows the lego plot of the extrapolated target position. In Figure 10 the x- and y-projections are given together with the expected combinatorical background, shown shaded. These measurements were so encouraging that the HERA − B collaboration spend a hughe effort in trying to reconstruct J/ψ mesons. The analyses of this data is ongoing.

5 SUMMARY

In this proceedings was shown how the HERA machine group and the HERA − B collaboration work together to make the technological challange of the HERA − B Experiment possible within the given timeconstraints. As example the vacuum system and the RF shield of the Vertex tank were described.

Results from the data taking periods of 1996 and 1997 established the functionallity of three different RF shieldings, the track reconstruction with the VDS, the functionallity of the Fast Control System and have proven the First Level Trigger to work.

6 REFERENCES

[1] H. Albrecht et al., HERA − B An Experiment to Study CP Violation in the B System Using an Internal Target at the HERA Proton Ring, Letter of Intent, DESY-PRC 92/04 (1992).

[2] H. Albrecht et al., HERA − B An Experiment to Study CP Violation in the B-System Using an Internal Target at the HERA Proton Ring, Proposal, DESY-PRC 94/02 (1994).

[3] E. Hartouni et al., HERA − B An Experiment to Study CP Violation in the B-System Using an Internal Target at the HERA Proton Ring, Technical Design Report, DESY-PRC 95/01 (1995).

[4] HERA − B VDS: http://pluto.mpi-hd.mpg.de/∼ktkno/www.html

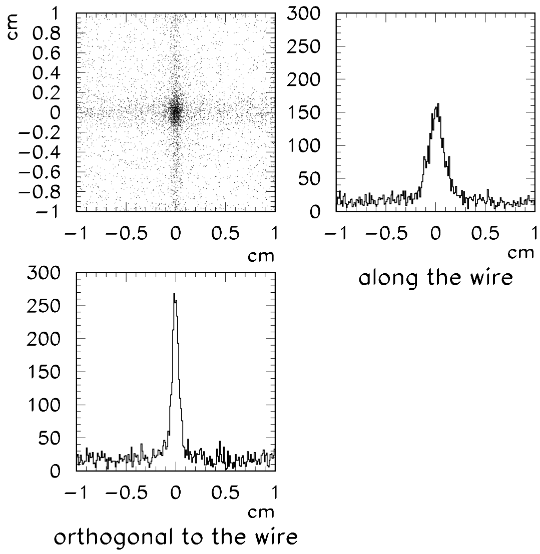

Figure 7: Distribution of hits on a single wire. The two dimensional distribution is shown together with its projections along (upper right) and orthogonal (lower left) to the wire.

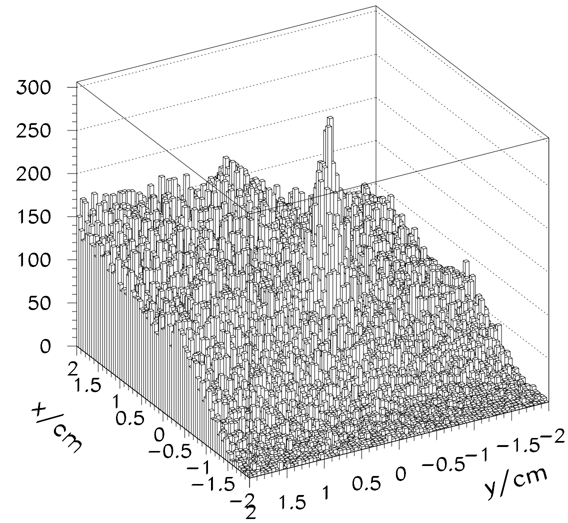

Figure 9: Lego plot of the extrapolated target position for ECAL triggered tracks

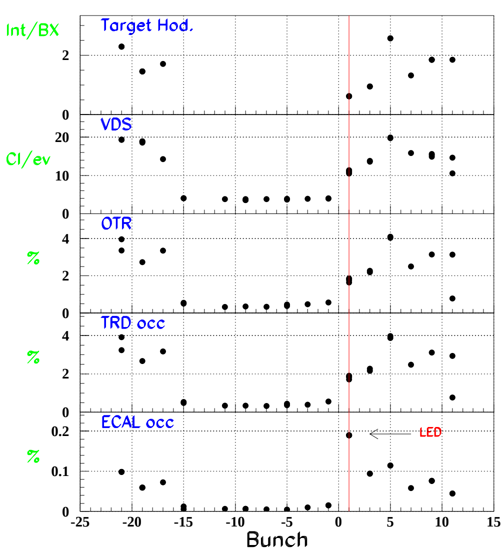

Figure 8: Measurements of interaction rate per bunch crossing measured by the Target hodoscopes, number of clusters per event in the Silicon and occupancies of OTR, TRD, and ECAL versus the bunch number.

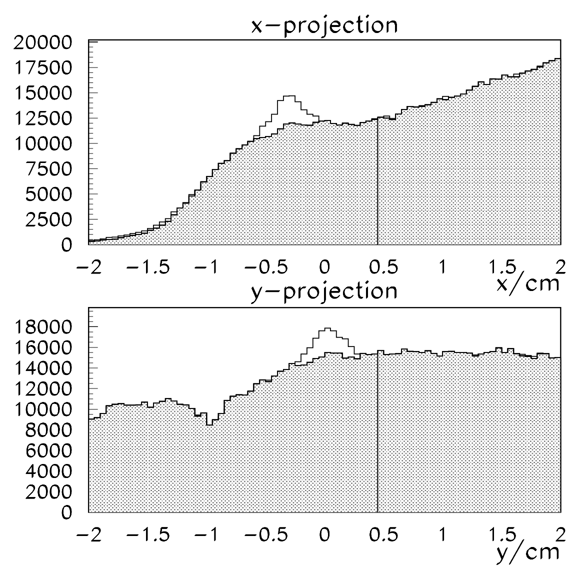

Figure 10: x- and y-prjections from Figure 9 with expected combinatorical background (shaded).

Near Beam Physics at HERA

M. Bieler
DESY, D 22603 Hamburg, Germany

Abstract

This paper gives an overview over near beam physics at the HERA electron–proton collider at DESY. After a short introduction to the HERA machine the main topics are the proton beam loss monitors, the proton beam collimation system, the wire target of HERA-B and the forward proton spectrometers of H1 and ZEUS.

1 HERA

The Hadron-Electron-Ring-Accelerator HERA is an accelerator facility for the investigation of electron–proton collisions [1], [2],[3],[4],[5].

It consists of two separate storage rings with a circumference of 6335 m each. They are located one upon another in a common tunnel 10–20 m underground. The proton beam is injected into HERA at an energy of 40 GeV and accelerated to the design energy of 820 GeV. It is guided in a superconducting magnet structure. For the electron ring a conventional magnet design was chosen whereas the normal conducting rf–system of the electron machine is supported by 16 superconducting resonators to reach the maximum energy of 30 GeV [6].

The geometry of the HERA–collider, as shown in fig. 1, is given by 4 straight sections where 4 experiments are situated. They are connected by 4 arcs. In the straight section “North” and “South” the two counter-rotating beams are bent and focused onto a common interaction point where the detectors of the experiments “H1” and “ZEUS” respectively are located to measure the e–p interactions. The beam separation is designed for a head-on collision of both beams.

In the straight section “East” the experiment “HERMES” measures the interaction of the polarized electron beam with an internal gas target. The electron and proton beam pass the experimental area of the detector in separate vacuum chambers.

In the straight section “West” the beam lines are also well separated and the Experiment “HERA-B” uses a wire target in the halo of the proton beam to investigate C-P violation in the B-system.

HERA was constructed by an international collaboration of more than 40 institutes and laboratories from 12 countries. Contributions were both in the form of construction and delivery of components for the facility as well as contribution to the manpower during the design and commissioning phase.

The construction of Hera started in 1984, and in 1990, after a period of 6 years both storage rings were technically completed. The commissioning phase, starting in 1991, was completed when luminosity was first achieved on October 20, 1991 with the collision of 10 counter-rotating bunches at the interaction regions North and South. In 1992 the detectors ZEUS and H1 were put in place and luminosity operation started. Since then beam currents and luminosity have been increased steadily and in 1997 proton peak currents of 100 mA in 180 bunches and positron peak currents of 40 mA in 189 bunches have led to an integrated luminosity of 36 inverse picobarn per year.

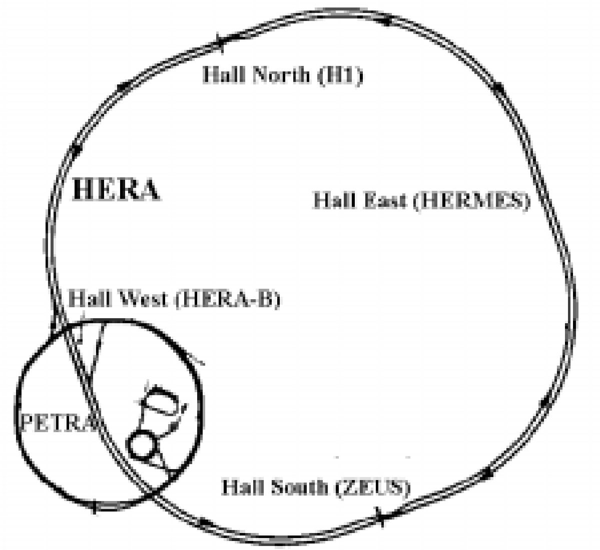

Figure 1: Geometry of the electron proton collider HERA. The bunches of the proton and electron machine collide at the interaction points “North” and “South” where the detectors of the experiments ZEUS and H1 are located. In the straight section “East” Hermes makes use of the electron beam, in straight section “West” HERA-B uses the proton beam.

2 PROTON BEAM LOSS MONITORS AT HERA

The proton beam loss monitors in HERA are distributed around the ring, one monitor on every quadrupole magnet. As the HERA electron ring, located about one meter below the proton ring, creates a significant background of synchrotron radiation, the proton beam loss monitors have to distinguish between synchrotron radiation photons and showers of charged particles from protons hitting the beam pipe. The proton beam loss monitors consist of two PIN diodes, two preamplifiers and a coincidence logic, integrated in a small housing, surrounded by a 2.5 cm lead shielding [7]. Fig. 2 shows a sketch of a beam loss monitor [8].

A single signal in just one diode caused by a synchrotron radiation photon is suppressed by the coincidence logic, whereas simultaneous signals in both diodes, caused by the shower of a lost proton, create an output signal with a length of less than 100 ns. With a bunch distance of 96 ns in HERA this leads to a maximum counting rate of one pulse per bunch crossing. A redesigned version of the HERA proton beam loss monitors is now commercially available [8].

The quench protection system for the superconducting

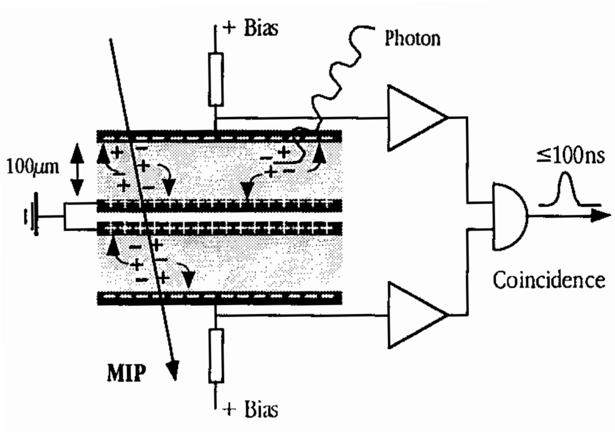

Figure 2: Sketch of a HERA proton beam loss monitor with two diodes, two preamplifiers and a coincidence logic

magnets of the HERA proton ring uses the counting rates of the beam loss monitors as a trigger criterion for the beam dump. After a beam dump the history of the rates of individual monitors prior to the beam dump can be inspected for a post mortem analysis. The rates of the individual beam loss monitors next to the proton collimators are used for the fine positioning of the respective collimators. The rates of the beam loss monitors next to the roman pots are used for their positioning, and the overall loss rates are used for the fine tuning of the betatron tunes and as a general background indicator.

3 PROTON COLLIMATORS AT HERA

The proton collimation system at HERA is described in detail in [9]. The collimators are located in 5 stations in the straight section west, with 2 or 4 jaws per station. In both the horizontal and the vertical plane there are one primary collimator and two secondary collimators, respectively. Ideal betatron phase advances between the jaws would be $\Delta\varphi = 30^o$ or $30^o + 180^o = 210^o$ and $\Delta\varphi = 150^o$ or $150^o + 180^o = 330^o$. The position of the collimators in HERA (in meters, right or left of the center of hall west), the actual phase advances between the collimators and their role as primary and secondary collimators are given in table 1. The position of the HERA-B wire target is also indicated. In both planes there are collimators at the right phase advance downstream of the wire target to intercept particles scattered by the wires.

Position	$\Delta\varphi_H$ (degr.)	$\Delta\varphi_V$ (degr.)	Function (horiz.)	Function (vert.)
WR 94	**0**	-28	Prim.	-
WR 33	85	**0**	-	Prim.
HERA-B	121	26	-	-
WL 19	**158**	74	Sec. 1	-
WL 105	189	**154**	-	Sec. 1
WL 150	**209**	**283**	Sec. 2	Sec. 2

Table 1: Position, betatron phase advances and function of the jaws of the proton collimator system

The collimator jaws are tungsten-copper conglomerate blocks, 60 mm wide, 80 mm high and 400 mm long (this is equivalent to 4 interaction length). The collimator jaws are not meant to serve as a beam dump. At least one accidental beam loss in a collimator jaw caused severe melting of the material and left a pencil shaped groove in the surface of the jaw.

The alignment of the surface of a jaw relative to the beam is about 100 μrad. The moving range of all jaws is from +50 mm (open) to -5 mm (beyond the center of the beam pipe) with a precision of $\pm 5\,\mu$m and a minimal gap of 1.2 mm between opposing jaws. Each jaw is equipped with a beam loss monitor, which is used to determine the position of the jaw relative to the beam.

For the collimator closing procedure at the beginning of a luminosity run, the rates of the beam loss monitors next to the collimators are used. First all jaws are moved from +50 mm to +15 mm. Then all jaws are moved to a position 3 mm wider than the position of the jaws during a typical luminosity run. During this move an increase of the counting rate of any beam loss monitor above a certain threshold would stop all collimators. The threshold is set a factor of 5 to 10 above the background counting rate measured with open collimators. Afterwards every single jaw is slowly moved to the beam until the counting rate at the adjacent beam loss monitor increases above the threshold. Then the jaw is stoped and moved back out by 0.2 mm. After the optimum collimator positions have been determined that way, all collimators are moved simultaneously to their optimum position by 0.2 mm. This procedure is relatively slow (15 minutes), but very effective. Once the collimators are closed, the experiments can turn on their sensitive components and only little fine tuning of the collimators is required to control the background during a luminosity run.

For the 1998 run, with HERA-B routinely operating the wire target, the collimator closing procedure will be modified in a way that HERA-B will move the wires into the beam halo before the collimators are closed. This procedure will help to further reduce collimator tuning if the wires are moved in or out during a luminosity run.

Fig. 3 shows the console application for the proton collimators. The upper part shows the status and position of the different collimator jaws relative to the beam pipe cross section. The lower part shows the counting rates of the proton beam loss monitors next to the collimators. The highest rates are seen at the collimator WL 19, just downstream of the HERA-B wire target.

The proton collimators and the adjacent beam loss monitors have been used as tools for many different beam diagnostic measurements (for details see [9]) like acceptance measurements, frequency analysis of beam loss rates, measurements of the transverse particle distribution in the beam, diffusion rates in the beam halo or diffusion rates due to beam beam interaction.

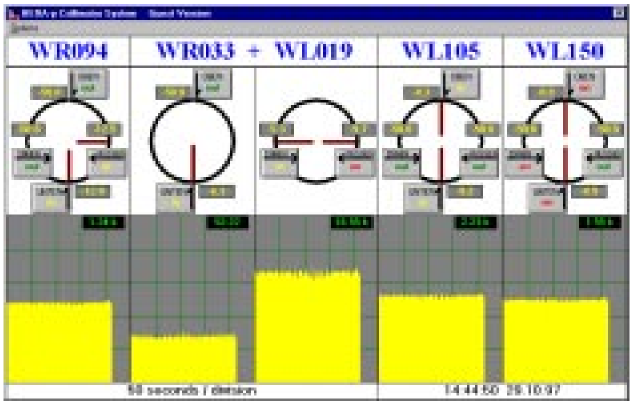

Figure 3: Console application for the proton collimators. The upper part shows the position of the different collimator jaws, the lower part shows the rates of the proton beam loss monitors next to the collimators.

4 THE HERA-B WIRE TARGET

The HERA-B experiment and the wire target are described in detail by C. Hast and K. Ehret in these proceedings. Here some aspects of the target operation from the machine operations point of view shall be mentioned.

The wire targets of HERA-B are moved into the halo of the proton beam. Their position relative to the beam is adjusted to a fixed interaction rate. This allows the target wires to follow slow motions of the beam due to thermal drifts.

At a typical interaction rate of 30 MHz at the target the beam loss monitors at the first collimator downstream see a beam loss rate of about 30 kHz, compared to about 1 kHz without target operation. The proton related backgrounds at the other experiments do increase when the wires are first moved in, but can usually be reduced again by carefully adjusting the collimator positions. The lifetime of the proton beam is reduced from about 1000 hours without target operation to less than 100 hours at interaction rates of 30 MHz. Fig. 4 shows the beam currents in HERA for two typical luminosity runs on September 11, 1997. During the run early in the morning there was no target operation of HERA-B. During the second run at 6 PM HERA-B went to an interaction rate of about 40 MHz. At that time a drastic change in the proton lifetime is visible.

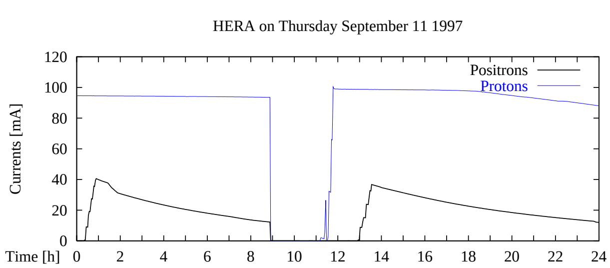

Figure 4: Beam currents in HERA for two typical luminosity runs on September 11, 1997. From 6 PM on HERA-B target operation limits the proton lifetime.

5 THE FORWARD PROTON SPECTROMETERS OF H1 AND ZEUS

In some electron–proton collisions at HERA the proton survives, gets a small transverse kick and/or looses a fraction of its energy and escapes from the detector through the beam pipe. In order to capture these protons, both H1 and ZEUS have installed forward proton spectrometers with up to six detector stations within a distance of 90 m downstream from the interaction point. These spectrometers make use of the vertical dipole magnets 70 m from the interaction point, which are used for the vertical separation of the beam pipes in the arcs of HERA. The detector stations are equipped with roman pots. These are thin housings for detectors, which can be moved into the beam pipe close to the beam.

Two detector stations of the forward proton spectrometer of H1 at 60 m and 80 m from the interaction point can be moved horizontally into the beam pipe, two vertical stations are at 80 m and 90 m from the interaction point. Coincidence of signals from the two vertical stations at 80 m and 90 m allows to reconstruct traces back to the interaction point. The energy acceptance of the vertical stations is roughly 500 - 750 GeV (at 820 GeV beam energy). The acceptance of the total system is about 10 %.

The vertical detectors are kept about 15 σ above the beam center. The actual position of the detectors with respect to the interaction point can be measured with a precision of 100 μm. At the beginning of a luminosity run, after the collimators have been closed, the roman pots are slowly moved into the beam pipe. The counting rate of a proton beam loss monitor downstream from the roman pot is observed. If the gradient of the counting rate increases above a certain threshold, the movement of the pot is stoped and then it is retracted by 200 μm. If the counting rates of the beam loss monitors or the counting rates of the detectors in the roman pots increase dramaticly during a luminosity run, the pots are retracted from the beam within a few seconds.

The detectors in the H1 roman pots consist of layers of 1 mm fibers. The fibers are grouped in layers of 25 fibers, 5 layers in one direction and another 5 layers tilted by 90 degrees. Such a fiber package together with two trigger tiles forms one detector and every roman pot is equipped with two detectors. The fibers are guided to photomultipliers which are located 50 cm away from the beam. Fig. 5 shows a sketch of one of the vertical roman pots of H1. A detailed description of the system can be found in [10] .

The leading proton spectrometer of ZEUS consists of more stations (3 vertical and 3 horizontal stations). Unlike the H1 pots, the ZEUS pots do not have a flat bottom, but a curved bottom surrounding the beam. The pots contain silicon detectors and amplifiers, both installed close to the beam. The advantage is a high energy acceptance and a high resolution of the detectors. Disadvantages are the need for radiation hard components and for cooling. Another disadvantage is the lack of flexibility due to the curved shape of the pots. If the beam drifts perpendicular to the di-

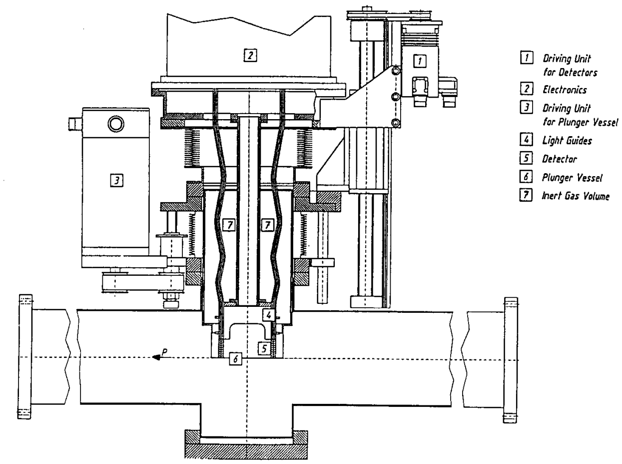

Figure 5: Sketch of one of the vertical roman pots of H1

rection of motion of the pots, the pots have to be removed from the beam until the old beam position is reestablished. If changes in the machine optics require an increase of the beam diameter at the pots, the pots have to be redesigned completely.

6 ACKNOWLEDGMENT

The information gathered in this paper was collected with the help of many colleagues from different groups. I would like to thank F. Willeke for carefully reading the manuscript and B. Holzer, K. Wittenburg, M. Seidel, M. Lomperski and W. Bartel for providing me with literature, drawings and fruitful discussions.

7 REFERENCES

[1] ‘HERA, A Proposal for a Large Electron Proton Colliding Beam Facility at DESY’, DESY HERA81-10 1981

[2] G.A. Voss, Proceedings of the 1st European Particle Accelerator Conference, Rome, June 1988

[3] B.H. Wiik,Proceedings of the 1989 Particle Accelerator Conference, Chicago, March 1989

[4] H. Kumpfert, M. Leenen,Proc. of the XIVth International Conference on High Energy Accelerators, Tsukuba 1989

[5] B.H. Wiik, Proceedings of the 2nd European Particle Accelerator Conference, Nice 1990

[6] D. Proch et al, ‘Superconducting Cavities for HERA’, Proceedings of the XVth International Conference on High Energy Accelerators, Hamburg 1992

[7] S. Schlögl,K. Wittenburg, ‘A Beam Loss Monitor System for HERA’, Proc. of the XVth International Conference on High Energy Accelerators, Hamburg 1992

[8] J. Bergoz, ‘Beam Loss Monitor User’s Manual’, Bergoz Precision Beam Instrumentation

[9] M. Seidel, ‘The Proton Collimation System of HERA’, DESY 94-103, June 1994

[10] The H1 Collaboration, ‘Proposal for a Forward Proton Spectrometer for H1’, H1 note H1-10/94-381, 1994, and DESY Internal Report PRC 94/03, 1994

Performance of the HERA-B Target and Interference with HERA Operation

K. Ehret[1]

Institut für Physik, Universität Dortmund, D 44221 Dortmund, Germany

Abstract

HERA-B is a fixed target experiment dedicated to study CP violation in the decay of neutral B mesons into the "gold platted" decay mode $B^0 \to J/\psi K^0_S$. An internal target in the halo of the 820 GeV HERA proton beam provides the source of B mesons in high rate fixed target proton-nucleus interactions. The target collects very efficiently the protons, before they get lost on any aperture limitation, to achieve the required constant interaction rate of 40 MHz. It operates parallel to HERA e-p luminosity data taking without significant disturbance of the other HERA experiments or the beam quality. This paper reviews the requirements and the main functionality of the HERA-B target. The different impacts on the target performance and various measurements are presented.

1 INTRODUCTION

One of the outstanding problems in high energy physics is the origin of CP violation, a phenomena discovered already 30 years ago in decays of neutral kaons. The most promising laboratory for CP violation studies are decays of neutral B mesons, where CP violating effects are expected to be large. Decay channels which can exhibit CP asymmetries are extremely rare, typically suppressed by 4 to 5 orders of magnitude. Cuts to select the events and to identify the b flavour reduces the useful rates further. Therefore a measurement of CP violation requires a large number of B produced mesons, i.e. a machine acting as a B factory. HERA-B uses the HERA protons to generate B mesons in 820 GeV proton-nucleus interactions on a fixed target. Here several tenths B mesons per second are rather easily produced, but the events contain a large number of particles besides the decay products of the B mesons. In addition the $b\bar{b}$ production cross section at HERA energy is six orders of magnitudes smaller than the total inelastic cross section. The ambitious challenge of the experiment are the detectors which will be operated in a very high rate environment and the triggers which have to provide a background reduction by six orders of magnitude.

The main goal of HERA-B is the observation of CP violation in the $B^0 \to J/\psi K^0_S$ decay mode (cp. Fig. 1) by measuring the asymmetry:

$$A_t = \frac{\Gamma(B^0 \to J/\psi K^0_S) - \Gamma(\bar{B}^0 \to J/\psi K^0_S)}{\Gamma(B^0 \to J/\psi K^0_S) + \Gamma(\bar{B}^0 \to J/\psi K^0_S)} = \sin 2\beta \sin xt/\tau_B,$$

[1] Klaus.Ehret@desy.de

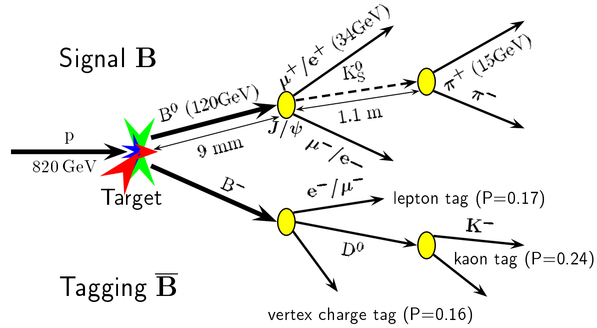

Figure 1: The "gold platted" $B^0 \to J/\psi K^0_S$ decay with some kinematical quantities at HERA-B .

where $x \approx 0.67$ is the mixing parameter, τ_B the lifetime of the B meson and $\sin 2\beta$ the term measuring CP violation.

Considering the cross section, the branching ratios, the trigger and the reconstruction efficiency of the HERA-B detector one ends up with a total efficiency of approximately 3×10^{-12}. A first significant CP measurements requires ≈ 1000 events and therefore 4×10^{14} interactions. This means one year (10^7 sec) running at a rate of 40 MHz. Regarding the HERA bunch frequency of 8 MHz, this leads to 5 simultaneous interactions per bunch crossing (bx).

HERA-B uses a set of 8 ribbons which are positioned around the beam at a distance of 4 - 6 r.m.s. beam widths, i.e. inside the beam halo or close to the beam core but outside the core. The main idea is to absorb protons, which leaves the beam core and would get lost anyhow, and bring them to interaction in the target (cp. Fig. 2). Such a wire target is mechanically stable, easy to operate and it gives well localized and separated main vertices. The operation of the target has to ensure that neither the beam quality is affected nor the e-p luminosity is reduced or the data taking of the other HERA experiments is disturbed by background. To achieve routinously the anticipated rate of 40 MHz it is essential that at least 50% of the halo protons are absorbed in the target before they get lost on any aperture limitation.

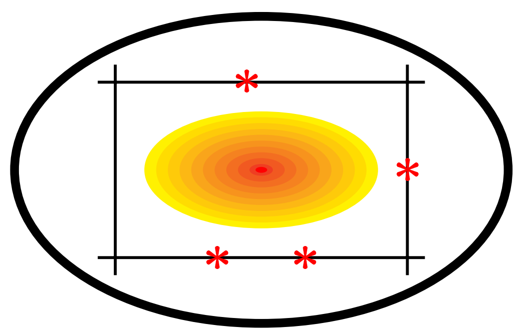

Figure 2: Basic idea of a halo target: protons which are drifting outwards interact on the wires before hitting any aperture limitation.

In this article the basic properties of the HERA-B target are reviewed. Main emphasis lies on the interference with HERA beam operation. After a brief description of the HERA machine and the experimental setup the main requirements and the basic functionality are summarized.

The impacts on the target efficiency are considered and the performance is discussed by a few selected measurements.

2 HERA

HERA [4] is a double storage ring designed for colliding a 820 GeV proton beam with a 30 GeV electron beam[2]. The rings with a length of 6335.8 m, their complicated injector chain and the four interaction regions are shown in Fig. 3. H1 and ZEUS are general purpose e-p experiments,

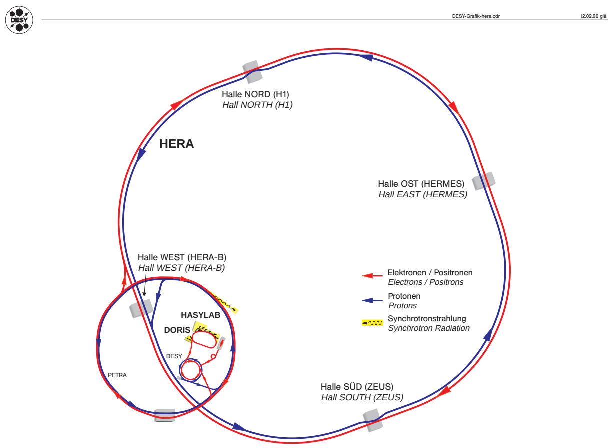

Figure 3: The HERA e-p ring at DESY in Hamburg.

the HERMES experiment in the east hall exclusively uses the polarized electron beam. The west straight section was rebuilt in the 1995/96 shutdown. All previously installed machine elements have been removed from the area to allow the installation of the 20 m long HERA-B detector in the west hall. In addition the optics was modified to comply with the various HERA-B requirements:

- low β function and low dispersion in the target area
- operation with the 2.1 Tm spectrometer magnet with both polarities and with switched off magnet
- compensation of the impact of the magnetic field on the polarization of the electron beam. Note that the HERA electron beam tube has to go through the detector, in 1 m distance of the proton beam tube, near the pole face of the HERA-B magnet.
- extent the proton collimator system to adopt to the new optics and to provide a powerful system to shield the other experiments against target induced background.

2.1 *HERA Proton Beam Parameter*

In Tab. 1 the typical proton beam parameter at the HERA-B target at WR09[3] are summarized. HERA operates at a proton energy of 820 Gev with currents up to 100 mA and with lifetimes of several hundred or even thousand hours. The protons are filled in 180 bunches with currents

HERA-p	x	y
Beta Function β	35 m	35 m
Alpha α	0	0.01
Typical emittance ϵ	$5 \cdot 10^{-9}$rad m	$4 \cdot 10^{-9}$rad m
spatial dispersion η	-470 mm	-1 mm
angular dispersion η'	-13.5 mrad	0
beam size σ	0.4 mm	0.35 mm

Table 1: Parameter of the proton beam at the HERA-B target position in 1996 and 1997. The horizontal direction is denoted by the index x, the vertical by y.

of around 0.5 mA ($7 \cdot 10^{10}$ protons), a bunch spacing of 96 nsec and a typical bunch length of 1 nsec. The detailed bx filling scheme is shown in Fig. 4.

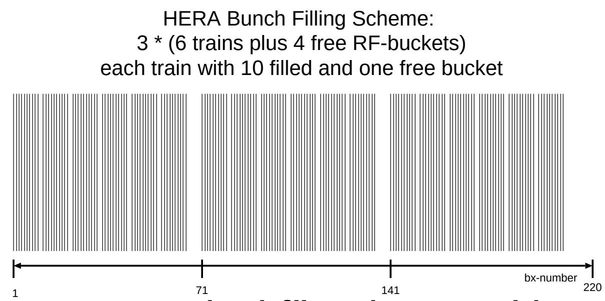

Figure 4: HERA p: bunch filling scheme. In total there are 220 RF buckets; the last 15 empty buckets are necessary to guarantee a secure beam dump.

2.2 *The Proton Collimator System*

The redesign of the proton collimator system [3, 5] required an optimized compromise between the limited available space, the capability to shield the other HERA experiments effectively against natural proton background and to catch protons, which are scattered under large angle in the target, before they hit the other HERA experiments [6]. The main design criteria is given by the optimum phase advance of secondary collimators with respect to the primary collimator or the target:

$$\Delta\phi^{opt} = m \cdot 180^o \pm \arccos(n_{p,t}/n_s),$$

where m is an integer number and $n_{p,t}, n_s$ are the amplitudes of the main collimator or target and the secondary collimator in units of beam sigma respectively. The system was built as a three stage collimator setup. The phase advances and the β functions are given in Tab. 2. A simulation code with particle tracking was developed to study the target induced background and the capability of the collimator system [7]. In the 1996 run it was proven that the collimator system has a high capability to catch scattered particles from the target and to shield the other experiments very efficient. This was a very important milestone in the cooperation with HERA and the HERA experiments; allowing long term high rate operation of the target.

[2]HERA operates usually with positrons - refered within this article as electrons.

[3]Notice the HERA naming convention used within this article: 4 quadrants (east, south, west and north) splitted in a right and left octant. Eg. WR09: WestRight - 9 m upstream of the west hall.

		Ψ_x/deg	type	β_x/m	η_x/mm	Ψ_y/deg	type	β_y/m	η_y/mm
KX0,KY0	WR094	0	p	140.1	-368.	0	p	79.0	5.6
KY1	WR033	-	-	-	-	27	s1	48.5	-13.5
Target	WR009	121	t	35.0	-470.	65	t	35.0	-1.
KX1	WL019	158	s1,t1	62.3	-87.	-	-	-	-
KX2,KY2	WL105	189	-	162.9	660.	182	t1	1040	-21.
KX3,KY3	WL150	209	s2,(t2)	41.6	510.	311	s2,t2	78.9	18.8

Table 2: Phase advance, beta functions and dispersion at collimators and targets. The following convention for the type notation is used: p -primary collimator, t - target, s1, s2 - two stages of secondary collimators for the primary collimator, t1, t2 - secondary collimators for the target.

2.3 Brief History: HERA and HERA-B Target

Since the first days of HERA operation the progress of the HERA-B target was closely related to the steadily ongoing development and improvement of the HERA proton ring.

1992: Shortly after HERA produced first e-p luminosity with 10 proton bunches and an integrated current of 1.5 mA first tests with the HERA-B target were carried out in autumn 1992. A simple test setup was installed in a freearea in the west right straight section at WR118. With one wire short term rates of 40 kHz with an efficiency up to 8 % have been achieved.

1993 HERA operates with 90 p-bunches and a current of 15 MHz. The target setup was significantly improved. With the four installed wires (movable pairs of wires at opposite beam sides with fixed distance) rates up to 8 MHz have been achieved. With a very simple setup of small drift chambers tracks pointing to the target has been observed.

1994 HERA is now operating with 50 mA of protons in 170 filled bunches. The natural lifetime of the p-beam exceeds 1000 h. To reach 40 MHz rate it was necessary to reduce the lifetime to less than 50 h; this didn't affect the HERA luminosity operation.

1995 The improved target mechanics allowed the independent movement of four wires from all four sides. Major improvements have been made in the automatic target steering, the monitoring and logging of external data (e.g. HERA information).

1996 HERA fills up to 80 mA protons in 180 bunches. The target with now 8 independent movable wires is mounted on the vessel of the HERA-B vertex detector system (VDS) and operated at the final location at WR09 with the final optics parameter. In long term high rate target operation the functionality and reliability of the HERA-B target has been demonstrated. A major milestone was the successful reduction of target induced backgrounds by means of the HERA collimator system, which opened the way for a successful corporation with the other HERA experiments. The distribution of the interactions along the target wire was measured with the vertex detector test setup.

1997 HERA exceeds 100 mA of filled proton current. The target is now nearly continuously in operation. Detailed investigation of the contributions of individual bunches gave solicitous results concerning the non proton bunch related interactions. A new wire insertion procedure helped to increase significantly the target running efficiency and to reduces the proton background and eases the optimization.

3 THE HERA-B TARGET

3.1 Requirements and Environment

The measurement of CP violation requires an interaction rate of around 40 MHz, i.e. 5 interactions per bunch crossing. One has to compare this with the natural loss rate of the proton beam. With a typical current of 80 mA (i.e. 10^{13} protons) and a lifetime of 100 hours the HERA proton beam just loses 30 MHz of protons. This demonstrates that the target has to collect very efficiently the protons before they get lost, and that the target has to scrape away protons from the tails of the beam in case the initial lifetime is too high. The target efficiency ϵ_T is defined as the ratio between the interaction rate in the HERA-B target and the total HERA proton loss rate, which is given by the current and the lifetime. A target efficiency above 50% is aspired not to reduce the proton lifetime below 50 hours. At this accepted level the target don't cut severely into the efficiency of the other HERA experiment because the HERA luminosity lifetime is usually less than 10 h, mainly determined by the electron lifetime and the emittance growth[4]. The interactions produced on the target follows the Poisson statistics:

$$p_\mu(n) = \frac{\mu^n}{n!} \exp(-\mu), \quad n = 0, 1, 2, 3, ...$$

where $p_\mu(n)$ describes the probability to observe n interactions in a bunch crossing (bx) if the mean number of interactions per bx is μ. The variance of the Poisson distribution is equal to the mean value μ, i.e. one gets a broad distribution. The capability of the HERA-B detector, optimized for a mean of five overlaid events, is limited by high occupancies and high radiation doses. The following lists summarizes the basic operation conditions to the target by means of the three most important efficiency requirements:

[4] $1/\tau_{lumi} = 1/\tau_p + 1/\tau_e + 1/\tau_{\epsilon-p} + 1/\tau_{\epsilon-e}$

Rate and Target Efficiency: To achieve the aspired rate of 40 MHz the impact on HERA and the other HERA experiments has to be small. This requires a very high target efficiency of at least 50% and an effective reduction of background produced in the target.

Running Efficiency: A nearly continuous operation of the target is necessary to obtain 10^7 sec measurement time within one year. The **target steering** has to be therefore very secure and has to avoid any harm or even the loss of the proton beam; which would then cost at least several hours to refill HERA. In addition it has to be very reliable, fast and easy to be operated. A proper **online monitoring** is necessary to recognize problems, e.g. in the rate stability or the background very early. And last but not least the **coordination** with HERA and the other HERA experiments is essential to obtain an effective use of filled proton beams.

Reconstruction Efficiency: Due to the limitations of the HERA-B detector capabilities in resolving events with very much interactions a constant rate without spikes but with equal distribution from all wires for all filled proton bunches is needed. In addition the interactions should come out of a small time window (≈ 1 nsec) within the 96 nsec bunch distance.

3.2 *Scattering on the Target and b Production*

Particles hitting the wire can interact or undergo quasi elastic scattering. At high energies (> 10 Gev) the cross sections depends only weak on the energy. The total cross section of protons impinging on a nuclei with atomic number $A > 4$ is given by:

$$\sigma_{tot} = 40\text{mb} \cdot A^{2/3}(1 + 0.5 \log_{10} A).$$

σ_{tot} is on the other hand given by the sum of the elastic and inelastic crossection ($\sigma_{tot} = \sigma_{el} + \sigma_{inel}$) with:

$$\sigma_{inel} = 33\text{mb} \cdot A^{2/3}(1 + 0.23 \log_{10} A).$$

The ratio σ_{el}/σ_{tot} can be parametrised within a few percent accuracy by:

$$\sigma_{el}/\sigma_{tot} = 0.205 \cdot A^{0.13}, \; A > 7.$$

The HERA proton beam energy of 820 GeV leads in a fixed target environment to a center of mass energy $\sqrt{s} \approx 40$ GeV, an energy not to fare above the b threshold. The background of normal inelastic interactions dominates b production by six orders of magnitudes. At HERA energies the gluon fusion processes, $gg \rightarrow b\bar{b}$, provides about 85% of the heavy quarks, the rest is produced by quark annihilation, $q\bar{q} \rightarrow b\bar{b}$. Fig. 5 shows the results of QCD calculations up to α_s^3 [8]. They predict a $b\bar{b}$ cross section of about 12 nb at 820 GeV beam energy, but with large uncertainties. The predicted value is in reasonable agreement with various measurements which also incorporates large uncertainties. This picture also clearly indicates that an increase in

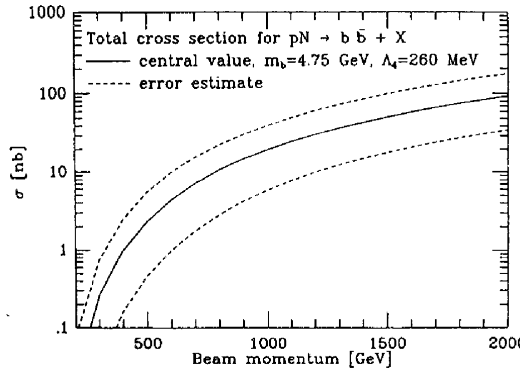

Figure 5: QCD calculations up to α_s^3 for $\sigma_{b\bar{b}}$.

the HERA proton energy, which is now under serious investigation[5] would increase the b-yield and therefore the signal to background ratio significantly. The $b\bar{b}$ cross section increases nearly linear with A:

$$\sigma_{b\bar{b}} = 12\text{nb} \cdot A^{0.98}.$$

Therefore the fraction of events with heavy quarks increases slowly with A. On the other side the mean number of tracks per interactions increases roughly like $\langle n \rangle = A^{0.2}$. For the experiment, mainly limited by the occupancy in the detector, one achieves a slight gain in the number of produced b quarks per interaction to the number of tracks per interaction in the range of 20-30% for heavy targets compared to light targets. There are more b's per interaction for heavy materials. Therefore one also gain in the number of vertices per bx - a number which is preferably small. But for the target material choice one has to take into account various other points like target efficiency, target induced background and momenta distribution of the tracks which usually prefers light materials.

3.3 *Basic Impacts on a Halo Target*

The basic idea of a halo target is to absorb protons which leaves the beam core and drift outwards and would get lost anyhow, and bring them to interaction in the target before they hit any aperture limitation in the beam tube. An efficient competition of the target with the collimators, which defines the aperture of the beam is needed. The interaction length λ_{int} of typical target materials is given in Tab. 3. A proton has to hit the 500μm long target several hundred times before an interaction occurs. Diffusion and the scattering in the target are the two important processes which determines the efficiency of the target. Fig. 6 shows a simplified sketch of the beam density with and without a target at the beam.

The number $N(t)$ of wire hits after t revolutions can be estimated by following consideration for a horizontally located target. The target wire is located at a position with a betatron amplitude T. A halo particle with given betatron amplitude $W > T$ occupy horizontal positions between

[5] For 1998 a run at 920 GeV is aspired.

Material	C	Al	Ti	Fe	Cu
Z	6	13	22	26	29
A	12.01	26.98	47.88	55.85	63.55
λ_{int}/cm	38.1	39.4	27.5	16.8	15.1
X_{rad}/cm	18.8	8.9	3.56	1.76	1.43
Θ_{sc}/μrad	24.	36.	47.5	52.	55.
$\langle\Delta$E$\rangle$/ MeV	438	433	360	382	380

Table 3: Atomic number A, mass Z, interaction length λ_{int}, radiation length X_{rad}, mean angular smearing Θ_{sc} and the mean energy loss $\langle\Delta\text{E}\rangle$ for various target materials.

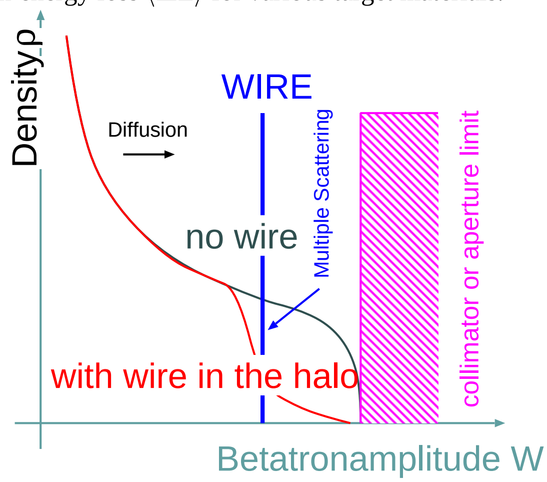

Figure 6: Basic impacts of a halo target.

$-W$ and $+W$ with $x(t) = W \cdot \sin\phi(t)$, depending on the betatron phase $\phi(t)$, see Fig. 7. Since the phase changes turn by turn with the tune Q, which is a not a simple rational number, the phase randomizes after several turns. The probability that the wire with horizontal width δ_x (typically 50μm) is hit can be approximated by:

$$dN/dt \approx \delta_x/(\pi\sigma_x\sqrt{W^2 - T^2}).$$

Depending on the detailed numbers and the coupling of the horizontal and vertical betatron motion one gets values of several ten-thousand to a few hundred-thousand turns before the proton interact in the wire, i.e. typical times in the order of a second.

Diffusion effects have a similar time scale and it is therefore important to consider them a little bit more in detail. The steep increase of the drift velocity v_D with the betatron amplitude W can be parametrised by:

$$v_D(W) = v_D(W_0)\left(\frac{W}{W_0}\right)^{\kappa}.$$

At a typical position of the target at 4 - 6 beam sigmas $v_D(W_0)$ lies between 0.1 and 10 σ/sec.

Before a proton gets absorbed it passes $N_{int} = \lambda_{int}/\delta_x$ times through the target and scatters in the target material. The total angular smearing due to scattering is given by:

$$\Theta^2_{sc} \approx \left(\frac{14\text{MeV}}{p}\right)^2 \cdot \frac{\lambda_{int}}{X_{rad}}.$$

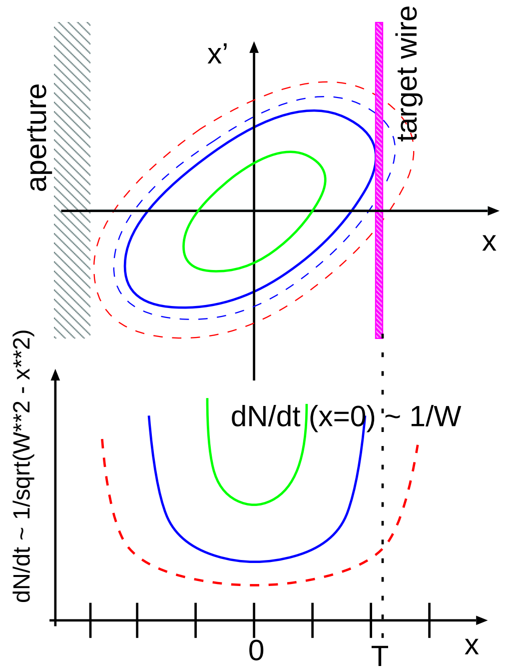

Figure 7: The horizontal phase space with a target wire at fixed position and the probability to find a particle at a given x position for particles with various betatron amplitudes.

Tab. 3 list this number for various materials and the HERA energy of 820 GeV. The scattering leads to an effective blow up of the beam which is determined by an increase of the squared betatron amplitude W:

$$\Delta(W^2) = \beta^2 \cdot \Theta^2_{sc};$$

a number which has to be compared with beam width $\sigma^2 = \beta^2 \cdot \epsilon^2 \approx 400\mu$m. Multiple scattering amounts therefore to a smearing of the betatron amplitude by a few σ which has to be added in quadrature to the betatron amplitude of the halo particles. The corresponding widening of the beam is one of the limiting factors to the efficiency of the target. The strong Z dependence of multiple scattering clearly prefers the use of light target materials. In addition a small β function is advantageous to minimize the widening of the beam.

Particles traverses the target also loses energy. The energy loss of 820 MeV protons per interaction length is summarized in Tab. 3. This energy loss leads to synchrotron oscillation in the longitudinal phase space and together with the non-vanishing dispersion in the target area to deviations from the design orbit in the transverse phase space. Some details will be discussed in section 5.5 in conjunction with the observation of non-bunch correlated interactions.

3.4 *Target Efficiency Simulation*

A simulation program was developed g[9] to study the basic properties of a halo target. Single halo particles are generated and tracked through the HERA proton machine until they are absorbed in the target or hit an aperture limitation. The particle tracking in linear optics uses single turn transport matrices, coupling is introduced artificially by a skew quadrupole. Diffusion is taken into account by the former given parametrisation; scattering and energy loss of protons in the target are simulated, losses or interactions are calculated. The simulation contains a lot of parameters, not all of them are well defined:

Geometries: the detailed information concerning the HERA ring geometries and its aperture limitation is rather complex and even not always well known. The simulation uses actually only one limit in each transversal direction; this seems to be a proper approach as long the collimator system defines the narrowest part of HERA.

Optics: The simulation assumes linear optics; the severe question is, whether the region outside 4 σ is dominated by nonlinear effects. At HERA nonlinear impacts are expected, e.g. the dynamic aperture or stable resonances in the halo region. But the very high intrinsic proton lifetime is an indication that the machine is even for larger betatron amplitudes in good approximation linear.

Diffusion: There exists just a poor knowledge and understanding about diffusion processes in the beam halo. Statistical physics with its basic transport equations together with some measured data provides the frame. The high proton lifetime and the interpretation of HERA-B target data indicates rather small drift velocities. A deeper understanding of beam halo dynamics is an important goal of actual and further target studies, and the simulation program is therefore a powerful tool.

Fluctuations: The real proton machine shows a wide variety of fluctuations and disturbances, something what is until yet neglected in the simulation.

The target efficiency is either limited by diffusion or by multiple scattering. In the first case more target material and material with larger Z improves the efficiency. But the HERA-B target is mainly dominated by multiple scattering[6]. Fig. 8 shows for this case the results of simulations with various target materials and different target positions for collimators located at 7 and 9 σ. The following list tries to summarize the most important results of the simulations:

- Low Z materials and low β are advantageous for the multiple scattering dominated case.
- To achieve $\epsilon_T \geq 50\%$ at least a 3 σ distance from the target to the aperture limitation is required.
- More material helps only in case of large diffusion.
- There is a good agreement between simulation and measurements, i.e. the main impacts are proper simulated. For the target operation point (4 - 5 σ) one gets similar absolute values for ϵ_T from the simulation.
- Fits to measurements over a complete scans requires usually a very steep slope for $v_D(s)$.

[6] due to the high proton lifetime. But diffusion still has an impact on the efficiency.

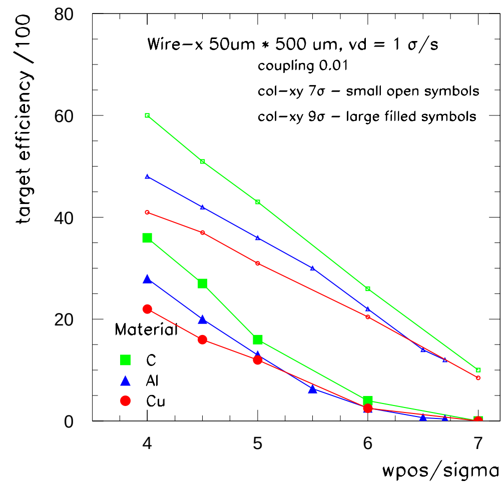

Figure 8: Target efficiency as function of the wire position for various target materials and two different collimator positions.

4 EXPERIMENTAL SETUP

4.1 Location and Mechanics

HERA-B uses a set of 8 ribbons with 50μm thickness parallel to the beam and 500μm length along the beam axis, which are positioned around the beam at a distance of 4 - 6 σ. The targets are grouped in two stations with a distance of 4 cm along the beam axis s. Within one station the 4 different targets are located at nearly equal s-positions and approaches the beam from all 4 different sides. Since the rebuilt of the HERA west right straight section the HERA-B target is located at WR09. The mechanics is mounted on a 2 m long vacuum vessel which mainly houses the HERA-B vertex detector system (VDS) [10]. Fig. 9 shows two photos of already mounted targets in the open VDS vessel. The targets are mounted on a ceramic fork and they are electrical connected to the outside of the vacuum vessel; providing a measurement of the interaction rate on a target by means of a induced charge measurement in the wire. The second photo shows a part of the RF shielding and the target cage in the VDS vessel. Protons are passing from right to left. The stepping motors which moves the wires have a nominal step-size of 50 nm. The precision and the clearance fit are in the μm range.

4.2 Counters and DAQ

Until yet mainly a test setup consisting of scintillating counters and silicon PIN diodes is used to monitor the targets. In 1996 the technical test run for the HERA-B sub-detectors, the various triggers and the data acquisition has started. The prototype detector delivers until yet mainly information for improved diagnostic, here esp. the VDS is very helpful (cp. Fig. 16). In the future the HERA-B detector will provide detailed information about rates, the contributions of individual wires etc. , which will be used for steering.

The DAQ system consists mainly out of scalers. ADCs,

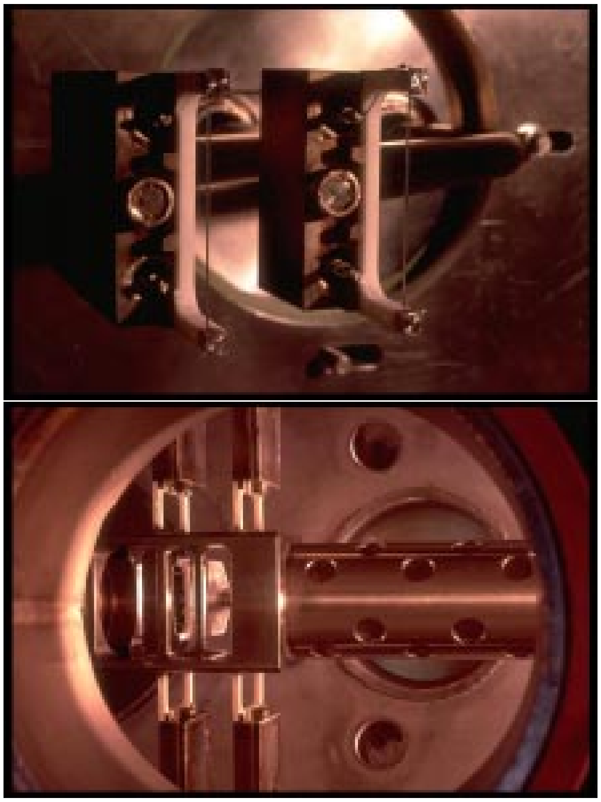

Figure 9: Targets mounted in the VDS vessel.

TDCs and especially a 40 MHz and 1 GHz FADC system provides detailed information e.g. on the event topology, the timing and the contribution of individual bunches. A large number of external data (HERA and other experiments etc.) are read from various online data servers and written into one common target online database. The target information (mainly rates and wire positions) is delivered through various servers to the other HERA-B subcomponents, to HERA, the other HERA experiments and is displayed online on the HERA WEB page[7]. The online monitoring is very essential, for the operation of the target as well as for the coordination with other groups. Already now usually at least 20 users request or display target informations.

4.3 Target Control

The target steering is based on direct measured rates and rather simple algorithm. To increase the rate the target moves in, to reduce the rate it moves out. Fig. 10 shows a sketch of the hardware setup. The steering code, implemented as a final state machine, handles fast beam finding, rate stabilization and equalization on several wires and it has to react very fast on emergencies. Security and to avoid any harm to the beam or other detectors is the highest priority in the steering concept. Therefore several levels of emergencies are implemented. The main steering takes place in a 10 Hz loop; rates are read out and the target movement is calculated, taking into account emergency conditions, the history and the slope of the rates. Close to the beam already a $\mathcal{O}$ (10 μm) step changes the rate by a factor of two. The equalization of individual wire contributions is just in a starting process. The test setup lacks from fast and significant measurements - but integrated low statistic devices shows already now very promising results. Finally the second level trigger will analyze vertex information of several kHz of events and provide the information to the target steering. Last but not least the target control has to be done by lot of different peoples on shift, i.e. it has to be very reliable and easy to run. TCC - the **T**arget **C**ontrol **C**enter provides therefore an easy to use graphical user interface.

[7] http://www-mpy.desy.de/desy-acc.html#HERA-B-Wire

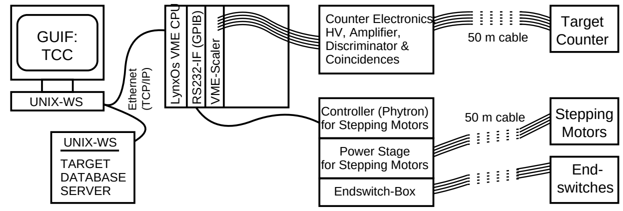

Figure 10: Setup of the **Ta**rget **Co**ntrol **S**ystem - TaCoS.

5 MEASUREMENT EXAMPLES

In the following section some basic properties and the performance of the HERA-B target are discussed on a few selected measurement examples.

5.1 Halo Target and Target Efficiency

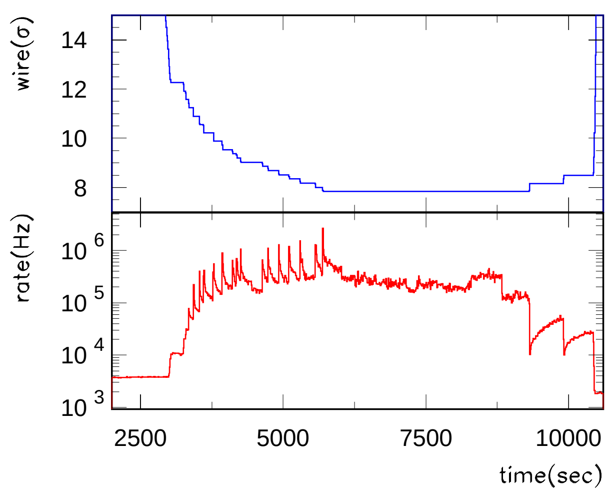

Figure 11: Target distance to the beam center and interaction rate as function of time.

Fig. 11 shows a typical target scan taken in 1993. After the target leaves the collimator shadow at about 12σ the trigger rate suddenly starts to rise. With each step towards the beam center the target scrapes away a part of the beam halo. This leads to a sharp rise in the rate which decays then within a few minutes to a new steady state. At a distance of about 8σ the rate remained at 200–300 kHz for about one hour. After retracting the target the rate drops suddenly and rises again until the halo is refilled. In Fig. 12 the target efficiency ϵ_T is shown for two different wire scans.

ϵ_T rises after the wire has left the collimator shadow at 12σ and becomes the dominating absorber if the target is moved closer to the beam. Efficiencies well above 50% have been reached. The importance of the collimator posi-

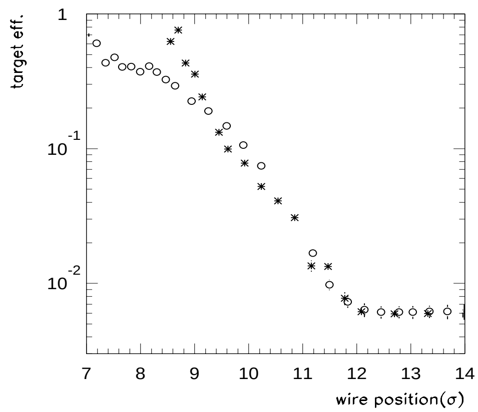

Figure 12: Target efficiency as a function of the distance to the beam center.

tion is demonstrated by the measurement shown in Fig. 13. Here the targets are kept at fixed positions and the collimator position is varied. The rate and the not plotted target ef-

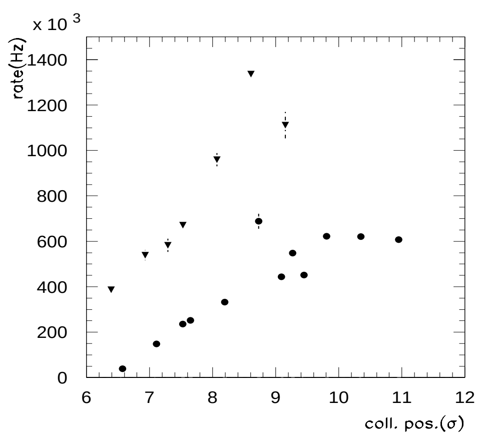

Figure 13: Interaction rate as a function of the collimator position. The targets are at fixed positions (dots: $\approx 6.5\sigma$; triangles: $\approx 5\sigma$).

ficiency ϵ_T rises with the collimator position. At around 9σ the aperture is limited by other devices, therefore no further increase is observed. To achieve high values of ϵ_T at least 3σ free aperture from the target position is required.

5.2 *Long Term High Rate Operation*

During the last years the feasibility of long term high rate target operations was proven. Fig. 14 shows a typical example with six hours continuous rates above 30 MHz, produced with four wires from one target station. The few large degradations (a) of the rate are triggered by the target emergency system, which retracts for safety reasons the wires to avoid huge spikes in the rate. During the run the targets move steadily closer to the beam (b) and scrape away protons from the bunch tails to keep the interaction rate constant. The wires approach to less than four sigma to the beam core. The scrapping of the beam leads to a clearly

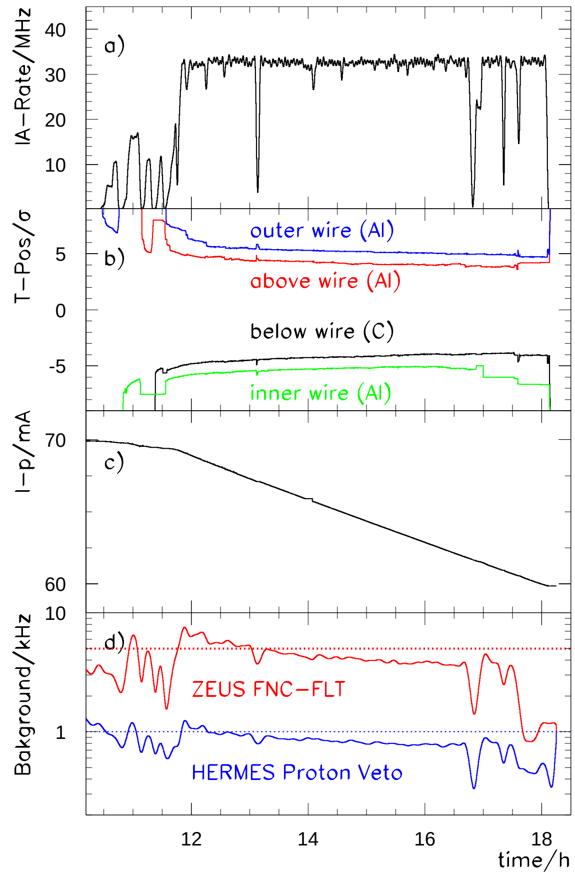

Figure 14: Interaction rate (a), wire position (b), proton current (c) and the two most critical background rates (d) of a typical HERA-B high rate target run.

visible reduction of the proton current and lifetime (c). In the above example the proton lifetime while high rate is between 45 h and 50 h. This results in a target efficiency ϵ_T between 60 and 65 %. Another important topic is the background at the other HERA experiments caused by large angle elastic proton nucleon scattering in the target wires. In Fig. 14 d) the both most critical background rates together with the limits for good running conditions are given. The limits for still acceptable background conditions are a factor of two higher. In the 1996 run it was proven, that the HERA optics modifications for the HERA-B experiment together with the extended and adjusted proton collimator system is very effective for the reduction of target induced background.

5.3 *Rate Stability and Fluctuations*

The investigation of the rate stability is a huge and very important topic because the efficiency of the final experiment relies on stable rates. The actual HERA operation conditions, with very high natural proton lifetimes, requires to aproach the targets close to the beam, scrape away protons and reduce the lifetime. The target operates at a very sharp edge of the beam, already μm steps alters the rate significantly. Artificial beam excitation to increase the halo population, e.g. by adding stochastic noise to a quadrupole and modulate the tune, could help to relax the situation. This is under serious investigation[8] and tests are planned for the 1998 operation. Fig. 15 illustrates that the interaction

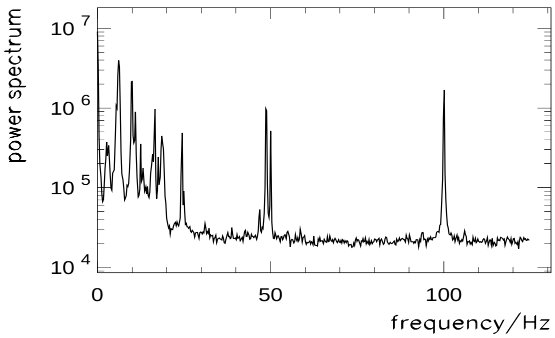

Figure 15: Power spectrum of the interaction rate showing typical lines from power supplies at 50 and 100 Hz but also lines from vibrations of machine elements.

rate (analyzed with a spectrum analyzer) presently reflects power supply lines and other external impacts.

5.4 Distribution of Interactions along the Wire

With the vertex detector installation in 1996 it was possible to measure the distribution of interactions along the target wires. Fig. 16 shows the transverse coordinates of track

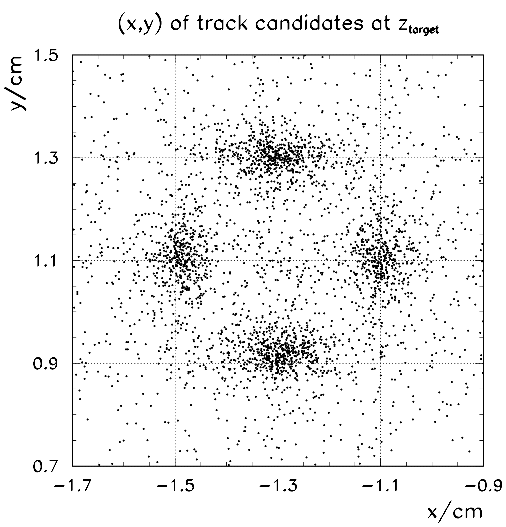

Figure 16: Target wires seen by the VDS.

candidates from the vertex detector plotted at the plane of the target wires. The clusters corresponds to individual wires. The background is purely dominated by combinatoric. The projection along the target wire has an rms-width around 500 μm, reflecting the intrinsic distribution on the wire folded with the vertex detector resolution of around 300 μm. The intrinsic width is therefore equal to the beam width of around 400 μm and not significantly smeared out by nonlinear effects in the beam halo.

5.5 Individual Bunch Contributions

The last topic discussed within this issue is the investigations of individual bunch contributions. All 180 filled HERA proton bunches contain usually within 10% the same current. For efficient data taking one aspires similar rate contributions from all bunches within a narrow time windows of 1 nsec width and equal distances of 96 nsec. Otherwise one loses efficiency due to high multiplicity events which cannot be resolved, low multiplicity events with less statistics and uncertainties in the drift-time measurement lowering the detector resolution.

Fig. 17 shows two measurements taken with a FADC system which samples the interaction rate signal with the fourfold bunch-frequency. The first measurement, taken

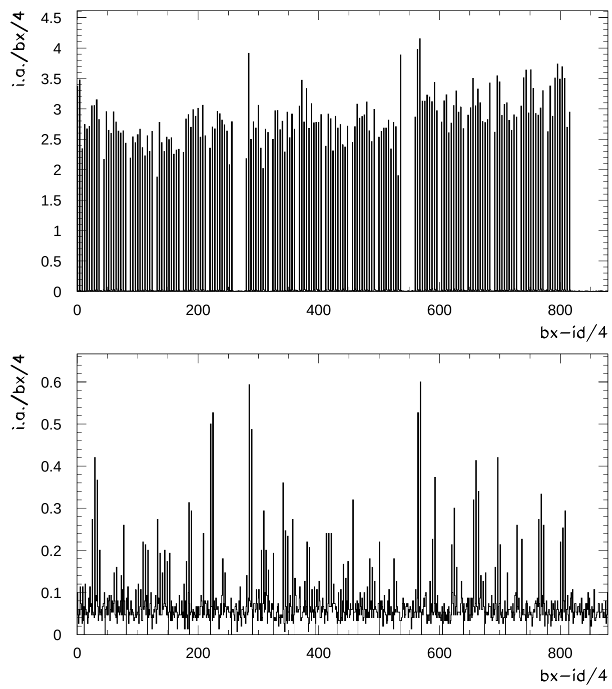

Figure 17: FADC measurement of individual bunch contributions.

with a wire at the inner beam side, reflects the bunch filling scheme; all 180 filled bunches contribute very similar and no interactions are coming out of the gaps between the bunches. The second example, taken with a wire on the outer beam side, indicates two problems:

BX-BX Variations: The individual bunches contribute very different. Similar shapes of the distribution are measured with wires from all sides. This indicates that the problem is most likely correlated with the emittance and/or the lifetime of the individual bunches. The problem originates most likely during the injection phase, caused e.g. by slight timing problems in one of the preaccelerators or the transfer to the next stage - and the protons preserve their history. In lot of examples one observes a systematic behavior which supports this explanation. HERA

[8] The problem is not to destroy the beam core and therefore the e-p luminosity.

is working on an improved timing and a feedback system, which hopefully cures this problem.

Non Bunch Correlated Interactions: Lot of interactions are not correlated with filled bunches. This is mainly observed on the outer beam side, no significant contributions are measured on the inner side. The amount of this out of proper time contributions varies from fill to fill. Within one fill these perturbing contributions saturates at a fixed level, exceeding in worse cases 10 MHz.

The reason for this non bunch correlated interactions is yet not finally verified. Most-likely it is correlated with the energy loss in the target and the dispersion in the target area. The mean energy loss of a 820 GeV proton (cp. Tab. 3) per interaction length is around 400 MeV, a value similar to the maximum momentum tolerance of the HERA proton RF system. Particles may cross the stable seperatrix in the longitudinal phase space and start to travel randomly along the beam tube. The horizontal dispersion in the target region shifts the orbit of theses particles by $\approx\ 0.5\sigma$ to the outer side, explaining that the effect is mainly absorbed on the outer side.

A simulation is under development to study this more in detail and to obtain a quantitative understanding, which is until yet missing. But the expectations into the simulation are limited, because as soon as additional nonlinear effects in the beam halo and interferences between the horizontal and vertical phase space are getting important one ends up with a rather complex and challenging beam dynamics study project. Therefore it's quite important to investigate the problem in some dedicated machine shifts in 1998; basic studies are the altering of the RF voltage and the movement either of the beam or of collimators at high dispersion points.

6 CONCLUSIONS

The HERA-B target is studied and improved since several years. Most of the fundamental problems like target efficiency ϵ_T, background and running efficiency are understood and solved. On its way to a full operational device it operates very reliable and is already now in nearly continuous operations. Open problems and subjects of further improvement are fluctuations, rate stability and the non bunch correlated interactions. As until now also further progress requires a close cooperation and the support of the HERA machine group. There is a very strong, but quite fruitful, interference and interaction with HERA; most problems can only be solved in a combined effort.

The HERA-B target operates not only near beam, but very close at the beam. Therefore it is a very sensitive device for beam diagnostic and it opens a wide area to study beam dynamics like halo population, diffusion, instabilities, fluctuations etc.

7 ACKNOWLEDGMENTS

The author likes to thank all members of the HERA-B target group for the enormous work they did. A cordial thanks to Thomas Lohse for providing his detailed knowledge, the simulation tools and his cooperation to resume, explain and discuss target related topics. A special thanks to the HERA shift crew and especially to F. Willeke and M. Seidel for all their support and the friendly collaboration. Thanks to the other HERA experiments for accepting us as the fourth HERA experiment. This work was supported by the Bundesministerium für Bildung, Wissenschaft, Forschung und Technologie under the contract number 057DO55.

8 REFERENCES

[1] 'HERA-B Proposal', by T. Lohse et al., DESY-PRC 94/02, 1994.

[2] 'Test of internal halo targets in the HERA proton ring', by C. Hast et al., NIM A354, 1995.

[3] 'HERA-B Design Report', by E. Hartouni et al., DESY-PRC 95/01, 1995.

[4] 'Near Beam Physics at HERA', by M. Bieler, this conference.

[5] 'The Proton Collimation System of HERA', by M. Seidel, DESY 94-103, 1994.

[6] 'Study of Background Caused by Scattering at the HERA-B Wire Target', by M. Seidel, DESY HERA 95-04, 1995.

[7] 'Simulation of Target Induced Background', by T. Lohse, private communication.

[8] P. Nason, S. Dawson and R.K. Ellis, *Nucl. Phys.* B **303**, 607 (1988), B **327**, 49 (1989), B **335**, 260 (1990).

[9] 'HERA-B Target Efficiency Simulation' by T. Lohse, private communication.

[10] 'HERA-B' by C. Hast, this conference.

A Forward Proton Detector at DØ

Andrew Brandt[1]
Fermi National Accelerator Laboratory, P.O. Box 500, Batavia, IL 60510; brandta@fnal.gov

Abstract

The addition of a Forward Proton Detector (FPD) as a new sub-detector of the DØ detector for Run II is discussed [1]. This paper describes the physics motivation for the FPD as well as its location and performance.

1 PHYSICS MOTIVATION

1.1 Overview of Diffractive Physics

Quantum Chromo-Dynamics (QCD), the current theory for strong interactions, has been very successful at describing and predicting many areas of particle physics. Its successes are limited, however, to the perturbative regime where the strong coupling constant is small. About 40% of the total $p\overline{p}$ cross section at the Tevatron is composed of elastic and diffractive scattering which are non-perturbative and cannot currently be calculated in QCD.

The properties of elastic and diffractive scattering are well-described by the phenomenology of pomeron exchange (Regge theory), where the pomeron is a color singlet with quantum numbers of the vacuum. The literature on diffractive dissociation is extensive and a few review articles are given in Ref. [2]. Regge theory predates the quark-gluon model, and it is not clear how to combine it with QCD. Definitions of the pomeron vary from a theoretical definition: "the highest Regge trajectory with quantum numbers of the vacuum, responsible for the growth in the hadronic cross section with $\sqrt{s}$ ", to an experimental one: "the thing that causes rapidity gaps". Many experiments have studied diffractive and elastic scattering at different center-of-mass energies, but due to the non-perturbative nature of the interactions, insight into the underlying process has been limited. The exact nature of the pomeron (Is it composed of quarks and gluons? Is it hard or soft? Is it the same object as a function of momentum transfer?) remains elusive, although recent theoretical ideas and experimental results are beginning to yield some answers. This brings us to the rather new field of hard diffraction.

Ingelman and Schlein [3] proposed that the observation of jets in diffractive events would probe the partonic nature of the exchanged object, whether it is the pomeron or something else. Their paper introduced the field of hard diffractive scattering, which refers to the subset of traditional diffractive interactions characterized by high transverse momentum (p_T) scattering. They assumed that the pomeron can be treated as an object that exists within a proton, and that it is thus sensible to define a flux of pomerons in the proton as well as a pomeron structure function. They proposed a gluonic pomeron with either a hard structure, as would be derived from two gluons sharing the pomeron momentum $\sim \beta(1-\beta)$, or a soft structure like the gluonic structure of the proton $\sim (1-\beta)^5$, where β is the momentum fraction of the parton with respect to the pomeron. With these assumptions they were able to make predictions for diffractive jet production cross sections and properties.

Figure 1 shows the diagram for hard single diffraction producing two jets, a scattered $\overline{p}$, and a rapidity gap (absence of particles in a certain region). This topology can either be tagged using a small angle spectrometer to detect and reconstruct the leading proton, or by the presence of a rapidity gap.

The first experimental results on this subject were published by the UA8 Collaboration at CERN, and showed the existence of jets in events with leading protons and that these jets had rapidity and longitudinal momentum distributions consistent with a hard pomeron structure [4]. There was also evidence for a "super-hard" or "coherent" pomeron, where the entire momentum of the pomeron participates in the hard scattering.

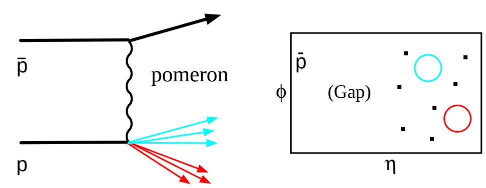

Figure 1: The diagram for a hard single diffractive interaction resulting in a final state with a scattered $\overline{p}$ and two jets. The η–ϕ plot shows the distribution of particles in this event including a rapidity gap near the scattered $\overline{p}$ and the circles which represent the two jets.

The study of hard diffractive processes has expanded dramatically in recent years and includes diffractive jet production at HERA and the Tevatron [5, 6, 7], diffractive W boson production [8], and rapidity gaps between high transverse energy jets [9, 10, 11, 12]. The available data samples, however, are generally statistically limited and do not have information about the scattered protons. The addition of large and precise data samples obtainable with the aid of the FPD will help to develop a more coherent picture of the pomeron.

1.2 Advantages of the FPD

Although rapidity gap studies can be used to gain some insight into the nature of the pomeron, these studies can be vastly improved through the addition of a Forward Proton Detector (FPD). Tagging the forward proton removes the ambiguity of a rapidity gap tag, which suffers from background due to low multiplicity non-diffractive events. The rapidity gap tag also does not give information on whether the scattered proton remains intact or is excited into a low-mass state, which could still yield a rapidity gap.

[1]For the DØ Collaboration

By detecting the scattered proton, one can measure its momentum (p) and thus derive two key variables $x_p = \mathrm{p}/\mathrm{p}_{\mathrm{beam}}$, the fractional longitudinal momentum of the scattered proton, and $t = (\mathrm{p}_{\mathrm{beam}} - \mathrm{p})^2$, the four-momentum transfer to the proton. Rapidity gap techniques do not give access to these two variables and thus lose important information about the diffractive process. The momentum fraction of the pomeron (ξ) is simply related to the momentum fraction of the proton by $\xi = 1 - x_p$. A measurement of the proton momentum thus gives the diffractive mass M_X through the equation $M_X = \sqrt{\xi} \cdot \sqrt{s}$, where $\sqrt{s}$ is the center-of-mass energy. The $|t|$-dependence of single diffraction has been measured to be $d\sigma/d|t| \sim e^{-b|t|}$, where $b \approx 6$ for inclusive single diffraction at $\sqrt{s} = 1800$ GeV [13]. The exact slope has a mild dependence on $\sqrt{s}$ and M_X, and has not been measured for hard diffractive events.

The ability to obtain large data samples and divide the data into mass bins facilitates the comparison of the data with theory in the form of phenomenological Monte Carlos, and allows studies of the pomeron structure in the pomeron-proton center-of-mass.

The use of a scattered proton as the diffractive tag also allows the full rapidity range of the detector to be exploited to study the diffractive system. This would in turn allow a search for the effects of the super-hard pomeron, which is expected to frequently result in back-scattered jets in the rapidity interval normally used to tag rapidity gaps. The super-hard pomeron is of great theoretical interest [14], part of which stems from the fact that if the entire pomeron momentum participates in the hard scatter, there is a dramatic increase in the cross section for the diffractive production of heavy objects, such as b quarks [15]. The cross section for hard double pomeron exchange is also enhanced by super-hard pomeron exchange [16, 17].

Hard double pomeron exchange, in which both the incoming proton and anti-proton emit a pomeron and the two pomerons interact to produce a massive system, can be studied effectively using the FPD. With both arms instrumented it would be possible to measure both the proton and anti-proton using the FPD, and jets using the central calorimeter. At the Tevatron a central system of about 100 GeV could be produced.

Although much can be learned about the pomeron at HERA, there are distinct advantages to studying hard diffraction at the Tevatron. Diffractive systems with mass greater than 450 GeV/c^2 can be produced at the Tevatron compared to only 70 GeV/c^2 at HERA. This allows for the production of high p_T objects at the Tevatron (such as W or Z bosons) as well as large jet cross sections. The super-hard pomeron can best be studied at the Tevatron; at HERA it can result only from a higher twist diagram, which is suppressed. Double pomeron exchange cannot be studied at an ep collider. Finally, one of the key results will stem from the comparison of pomeron structure in ep and $p\overline{p}$ collisions. If the pomeron behaves like a particle it should have consistent structure independent of the nature of the probe (electron or proton).

1.3 Physics Motivation Summary

The dramatically expanding field of hard diffraction has been driven by experimental results. More precise results are needed to improve the understanding of the nature and structure of the pomeron and distinguish between different theoretical models. There is a rich, timely program of physics that can be accessed with the addition of the FPD to the DØ experiment. This includes

- Studies of pomeron structure using diffractive jet production, including the dependence on ξ and $|t|$.
- Search for diffractive production of heavy objects and combining different hard diffractive channels to determine the quark and gluon content of the pomeron.
- Search for the super-hard pomeron.
- Studies of double pomeron exchange.
- Search for "new physics" such as glueballs, centauros, and Higgs bosons.
- Determination of pomeron universality in conjunction with HERA results.

The understanding of strong interactions is incomplete without inclusion of soft and hard diffractive processes. The Tevatron is the ideal collider to study this physics due to the large center-of-mass energy available, and the addition of the FPD will greatly augment the physics capabilities of the DØ detector.

2 THE FPD LAYOUT AND ACCEPTANCE

The Forward Proton Detector is a series of momentum spectrometers which make use of machine magnets along with points measured on the track of the scattered proton (or anti-proton) to calculate its momentum and scattering angle ($\theta \sim \sqrt{t}$). The points are measured using detectors located in Roman pots, which are typically stainless steel pots or containers that allow the detectors to function outside of the machine vacuum but close to the beam. Particles traverse thin steel windows at the entrance and exit of each pot. The pots are remotely controlled and can be moved close to the beam (within a few mm) during stable beam conditions and retracted otherwise.

2.1 Dipole Spectrometer

Figure 2 shows the proposed location of the Roman pots that will comprise the Forward Proton Detector, where A refers to the outgoing anti-proton side, P the outgoing proton side, Q represents the low beta quadrupole magnets, D the dipole magnets, and S the electrostatic separators. The dipole spectrometer consists of two Roman pot detectors (A_{D1} and A_{D2}) located after the bending dipoles about 57

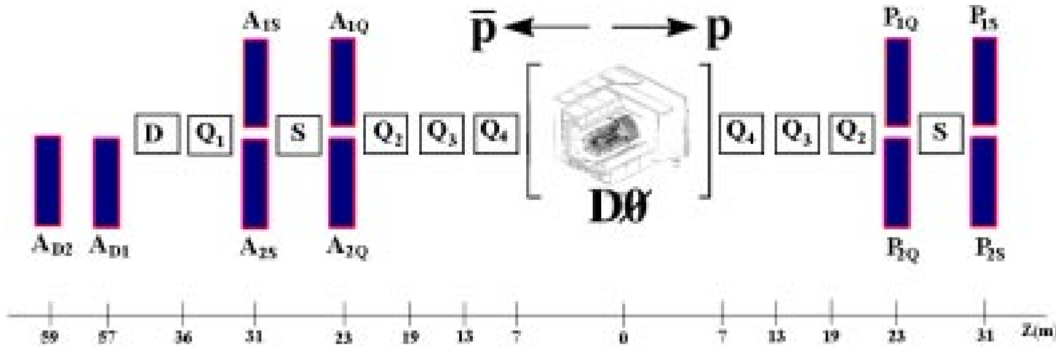

Figure 2: Placement of Roman pot detectors near the DØ interaction region. The horizontal scale shows the distance from the interaction point in meters. Each of the independent momentum spectrometers consists of two Roman pots (represented by black rectangles) in combination with the machine magnets as described in the text.

meters downstream of the interaction point on the outgoing $\overline{p}$ arm. The other Roman pots in the figure are components of the quadrupole spectrometers discussed in the next section. The dipole spectrometer pots are located inside the Tevatron ring in the horizontal plane to detect scattered anti-protons that have lost a few percent of the original beam momentum. These are the equivalent positions of the CDF pots (E-876) [18] which were added at the end of Run I. There are no known obstacles to implementing this portion of the FPD as the optics are roughly the same at CDF and DØ, and there is space available at the equivalent location near DØ. It is not possible to instrument the outgoing proton side with a dipole spectrometer without major modifications to the accelerator (not being considered).

A single dipole spectrometer with acceptance characteristics similar to that of the Run I CDF spectrometer has two principal limitations: hard double pomeron exchange cannot be studied using p and $\overline{p}$ tags since only the $\overline{p}$ arm is instrumented, and the acceptance is restricted to a relatively large ξ region where the backgrounds from other processes are large and hard to understand.

To remove these limitations, the FPD discussed in this document is optimized to improve the acceptance and also includes quadrupole spectrometers.

2.2 Quadrupole Spectrometers

There is currently no space near DØ for Roman pots other than for dipole spectrometer pots A_{D1} and A_{D2}. The instrumentation of both the outgoing proton and anti-proton arms requires modifications to the machine lattice to create space for the detectors. The proposal here involves moving the three low beta quadrupoles on each side (Q_4, Q_3, and Q_2) about two-thirds of a meter closer to the interaction region, in order to create two one-third meter spaces for the Roman pot stations. Roman pots would be located at either end of the electrostatic separators, which would be moved one-third of a meter closer to the interaction region. The area within the bypass is the only "warm" section of beam pipe in reasonable proximity to the DØ detector, and is thus the obvious choice for the location of Roman pots.

Preliminary studies indicate that the quadrupoles can be supported while maintaining or even reducing the current deflection of the closest quadrupole without a major redesign. This can be accomplished by reinforcing and lengthening the shelf that extends from the main girder that currently supports the quadrupoles. Preliminary studies of the bypass modifications indicate that this is a minor modification assuming that a sufficient vacuum is maintained. Complete engineering studies are in progress.

The FPD thus will consist of six Roman pot stations, the aforementioned A_D, which has two stations, plus four stations that use the quadrupole magnets to measure the proton (P_Q and P_S) or anti-proton (A_Q and A_S) trajectory instead of the dipole magnets.

An ideal proton detector would be an annular detector with full ϕ acceptance close to the beam. Since it is necessary to remove the detector during injection of the beam for stability and radiation considerations, such a design is impractical. The proposal maximizes the acceptance for protons and anti-protons by allowing pots in both the horizontal and vertical planes.

With this design there are eight independent quadrupole spectrometers, four on each side of the interaction region (two each in the x and y directions). This gives a total of 18 pots, 2 dipole pots and 16 quadrupole pots. An example of a quadrupole spectrometer is the P_1 spectrometer (first proton spectrometer) shown in Fig. 2, which has the pot P_{1Q} located after the Q_2 quadrupole about 23 m from the interaction point, and P_{1S} located about 31 m from $z = 0$. A proton deflected to the left of the beam axis would be detected in this spectrometer while a proton scattered to the right would be detected in the P_2 spectrometer in pots P_{2Q} and P_{2S}. There would also be P_3 and P_4 spectrometers (not shown in Fig. 2 for simplicity) for protons scattered above and below the beamline. Analogous spectrometers are located on the anti-proton side.

2.3 Tracking Studies

To study the acceptance of the spectrometers, we used a tracking program provided by the Beams Division [19]. This program tracks particles through each element of the lattice, using the measured lengths and magnetic fields of the elements. The Run II beam energy of 1 TeV was assumed in the lattice calculations, and a modified version of the dispersion-free lattice taking into account the moved quadrupoles was used [20].

The acceptance is critically dependent on the distance of the detector from the beam axis, which depends on the beam width (σ). Table 1, which is extracted from a detailed study of the background from accelerator losses [21], shows the 8σ beam widths at the proposed Roman pot locations (dipole pots are only useful in the horizontal plane). Roman pots placed at 8σ from the beam could detect scattered p's and $\overline{p}$'s with displacements larger than than this. A comparison of the Q and S rows of the table for p's and $\overline{p}$'s reveals that for this lattice the horizontal plane for protons is equivalent to the vertical plane for $\overline{p}$'s and vice versa.

Roman Pot Station	$8\sigma_x(\mathrm{mm})$	$8\sigma_y(\mathrm{mm})$
A_{D1}	5.64	-
A_{D2}	5.01	-
A_Q	14.5	6.77
A_S	13.1	4.61
P_Q	6.78	14.4
P_S	4.66	13.0

Table 1: 8σ positions at the Roman pot locations.

The tracking program is used to map out the acceptance in $|t|$ and ϕ. For a track to be accepted, it must remain within the beam pipe (inner radius of 35 mm) and within the separator aperture (25 mm). It must also pass through the active area of the detector in both pots, which is assumed to cover $x_{min} < x < x_{min} + 20$ mm and $-10 < y < 10$ mm for horizontal pots (x and y are interchanged for vertical pots). The x_{min} (y_{min}) values are obtained from the $8\sigma_x$ ($8\sigma_y$) column in Table 1.

The acceptance is maximized by minimizing the distance between the detectors and the beam axis. This distance is limited primarily by the halo rates which increase as the pots are inserted closer to the beam. Using an initial intensity of 10^{13} protons per bunch, we have determined that the beam halo rates for an 8σ pot location are on the order of 10^5 protons/second in the quadrupole pots [21], and a factor of two higher in the dipole pots. The halo rates decrease by about a factor of three at 9σ and sharply decrease further with larger pot displacements. There is some dependence on the assumptions and exact collimation scheme, which has not been tuned to minimize the rates at the pot positions. The real rates will have to be measured and the exact pot displacements will then be determined. The current studies indicate that a reasonable pot location is between 8 and 9σ for quadrupole pots and 10σ for dipole pots.

2.3.1 Spectrometer Acceptance

A proton is considered to be accepted by the spectrometer if it passes through the active area of both detectors while remaining within the limiting aperture of the beam pipe throughout its entire trajectory. The acceptance is determined as a function of the initial conditions of the anti-proton (ϕ, $|t|$, and ξ). The geometric (ϕ) acceptance of the (a) quadrupole spectrometers at 8σ (b) dipole spectrometer at 10σ is shown in bins of ξ and $|t|$ in Fig. 3. The size of the boxes are proportional to the geometric acceptance with the larger boxes representing larger acceptance. A quadrupole spectrometer requires a minimum angle or $|t|$ to accept scattered protons, while a dipole spectrometer requires a minimum momentum loss, resulting in the different behavior observed in the two parts of the figure. For the quadrupole case there is no acceptance for $|t| < 0.5\,\mathrm{GeV}^2$, but the intermediate and high $|t|$ geometric acceptance are quite good, while for the dipole case the acceptance is especially good for $0 < |t| < 0.5$ GeV^2 and high ξ ($\xi > 0.02$).

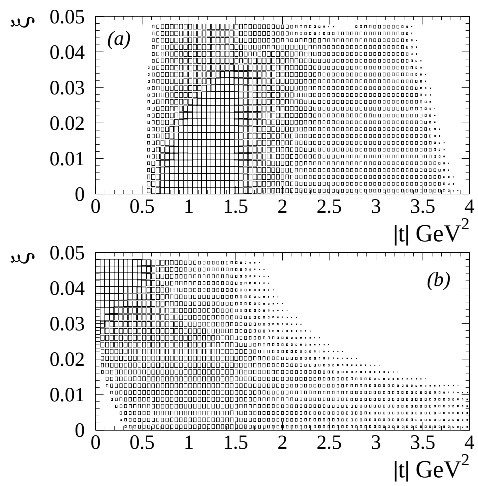

Figure 3: The geometric acceptance in bins of ξ and $|t|$ for (a) the quadrupole spectrometers (p or $\overline{p}$) at 8σ displacements (b) the dipole spectrometer ($\overline{p}$ only) at 10σ displacements. The acceptance in each bin is proportional to the size of the box, with the largest box representing 83(100)% acceptance for the quadrupole (dipole) spectrometers.

We calculate the total acceptance by integrating over the ϕ and $|t|$ values accepted by the pots. The $|t|$ dependence is included using the relation $d\sigma/dt \sim e^{-b|t|}$, where $b = 4.2 - 0.5ln(\xi)$ from Ref. [13]. This expression is valid for single diffractive and most likely double pomeron events, but for elastic events $b \approx 17$ [22]. The total acceptance is dominated by the $|t|$ acceptance, since the cross section falls so steeply with $|t|$. For the quadrupole case, the total acceptance has little ξ dependence and is stable at about 1.4%, whereas the dipole acceptance ranges from a couple percent at ξ near zero to 35% at an intermediate $\xi = 0.02$ and 96% at $\xi = 0.05$.

The situation for the DØ dipole spectrometer will be much improved over the Run I CDF case which had little acceptance for $\xi < 0.05$. The Roman pot design under consideration, discussed in Sec. 3.1, should result in a dead area on the order of 100 μm, instead of a few millimeters. The separation of the beams is more advantageous at the DØ location, with the $\overline{p}$ beam located 0.3 mm closer to the pots than the proton beam [23]. We will be preparing for a long run and will have adequate time to study the halo rates in order to minimize the pot displacement. The long running period will allow us to obtain large data samples even if the acceptance were significantly less than 1%. We consequently expect to have acceptance to ξ near zero.

The total acceptance in general does not depend strongly on the width of the active area of the detector, as the bulk of the acceptance is in the center of the detector. Doubling the width from 2 to 4 cm only increases the overall acceptance by a few percent of its nominal value, since this only improves the acceptance for very rare high $|t|$ events, and decreasing the width from 2 to 1.5 cm also has little effect.

As mentioned earlier, the total acceptance is quite sensitive to pot position, decreasing by about a factor of three for each additional σ unit. The acceptance is also sensitive to the final details of the lattice (which could affect the acceptance by roughly a factor of two in either direction), and the emittance (which would affect the acceptance if it is much smaller or larger than the expected value).

We have also studied the issue of beam crossing angles, which may be needed in the case of 132 nsec running to avoid parasitic collisions [24]. The addition of a crossing angle does not dramatically affect the acceptance. It results in a slight improvement for the dipole pots by moving the proton beam further away from the pots. For the quadrupole pots, the acceptance is improved for some spectrometers and degraded for others with an overall effect of less than a factor of two. The addition of a crossing angle, although not desirable from complexity and symmetry arguments, does not significantly affect the overall acceptance and does not compromise the goals of the FPD.

2.3.2 Resolution

The transport matrix obtained from the tracking program can be used to derive the resolution expected from the spectrometers. The position resolution depends on the point resolution of the detector and multiple scattering, which are estimated to be about 0.1 mm and 0.04 mm, respectively, for the detector discussed in Sec. 3.2. It is also sensitive to the uncertainty in the beam position at the pot locations. The average beam position can be measured very well using elastic events, and deviations from this position are expected to be about 0.1 mm [21]. Adding these resolutions in quadrature gives a position uncertainty of about 0.15 mm. This yields estimated resolutions of $\delta\xi = 0.0012$ and $\delta t = 0.018\sqrt{t}$. In practice, the $|t|$ resolution is dominated by the 0.06 mrad angular dispersion of the beam, which corresponds to $\delta t = 0.12\sqrt{t}$.

2.4 *Acceptance Summary*

Tracking studies show that with reasonable assumptions about Run II conditions, the Forward Proton Detector will have quite good acceptance for detecting scattered protons and anti-protons. The dipole spectrometer has excellent acceptance for anti-protons, especially at low $|t|$ and high ξ. The addition of quadrupole spectrometers allows the tagging of protons, and thus double pomeron and elastic events (which are crucial for alignment and calibration), as well as generally improving the intermediate and high $|t|$ acceptance. Our design with spectrometers in both the horizontal and vertical planes makes this acceptance very robust, and insulates us against accelerator uncertainties. Although the $\overline{p}$ quadrupole pots have inferior total acceptance to the dipole pots, they improve the $|t|$ coverage, are crucial for elastics and halo rejection, and will allow the calibration of the dipole spectrometer.

3 DETECTORS

3.1 *Roman Pots*

Figure 4 shows a sketch of the front view and the side view of a Roman pot. Each pot is a small steel box that completely encases the scintillation fiber detector (described in the next section) and keeps it isolated from the machine vacuum, although the pot itself remains inside the machine vacuum. The dimensions are labelled on the figure and show that the pot is very compact, with a length of only 3.8 cm along the beamline, a height of 13 cm, and a width of 7 cm. The width and height are determined by the bending radius of the fibers. The pot will be fully retracted in a bay area for beam injection, and can be moved into the beam pipe at a position close to the beam for normal running. A small diameter bellows surrounds the cylindrical chimney and supports the structure. The chimney is used to route the fibers to the phototubes.

The Roman pot is composed of 2 mm thick steel except for a thin window which brackets the active area of the detector traversed by the scattered protons. The window is composed of a 50 μm stainless steel foil in order to reduce multiple scattering. Once the detector is placed inside the box, a steel lid with a cylindrical chimney is welded to the top of the box. A low viscosity epoxy will be injected through the chimney in order to fill the remaining space on either side of the detectors, thus creating a solid one-piece detector. The box design produces the smallest possible pot, reducing the space needed in the beam pipe region. This allow us to have pots in both the x and y planes in order to maximize the acceptance. Another advantage of this design is a much lower cost relative to standard Roman pot designs which are at atmospheric pressure on one side, and require a pressure compensation system to combat the forces caused by the imbalance in pressure between the inside and outside

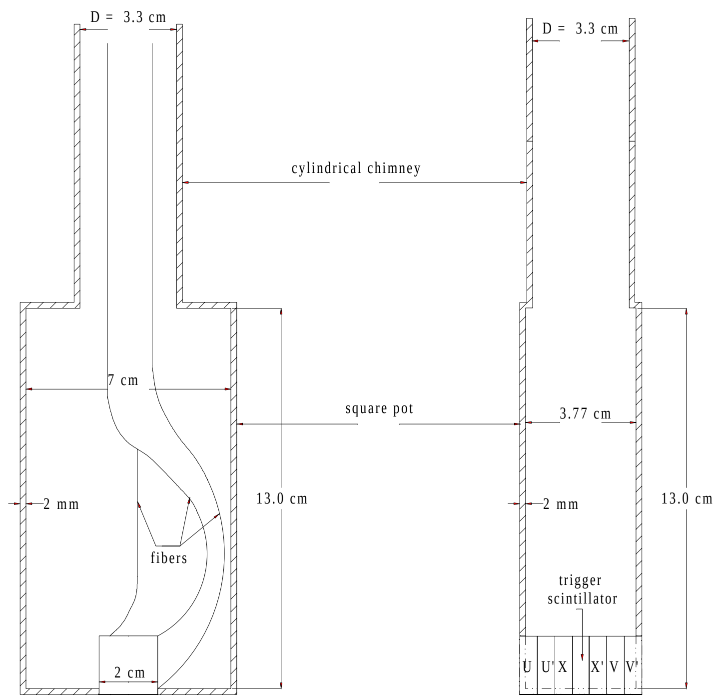

Figure 4: A front and side view of the Roman pot and detector described in the text.

of the pot. Our design also only requires a small diameter bellows and a small range of motion.

A stepping motor drives a cam system that moves the pot along the direction of the chimney axis. A system of bearings keeps the box movement from deviating from the direction perpendicular to the beam line. The position sensing system is based on two high precision linear potentiometers (LVDT's), one performing the primary position measurement and the second providing redundancy. The whole positioning system will be capable of a displacement precision of better than 25 μm.

3.2 Detectors

Each Roman pot contains a small scintillator for triggering and timing and a six-plane scintillating fiber detector, which is used to determine the (x, y) coordinate of the deflected proton at the pot position. The detector is comprised of stacked ribbons of four fibers oriented such that the scattered proton (or anti-proton) would pass through all four fibers to maximize the light output. The stacked ribbons have a one-third ribbon width spacing.

The use of 0.8×0.8 mm square scintillating fibers would allow a theoretical resolution of about 80 μm. The estimated radiation dose of the detector is 0.03 Mrad per year of normal running. A full hit by the proton beam corresponds to 0.3 Mrad, or ten years of normal run. Studies have shown that a 1 Mrad dose reduces the fiber attenuation length to 40% of its original value [25]. However, due to the short length of our fibers (2 cm) the reduction in attenuation length is not important even with several beam accidents.

3.2.1 Fiber Readout and Trigger

The scintillating fibers are connected to clear fibers that are bundled together in groups of four and connected to one channel of a multi-anode photomultiplier tube (MAPMT). Four fibers per channel will give about 10 photoelectrons and fit comfortably within the pixel size of the MAPMT, which has good gain uniformity among its 16 anodes with negligible cross-talk. There will be 112 channels per pot, so seven 16 channel tubes will be required for each pot.

The MAPMT's can be read out by a standard Central Fiber Tracker (CFT) trigger board, with one trigger board required for each of the nine spectrometers. The total number of channels needed per spectrometer is 224 which is well below the trigger board limit of 512 channels. The signals from the MAPMT will be passed through the existing front-end chip, modulo the minor modifications to the components necessitated by the exact signal size and shape. These boards were designed to allow for different input signals since they are being used by the central and forward preshower detectors in addition to the central fiber tracker, thus the modification of these components will not be difficult or costly. The front-end chip outputs signals to the SVX-II chip [26] for digitization. The SVX-II chip will then store the information from the fiber hits in the standard event data block. The front-end chip also outputs a TTL signal for use in the trigger logic.

The Level 1 (hardware) trigger logic is formed in gate array chips which combine the hit fiber information along with a table-lookup incorporating the transport matrix equations to give the ξ and $|t|$ of the track. A preliminary study of the tracking equations indicates that about 500 equations will be necessary to specify a typical ξ and $|t|$ range, well below the 8000 equations available on the trigger board. The total time required for the FPD Level 1 decision is about 800 nsec, 400 nsec for proton transit and return of the signal to the DØ region and another 400 nsec for the trigger logic and transit to the Level 1 framework. This is well within the 4.2 μsec time allowed for a Level 1 decision. The Level 1 framework will automatically synchronize the FPD decision with all other Level 1 decisions, so timing will not be a problem.

The nine CFT trigger cards will transmit their trigger decisions to the FPD trigger manager. The manager will combine these independent trigger decisions into L1 "and/or" terms for the L1 Framework. The FPD trigger manager will be housed in a single crate. This crate will be a smaller version of the CFT and Muon L1 trigger managers and will not require additional design or engineering. This readout system has the great advantage of using existing DØ trigger boards such that the data storage and triggering are completely DØ standard.

Other detector options, such as silicon or gas microstrip detectors, suffer from dead areas at the bottom of the detector and difficulties in triggering at Level 1 and would require significant development. In conclusion, we have not been able to identify a cheaper, more reliable option than a scintillating fiber detector readout with multi-channel phototubes.

4 DATA TAKING

4.1 Data Taking Strategy

The FPD is designed to be a sub-detector of DØ and will be well-integrated into the DØ trigger framework. Due to the relatively small number of channels (about 2000 compared to hundreds of thousands for other sub-detectors), this detector will have a negligible effect on the event size. It should be read out on every event since any standard type of physics process below mass threshold can be produced diffractively.

It will also be necessary to have a few dedicated triggers which demand tracks at the trigger level. Dedicated triggers will be required for diffractive jet production, double pomeron exchange, and elastic scattering.

To minimize the bandwidth for these dedicated triggers, the capability to cut on ξ at Level 1 is essential (See Sec. 3.2.1). This allows the different triggers to only accept tracks in the kinematic range of interest. In addition to the requirement of a p or $\overline{p}$ (and in some cases jets), the dedicated triggers must include elements to reject multiple interaction and halo backgrounds.

4.2 Fake Background

A serious concern about triggering on hard diffraction is the frequency of multiple $p\overline{p}$ interactions in the same bunch crossing. The superposition of a low mass diffractive event with a hard scattering event is an important background since this combination can fake a hard diffractive signal. Fortunately, this background is dominated by very low mass diffraction which could not produce jets and can easily be rejected at Level 1 by a cut such as $\xi > 0.004$. In addition a single interaction requirement can be imposed at Level 1 using timing information from the Level Ø detector (an array of scintiallators located between the central and endcap calorimeters). The Level 1 background rates will be small and comparable to the signal rates (few HZ). At Level 3 (software trigger) or offline, this background can be reduced to near zero using a single interaction algorithm or tool, which can use the silicon information to demand a single vertex, compare the event time from the trigger scintillators and from Level Ø, and demand conservation of longitudinal momentum.

A detailed study of the overlap of a halo event with a hard scattering event indicates that this background will also not be a problem, due to the ξ cut which eliminates most of the halo, and the multiple interaction cuts.

4.3 Accelerator Background at DØ

With no Roman pots, the accelerator-induced background is expected to be at most a few percent of the background from $p\overline{p}$ interactions. The DØ sub-detector most sensitive to accelerator related background is the forward muon spectrometer. Studies have been performed to quantify the increase in background due to the Roman pots compared to the baseline case with no pots.

A contribution to background rates of beam halo interactions with the pots is calculated assuming an intensity of 10^{13} protons per bunch and 10^{12} anti-protons per bunch and a luminosity of $1 \cdot 10^{32}$ cm$^{-2}s^{-1}$ (as in the halo studies). The halo protons scattered by the pots and secondary particles generated in inelastic nuclear interactions with the pots and accelerator components are then passed through detailed simulations with the MARS code. These simulations combine the magnetic fields and the pot, separator, quadrupole, dipole, tunnel, shielding, and DØ forward muon spectrometer geometry, yielding a three dimensional distribution of particles entering the DØ sub-detectors. The ratio of the number of hits from accelerator background in the muon chambers (located at 6, 8, and 10 meters from the interaction point) with and without Roman pots is then determined. This ratio is about 4.5 for 8σ pot positions and 1.5 for 9σ pot positions, implying a total increase in background rates of at most 15% for 8σ and a few percent for 9σ. The effect of a small increase in the background rates to the muon system should be minor. Detailed simulations of the backgrounds to the silicon detector show that these are also negligible compared to the interaction related background. The conclusion from the background studies is consistent with that of the halo studies: the pots can likely be positioned between 8 and 9σ. The actual running position will clearly have to be determined experimentally.

4.4 Data Taking Summary

The addition of the FPD will have little impact on backgrounds at DØ or the overall trigger rates, at most at the few percent level. Many handles exist to reject backgrounds to hard diffraction, and with early data an optimized trigger list can be formed. Large data samples can be obtained with little background, and will allow us to study the full physics menu discussed earlier.

5 CONCLUSIONS

For the next ten years the Tevatron offers the best possibility to understand pomeron exchange and the transition between non-perturbative and perturbative QCD. The addition of the FPD would greatly increase the physics reach of the hard diffractive physics program with no negative impact on the current DØ physics program. The measurements of jets and particles will be done with the upgraded DØ detector, which will be very well suited to this purpose. The FPD will be used to ensure that large diffractive data samples are obtained and that they can be divided into ξ and $|t|$ bins. It will allow accurate determination of pomeron structure and hard diffractive cross sections, permitting us to greatly expand the knowledge of the field of hard diffraction.

6 ACKNOWLEDGEMENTS

We thank the staffs at Fermilab and collaborating institutions for their contributions to this work, and acknowledge support from the Department of Energy and National Science Foundation (U.S.A.), Commissariat à L'Energie Atomique (France), State Committee for Science and Technology and Ministry for Atomic Energy (Russia), CNPq (Brazil), Departments of Atomic Energy and Science and Education (India), Colciencias (Colombia), CONACyT (Mexico), Ministry of Education and KOSEF (Korea), and CONICET and UBACyT (Argentina).

7 REFERENCES

[1] DØ Collaboration, "Proposal for a Forward Proton Detector at DØ", Proposal P-900 submitted to the Fermilab PAC; A. Brandt *et al.* FERMILAB PUB–97-377.

[2] G. Alberi and G. Goggi, Physics Reports **74**, 1 (1981); K. Goulianos, Physics Reports **101**, 169 (1983). A. Donnachie and P.V. Landshoff, Nucl. Phys. B **244**, 322 (1984); B **267**, 690 (1986).

[3] G. Ingelman and P. Schlein, Phys. Lett. B **152**, 256 (1985).

[4] A. Brandt *et al.* (UA8 Collaboration), Phys. Lett. B **297**, 417 (1992).

[5] A. Doyle, *Workshop on HERA Physics, "Proton, Photon, and Pomeron Structure"*, GLAS-PPE/96-01.

[6] A. Brandt (DØ Collaboration) *Proceedings of the 11th Topical Workshop on Proton-Antiproton Collider Physics*, Abano Terme, Italy, 1996.

[7] P. Melese (CDF Collaboration) *Proceedings of the 11th Topical Workshop on Proton-Antiproton Collider Physics*, Abano Terme, Italy, 1996; *Proceedings 1996 Divisional Meeting of the Division of Particles and Fields*, Minneapolis, MN, 1996.

[8] F. Abe *et al.* (CDF Collaboration), Phys. Rev. Lett. **78**, 2698 (1997).

[9] S. Abachi *et al.* (DØ Collaboration), Phys. Rev. Lett. **72**, 2332 (1994).

[10] F. Abe *et al.* (CDF Collaboration), Phys. Rev. Lett. **74**, 855 (1995).

[11] S. Abachi *et al.* (DØ Collaboration), Phys. Rev. Lett. **76**, 734 (1996).

[12] M. Derrick *et al.* (ZEUS Collaboration), Phys. Lett. B **369**, 55 (1996).

[13] F. Abe *et al.* (CDF Collaboration), Phys. Rev. D **50**, 5535 (1994).

[14] L. Frankfurt and M. Strikman, Phys. Rev. Lett. **63**, 1914 (1989); **64** 815 (1990).

[15] G. Alves, E. Levin, and A. Santoro, Phys. Rev. D **55**, 2683 (1997).

[16] J. Pumplin, Phys. Rev. D **52**, 1477 (1995).

[17] A. Berera and J. Collins, Nucl. Phys. B **474**, 183 (1996).

[18] "Proposal for Hard Diffraction Studies in CDF", (CDF Collaboration), CDF/CDFR/2940, (1995).

[19] Tracking program provided by M. Martens, L. Michelotti.

[20] J.A. Johnstone, "Report to the Low Beta Study Group", Fermilab Internal Report, (1994).; J.A. Johnstone, private communication (1996).

[21] A. Brandt, A. Drozhdin, and N. Mokhov, "The DØ Roman Pots Detector Beam Loss Simulations", unpublished (1997).

[22] F. Abe *et al.* (CDF Collaboration), Phys. Rev. D **50**, 5518 (1994).

[23] P. Bagley (Beams Division), private communication.

[24] P. Bagley *et al.*, "Summary of the TeV33 Working Group", *Proceedings of 1996 DPF Study on New Directions for High-energy Physics (Snowmass '96)*, Snowmass CO (1996).

[25] C. Kim and A. Bross, "Attenuation and Radiation Damage Studies of Multi-clad Optical Fiber", unpublished (1996).

[26] T. Zimmerman *et al.*, "The SVX II Readout Chip", IEEE Trans. Nucl. Sci., Vol. 42, No. 4, August 1995.

Hard Diffraction in CDF

Michael G. Albrow
Fermi National Accelerator Laboratory, P.O. Box 500, Batavia, IL 60510

Abstract

Although QCD describes well strong interactions involving large momentum transfers (*hard collisions*) there is a subset which is not understood, namely color singlet exchange or pomeron exchange. We have been studying this using detectors very close to the beams (in "roman pots") to *tag* the pomeron.

1 INTRODUCTION

If one measures the momentum, p, spectrum of small angle (anti-)protons at the Tevatron, dividing p by the beam momentum to get the fractional quantity called Feynman-x, x_F, the distribution has a peak at x_F = 1.0 due to elastic scattering. However inelastic collisions, which by definition have more particles than just $p + \bar{p}$ in the final state, show a distribution peaking up from a flattish distribution extending to about x_F = 0.95 to two orders of magnitude higher by x_F very close to 1.0. For example distributions see Figs 13(a) and 14(a) of Ref. [1] These data were taken in an earlier manifestation of roman pot detectors in CDF. This inelastic peak is attributed to *Single Diffractive Excitation, SDE,* in which one of the beam particles has been diffractively dissociated (or excited to a massive state, mass M) which breaks up to hadrons. Current thinking is that at the high energies of the Tevatron elastic scattering is mediated by the exchange of an entity called the pomeron. At low energies the exchange of virtual mesons such as π, ρ is important but these die away as the center of mass energy $\sqrt{s}$ increases. We do not know whether it makes sense to consider the pomeron as having a well-defined structure in terms of quarks and gluons (like all *real* strongly interacting particles) but it is a good working hypothesis. In the early days of QCD F.Low suggested that it is mainly two gluons in a colorless state (a single gluon is always colored and exchanging it could not leave the proton intact).

Single Diffractive Excitation can then be viewed as due to the emission of a pomeron from the $\bar{p}$ (e.g.) followed by it interacting with the p. The pomeron carries a momentum fraction ξ = 1 - x_F of the $\bar{p}$ and then M = $\sqrt{\xi}\sqrt{s}$. Another attribute of the pomeron is its 4-momentum-transfer-squared t, which is always negative and is equivalent to its mass-squared. If we know the (vector) momentum of the incident and outgoing $\bar{p}$ the pomeron is tagged, and we know its t and ξ. We can then do a Lorenz transformation to the c.m. frame of the pomeron-proton "collision" and study the final hadronic state.

If the pomeron consists of quark and/or gluon constituents they can undergo hard scattering on the q/g of the proton and make high-E_T jets. These were first observed by UA8 [2] at the CERN $Sp\bar{p}S$ Collider. By measuring the jets, and knowing the structure function of the proton (the q and g distributions in terms of Bjorken-x = p_{parton}/p_{proton}) we can measure the structure functions of the pomeron (in terms of β = $p_{parton}/p_{pomeron}$). Actually, just by measuring jets we get some combination of q and g structure functions. Measuring another process such as Drell-Yan lepton pairs from $q\bar{q}$ annihilation, W or heavy flavor production will help separate these. A most important question is whether the pomeron structure function thus obtained agrees with that found by probing it with virtual photons at HERA. These couple directly only to the charged q and $\bar{q}$ in the pomeron. Even if the "soft" pomeron at very low Q^2, the 4-momentum squared of the probing photon, were purely gluons some q and $\bar{q}$ would be present by "evolution" (e.g. $g \rightarrow q\bar{q}$) in the HERA measurements. Agreement (or not) between Tevatron and HERA measurements will tell us whether this quasi-particle paradigm is making sense; how far can we push it? Theorists, if they think about these things at all, usually consider the pomeron to be much more complicated. But progress has been very slow. We take an experimental approach. What is the (Q^2, β) dependence of the q and g densities? Are they dependent on $|t|$? Or on ξ?

Single diffractive collisions producing dijets have an antiproton (the CDF Run Ic pots were on the downstream $\bar{p}$ side) near the beam rapidity ($y_{beam} = ln\sqrt{s}/m_p = 7.5$) and then a rapidity gap, i.e. no particles in an angular region from about η_{max} to y_{beam}. Here pseudorapidity η = $-ln.tan\frac{\theta}{2}$ and η_{max} = $-ln\xi$. A rapidity gap of 3 units corresponds to ξ = 0.05 or x_F = 0.95. This is the region where diffraction (i.e. pomeron exchange) becomes dominant. For smaller gaps or smaller x_F other exchanges (virtual π, ρ) become increasingly important. This "boundary" corresponds to an excited mass (the $\sqrt{\hat{s}}$ of the pomeron-proton collision) which was 14 GeV at the ISR ($\sqrt{s} = 63$ GeV), 140 GeV at the $Sp\bar{p}S$ ($\sqrt{s} = 630$ GeV), and 400 GeV at the Tevatron. Here we can really get into the realm of *hard* collisions, probing very small distances where the notion of partons makes most sense. Because of the higher energy compared to the $Sp\bar{p}S$ we have much larger rates for jets and can go to higher jet transverse energies E_T. There is also more rapidity available (which is better for gap physics). All in all the Tevatron is much better than the $Sp\bar{p}S$ (as well as the fact that it still exists!).

One of the most sensitive variables to the pomeron structure is the rapidity distribution of the produced high E_T jets. For illustration, suppose that the β distribution is either *soft* with low-β favored, $(1-\beta)^5$, *hard* with medium β favored, $\beta(1-\beta)$, or *superhard* with $\beta \approx 1$. Fig. 1 shows the pseudorapidity distributions of jets in these cases for two M bands. Tagging of the pomeron is needed to measure the diffractive mass M, or equivalently its boost.

However even without detecting the forward antiproton one can use the presence of rapidity gaps to see diffractive dijet signals and constrain pomeron structure. We had a trigger in CDF which required two jets, both forward ($\theta < 20^\circ, \eta > 1.8, E_T > 20$ GeV). We then looked on the

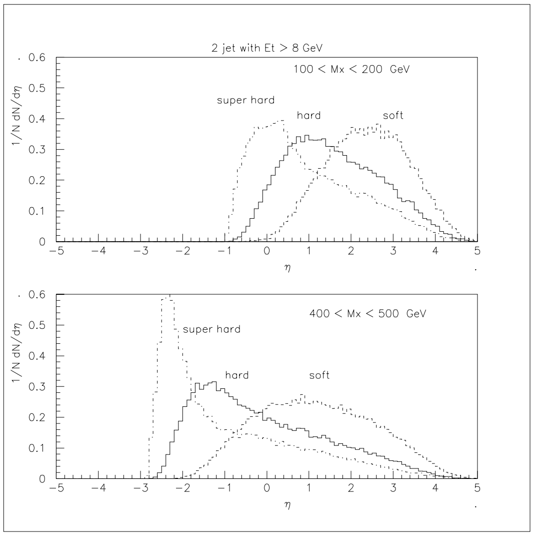

Figure 1: Rapidity distributions of diffractively produced jets for soft, hard and superhard parton/pomeron distributions.

other side, where a rapidity gap might be, at the number of calorimeter towers ($2.4 < \eta < 4.2$) with a hit and the number of "Beam Beam Counters" ($3.2 < \eta < 5.9$) with a hit. Plotting these against each other, Fig. 2, one sees a special class of about 1% of the events with no hits in either detector, i.e. a rapidity gap of 3.5 units, with a modest background which can be estimated from the rest of the distribution.

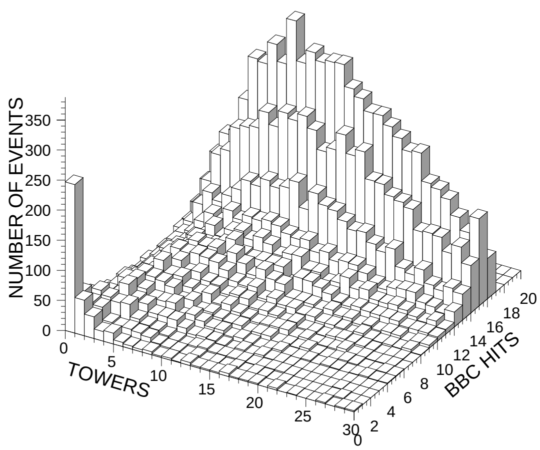

Figure 2: Multiplicity of hits in forward calorimeter towers vs. BBC hit multiplicity distribution, rapidity hemisphere opposite two jets. Diffractive signal shows in bin (0,0).

This study finds that the fraction of jets (in the kinematic region defined above) which are diffractively produced is [0.75 $\pm$ 0.10]%; the jets have a similar E_T distribution. Diffractive events have fewer third jets and the two leading jets are better balanced than in non-diffractive events.

2 ROMAN POTS IN CDF: ROUND 2, DEC 1995-FEB 1996

In diffractive collisions the elastic or "quasi-elastic" scattered antiproton stays inside the beam pipe for tens of meters. The longitudinal momentum is either p_{beam} (elastic) or $x_F.p_{beam}$ (SDE). The transverse momentum p_T is approximately $\sqrt{-t}$ where $|t|$ has a very steeply falling distribution: e^{bt}. The slope b is about 17 GeV^{-2} for elastic scattering and about 7 GeV^{-2} for diffractive scattering (although the latter depends on M). So nearly all diffractively scattered particles have angles less than 1 mr. To detect them, and to get to small $|t|$ to get a large part of the cross section, the usual procedure is to use vacuum chamber *pots* containing detectors in the atmosphere which can be moved very close (8σ or 10σ) to the circulating beams at the beginning of a run. These are usually called "Roman Pots" after the CERN-Rome group at the ISR which first used the idea. (Sometimes we call our Run Ic pots "Tokyo Pots" because our Japanese collaborators made them.) These pots have to be placed where the machine is warm. Possibilities for CDF on the outgoing antiproton side are:

• In front of the first quadrupole Q4 (about 7 m). No momentum information and acceptance only for large $|t|$.

• Before and/or behind the (warm) electrostatic separators between Q2 and Q1. There is little space for pots here with the existing machine configuration, although it is not excluded that a very compact detector could be inserted and in CDF we are presently looking at this possibility. DØ has proposed [3] to move quadrupoles and expand the warm space at the entrance and exit of the es-separators to put sets of pots, 4 at each location. The acceptance of such detectors goes all the way to ξ = 0 but is limited to $|t| \geq 0.5$ GeV^2 or so depending on beam conditions. A good feature of detectors in this location is that they can be placed on both beams, while there is only room for the dipole spectrometer discussed below on the antiproton side (the machine is asymmetric).

• Between the third and fourth dipoles (A48-3 and A47-5), about 56 m from BØ there is a warm space of nearly 3 m. The quasielastically scattered particles are bent more than the elastic/beam particles and one can get essentially 100% acceptance for them (even at zero $|t|$, if $\xi > 0.05$) by placing detectors on the inside of the ring in the horizontal plane. The acceptance does extend to ξ = 0 (low mass SDE or elastics) for $|t|$ values like that of the quadrupole spectrometers. However the rates are low because, apart from the cross sections being small the azimuth (ϕ) acceptance is reduced by having a single detector on the inside of the ring. It is in this short straight section that a group of us proposed [4] to put a set of three pots with detectors separated by about 1 m. It was proposed to the PAC in February 1995, still "subject to the approval of the CDF Collaboration", and the pots were installed in the Tevatron the following September for commissioning in November, just in time to get some good data before the end of Run I in February.

There were three identical pots, shown in Fig. 3.

Each has a trigger scintillator 21 mm $\times$ 21 mm $\times$ 6 mm read out by a H3171 PMT. Bundles of square (0.8 mm $\times$ 0.8 mm) SCSF81 scintillating fibers in x and y directions gave these co-ordinates with about 120 μm precision. The arrangement (see Fig. 4 was to have ribbons of 4-fibers in

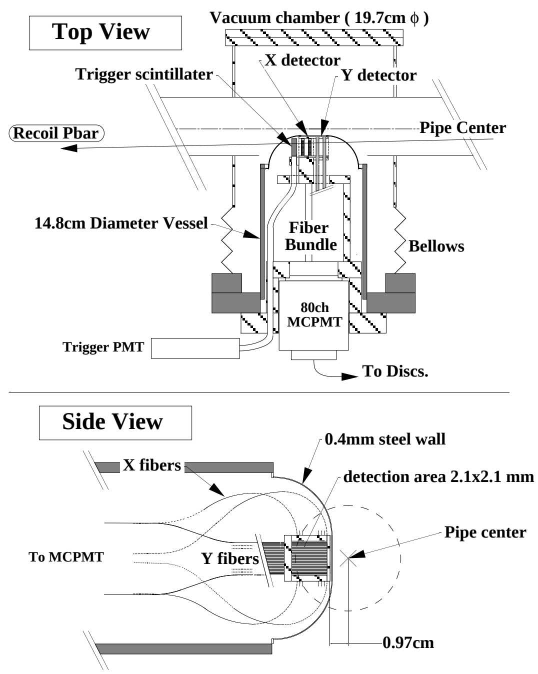

Figure 3: Top and side (particle's eye) views of one (of three) pot detectors in CDF for Run Ic.

line (to get plenty of signal) which would go to a single pixel of a H5828 Multi-anode PMT.

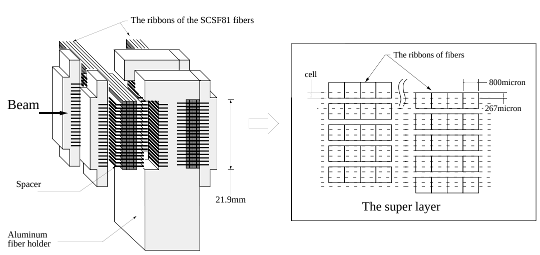

Figure 4: Arrangement of scintillating fibers in a pot detector.

Two staggered layers of these ribbons defined bins of width 800/3 = 267 μm depending on whether one or two ribbons were hit. Precision aluminum fiber holders positioned the fibers to about 20 μm. The distance between the active edge of this hodoscope and the vacuum side of the 0.5 mm stainless steel pot wall was 1.48 mm. After the beams had been made stable and cleaned, the pots were were individually moved in with their positions read out by LVDT devices. The alignment was at the level of 25 μm. It was found that the pots could be moved in to a distance of about 10 mm from the center of the p-beam, which was (unfortunately) the nearer of the two beams, without causing any observeable extra backgrounds in the CDF and DØ detectors and with a reasonable rate in the pots themselves (measured by $S1.S2.S3$ concidences). Our philosophy was to (a) not ask for any special beam conditions (b) be able to keep the pots in for all CDF data taking. Getting as close to the beam as possible is not the major issue for this physics, which is mostly high-M diffraction and the θ = 0 particles are accepted inside the pot detectors. However some increase in the acceptance to smaller t, ξ is desireable and will be achieved in Run II by inverting the polarity of the es-separators. This will shift the $\bar{p}$ beam some 3.5 mm closer to the inside of the ring. The "pot-p" beam center distance will stay the same because this is the dominant constraint. The $\bar{p}$ beam halo is smaller. As a result we will get extra acceptance to small t, ξ in Run II without any modifications to the pot/detector.

During a run the "inclusive pot trigger" was based on a coincidence of the three pot scintillators gated by $\bar{p}$-crossing time . Depending on run conditions some 60-80% of these events have exactly one 3-point track in both the x-view and the y-view. Fitting straight tracks and measuring residuals gives a relative alignment check and confirms about 120 μm resolution per detector.

The acceptance of the pot detectors can be understood from Fig. 5.

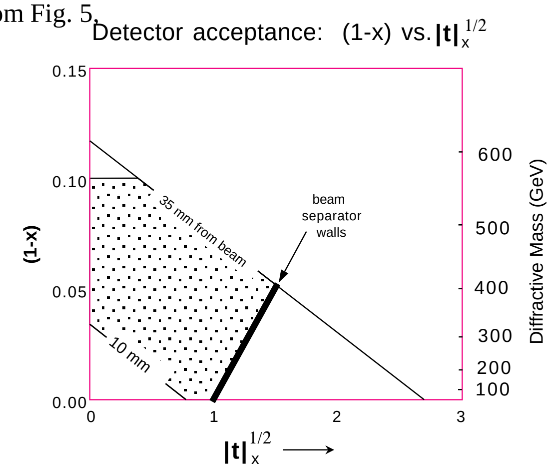

Figure 5: Region of acceptance of pot spectrometer.

which shows the plane $\xi = (1 - x_F) \approx M^2/s$ vs $\sqrt{t} \approx p_T$. This is from our proposal. Contours of fixed distance from the beams are diagonal, so that the 10 mm limit shown excludes the low-$|t|$, low-M^2 corner where the cross section is highest; however this is not so bad for the interesting high mass events. For $\xi \approx$ 0.45 the acceptance goes all the way to t = 0 and at low $|t|$ is 100% (full-ϕ coverage). Lines of fixed slope $\theta = dx/dz$ are nearly horizontal . 1 mrad change in θ corresponds approximately to 0.01 change in ξ; the resolution is about $\frac{1}{10}$ smaller. Data distributions from inclusive pot triggers show the behavior expected from this figure, or rather from the acceptance A($\xi, |t|$) together with the known shape of the inclusive diffractive cross section.

Another instructive set of diagrams is made by selecting antiprotons at various x_F, t and all ϕ and plotting where they hit the pot detectors in x, y. As x_F decreases from 1.0 to 0.90 the $|t|$ = 0 point moves from being (obviously) coincident with the beam, to the left and entering the detector 10 mm from the beam by x_F = 0.96, at the same time the contours of constant $|t|$, which were approximately circles at x_F = 1.0, become focussed-down ellipses (major axis horizontal). This dipole spectrometer has very good acceptance for x_F less than about 0.96; if good acceptance at x_F

= 0.98 were required moving another mm or two closer to the beam does not help much because particles with rather small $|t|$ are all around the beam ... you start to need detectors above, below and on the right side (outside the ring) as well. The quadrupole spectrometers now proposed by DØ have U,D,L,R pots for this reason.

The fact that cross sections peak sharply at $|t|$ = 0 together with the feature that this point moves in x, y through the detector with changing ξ provides a nice check or calibration of the distance of the detectors from the unscattered beam. A scatter plot of dx/dz vs x for events with a single pot track and a central vertex shows a sharply populated ridge corresponding to $|t|$ = 0. Alternatively if we calculate the distribution of $|t|$ we find a good exponential all the way to $|t|$ = 0 only when the x distance of the pots from the antiproton beam is correct. Noting that the position of the antiproton beam can shift at the level of 1 mm from run to run, this is a useful check to apply. Beam Position Monitors just downstream (as seen by the $\bar{p}$) of the pots provide the primary information.

3 DIFFRACTIVE DATA WITH POTS

Commissioning of the pot detectors with beam started in mid-November 1995 (Run Ic); after a short period at 1800 GeV the machine operated at 630 GeV until the end-of-year shutdown. This run was important for us because it was the energy of the CERN $Sp\bar{p}S$ run of experiment UA8 which needed a direct comparison. Even though several channels of the fiber read-out were still not working for this (and could not easily be fixed due to the limited access to the tunnel), we obtained very useful diffractive dijet data thanks to two facts: (1) the acceptance in ξ is the same at 630 and 1800 GeV but the acceptance in $|t|$ comes down by the ratio of p^2_{beam} so we accept larger cross-sections (2) Features such as the β-distributions in the pomeron can be studied independently of details of the acceptance for the forward $\bar{p}$. We have about 1000 events with a pot track + two jets above 7 GeV which are now being studied. For the 5-6 weeks of 1800 GeV running in 1996 the problems of dead channels were fixed. We took data with a "pot inclusive" trigger heavily prescaled and pot + dijet triggers, the total rate being limited to a few percent of the total CDF trigger rate by decisions on overall physics goals. However we were lucky to profit from two days of special low luminosity running for experiment E811 when we got internal priority in CDF and collected several million diffractive events, including 2500 with two jets above 10 GeV in E_T. The E_T spectrum of the diffractive di-jet sample is extended above 25 GeV using the more exclusive trigger and the higher luminosity data set, but care is required to select single interactions (vertex requirement) especially at high luminosity. These events are "gold plated" in that the pomeron is tagged, one can transform events to the pomeron-proton c.m. frame and derive β for each event. That distribution can then be corrected for the acceptance, effectively convoluted with the β-dependence of the hard scattering cross section and known parton distribution in the proton, to extract the β-distribution in the pomeron.

4 WHAT DID TEVATRON (CDF+DØ)TEACH US (SO FAR)?

• Rapidity gaps (especially as an excess of events in "bin 0") are established as a signature of diffraction. Observing the edge of the gap with forward detectors gives ξ, approximately, but t is unknown.

• A superhard pomeron exists, jet-gap-jet configuration.

• Single diffractive excitation of dijets at the level of 1% of all dijets roughly independent of E_T is confirmed.

• Single diffractive excitation of $W^\pm$ has been observed by CDF, also at the level of about 1%. From this and the rate of dijet production we can conclude that at $Q^2 \approx 10^3$ GeV^2 the fraction of the pomeron's momentum carried by gluons is about 60$\pm$30 % gluons.

• SDE of heavy flavors (b, c) has been observed.

• There is evidence for dijets in double pomeron exchange. In CDF these events have a pot track, two central jets above 7 GeV, and a "bin-0" excess on the opposite side. In DØ they have gaps on both sides.

Most of these studies are on-going, and DØ are also very active in the field (see the talk by A.Brandt).

5 WHAT WE WOULD LIKE (AT THE TEVATRON)

Accepting at least provisionally the paradigm pomeron = quasiparticle with mass = $\sqrt{|t|}$, we would like to measure its full structure functions:

$$g(\beta, Q^2, t, \xi)$$

and

$$q(\beta, Q^2, t, \xi)$$

• Any apparent dependence on ξ is likely to be due to a varying admixture of non-pomeron reggeons. Data at different $\sqrt{s}$ and t could help to sort this out.

• No dependence of the structure on t is expected but who knows? A comparison near t = 0, medium and large $|t|$ should be made.

• Q^2 dependence should be given by QCD evolution (DGLAP) and is a very important test, but the range of ln(Q^2), defining $Q^2 = E_T^2$ e.g., is limited.

• β-dependence is perhaps the most interesting issue at the present time. Is there a "superhard" component which UA8 claimed caused 30% of the time the entire momentum of the pomeron to participate in the hard scatter ($\beta \approx 1$)?

• We must resolve the issue of pomeron "flux" and its normalization by comparing SDE and double pomeron cross sections, and HERA measurements.

6 IMPROVEMENTS FOR RUN II

6.1 Pot Spectrometer

We are proposing to use the same dipole spectrometer that we had in Run Ic in Run II. However we will be able to get about 3.4 mm closer to the relevant $\bar{p}$ beam by inverting the polarity of the electrostatic separators around BØ , which in Run Ic had the more intense and larger p beam closer to the pots. Hopefully autocleaning techniques will allow the pots to be kept in throughout normal CDF/DØ data taking at a distance of order 8-10 σ horizontally. At the Near Beam Symposium I mentioned some possible detailed refinements: modifying the fiber/pot assembly to gain a fraction of a mm; having different standard positions according to beam conditions; having a fiber-driven trigger processor to select $A(\xi, t)$; etc. Since then, we have decided to leave a well-working system alone, and just to profit from flipping the e-s separator polarity.

6.2 Miniplugs

The present plug calorimeters in CDF will be replaced by improved plugs extending down to $\theta = 3^\circ$ or $\eta = 3.6$. Further coverage is very important for forward gap physics, and we have proposed "miniplugs" to extend the coverage to about 0.5° or $\eta = 5.3$. These will be cylinders of lead plates with liquid scintillator read out by wavelength shifting fibers to multi-anode pmts. This scheme gives excellent transverse spatial resolution allowing good rapidity-gap-edge definition. The proposal still has to be endorsed by CDF and financed.

6.3 Beam Scintillator Counters

We would like to extend the detection of particles, and hence of rapidity gaps, over as much as possible of the region between the hole in the miniplugs and the dipole spectrometer 56 m downstream (also on the East side where there is no warm space for a dipole spectrometer). This could be (at least mostly) done by small lead-scintillator sandwiches in mini-pots moving in as close as possible to the beams near 7 m from BØ before the first (cold) quadrupole. Such mini-pots were used to maximize the coverage in a total cross section measurement [5]. However a simpler scheme, which would have the (probably important) advantage of not intruding into the vacuum pipe, is to fit BSC = Beam Shower Counters closely around the beam pipe at four locations (for the $\bar{p}$ side: entrance to first cold section at Q4, exit of Q2, entrance of Q1 and exit of A48-3 dipole. Together these counters should have a high probability of detecting showers caused by the high momentum particles hitting the vacuum pipe and interacting. They may not be 100% efficient as rapidity gap detectors, but they are cheap and simple and their performance can be studied using correlations with the dipole pot spectrometer. They could be very useful in cleaning up double pomeron exchange candidates on the East side, where there is not space for a pot spectrometer.

6.4 Triggers

Note that *ALL* recorded CDF events $(W, Z, top, Higgs, etc!)$ read out the pots (and other very forward detectors) and so we can study the diffractive component of these events without special triggers. However a trigger with (e.g.) two 20 GeV jets has such a high cross section that it is heavily prescaled, but if one requires a pot track in addition we can remove or reduce the prescale factor and get much more statistics on pot+dijet. Rapidity gaps can also be used effectively in diffractive triggers, but it is very important to back them up by data sets that did *not* require the gap in order to study the signal:background. In fact all components of any multi-component trigger should be run alone and in combinations, right down to the totally inclusive beam-crossing trigger. (One can select single vertex events and use this sample for monitoring detector behavior as well as for minimum bias and soft diffractive physics.) In Run II rapidity gaps in the trigger will have the extra benefit of vetoing multiple interactions, which will be of little or no value for diffractive studies. The aim of a good set of diffractive triggers is to do lots of additional physics without affecting the rest of the program except at the few percent level in tape written and events to analyze.

6.5 Experience

Last but not least, the experience gained during Run Ic and the physics we will have learned (when the analyses are all complete!) will hopefully together help us to ask, and answer, the important questions quickly. I would like to note here the great value of close collaboration between the experiment/detector side and the accelerator side, as stressed by this Near Beam Workshop, and in our particular case by having Craig Moore working with us.

7 REFERENCES

[1] F.Abe et al., Phys.Rev.**D 50** (1994) p.5535.

[2] R.Bonino et al., Phys.Lett **B 211** (1988) p.214.

[3] A.Brandt et al., Fermilab-P-900, FERMILAB-Pub-97/377 (Nov.97)

[4] M.Dennino et al., CDFR/**2940**, Fermilab-P-876 (Feb.95)

[5] F.Abe et al., Phys.Rev.**D 50** (1994) p.5550.

THE VARIABLE DENSITY GAS JET INTERNAL TARGET FOR EXPERIMENT 835 AT FERMILAB

D. Allspach, A. Hahn, C. Kendziora, and S. Pordes,
Fermi National Accelerator Laboratory, Batavia, IL, USA

G. Boero, G. Garzoglio, M. Macri, M. Marinelli, M. Pallavicini, and E. Robutti,
Istituto Nazionale di Fisica Nucleare e Universita di Genova, Italy

Abstract

The hydrogen Jet Target for Experiment 835 (Charmonium spectroscopy) at the Fermilab Antiproton Accumulator can provide a variable density cluster stream up to $3.2 \cdot 10^{14}$ atoms/cc in order to allow an instantaneous luminosity greater than $2 \cdot 10^{31}$ $cm^{-2}s^{-1}$. This result can be achieved due to the helium refrigerated expansion stage which provides the cluster stream and due to the pumping and the alignment system which significantly lower the background gas. Details on the construction and the performances, measured in the laboratory and during the run, are discussed.

1. INTRODUCTION

The use of internal gas jet targets in high energy physics experiments [1] provides a source of interaction with unique characteristics. Its main feature resides in the efficient use of the particle beam coasting in the storage ring: this is most important when the beam requires a long time and high cost to be accumulated and maintained, as in the case of antiproton beams.

The main problem arising with the use of internal targets is their effect on the beam lifetime and properties (such as size and momentum). The development of stochastic cooling techniques applied to horizontal and vertical betatron oscillations and to momentum (synchrotron) oscillations led to excellent results in recent years. In particular, hydrogen jet targets were built by the Genova I.N.F.N. group for experiments R704 [2], PS202 [3], PS210 [4] at CERN and for E760 [5] at Fermilab.

The success of the E760 program led to the decision to begin a new experiment identified as E835 [6]. The antiproton beam is produced in the Fermilab Antiproton Source. A 120 GeV proton beam focused on a fixed target yields approximately one antiproton for every 10^6 protons. Roughly $8 \cdot 10^{11}$ antiprotons can be collected over a period of 24 hours. With this quantity of antiprotons circulating in the Antiproton Accumulator, the beam has a current of 80 mA. In the absence of the hydrogen gas jet stream, the antiproton beam lifetime is around 400 hours. During experimentation an interaction rate of 1.4 MHz between the jet stream and the antiproton beam is chosen resulting in a beam lifetime of about 50 hours.

In order to maximize the amount of collectable data, the interaction rate is kept constant. While taking data with a single stack of antiprotons, the antiproton current varies from 80 mA to about 5 mA. The E835 jet target has the capability of varying the density from $1 \cdot 10^{13}$ to $3.2 \cdot 10^{14}$ atoms/cc, which provides a constant luminosity of $2 \cdot 10^{31}$ $cm^{-2}s^{-1}$ during most of the run. Those values need to be compared with a peak density of $6 \cdot 10^{13}$ atoms/cc reached for E760. At the same time, the jet should maintain the characteristics of excellent spatial definition and a low background gas level.

The upgrade program, carried out by the Fermilab Research Division and Genova I.N.F.N. section, required substantial modifications to the former E760 system. These modifications include:

(1) Lowering the stagnation temperature of the hydrogen gas supplied at the jet source nozzle such that the density of the hydrogen jet stream is increased.

(2) Improving the system pumping speed acting on the vacuum chamber in which the gas jet is located. This reduces the interaction rate of the antiproton beam with the background gas associated with the jet stream.

(3) Controlling the source position in the plane normal to the jet stream and its angular position. This results in a perfect alignment of the jet stream with respect to the antiproton beam. This minimizes the quantity of gas which enter the Antiproton Accumulator, but is not directly absorbed by the sink system: this constitutes the background gas.

This paper is organized as follows. Section 2 outlines some properties of cluster jet targets and describes how they are produced through gas expansion in a properly shaped nozzle. Section 3 deals with the central point of the program upgrade, describing the differential pumping system of the machine and the temperature and pressure control of the gas jet system. The method used to measure jet flux and speed, required for determining density, is also described. Results from these measurements are used to draw conclusions on actual system performance.

2. THE JET SOURCE

The gas jet used for the E760-E835 target belongs to the so-called "cluster jet" type, in which the core of the jet is made up of micro droplets, or "clusters" of condensed matter (in our case hydrogen).

The cluster jets are produced through expansion of a gas through a convergent-divergent nozzle in condition of high pressure and low temperature (see Fig. 1). The sudden decrease in pressure and temperature caused by expansion sets the gas in a supersaturated state and favors the formation and growth of clusters whose size may vary from 10^7 to 10^8 molecules [7].

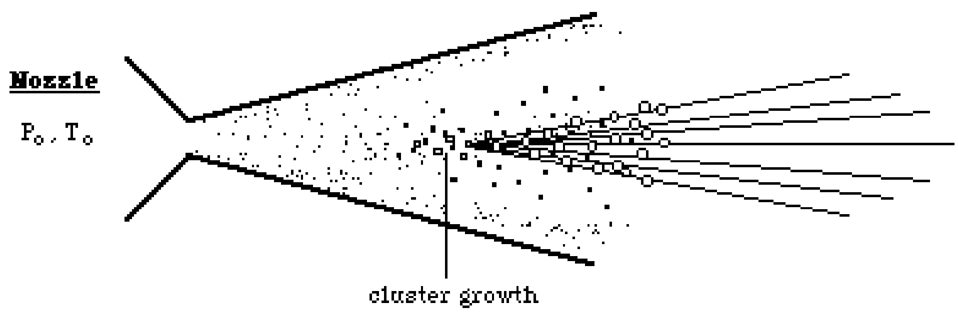

Fig. 1: Condensation and formation of the cluster stream, due to the adiabatic expansion of the gas inside the trumpet shaped nozzle.

Despite the complexity of the condensation process, a qualitative treatment is possible using thermodynamic equations for isentropic expansion [8]:

$$T = T_0\left(1+\frac{\gamma-1}{2}M^2\right)^{-1}$$

$$v = M\sqrt{\frac{\gamma R T_0}{m}}\left(1+\frac{\gamma-1}{2}M^2\right)^{-\frac{1}{2}}$$

$$P = P_0\left(1+\frac{\gamma-1}{2}M^2\right)^{-\frac{\gamma}{\gamma-1}}$$

$$\rho = \rho_0\left(1+\frac{\gamma-1}{2}M^2\right)^{-\frac{1}{\gamma-1}}$$

where P_0, T_0 and ρ_0 are the initial gas pressure, temperature and density, defined by the nozzle status; P, T and ρ are the gas conditions during the expansion; M is the Mach number and $\gamma = c_p/c_V$.

From the previous formulae it can be seen that for suitable values of P_0 and T_0 the point representing the state of the gas in the *P-T* diagram can move into the liquid side of the saturation curve (Fig. 2 [7]), thus starting the condensation process.

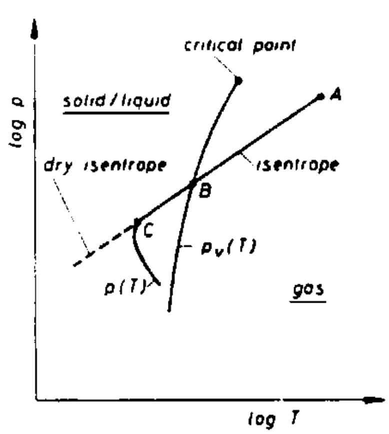

Fig. 2: Isentropic curve for a particular expansion and transition curve on the pressure and temperature plane.

The clusters constitute the core of the gas flow exiting the nozzle. They show the remarkable property of having a very narrow speed distribution, which cause them to form a high density jet with directional spread within a small cone (few degrees) around its axis (for the experiment we use only a fraction of this angular range; the remaining gas needs to be pumped out). This feature can be enhanced by choosing an appropriate shape for the nozzle. Best results have been achieved with trumpet-shaped nozzles: this is therefore the shape we chose as well. Our nozzle has an opening angle of 3.5°, a divergent length of 8 mm and a throat diameter of 37 µm.

The working points for the nozzle pressure (P) and temperature (T) are based on the following factors. It is sensible to expect that, for a given pressure, the core of the cluster stream becomes denser as the temperature decreases. Therefore, to increase the gas jet density, with the minimum background, one should increase the pressure and decrease the temperature, but avoid the phase transition. The saturation curve is the upper border which limits the pressure for a given temperature. This border defines the curve to be followed to achieve the higher jet densities (Fig. 12).

To be able to use the jet as a target inside a storage ring, one has to isolate the cluster jet stream from the remaining ("background") gas exiting the nozzle. The primary reason is to prevent large quantities of gas from entering the accumulator pipe, where a high vacuum must be kept at all times. This is achieved by making use of a differential pumping system (Fig. 3), with the jet crossing a series of chambers which are independently evacuated.

The dimensions of the jet at the interaction region (7 mm) is set from the skimmer between the second and the third chamber (see "second skimmer" in Fig. 6), which, having an aperture diameter of 4.3 mm, selects the dense core of the jet (1.5°). The first skimmer eliminates most of the gas exiting the nozzle, selecting a jet angle of 3°; it has a diameter of 1.4 mm. It has been possible to minimize the conductance of this skimmer, and the background gas as well, by the use of the nozzle alignment system: horizontal, vertical and angular movements are allowed. An ion gauge, mounted on the

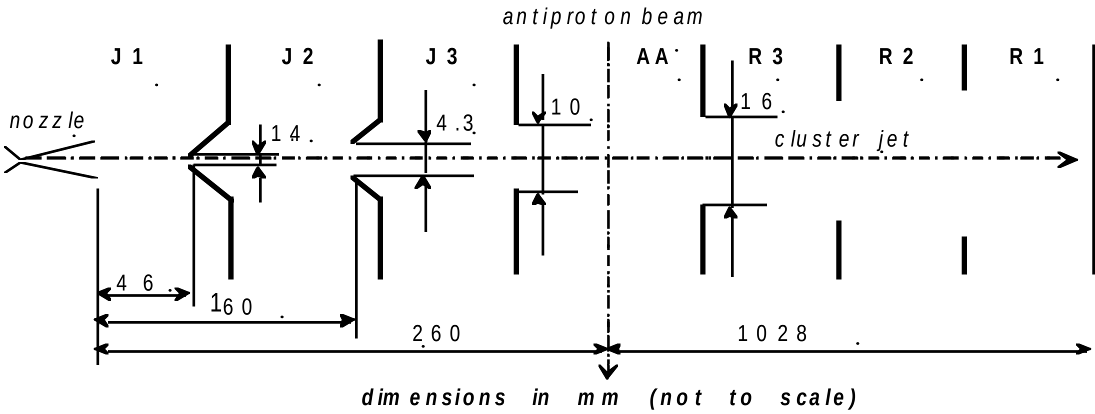

Fig. 3: Schematic of the seven chamber differential pumping system.

geometrical axis of the vacuum chambers and located in the last recovery chamber, helps the alignment of the jet. In table 1 [9] is written the conductance of each skimmer and diaphragm between the chambers.

3. GAS JET SETUP

Pumping system.

The configuration of the *pumping system* is the result of a trade-off between the need to have high pumping speeds and the space limitations imposed on the Jet Target by the presence of the E835 detector just downstream of the interaction point (Fig. 4).

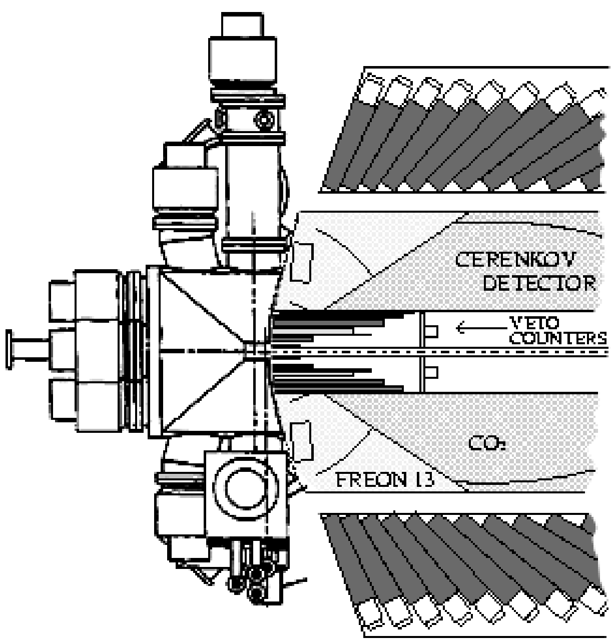

Fig. 4: The detector of E835 in the region next to the jet target.

Ten turbomolecular pumps (TMP's) are installed directly onto the chambers. Eight of these have a capacity of 1000 L/s and two are rated for 3500 L/s. The actual pumping speed in each chamber has been measured by the use of a calibrated hydrogen flow (see Table 1) [9]. The conductance of the skimmer and diaphragms between chambers have been measured with the same method as well.

Due to the low compression ratio of the turbomolecular pumps for hydrogen, the pumping system has been designed to avoid limiting the pressure in the high vacuum zone of each pump due to the rough vacuum pressure. To achieve this result, two additional turbomolecular pumps are used as booster pumps downstream of the pumps on the J2, J3, AA1, AA2, R1, R2 and R3 chambers. Also included are three positive displacement blowers and two roughing pumps (see Fig.5).

Hydrogen supply line.

To control the hydrogen gas pressure at the nozzle inlet, a multiple loop controller is used. A high performance pressure transmitter provides the pressure reading to the controller. An electromagnetically operated flow control valve is then positioned by the controller in order to maintain the gas set pressure. The operating range is 3 - 120 psia with a precision of 0.5 psi.

Before entering the refrigeration system, the hydrogen gas is purified by mechanical filters and a liquid nitrogen cold trap. This is to avoid plating contaminants in the refrigerated hydrogen circuit and to prevent the small aperture of the nozzle from becoming partially or completely clogged.

Temperature control.

The nozzle through which the H_2 passes is located inside the J1 chamber (Fig. 6)[10]. The cooling is achieved by the use of a two stage helium cryocooler, commercially rated for 9W at 20K. The coldest second stage extension is thermally coupled to a copper spool through which the hydrogen gas flows: here it is cooled down to its stagnation temperature before expansion. The nozzle is kept in place by a metallic support (*nozzle holder*): this is thermally coupled to the spool by copper cables to ensure mobility of the nozzle.

All of this is enclosed in a vacuum tight structure. To reduce heat transfer by radiation from the shell walls to the nozzle and coldfinger of the cryocooler, shields cooled with liquid nitrogen are installed. The cryocooler

Pumping Speed for N_2	**Pumping Speed for H_2**	**Conductance for H_2**
S_{J1} = 1180 lit/sec	S_{J1} = 1450 lit/sec	
	S_{J2} = 650 lit/sec	$C_{J1\text{-}J2}$ < 2 lit/sec
S_{J3} = 480 lit/sec	S_{J3} =660 lit/sec	$C_{J2\text{-}J3}$ = 6 lit/sec
S_{AA} = 115 lit/sec	S_{AA} = 520 lit/sec	$C_{J3\text{-}AA}$ = 25 lit/sec
S_{AA1} = 520 lit/sec	S_{R3} =700 lit/sec	$C_{AA\text{-}R3}$ = 40 lit/sec
	S_{R2} = 740 lit/sec	$C_{R3\text{-}R2}$ = 100 lit/sec
S_{R1} =1130 lit/sec	S_{R1} =2350 lit/sec	$C_{R2\text{-}R1}$ = 150 lit/sec

Table 1. Measured values of the pumping speed (N_2 and H_2) and conductance (H_2). These pumping speeds are measured for pressures below $5 \cdot 10^{-4}\,torr$. The AA pumping speed during the test was limited by the system used for the cluster-jet shape measurements.

extension (whose temperature can reach values as low as 10K), has installed another shield around it and is cooled to about 50K by the first stage of the cryocooler.

The cooling and expansion stage is located just upstream of the J1 chamber radiation shield. This shield decouples the nozzle holder from the radiation heat transfer. Furthermore, cooling the gas around the nozzle, it reduces the mean energy transferred to the cluster for scattering processes. This virtually eliminates the evaporation of H_2 molecules from the clusters.

The nozzle is nearly the coldest component of the hydrogen circuit. As pointed out in section 2, the useful working temperature range of the nozzle for data taking is from 15K to 40K. The sensitivity of the temperature control in this range is better than 0.01K. The nozzle temperature is sensed with a calibrated germanium resistance thermometer located on the nozzle holder. The sensor is positioned in a cavity whose dimensions create a close sliding fit with the sensor. A vacuum grease with good thermal conductance is used to minimize the contact resistance. A 16 bit temperature controller reads the nozzle temperature and provides an analog voltage output to a heater foil wrapped around the nozzle coupling spool. The result is a difference of about 2K between the cooler spool and the nozzle holder, due to a 2W heater load on the latter.

The time response of both the temperature and the pressure control has been designed to be around 10 sec. Other parameters, which have an effect on the interaction rate such as the beam current, vary with the time scale of hours. The noise is insignificant.

Given this kind of control, it is possible to maintain the density to within 20%.

Measurements of the Density and Flow of Background Gas.

To determine the jet density, the three parameters which are in the following formula have been independently measured.

$$\rho = \frac{\Phi_{Jet}}{A_{jet} \cdot V_{Cl}} \tag{3.1}$$

The cross sectional area of the jet in the interaction region depends only on the geometry of the skimmer system. The conical shape of the jet is defined by the aperture of the skimmer between chambers J2 and J3 (Fig. 6) and from the distance of the latter to the nozzle. A direct measurement of this area has been made by passing a needle through the jet. The clusters which strike the needle at room temperature evaporate completely. Using an ion gauge, it is possible to record the consequent pressure increase in the interaction region and to therefore define the spatial width of the jet. Due to the "L" shape of the needle used, the area has been measured both horizontally and vertically, verifying that its shape is indeed circular. It has also been shown that the jet shape does not vary by changing the nozzle temperature and pressure (Fig. 7).

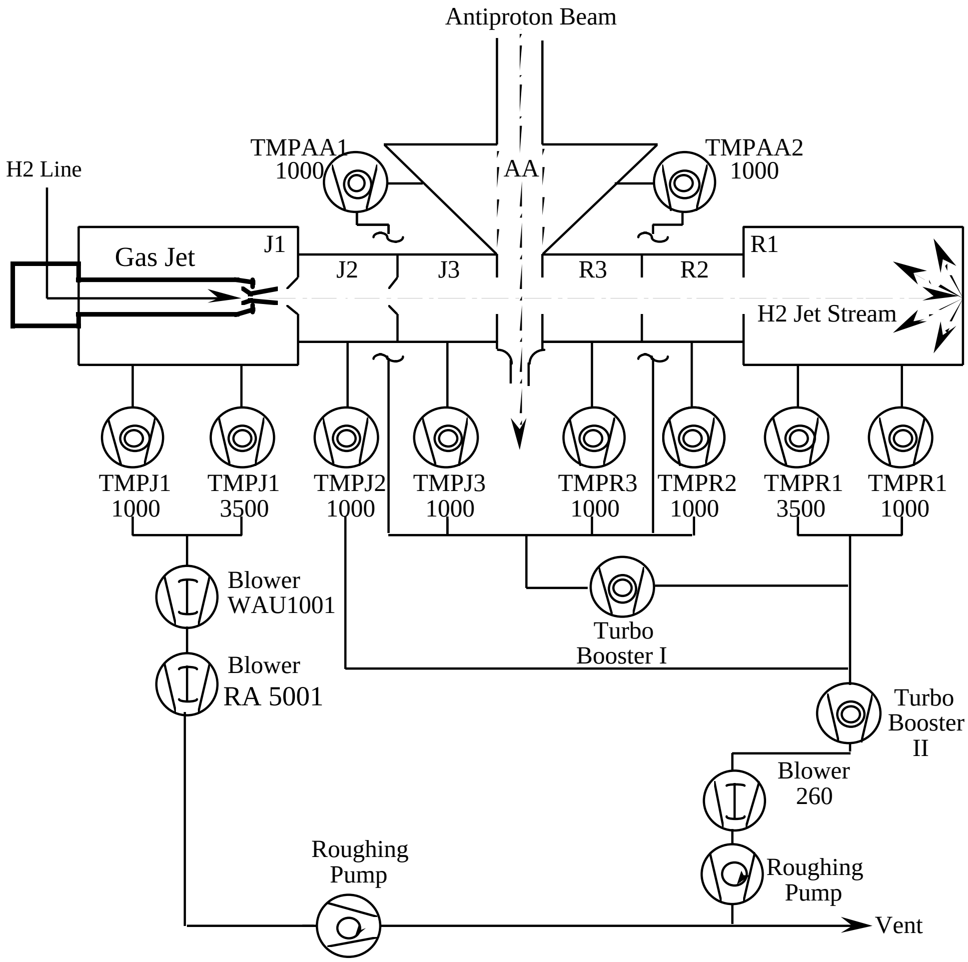

Fig. 5: The Jet Target Pumping System. The structure has been designed to prevent limitation of the chamber pressure by the compression ratio of the pumps.

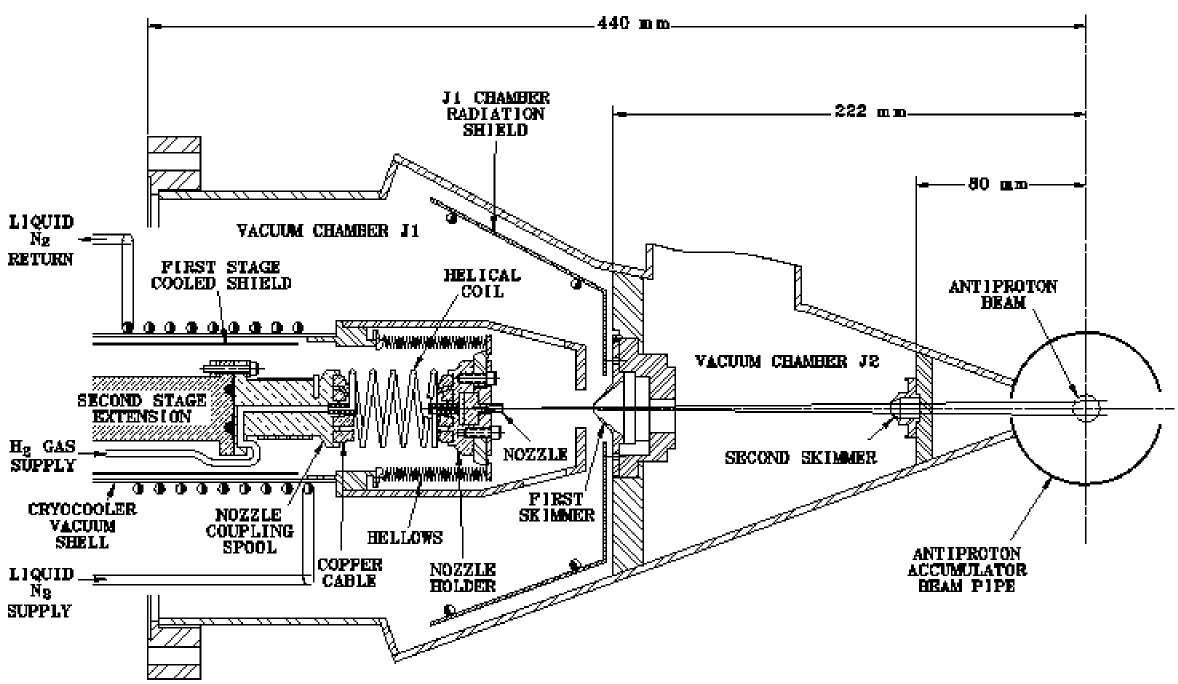

Fig. 6: Hydrogen Gas Jet components located in the J1 Vacuum Chamber.

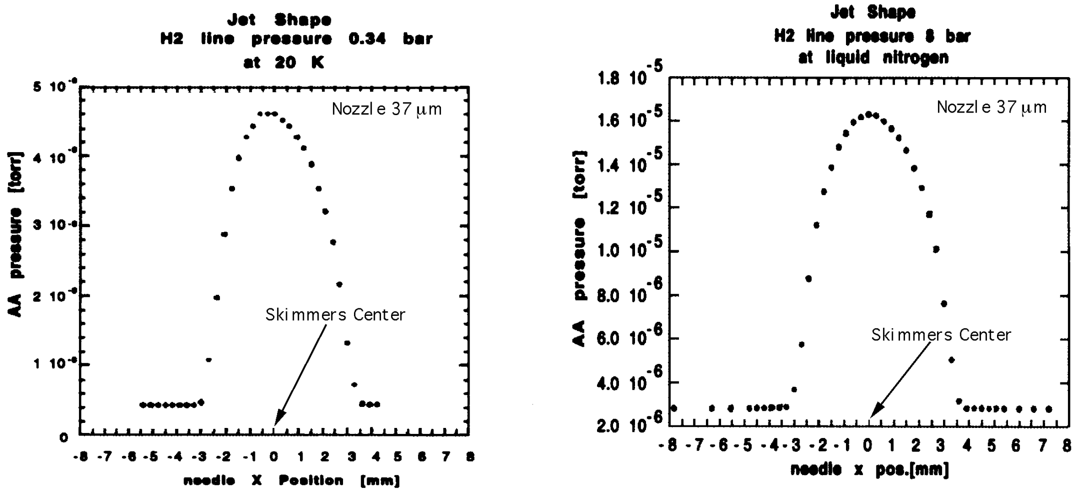

(*a*) (*b*)

Fig. 7: Density distribution of the jet in the region of intersection with the antiproton beam. *a*) shape at 20K, 0.34 bar; *b*) shape at 77K, 8 bar.

The value obtained for this area is A_{jet} = (3.9 ± 0.5)·10^{-5} m^2 (diameter ~ 7 *mm*). The flow Φ_{Jet} has been determined using the equation:

$$\Phi_{Jet} = \frac{S \cdot P}{R \cdot T} \qquad (3.2)$$

The pressure, P, is measured inside chamber R1 as this is where the cluster jet is destroyed; the pumping speed, S, has been previously determined; T is room temperature; and, R is the universal gas constant. The pumping speed in R1, as in each chamber, has been measured by the use of a calibrated hydrogen flow (see Table 1), using again equation 3.2.

An independent measurement of the flow has been done by integrating the distributions in Fig. 7. The two measurements are consistent within the experimental errors.

The cluster speed has been measured by determining the time of flight from the interaction area to R1. This length (basis of the measurement) is 850 mm. The instrument used was a chopper installed on the jet. Using a lock-in amplifier, the phase difference between the modulate signal in R1 and a trigger has been measured for different values of the chopper frequency revolution.

The time of flight t_{of} is given by:

$$t_{of} = \frac{1}{2}\frac{1}{360}\frac{\mathrm{d}(\Delta\Phi)}{\mathrm{d}f}$$

where $\Delta\Phi$ is the phase difference and f is the revolution frequency of the chopper.

Figure 8 shows the typical trend of the cluster speed for a constant nozzle temperature, changing the pressure. It is possible to see that, at T=30K, for values of the pressure greater than 20 psia, the speed saturates.

It is possible to compare these results with the value given from the Kinetic Theory:

$$V_{Cl} = \sqrt{\frac{2R}{W}\left(\frac{\gamma}{\gamma - 1}\right)T}$$

where W = 2.016 10^{-3} Kg/mole , T is the nozzle temperature, R is the universal gas constant and $\gamma = c_P / c_V$ (for molecular hydrogen at low temperature equal to $5/3$). Fig. 9 shows the results.

For temperatures lower than 20K, the experimental points are very different from the theoretical trend because the pressure at which the hydrogen passes from gas to liquid is lower than the pressure for observing the speed saturation. For these values of the temperature, Fig. 9 shows the maximum speed measured. The upper limit in the width of the speed distribution has been estimated at ±10%.

Using formula 3.1, the jet density and background gas in AA have been plotted for various pressures. Fig 10 shows one of these plots at a constant temperature of 25K. Notice the trend of the curves. In choosing operating points for the jet target, pressures and temperatures resulting in the characteristic peaks are preferred.

Changing the nozzle pressure and temperature according with the trend described in Section 2, it is possible to achieve densities from $1 \cdot 10^{13}$ atoms/cc to $3.2 \cdot 10^{14}$ atoms/cc. This is more than a factor of 5 higher than the maximum density reached in E760 ($6 \cdot 10^{13}$ atoms/cc).

Considering the width of the density distribution (Fig. 7), it is possible to plot the density distribution in atoms/cm^2 (Fig. 11).

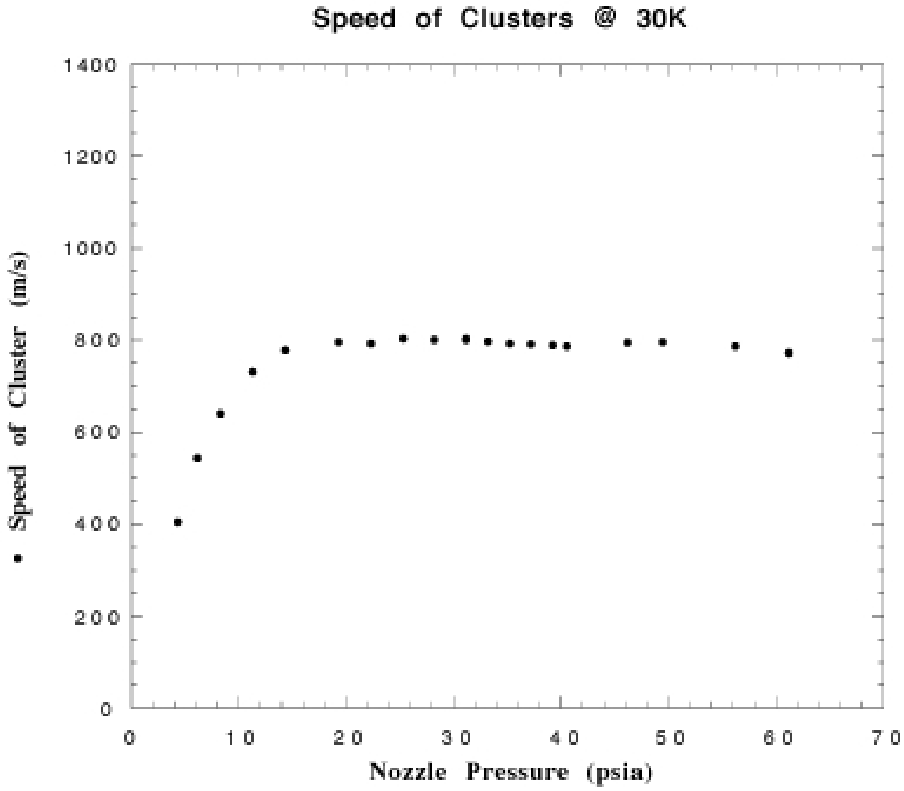

Fig. 8: The cluster speed at 30K, varying the nozzle pressure. For pressure higher than 20 psia the speed distribution saturates.

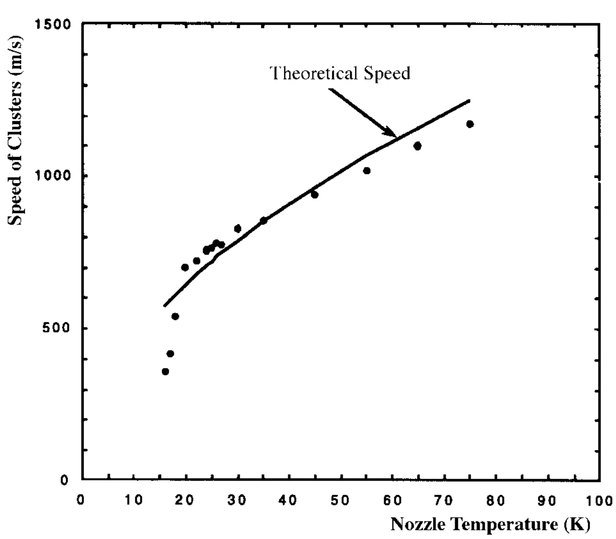

Fig. 9: Results from the cluster speed measurements. The continuous line shows the values given by the kinetic theory.

Fig. 12 shows the nozzle temperature and pressure chosen and the corresponding density values. These conditions have been reproducible throughout the last 9 months of running.

From the pressure inside the Antiproton Accumulator we know that the diffused gas along the entire length is about 5% of the gas which constitutes the target. In other words, 95% of the interactions occur in the interaction area monitored by the final state detector. This is a great improvement as compared to E760 for which the diffused gas percentage of 40%.

Adjusting the temperature and pressure according to the conditions shown in Fig. 12, it is possible to keep the instantaneous luminosity of the experiment at a constant value, typically $2 \cdot 10^{31}$ $cm^{-2}s^{-1}$ (Fig. 13).

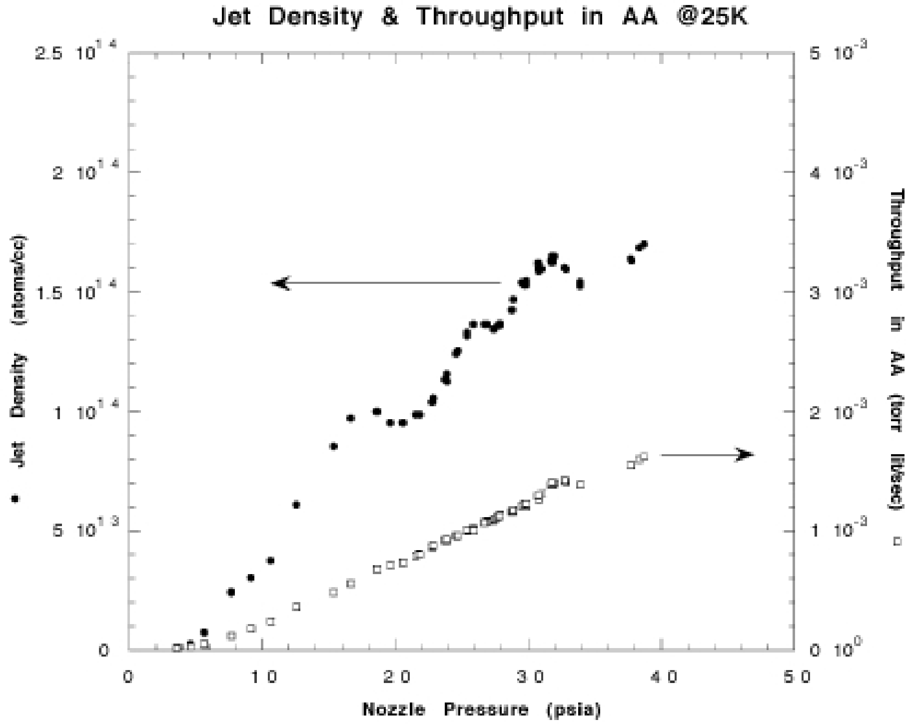

Fig. 10: Jet Density at a nozzle temperature of 25K. Also shown is the throughput of the background gas diffused in the Antiproton Accumulator.

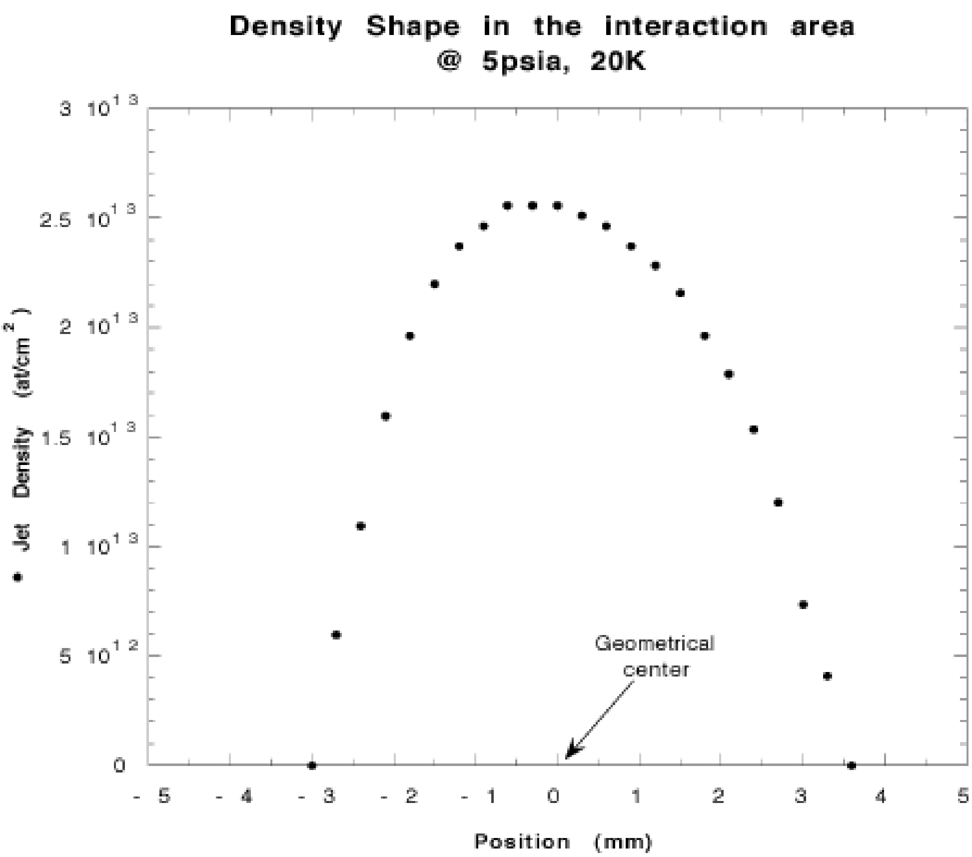

Fig. 11: The density in atoms/cm^2 in the interaction region with the antiproton beam. On the x axis, 0 represent the theoretical axis of the jet.

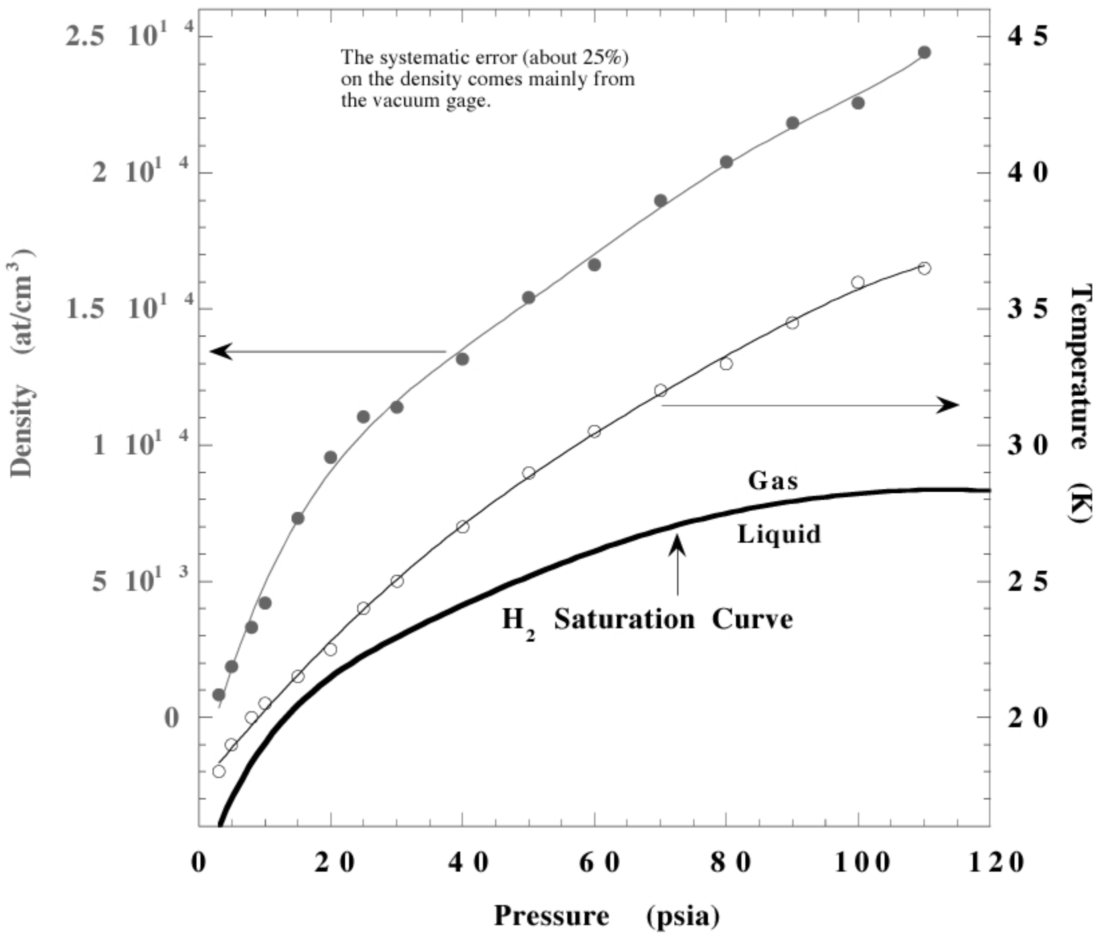

Fig. 12 The "open circle" curve (right axis) shows the Temperature vs. Pressure condition of the nozzle chosen for varying density. The "full circle" (left axis) curve shows the Density vs. Pressure obtained for that pressure and temperature. The thick black line is the saturation curve for hydrogen.

4. CONCLUSIONS

The internal Gas Jet Target for E835 (Charmonium spectroscopy) at the Fermilab Antiproton Accumulator is an upgraded version of the system used in E760. It's main feature is the cryocooler expansion stage, which allows much higher densities ($3.2 \cdot 10^{14}$ atoms/cc), and a better pumping system which, together with the new alignment system, lowers the background gas. Using the Target in a new operational mode, the variable density, we have obtained a substantial increase in the integrated luminosity of the experiment.

5. ACKNOWLEDGMENTS

The work which has made possible the achievements in the target performances is the result of a splendid collaboration between two Fermilab groups: the PAB support group (in particular R. Davis, D. Miller) and the Cryogenic group (in particular the staff of Lab 3) and the INFN technical services; the mechanical workshop (in particular F. Conforti, G. Franzone, P. Pollovio and E. Vigo), the mechanical project service (in particular G. Massari) and E. Bozzo. We would like to acknowledge the work of all the people that made possible the construction and use of the first version of the target used in Experiment 760.

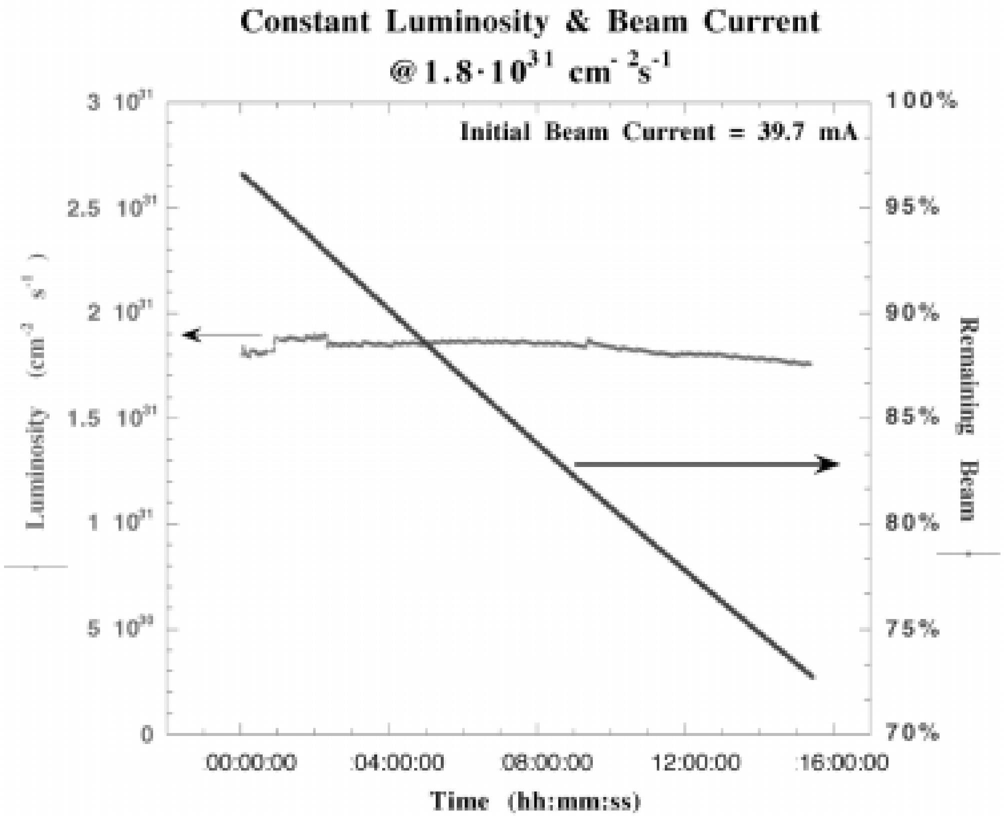

Fig. 13: A 16 hour period of data taking in which the instantaneous luminosity is kept at about $2{\cdot}10^{31}$ $cm^{-2}s^{-1}$. The antiproton beam current varies from 39.7 mA to 29 mA.

REFERENCES

[1] M. Macri, *Gas Jet Targets*, CERN 84-15 (1984)
M. Macri, in *Internal Gas Jet Targets for Nuclear and Particle Physics Experiments in Hadronic Physics at Intermediate Energies*, T. Bressani Editor, Elsevier Sc. Pub. (1987)

[2] C. Baglin et al., *Nucl. Phys*. B286:85 (1987)

[3] L. Bertolotto et al., *Phys. Lett*. B345:325 91995)

[4] G. Baur et al., *Phys. Lett*. B368:251 (1996)

[5] R. Cester and P. A. Rapids, Annu. Rev. Nucl. Part. Sci. 44 (1994), 329

[6] T. A. Armstrong et al., Fermilab Proposal 835 (1992)

[7] O. F. Hagena, W. Obert, *J. Chem. Phys.* 59:1793 (1972)
J. Gspann, K. Korting, *J. Chem. Phys*. 59:4726 (1973)

[8] D. R. Miller, *Free jet sources*, in *Atomic and molecular beam methods*, vol. I, p. 14, G. Scoles ed., Oxford Univ. Press (1988)
M. Kappes, S. Leutwyler, *Molecular beams of clusters,* in *Atomic and molecular beam methods*, vol. I, p. 380, G. Scoles ed., Oxford Univ. Press (1988)

[9] D. H. Allspach et al., *The E760 Jet Target: measurements of performance at 77K*, Fermilab-TM-1915, Nov. 1994

[10] D. H. Allspach et al., *Refrigerated Hydrogen Gas Jet for the Fermilab Antiproton Accumulator*, in *Advances in Cryogenic Engeneering*,vol. 41, p. 685, P. Kittel ed., Plenum Press,NY (1996)

BTeV/CØ

Daniel M. Kaplan[1]
Illinois Institute of Technology, Chicago, IL 60616, USA

Abstract

The physics goals and techniques of the proposed BTeV experiment at the C0 Tevatron interaction area are summarized, with emphasis on aspects of the experiment that depend on near-beam issues. BTeV aims to carry out a comprehensive study of rare processes (especially *CP* violation) in charm and beauty decay starting in collider Run II. Vertex detectors will be deployed within a few mm of the beam. Early running may employ a wire target in the beam halo.

1 INTRODUCTION

The BTeV collaboration is proposing to carry out a dedicated heavy-quark collider experiment in the C0 interaction region at the Tevatron. The main goals of BTeV are to search for *CP* violation, mixing, and rare flavor-changing neutral-current (FCNC) decays of b- and c-quark hadrons at unprecedented levels of sensitivity. Each year of BTeV collider operation is expected to produce $\mathcal{O}(10^{11})$ b hadrons and $\mathcal{O}(10^{12})$ c hadrons, to be compared with $\mathcal{O}(10^7)$ of each available at the e^+e^- "B Factories" and $\mathcal{O}(10^9)$ b events per year at the HERA-B fixed-target experiment. The BTeV spectrometer is being designed to make optimal use of the produced samples, avoiding many of the compromises necessary in general-purpose detectors.

The rationale for sensitive b-quark studies has been discussed extensively [1]-[3]. In a nutshell, the goal is to test thoroughly the Kobayashi-Maskawa (KM) [4] mechanism – the Standard-Model explanation for *CP* violation – in a regime in which large effects are expected, as opposed to the $\mathcal{O}(10^{-3})$ effects observed in the K^0 sector [5, 3]. The KM model, while compatible with all known experimental evidence, is not unique, and it is appropriate to regard the origin of *CP* violation as a key unsolved problem of contemporary science. The baryon asymmetry of the universe leads us to think [6] that *CP* violation beyond that predicted in the KM model should exist [7]. The over-arching question in particle physics today is, what "new physics" underlies the Standard Model?[2] It is possible that K^0 *CP* violation arises in part or even entirely from physics outside the Standard Model, in which case it is the only new-physics signature that has already been observed.

Many experiments now seek to address this topic. The B-Factory and HERA-B groups are vying to be the first to observe *CP* violation in B decay, and the CDF and D0 groups are not far behind. However, it is likely that these efforts, while adequate to observe effects, will not suffice for the thorough investigation that the importance of the topic demands.

High-sensitivity charm studies are complementary to beauty studies. In the Standard Model, *CP* violation, mixing, and FCNC decays, all relatively large in beauty, are drastically suppressed in charm [8]. Any contribution from new physics will thus stand out dramatically. For example, new physics might be Higgs-like and couple to quark mass [9], or might couple more strongly to "up-type"[3] than "down-type"[4] quarks [10]. In such scenarios, charm has the biggest new-physics signal-to-background ratio of any quark. On the experimental side one has (compared to beauty) large production cross sections, large branching ratios to final states of interest, and straightforward tagging via the $D^{*+} \to D^0\pi^+$ decay chain. The experimental approach taken by BTeV, featuring a primary trigger based on the presence of secondary vertices, naturally provides high charm and beauty sensitivity simultaneously. We can thus carry out a "two-pronged assault" on the Standard Model.

2 STANDARD-MODEL *CP* VIOLATION

2.1 The CKM Quark-Mixing Matrix

The KM mechanism for *CP* violation invokes a non-zero phase in the Cabibbo-Kobayashi-Maskawa (CKM) quark mixing matrix [11, 4],

$$V = \begin{pmatrix} V_{ud} & V_{us} & V_{ub} \\ V_{cd} & V_{cs} & V_{cb} \\ V_{td} & V_{ts} & V_{tb} \end{pmatrix} .$$

The matrix V parametrizes the coupling of the W bosons to the quarks in a way that allows the generations to mix. For example, instead of coupling the u quark only to the d, W^+ emission couples the u to the linear combination

$$V_{ud}|d\rangle + V_{us}|s\rangle + V_{ub}|b\rangle ,$$

with similar expressions for the couplings to the c and t quarks. This generation mixing provides an explanation for the observed non-stability of the s and b quarks.

As is well known, for two generations of quarks, the quark mixing matrix is real and has one free parameter, the Cabibbo angle [11]. Being unitary, for three quark generations the matrix depends on only four independent parameters, including one non-trivial phase [4]. Certain decays can occur via more than one Feynman diagram in such a way that the interference term between the diagrams contains this phase. When the decay width for such a reaction is compared to that for the *CP*-conjugate reaction, the dependence on the CKM phase (whose sign changes under *CP*) can result in a *CP* asymmetry, *e.g.*

$$A \equiv \frac{\Gamma(B \to f) - \Gamma(\overline{B} \to \overline{f})}{\Gamma(B \to f) + \Gamma(\overline{B} \to \overline{f})} \neq 0 ,$$

[1] For the BTeV Collaboration

[2] The Standard Model, while consistent with all established experimental results, has more than twenty free parameters (the lepton masses, quark masses and mixing parameters, coupling constants, Weinberg angle, Higgs mass, etc.) and thus is generally considered to be only an approximation. New physical effect(s) yet to be discovered are presumed to determine the values of these parameters.

[3] *i.e.*, the u, c, and t quarks

[4] *i.e.*, the d, s, and b quarks

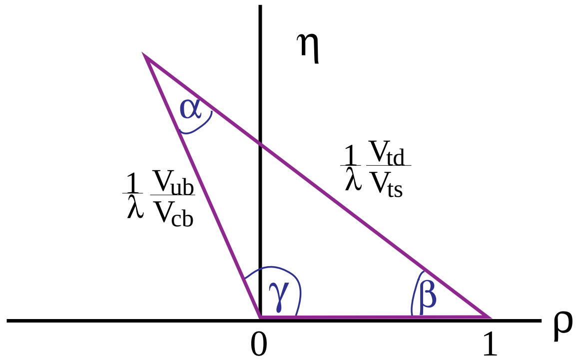

Figure 1: The "unitarity triangle" for couplings of the b quark, expressed in terms of the λ, ρ, and η variables of the Wolfenstein parametrization [12] of the CKM matrix.

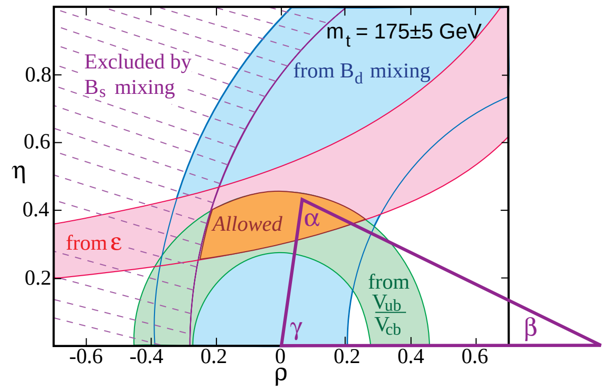

Figure 2: Current knowledge of the CKM triangle, based on experimental constraints on the lengths of its sides from B decays, and on the position of its apex from the ε parameter of K^0 *CP* violation, with estimated 1σ error bands.

which will depend on the decay time if the interference involves $B\overline{B}$ mixing.

The unitarity of the CKM matrix further implies that the product of any two of its rows or columns be zero. One such relationship is

$$V_{ud}V_{ub}^* + V_{cd}V_{cb}^* + V_{td}V_{tb}^* = 0\,.$$

This relationship constrains mixing rates and *CP* asymmetries in various decays of beauty hadrons. Since it states that three complex numbers sum to zero, it can be visualized as defining a triangle in the complex plane (Fig. 1). Because (unlike the case in the K^0 and charm sectors) the sides of this triangle are all roughly similar in length [2] (Fig. 2), the angles are expected to be large. Since the angles determine the *CP* asymmetries, these should be uniquely large in beauty decays.

2.2 Studying the Unitarity Triangle

The task of verifying the KM model then reduces to measuring enough of the mixing and asymmetry parameters to prove that the triangle is indeed closed, *i.e.* that its angles and the lengths of its sides are consistent. In addition it must satisfy constraints from *CP* violation in the K^0 sector (Fig. 2). Ideally one would make enough different measurements to verify that *all* decays constrained by the unitarity triangle satisfy the constraints. This task is made difficult by the small branching ratios for interesting B-hadron final states (*e.g.* 1.7×10^{-5} for $B_d \to J/\psi K_S \to \mu^+\mu^-\pi^+\pi^-$), thus a large $b\bar{b}$ production cross section is required. Since $\sigma_{b\bar{b}} \sim 100\,\mu$b at $\sqrt{s} = 2\,$TeV, the Tevatron collider is a natural venue for such studies.

The angle β can be determined from the *CP* asymmetry in $B_d \to J/\psi K_S$ with essentially no theoretical uncertainty. Since this mode also has a clean experimental signature in the $J/\psi \to$ dileptons decay and (compared to other modes with large expected *CP* asymmetries) a relatively large compound branching ratio, it is sometimes called the "golden" mode for B *CP* violation. Its *CP* asymmetry is expected [2] to be $\sim$0.5 in the Standard Model and is likely to be measured by $\approx$2002 in the next round of experiments.

The other two angles of the unitarity triangle are considerably harder to determine. It is often stated that α is measured in $B_d \to \pi^+\pi^-$. The measurement suffers from significant drawbacks. First, the branching ratio is small ($< 1.5\times10^{-5}$ at 90% C.L. [13]) and has yet to be definitively established. Second, the larger branching ratio observed for $B_d \to K^+\pi^-$ [13] imposes stringent experimental requirements on hadron identification and mass resolution to allow adequate suppression of $K\pi$ background, and also implies a significant contribution to $BR(B_d \to \pi^+\pi^-)$ from penguin diagrams, whose *CP* asymmetry is difficult to relate to CKM angles. Nevertheless, the measurement of the *CP* asymmetry in $B_d \to \pi^+\pi^-$ will be an important step forward and will furnish a significant constraint on models of *CP* violation.

Various methods of determining γ have been discussed and have various advantages and drawbacks. A promising method appears to be comparison of branching ratios for $B^+ \to \overset{(}{\overline{D^0}}\overset{)}{} K^+$ and $B^- \to \overset{(}{\overline{D^0}}\overset{)}{} K^-$ [14]. Both of these can occur via two processes that interfere, namely $B^+ \to \overline{D^0}K^+$, $\overline{D^0} \to K^+\pi^-$ and $B^+ \to D^0K^+$, $D^0 \to K^+\pi^-$ (and charge-conjugates). Since the first proceeds via $b \to u$ conversion while the second includes a doubly Cabibbo-suppressed D^0 decay, both are highly suppressed processes, leading to the favorable situation where the interference between them can have a relatively large effect (of order unity) on branching ratios. On the other hand, the branching ratios for these modes are expected to be $\mathcal{O}(10^{-6})$. Another method is via the mixing-induced *CP* asymmetry in $B_s(\overline{B_s}) \to D_s^{\mp}K^{\pm}$; this measurement will require excellent decay-time resolution given the rapid expected $B_s\overline{B_s}$-mixing oscillations.

We see that a complete test of the KM model will require very large B samples. Only hadroproduction can supply such large numbers of events. Furthermore, since several of the decay modes of primary interest are to all-hadronic final states, a significant physics penalty is paid if the typical B trigger, requiring high-p_t leptons from semileptonic or $B \to J/\psi$ decays, is employed. We are thus led to the BTeV strategy: a first-level trigger based on decay-vertex reconstruction.

BTeV's sensitivity has been estimated [15] as ±0.04 in $\sin 2\beta$ and (ignoring penguin contributions) ±0.1 in $\sin 2\alpha$. These are for one year of running at the nominal luminosity of 5×10^{31} cm^{-2}s^{-1}. We are investigating our sensitivity to γ and also the possibility of running at higher luminosity.

3 NON-STANDARD-MODEL *CP* VIOLATION

A variety of extensions to the Standard Model (SM) have been considered in which *CP*-violating phases can arise elsewhere than in the CKM matrix. Possible non-Standard sources for *CP* violation include additional Higgs doublets, non-minimal supersymmetry, massive W's with right-handed couplings ("left-right-symmetric" models), leptoquarks, a fourth generation, etc. [3, 16]. Such mechanisms could be responsible for all or part of K^0 *CP* violation.

These models have various attractive features. For example, an enlarged Higgs sector is a relatively natural and straightforward extension of the SM, especially since we know of no reason (other than Occam's Razor!) why, assuming Nature opted to implement the Higgs mechanism, she should have stopped after only one physical Higgs boson. Left-right-symmetric models are appealing in that they provide a unified explanation for both parity and *CP* violation. And in such extensions of the SM, the CKM phase could be exactly zero, perhaps due to some yet-to-be-determined symmetry principle – a less arbitrary scenario than the SM, in which the value of the CKM phase is a free parameter.

Typically these alternative models for *CP* violation lack the distinctive feature of the SM that *CP* asymmetries are largest in the B sector. Many of them can lead to *CP* violation in charm decay at the 10^{-3} to 10^{-2} level and have the additional distinctive signatures of large flavor-changing neutral currents or mixing in charm. While direct *CP* violation at the 10^{-3} level in Cabibbo-suppressed charm decays is a prediction of the Standard Model [17], its observation in Cabibbo-favored or doubly Cabibbo-suppressed decays would constitute unambiguous evidence for new physics, as would the observation of indirect *CP* violation in charm. At the levels discussed in the literature, such effects could be detectable in BTeV, which could reconstruct 10^8 to 10^9 charm decays, but more simulation is required to assess backgrounds and systematics [18].

4 THE BTEV SPECTROMETER

The proposed BTeV spectrometer (shown schematically in Fig. 3) covers the forward and backward regions at the new C0 Tevatron interaction area. The instrumented angular range is $0.01 \lesssim |\tan\theta| \lesssim 0.3$. Monte Carlo simulation shows that such coverage includes ~50% of all B and D decays.

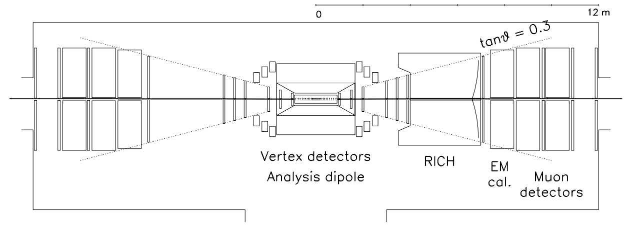

Figure 3: Sketch of BTeV Spectrometer.

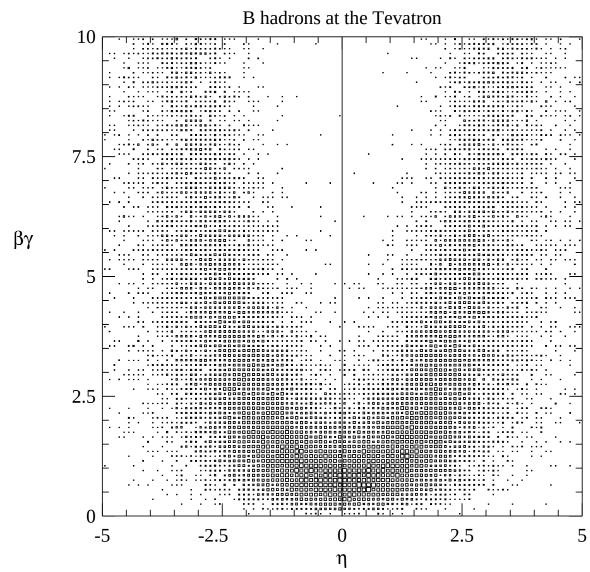

Figure 4: Relativistic boost factor $\beta\gamma$ *vs.* pseudorapidity η of B hadrons produced at the Tevatron Collider.

Compared to the "central-geometry" case (*e.g.* CDF and D0), this "forward-geometry" configuration accepts relatively high-momentum particles (see Fig. 4). It also leads to an advantageous vertex-detector arrangement, consisting of detector planes inside the vacuum pipe oriented perpendicular to the beam (Fig. 5), allowing substantially better reconstruction of decay proper time. Another key advantage of forward geometry is the feasibility of effective hadron identification. Because QCD mechanisms of $b\bar{b}$ production yield quark pairs that are closely correlated in rapidity ($|y_b - y_{\bar{b}}| \lesssim 1$), there is little disadvantage in omitting the small-rapidity region: when the decay products of one B hadron are detected in the forward (or backward) region, decay products of the second ("tagging") B have a high probability to be detected there also.

In addition to large acceptance, the apparatus must have high interaction-rate capability, an efficient trigger for heavy-quark decays, high-speed and high-capacity data acquisition, good mass and vertex resolution, and good particle identification. Of these requirements, the most challenging are the trigger and the particle identification. We intend to trigger primarily on the presence of a decay vertex separated from the primary vertex [19]. To reduce occupancy and facilitate vertex reconstruction at trigger

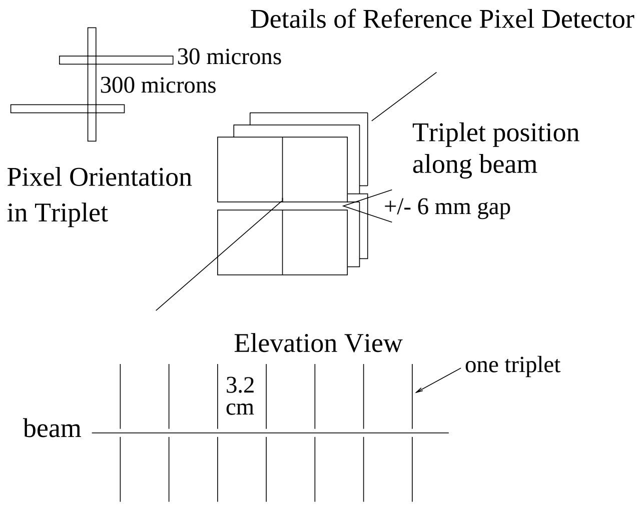

Figure 5: Proposed arrangement of BTeV vertex detector.

level 1, pixel detectors will be used for vertex reconstruction. For efficient, reliable, and compact particle identification, we will build a ring-imaging Cherenkov counter. In other respects the spectrometer will resemble existing large-aperture heavy-quark experiments; see Refs. [15, 20] for more detailed discussions.

5 NEAR-BEAM ISSUES IN BTEV

5.1 Size of vertex-detector beam gap

A key point in the reconstruction of decay vertices in forward geometry is the dependence of the impact-parameter resolution on the transverse distance of the vertex detectors from the beam [21]. This is illustrated in Fig. 6. For sufficiently fine pixel resolution, the impact-parameter resolution will typically be dominated by multiple coulomb scattering in the first detector plane that the particle encounters. The effective r.m.s. scattering angle $\delta\theta_y$ in the y-z view for a charged particle of momentum p traversing a detector of thickness X and radiation length X_0 is [22]

$$\delta\theta_y \approx \frac{0.015\,\mathrm{GeV}}{p}\sqrt{\frac{X}{X_0}}\,.$$

(The thickness X of course must include substrate, readout electronics, and RF shielding.) If the particle encounters the first detector at a longitudinal distance z from the vertex and transverse distance y from the beam, the scattering contribution to impact-parameter resolution is

$$\begin{aligned} \delta y &\approx z\delta\theta_y \\ &\approx y\left(\frac{0.015\,\mathrm{GeV}}{p_y}\sqrt{\frac{X}{X_0}}\right)\,. \end{aligned} \tag{1}$$

A similar equation holds for the x-z view, where δx also depends on p_y since the beam gap is assumed to be in y.

We see that the impact-parameter error is proportional to the transverse distance of the track from the beam at the first measurement plane encountered by the particle. To minimize the scattering contribution, it is thus important to keep the beam gap as small as possible. The other parameters appearing in Eq. 1 are less subject to control by the experimenter: the distribution of p_y is determined by the mass and production and decay dynamics of the particle to be studied, and X/X_0 is fixed by signal/noise, mechanical support, and cooling issues. Furthermore, the dependence on X/X_0 is as the square root, so while thickness should be minimized, it is difficult to make a big impact in this way.

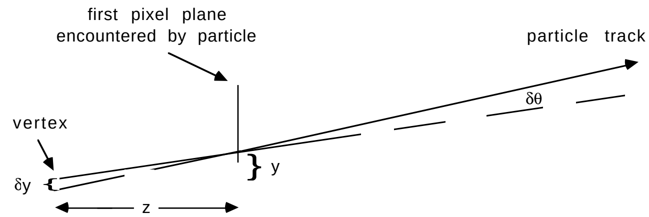

Figure 6: Illustration of dependence of vertical impact-parameter error δy on scattering angle $\delta\theta$ in first pixel plane.

Fig. 7 shows the dependence of the proper-time resolution on the size of the beam gap for simulated $B_s \to J/\psi K^*$ events. (The time resolution in this mode is an indicator of physics reach for studies of B_s mixing, a challenging measurement in b physics.) As the half-gap $y_{\min}$ is decreased from 9 mm to 3 mm, the r.m.s. resolution improves by about a factor of 2. In addition, since cuts on vertex separation must be made in order to suppress background, the number of events in the final sample increases by more than a factor of 2. This indicates the substantial improvement in physics reach that is possible if the vertex detectors can be moved closer to the beam. With the nominal 6 mm half-gap, the reach in x_s (the parameter that relates the B_s mixing rate to its decay rate) is about 40, *i.e.* if $x_s = 40$ we expect to obtain a 5-standard-deviation signal for B_s mixing in about one year of running at $\mathcal{L} = 5\times10^{31}\,\mathrm{cm^{-2}s^{-1}}$. This should be compared with the Standard-Model prediction $x_s < 60$ and the current experimental lower limit $x_s > 15$ [23].

The size of the half-gap is in principle limited from below by two effects: 1) radiation damage in the vertex detectors and 2) creation of backgrounds at the other interaction regions. In practice the first limit will be reached well before the second! For silicon detectors with a 4 mm half-gap, the radiation-damage limit ($\sim 10^{14}$ minimum-ionizing particles/cm^2) is reached in $\approx$1 year of running at $\mathcal{L} = 5\times10^{31}\,\mathrm{cm^{-2}s^{-1}}$. Development of diamond pixel detectors may allow a smaller gap.[5]

5.2 Wire-target running in C0

The commissioning of a third collider interaction region is likely to be a complex process, and simultaneous collider

[5] Subsequently to this Symposium, vertex-detector geometries with a square beam hole instead of a full-width gap have been simulated and found to improve physics reach substantially, *e.g.* the B_s-mixing reach for one year of running at $\mathcal{L} = 5\times10^{31}\,\mathrm{cm^{-2}s^{-1}}$ increases to $x_s \approx 65$.

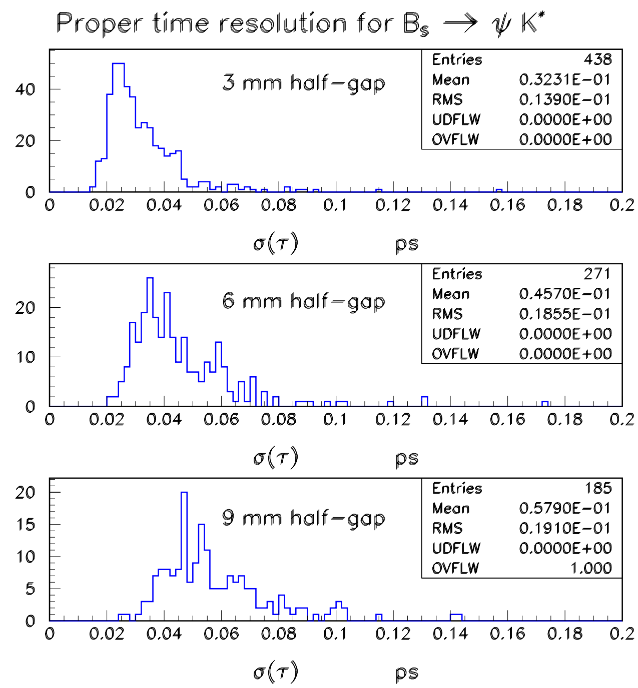

Figure 7: Simulated distribution of proper-time resolution for $B_s \to D_s\pi$ events for three different values of $y_{\rm min}$.

luminosity in all three areas might not be available during the first years of Collider Run II. It has thus been envisaged since the earliest consideration of the C0 program [24] that a significant portion of the early running might be carried out using a wire or pellet target in the halo of the proton or antiproton beam. This could afford an early opportunity for commissioning of detectors. Since it would provide a source of primary interactions localized at a known point or along a known line in space, it could also be invaluable for testing the vertex trigger.

While halo running would be essentially useless for beauty due to the small fixed-target b cross section [25], surprisingly, the charm reach could be comparable in fixed-target and collider modes. The increase in charm cross section at $\sqrt{s} = 2$ TeV compared to 43 GeV has not been measured but is presumed to be a factor $\gtrsim$10. However, if only one spectrometer arm is instrumented at first, fixed-target has a factor-of-3 advantage in geometrical acceptance, and a factor $\approx$4 in cross section can be made up by taking advantage of the target-A dependence of charm production ($\sigma_{c\bar{c}} \propto A^1$ [26] *vs.* $A^{0.71}$ [22] for the total inelastic cross section which limits the interaction rate). Finally, triggering on charm is likely to be considerably more efficient in fixed-target mode, where the moderate p_t ($\lesssim$1 GeV) of charm decay products stands out more prominently relative to minimum-bias background: in fixed-target a factor $\approx$100 in background suppression is available *before* vertex reconstruction [15], perhaps allowing charm triggering in the short-lifetime regime (proper time $<$ 1 ps) crucial to studies of charm mixing in $D^0 \to$ hadrons decays [27].

A possible physics advantage of halo running has also been suggested [28]. Biases in charm mixing studies may arise from $b \to c$ cascade decays. These would be suppressed by two orders of magnitude in fixed-target relative to collider mode, due to the reduced beauty production cross section.

Assuming a 1 MHz rate of inelastic interactions, $> 10^8$ charm decays can be reconstructed per year (10^7 s) of fixed-target operation. For example, the rate of $D^0(\overline{D^0}) \to K^\mp\pi^\pm$ is estimated as [29]

$$\begin{aligned} n_{D^0(\overline{D^0})\to K\pi} = & \quad 10^7{\rm s} \cdot 10^6{\rm int./s} \cdot \\ & 6.5\times 10^{-4} A^{0.29} D^0(\overline{D^0})/{\rm int.} \cdot \\ & 4\% \cdot 10\% \qquad (2) \\ = & \quad 1\times 10^8\,, \end{aligned}$$

where the last two factors appearing in Eq. 2 are $BR(D^0 \to K^-\pi^+)$ and the product of acceptance and reconstruction efficiency. Other decay modes will increase the total by a factor $\sim$3. This interaction rate implies $\approx$0.4 interactions/crossing with 396 ns bunch spacing and $\approx$0.1 with 132 ns spacing, low enough that p_t-based triggers should not be badly affected by pile-up. That a 1 MHz interaction rate is feasible with a halo target follows from the work of the HERA-B collaboration, who have demonstrated 30 MHz with wire targets in the halo of the HERA proton beam [30]. However, the Tevatron scraping and collimation procedures may need considerable rethinking, since high-rate operation of a halo target requires that the target compete efficiently with the collimators.

6 CONCLUSIONS

If approved, BTeV will be the state-of-the-art charm and beauty experiment in the mid-2000's period. The near-beam environment will be key to the experiment's physics reach:

- Minimizing the size of the vertex-detector beam gap will both maximize the number of events satisfying analysis cuts and optimize their vertex resolution.
- Early charm sensitivity at a competitive level may depend on halo targeting.

7 REFERENCES

[1] See for example A. J. Buras, in *Proc. Beauty '95*, N. Harnew and P. Schlein, eds., Nucl. Instrum. Meth. **A368**, 1 (1995).

[2] A. J. Buras and R. Fleischer, "Quark Mixing, CP Violation and Rare Decays After the Top Quark Discovery," TUM-HEP-275/97, TTP97-15, hep-ph/9704376, to appear in **Heavy Flavours II**, A. J. Buras and M. Lindner, eds., World Scientific;
A. Ali and D. London, Nucl. Phys. Proc. Suppl. **54A**, 297 (1997);
S. Stone, "The Goals and Techniques of BTeV and LHC-B," HEPSY-97-3, hep-ph/9709500, to appear in *Proc. Int'l School of Physics, 'Enrico Fermi:' Heavy Flavor Physics –*

A Probe of Nature's Grand Design, Varenna, Italy, 8–18 July 1997.

[3] See for example J. L. Rosner, "Present and Future Aspects of *CP* Violation," hep-ph/9506364, in **Particles and Fields: Proc. 8th Jorge Andre Swieca Summer School**, J. Barcelos-Neto, S. F. Novaes, V. O. Rivelles, eds., World Scientific, 1996, p. 116;
B. Winstein and L. Wolfenstein, Rev. Mod. Phys. **65**, 1113 (1993).

[4] M. Kobayashi and T. Maskawa, Prog. Theor. Phys. **49**, 652 (1973).

[5] J. H. Christenson, J. W. Cronin, V. L. Fitch, and R. Tourlay, Phys. Rev. Lett. **13**, 138 (1964).

[6] A. D. Sakharov, Pis'ma Zh. Eksp. Teor. Fiz. **5**, 32 (1967) [JETP Lett. **5**, 24 (1967)];
E. W. Kolb and M. S. Turner, "Baryogenesis," in **The Early Universe**, Addison-Wesley, 1990, p. 157.

[7] H. Quinn, Nucl. Phys. Proc. Suppl. **50**, 17 (1996);
P. Huet and E. Sather, Phys. Rev. D **51**, 379 (1995).

[8] G. Burdman, "Charm Mixing and *CP* Violation in the Standard Model," in **The Future of High-Sensitivity Charm Experiments**, *Proc. CHARM2000 Workshop*, Fermilab, June 7–9, 1994, D. Kaplan and S. Kwan, *eds.*, FERMILAB-Conf-94/190, p. 75, and
"Potential for Discoveries in Charm Meson Physics," in **Workshop on the Tau/Charm Factory**, J. Repond, *ed.*, Argonne National Laboratory, June 21–23, 1995, AIP Conf. Proc. No. 349 (1996), p. 409;
S. Pakvasa, "Charm as Probe of New Physics," in **The Future of High-Sensitivity Charm Experiments**, *op. cit.*, p. 85, and
"Flavor Changing Neutral Currents in Charm Sector (as Signal for New Physics)," to appear in *Proc. Symp. on Flavor Changing Neutral Currents: Present and Future Studies (FCNC 97)*, Santa Monica, CA, 19–21 Feb. 1997.

[9] I. I. Bigi, "On Charm Decays: Present Status and Future Goals," in **Charm Physics**, *Proc. Int. Symp. on Charm Physics*, Beijing, China, June 4–16, 1987, Gordon and Breach (1987), p. 339.

[10] W. Buchmuller and D. Wyler, Phys. Lett. **177B**, 377 (1986) and Nucl. Phys. **B268**, 621 (1986);
Miriam Leurer, Phys. Rev. Lett. **71**, 1324 (1993);
A. Hadeed and B. Holdom, Phys. Lett. **159B**, 379 (1985).

[11] N. Cabibbo, Phys. Rev. Lett. **10**, 531 (1963).

[12] L. Wolfenstein, Phys. Rev. Lett. **51**, 1945 (1983).

[13] R. Godang *et al.*, "Observation of Exclusive Two Body B Decays to Kaons and Pions," CLNS 97-1522, CLEO 07-27, hep-ex/9711010 (1997).

[14] D. Atwood, I. Dunietz, and A. Soni, Phys. Rev. Lett. **78**, 3257 (1997);
I. Dunietz, "Beautiful CP Violation," to appear in **Twenty Beautiful Years of B Physics**, Proc. of the b20 Symposium, Illinois Institute of Technology, Chicago, IL, June–July 1997, R. A. Burnstein, D. M. Kaplan, and H. A. Rubin, eds., AIP Press.

[15] A. Santoro *et al.*. "An Expression of Interest for a Heavy Quark Program at C0," May 1997.

[16] J. F. Donoghue, B. R. Holstein, and G. Valencia, Int. J. Mod. Phys. A, **2**, 319 (1987).

[17] M. Golden and B. Grinstein, Phys. Lett. B **222**, 501 (1989);
F. Buccella *et al.*, Phys. Lett. B **302**, 319 (1993) and **379**, 249 (1996).

[18] For a more detailed discussion of new-physics reach in charm see D. M. Kaplan, Nucl. Phys. B (Proc. Suppl.) **50**, 260 (1996).

[19] D. Husby *et al.*, "Design of a Secondary Vertex Trigger System," in *Proc. 5th Int. Conf. on Electronics for Particle Physics*, eds. G.J. Blanar and R.L. Sumner, (LeCroy Corp., Chestnut Ridge, NY, 1995);
R. Isik *et al.*, U. of Pa. Report UPR-234E (1996).

[20] S. Stone, "The BTeV Program," to appear in proc. B Physics and *CP* Violation, Honolulu, HI, March 1997;
J. N. Butler, "Prospects for Heavy Flavor Physics at Hadron Colliders," to appear in **Fundamental Particles and Interactions**, proc. of Frontiers in Particle Physics, Vanderbilt Univ., Nashville, TN, May 1997, Robert S. Panvini and Thomas J. Weiler, eds., AIP Press;
P. L. McBride, "BTeV," to appear in **Twenty Beautiful Years of B Physics**, *op. cit.*

[21] W. Selove, in *Proc. Workshop on B Physics at Hadron Accelerators*, eds. C.S. Mishra and P. McBride, FERMILAB-Conf-93/267 (1993), p. 617.

[22] R. M. Barnett *et al.* (Particle Data Group), Phys. Rev. D **54**, 1 (1996) and 1997 off-year partial update for the 1998 edition available on the PDG WWW pages (URL: http://pdg.lbl.gov/).

[23] V. Andreev *et al.*, "Combined Results on B^0 Oscillations: Update for the Summer 1997 Conferences," LEP-BOSC 97/2, Aug. 18, 1997.

[24] J. Peoples, private communication;
J. Peoples, comments at the C0 Workshop, Fermilab, Dec. 4–6, 1996.

[25] D. M. Jansen, *et al.*, Phys. Rev. Lett. **74** (1995) 3118.

[26] M. J. Leitch *et al.*, Phys. Rev. Lett. **72**, 2542 (1994).

[27] E. M. Aitala *et al.*, Phys. Rev. D **57**, 13 (1998).

[28] D. M. Kaplan, "A Future Charm Facility," to appear in *Proc. Symp. on Flavor Changing Neutral Currents: Present and Future Studies (FCNC 97)*, Santa Monica, CA, 19–21 Feb. 1997, IIT-HEP-97-1, hep-ex/9705002.

[29] The charm rate per inelastic interaction at 1 TeV beam energy is conservatively estimated by averaging results on charged- and neutral-D production by 800 GeV proton beams from R. Ammar *et al.*, Phys. Rev. Lett. **61**, 2185 (1988); K. Kodama *et al.*, Phys. Lett. B **263**, 573 (1991); and M. J. Leitch *et al.* (*op. cit.*), assuming linear A dependence as observed by Leitch *et al.*

[30] K. Ehret, "Performance of the HERA-B Target and Interference with HERA Operation," this Symposium.

A Zero Degree Experiment at the Tevatron Collider

Lawrence W. Jones and Michael J. Longo
University of Michigan, Ann Arbor, MI 48109-1120

Abstract

A small experiment has been proposed for the C0 experimental area at the Tevatron collider to study the production of particles at and close to zero degrees. Such data will fill a glaring gap in the systematic study of strong interactions. Besides enabling better theoretical understanding of the relevant QCD processes, it will supply valuable input to the design of collimators and beam scrapers. It will also resolve long-standing ambiguities and explore intriguing anomalies reported from cosmic ray data.

1 INTRODUCTION

A proposal (P-899) has been submitted to the Fermilab management for a small experiment on "Particle Production at 0^0 from the Collider" by a group of physicists from the University of Michigan, the University of Tennesee, Case Western Reserve University, Lousiana State University, and Fermilab. The spokesman is Michael J. Longo from Michigan. Briefly, the objective is to measure the production of hadrons and leptons produced down to and including zero degrees, data which have been unavailable from almost all energies above those explored with fixed-target bubble chamber exposures about 20 years ago. The experiment would utilize the C0 experimental area within the window of time between the re-commissioning of the Collider and the installation of the B-TeV detector.

2 MOTIVATION

The motivations for this experiment are at least three. First, the physics of 'soft QCD' processes has been very little explored, and substantial theoretical questions remain. The physics of Pomeron exchange, etc., has attracted increasing attention, as attested by the discussions at workshops on "Small x and Diffractive Physics" held at Argonne and Fermilab in recent years. A recent summary of the relevant physics issues may be found in the FELIX Letter of Intent [1] submitted to the CERN LHC Committee this past August.

Second, this physics is clearly related to the design of beam scrapers, collimators, and to the properties of beam halos; and hence very directly relevant to the objectives of this conference. Without doubt, better knowledge of the small-angle particle production will lead to better design of collimators and related beam-cleaning hardware. This falls in the category of what Leon Lederman has referred to as 'engineering physics'.

Third, cosmic ray physics is dominated by energy flow, and this, in turn, by particles produced in the far-forward direction (extreme values of pseudorapidity). And yet essential quantities such as the average inelasticity in a nucleon-nucleon collision are very poorly known and subject to widely- varying assumptions. The inelasticity of a nucleon-nucleon collision, wherein the target nucleon is intitially at rest (the cosmic ray situation), is given by: $K = [1 - (E_s/E_o)]$, where E_o is the incident particle (e.g. proton) energy and E_s is the energy of the most energetic final-state baryon. The state of confusion on average inelasticity is reflected in Figure 1 from a recent publication [2].

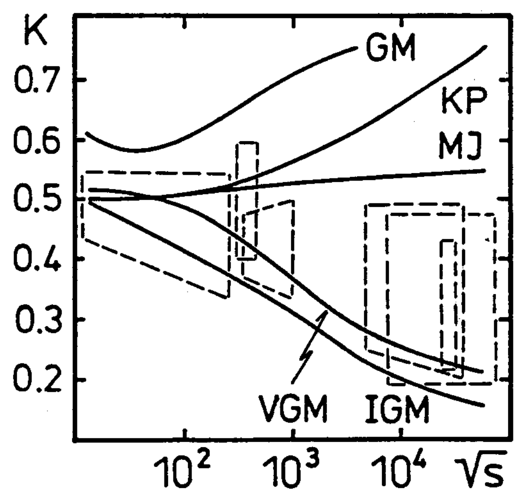

Figure 1: Energy dependence of average inelasticity in p-p reactions inferred from various cosmic ray data (dashed boxes) and from predictions of different theoretical models and simulations.

Although the energy of cosmic rays, as interpreted through air showers or air Cherenkov radiation, is not affected by this uncertainty (at very high energies, virtually all of the primary cosmic ray energy eventually appears in the electromagnetic component), the interpretation of such quantities as muon-electron ratio and depth of maximum numbers of particles in an air shower depends on both the primary cosmic ray particle mass number and on this inelasticity. This essential ambiguity between average inelasticity and the nuclear composition of the primary cosmic rays has frustrated the interpretation of cosmic ray data for decades. At primary energies above $10^{14} eV$, the low flux makes direct observation of the incident cosmic ray particles impossible (with satellites or balloons), hence our knowledge is totally reliant on indirect observations at ground level. Given the increasing interest in cosmic ray physics by the particle physics community (as evidenced, for example, by the Fermilab participation in the Auger Project), accelerator results which are of direct use in interpreting cosmic ray data have become quite timely.

In addition, the forward physics-dominated cosmic ray data continue to suggest new physics; anomalous phenomena (Chirons, Halos, Centauros, large cross sections for heavy flavor production, etc.) which have not been seen -

or hardly explored - in accelerator data [1].

3 HISTORICAL BACKGROUND

The hydrogen bubble chambers at Fermilab and CERN, working with pion and proton beams, collected inclusive data at energies of 300 - 400 GeV, and of course have good, inclusive data on production of charged hadrons down to and including zero degrees. There were subsequent Fermilab neutron data from 400 GeV protons at zero degrees, as well as charged pion and proton production data from 100 and 175 GeV protons with a forward magnetic spectrometer. At the CERN ISR, with $\sqrt{s} = 60\ GeV$, zero degree production data on neutrons were again taken, as well as small angle negative hadron data. And at the CERN $Sp\bar{p}S$ ($\sqrt{s} = 540\ GeV$), UA5 data were taken on neutral pion production at angles greater than 1.6 mr. These data have been nicely reviewed by Voyvodic in 1992 [3].

However, the rather surprising observation remains that there is little comprehensive inclusive data on particle production at small angles from the colliders. The modest time and effort required for this proposed experiment will thus have an impact out of proportion to the overall cost of the required effort.

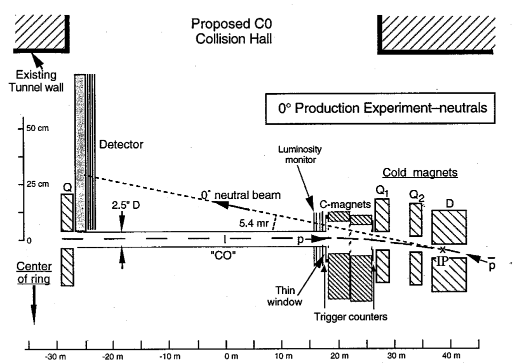

Figure 2: Experimental configuration for 0^0 neutral measurement. Note the transverse-longitudinal scale ratio of 40:1. The interaction point (IP) is about 38 m from the center of the straight section.

4 EXPERIMENTAL DETAILS

This experiment proposes to observe neutrons and gammas (from neutral pions) produced at zero degrees by locating the $\bar{p}-p$ intersection region within a superconducting bending magnet of the machine lattice, as sketched in Figure 2. Here it is seen that the zero degree neutral secondaries reach a detector about 30 cm outside the circulating beams at the opposite end of the straight section, more than adequate for a calorimeter which will contain the lateral spread of the hadronic cascade.

In this situation, the interaction point is moved to a point 38 m from the center of the C0 straight section. One obvious consequence of this is that this experiment would require dedicated running for its data collection. However, as the inclusive data come very fast, even with modest luminosity, it is estimated that the entire dedicated running time required to complete this experiment is less than a week.

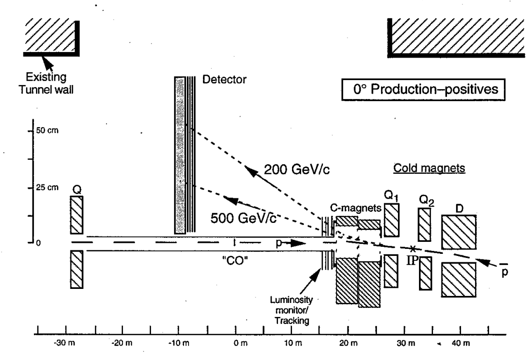

Figure 3: Configuration for the study of 0^0 production of 200 GeV/c and 500 GeV/c positive secondaries. Lower momenta can be studied with the IP moved farther to the left.

By shifting the intersection point closer to the center of the C0 straight section, different ranges of positive and negative secondary momenta with production angles at and near 0^0 may be studied, as illustrated in Figures 3 and 4. Note that the zero degree production refers to the antiproton direction, hence the produced negatives include the beam inelastic $\bar{p}$s,

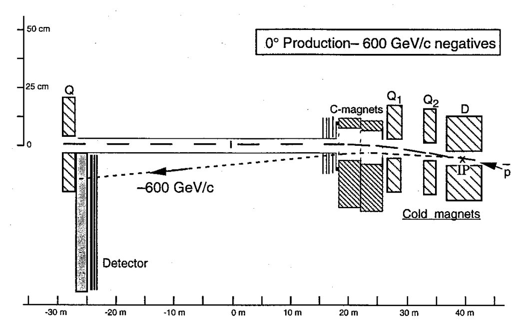

Figure 4: Arrangement for the study of (approximately) 600 GeV/c negative production at 0^0. Here the IP is 40.5 m from the center of C0. Up to 900 GeV/c negatives at 0^0 can be measured with the IP at 52 m.

A summary of the ranges of momenta of positive and negative, as well as neutral secondaries produced at 0^0 and small angles for different locations of the intersection point (relative to the center of C0) is given in Table I.

Note that the two gammas from a 100 GeV π^0 are separated by about 17 cm at the calorimeter detector 60 m from the production point, hence both gammas are detected for most high energy π^0s produced near 0^0. However this suggests that it would be practical to look on opposite sides of the beam pipe for decay products of more massive short-lived objects, such as the J/Ψ and the Υ. Figure 5 is a sketch of the intersection point and detector configuration

Table 1: Range of momentum accepted at $p_T = 0$ and p_T range for a typical momentum for various IP locations. Momenta are in GeV/c.

IP Location and geometry	Charge	Momentum Range for $p_T = 0$	P_T^{min} and P_T^{max} @ Particular Momenta
20 m	0	–	1.2 to 3.2@100
	pos	15 - 35	0 to -1.2@25
Fig 5.	neg	15 - 36	0 to -1.3@25
25 m	0	–	0.75 to 2.4@250
	pos	150 - 500	0 to -4.7@300
Fig. 5	neg	136 - 250	0 to -3.4@200
30 m	0	–	0.4 to 1.4@250
Fig. 3+	pos	180 - 600	0 to 0.9@380
Fig. 4	neg	155 - 290	0 to 0.7@220
38 m	0	5 - 1000	0 to 0.8@500
Fig. 2	pos	–	-1.6 to -2.8@600
Fig. 4	neg	360 - 500	0 to 0.6@430
50 m	neg	860 - 900	1.1 to 1.2@1000
Fig. 4			

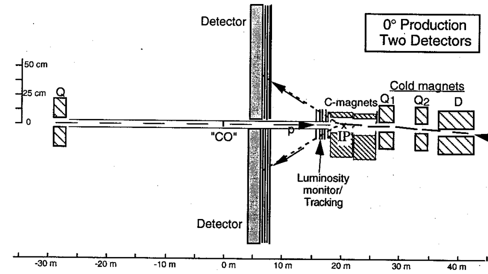

Figure 5: Proposed configuration of two detectors for 2-particle final states. The transverse-longitudinal scale ratio here is 20:1. The symmetric decay of a 160 GeV/c J/Ψ (or a 480 GeV/c Υ) produced at 0^0 is illustrated.

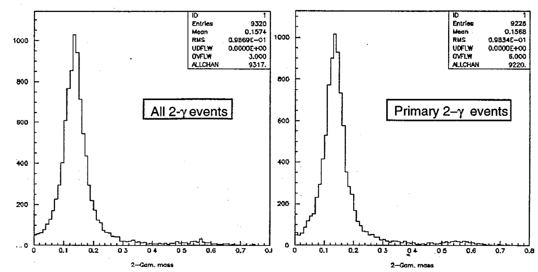

Figure 6: Reconstructed 2γ masses for all events with only 2γs and for 2γ events coming directly from the $p\bar{-}p$ collision region.

for such studies.

Data would also be collected on K-short and Λ production. In this context, it is worth recalling that cosmic ray balloon-borne detectors report anomalously large heavy flavor production in forward directions, to which this experiment would be sensitive [4]. Monte Carlo studies have been carried out to explore the invarient mass resolution of the proposed calorimeter detector to different final state particles; as an example, the observed invarient mass distribution observed for π° is sketched in Figure 6. Here the pions are produced according to a PYTHIA simulation, and the effect of the detector and accelerator component configurations modeled by GEANT. Similar distributions have been obtained for η's, K's, and Λ's.

A search will also be made for evidence of other unusual phenomena, such as Disoriented Chiral Condensates (DCC), the phenomenon suggested as the physics behind the reported cosmic ray Centauro phenomena [5].

5 SIGNAL BACKGROUND

Studies of the backgrounds anticipated have been modeled, assuming particle distributions at the primary interaction (beam-beam or beam-gas) as generated by PYTHIA, and then propagating the reaction products according to the GEANT simulation. From these simulations, the particle background in the detectors appears manageable. This is in accord with our experience with MiniMax, also in the C0 collision area, where we learned that the most critical element was the thin window between the intersection point and the detectors. Here the situation is, in fact, more favorable because the collisions occur within a bending magnet, and most reaction products are swept into the magnet structure before they leave the dipole. In addition, the vacuum in the superconducting dipole is very good, $\ll 10^{-11}$ torr, so that beam-gas interactions should not be a problem. The luminosity near the end of the C0 straight section will be about $2 \times 10^{28} cm^{-2} sec^{-1}$, corresponding to an event rate of about 1500 Hz. The luminosity may be somewhat less further back into the magnet lattice; in any case, absolute rates are not a problem. The detector, relying primarily on calorimetry with a threshold of about 5 GeV, will be insensitive to the soft particle albedo which may diffuse into the straight section.

6 ENGINEERING CONSIDERATIONS

The installation of this small experiment will require minimal impact on the Tevatron program. A special vacuum tank will be necessary, with thin windows along the trajectories of the particles to be studied (as sketched in the figures). The Lambertson magnets, used for the Tevatron abort, will be moved prior to installation of the B-TeV detector, and it would be convenient for this experiment if they were not present. The existing 'C' magnets are shown; additional bending may be required to replace that provided by the Lambertsons. This can all be engineered to be compatible with this experiment with very modest incremental cost and with good communication between the Laboratory, the BTeV group, and this collaboration. The requested running time is very short; less than a week of data collection is required. Tune-up can be carried out with beam-gas interactions, totally parasitically. In view of the expected time window between commissioning of the Tevatron and installation of the BTeV experiment, this experiment would optimise the utilization of the Tevatron through this period.

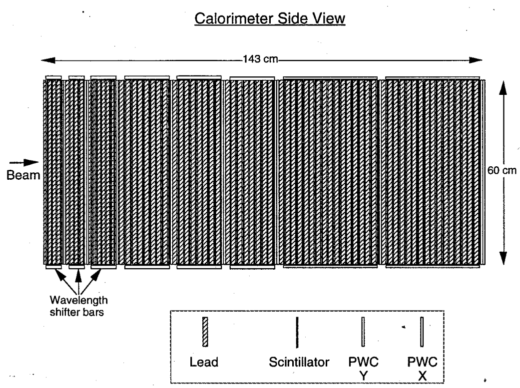

Figure 7: Cross-sectional view of one of the proposed calorimeters. There are lead plates of 1 cm thickness (electromagnetic, front sections) and 1.5 cm (remainder) (total: 114 plates) separated by scintillator, totalling 10.4 nuclear interaction lengths. The scintillators would be read out in 8 depth samplings. The locations of X-Y proportional wire plane pairs are also shown.

7 DETECTORS

The detectors would be calorimeters made of high-Z absorber plates interleaved with scintillator sheets, with proportional wire chambers inserted at several depths to localize the X-Y vertex coordinates of converting neutral hadrons and gammas. Hadron - gamma identification would be obtained from the longitudinal development of the cascades. The calorimeters would be preceeded by wire chambers to track incident charged particles, and muon chambers would follow the calorimeters. Two calorimeters would be used, one on the inner side and one on the outer side of the ring. An energy resolution of 15%/$\sqrt{E}$ for electrons and γs, and of 60%/$\sqrt{E}$ for charged hadrons (E in GeV) has been assumed, following general experience. The structure of the proposed calorimeter is sketched in Figure 7.

Additional thin chambers and counters would be located just outside the vacuum chamber thin windows for luminosity monitoring and for tracking of charged secondaries.

8 CONCLUSION

It has been noted that, whenever a new region of physical parameter space is explored, surprises should be expected. This experiment indeed will open a new domain of rapidity/pseudorapidity space, so far largely unexamined at particle accelerators. We look forward to the opportunity to undertake this exploration.

9 ACKNOWLEDGEMENTS

This work has been supported by the U.S. Department of Energy and the National Science Foundation.

10 REFERENCES

[1] FELIX; *A full acceptance detector at the LHC*, Letter of Intent, CERN/LHCC 97-45, LHCC/110; 1 August 1997.

[2] Z. Wlodarczyk **J. Phys. G. 19** L133 (1993).

[3] L. Voyvodic *Very High Energy Cosmic-Ray Interactions 1992, AIP Conf. Proc. 276* p. 231 (1992).

[4] H. Wilczynski, Nucl Phys. B (Proc. Suppl.) **52B**, 81 (1997).

[5] C. M. Lattes, Y. Fujimoto, and S. Hasegawa, Physics Reports **65** (1980). L. W. Jones *Proc. of the XXV International Cosmic Ray Conf., Vol 6* p. 29 (1997).

Forward Measurements in RHIC and LHC Heavy Ion Collisions

Sebastian N. White
Brookhaven National Laboratory, Upton, New York 11973

Abstract

Two mechanisms for forward, correlated neutron emission in heavy ion collisions motivate the construction of compact hadron calorimeters to be placed downstream of interaction regions at RHIC and LHC. Plans are now underway to build such detectors. Here we discuss recent progress in understanding their role and performance requirements.

1 INTRODUCTION

If the number of forward neutrons can be measured along both beam directions in RHIC and LHC heavy ion collisions, this information will be used both for monitoring Luminosity through the Correlated Coulomb Dissociation rate and as a tool for measuring centrality of hadronic collisions on an event-by-event basis.

What is needed for luminosity monitoring is a clean reaction with straightforward detector acceptance. The photonuclear process proposed here results in coincident beam energy neutron emission along each beam direction. RHIC and LHC collider designs are compatible with detectors covering $\sim 100\%$ of the required solid angle with $\sim 10 \cdot 10cm^2$ area. Similar detectors have been exposed in beam tests and a fixed target heavy ion experiment.

What is needed for event characterization is a measure of the nuclear overlap in a hadronic collision. In fixed target heavy ion experiments small aperture **Z**ero **D**egree **C**alorimeters are used to measure centrality via the disappearence of beam energy spectators. At a collider, beam energy fragments follow the beam orbit but unbound protons and neutrons will leave the beam tube after the first bending magnet (since Z/A of the beams is $\sim \frac{1}{2}$). Since we propose to measure only the neutrons at RHIC and fluctuations in spectator fragmentation could wash out the effectiveness of recording only neutron spectators , a short experiment was performed at CERN this year.

2 MUTUAL COULOMB DISSOCIATION AND LUMINOSITY MONITORING

The Coulomb dissociation of a single beam nucleus in collisions of identical beam species has already been considered in some detail for RHIC [3],[2]. This process is of interest because it is one of the limiting factors affecting beam lifetime. However, we do not consider it interesting as a diagnostic tool since it is not easily distinguished from ”single beam” backgrounds. On the other hand, we have found that a simple extension of the Weizsacker-Williams treatment of this process reveals a large component of dissociation as mutual [1]. The coincident detection of neutrons along each beam direction, as depicted in Fig. 1, makes the process cleaner and suitable for Luminosity monitoring.

The cross section for heavy ion dissociation may be accurately expressed in terms of the (experimentally known) photodissociation cross sections, $\sigma_{ph}(\omega)$, of the same nucleus over an appropriate range of photon energies.

$$\sigma_{dis} = \frac{2\alpha Z_p^2}{\pi\gamma^2}\int d\omega\omega\sigma_{ph}(\omega)\int_{b_0}^{\infty} b\, db K_1^2(\frac{b\,\omega}{\gamma}). \quad (1)$$

Since we want to calculate the mutual dissociation cross section for the two colliding nuclei, we define a dissociation probability, P(b), as a function of impact parameter b

$$\sigma_{dis} = 2\pi\int_{b_0}^{\infty} P(b) b\, db. \quad (2)$$

Then inverting the order of integration in Eq. (1) we have

$$P(b) = \frac{\alpha Z_p^2}{\pi^2\gamma^2}\int d\omega\omega\sigma_{ph}(\omega)K_1^2(\frac{b\,\omega}{\gamma}). \quad (3)$$

We neglect, for the moment, the fact that P(b) approaches unity at grazing impact in our case. We instead give a first order expression for correlated dissociation, $\sigma_{cd}^{(1)}$, which we subsequently correct to preserve unitarity. We then have

$$\sigma_{cd}^{(1)} = 2\pi\int_{b_0}^{\infty}\Big[P(b)\Big]^2 b\, db, \quad (4)$$

which may be evaluated numerically using the data on $\sigma_{ph}(\omega)$. As discussed in ref.[1], the resulting cross sections are sensitive to impact parameter cutoff (b_0) at the level of 10 to 15%. Taking $b_0 = 15$ fermi, we found σ_{cd} =3.9 barns at RHIC top energy with gold beams and 7.2 barns at LHC top energy with Pb beams.

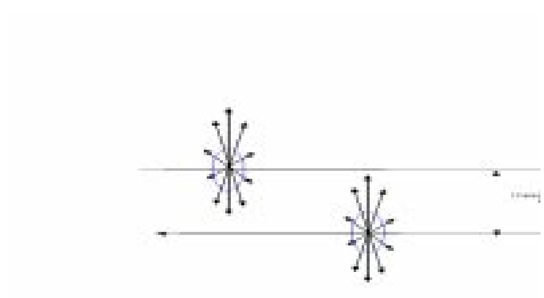

Figure 1: Peripheral collision of Heavy Ion beams at impact parameter,b, for which a Coulomb Dissociation Probability is computed.

3 EXPERIMENTAL CONSIDERATIONS, DETECTOR REQUIREMENTS

The spectrum of emitted neutrons determines the design criteria for the luminosity monitor detectors. Their lab energy and angular distributions were calculated from photonuclear data. In the target frame, neutrons are emitted with $\leq$ 10MeV of kinetic energy. This results in a very small energy spread and opening angle when seen in the laboatory frame.

More than half of the inclusive dissociation cross section results in single neutron emission with a lab energy spread of $\sigma \leq 10\% \times E_{beam}$. So the measured linewidth will be determined by the detector resolution which we require to be $\leq 20\%$ @ 100 GeV. The angular distribution is limited to a cone of 1.4mr opening angle at RHIC top energy (± 2.5cm at the ± 18m location of the detectors in RHIC. The neutron calorimeter response should be flat over this area. The final requirement on the 2 calorimeters comes from the possibility of time difference measurement to locate the interaction point. We require $\sigma_t = 300$psec.

4 EVENT CHARACTERIZATION WITH A NEUTRON CALORIMETER

In a special run of NA49 [4], "centrality" of 158GeV/n Pb + Pb target collisions was measured simultaneously using a large angle "ring" calorimeter and a forward (ZDC) calorimeter, $\sim$ 25m downstream of the target. A magnet between the target and ZDC separated the fragments so that different species could be measured independently. The resulting geometry, shown in Fig. 2, is identical to the configuration around the RHIC neutron detector location. The "fragment" region corresponds to the orbit of one stored beam.

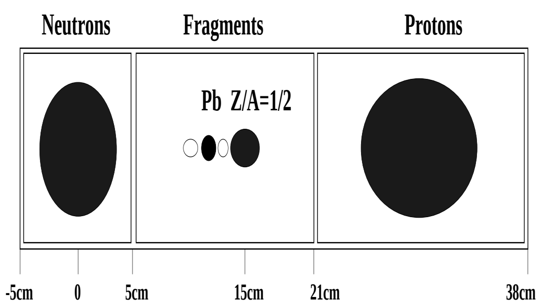

Figure 2: Fragment distribution at the forward calorimeter in the NA49 test.

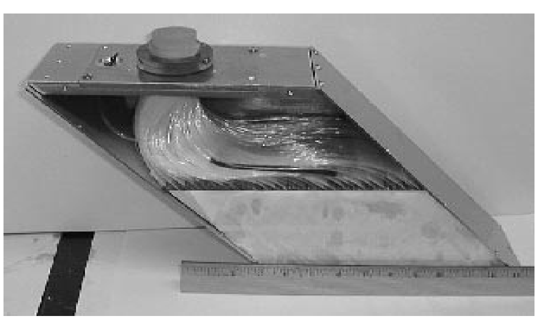

Figure 3: A 2λ ZDC calorimeter section. The beam enters from the lower right.

These data were analyzed with event characterization at RHIC in mind, where we expect to place one ZDC on either side of the interaction regions. To the extent that the experiments at RHIC differ from one another the fact that they share one detector for event characterization is expected to be an asset in comparing results.

The NA49 test addressed the question of the effectiveness of measuring only the spectator energy carried by free neutrons. Since some data already exist on fragmentation into neutrons at 1GeV/nucleon and fragmentation is expected to vary slowly with energy, the NA49 test makes a firm prediction for neutron multiplicities vs. cenrality at RHIC.

We plotted the measured energy in the ring calorimeter vs the multiplicity of each fragment type. In this way the effective resolution in E_t could be predicted assuming that only neutrons or neutrons and protons are detected in RHIC experiments.

A Preliminary conclusion from this analysis confirm that the sensitivity of the neutron calorimeter to "centrality" is already adequate (adding proton measurement does not qualitatively improve the resolution). A large neutron multiplicity (~ 10) is observed even in the most central events even those which correspond to the highest E_t bins.

We conclude that the ZDC's efficiency for producing a coincident signal in each beam direction will be close to unity for both central and peripheral hadronic collisions and that the energy measurements in the RHIC ZDC's can be used for selecting data with different centrality much as has been done in fixed target Heavy Ion experiments at the Brookhaven AGS and the Cern SPS.

5 CALORIMETER DESIGN

Prototype RHIC calorimeters are being prepared for beam tests later this year. The preferred design uses a cerenkov light fiber readout (QCAL) with fiber layers oriented at 45^o to the beam direction [5]. Simulations have shown that a hadronic shower resolution of $\leq 20\%$ at 100 GeV can be achieved with a 10 cm wide by 8λ deep module with 5mm thick Tungsten plates. We are currently testing both a Copper and a Tungsten version at CERN.Once a design is selected based on beamtest results, identical modules will be installed in each RHIC experiment.

One PMT signal from the 1st 2λ deep section (shown in Fig. 3.) on each side will be used for timing. Both the coincidence rate and the time difference distribution (which is related to the length and average position of the interaction region) will be available and updated at a rate of a few Hertz in the RHIC control room.

6 REFERENCES

[1] A. J. Baltz and S.N.White, BNL-63127.

[2] M. J. Rhoades-Brown and J. Weneser, BNL-47806.

[3] A. J. Baltz, M. J. Rhoades-Brown, and J. Weneser, BNL-63069.

[4] T.Alber et al.(na49 collaboration) manuscript in preparation.

[5] M.Lundin et al., Nucl. Inst. and Meth. A 361 (1995) p.161

FELIX – a Full Acceptance Detector at the LHC

Cyrus Taylor
Dept. of Physics, Case Western Reserve University, Cleveland, OH 44106 USA
Valentina Avati and Karsten Eggert
CERN, Geneva, Switzerland
Presented by C. Taylor[1]

Abstract

The FELIX collaboration has proposed the construction of a full acceptance detector for the LHC, to be located at Intersection Region 4, and to be commissioned concurrently with the LHC. The primary mission of FELIX is QCD: to provide comprehensive and definitive observations of a very broad range of strong-interaction processes. This paper reviews the detector concept and performance characteristics, the physics menu, and plans for integration of FELIX into the collider lattice and physical environment. The current status of the FELIX Letter of Intent is discussed.

1 INTRODUCTION

FELIX will be the first full acceptance detector at a hadron collider. It will be optimized for studying the structure of individual events over all of phase space (see Figure 1). FELIX will observe and measure all charged particles, from the central region all the way out to diffractive protons which have lost only 0.2% of their initial energy. It will even see elastic protons which have a momentum transfer of at least 10^{-2} GeV^2. This comprehensive, precision tracking is accompanied by equally superb electromagnetic and hadronic calorimetry. FELIX will observe and measure photons and neutrons down, literally, to zero degrees, giving it an unparalleled ability to track the energy flow. In contrast, the other LHC detectors are sensitive over only a fraction of phase space and see less than 10% of the typical energy flow. FELIX is thus uniquely able to pursue physics complementary to that of the other detectors planned for the LHC.

The FELIX design involves the coordinated arrangement of three distinct systems: the magnetic architecture responsible for getting the beams through the I4 straight section, the tracking system, and the calorimetry. Each system must be complete in its own right, without compromising the characteristics of the other systems. The magnetic apertures must not be limiting apertures of either the tracking or calorimeter systems. There must be sufficient physical space for both tracking and calorimetry. The calorimeters must be physically large enough to have good resolution, and must not interfere with either the tracking or the magnetic systems.

All of this requires a lot of space, and the detector must be carefully integrated into the design of the machine. Full acceptance cannot be achieved by "adding on" to central detectors optimized for high p_T physics. Here FELIX is fortunate. The decision to split the RF cavities at I4, moving them to $\pm$ 140 m from the interaction point (IP), combined with the fact that FELIX's "low" luminosity permits the focusing quadrupoles to be moved more than 120 m from the IP, provides the necessary longitudinal space. I4 is also ideal from the point of view of transverse space. The beams are separated by 42 cm at the location of the RF cavities, providing room for zero degree calorimetry. Since the existing infrastructure, including the ALEPH solenoid, can be re-used with minimal modifications, I4 is clearly a superb location for a full acceptance detector. (The central part of FELIX, which nicely fits into the existing cavern, and the extensions upstream into the forward regions, are shown in Figure 2.)

Nevertheless, the task of integrating a detector with genuinely full acceptance into the available space at I4 is not trivial. The FELIX Letter of Intent [1] outlines how it can be done, using well-understood magnets and compact detectors, for a comparatively modest price: we estimate a cost of about 25 MCHF for the machine magnets and the infrastructure, and about 50 MCHF for the detector outlined here and presented in more detail in the FELIX LoI.

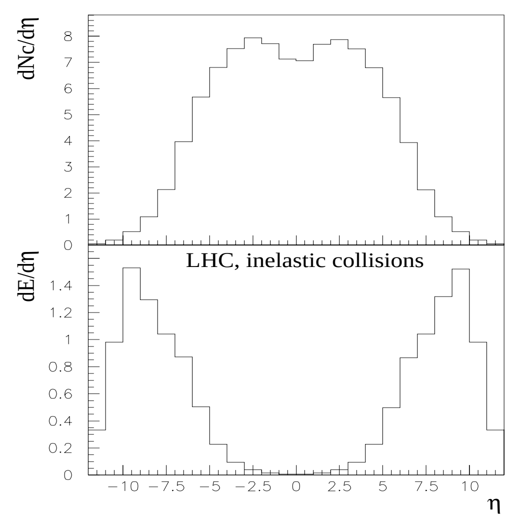

Figure 1: The pseudorapidity distribution of charged particles and of the energy-flow at $\sqrt{s}$ =14 TeV.

2 PHYSICS OVERVIEW

The heart of the FELIX physics agenda is QCD: FELIX will be the ultimate QCD detector at the LHC.

Surprisingly, the need for such a detector is not obvious to many members of the high energy community. In part, this may be because of the success of the interplay between theory and experiment in the case of electron-positron collisions. The cleanliness of the process, together with the low event rate and full-acceptance capability of the detectors, has led to an especially fruitful interaction between the

[1] For the FELIX Collaboration

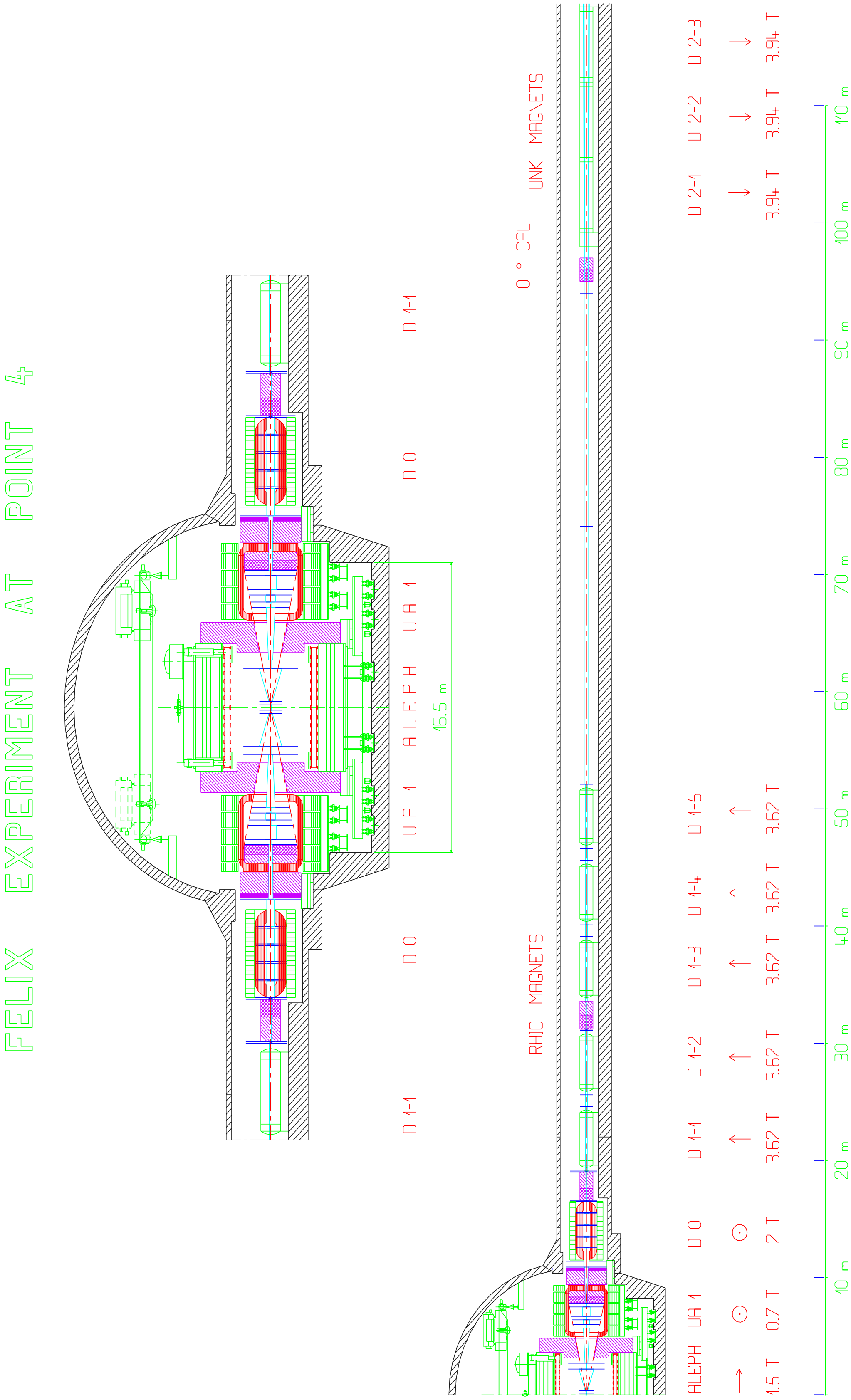

Figure 2: Sketch of the FELIX experiment in central and very forward region.

QCD aspects of that experimental program with the remainder.

The case of hadron-hadron collider physics is quite different. The high-p_T, low cross section physics is accessed by highly selective triggers. The phase-space acceptance of the detectors is largely limited to the central rapidity region. Full acceptance has not been attained since the bubble-chamber era of fixed-target physics. Therefore the basic data base is much more limited.

This situation is all the more serious because of the great variety in event classes for hadron-hadron collisions. There are soft collisions with large impact parameters; angular momenta of tens of thousands instead of the unique $J = 1$ of the e^+e^- world. Central collisions produce much higher multiplicities than are seen in e^+e^- annihilation. There are the diffraction classes of events, with and without jet activity, that comprise several to tens of percent of typical subsamples (if seen in full acceptance) and which present a major challenge to theory. There are poorly understood strong Bose-Einstein-like correlations seen at very low p_T and low relative p_T in hadron-hadron collisions which do not occur in e^+e^- collisions. But at collider energies this is only based on one sample of low-p_T data from UA1, because until now no other detector has had the measurement capability. Finally, there is little if any data in the forward fragmentation regions, where cosmic ray experiments insistently claim that anomalies exist.

Given this richness of phenomena, and given the importance of QCD to the interpretation of the new-physics data expected to emerge from the LHC, it is clearly very important to improve the data-base with an LHC detector and experimental group fully dedicated to the observation and interpretation of as broad a range of QCD phenomena as possible. This is of course the mission of the FELIX initiative.

Many of these new opportunities in QCD physics at the LHC are not well known, and the FELIX collaboration has accordingly placed high priority in in providing a description of them in the FELIX LoI. We briefly summarize a few of the main themes here.

2.1 Parton densities can be measured to extremely small x, below 10^{-6}

The parton densities at small x are themselves a very important thing to measure. Up to now HERA has provided data down to x values of order 10^{-4} for Q^2 in the perturbative domain of several GeV^2. FELIX will have the capability to extend these measurements to x values below 10^{-6} via observation of dileptons, low-mass dijets, and low-mass jet-photon systems carrying large longitudinal momenta. In this regime one expects (especially for proton-ion collisions) the breakdown of the usual DGLAP/BFKL evolution-equation formalism and significant nonlinear effects to be observed.

2.2 Minijet production in hadron-hadron collisions is strongly energy dependent

The need for a vastly improved QCD data-base for hadron-hadron collisions is made even more urgent by the fact that qualitative changes are expected even in the structure of generic events because of the rapid increase with energy of gluon parton densities in the primary protons. Thanks to the measurements at HERA, this is not only the theoretical expectation but also a data-driven one. The parton densities at a $5 - 10$ GeV scale become so large that minijet production in central collisions may become commonplace, with minijet p_T large enough for reasonably clean observability. These very high parton densities create, at a perturbative short distance scale, “hot spots” in the spacetime evolution of the collision process within which there may be thermalization or other nonperturbative phenomena not easy to anticipate in advance of the data. Particle spectra themselves may evolve to something quite distinct from what has been so far observed, with strangeness, heavy flavors, and/or baryon and antibaryon production enhanced. Especially in central proton-ion collisions, where the total gluon-gluon luminosity per collision is maximized, and where the evolution of a single proton fragment is followed, one can expect this class of phenomena to be most prominent and surprises most probable.

2.3 Diffractive final states are endemic, many are important, and some are spectacular

Diffractive final states will comprise almost 50% of all final states at the LHC. The soft diffraction at very large impact parameter, which perhaps sheds light on pion-cloud or glueball physics, is at one extreme, and hard diffraction, where rapidity gaps coexist with jets, is at the other. There are a large variety of hard diffraction processes, including some with two and three rapidity gaps, which are of basic interest to study. In this class there are expected to be, for example, an extraordinary class of events where the complete event consists of a coplanar dijet accompanied by the two unfragmented beam protons detected in Roman pots, and absolutely nothing else in the detector. Certainly ATLAS and CMS can also detect such events, provided they sacrifice a luminosity factor of about 30 relative to their hard-earned peak luminosity. However, to really understand this event class, one will need, at the very least, to examine the t-distribution of the Roman-pot protons, as well as to study the generalizations of this process to the cases where one or both of the protons undergoes soft diffraction dissociation to a low mass resonance or a high mass continuum, or to a high-p_T system containing a tagging jet. Only FELIX would have such a capability.

In addition to this class of hard diffraction and very soft diffraction processes, there is another very interesting class of semihard diffractive phenomena associated with the conjectured fluctuation of the initial-state projectile into a transversely compact configuration, which therefore interacts with an unusually small cross section. Evidence for this is seen in vector-meson photoproduction at HERA, especially J/ψ production, which exhibits the expected rapid increase of cross section with energy. Also at Fermilab, diffraction dissociation of a high energy pion into dijets, with all the initial pion energy going into the dijet system, is being studied by experiment E791. Exactly the same process is available at the LHC with FELIX, as well as a similar process where one beam proton dissociates diffractively into three jets, one for each quark. The A dependence of these processes is remarkable, roughly $A^{4/3}$, because this diffractive process should occur even in central collisions, thanks to the small size of the initial configuration.

2.4 Particle production from deep within the light cone may exist and deserves careful searches

The existence of events with a very high final-state multiplicity of minijets and their associated hadrons has other implications. The products of such interactions for the most part can be expected to explode from the initially compact collision volume in all directions at the speed of light. Because of the high multiplicity density, the time of hadronization of all these degrees of freedom will be lengthened from the usual low-energy value of 1-2 fm to several fm. Up to this time of hadronization, the expanding "fireball" containing most of the partonic collision products is arguably a rather thin spherical shell, of thickness of order a fm. So even before hadronization there is a large interior volume of hundreds of fm^3, isolated from the exterior vacuum, which may evolve toward a chirally disordered vacuum. Consequently in such events there might be a large pulse of semi-classical, coherent pions of relatively low p_T emitted when this false vacuum eventually decays: disoriented chiral condensate. This is at present only a speculative possibility, although experimental searches, especially in the context of ion-ion collisions, are underway.

More generally, one may ask: if disoriented vacuum is not what is in the interior of this quasi-macroscopic fireball, what is? If the interior "vacuum" is broken into domains of various chiral orientations, then topological obstructions might lead to production of (Skyrmionic) baryons and antibaryons of unusually low p_T. And if there is activity deep inside the light cone, no matter what it is, then this activity has eventually to be turned into emission of particles; hence a new particle production mechanism which deserves to be studied. It would seem that the only alternative available for the $absence$ of new phenomena emergent from the deep interior of the light cone under these circumstances is that that region relaxes back to the true vacuum, despite its being isolated from the true vacuum by a fireball shell and despite there not being enough elapsed time for chiral orientation to be distinguished energetically from chiral disorientation.

2.5 Collisions with very high impact-parameter may probe the chiral vacuum structure

In general, the chiral vacuum condensate is distorted in the neighborhood of impurities such as an isolated proton. This is just the long-range pion cloud surrounding it. The pion-cloud structure can be probed especially well in high energy pp collisions at very large impact parameters, say 2 to 3 fm. These interactions are, because of the larger radii of interaction at the LHC, a bigger component of the cross section, and can lead to larger final-state multiplicities than found at lower energies. Perhaps here too there may be coherence in the structure of the pion emission, and this class of events may turn out to be of special interest. Again a detection capability at very low p_T, 100 MeV and less, as possessed by FELIX, is important for such studies.

2.6 New opportunities exist for tagging event classes

Together with these many novel phenomena, there will be new methods for experimentally tagging different kinds of events. The impact parameter of the collision is obviously of importance to determine event-by-event. This is done routinely in ion-ion collisions via zero degree measurements of nuclear fragments and by the amount of transverse energy produced. At the LHC, the FELIX instrumentation in the forward direction allows a data-driven approach for attacking the problem by the former method. The large yield of minijets, strongly dependent upon impact parameter, may allow the latter method, based upon transverse energy production, to be used more effectively at the LHC (by all detector groups) because of the stronger correlation of multiplicity with impact parameter than at lower energy. A combination of both methods, unique to FELIX, is likely to be the best of all.

A second important tag available to FELIX is the choice of beam. By tagging on a leading neutron or Δ^{++} at very low t, one can reasonably cleanly isolate the one-pion-exchange contribution, and thereby replace the LHC pp collider with a somewhat lower energy, lower luminosity πp collider. In a similar spirit, and including Λ tags, one can study collisions of any combination of π, K, or p with each other. The beam-dependence of phenomena has historically been of considerable importance, and it may find important applicability, especially with respect to questions of valence-parton structure, at the LHC energy scale.

A special case of these tags is that of a photon tag in ion-ion collisions, via forward detection of the undissociated ions. The luminosity for $\gamma\gamma$ collisions is very high, and the capability of FELIX to exploit this luminosity is also very high.

Another class of tags which has been underutilized is the diffractive tag, where leading protons are detected via Roman-pots. As discussed above, this leads to a very rich stratum of up-to-now poorly-measured, poorly understood, but potentially important physics.

Finally, there may be pattern tags. The event structure in final states containing jets is dependent upon the color flow. Typically, neighboring jets in phase space are connected by a partonic color line (antenna). For quarks, one antenna line emerges from the jet, for gluons two. Along these antenna lines in phase space, hadronization and minijet production is enhanced. Recently the Tevatron collider exper-

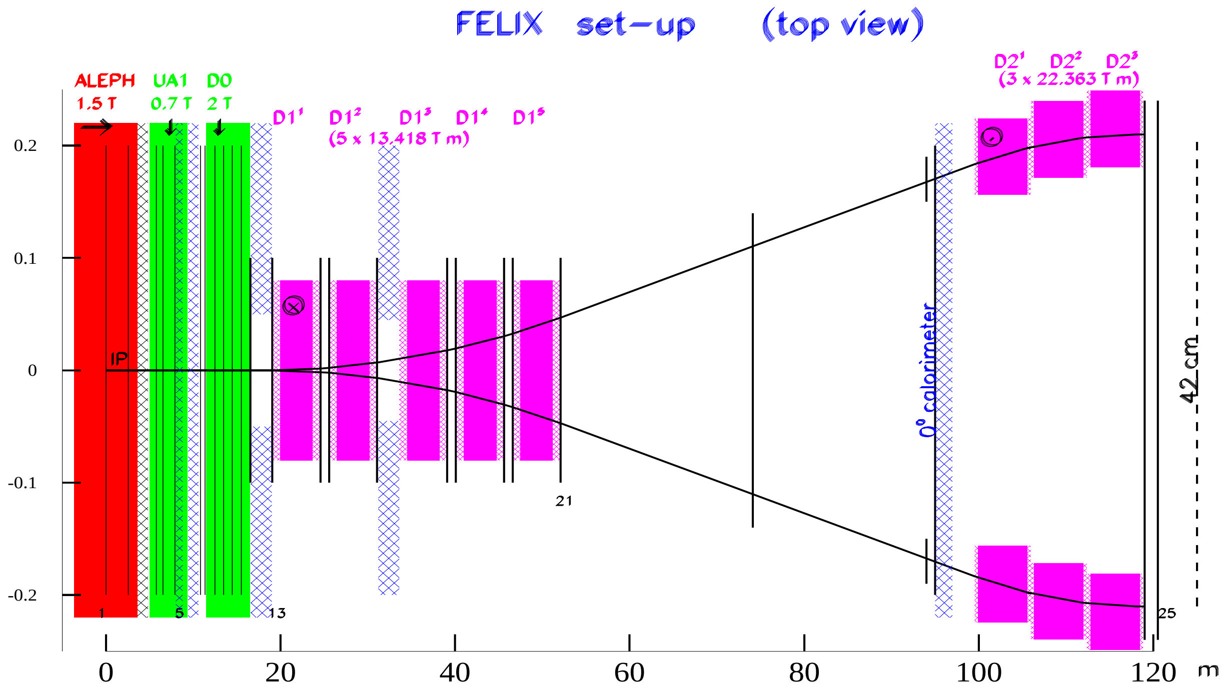

Figure 3: The top view of the FELIX detector. The different magnets, calorimeters (hatched areas), tracking stations (vertical lines) and the beam trajectories in the horizontal plane are indicated.

iments have observed these effects. In principle this technique might allow one in the future to identify in an individual multijet event quarks versus gluons, and even fully classify the event structure according to the color flow. Clearly such a pattern-analysis technique is very difficult, and needs to be data-driven. FELIX, with full acceptance, will be optimal for making the attempt.

3 THE FELIX DETECTOR

We now introduce the major features of the FELIX design.

3.1 A tunable insertion at I4

A full acceptance detector must be able to analyze the global structure event-by-event. This means that it should run at a luminosity no greater than $\mathcal{L}\sim 10^{32}$ cm^{-2} s^{-1}; that is, with less than about one interaction per crossing. This luminosity can be achieved at I4 by means of an insertion which can be tuned from $\beta^* = 23$ m to $\beta^* = 900$ m without changing the magnetic elements.

There are two significant features of this insertion. First, the final-focus quadrupoles can be placed more than 120 m from the IP, providing the space needed to accommodate the FELIX dipoles. Second, it is economical. The necessary quadrupoles are already in the LHC baseline design.

The ability to tune the insertion also has several nice features. At $\beta^* = 900$ m, FELIX is optimized for the study of low-t elastic scattering. At $\beta^* = 110$ m, where FELIX's luminosity is about 4 x 10^{31} cm^{-2} s^{-1} when the LHC is at design luminosity, the beam size in the heart of FELIX detector ($\pm$ 120 m) is minimized, permitting the Roman pot detectors in these locations to come as close as 3 mm to the beam. Finally, $\beta^* = 23$ m permits FELIX to reach luminosities as high as 2 x 10^{32}cm$^{-2}s^{-1}$.

3.2 Well-understood magnets

FELIX will implement a "kissing scheme" in which the two beams are brought together at 0^o in the horizontal plane and then returned to the same inner or outer arc (See Figure 3). To accomplish this, we need some 67 T-m to first bring the beams together (D2 magnets), and then another 67 T-m (D1 magnets) to make them parallel. This has to be accomplished within the 120 m available. Both sets of magnets must be superconducting machine dipoles. The D1 magnets must also have large bores, to accomodate both beams and to provide acceptable tracking and calorimetry apertures.

FELIX is fortunate that Brookhaven National Laboratory (BNL) has designed large aperture superconducting dipole magnets for use at RHIC. With a coil aperture of 18 cm and a design field of 4.28 T (FELIX will use them at 3.62 T), these magnets are suitable for use as D1 magnets. BNL is committed to producing these magnets for RHIC and thus will be able to supply well-understood magnets on the FELIX time scale.

The constraints on the D2 magnets are somewhat less severe, and several options are available. Of these, FELIX proposes existing superconducting dipoles constructed as prototypes for UNK. While these are single aperture magnets, the 42 cm beam separation permits two UNK cold masses to be assembled in a common cryostat for use as D2 magnets.

In order to avoid parasitic beam-beam interactions and long-range tune shift effects, the beams will collide with a vertical crossing angle of ± 0.5 mrad. To do this while optimizing the match of the magnetic architecture to tracking and calorimetry, we propose to re-use the existing UA1 magnet, split longitudinally into two halves and equipped with new coils. We will also build two 5 meter long, 2 T warm dipole (D0) magnets.

The magnetic architecture is completed by the re-use of the existing ALEPH solenoid, which is well-matched with the use of the UA1 magnet.

An important feature of this overall design is that the strengths of the magnetic fields increase in the forward direction, always well-matched to the typical momenta of the particles, resulting in momentum resolution which is reasonably uniform over all of phase space.

Finally, we note that all magnets can be accommodated in the existing Aleph collision hall and adjacent tunnels without any significant civil construction.

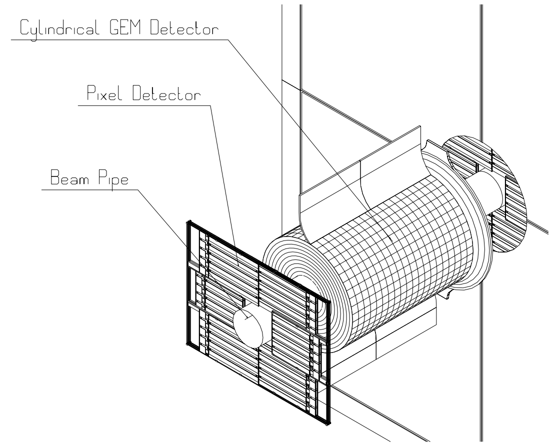

Figure 5: A schematic view of a tracking station based on Si pixel detectors and a micro-TPC. Note that several large-area GEM chambers have been removed to improve visibility of the micro-TPC.

3.3 Compact, precise tracking

Some 50 tracking stations, located as far as 430 m from the IP, are needed to ensure full acceptance and uniform resolution. The positions of most of the stations (vertical lines) are indicated in Figure 3. FELIX will instrument radially outward, emphasizing compact, near-beam tracking. How close we will approach the beams depends on the location. In general, we will use Roman pot detectors to aggressively approach the beams wherever the location is accessible and the pot mechanical structure does not interfere with other tracking or calorimetry. Elsewhere, we propose to use fixed-radius tracking, approaching to within 2.5 cm of the beams. The acceptance for charged particles as a function of pseudorapidity (a) and their momenta (b) (see Figure 4) is almost 100% over the entire phase space.

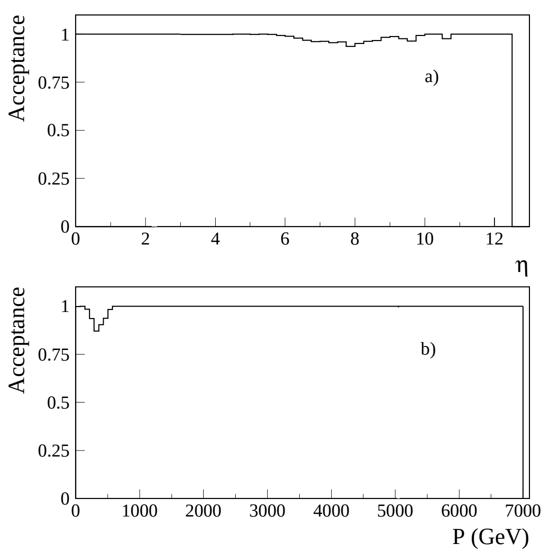

Figure 4: The acceptance in FELIX for charged particle momentum measurements as a function of (a) the pseudorapidity; and (b) the momentum of the particles.

An important consideration is the occupancy within the tracking detectors. High particle densities close to the beam pose a significant pattern recognition problem. Each tracking station should thus have sufficient resolution and redundancy to be able to locally reconstruct track segments. Track segments are then matched, station-to-station, resulting in a very powerful spectrometer.

These considerations lead to a common conceptual design for most FELIX tracking stations, based on two technologies: Si pixel detectors out to radii of about 8 cm, supplemented by Gas Electron Multiplier (GEM) chambers at larger radii. We are also exploring the possibility of using GEM as the basis for very compact micro-TPC's. A conceptual design for a "standard" fixed-radius tracking station are shown in Figure 5. The same technologies will be used for a compact microvertex detector.

3.4 Forward calorimetry

FELIX proposes four calorimeters on each side of the IP to provide complete electromagnetic and hadronic calorimetry for angles $\theta < 0.2$ radian, that is, for $|\eta| > 2.3$. The coverage of the calorimeters is illustrated in Figure 6. The interplay with the magnets and tracking systems is illustrated in Figures 2.

The calorimeters must have superb energy and spatial resolution, and must provide the information needed to identify neutrons, electrons and gammas. This must be done in limited space, and in a high-radiation environment. These considerations determine the structure of the calorimeters, the choice of sampling materials and the kinds of photodetectors and front end electronics which can be used for the readout.

The UA1 endwall calorimeter, which is expected to have a radiation dose of less than 5 Mrad for 10 years running,

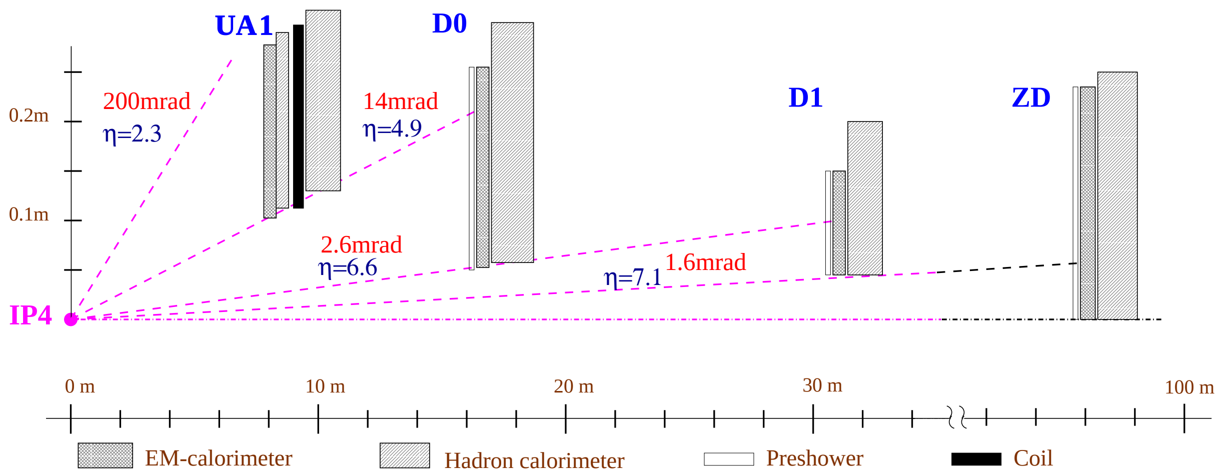

Figure 6: Schematic view of FELIX forward calorimetry.

is a sampling calorimeter based on plastic scintillators and wavelength shifting fibers. The very forward (D0, D1 and Zero Degree calorimeters) see much higher radiation levels, and will thus be "spaghetti"-type calorimeters, based on either thin capillaries filled with liquid scintillator or on quartz fibers. All three very forward calorimeters are similar in construction, differing only in their overall dimensions. Each consists of a preshower detector, an EM calorimeter, and two hadron calorimeter sections.

4 RECENT HISTORY

After the presentations of J.D. Bjorken and K. Eggert about possible forward physics in pp and p-A collisions at the LHCC "Workshop on Further Physics Topics" (Nov. 1994) the LHCC Committee recommended this kind of physics by noting: *"The LHCC noted the interest in diffraction, and expects that such studies may also form part of the LHC experimental programme. The committee encourages interested parties to work together on an integrated approach towards this physics, whilst bearing in mind the LHC physics priorities already established"*

When the possibility for a new interaction region in I4 became reality (summer 1995) several workshops took place to discuss the layout of a full acceptance detector.

In May 1996 the LHCC defined new rules for coming activities : *" The LHCC urges that any new experimental intiative should be consistent with the restricted resources likely to be available, and combined as far as possible with one of the foreseen experiment."*

In an Oct. 1996 memorandum[2] to the LHCC, FELIX responded to these new guidelines by describing, in detail, the FELIX set-up, strategy and financial assumptions. The group received general encouragement from the CERN management to go ahead with the Letter of Intent.

During the spring and summer of 1997, the FELIX collaboration mobilized for the preparation of the LoI, which was submitted to the LHCC in August 1997.

In November 1997, the LHCC chose to address the FELIX Letter of Intent, finding

... that the FELIX LoI is not responsive to these guidelines. While the physics topics addressed by the programme proposed in the LoI are of interest (particularly the complete reconstruction of diffractive events), the likely costs of constructing the proposed dedicated detector and of the modifications to the LHC collider are very high in comparison with the probable physics output. Finally, the composition and strength of the collaboration seem inadequate for carrying out a strong programme addressing these physics topics. [3]

The CERN Research Board has since endorsed the decision of the LHCC.

The FELIX collaboration believes that these decisions were reached in a precipitate manner, with gross violation of due process. In particular, there has been no thorough scientific review of the FELIX proposal. Indeed, a primary grievance is that the LHCC referees never contacted the proponents before arriving at its negative conclusion, nor were the proponents permitted to directly present the initiative in person to the committee. Important issues, including possible staging scenarios to reduce cost, and ongoing efforts to build collaboration strength, were thus never presented to the committees.

The justification of the decision which has been presented by the LHCC, the Research Board and by the Director General clearly has to do with costs: CERN is under great financial stress, and the issue of affordability is of course a very real one, an issue not unnoticed by the collaboration. It is clear that the FELIX collaboration as presently constituted is far from being able to provide the resources, a point which was reinforced in private discussions by the CERN Director General, who has indicated that he might have considered the FELIX LoI more seriously if the Collaboration would have been stronger, and with more collaborators from CERN Member States.

FELIX has formally protested both the conclusions of the LHCC and the procedure by which the FELIX LoI has been considered by the LHCC.

The LHCC and Research Board have, however, raised several critical points. FELIX had originally expected to address such issues via direct interaction with the referees and the LHCC through the usual procedures. In the present situation, we believe that the best way of proceeding is to present an addendum to the FELIX LoI to the LHCC which will contain a thorough discussion of the following points:

- the complementarity of the capabilities of FELIX with those of the already foreseen experiments;
- staging scenarios for the FELIX detector; including
- the possibility to construct a preliminary version of the FELIX experiment at FNAL, HERA or RHIC with a stronger collaboration to demonstrate both the technical feasibility as well as to obtain a first glimpse of the physics.

FELIX welcomes all additional collaborators, and will continue to expand the collaboration, with particular emphasis on CERN member states. FELIX will also work to identify funding sources. Finally, the entire FELIX collaboration will continue to work on substantive issues as outlined above, and in the LOI. In particular, we are proceeding with the design and construction of a prototype forward tracking station, as sketched in Figure 5, to be tested at one of the current generation of colliders. Prototypes of the various forward calorimeters are also under construction.

FELIX looks forward to a more positive response from the Committees. It is clear, however, that more people must soon join the effort if FELIX is to succeed.

5 ACKNOWLEDGEMENTS

Many people have made invaluable contributions to FELIX without formally joining the collaboration. We would particularly like to acknowledge the contributions of the approximately 100 people in this category who directly contributed to the preparation of the FELIX Letter of Intent, and who are thanked in that document by name.

6 REFERENCES

[1] The FELIX Collaboration. "FELIX, A Full Acceptance Detector at the LHC, Letter of Intent". CERN/LHCC 97-45, LHCC/I10, 1 August 1997. The full text of the LoI is available on the web at the FELIX webpage http://www.cern.ch/FELIX

[2] J.D. Bjorken, K. Eggert and C. Taylor, Progress Report about FELIX, LHCC 96-37, http://www.cern.ch/FELIX/News/memor.html

[3] LHCC Minutes, CERN/LHCC 97-61:LHCC31

II. BEAM DYNAMICS AND BEAM HALO

Modulational Effects in Accelerators[1]

T. Satogata
Brookhaven National Laboratory
Building 1005S–3, PO Box 5000, Upton, NY, 11973-5000
USA

Abstract

We discuss effects of field modulations in accelerators, specifically those that can be used for operational beam diagnostics and beam halo control. In transverse beam dynamics, combined effects of nonlinear resonances and tune modulations influence diffusion rates and tail transport, and some qualitative control of loss rates with applied tune modulation has been demonstrated. In the longitudinal domain, applied RF phase and voltage modulations provide mechanisms for parasitic halo transport, useful in slow crystal extraction. Experimental experiences with transverse tune and RF modulations are also discussed.

1 INTRODUCTION

In the past several decades, the hadron beam dynamics community has expended considerable effort to understand the effects of power supply ripples and magnetic field modulations. For example, transverse tune modulation in conjunction with nonlinear resonances is well established as a significant contributor to beam lifetime. This experience has led to the suggestion of methods, both transverse and longitudinal, that use magnet modulations to control dynamic beam loss and halo population.

This paper briefly reviews modulation phenomena impacting beam halo population and transport, and long-term ($> 10^6$ turns) beam and luminosity stability, as well as recent uses of modulations in beam diagnostics.

2 EXAMPLES OF MODULATION

Noise at some level is always present in a synchrotron, and excites the beam at broad-band frequencies. The broad frequency spectrum arises from a configration of multiple noise sources including ground motion, local industrial activity, and electrical noise. Noise is also routinely applied to transverse dampers to excite coherent beam oscillations for tune measurements.

Transverse tune modulation also arises from several sources. Dominant main bus power supply ripples range from 50–1200 Hz at 50 or 60 Hz harmonics, with tune widths ΔQ up to 10^{-4}. Chromatic tune modulation changes frequency with the synchrotron tune Q_S, typically from 50–500 Hz, and can create tune spreads up to $\Delta Q \approx 10^{-3}$ — it is worst at injection, where beams have their largest momentum spread. Controlled tune modulation can be applied up to 1 kHz (or faster, with ferrite magnets), with strengths up to $\Delta Q = 10^{-2}$.

[1]Work performed under the auspices of the US Department of Energy

Accelerator RF systems lack the DC regulation and spectral modulation found at power frequency harmonics in main magnets. However, RF phase and amplitude modulation are used during transfer and storage cogging, and in parametric feedback loops used to control multibunch instabilities. The frequencies most relevant to slow dynamics and halo control range from low frequencies to the synchrotron frequency, Q_S.

3 MODULATIONS AND BEAM DIAGNOSTICS

3.1 Narrow-band excitation and response

The SPS and LEP Q-meter systems allow application of white noise, single-frequency excitation, and frequency-swept dipole modulations (chirps) on a transverse damper. The transverse tunes are then calculated with overlapping FFTs of digitized turn-by-turn BPM signals, allowing tracking of the SPS tune through an acceleration cycle.

Calculations and experience have demonstrated that transverse emittance growth as low as 10% is achievable for 150 tune measurements through the SPS acceleration cycle, with short chirped modulations. PLL feedback and tune tracking also gives reasonable growth rates with much smaller narrow-band feedback, but requires careful tuning and balance between bandwith and precision to achieve similar results [1].

3.2 Beam-based instrument and optics calibration

In several electron storage rings, quadrupole modulation has been used to dead-reckon deviations of the closed orbit from quadrupole magnet optical centers, without requiring absolute knowledge of relative magnet and BPM survey calibrations. Harmonic analysis of BPM signals at the modulation frequency can indicate magnet deviations with precisions of $100\mu\mathrm{m}$, using modulation strengths as low as 0.03% of the magnet strength. However, such a method requires individual shunts and power supplies for modulated quadrupoles [2].

These methods have also been used to accurately measure relative phase advances between BPMs in LEP, and thus make lattice optics measurements parasitically during the course of operations. Such methods might be applied to measure lattice optics through acceleration ramps [3].

3.3 Instability damping

Recently, chromaticity modulation has been suggested as a means to damp the transverse head-tail instability, which limits single-bunch intensities in some machines. Modulation of the chromaticity over the RF synchroton period would create an incoherent transverse tune spread over the beam, creating enough phase mixing to raise the threshold of instability by orders of magnitude. This is the first example of nonlinear modulations applied to beam stability, and investigations of the dynamical implications of sextupole modulations are ongoing [4].

4 TRANSVERSE TUNE MODULATION

During storage and collisions, nonlinear beam-beam effects, as well as error fields in main magnets and nonlinear correction magnets, produce nonlinear resonances in transverse phase space. Since a complete discussion of two-dimensional resonances is inappropriate here, we shall restrict this discussion to isolated one-dimensional resonances. Motion under the influence of these resonances has been extensively studied, and is applicable to processes described in later sections. Further details and references may be found elsewhere [5].

Motion within an isolated one-dimensional resonance is characterized by the appearance of "resonance islands" in transverse phase space (Figure 1). Moving to a coordinate system near the center of one of these islands, this behavior may be parameterized with pendular equations of motion. The frequencies of oscillation within the resonance island, around the central fixed points, range from zero near the separatrix to Q_I, the "island tune", very near the fixed point at the center of the island. Like the dynamical whisker map and simple RF synchrotron motion, motion near the separatrix has very low frequency, and thus is highly sensitive to perturbations such as tune modulation.

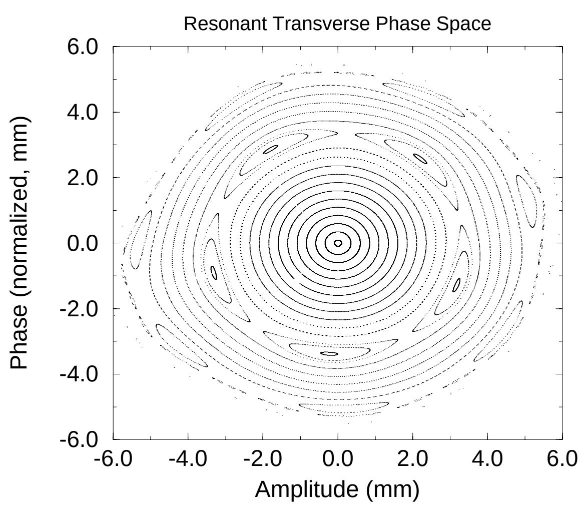

Figure 1: Two sets of resonances, $Q = 2/5$ and $Q = 3/7$, in one-dimensional normalized transverse phase space. Motion is stable up to more than 6 mm in the tails, and the core motion is regular and unperturbed by the nearby resonances.

4.1 Parameterization and character of tune modulation

As with driven pendulum motion, particle motion near and within resonances is highly sensitive to tune modulations with frequencies near the island tune Q_I. Weak resonances have small island tunes (on the order of $Q_I = 10^{-5}$ to $Q_I = 10^{-10}$) and small spatial extent. Very strong resonances, usually created explicitly by nonlinearities during beam dynamics studies, have larger island tunes up to $Q_I = 10^{-3}$ or more.

One-dimensional transverse tune modulation may be parameterized by

$$Q = Q_0 + q \sin(2\pi Q_M t), \quad [t] = \text{turns} \tag{1}$$

where (q, Q_M) are the tune modulation strength (in tune units) and frequency. The behaviors of isolated one-dimensional resonances under the influence of tune modulation has been extensively studied in the past decade. This has produced complementary approaches that can be summarized by a parameterized tune modulation phase diagram, Figure 2.

This figure, when interpreted properly, is particularly powerful. Two parameters of the tune modulation, strength and frequency, and one parameter of resonance strength can be used to qualitatively predict the dynamics of a nonlinear system. When multiple resonances under the influence of tune modulation interact, e.g. at large particle amplitudes in the beam halo, controllable tune modulation can play a significant role in halo transport and slow beam loss.

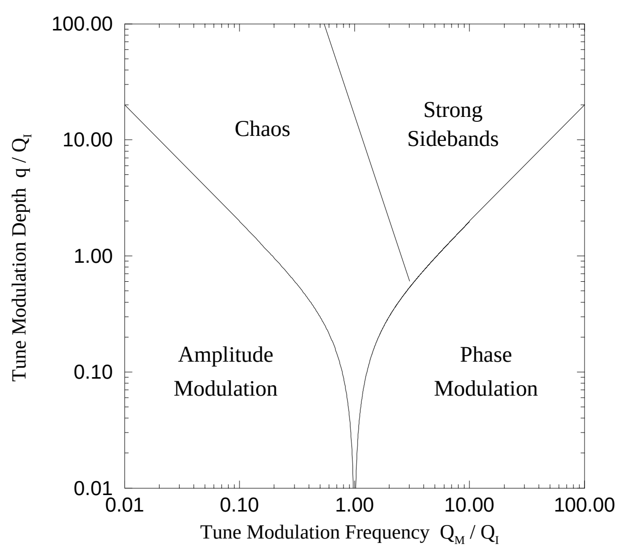

Figure 2: A parameterized tune modulation phase diagram. Resonant motion phases include stable motion (amplitude and phase modulation), the creation of isolated sideband resonances (strong sidebands), and thick bands of bounded stochastic motion (chaos) [6, 7, 8].

4.2 Modulational diffusion

Overlapping resonances and stochastic motion create amplitude growth and beam loss over timescales ranging from tens to millions of machine turns. Since strongly resonant and stochastic motion are avoided in the course of operations, practical interests in slow tail transport and beam loss concentrate on slow diffusive mechanisms. Though transverse diffusion in hadron colliders is partly created by noise growth, efforts have concentrated on other sources (such as tune modulation) that provide operational access to correction and control.

The most promising of these sources is modulational diffusion, originally applied by Chirikov. Here tune modulation creates small bands of stochastic motion in one-dimensional resonances, for resonances that have appropriate small strengths and island tunes. (See Figure 2.) This stochastic motion, though bounded, serves as a noise source that can be coupled into other dimensions of particle motion, thus creating slow diffusion. Simulations of modulational diffusion with realistic magnet and beam-beam nonlinearities and chromatic tune modulation have agreed within factors of two with observation [5, 8].

4.3 Experience: FNAL, IUCF, CERN, HERA-p

Beam capture onto resonances has been observed in experiments at FNAL [6] and IUCF [7], and measurements of strong resonances created by controlled nonlinearities have been demonstrated to agree with simulations and theory.

In a series of experiments at CERN and DESY, resonant slow diffusion has also been observed, similar to experiments performed in FNAL's E778 experiments [8, 9]. Loss rates were demonstrated to depend strongly on the presence and character of tune modulation, and transverse diffusion coefficients were measured. However, these loss rates were also shown to depend strongly on machine conditions, creating difficulties with reproducibility.

Diffusion and loss rates in the HERA-p halo have been controlled by compensating 100 and 300 Hz quad bus ripple lines with external tune modulation [10, 8]. After tuning, this compensation reducted proton losses by up to 40%. This experiment also demonstrated the use of PLL circuits to measure tune modulation from beam-based measurements, instead of inferring tune modulation from measurements of quad bus ripple.

More recently, another compelling argument has proposed that modulational diffusion is the source of the operational HERA-p dynamic aperture [11].

Transverse tune modulation, combined with knowledge of magnet and beam-beam nonlinearities, can be used to qualitatively control beam loss and halo growth. However, the many sensitive dependencies on machine parameters (e.g. base tunes, chromaticities, beam momentum spread, magnetic nonlinearities) make quantitative control difficult at best, and do not provide a very promising or sophisticated way to control beam halo and long-term beam loss.

5 LONGITUDINAL VOLTAGE MODULATION

During beam storage and collisions, longitudinal phase space is significantly simpler than the transverse. Typically a single storage RF voltage is applied, creating RF buckets that are dynamically equivalent to free pendula. The synchrotron frequency $Q_S(\delta)$ depends smoothly on momentum offset $\delta \equiv \Delta p/p$, ranging from the base synchrotron frequency Q_{S0} at small amplitudes to zero at the separatrix, $\delta = \delta_{\max}$. (See Figure 3.)

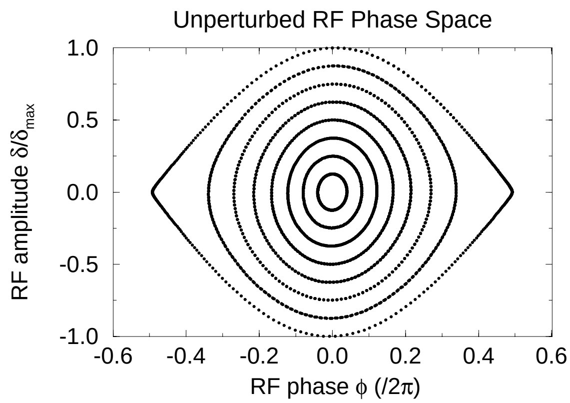

Figure 3: Typical RF phase space at beam store. This motion is parameterizable as a pendulum, with synchrotron frequencies ranging from $Q_{S0} = 0.008$ at the center fixed point to zero at the separatrix.

Due to the character of RF feedback and control, the two simplest quantities to modulate are RF voltage and synchronous RF phase. RF phase modulation, however, moves RF bucket fixed points, and has the unfortunate side effect of modulating the location of experimental interaction points. RF voltage modulation instead modulates the beam momentum width by varying the bucket size. Useful voltage modulation strengths incur changes much smaller than the total beam momentum width, and should not have any observable effects on colliding beam experiments.

When RF voltage modulation of the form

$$\frac{\Delta V}{V} = q \cos(2\pi Q_M t) \quad [t] = \mathrm{turns} \qquad (2)$$

is applied, the pendular RF phase space of Figure 3 becomes that of a parametrically driven pendulum [12]. Since pendulum motion is nonlinear, a primary nonlinear resonances is driven at amplitude $\delta_{\rm res}$ where $Q_M = 2Q_S(\delta_{\rm res})$, and the region near the RF separatrix becomes stochastic. Multiple voltage modulations may be applied, creating several resonances,

Modulation strengths significantly less than 1% of the RF voltage can create large resonance islands, as shown in Figure 4. Furthermore, beam within these resonance islands can be moved radially in the RF bucket with adiabatic changes to the voltage modulation frequency.

5.1 RF bucket halo transport

Following Gabella, et al. [13], one can use the resonances created by several RF voltage modulations to construct an integrated slow extraction system for crystal extraction. Particles are adiabatically moved outwards from the beam core to a "drive" resonance at a large momentum amplitude

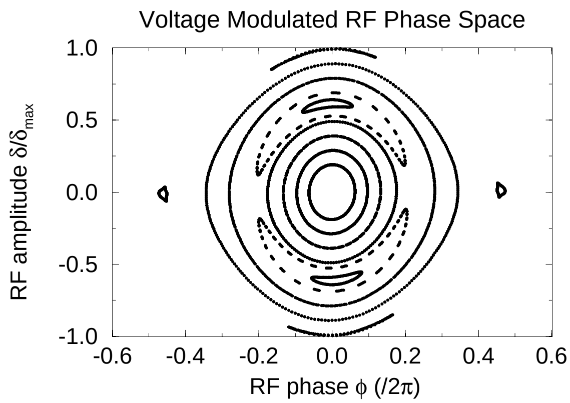

Figure 4: RF phase space as in Figure 3, with RF voltage modulation of depth $q = 0.002$ and frequency $Q_M = 1.8Q_{S0}$. Note the two large primary resonance islands, with small higher-order islands crated near the separatrix.

in the RF bucket. They then diffuse into the drive resonance through a web of weak stochastic resonances. Once within the drive bucket, particles are smoothly moved outwards to amplitudes that achieve penetration depths consistent with efficient crystal extraction.

Such a system requires several simultaneous voltage modulations of varying frequencies and amplitudes. The drive bucket frequency is low and constant, to place the drive bucket at a large momentum offset in RF phase space. The "feed" bucket, which captures particles near the core and moves them outwards, must ramp in frequency from $Q_M \approx 1.95Q_{S0}$ down to near the drive bucket frequency. Theoretical hamiltonian considerations give a maximum frequency ramping rate of

$$\frac{dQ_M}{dt} < 2\pi Q_S^2(\delta_{\text{res}}) \tag{3}$$

to maintain adiabatic capture. Furthermore, the feed bucket must be powered suddenly at the beginning of every ramp, to capture beam nonadiabatically in the core. Three to five additional modulations are added to create weak stochasticity around the drive resonance. Gabella, et al. state that this improves transfer efficiency.

Though such an extraction system is complicated by the many modulation parameters, it allows elegant control of extraction parameters such as spill rate. Because this system extracts particles by moving them to large momentum, it also requires that extraction be performed at a point of high horizontal dispersion.

5.2 Experience: IUCF, FNAL, CERN SPS

5.2.1 IUCF experiments and theory

Following the development of methods to track the synchrotron motion of an electron-cooled proton beam, RF voltage and frequency modulation have been extensively

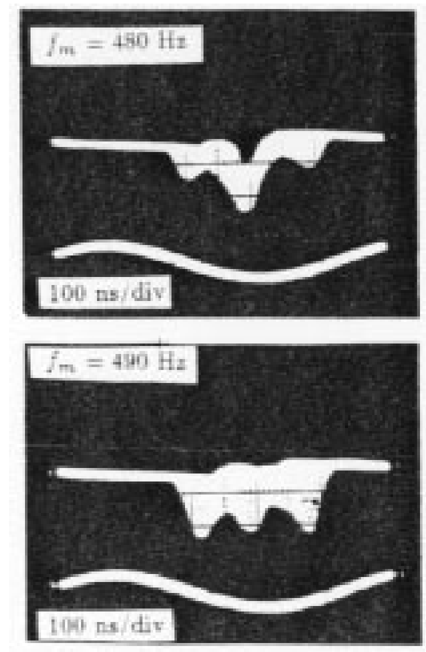

Figure 5: The longitudinal beam distribution for many turns, acquired from a high-dispersion BPM sum signal over many synchrotron periods as observed in IUCF for two different voltage modulation frequencies [15]. Beam capture in resonance islands is clearly visible.

studied in a series of nonlinear dynamics experiments performed at IUCF [14, 15]. Beam capture in RF resonance islands has been observed (Figure 5), and locations of resonance islands have been shown to agree very well with theory. Many of their results on parametric oscillators and driven resonances are applicable to both the transverse and longitudinal domains.

Other relevant work on RF dynamics investigated by the IUCF group includes double RF systems and barrier bucket dynamics. When combined with resonant behavior and RF voltage modulations, the results may be applied to RF manipulations ranging from transition crossing to efficient rebucketing [16, 17, 18].

5.2.2 FNAL and CERN crystal extraction

Experiments with crystal extraction, such as those performed at the CERN SPS and Fermilab Tevatron, have produced extraction efficiencies ranging up to approximately 30%. These experiments have suffered from the necessary limitation of crystals placed at low-dispersion areas, disallowing the opportunity to investigate RF-based extraction schemes such as those described above. Instead, tails were populated in the full phase space by application of noise on transverse dampers, or the beam was kicked into large betatron oscillations to physically overlap circulating beam tails with the extraction crystal [19].

6 SUMMARY

Single-frequency and narrow-band modulations are becoming more common with the advent of high-sensitivity systems in beam instrumentation. Minute responses to small excitations are locked and tracked while minimizing beam disturbances, and create the opportunity for understanding and experience with beam response during operations. Previous approaches using broad-band noise are unfriendly to luminosity requirements of colliding-beam experiments.

There have been qualitative and quantitative successes in the realms of nonlinear dynamics and magnet modulations, both transversely and longitudinally. In particular, tune modulation and transverse nonlinear dynamics have been combined to qualitatively affect slow tail transport and loss, though there are complex dependencies on even small changes in machine parameters. Transverse tune modulation may be controlled via feedback, but it is not a promising mechanism in the search for delicate slow extraction mechanisms during collider operations. The changing nature of beam sizes and beam-beam forces, and the resonances they create, is enough to limit the functionality of this approach.

RF space particle transport is more promising than the transverse, owing to the simpler nature of RF dynamics, the lack of strongly driven resonances, and the slower characteristic frequencies of motion. RF voltage modulation is accessible at frequencies and strengths required for low-intensity tail repopulation, and a promising parasitic mechanism has been proposed for crystal extraction [13]. However, RF extraction methods are only applicable for crystals placed in high-dispersion areas. As of the present there are no known plans to experimentally investigate high-dispersion crystal extraction.

7 REFERENCES

[1] C. Boccard et al., "Tune Measurements in the SPS as Multicycling Machine", in *Proceedings of the 1996 European Particle Accelerator Conference* (IEEE, Sitges, 1996), Vol. 2, p. 1600.

[2] J. Deregel et al., "Proposal of a K-Modulation System for the LHC Quadrupoles", LHC Project Report 4, 1996.

[3] P. Castro-Garcia, "Luminosity and Beta Function Measurement at the Electron-Positron Collider Ring LEP", Ph.D. thesis, CERN-SL-96-070-BI, 1996.

[4] Wen-Hao Cheng, A.M. Sessler, and J.S. Wurtele, "Damping of the Transverse Head-Tail Instability by Periodic Modulation of the Chromaticity", Phys. Rev. Lett. **78**, 4565 (1997) .

[5] T. Satogata, "Nonlinear Resonance Islands and Modulational Effects in a Proton Synchrotron", Ph.D. thesis, Northwestern University, February 1993.

[6] T. Satogata et al., "Driven Response of a Trapped Particle Beam", Phys. Rev. Lett. **68**, 1838 (1992) .

[7] Y. Wang et al., "The Effects Of Tune Modulation On Particles Trapped In One-Dimensional Resonance Islands", Phys. Rev. E **49**, 5697 (1994) .

[8] W. Fischer, "An Experimental Study on the Long-Term Stability of Particle Motion in Hadron Storage Rings", Ph.D. thesis, Universitat Hamburg, DESY 95-235, December 1995.

[9] T. Chen et al., "Measurements of a Hamiltonian System and their Description by a Diffusive Model", Phys. Rev. Lett. **68**, 33 (1992) .

[10] O.S. Brüning and F. Willeke, "Reduction of Particle Losses in HERA by Generating an Additional Harmonic Tune Modulation", in *Proceedings of the 1995 IEEE Particle Accelerator Conference* (IEEE, Dallas, 1995), Vol. 1, p. 420.

[11] F. Zimmermann, "Transverse Proton Diffusion", Particle Accelerators 49(N2) 67-104, 1995.

[12] S. Peggs, "Proton Mining — Dual Frequency Amplitude Modulation", May 9, 1991, FNAL AP note 91-001.

[13] Gabella, Rosenzweig, Kick, Peggs, "RF Voltage Modulation at Discrete Frequencies, with Applications to Crystal Channeling Extraction", Particle Accelerators, 1993, Vol 42(3-4), pp. 235-257.

[14] M. Ellison et al., "Driven Response of the Synchrotron Motion of a Beam", Phys. Rev. Lett. **70**, 591 (1993) .

[15] D. Li et al., "Experimental measure of resonance islands induced by RF voltage modulation", Phys. Rev. E **48**, R1638 (1993) .

[16] S.Y. Lee et al., "Parametric Resonances in Synchrotrons with Two RF Systems", Phys. Rev. E **49**, 5717 (1994) .

[17] S.Y. Lee and K.Y. Ng, "Particle Dynamics in Storage Rings with Barrier RF Systems", Phys. Rev. E **55**, 5992 (1997) .

[18] J.Y. Liu et al., "Bifurcation of Resonance Islands and Landau Damping in the Double-RF System", Phys. Rev. E **50**, R3349 (1994) .

[19] C.T. Murphy et al., "First Results From Bent Crystal Extraction at the Fermilab Tevatron", in *Proceedings of the Workshop on Channeling and Other Coherent Crystal Effects at Relativstic Energies* (Aarhus, Denmark, 1996).

Coherent Nonlinear Phenomena in High Energy Synchrotrons: Observations and Theoretical Models

P. L. Colestock, L. K. Spentzouris, and S. I. Tzenov

Fermi National Accelerator Laboratory, P.O. Box 500, Batavia, IL 60510; colestoc@fnalv.gov

Abstract

Nonlinear waves have been observed in synchrotrons for years but have received little attention in the literature. While pathological, these phenomena are worth studying on at least two accounts. First, the formation of solitary waves may lead to droplet formation that causes significant beam halo to develop. It is important to understand the conditions under which such behavior may be expected in terms of the machine impedance. Secondly, a variety of nonlinear processes are likely involved in the normal saturation of unstable oscillations, leading to the possibility that low-level, but potentially broadband fluctuation spectra may develop. The resulting fluctuation spectra carry indirectly the signature of the machine impedance. In this work we review a number of observations of nonlinear longitudinal waves made in Fermilab accelerators, and make a first attempt to develop appropriate theoretical models to explain these observations.

1 INTRODUCTION

Over the years, nonlinear wave phenomena have received scant attention in high energy synchrotrons, in part, because of the mathematical difficulty of this subject, but also due to the fact that nonlinear wave motion is usually associated with a pathological state of an accelerator that is best to be avoided. While this is indeed true for the most violent nonlinear effects, a broad class of low-level processes may be playing a role in many present machines, and the drive for ever higher beam intensities may lead to the widespread occurrence of nonlinear wave phenomena.

In particular, in the case of the dynamical behavior in the vicinity of an intense, stored beam, we are interested in the formation of beam halo, either as a diffuse cloud, represented by a departure from a Gaussian distribution, or as droplets which may occur in a type of phase transition at beam's edge due to coherent modes. In addition, it is useful to study the formation of an equilibrium state, if it exists, between a broad spectrum of marginally stable modes and some weak dissipative mechanisms that can lead to a saturated state of low-level turbulence, which, in turn, can affect the rate at which the halo population is generated. These phenomena can be expected to be most prevalent in hadron rings owing to the weakness of the damping mechanisms, and our attention in this paper is focussed on this case.

While these subjects are mathematically complex, a rich literature already exists in the field of plasma physics that deals with these questions, although the interparticle force predominantly considered in this literature is due to space charge alone. At the relativistic energies typical in modern accelerators, the interaction between particles is dominated by wall image currents, i.e. the wakefields, which complicates the nature of the interaction, but can also lead to a wider variety of wave phenomena. It is our aim in this work to highlight observations of nonlinear wave phenomena in high-energy synchrotrons and to point out methods of analysis from plasma physics that can be applied to the study of these topics.

The types of wave behavior in beams may be classified according to the degree of nonlinearity, in parallel with the concepts in plasma physics. In the linear regime, a resonant mode can be driven resulting in a response at the drive frequency which is characteristic of the beam intensity and the nature of the wakefield, or impedance, of the machine. When detected by a suitable pick-up, the driven response can shed light on the properties of the wakefields and the proximity of the beam to the stability threshold. This so-called transfer function method [1] is widely used to study accelerator stability.

If an accelerator is operated just above its stability limit, the most unstable mode is driven into exponential growth by the wakes, reaching a saturated, though marginally stable, state as the beam distribution is altered by the growing waves. If the spectrum of unstable modes is sufficiently broad, the phase of the perturbation is effectively random, and the interaction of waves and particles leads to particle diffusion in phase space, known in plasma physics as quasi-linear diffusion [2]. The analog in beams, known as the 'overshoot' phenomenon, has been studied [3],[4], although the applicability of this model is unclear owing to the typically narrow unstable spectrum found in many storage rings. A recent numerical study of this phenomenon that shows the complexity of the interaction is found in ref. [5].

However, particularly in hadron rings where the absence of synchrotron damping allows virtually unimpeded mode growth, unstable waves can grow to finite amplitudes that permit a significant fraction of the beam to become trapped in its own wake. The resulting wave motion couples to the trapped particles in such a way as to give rise to slowly damped oscillations. This phenomenon is known as nonlinear Landau damping in the plasma physics literature [6] (in comparison to linear Landau damping which is part of the linear beam response). It is to be expected that where a discrete spectrum of unstable waves can occur, as is often the case in a synchrotron, that nonlinear Landau damping can play an important role.

At the next higher level of nonlinear interaction, coherent modes can resonantly interact in a process known as the three- wave interaction [7]. This leads typically to a cascade in frequency which, due to the harmonic character of many modes in storage rings, readily occurs and can cause a broadening of the original unstable spectrum. This phenomenon has been studied in the simple case of longitudinal oscillations in a coasting beam, [8] and it can be expected that similar wave-wave coupling can occur in the transverse plane and in bunched beams as well, albeit with different resonance conditions.

If the coherent motion is particularly violent, and sufficiently dissipative, then the trapped portion of the beam can self-extract from the core of the beam distribution, forming droplets at the beam edge that can be self-sustaining. These are, presumably, a form of solitary wave, or soliton, which is perhaps unique to a high-energy synchrotron due to the complex character of the wake field. Such solitary waves may be a primary producer of halo particles for weakly-damped hadron rings.

In general, we are interested in the final state of these various nonlinear interactions: the condition where the coherent modes reach marginal stability through either a change in the beam distribution, or through frequency spreading of the spectral distribution. In the latter case, the phonons themselves can be thought of as comprising a fluid which comes into equilibrium, the details of which depend on the inter-phonon interaction. In the plasma physics literature, scaling laws for the resulting turbulent fluctuation spectrum have been derived ([9] and references contained therein). For our purposes, we would like to understand how aspects of the machine impedance, and therefore the detailed design, contribute to the form of the equilibrium turbulent spectrum, if it exists.

In this paper we review the observations made at Fermilab [8] in stored high energy hadron beams and compare the observations with numerical simulations. Our experimental studies, and thus our theoretical work, have been focussed on the phenomena in perhaps the simplest of all cases, that of longitudinal oscillations of a coasting, or unbunched, beam in a storage ring. As such, the surface of this subject has only been scratched, and our aim here is to outline the steps that would have to be taken to study any of the many other possible situations where nonlinear waves can occur. Moreover, we would like to underscore the importance of understanding turbulence in beams that we feel will be playing an increasingly important role as beams are more commonly run close to, or even above, their linear stability boundaries.

2 REVIEW OF BASIC PHENOMENA

2.1 Stability in Particle Beams

In the case of a high-energy stored beam, the growth of coherent wave motion is normally undesireable. Wakefields can drive such waves, though the mode growth is counteracted by damping due to the spread in frequencies of the individual particles making up the beam, and this damping effect was first derived for a plasma, known as Landau damping [10]. A well known technique for determining the linear stability boundary of a beam is to excite driven oscillations on the beam and to monitor the amplitude and phase of the beam's response, which includes the effects of wakefields. This technique, known as a beam transfer function, [1], yields for longitudinal motion in a coasting beam a response of the form

$$R(\Omega) = \frac{1}{\frac{i(e\omega_s)^2}{2\pi}\int_{-\infty}^{\infty}\frac{\frac{\partial f_o}{\partial \epsilon}}{\Omega - m(\omega_s + k_o\epsilon)}d\epsilon} + Z(\Omega) \quad (1)$$

where ω_s is the harmonic revolution frequency, f_o is the longitudinal particle distribution function, ε is the energy deviation, k_o is the frequency dispersion factor and $Z(\Omega)$ is the machine impedance. This function is directly related to the dispersion relation for longitudinal modes given by

$$D_m(\Omega) = 1 + Z(\Omega)\frac{i(e\omega_s)^2}{2\pi}\int_{-\infty}^{\infty}\frac{\frac{\partial f_o}{\partial \epsilon}}{\Omega - m(\omega_s + k_o\epsilon)}d\epsilon \quad (2)$$

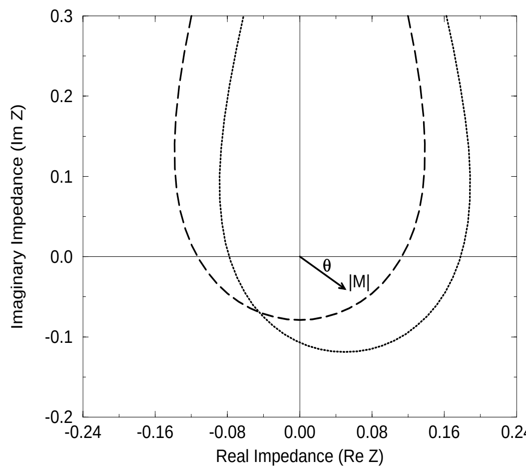

Figure 1: Theoretical shift of the beam response due to an impedance. The curve centered on the origin (dashed) is the response when there is no impedance, and the displaced curve (dotted) is the response when there is an impedance of $(Z_x, Z_y) = (.05, -.04)$. The magnitude of the impedance is $|\mathrm{M}| = \sqrt{Z_x^2 + Z_y^2} = .064\Omega$, and the phase is $\theta = -39°$. The beam distribution used was Gaussian in energy, and the beam parameters were arbitrary.

The stability boundary can be depicted in the impedance plane as the curve for which $Im(\Omega) = 0$, as shown in Fig.1. The machine impedance can be extracted from the measurements as an offset of the centroid of the stability curve, provided the beam distribution is known, assumed to be Gaussian here.

2.2 The Three-Wave Interaction

Weakly nonlinear processes are described using the same techniques as in linear stability theory, with the exception that a second-order frequency mixing term is included in the description of the dynamics. The effect of the frequency-mixing leads to a resonant coupling phenomenon by which modes at two separate frequencies couple to produce a response at a third frequency, a process known as three-wave or parametric coupling. The process is characterized by selection rules such that

$$\omega_1 = \omega_2 + \omega_3 \tag{3}$$

corresponding to conservation of energy among the waves. A similar condition applies to the mode wavenumbers, corresponding to conservation of momentum. Due to the periodicity in a ring, this condition can be readily satisfied for a large number of normal modes. We have studied the coupling for longitudinal modes theoretically and found three-wave coupling obeys a dispersion relation that couples the linear response of harmonic m and m-n through an idler mode at harmonic n.

$$\begin{aligned} & D_m(\Omega)D_{m-n}(\Omega-\Omega_0) = \\ & \qquad \frac{I_0^2 Z_m(\Omega) Z_{m-n}(\Omega-\Omega_0) V_0 V_0^* \beta^8}{64\pi^5 m^2 (m-n)^2 \eta^4 \left(\frac{\sigma_\varepsilon}{E_0}\right)^8 (E_0[eV])^4} \\ & \quad \times \int_{-\infty}^{\infty} \frac{x e^{-x^2}}{[\varepsilon-\xi_1][\varepsilon-\xi_2]^2}\, dx \\ & \quad \times \int_{-\infty}^{\infty} \frac{x e^{-x^2}}{[\varepsilon-\xi_1]^2[\varepsilon-\xi_2]}\, dx \end{aligned} \tag{4}$$

where the drive frequency is at $\Omega_o = n\omega_s$ and

$$\begin{aligned} x &= \frac{\varepsilon}{\sqrt{2}\sigma_\varepsilon}, \\ \xi_1 &= \frac{1}{\sqrt{2}\sigma_\varepsilon m k_0}(\Omega - m\omega_s), \\ \xi_2 &= \frac{1}{\sqrt{2}\sigma_\varepsilon (m-n) k_0}(\Omega - \Omega_0 - (m-n)\omega_s), \end{aligned}$$

and V_o is the drive amplitude, I_o is the beam current, η is the slip factor, $\frac{\sigma_\epsilon}{E_o}$ is the fractional energy spread and E_o is the beam energy.

The implication of Eq. 4 is that three-wave coupling is most likely near the stability threshold for any of the modes involved. The selection rule Eq. 3 leads to a single-sided coupling, which was observed experimentally, as shown in Fig. 2.

An interesting issue to investigate is how the power in the excited modes varies in time, especially in the presence of damping. Experimental observations indicate that a very regular cascade toward lower frequencies takes place, evidently due to successive three-wave coupling events. This behavior is typical for a dissipative system with sufficiently high mode density, and may be described by the following system of equations for the mode amplitudes.

$$\frac{\partial A_m}{\partial t} = s_m e^{i\phi} V_{mnk} A_n A_k \tag{5}$$

where the matrix element of the interaction has been symbolized as V_{mnk}, and is defined by as the following,

$$V_{mnk} = \frac{-i\frac{2(e\omega_s)^3}{\sqrt{\epsilon_0}(2\pi)^2} Z \int_{-\infty}^{\infty} \frac{\partial}{\partial\varepsilon}\left(\frac{\frac{\partial f_0}{\partial\varepsilon}}{\omega_k-(k)\omega(\varepsilon)}\right)\frac{1}{[\omega_m - m\omega(\varepsilon)]}\, d\varepsilon}{\left[\left|\frac{\partial D_m}{\partial\omega_m}\right|\left|\frac{\partial D_n}{\partial\omega_n}\right|\left|\frac{\partial D_k}{\partial\omega_k}\right|\right]^{\frac{1}{2}}} \tag{6}$$

It is worthwhile to note that as the multiplicity of modes becomes sufficiently dense, the coupling between waves governed by Eq. 6 can lead to a solitary wave phenomenon [11], and this subject will be described further in a later section. In the above mentioned work, only the interaction of longitudinal modes has been considered. It is also reasonable to expect that transverse modes can be coupled, especially where nonlinearities can play an important role, such as in the beam-beam interaction. This should be a fruitful area for further study.

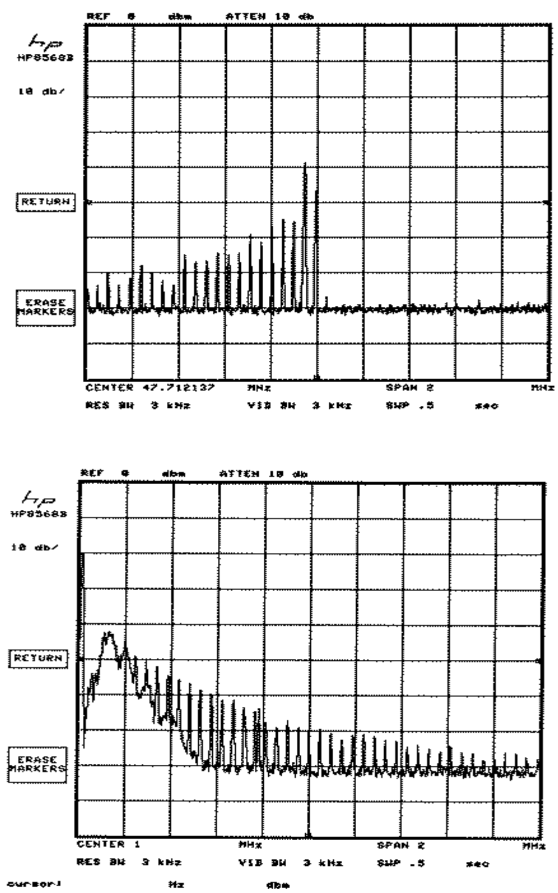

Figure 2: Three-wave coupling spectrum for longitudinal modes in a coasting beam in the Tevatron, 150 GeV beam. Excitation at h = 1000, (47.712 MHz) as shown in the upper graph, led to successive excitation of lower sidebands accompanied by low frequency modes, shown in the lower graph, which satisfy the selection rule. The lower graph begins at zero frequency and in each figure the frequency span is 2 MHz. The vertical amplitudes are in arbitrary units but the scales are logrithmic.

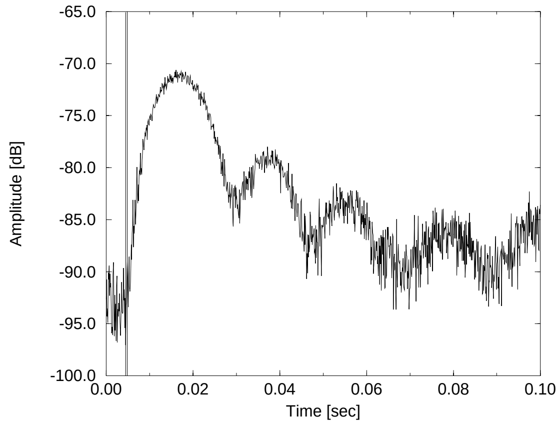

Figure 3: Power versus time at h = 105 in response to a 0.5 msec drive pulse. The placement and duration of the drive pulse has been drawn in for reference. An impulse excitation leads to slowly decaying amplitude oscillations as trapped particles exchange energy with the wakefield.

2.3 Nonlinear Landau Damping

Sufficiently large wakefields disturb an initially smooth particle distribution by trapping particles within the potential wells of the waves generated. The particle motion decoheres with a time constant that is significantly longer than the inverse frequency spread, or linear Landau damping time. The trapped particles undergo synchrotron oscillations in the self-generated potential wells, alternately exchanging incremental energy with the wakefields. The combination of energy dispersion of the particles and the nonlinearity of the voltage waveform eventually causes phase mixing of the coherent motion. This nonlinear damping process is called nonlinear Landau damping, and was first studied in plasma physics. [6], [12] - [16].

Experiments were carried out in the Fermilab Main Ring which clearly showed the signature of nonlinear Landau damping. In these studies, a short pulse of rf power was applied to the beam using an rf cavity at h=106 (5.03 MHz). The resulting response showed a characteristic response whose envelope decayed not exponentially but in an oscillatory manner, as shown in 3. This behavior is attributed to the exchange of energy between trapped particles and waves as described above. Both analytic [16], [12], [15], and numerical work [14], on nonlinear Landau damping has been carried out which descibes the behavior we have observed. This result will also be discussed further in a later section on simulations.

It has also been pointed out [16] that the advent of particle bunching is accompanied by the appearance of coherent power in higher harmonics of the fundamental frequency of the wakefield as the trapped particle bunches compress within the potential wells. Such behavior has indeed been observed in the experiments described above [8]. This compression of the bunch length is essentially wavefront steepening which is a prerequisite for the formation of solitons.

2.4 Solitary Waves.

The formation of solitons in a beam is of interest, since solitons may well be the vehicle which carries coherent energy in a highly turbulent state that might occur in a beam with weak damping. A vast literature on solitons in various media exists [17] - [20], though little effort has been given to this subject in ultra-relativistic beams. In particular, solitons in plasmas have been studied extensively, [18], [20], which depend on the particular nonlinearity introduced by the Coulomb force, i.e. space charge. A similar space charge limit was studied for a coasting beam [21], [22], and for a resonator impedance, [23], leading to the possibility that solitons may exist in high energy beams under certain conditions.

Since a wakefield force is fundamentally more complex than the space charge force, it can be assumed that the characteristics of a soliton will also be unique to the case of a high-energy beam. In particular, it is interesting to know what the impact of the wakefield dissipation has on the solitary wave behavior. Results from a variety of beam experiments suggest that long-lived solitary structures may form and extract themselves from the core of the beam over long times [24], [25]. In other work, transient solitary waves seem to appear [8]. In all cases, solitons may be viewed as phase-space droplets that appear in the beam, and under some conditions, give rise to a phase-transition and clumpy halo formation. From this point of view, it is valuable to understand their dynamics.

To this end we sketch here the results of an analytic study of longitudinal solitons on a coasting beam due to a general resonator impedance. This reperesents the simplest possible scenario for understanding such phenomena, will illustrate the mathematical procedure and serves as the starting point for more complex situations. For the reader's sake we note that many steps have been omitted from the following derivation for reasons of space. Full details will be given in forthcoming work [26]. The model equations for the dynamics are given by the following system

$$\frac{\partial f}{\partial T} + v\frac{\partial f}{\partial \theta} + \lambda_1 V\frac{\partial f}{\partial v} = 0,$$

$$\frac{\partial^2 V}{\partial T^2} + 2\gamma\frac{\partial V}{\partial T} + \omega^2 V = \frac{\partial I}{\partial T}, \tag{7}$$

$$I\left(\theta;T\right) = \int dv v f\left(\theta,v;T\right),$$

where $f\left(\theta,v;T\right)$ is the longitudinal distribution function, V is the voltage on a resonator of $\gamma = \frac{\omega}{2Q}$, $\omega = \frac{\omega_r}{\omega_s}\,\omega_r$ being the resonator frequency, and I is the instantaneous beam current. Time t has been normalized as $T = \omega_s t$. Furthermore $v = \frac{1}{\omega_s}\frac{d\theta}{dt} = 1 + \frac{k_o\varepsilon}{\omega_s}$ is the dimensionless angular velocity of a beam particle and

$$\lambda_1 = \frac{e^2 R k_o \gamma}{\pi},$$

where R is the resonator shunt impedance. Using standard moment techniques [28] on the above equations, we may pass over to the hydrodynamic picture of longitudinal beam motion and start from the system of gas-dynamic equations

$$\frac{\partial \rho}{\partial T} + \frac{\partial}{\partial \theta}(\rho u) = 0,$$

$$\frac{\partial u}{\partial T} + u\frac{\partial u}{\partial \theta} = \lambda V - \frac{\sigma_v^2}{\rho}\frac{\partial \rho}{\partial \theta}, \qquad (8)$$

$$\frac{\partial^2 V}{\partial T^2} + 2\gamma\frac{\partial V}{\partial T} + \omega^2 V = \frac{\partial}{\partial T}(\rho u),$$

where ρ and u are the density and the mean velocity moments of the distribution, respectively, (the variables ρ and V have been appropriately scaled) and $\lambda = \rho_o \lambda_1$. ($\rho_o$ = constant is the equilibrium beam density.) Using a renormalization group approach [26], [27], we may derive a set of amplitude equations for the rescaled beam density R_o, the current velocity u_o and the mode envelope function E.

Before proceeding, we would like to examine the stability problem of stationary waves in this system, which can be done without a formal solution of the amplitude equations. The approach, introduced by Sagdeev [18], is to look for forms of the nonlinear equations which correspond to harmonic motion in an effective potential well. Such states, if they exist, are conjectured to be allowed solitary waves in the nonlinear system. To this end let us write down the full system of amplitude equations, which after appropriate scaling reads as

$$\frac{\partial \widetilde{\rho}}{\partial \tau} + \frac{\partial}{\partial \Theta}(\widetilde{\rho}\widetilde{v}) = 0,$$

$$\frac{\partial \widetilde{v}}{\partial \tau} + \widetilde{v}\frac{\partial \widetilde{v}}{\partial \Theta} = -c_u^2\left(\frac{1}{\widetilde{\rho}}\frac{\partial \widetilde{\rho}}{\partial \Theta} + \frac{\partial |\psi|^2}{\partial \Theta}\right), \qquad (9)$$

$$i\frac{\partial \psi}{\partial \tau} + i\gamma b\psi + (1-\widetilde{\rho})\psi = -\left(1 - \frac{2i\gamma}{\omega_o}\right)\frac{\partial^2 \psi}{\partial \Theta^2} +$$

$$+\frac{2i}{\omega_o b}\left(1 - \frac{i\gamma}{\omega_o}\right)\frac{\partial(\widetilde{\rho}\widetilde{v}\psi)}{\partial \Theta} + \frac{i}{\lambda b^2}\psi\frac{\partial \widetilde{\rho}}{\partial \tau},$$

where

$$\widetilde{\rho} = 1 + R_o \qquad ; \qquad \widetilde{v} = \frac{ab\omega_o}{2}(1+u_o),$$

$$\psi = \frac{|\lambda|}{\omega_o \sigma_v} E e^{-\gamma T}$$

are the new (rescaled) dependent variables. The coefficients entering the above expressions are specified as follows:

$$a = \frac{2}{\sqrt{\sigma_v^2 + 3}} \qquad ; \qquad b = \frac{2\omega_q}{\lambda},$$

$$c_u = \frac{a\omega_o\omega_q\sigma_v}{|\lambda|},$$

where σ_v is the normalized beam energy spread. The new independent variables (time τ and azimuthal position Θ) are given by

$$\tau = \frac{T}{b} \qquad ; \qquad \Theta = \frac{a\omega_o\theta}{2}.$$

Moreover in the above set of equations the following notations have been adopted

$$\omega_o^2 = \omega^2 - \lambda \qquad ; \qquad \omega_q^2 = \omega_o^2 - \gamma^2,$$

In order to proceed, we have to further assume that the resonator is weakly damped, namely the high-Q case. For this case $(\gamma = 0)$ the ansatz

$$\widetilde{\rho} = \widetilde{\rho}(z) \qquad ; \qquad \widetilde{v} = \widetilde{v}(z),$$

$$\psi = A(z)e^{i[(a+v_o)z/2+\Omega\tau]} \quad ; \quad z = \Theta - v_o\tau$$

leads to a system of differential equations for $\widetilde{\rho}$, $\widetilde{v}$ and ψ admitting the following integrals of motion

$$C_1 = \widetilde{\rho}(\widetilde{v} - v_o),$$

$$C_2 = \frac{C_1^2}{2\widetilde{\rho}^2} + c_u^2\left(A^2 + \ln\widetilde{\rho}\right), \qquad (10)$$

$$2E = \left(\frac{dA}{dz}\right)^2 + \left[1 - \Omega + \frac{1}{4}(a+v_o)^2\right]A^2 -$$

$$-1 + \widetilde{\rho} + \frac{C_1^2}{c_u^2\widetilde{\rho}}.$$

These integrals of motion suggest that the stability of stationary waves can be equivalently described in terms of motion of a single particle in a (pseudo)- potential well. Indeed, the function

$$U(A) = \left[1 - \Omega + \frac{1}{4}(a+v_o)^2\right]A^2 -$$

$$-1 + \widetilde{\rho} + \frac{C_1^2}{c_u^2\widetilde{\rho}} \qquad (11)$$

provided $\widetilde{\rho}$ is expressed in terms of A from the second integral, comprises a pseudo-potential function. In Fig. 4 we

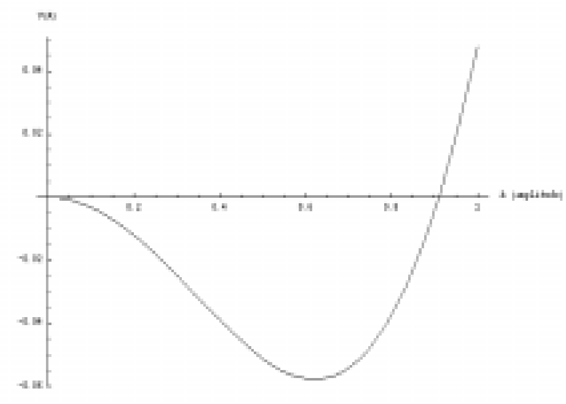

Figure 4: Pseudo-potential based on the nonlinear wave equations for a coasting beam. A minimum in this potential indicates the possibility for solitary waves (cavitons) to form.

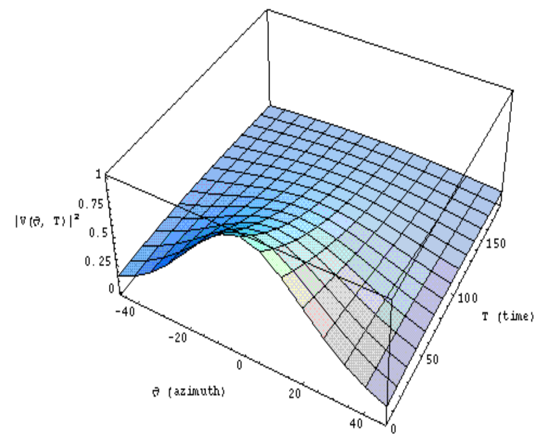

Figure 5: Voltage amplitude evolution of the solitary wave due to a resonator impedance. In the frame of the wave, the amplitude persists for long times but eventually damps as the soliton decelerates away from the beam core, and hence, the resonator's resonant frequency.

show $U(A)$ for the simplest case of constant current velocity $\widetilde{v} = v_o$ $(C_1 = 0)$. We note that a minimum in this pseudo-potential corresponds to solitary waves that can be effectively "trapped" in this potential well.

In the following, we can proceed to find approximate closed-form solutions of these nonlinear equations, which will allow us to explicitly find the time behavior of the solitary waves in the presence of dissipation. Eliminating of the current velocity from the complete set of amplitude equations and expressing $\widetilde{\rho}$ in terms of $|\psi|^2$

$$\widetilde{\rho} = 1 - |\psi|^2 \tag{12}$$

we finally arrive at the damped nonlinear Schrödinger equation

$$i\frac{\partial \psi}{\partial \tau} + i\gamma b\psi =$$

$$-\left(1 - \frac{2i\gamma}{\omega_o}\right)\frac{\partial^2 \psi}{\partial x^2} + \frac{a\gamma}{\omega_o}\frac{\partial \psi}{\partial x} - |\psi|^2\psi, \tag{13}$$

where

$$x = \frac{a}{2}\left(\omega_o \theta + \frac{2T}{b}\right).$$

Eq. 13 admits closed form solutions that indicate solitary waves can exist, but due to the dissipation in the model, eventually disappear after initial generation. We interpret this behavior as a gradual shrinking of the potential well that occurs when the trapped particles have decelerated sufficiently from the the resonantor frequency. The results for the voltage amplitude and soliton (caviton) density are shown in Figs. 5 and 6 respectively. We note that a similar equation has been derived [22] from an entirely different perspective. It is also worth noting that Eq. 13 is a special case of the complex, cubic Ginzburg-Landau equation [29], widely used to study various pattern formation phenomena and coherent structures.

2.5 Turbulence.

The study of turbulence in beams is valuable primarily because it may be a universal phenomenon, at least at low levels, which plays a role in determining the limiting phase-space density in any machine. The effect has likely been small in machines well below their stability thresholds, however, as intensities have been pushed closer to stability limits, nonlinear wave interactions can occur which lead to a marginally stable equilibrium. A first attempt at determining the fluctuation spectrum for a beam was obtained by considering the equilibrium state of a Gaussian beam [30]. The resulting spectrum was related to the linear dielectric function and showed that the fluctuation density would be strongly peaked for cases near the linear stability limit. It is our conjecture that such a situation may have occurred in the Fermilab Tevatron during recent attempts to realize stochastic cooling of bunched beams [31]. A broad, stationary spectrum of fluctuations was observed at many times the expected Schottky, or shot noise, levels. The harmonic generation observed in the Fermilab Main Ring mentioned above is consistent with these observations as well. It is our aim in this paper to outline a theoretical approach to understand the formation of an equilibrium spectrum and to understand the spectral amplitude dependence on the character of the machine impedance.

The approach taken is to develop a statistical description of fluctuations for an ensemble of coupled modes. This may be viewed as a development of the amplitude equations associated with coupled modes, as in Eq. 6. The interaction between modes may be three-wave, as given in 6, or higher-order. In this work, we outline a general procedure, but keep only interactions up to the three-wave level. The result will

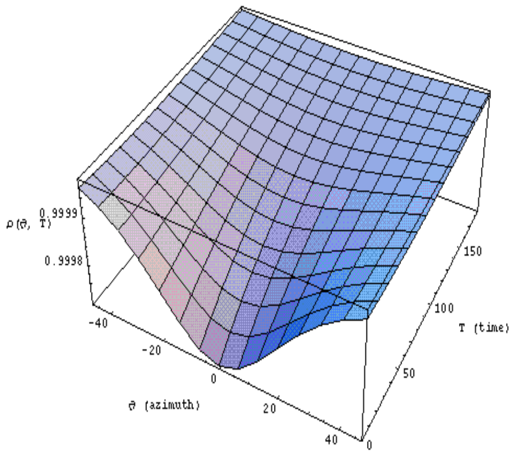

Figure 6: Caviton density evolution. A density depression associated with the solitary wave decreases in amlitude at long times as the wave amplitude itself decreases.

be a scaling law for the envelope of the fluctuation spectrum.

The starting point for our analysis is the system of equations for the fluctuation δN of the microscopic phase space density and the fluctuation δV of the voltage [9]

$$\left(\frac{\partial}{\partial\theta}+v\frac{\partial}{\partial\sigma}+\lambda V\frac{\partial}{\partial v}\right)\delta N=$$

$$-\lambda n\frac{\partial f}{\partial v}\delta V-\lambda\frac{\partial}{\partial v}\left[\delta N\delta V-\langle\delta N\delta V\rangle\right],$$

$$\frac{\partial^2\delta V}{\partial\sigma^2}-2\gamma\frac{\partial\delta V}{\partial\sigma}+\omega^2\delta V=-\frac{\partial\delta I}{\partial\sigma},$$

$$\delta I=\int dv\,(1+v)\,\delta N\,(\sigma,v;\theta)$$

written in the variables $\sigma=\theta-\omega_s t$ and $v=k_o\varepsilon/\omega_s$. Fourier transforming the above equations and using the concept of slowly varying amplitude of weakly nonlinear waves one obtains the following equation

$$\left(\frac{\partial}{\partial\theta}+\Omega_g\frac{\partial}{\partial\sigma}-\Gamma_k\right)\delta V_k=-\frac{i}{\left(\frac{\partial\epsilon}{\partial\Omega}\right)_{\Omega_k}}$$

$$\times\sum_{k_1+k_2=k}\kappa_2\left(k,\Omega_{k_1}+\Omega_{k_2};k_2,\Omega_{k_2}\right)$$

$$\times\left(\delta V_{k_1}\delta V_{k_2}-\langle\delta V_{k_1}\delta V_{k_2}\rangle\right)e^{i\theta\left(\Omega_k-\Omega_{k_1}-\Omega_{k_2}\right)}+\ldots\quad(14)$$

for the amplitudes δV_k, where

$$\epsilon\,(k,\Omega)=1+i\lambda nZ\,(k)\int\frac{dv\,(1+v)}{\Omega-kv+io}\frac{\partial f}{\partial v},$$

is the dielectric permittivity and

$$\kappa_2\,(k,\Omega;k_1,\Omega_1)=\frac{n\lambda^2Z\,(k)}{2\gamma}\int dv\,(1+v)$$

$$\times\frac{1}{\Omega-kv+io}\frac{\partial}{\partial v}\left(\frac{1}{\Omega_1-k_1v+io}\frac{\partial f}{\partial v}\right)$$

is the second order susceptibility of the beam. Here

$$Z\,(k)=\frac{ik}{k^2-\omega^2+2i\gamma k}$$

is the familiar resonator impedance function and

$$\Omega_g=-\left\{\frac{\partial Re\left[\epsilon\,(k,\Omega)\right]}{\partial k}\left[\frac{\partial Re\left[\epsilon\,(k,\Omega)\right]}{\partial\Omega}\right]^{-1}\right\}_{\Omega=\Omega_k}$$

$$\Gamma_k=\left\{Im\left[\epsilon\,(k,\Omega)\right]\left[\frac{\partial Re\left[\epsilon\,(k,\Omega)\right]}{\partial\Omega}\right]^{-1}\right\}_{\Omega=\Omega_k}$$

are the group velocity of waves and the damping factor respectively. For the slowly evolving part A_k of the wave amplitude δV_k it is straightforward to derive the equation

$$\left(\frac{\partial}{\partial\theta}+\Omega_g\frac{\partial}{\partial\sigma}+i\omega_k-\Gamma_k\right)A_k=$$

$$=i\sum_{k+k_1=k_2+k_3}S\,(k,k_1,k_2,k_3)$$

$$\times\left(A^*_{k_1}A_{k_2}A_{k_3}-A_{k_2}\left\langle A^*_{k_1}A_{k_3}\right\rangle-\left\langle A^*_{k_1}A_{k_2}A_{k_3}\right\rangle\right),\quad(15)$$

where

$$S\,(k,k_1,k_2,k_3)=\frac{\kappa_2\,(k-k_2,\Omega_{k_3}-\Omega_{k_1};k_3,\Omega_{k_3})}{\sqrt{\omega^2-\lambda n}\left(\frac{\partial\epsilon}{\partial\Omega}\right)_{\Omega_k}\left(\frac{\partial\epsilon}{\partial\Omega}\right)_{\Omega_{k-k_2}}}$$

$$\times[\kappa_2(k,\Omega_{k_2}+\Omega_{k-k_2};k-k_2,\Omega_{k-k_2})$$

$$+\kappa_2(k-k_2,\Omega_{k_2}+\Omega_{k-k_2};k_2,\Omega_{k_2})],$$

$$\omega_k=\Omega_k-sign\,(k)\sqrt{\omega^2-\lambda n}.$$

Averaging of the equation for A_k yields the kinetic equation for waves

$$\left(\frac{\partial}{\partial\theta}+\Omega_g\frac{\partial}{\partial\sigma}-2\Gamma_k\right)I_k=$$

$$=2\pi\sum_{k+k_1=k_2+k_3}\left|S\,(k,k_1,k_2,k_3)\right|^2$$

$$\times\delta\left(\omega_k+\omega_{k_1}-\omega_{k_2}-\omega_{k_3}\right)$$

$$\times\left(I_{k_1}I_{k_2}I_{k_3}+I_kI_{k_2}I_{k_3}-I_kI_{k_1}I_{k_3}-I_kI_{k_1}I_{k_2}\right),\quad(16)$$

where

$$\langle A_k A_{k_1} \rangle = I_k \delta(k + k_1).$$

Dimensional analysis of the kinetic equation for waves gives the following fluctuation spectrum law of Kolmogorov type

$$I_k \sim const * k^{-7/3}. \tag{17}$$

We note that this power law spectrum, which in this case is due to a resonator, would indeed lead to the type of broad fluctuation spectrum seen in experiments. However, at this time, a detailed study of the scaling of the observed spectrum has not been made. An extension of the above work to consider bunched beams, and other types of machine impedance would be very worthwhile.

3 SIMULATIONS

In this work, we are interested in demonstrating examples of the nonlinear wave behavior we have described analytically. No attempt is made to closely model a real device, though this could be done with the building blocks we provide here. We shall concentrate on the longitudinal plane, as explained above, and carry out simulations exculsively on a coasting, (unbunched) beam, for simplicity. We adopt the resonator model described above and follow approximately the procedure adopted in early simulation work [32]. The particle evolution equations are given by

$$\begin{aligned} \frac{d\epsilon}{dt} &= 2\pi e\omega_s V(t) \\ \frac{d\theta}{dt} &= -\eta\epsilon \\ \frac{dV}{dt} &= \frac{\omega_r R}{Q}(I - I_1) - \frac{\omega_r}{Q}V \\ \frac{dI_1}{dt} &= \frac{\omega_r Q}{R}V \end{aligned} \tag{18}$$

where ϵ is the energy deviation from the synchronous energy and V is the voltage induced in a resonator with shunt impedance R, resonant frequency ω_r and quality factor Q. I is the instantaneous current given as the projection of phase-space onto the θ axis

$$I = \frac{e\omega_s}{2\pi}\int_{-\infty}^{\infty} f d\epsilon$$

The energy dispersion η is assumed to be a constant and the particle distribution is advanced each time step according to Eq. 18. Then the current is computed, followed by the voltage on the resonator using Eq. 18. Results for the case of a coasting beam are shown in Figure 7 - 9. The simulation parameters are given in Table 1.

In Fig. 7, the phase-space distribution is shown, initially assumed to be uniform in θ and Gaussian in energy. After 500 time steps, the resonator has developed a sinusoidal voltage from the initial noise level (due to the finite number of particles) which has succeeded in bunching a large fraction of the beam and synchrotron motion in the resulting potential well is taking place. The synchrotron motion can also be thought of as synonymous to the wave-breaking process which has been described in plasma physics [12]. As time proceeds, Fig. 8, shows a deceleration of the trapped particles from the core of the beam, and the decelerated portion remains well-organized, and even intensifies as its length is foreshortened. The voltage in the resonator then becomes phase-locked to the 'droplets' and the voltage amplitude oscillates as they move in and out of phase with the remaining coherent structure in the beam's core. We note that the droplets thus formed bear the characteristics of the solitons discussed in the previous section, remaining self-organized for long times.

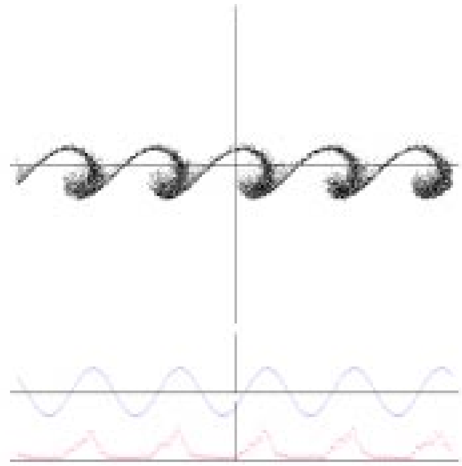

Figure 7: Simulation after 500 time steps for the model problem listed in Table 1. The upper portion represents $\varepsilon - \theta$ phase-space. The middle curve is the cavity voltage as applied to different portions of the beam and the bottom curve is the projection of phase-space on the theta-axis, representing the instantaneous current. The resonator wakefields have caused bunching which shows significant particle trapping and consequent wave overturning. The particle current shows strong local intensification of the beam density corresponding to the solitons.

As the dissipation in the impedance continues to decelerate the solitons Fig. 9, the resonator voltage drops due to the high Q value, or narrow bandwidth, assumed. This, in turn, reduces the deceleration rate and the depth of the potential wells that can sustain the solitons. As such, a steady state can be reached where the remaining trapped particles reach a stable equilibrium outside the beam, in accord with the analytic model for solitary waves. The envelope of the cavity voltage and the mean energy deviation of the solitons are shown in Fig. 10, indicating deceleration of the trapped particles. A steady state is eventually reached, though not shown, where the solitons have moved sufficiently off resonance that the deceleration ceases.

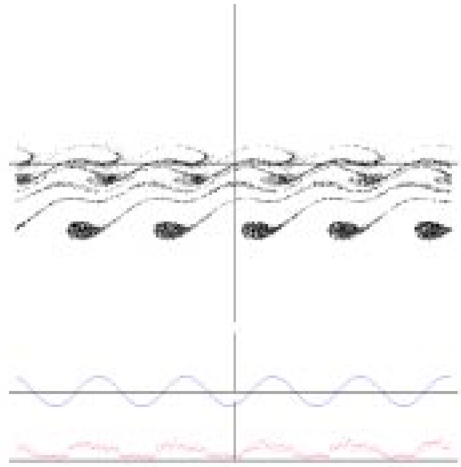

Figure 8: Phase-space after 1000 time steps. Portions of the originally trapped particle population have decelerated from the core due to the finite resistivity of the wakefields. The solitons remain, however, well-organized as they experience deceleration. Both the cavity voltage and the density perturbations have decreased, but persist for long times. The diagrams have the same meaning as in the previous figure.

We show the final results for a low-Q cavity in Fig. 11. These are qualitatively the same as in the previous case, but the structure of the solitons has taken on a decidedly random character. This is evidently due to the fact that the fractional contribution of noise to the cavity voltage is larger, owing to the wider bandwidth of the cavity, resulting in a more random distribution of potential well sizes. Droplet, or soliton formation, still occurs, but the resulting fluctuation spectrum is broader. The onset of the solitary waves can be viewed as a phase transition at the beam's edge produced by the resonator's wakefield. This is the case, we believe, that is most frequently encountered in actual machines.

Table 1: Model Simulation Parameters

Parameter	Value
Resonator Impedance	100 Ohms
Slip Factor η	.001
Resonator Quality Factor	10.
Typical Beam Energy Spread σ_ε/E_0	$1-4\times10^{-3}$
Number of Particles	10000

We note that the fluctuation spectrum associated with the above distribution is due to the ensemble of strongly nonlinear waves and is likely beyond the realm of the three-wave interaction described in the scaling law in the previous section. An interesting study to be carried out is the experimental and theoretical determination of the spectral shape in a machine whose impedance is well-known.

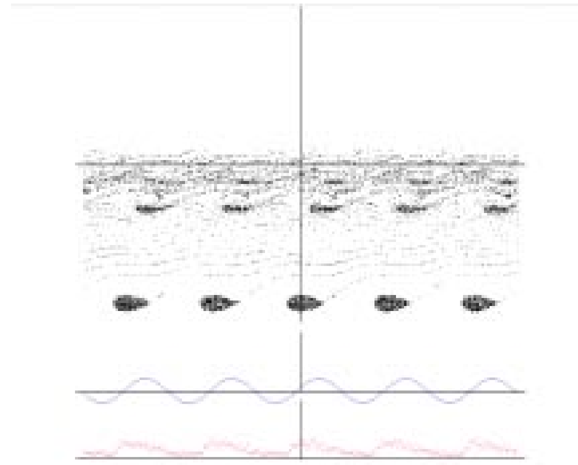

Figure 9: Phase-space after 2000 time steps. The beam core is now largely decohered, however, the solitons continue to decelerate slowly and maintain the remaining cavity voltage well off resonance. The diagrams have the same meaning as in the previous figure.

4 CONCLUSIONS

In this work we have attempted to outline various levels of nonlinearity in coherent interactions in high-energy beams. Besides the general academic interest of nonlinear dynamics, for which high-energy beams provide an excellent testing ground, there are at least two areas where the study of nonlinear waves can find application in accelerator physics.

The first is the study of halo formation in which the nonlinear evolution of coherent fluctuations can lead to soliton, or droplet, formation, as described in previous sections. While there is suggestive experimental evidence that such states can occur, there has been little detailed study of this phenomenon, and we assert that there is much to be learned about machine wakefields through the study of solitary waves and their interactions. Specifically, we have only considered the simplest case, that of longitudinal waves in an unbunched beam, and there are many other cases of interest in high-energy accelerators.

The second application is the study of non-equilibrium fluctuations driven by wakefields. Nonlinear mode-mode coupling permits a frequency cascade, both toward lower and higher frequencies via separate processes. The photon distribution that results is an equilibrium between the nonlinear interactions producing the cascade and weak dissipative mechanisms. These mechanisms are assumed to be related to the broadband impedance of the machine, though other mechanisms may also be responsible. We have carried out a model calculation for a specific form of impedance that yields a specific scaling law for the turbulent spectrum. A number of assumptions come into play in the development of this model and the situation is ripe for careful experimental testing. The benefit of this study is the understanding of the significance of low-level turbulence in the limiting parameters of a given accelerator.

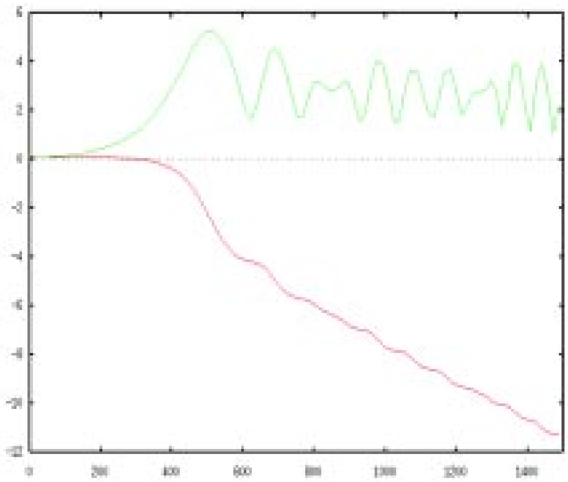

Figure 10: Cavity voltage envelope and mean energy deviation. The upper curve is the envelope of the cavity voltage, showing the exchange of energy between the soliton and the wakefield. The lower curve is the mean energy of the perturbation, which descends away from the beam, but eventually reaches an equilibrium (not shown) where the deceleration ceases.

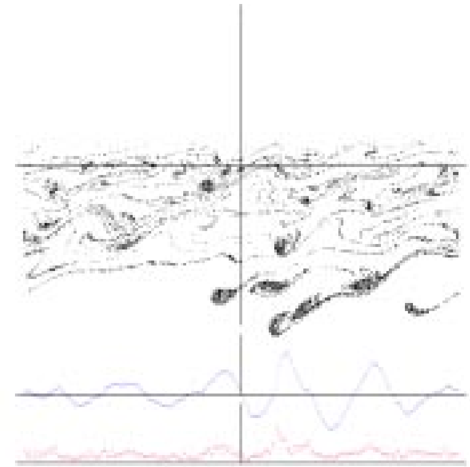

Figure 11: Simulation results for low-Q case. The comparative contribution of noise to the dynamics is larger owing to the increased bandwidth of the resonator. Solitary waves still develop, but the associated fluctuation spectrum is broader.

5 ACKNOWLEDGEMENTS

The authors are indebted to Prof. Nigel Goldenfeld for helpful discussions, and to Dr. David Finley for his enlightened support of this work.

6 REFERENCES

[1] A. Hofmann, Single-beam Collective Phenomena - Longitudinal,CERN 77-13, July 1977.

[2] C. F. Kennel and F. Engelmann, Velocity Space Diffusion from Weak Plasma Turbulence in a Magnetic Field, *Physics of Fluids*, 9, 1966.

[3] Y. Chin and K. Yokoya, *Physical Review D*, Vol. 28, 1983

[4] A. Bogacz and K. Y. Ng, Nonlinear Saturation of the Longitudinal Modes of a Coasting Beam in a Storage Ring, *Physical Review D*, D36, 1987

[5] A. Gerasimov, Longitudinal Bunched-Beam Instabilities Going Nonlinear: Emittance Growth, Beam Splitting and Turbulence, *Physical Review E*, Vol. 49, 1994

[6] T.M. O'Neil, Collisionless Damping of Nonlinear Plasma Oscillations, *The Physics of Fluids*, Vol. 8, Dec 1965.

[7] K. Nishikawa, Parametric Excitation of Coupled Waves I.General formulation, *Journal of the Physical Society of Japan*, Vol. 24, 1968.

[8] L. K. Spentzouris, Ph.D. Thesis, Northwestern University, 1996.

[9] V. E. Zakharov, Kolmogorov Spectra in Weak Turbulence Problems, Handbook of Plasma Physics, Eds. M. N. Rosenbluth and R. Z. Sagdeev, Elsevier, 1984.

[10] T. H.. Stix, The Theory of Plasma Waves, American Institute of Physics, New York, 1992.

[11] E. Fermi, J. Pasta and S. Ulam, Studies of Nonlinear Problems, Los Alamos National Laboratory Report LA-1940, 1955.

[12] J. Dawson, On Landau Damping, *The Physics of Fluids*, Vol. 4, Number 7, Jul 1961.

[13] J. H. Malmberg and C. B.Wharton, *Physical Review Letters*, Vol. 17, 175, 1966.

[14] I.H. Oei and D.G. Swanson, Self-consistent Finite Amplitude Wave Damping, *The Physics of Fluids*, Vol. 15, Number 12, Dec 1972.

[15] J. Canosa and J. Gazdag, Threshold Conditions for Electron Trapping by Nonlinear Waves, *The Physics of Fluids*, Vol. 17, Number 11, Nov 1974.

[16] T.M. O'Neil, J.H. Winfrey, and J.H.Malmberg, Nonlinear Interaction of a Small Cold Beam and a Plasma, *The Physics of Fluids*, Vol 14, Number 6, June 1971.

[17] P. G. Drazin and R. S.Johnson, Solitons: An Introduction, Cambridge University Press, Cambridge, 1989.

[18] R. Z. Sagdeev, D. A. Usikov and G. M. Zaslavsky, *Nonlinear Physics*, Harwood Academic, London, 1988

[19] A.C. Scott, F.Y.F. Chu, and D.W. McLaughlin, The Soliton: a New Concept in Applied Science, *Proceedings of the IEEE*, Vol 61, Number 10, Oct 1973.

[20] R. C. Davidson, Methods in Nonlinear Plasma Theory, Academic Press, New York, 1972.

[21] J.J. Bisognano, Solitons and particle beams, *Particles and fields series 47, High Brightness Beams for Advanced Accelerator Applications*, AIP Conference Proceedings 253, College Park MD, 1991.

[22] R. Fedele, G. Miele, L. Palumbo, and V. G. Vaccaro, Thermal Wave Model for Nonlinear Longitudinal Dynamics in Particle Accelerators, *Physics Letters*, A 179, 407, 1993.

[23] P. L. Colestock, S. Assadi and L. K.Spentzouris, Nonlinear Collective Phenomena in High-Energy Synchrotrons, Proc. ICFA Workshop on Nonlinear and Collective Phenomena in Beam Physics, AIP Proc. 395, Arcidosso, 1996.

[24] M. Q. Barton and C. E. Nielsen, Longitudinal Instability and Cluster Formation in the Cosmotron, Proc. Int. Conf. on High-Energy Accelerators, Sept. 6-12, 163, 1961.

[25] R. A. Carrigan, Private Communication

[26] S. Tzenov and P. L. Colestock, To Be Published

[27] L.-Y. Chen, N. .Goldenfeld and Y.Oono, Renormalization Group and Singular Perturbation: Multiple Scales, Boundary Layers and Reductive Perturbation Theory, *Phys. Rev E*, Vol. 54, 376, 1996.

[28] Y. L. Klimontovich, *Statistical Physics*, Harwood Academic Publishers, Chur. 1986.

[29] M. C.Cross and P. C.Hohenberg, Pattern Formation Outside of Equilibrium, *Reviews of Modern Physics*, Vol. 65, 851, 1993.

[30] V. V. Parkhomchuk and D. V. Pestrikov, Thermal Noise in an Intense Beam in a Storage Ring, *Sov. Phys. Tech. Phys.*, Vol. 25, 7, 1980.

[31] G. P. Jackson, Bunched Beam Stochastic Cooling in the Fermilab Tevatron Collider, Proc. Montreaux Workshop on Beam Cooling and Related Topics, CERN Geneva, CERN-94-03, 127, 1993.

[32] E. Keil and E. Messerschmid, Study of Non-Linear Effects of a Resonant Cavity on the Longitudinal Dynamics of a Coasting Particle Beam, *Nucl. Inst. and Methods*, Vol. 128, 203, 1975.

Beam-Beam Interactions

W. Chou
Fermi National Accelerator Laboratory, P.O. Box 500, Batavia, IL 60510

Abstract

This paper gives a brief review of the beam-beam interactions of the hadron beams. Some recent results on the Pacman effect and dynamic aperture studies are also included.

1 INTRODUCTION

No matter how "perfectly" a collider could be built (*e.g.*, good vacuum, small magnet errors, little non-linearity and low coupling impedance, *etc.*), beam-beam interactions will be the ultimate limit of its performance. These interactions will cause particle losses, emittance growth, tune shifts, orbit displacements, beam instabilities, non-linear resonances and will limit the dynamic aperture and the beam current and beam lifetime. Because interactions of hadron beams are quite different from that of lepton beams, we will content ourselves with the study of hadron beams in this paper.

There have been extensive machine studies on beam-beam interactions at the Tevatron at Fermilab and the S$p\bar{p}$S at CERN. There were also intensive theoretical and computational beam-beam studies at the former SSC and for the future LHC. [1, 2, 3] We will briefly review these results. We will also discuss some new results recently obtained from the LHC work, mainly on the Pacman effect and dynamic aperture.

2 STRONG BEAM-BEAM INTERACTIONS

2.1 Inelastic scattering

This is what a collider is built for. This process generates the events that detectors will record and the experimentalists will analyze. It also results in particle losses. The loss rate is:

$$\frac{dN}{dt} = \mathcal{L}\sigma_{\rm inel} \tag{1}$$

which gives the beam lifetime due to luminosity. Take the LHC as an example. The total number of particles per beam is 2.8×10^{14}, the luminosity $\mathcal{L}$ is 10^{34} cm^{-2}s^{-1}, the inelastic cross section $\sigma_{\rm inel}$ is about 60 mb, and there are two high luminosity interaction points (IPs). These numbers give a beam lifetime of about 65 hours.

2.2 Elastic scattering

The proton-proton elastic scattering contributes to the emittance growth. The growth rate is given by (per IP):

$$\frac{d\epsilon}{dt} = \frac{N_{\rm B} f_0}{4\pi\epsilon}\sigma_{\rm el}\sigma_\alpha^2 \tag{2}$$

The meaning of the symbols can be found in the Glossary. The RMS value of pp elastic scattering angle in the center of mass system (CMS), σ_α, is

$$\sigma_\alpha = \frac{hc}{E_{\rm c.m.}\sqrt{2\pi\sigma_{\rm T}}} \tag{3}$$

In the LHC, for colliding beams with $E_{\rm c.m.}$ = 14 TeV and $\sigma_{\rm T} \approx$ 100 mb, one finds $\sigma_\alpha = 11$ μrad. Using $N_{\rm B} = 1 \times 10^{11}$, $f_0 = 11.2$ kHz, $\epsilon = 5 \times 10^{-10}$ m-rad, $\sigma_{\rm el}$ = 40 mb, one gets a growth rate of about 1×10^{-16} m-rad/s per IP.

3 ELECTROMAGNETIC BEAM-BEAM INTERACTIONS

There are two types of interactions: head-on and long range (which is also called parasitic crossings). The characteristic quantity of these interactions is the beam-beam parameter ξ. It is sometimes also called the Amman-Ritson parameter to honor the two physicists who first investigated it in 1960. Consider two counter-circulating round bunches. At small amplitude, the opposing bunch looks like a lens with the strength:

$$f = \frac{N_B r_p}{\gamma\sigma_x^2} = \frac{N_B r_p}{\gamma\epsilon\beta^*} \tag{4}$$

The tune shift per IP is:

$$\xi = \frac{\beta^* f}{4\pi} = \frac{\beta^* N_B r_p}{4\pi\gamma\epsilon\beta^*} = \frac{r_p}{4\pi}\cdot\frac{N_B}{\epsilon_N} \tag{5}$$

Note that this parameter is independent of the beam energy and the beta-function and, apart from a constant, is equivalent to the beam brightness N_B/ϵ_N. This perhaps surprisingly simple result makes this parameter very useful. It is one of the basic parameters in the design of any collider. (Note that the brightness is also limited by the space charge effect in the first circular accelerator in the injector chain.) The design value of ξ is 0.0034 for the LHC and 0.0009 for the SSC.

3.1 Tune shift and tune spread

The most significant beam-beam effect observed at the Tevatron and S$p\bar{p}$S is the slow diffusion, which is believed to be caused by high order betatron resonances. It leads to particle losses that in turn decrease the beam lifetime and create background in detectors. The head-on tune shift per IP (which is also the tune spread) is:

$$\Delta\nu_{\rm HO} = \xi\left(\frac{2R_{\rm re}^2}{1+R_{\rm re}}\right) \tag{6}$$

where $R_{\rm re}$ is the luminosity reduction factor due to the crossing angle and equals:

$$R_{\rm re} = \left(1 + \left(\frac{\theta\sigma_s}{2\sigma_x}\right)^2\right)^{-1/2} \tag{7}$$

For long range interactions, the tune shift per IP is:

$$\Delta\nu_{\rm LR} = \xi\cdot\frac{N_p}{n^2} \tag{8}$$

where n is the full crossing angle in units of $\sigma_{x'}$, N_p is the number of parasitic crossings and equals:

$$N_p = \frac{4L^*}{S_B} \tag{9}$$

The long range tune spread per IP is:

$$\delta\nu_{\rm LR} = \xi \cdot \frac{3N_p a^2}{2n^4} \tag{10}$$

where a is the betatron oscillation amplitude in units of σ_x. It is seen that long range interactions are more complicated and are dependent upon many parameters, in particular, on the crossing angle n. As a matter of fact, the introduction of a crossing angle is mainly for the purpose of reducing long range beam-beam effects.

In order to control the slow diffusion, it is required to keep the total tune spread (head-on + long range + non-linear magnetic field effects) within a "tune budget," which is usually about 0.02. The working point is so chosen such that all the resonances below the 10th order can be avoided when the total tune spread is kept within this budget. There are several such regions on the tune diagram near the diagonal that one can choose from. It is interesting that different machines seem to have different preferences. For example, the Tevatron chooses a tune near 0.415, the former SSC near 0.285, and the S$p\bar{p}$S near 0.31 (which is also likely to be the choice for the LHC).

The linear tune shift can be compensated by retuning the quadrupoles. Alternate crossing planes at $90°$ relative to each other (*e.g.,* alternate horizontal and vertical crossings, or $45°$ tilted crossing planes) can also effectively cancel the tune spread. But the Pacman effect makes it difficult, see Section 3.4 below.

3.2 Orbit distortion

Long range interactions will also cause orbit distortion:

$$\Delta x = \frac{8\pi\xi N_p}{n} \tag{11}$$

Therefore, fine steering is desired near the IP's for orbit corrections. But again, the Pacman effect further complicates the corrections (see 3.4).

3.3 Coherent effects

Both head-on and long range interactions can produce coherent beam-beam effects. The rigid dipole modes (π-mode and σ-mode) and higher order multipole modes can be studied by theoretical modelling and by computer simulations. The results are usually expressed in terms of the stability boundary in the (ξ, ν_β) space for checking if there would be enough room for the working area during normal machine operations.

3.4 Pacman effects

In a collider, the bunch train contains several injection gaps and an abort gap. Bunches that in the interaction regions are circulating past gaps of missing bunches in the counter-circulating beam are called the Pacman bunches. Such bunches will suffer anomalous tune shifts and orbit displacements different from the "average" bunches circulating relative to a locally fully filled beam. Therefore if the machine is optimized for average bunches the Pacman bunches will not be in an optimized environment and may suffer enhanced losses. However, loss of a Pacman bunch will create new Pacman bunches in the counter-circulating beam, and over the course of time holes will develop in both beams and eventually the beams may be destroyed. When the IPs are symmetrically placed with separations of half the ring circumference, a circulating bunch encounters the identical pattern of counter-circulating bunches at each IP. For this special case the Pacman effects at the paired IPs are related and the IPs can be configured to cancel or minimize the Pacman anomalies. Irrespective of the phase advance between the IPs, the anomalous tune shift is cancellable by crossing planes at 90° relative to each other at the two IPs. However, the anomalous orbit shifts can at best be minimized by a "best" choice of phase separations between the IPs, namely, separated in phase by half the phase advance around the ring. Ref. [4] shows that the orbit distortion at the two IPs, A and B, is:

$$|\Delta x_A| \text{ and/or } |\Delta x_B| \geq \frac{1}{2}\Delta x \tag{12}$$

For the symmetric case one has:

$$|\Delta x_A| = |\Delta x_B| = \frac{1}{2}\Delta x \tag{13}$$

Thus the symmetric case represents the optimum configuration.

At the LHC using a β^* of 50 cm, an emittance of 5×10^{-8} cm-rad, a θ of 200 μrad, a $\Delta\nu_{\rm HO}$ of 0.0034 per IP, and N_p equal to 9 (for the so-called run away Pacman effect), the orbit displacement in the symmetric case is 0.06 σ_x or 1 μm for a beam with a σ_x of 16 μm. Such an orbit displacement is very small and will contribute minimally to instability.

3.5 Dynamic aperture

The dynamic aperture during collisions is mainly determined by the beam-beam interactions as well as by the multipole errors of the low-β quads in the interaction regions. Among other factors, it has a strong dependence on the crossing angle. On the one hand, larger crossing means less long range beam-beam interactions. Thus, the dynamic aperture limited by beam-beam would become bigger. On the other hand, however, the dynamic aperture limited by the low-β quads would be smaller because of poor field qualities when beams move further away from the magnet axis. Therefore, when the crossing angle increases, the dynamic aperture would at first increase (which is the beam-beam dominated region); after reaching a maximum value, it would decrease (which is the field error dominated region). Numerical studies by long term tracking for the LHC have confirmed this prediction. [5]

Table 1. Comparison of Machine Parameters

Machine	DORIS I	HERA	SSC	LHC
ξ	0.01	0.0006	0.0009	0.0034
ν_s	0.03	0.01	0.0012	0.0021
$\theta\sigma_s/\sigma_x$	0.7	4	0.45	0.48

This study is important because it plays a big role in the requirement of the low-β quad aperture. If the aperture is too small, one will not be able to open up the crossing angle to the preferred size. As a consequence, the dynamic aperture could be severely limited by the beam-beam effects. Use the LHC as an example. Its low-β quad aperture is 70 mm. The design value of the crossing angle is 200 μrad. [3] But tracking studies show that, in order to have a dynamic aperture of 7-8 σ_x, the crossing angle needs to be increased to about 300 μrad. [5] This lead to a new space budget of the quad aperture and a re-design of the shielding inside the quads for making a larger crossing possible.

3.6 Synchro-betatron resonance

The crossing angle may excite synchro-betatron resonances. There are three key parameters that will determine the strength of these resonances, namely, the beam-beam parameter ξ, the synchrotron tune ν_s, and the normalized crossing angle $\theta\sigma_s/\sigma_x$. Table 1 is a comparison of these parameters in four machines: the DORIS I, the HERA, the SSC and the LHC (of which $\theta = 200$ μrad is used). The synchro-betatron resonance was a major concern of the two DESY machines. However, it is seen from the table that this effect should not be as critical in the SSC or the LHC. For example, based on Piwinski's theory [6], simulations were done for the SSC and showed that, with $\theta = 150$ μrad, only the satellites of the resonances up to the order of six could be harmful to the beams. Between these resonances there was enough space for the working area. [7]

4 DISCUSSIONS

The strong beam-beam interactions give rise to particle losses and emittance growth. These interactions and other effects (*e.g.,* intrabeam scattering, synchrotron radiation, residual gas scattering, beam collimation and external excitations) lead to the evolution of machine luminosity, which can readily be calculated. [8]

The electromagnetic beam-beam interactions have been studied in the past four decades. One has achieved relatively good understanding of the effects on the tune shift, orbit distortion, dynamic aperture and synchro-betatron resonances by means of the weak-strong or weak-weak model. However, less successful is the strong-strong model, which is more complicated and is a real challenge in the investigations. Because it is one of the main causes of the formation of the beam halo, it certainly deserves more attention in the future study of the near beam physics.

5 REFERENCES

[1] SSC Conceptual Design, SSC-SR-2020 (March 1986).

[2] SSC Site-Specific Conceptual Design, SSCL-SR-1056 (July 1990).

[3] LHC Conceptual Design (Yellowbook), CERN/AC/95-05 (October 1995).

[4] D. Ritson and W. Chou, "Minimizing the Pacman Effect on the Closed Orbit," submitted to *Particle Accelerators*, also see FERMILAB-TM-2029 (1997).

[5] W. Chou and D. Ritson, CERN LHC Project Report 123 (1997); also see FERMILAB-Conf-97/195 (1997).

[6] A. Piwinski, IEEE Trans. on Nucl. Sci. NS-24, 1408 (1977).

[7] W. Chou and A. Piwinski, Proc. B Factory Workshop, SLAC, April 6-10, 1992, SLAC-400, p.134 (November 1992).

[8] W. Chou, S. Dutt, T. Garavaglia and S. Kauffmann, Proc. 1993 Particle Accelerator Conference, Washington, D.C., May 17-21, 1993, p. 3609.

Glossary

N	Total number of particles in a beam
t	Time
$\mathcal{L}$	Luminosity
$\sigma_{\rm inel}$	Inelastic cross section
$\sigma_{\rm el}$	Elastic cross section
$\sigma_{\rm T}$	Total cross section
ϵ	RMS transverse emittance
$N_{\rm B}$	Number of protons per bunch
f_0	Revolution frequency
σ_α	RMS pp elastic scattering angle in CMS
h	Planck's constant
c	Speed of light
$E_{\rm c.m.}$	Energy in the center of mass system
$\epsilon_{\rm N}$	Normalized RMS transverse emittance
$r_{\rm p}$	Classical proton radius
γ	Relativistic factor
β^*	β-function at the interaction point
ξ	Beam-beam (Amman-Ritson) parameter)
θ	Full crossing angle in unit radian
n	Full crossing angle in units of $\sigma_{x'}$
a	Betatron oscillation amplitude in units of σ_x
$R_{\rm re}$	Luminosity reduction factor due to crossing
L^*	Effective interaction distance
$S_{\rm B}$	Bunch spacing
ν_β	Betatron tune
ν_s	Synchrotron tune
σ_x	RMS beam transverse spatial size
$\sigma_{x'}$	RMS beam transverse angular size
σ_s	RMS bunch length
$\Delta\nu_{\rm HO}$	Head-on beam-beam tune shift
$\Delta\nu_{\rm LR}$	Long range beam-beam tune shift
$\delta\nu_{\rm LR}$	Long range beam-beam tune spread
N_p	Number of parasitic crossings
Δx	Orbit distortion in units of σ_x

Long-Term Stability in Hadron Colliders with Tune Modulation

W. Scandale[1]
CERN, LHC Division, CH-1211 Geneva, Switzerland

E. Todesco
Department of Physics, Via Irnerio 46, 40126 Bologna, Italy

Abstract

The single-particle betatron motion is analysed in hadron colliders dominated by field-shape imperfections, like the CERN-LHC with injection optics. The aim is to evaluate the effect of tune ripple and momentum deviation on long-term stability. An empirical formula with three free parameters is proposed to interpolate the dynamic aperture versus the stability time. The dynamic aperture turns out to decay with a power of the inverse logarithm of the stability time. Tracking data fit well with the empirical formula, and extrapolation by at least one order of magnitudes in the stability time is shown to be reliable.

1 INTRODUCTION

In this paper we present some recent results [1] about the study of long-time stability of single-particle motion in hadron colliders. For planned machines such as the LHC [2], the beam is expected to make $10^7 - 10^8$ revolutions at injection before energy ramping, and during this time the nonlinearities due to the imperfections of the magnets can provoke slow particle losses and diffusion [1, 3, 4, 5]. The estimate of the relevance of these phenomena can be hardly carried out using brute-force tracking, even with the aid of modern supercomputers, and therefore alternative approaches should be worked out. Several studies have been carried out by accelerator physicists [6, 7, 8, 9, 10, 11, 12, 13, 14]. Indeed, diffusion due to a cocktail of nonlinearities and tune modulation is observed in several fields of physics, and relevant contributions have been given by many authors (see for instance [15, 16, 17]).

In Refs. [1, 4] we have proposed an empirical approach to the problem of long-term stability, based on the idea of survival plots [6, 7, 18]. In these diagrams, one plots the stability time versus the initial amplitude, in order to find out a trend for the long-term stability. Indeed, due to the intricate structure of the phase space close to the dynamic aperture, these plots are far from being regular. The crucial point is to replace a single amplitude with an average over several amplitudes, taken with different ratios between the linear invariants [19]. Using this procedure, the irregularities of the phase space disappear, and the dynamic aperture turns out to be a rather smooth function of the stability time, that can be well interpolated using the following empirical formula [1]

$$D(N) = A + \frac{B}{\log^{\kappa} N}. \tag{1}$$

The above formula implies that, if $A > 0$ and $\kappa > 0$, the phase space is divided into two parts: one inner region inside A, that according to the extrapolation is stable for infinite times, and an outer region whose emptying rate is proportional to the power of the logarithm of the stability time. In this outer region, even though approximate invariants could still be defined with some precision, the integrable structure of the phase space is destroyed, and one is left with a wide chaotic band. These two regions correspond to the thin layer diffusion and to the thick layer diffusion respectively, according to the terminology used in Ref. [16]. When $A < 0$ or $\kappa < 0$ the first region disappears, and all the phase space is a wide chaotic band whose particles will escape sooner or later.

This kind of scenario has been originally described for a 4D Hènon mapping [4] with linear frequencies close to resonances 5 and 6; this simple model has allowed a deep numerical investigation of the phenomenology of long-time losses. The case of a modulated Hènon map has also been considered, showing that the same formula holds, the contribution of the modulation being essentially a reduction of the exponent κ [see Eq. (1)]. Following the same approach, analogous simulations have been carried out for a realistic LHC model, finding out very similar behaviours. In this paper we show the data of the modulated Hènon map, and of the LHC with different momentum deviations and modulational amplitudes. It turns out that the effect of the modulation and of the momentum deviation are rather similar, being analogous to the case of the modulated Hènon map.

The above method allows one to extrapolate the empirical formula (1) to predict long-term stability with a limited set of tracking data. We show that, in the modulated Hènon mapping, using tracking data up to 10^5 turns it is possible to predict up to 10^7 turns within 5% of relative error. This extrapolation method is currently used at CERN for the LHC simulations [20].

This approach lacks a theoretical justification of the empirical formula (1). In the case without modulation, the formula can be interpreted through the Nekhoroshev theorem [21], but this argument does not hold for the modulated case. It would be desirable to have a theoretical framework to justify the empirical formula and the associated scenario that has been worked out through the analysis of tracking data.

The plan of the paper is the following. In Section 2 we discuss the analysed models. Section 3 is devoted to the dynamic aperture definition. In Section 4 we present the numerical data.

[1] e–mail: Walter.Scandale@cern.ch

2 MODELS

2.1 Modulated Hénon map

The modulated 4D Hénon map reads

$$\begin{pmatrix} x^{(n+1)} \\ p_x^{(n+1)} \\ y^{(n+1)} \\ p_y^{(n+1)} \end{pmatrix} = \mathbf{L} \begin{pmatrix} x^{(n)} \\ p_x^{(n)} + [x^{(n)}]^2 - [y^{(n)}]^2 \\ y^{(n)} \\ p_y^{(n)} - 2x^{(n)}y^{(n)} \end{pmatrix} \qquad (2)$$

where (x, p_x, y, p_y) are the phase space coordinates, and the linear part of the map **L** is the direct product of two two-dimensional rotations whose linear frequencies $\omega_x^{(n)}$, $\omega_y^{(n)}$ are slowly varying with the discrete time n according to

$$\omega_i^{(n)} = \omega_{i0}\left(1 + \epsilon \sum_{k=1}^{m} \epsilon_k \cos(\Omega_k n)\right) \qquad i = x, y \qquad (3)$$

We considered one main frequency $\Omega_1 = 2\pi/868.12$, $\epsilon_1 = 10^{-4}$, and six harmonics with relative amplitudes ranging from 0.7 to 0.07. These data correspond to the tune modulation due to the observed ripple in the quadrupoles of the SPS, see Ref. [1] for more details. The linear frequencies ω_{x0} and ω_{y0} are fixed to 0.168 and 0.201 in order to have relevant long-term phenomena. We analyse the dependence of the dynamic aperture on the amplitude ϵ of the modulation, that has been varied between 1 and 64.

2.2 LHC lattice

The lattice of the LHC used in this study is Version 4.3 described in Ref. [1, 22]. It includes field-shape errors (both systematic and random), the set of multipolar correctors, and of chromaticity correctors. Linear imperfections that induce finite closed orbit or linear coupling are disregarded. To take into account the operational difficulty of the chromatic correction in a real machine, we set $Q' = 2$.

The numerical results refer to particles tracked with different initial momentum deviation $\Delta p/p$, that ranges from 0.0001 to 0.00075. A momentum deviation of 0.0001 gives rise to a tune oscillation of $2 \cdot 10^{-4}$ amplitude at the synchrotron frequency.

The tune modulation is obtained by summing up seven sine-waves with the same relative amplitudes and frequencies as those used for the Hènon map. The global amplitude is varied by a multiplicative factor ϵ that ranges from 1 to 8.

3 DYNAMIC APERTURE DEFINITION

In a previous work [19] we have proposed a definition of dynamic aperture as a function of the number of turns N as the first amplitude where particle loss occurs before N turns, averaged over the phase space. Particles are started along a 2D polar grid in the coordinate space (x, y):

$$x = r\cos\theta \qquad y = r\sin\theta \qquad (4)$$

and the initial momenta p_x p_y are set to zero. Let $r(\theta; N)$ be the last stable initial condition along θ before the first loss at a turn number lower than N occurs. Then the dynamic aperture is defined as

$$D(N) = \left(\int_0^{\pi/2} [r(\theta; N)]^4 \sin 2\theta d\theta\right)^{1/4}. \qquad (5)$$

With respect to the approach used in several long-term simulations (see for instance [6, 18, 23]), where a fixed value of θ is considered in order to speed up simulations, this definition provides a smoother dependence of D on N, thus allowing to derive interpolating formulae and to extrapolate them to predict long-term particle loss. For the above formula one can estimate the associated error, that depends on the grid steps used to scan along r and θ. More details can be found in Ref. [1].

4 NUMERICAL DATA

4.1 Modulated Hènon map

We considered 100 steps in the initial conditions for 30 different angles θ [see Eq. (5)]; each initial condition was iterated for 10^7 turns. The dynamic aperture as a function of the stability time N was computed using Eq. (5). In Figures 1–5 we show the DA with the associated error (bars), and the interpolation through Eq. (1) (solid line). When $A > 0$ and $\kappa > 0$, the asymptotic value of the dynamic aperture A is shown (dashed line). We considered the model without modulation (Figure 1) and the modulated case with increasing values of the amplitude ϵ (see Eq. (3)). The fitting values of the parameters and the associated errors are shown in Table 1. The estimate of the errors of the fitting parameters is worked out through standard methods of numerical analysis, even though some care is needed since the fitting function is nonlinear in the exponent κ (see Ref. [1] for more details). We used a confidence level of 95%. One can make the following observations.

- The χ^2 of the fit is always around one: this implies that the data well fit with Eq. (1). A slight deterioration of the fit is observed for the largest modulational amplitude $\epsilon = 64$.
- The errors associated to the fitting parameters are rather large. Nevertheless, one can observe that the exponent κ decreases with increasing modulational amplitudes. Moreover, the parameter B weakly depends on ϵ for small ϵ.
- For small ϵ the extrapolation of the formula (1) predicts a hard core of particle stable for infinite times (i.e. $\kappa > 0$ and $A > 0$). When ϵ reaches a certain limit, all the phase space becomes unstable: this is in qualitative agreement with experiments on existing machines.
- The extrapolation value of the dynamic aperture A at infinity is rather well defined for very small modulational amplitudes ($\epsilon = 0, 1$), but becomes very loose

when the amplitude increases ($\epsilon = 4$). In these cases the prediction for infinite times becomes questionable, and only an extrapolation over finite time (a few orders of magnitude) seems reliable.

Using the tracking data up to 10^5 and up to 10^6 turns we extrapolated the dynamic aperture up to 10^7 turns. The comparison with tracking at 10^7 turns is given in Table 2. The extrapolation is always in agreement with tracking within the errors. Extrapolation from 10^5 to 10^7 allows a dynamic aperture prediction within 5% of relative error.

4.2 LHC lattice

For the LHC model described in section 2.2 we carried out simulations with 100 steps and 17 angles, up to 10^6 turns. Beside the purely four-dimensional case (coasting beam), we also considered several off momentum energies $\Delta p/p$ from 0.0001 to 0.00075. Tracking data and the fitting function are shown in Figures 6–10. Moreover, we fixed the momentum deviation to 0.0001 and we switched on the tune modulation with increasing amplitudes $\epsilon = 1, 2, 4, 8$. Tracking data and the fitting function are shown in Figures 11–14. The fitting parameters κ, A, B, and the χ^2 are shown in Table 3. It turns out that the situation is rather analogous to the case of the modulated Hènon mapping.

- The fit is rather good in all cases: the χ^2 is of the order of one. A deterioration of the fit is observed for large momentum deviations.
- The exponent κ decreases with the increasing modulational amplitude and with the momentum deviation.
- Extrapolation at infinity of the DA is well defined only for the four-dimensional case.
- The parameter B seems to be independent of ϵ and $\Delta p/p$ for small ϵ and $\Delta p/p$ (see $\epsilon = 0$, $\Delta p/p = 0.0001$, and $\epsilon = 1$, $\Delta p/p = 0.0001$).

We compared the extrapolation of the DA from 10^5 to 10^6 with actual tracking at 10^6: the results (see Table 4) are in agreement and the error is within 5%. Unfortunately it was not possible to compare the extrapolation of 10^5 to 10^7 with actual tracking, since it is too onerous.

5 ACKNOWLEDGEMENTS

We wish to acknowledge G. Turchetti for useful discussions and M. Giovannozzi for very relevant contributions.

6 REFERENCES

[1] M. Giovannozzi, W. Scandale, E. Todesco, *Phys. Rev. E* , (1998) in press.

[2] The LHC Study Group, *CERN* **95-05** (1995).

[3] F. Schmidt, F. Willeke and F. Zimmermann, *Part. Accel.* **35**, (1991) 249–256.

[4] M. Giovannozzi, W. Scandale, E. Todesco, *Part. Accel.* **56**, (1997) 195–225.

[5] W. Fischer, M. Giovannozzi, F. Schmidt, *Phys. Rev. E* **55**, (1997) 3507–20.

[6] Y. Yan, *SSC* **500** (1991).

[7] A. Chao, *AIP Conf. Proc.* **230**, (1990) 203.

[8] D. Brandt et al., in *EPAC 90*, edited by P. Marin and P. Mandrillon (Edition Frontières, Gif sur Yvette, 1991) pp. 1438.

[9] T. Chen et al., *Phys. Rev. Lett.* **68**, (1992) 33–6.

[10] Y. Wang et al., *Phys. Rev. E* **49**, (1994) 5697–5705.

[11] O. S. Brüning, *Part. Accel.* **41**, (1993) 133–51.

[12] A. Gerasimov, *CERN-SL (AP)* **92–30** (1992).

[13] R. L. Warnock and R. D. Ruth, *Physica D* **56**, (1992) 188.

[14] F. Schmidt, *LHC Project Note* **30** (1996).

[15] B. V. Chirikov, *Phys. Rep.* **52-5**, (1979) 263–379.

[16] B. V. Chirikov, M. A. Lieberman, D. L. Shepelyansky, F. M. Vivaldi, *Physica D* **14**, (1985) 289–304.

[17] A. I. Neishtadt, *Sov. J. Plasma Phys.* **12**, (1986) 568–73.

[18] F. Galluccio and F. Schmidt, in *Third European Particle Accelerator Conference*, edited by H. Henke (Edition Frontiéres, Gif sur Yvette, 1993) pp. 640–642.

[19] E. Todesco, M. Giovannozzi, *Phys. Rev. E* **53**, (1996) 4067.

[20] M. Böge and F. Schmidt, in *Beam stability and nonlinear dynamics*, edited by Z. Parsa (AIP, New York, 1997).

[21] G. Turchetti, private communication.

[22] W. Scandale et al., in *PAC 95*, (IEEE, Piscataway, 1995) pp. 2844–46.

[23] Z. Guo., T. Risselada, W. Scandale, *AIP Conf. Proc.* **255**, (1992) 50–65.

Table 1. Interpolation parameters for the Hènon map

ϵ	κ	A	B	χ^2
0	$1.4^{+0.5}_{-0.5}$	$0.43^{+0.03}_{-0.06}$	$0.6^{+0.3}_{-0.1}$	1.5
1	$1.2^{+0.5}_{-0.5}$	$0.40^{+0.04}_{-0.09}$	$0.6^{+0.2}_{-0.1}$	1.7
4	$0.6^{+0.5}_{-0.4}$	$0.24^{+0.13}_{-0.56}$	$0.6^{+0.5}_{-0.0}$	2.3
16	$0.1^{+0.4}_{-0.5}$	-1.5	2.3	0.9
64	$-0.5^{+0.4}_{-0.3}$	$1.0^{+2.0}_{-0.2}$	$-0.3^{+0.2}_{-2.0}$	3.7

Table 2. Comparison of extrapolated dynamic aperture and tracking for the modulated Hénon map

ϵ	Extrapolation from 10^5 to 10^7	Extrapolation from 10^6 to 10^7	Tracking at 10^7
0	$0.46^{+0.02}_{-0.03}$	$0.47^{+0.02}_{-0.02}$	$0.47^{+0.01}_{-0.01}$
1	$0.46^{+0.02}_{-0.02}$	$0.46^{+0.01}_{-0.01}$	$0.46^{+0.01}_{-0.01}$
4	$0.45^{+0.02}_{-0.03}$	$0.45^{+0.01}_{-0.02}$	$0.44^{+0.01}_{-0.01}$
16	$0.41^{+0.03}_{-0.05}$	$0.41^{+0.02}_{-0.01}$	$0.40^{+0.01}_{-0.01}$
64	$0.37^{+0.03}_{-0.04}$	$0.36^{+0.02}_{-0.02}$	$0.33^{+0.01}_{-0.01}$

Table 3. Interpolation parameters for the LHC

ϵ	$\Delta p/p \cdot 10^5$	κ	A	B	χ^2
0	0	$1.9^{+1.1}_{-1.2}$	$12.0^{+0.3}_{-1.7}$	9^{+9}_{-3}	0.4
0	10	$0.8^{+1.0}_{-1.1}$	9.6	8	1.0
0	30	$-0.4^{+0.6}_{-0.6}$	20	-4	1.8
0	50	$-0.3^{+0.5}_{-0.5}$	23	-7	3.8
0	75	$-0.3^{+0.4}_{-0.4}$	24	-9	3.8
1	10	$0.3^{+0.9}_{-1.0}$	3.4	13	1.4
2	10	$-0.1^{+0.9}_{-0.8}$	42	-26	2.0
4	10	$-0.1^{+0.8}_{-0.7}$	47	-30	1.0
8	10	$-0.2^{+0.5}_{-0.5}$	33	-16	1.3

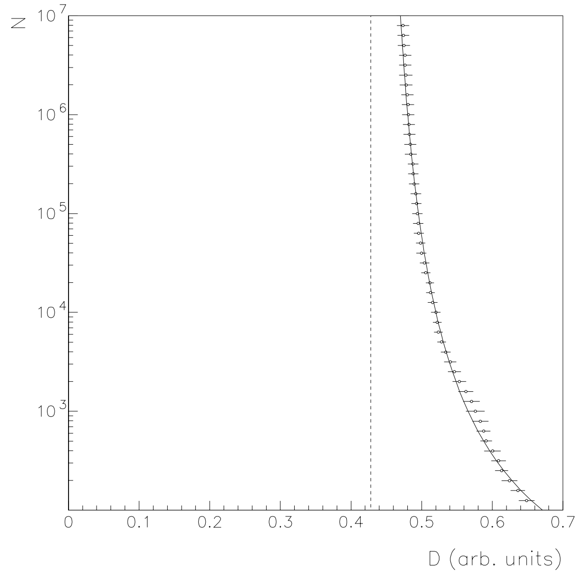

Figure 1: Interpolation of dynamic aperture data (bars) with empirical formula (solid line) for the Hènon map without modulation.

Table 4. Comparison of extrapolated dynamic aperture and tracking for the LHC

ϵ	$\Delta p/p \cdot 10^5$	Extrapolation from 10^5 to 10^6	Tracking at 10^6
0	0	$12.3^{+0.1}_{-0.4}$	$12.3^{+0.2}_{-0.2}$
0	10	$11.7^{+0.2}_{-0.4}$	$11.5^{+0.2}_{-0.2}$
0	30	$10.7^{+0.3}_{-0.5}$	$10.6^{+0.2}_{-0.2}$
0	50	$9.8^{+0.4}_{-0.4}$	$10.3^{+0.2}_{-0.2}$
0	75	$9.3^{+0.3}_{-0.5}$	$9.6^{+0.2}_{-0.2}$
1	10	$11.4^{+0.4}_{-0.4}$	$11.1^{+0.2}_{-0.2}$
2	10	$11.1^{+0.5}_{-0.5}$	$10.7^{+0.2}_{-0.2}$
4	10	$10.6^{+0.5}_{-0.5}$	$10.4^{+0.2}_{-0.2}$
8	10	$10.0^{+0.5}_{-0.7}$	$10.1^{+0.2}_{-0.2}$

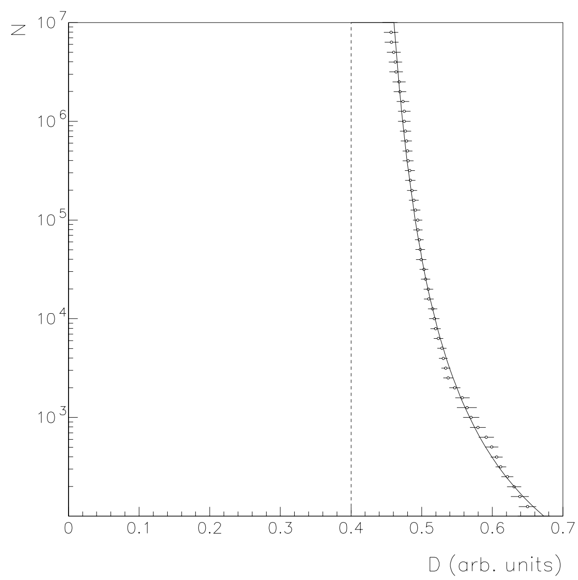

Figure 2: Interpolation of dynamic aperture data (bars) with empirical formula (solid line) for the modulated Hènon map with $\epsilon = 1$.

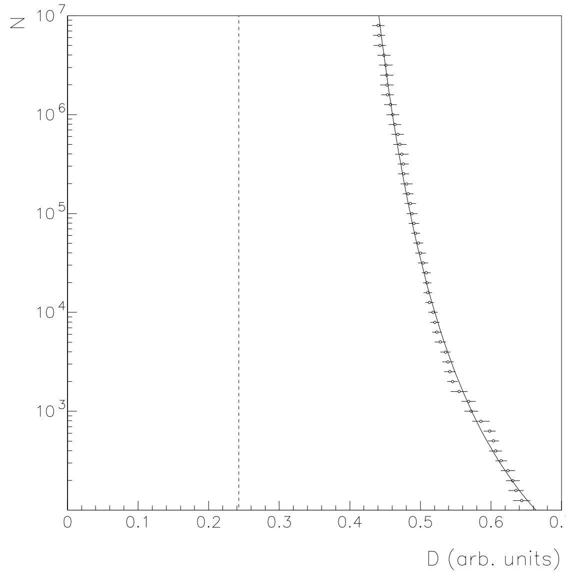

Figure 3: Interpolation of dynamic aperture data (bars) with empirical formula (solid line) for the modulated Hènon map with $\epsilon = 4$.

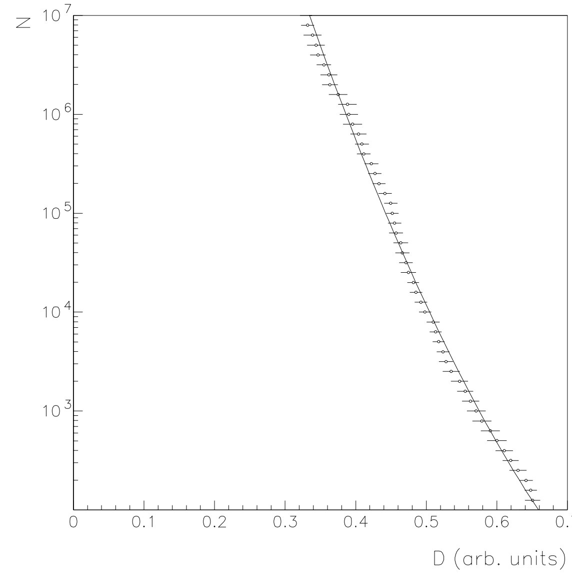

Figure 5: Interpolation of dynamic aperture data (bars) with empirical formula (solid line) for the modulated Hènon map with $\epsilon = 64$.

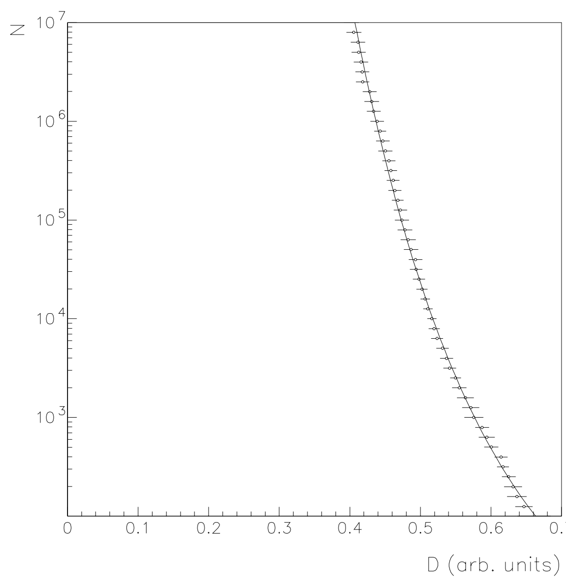

Figure 4: Interpolation of dynamic aperture data (bars) with empirical formula (solid line) for the modulated Hènon map with $\epsilon = 16$.

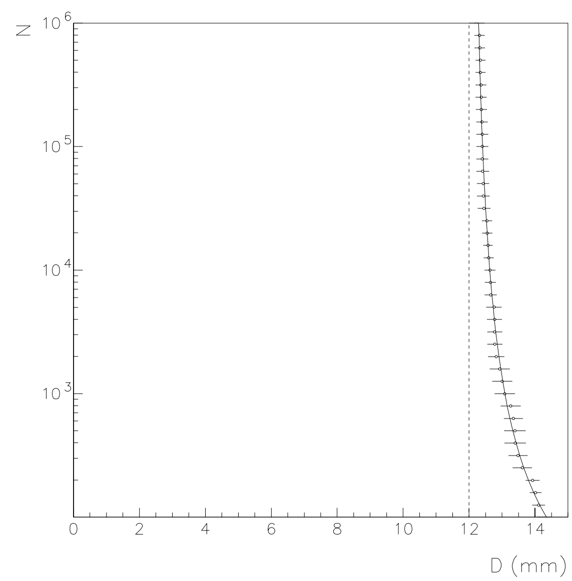

Figure 6: Interpolation of dynamic aperture data (bars) with empirical formula (solid line) for the LHC without off-energy and without modulation.

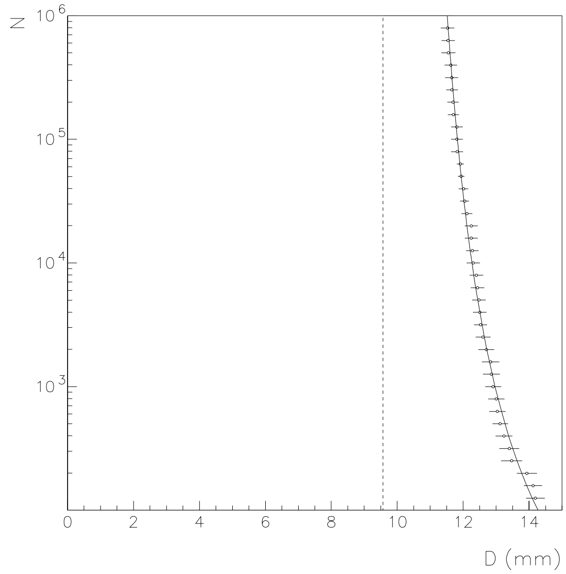

Figure 7: Interpolation of dynamic aperture data (bars) with empirical formula (solid line) for the LHC with $\Delta p/p = 0.0001$ and without modulation.

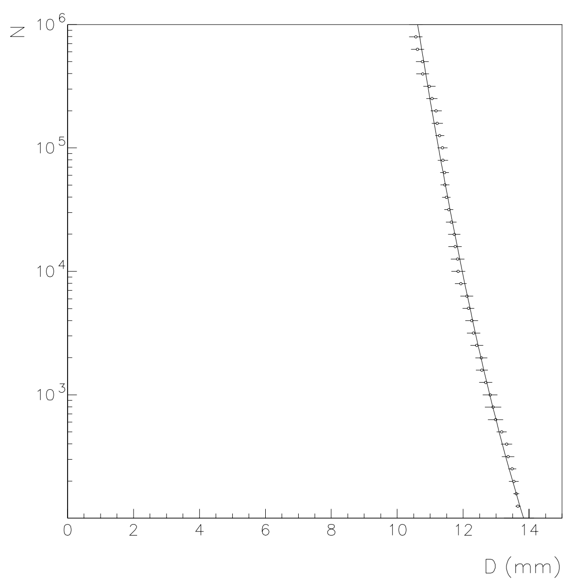

Figure 8: Interpolation of dynamic aperture data (bars) with empirical formula (solid line) for the LHC with $\Delta p/p = 0.0003$ and without modulation.

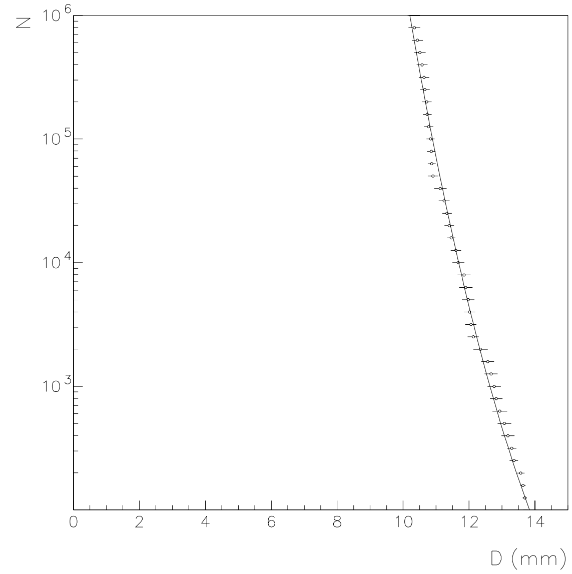

Figure 9: Interpolation of dynamic aperture data (bars) with empirical formula (solid line) for the LHC with $\Delta p/p = 0.0005$ and without modulation.

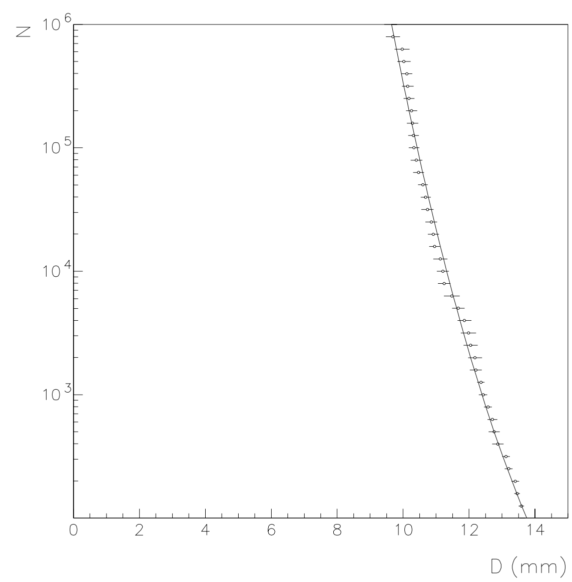

Figure 10: Interpolation of dynamic aperture data (bars) with empirical formula (solid line) for the LHC with $\Delta p/p = 0.00075$ and without modulation.

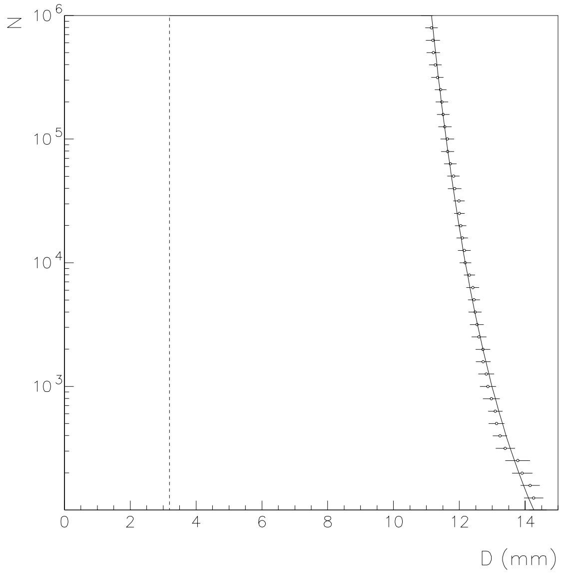

Figure 11: Interpolation of dynamic aperture data (bars) with empirical formula (solid line) for the LHC with $\Delta p/p = 0.0001$ and with modulation $\epsilon = 1$.

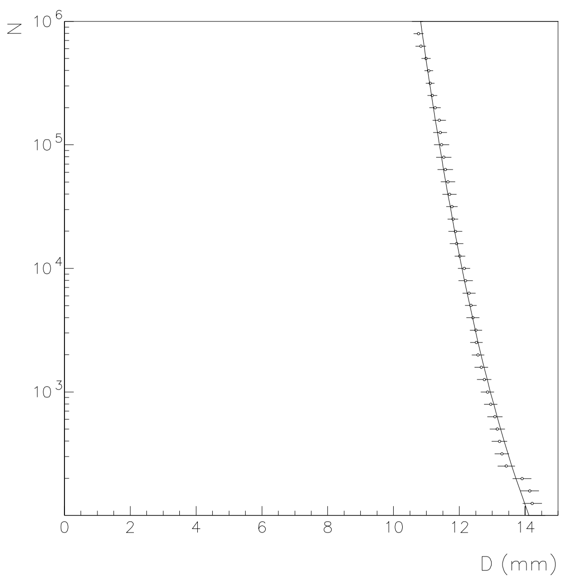

Figure 12: Interpolation of dynamic aperture data (bars) with empirical formula (solid line) for the LHC with $\Delta p/p = 0.0001$ and with modulation $\epsilon = 2$.

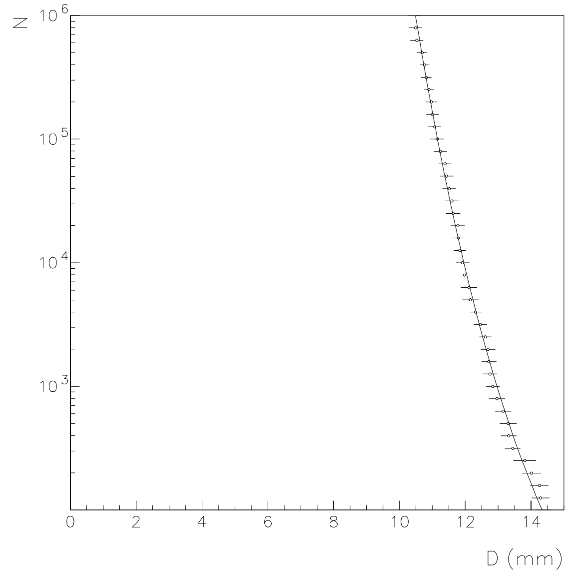

Figure 13: Interpolation of dynamic aperture data (bars) with empirical formula (solid line) for the LHC with $\Delta p/p 0.0001$ and with modulation $\epsilon = 4$.

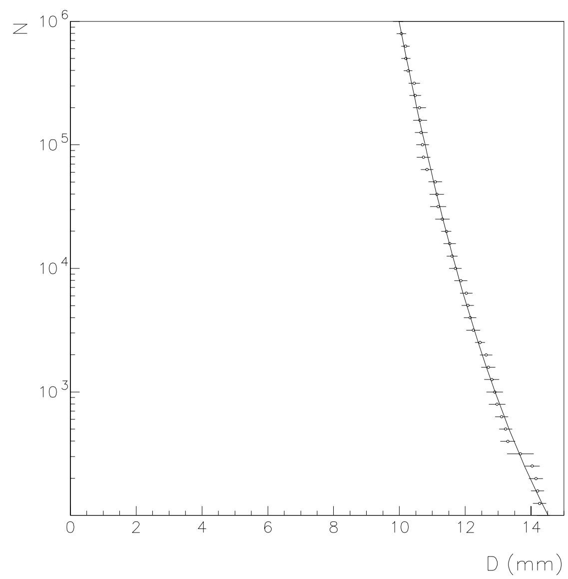

Figure 14: Interpolation of dynamic aperture data (bars) with empirical formula (solid line) for the LHC with $\Delta p/p = 0.0001$ and with modulation $\epsilon = 8$.

III. BEAM COLLIMATION

Proton Collimation in TeV Colliders

N. Catalan Lasheras, G. Ferioli, J.B. Jeanneret, R. Jung, T. Trenkler[1]
CERN, SL Division
D. Kaltchev
TRIUMF, Vancouver

1 INTRODUCTION

In high intensity proton colliders with superconducting magnets, quenches induced by beam losses are unavoidable in the absence of a collimation system. We will show that a single stage collimator system cannot suffice at TeV energies. We discuss a two-stage collimation system first as an optical system then considering true scattering in collimator jaws, giving some emphasis to the LHC project. Finally, we present the preliminary measurements done at 120 GeV/c in the SPS ring with a simplified three stage collimation system.

2 PROTON LOSSES AND QUENCH LEVELS

Proton losses can be divided in three basic classes, namely injection, ramping losses and steady losses in collision. In all these cases and in the absence of a collimation system the losses might be concentrated near one location which is the aperture limitation of the ring. The following numerical values are related to the nominal LHC parameters. The effective longitudinal spreading at the loss point is strongly dependent of the local parameters, but can be as low as $\Delta L \approx 10$ m, computed with the average betatronic angle at the effective local vacuum chamber radius.

An injected batch has $N_p = 2.4\,10^{13}$ protons and is 6 μs long. The ratio between actual and tolerable losses is

$$r = \frac{f N_p}{\Delta n_q \Delta L} = 240 \tag{1}$$

with $f = 0.1$ a somewhat arbitrary fraction of the batch lost immediatly and $\Delta n_q = 10^9$ pm^{-1} the quench level for fast losses (see below Section 2.1 and Table 2).

At ramping, RF-untrapped protons are not accelerated and migrate slowly towards the vacuum chamber. The flash of losses lasts $\Delta t \approx 0.1$s, i.e. more than the time needed to make use of the helium trapped in the cable, allowing $\Delta n_q = 2.5\,10^{10}$ pm^{-1} (see below Section 2.1 and Table 2). The full stored intensity is $N_p = 3\,10^{14}$ protons. With again $f = 0.1$ we obtain using (1) $r = 125$.

In collision, the halo is fed by elastic scattering in $7+7$ TeV collisions, at a rate of $\dot{n}_{el} \approx 10^9$ ps^{-1} for two experiments with $\mathcal{L} = 10^{34}$cm^{-2}s^{-1} and $\sigma_{el} = 40$ mbarn . The scattered protons are emitted at an angle close to the beam divergence at the crossing point [1] and slowly enlarge the transverse beam tail. Losses associated to transverse diffusion related to machine imperfections are estimated

[1]Formerly CERN–SL Division, now at Siemens-Matsushita OHG, Deutschlandsberg, Austria

Table 1: Maximum density of energy deposited in the coil magnet by a proton impacting the vacuum chamber at the betatronic angle (see text).

p [Tev/c]	ε_{max} [J cm^{-3}]	L_{eff} [m]	ε_{dist} [Jm cm^{-3}]
.45	$1.4\,10^{-11}$	1.0	$1.4\,10^{-11}$
7	$9.2\,10^{-10}$	0.7	$6.5\,10^{-10}$

from SPS collider experience. With a lifetime of $\tau_{beam} \approx$ 50 hours the losses would be $\dot{n}_{beam} = N_p/\tau_{beam} \approx 2\,10^9$ ps^{-1}, for a total $\dot{N}_{loss} = \dot{n}_{beam} + \dot{n}_{el} \approx 3\,10^9$ ps^{-1}. The steady quench level will be $\dot{n}_q \approx 8\,10^6$ pm^{-1}s^{-1} (see below Section 2.2 and Table 3). In this case $r = \dot{N}_{loss}/(\dot{n}_q \Delta L) = 30$, without taking into account large fluctuations of the losses associated to short term instabilities of the beam halo.

In all three cases, the factor r is much larger than the allowed value $r = 1$. The sole good way to lower r is to use collimators which both absorb protons or dilute in phase and amplitude those one that are scattered back into the aperture of the ring.

2.1 Transient quench levels

This section summarises the content of the report [2]. The transient quench level of a magnet is quantified basically by the amout of energy per unit volume ΔQ which is needed to raise the temperature of the coil above its critical value T_q. To compute the number of protons lost locally which induce a quench, the average shower (hadronic and electromagnetic) developped by a proton impacting the vacuum chamber near the coil of the magnet was simulated with the CASIM code [3]. This allows to compute the maximum density of the energy release ε_{max} by the shower in the coil. In practice, apart from a few pathological cases, the proton losses are spread over distances longer than the effective length of the showers $L_{eff} \sim 1$ m. Therefore, instead of ε_{max}, the quantity $\varepsilon_{dist} = \varepsilon_{max} L_{eff}$ is used. Numerical values are given in Table 1.

The number of protons Δn_q which must be lost locally to induce a quench is

$$\Delta n_q = \frac{\Delta Q}{\varepsilon_{dist}} \tag{2}$$

where Δn_q has the units protons m^{-1}. For a given T_q, the heat reserve is the integral of the specific heat between the bath of helium $T_o \approx 1.9K$ and T_q with $T_q \approx 9$K at injection beam energy and $T_q \approx 2.8K$ at top beam energy.

The heat reserve $\Delta Q(T_q)$ depends also on the duration of the transient loss. The cable of the coil is made of wires closely packed in an insulator, through which the helium flows too slowly to contribute in the case of transient losses (see next section). On the other hand, the heat reserve of the helium trapped between the wires contributes but the heat transfer is limited by the film of bubbles which develops at the interface of the two media above a critical value. The

Table 2: Heat reserve and allowed transient losses of protons at injection momentum (upper part) and top momentum (lower part) in LHC, see text. First two lines, metallic contribution only. Third line with trapped helium included. The uncertainty on these values is about $\pm 50\%$.

Δt [ms]	ΔQ [J]	ε_{dist} [Jm/cm^{-3}]	Δn_q [pm^{-1}]
< 3	$4\ 10^{-2}$	$3.8\ 10^{-11}$	10^9
6	$4\ 10^{-2}$	$1.4\ 10^{-11}$	$3\ 10^9$
> 50	$35\ 10^{-2}$	$1.4\ 10^{-11}$	$2.5\ 10^{10}$
Δt [ms]	ΔQ [J]	ε_{dist} [Jm/cm^{-3}]	Δn_q [pm^{-1}]
< 1	$8\ 10^{-4}$	$1.3\ 10^{-9}$	$6\ 10^5$
3	$8\ 10^{-4}$	$6.5\ 10^{-10}$	$1.2\ 10^6$
> 10	$3\ 10^{-2}$	$6.5\ 10^{-10}$	$4.6\ 10^7$

Table 3: Allowed steady losses of protons (see text). The uncertainty on these values is about $\pm 50\%$.

p [Tev/c]	W_q [W]	ε_{dist} [Jm/cm^{-3}]	$\dot{n}_q$ [p(ms)$^{-1}$]
.45	10^{-2}	$1.4\ 10^{-11}$	$7\ 10^8$
7	$5\ 10^{-3}$	$6.5\ 10^{-10}$	$8\ 10^6$

critical volumetric transfer of power is estimated to $\phi_V = 8$ Wcm^{-3} at injection and $\phi_V = 4$ Wcm^{-3} at 7 TeV. The critical time scale to allow the use of the trapped helium is thus $\Delta t = \Delta Q(T_q)/\phi_V$. The contribution of the helium to $\Delta Q(T_q)$ is integrated numerically using experimental data [4].

At shorter time scale, the sole metallic part of the cable contributes to $\Delta Q(T_q)$. In spite of some modifications related to the superconducting state of the NbTi, the specific heat of the wires is dominated by the cubic dependence on T of the Debye theory. The contribution of the metal to $\Delta Q(T_q)$ is therefore small at 7 TeV when compared to the one of the helium, even if the last one occupies only five per cent of the volume of the cable.

At a further smaller time scale $\delta t \sim$ 2ms, below the temperature decay time across the section of the cable, ε_{dist} must be multiplied by a factor 2-3, to take into account the radial variation of the energy deposition inside the cable $\varepsilon_{dist}(r)$. Above that critical value, the average radial value can be used.

Δn_q as computed with (2) for the three different time scales discussed is given in Table 2. Linear interpolation can be used between the caracteristic time scales, keeping in mind that all values are certainly not more precise than a factor two.

2.2 Steady quench levels

The steady power which can be evacuated by the coils while staying below the critical temperature is related to the electrical insulation of the cables. The heat is evacuated off the cables by the exchange of helium through this insulator. The allowed flux of energy per unit volume of cables given in Table 3 are the result of a compromise between the electrical resistivity and the porosity of the insulator. These values are measured on sample coils. The allowed steady rate of protons is given by $\dot{n}_q = W_q/\varepsilon_{dist}$.

The comparison of the allowed transient losses $\Delta Q = 8\ 10^{-4}$ J at the time scale $\Delta t = 3\ 10^{-3}$s (top energy, table 2) with the amount of energy removed by steady conduction during the same time $\delta Q_{cond} = W_q \Delta t = 1.5\ 10^{-5}$ J, indicates that close to their upper limit transient losses rely only on local heat reserve.

3 A SINGLE COLLIMATOR AND TRANSVERSE DIFFUSION OF THE HALO

To be efficient, a primary collimator must be placed inside the short term dynamic aperture (short term meaning here < 1000 turns). In the LHC it will be at a normalised transverse depth of $n_1 = x/\sigma_x \sim 6$. In this range of amplitudes, the transverse drift speed v_d of the halo cannot be predicted either precisely or reliably. At the CERN antiproton-proton collider, in collision somewhat below the beam-beam limit, an experiment indicated $v_d \approx 3\ \sigma$/s at $n_1 = 6$ [5]. LHC tracking data without ripple at injection energy indicate $v_d < 0.05\ \sigma$/s [6]. For given v_d, a distribution of impact parameter, parametrised by a range Δb is obtained by a simple multiturn tracking. Some values are given in Table 5. The computed Δb must be compared to the critical impact parameter b_c, beyond which an impacting proton is more likely to be absorbed instead of being scattered out of the jaw by multiple coulomb scattering or nuclear elastic scattering (this last process being ignored in the rest of this section). The computation of b_c is made in section 3.2. By comparing Δb to b_c in Table 5, we can conclude that in LHC, at least at injection we will be in a regime of strong outscattering.

3.1 Side escape by multiple coulomb scattering

Multiple coulomb scattering is described by the Moliere theory, which is a formalism of diffusion applied to a large number of small successive transverse kicks applied to a charged particle passing through matter [7]. The number of scatterers per millimeter is very high. Both the angular distribution, with the polar angle θ, $dN/d\theta_{mcs}(s)$ and the spatial transverse one $dN/d\Delta_{mcs}(s)$ of the protons around the original axis of flight are gaussian up to ~ 3 standard deviations. The dependence on a given monoatomic material is contained mostly in the radiation length L_R (see Table 4). The standard deviations of $dN/d\theta_{mcs}(s)$ and $dN/d\Delta_{mcs}(s)$ are (with units m and TeV/c)

$$\theta^o_{mcs}(s) = \frac{13.6\ 10^{-6}}{p}\left(\frac{s}{L_R}\right)^{1/2}$$
$$\text{and}\ \ \Delta^o_{mcs}(s) = \frac{7.8\ 10^{-6}}{p}\left(\frac{s^3}{L_R}\right)^{1/2}. \qquad (3)$$

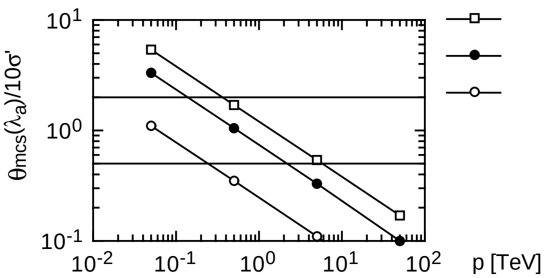

Figure 1: The m.c.s angle after one absorption length, normalised to an effective machine aperture of 10 r.m.s beam units for different materials. The two lines delimit the momentum range in which the outscattering density is high in the aperture of the ring.

Table 5: An estimator of the impact parameter range Δb of the proton in LHC computed with $v_d = 1\ \sigma$/s, at the normalised transverse distance from the beam axis $n_1 = 6$, compared to the critical impact parameter b_c below which outscattering by the collimator edge is important.

p [TeV/c]	Δb [μm]	b_c [μm]
.45	4	12
7	1	0.7

Disregarding edge escape, the proton flux is attenuated exponentially along the collimator by nuclear absorption, with the absorbtion length $\lambda_{abs}(Z)$ (see Table 4). The angular distribution of the protons escaping a collimator can therefore be estimated using (3) with $s = \lambda_{abs}(Z)$. This quantity, normalised to an effective machine aperture of $10\sigma'$, where σ' is the r.m.s beam divergence at the collimator location, is plotted in Figure 1 for different materials. Two cases are favourable for collimation . At low momentum ($p < 100$ GeV), and using a heavy target, the scattered protons are spread much beyond the the aperture. Most of them are lost nearby the collimator and the rest is strongly diluted in the aperture area. At high energy ($p > 10$ TeV), by using a light target, the scattered protons stay well inside the aperture. They will do many turns and finally be absorbed by the collimator which is their sole obstacle at small amplitude. In the intermediate momentum range (the case of LHC), a high intensity cannot be cleaned by a single collimator, if the beam loss rate is high in the sense of Section 2.

3.2 Critical impact parameter

The critical impact parameter b_c is computed by using (3) with again $s = \lambda_{abs}(Z)$. The quantity $\lambda_{red}(Z) = (\lambda_{abs}^3/L_R)^{1/2}$ is given in Figure 2 for several materials. Interestingly, the metals of interest for collimation (good heat conductivity and good vacuum properties) all have a similar λ_{red}, with no visible dependence on Z. Thus, the critical impact parameter is approximately metal-independent and

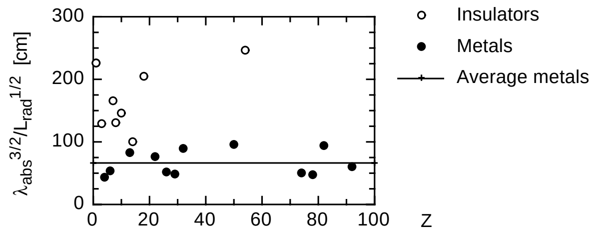

Figure 2: The reduced length λ_{red} as a function of the atomic number Z. For metals (black dots), λ_{red} is nearly constant with an mean value $\lambda_{red} = 0.66$ m and a relative variance $\sigma(\lambda_{red})/\lambda_{red} = 0.3$.

equal to (with units μm and TeV).

$$b_c = 5.2/p\,. \tag{4}$$

3.3 Secondary collimator material

The wide angular range of protons scattered off the primary collimator implies a somewhat uniform distribution of impacts on the secondary collimators . Provided they are long enough ($\sim 5\lambda_{abs}$), tertiary particles will be mostly issued from a surface layer of thickness b_c. The Z-indepence of b_c therefore allows to choose freely the material of the secondary collimators . Other parameters will be considered (physical length and radiation length, thermal conductivity, resistance to shock waves for exemple).

3.4 Secondary collimators needed

At Tev energies, the outscattering rate off a primary collimator is close to unity. The use of a two-stage collimation system is therefore mandatory.

4 OPTICS AND COLLIMATION

The material discussed here is fully developped in [8],[9] and [10], to which the reader can to refer for more details and full demonstrations. In this section we do not consider true scattering in collimators , which is introduced in Section 6. We only do optics and geometry in the four dimensional phase space . We consider the primary collimators as pure isotropic scatterers and secondary collimators as black absorbers. Our criterion to define an optimal two-stage collimation system is to minimise the surface occupied by the secondary halo in the plane of the normalised amplitude $A_X - A_Y$, or the largest distance to the origin of this same surface as it is delimited by the secondary collimators .

4.1 Numerical exemple

To illustrate numerically some results and to help comparing different systems with each other, we will use some identical basic parameters in further sections. The jaws of the primary collimators will always be retracted by $n_1 = 6$ normalised transverse r.m.s. beam radius and the jaws of

Table 4: The nuclear absoption and the radiation lengths in metric units for some Z-values. Cross-sections are valid in the few hundred GeV range. σ_{dd} at 450 GeV/c. λ_{abs} and L_R in [cm]. All cross-sections in [mbarn]. b_{pN} in $[\mathrm{GeV}^{-2}\mathrm{c}^2]$.

Element	Z	A	λ_{abs}	L_R	σ_{abs}	$\sigma_{pN,el}$	n_{pp}	$\sigma_{pn,el}$	σ_d	b_{pN}
H	1	1	720	865	33	-	-	7	3.4	12.0
Be	4	9	40	35	200	70	3.2	22.4	11	75
Al	13	27	39	8.9	420	210	4.7	32.7	16	120
Cu	29	63.5	15	1.4	780	450	6.2	43.4	21	220
W	74	207	9.6	0.35	1650	1120	9.2	64.4	31	450

the secondary collimators always by $n_2 = 7$. All other quantities will be deduced from these two numbers. These numbers are presently a kind of canonical set used for LHC collimation studies. They can of course be changed to any other value for another application.

4.2 Normalised coordinates

The phase coordinates (z, z') of the two transverse directions are normalised at each point along the ring with

$$\mathbf{Z} = \begin{pmatrix} Z \\ Z' \end{pmatrix} = \frac{1}{\sigma_z} \begin{pmatrix} 1 & 0 \\ \alpha_z & \beta_z \end{pmatrix} \begin{pmatrix} z \\ z' \end{pmatrix} \tag{5}$$

z standing here for either the x or y direction, s being the longitudinal coordinate, $\alpha(s)$ and $\beta(s)$ the Twiss functions and $\sigma = (\epsilon\beta(s))^{1/2}$ the transverse r.m.s beam size. The transfer matrix M_{12} transporting a particle from s_1 to s_2 in the normalised coordinates (Z, Z') is then simply the rotation

$$M(\mu) = \begin{pmatrix} \cos\mu & \sin\mu \\ -\sin\mu & \cos\mu \end{pmatrix} \tag{6}$$

with μ being the betatronic phase advance between $s1$ and $s2$. The betatronic motion is thus reduced to a harmonic motion, where the betatronic phase advance plays the role of the time, or of the longitudinal coordinate s. In the normalised phase space, the invariant amplitude of a particle in one transverse direction (or 2D-phase space) is $A = (Z^2 + Z'^2)^{1/2}$. The 4D-amplitude is $A = (A_x^2 + A_y^2)^{1/2}$.

4.3 One dimensional betatronic collimation

The proton which drifts slowly outwards touches the collimator when being very close to its maximum spatial extension $\mathbf{Z_o} = (n_1, 0)$ (Figure 3). By scattering in the collimator it gets an angular kick $Z' = K_z$, distributing uniformly the protons along the line $\mathbf{Z_1} = (n_1, K_z)$. The sole free parameter to choose the location of a secondary collimator is the phase advance μ between the primary collimator and the secondary collimator. The minimisation of the secondary halo amplitude is done by cutting the line $Z = n_1$ with a secondary collimator at the phase advance [8]

$$\cos\mu_{opt} = \pm\frac{n_1}{n_2}. \tag{7}$$

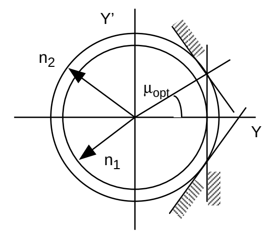

Figure 3: One dimensional betatronic collimation. A particle is scattered close to its maximum transverse position $Z = n_1$. If it is not absorbed, it is scattered along the vertical line $Z = n_1$. If a secondary collimator is at the depth n_2, the shortest cut along this line is made with a secondary collimator at the phase advance μ_{opt}.

The maximum secondary amplitude escaping the two-stage collimation system is the absolute possible minimum $A_{cut}^{min} = n_2$ which is equal to the secondary collimator aperture. This is obtained by transporting $\mathbf{Z}_1$ at μ_{opt}, or $\mathbf{Z}_2 = M(\mu_{opt})\mathbf{Z}_1$. Then, using (7) it follows $Z_2 = n_1^2/n_2 + (1 - n_1^2/n_2^2)^{1/2}K_z$. Cutting at $Z_2 = n_2$ finally gives $K_{cut} = K_z = (n_2^2 - n_1^2)^{1/2}$ and $A = (Z_1^2 + K_{cut}^2)^{1/2} = n_2$. The two signs in (7) corresponds to cutting each of the two half lines $Z = n_1$, $Z' > 0$ and $Z' < 0$.

4.4 Two dimensional betatronic collimation in $X - Z$ symmetric optics

The particular optics which has the property $\mu_x(s) = \mu_y(s)$ (or equivalently $\beta_x(s) = \beta_y(s)$) was studied because a soft symmetric low-β insertion, which has this property, was envisaged for a time for the cleaning system of LHC [11]. Later, it appeared that this particular case is the sole one which we have been able to treat analytically. We use it here to show that a two dimensional collimation system is not a simple extension of the one dimensional case discussed above.

The closest extension of the one dimensional system in two dimensions is the use of circular collimators (circular in normalised coordinates, approximated for exemple by eight jaws in a real case), with a radial aperture n_1 for the primary collimator and n_2 for the secondary collimators. To simplify the present discussion, we consider only the impact point on the primary collimator at $(X, Y) = (n_1, 0)$.

The treatment of the other azimuth is done in [8]. The non trivial difference with a one dimensional system appears at the impact point in the primary collimator where scattering populates every azimuthal direction in the $X' - Y'$ plane.

Let us write the coordinates of the proton before scattering

$$\mathbf{A_o} = (X, X', Y, Y') = (\mathbf{X}, \mathbf{Y}) = (n_1, 0, 0, 0) \quad (8)$$

We limit our discussion to two extreme cases, which we call parallel and orthogonal scattering. Parallel means scattering in the plane of the original betatronic oscillation, i.e. $(X', Y') = (k_x, 0)$ in our case of azimuth. Orthogonal scattering is when $(X', Y') = (0, k_y)$.

Parallel scattering leaves intact the Y-amplitude, i.e. $A_y = 0$ before and after scattering . The problem is therefore reduced to the one dimensional case and is solved by installing two circular collimators at $\cos\mu_{opt} = \pm\frac{n_1}{n_2}$.

The coordinates of the proton after orthogonal scattering are

$$\mathbf{A_1} = (\mathbf{X_1}, \mathbf{Y_1}) = (n_1, 0, 0, k_y) \text{ with } k_y \epsilon [-\infty, \infty]. \quad (9)$$

In the abscence of coupling, there is no way to cut on the X-amplitude $A_X = n_1$ which is smaller then the secondary collimator aperture n_2. To cut efficiently on the Z-amplitude, we must place an additional secondary collimator where the angle is entirely converted to amplitude, i.e. at phase advance $\mu = \pi/2$ from the primary collimator . $\mathbf{A_1}$ transforms to

$$\mathbf{A_2} = (M(\pi/2)\mathbf{X_1}, M(\pi/2)\mathbf{Y_1}) = (0, -n_1, k_y, 0) \quad (10)$$

The secondary collimator cuts on Y at $k_z \leq n_2$. The largest vector leaving that collimator is then

$$\mathbf{A_2} = (n_1, 0, n_2, 0) \text{ with } A_2 = (n_1^2 + n_2^2)^{1/2}. \quad (11)$$

A_2 is the largest combined amplitude passing the secondary collimators and occurs in the case of orthogonal scattering. The intermediate cases between parallel and orthogonal scattering are cut in amplitude at values in the range $A \epsilon [n_2, A_2]$ [8]. The limits are identical at other $X - Y$ azimuths. With our numerical set, the secondary halo extends up to $A_2 = 9.2$.

The important result is that, at least in the kind of optics used in this section, with optimal secondary collimator locations, the cut in amplitude is done at a value somewhat larger than the secondary collimator aperture. We will see that this result remains true in any kind of optics, if the cleaning section is of reasonably finite length.

Other optics

FODO optics of different phase advance per cell were explored, by fitting the circular collimator locations with numerical methods [8]. The result, expressed by the largest secondary amplitudes was always less performant than the symmetric low-beta section discussed here above.

Rectangular collimators

If the number of collimators is an issue or conversely, if the geometrical aperture of the ring is large enough, rectangular collimators (X and Z jaws only) can be used. The degradation of the performance in amplitude cut relative to cicular collimators is $\sim 20\%$ [8].

5 LOCATING COLLIMATORS IN ARBITRARY OPTICS. THE LHC CLEANING INSERTION.

The general case of finding the best solution of primary and secondary collimator locations in an arbitrary optics requires a numerical approach. The DJ code [9],[10] allows to locate both in longitudinal position and $X-Z$ azimuth an arbitrarily large number of jaws (here and below, jaw stands for a pair of transversely opposite jaws). It is found more efficient at the same hardware cost to abandon the use of circular collimators , anyway approximatted by eight flat jaws, and to let the location and the azimuth of every jaw free in the fit. The number of free parameters is therefore $N_{par} = 2N + 3 = 27$ for the equivalent of three circular collimators $(3 \cdot 8)$ and three primary jaws, the last ones being kept horizontal,vertical and skewed at $45°$. The function to be minimised can be the radius A_{max} of the smallest circle surrounding the geometrical edge of the secondary halo. A_{max} is not a smooth function and classical minimum finding methods often fail to find a good solution. The simulated annealing method [12] is used instead. This algorithm always find several good solutions, allowing to choose one which does not create hardware conflicts.

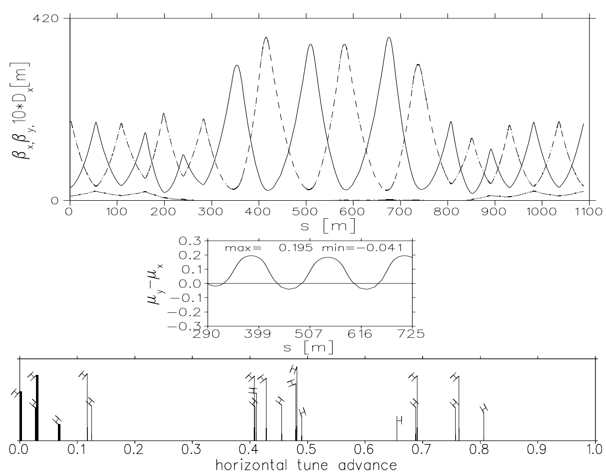

Figure 4: IR7 lattice and tune-split functions for LHC version 5.0, with the IR7 quadrupoles tuned for high positive tune split, giving $A_{max} = 8.45\sigma$. The range of tune advance (in 2π units) corresponds to the range $s \ \epsilon \ [290, 725]$.

Several FODO like optics were tried for LHC, with different phase modulation $\mu_z - \mu_x$. The better result $A_{max} = 8.4$ is obtained for the largest achievable $(\mu_z - \mu_x)$ in an insertion which has a total phase advance $\mu_x \approx \mu_z \approx 2\pi$ (see Figure 4). Our interpretation of the result is that a large phase modulation allows to catch more of the 'orthogonally' scattered protons (Section 4.4). On this point, see also [13]. The absolute value of A_{max} is quite good and anyway better then the optimum reached with the symmetric insertion of Section 4.4.

6 SCATTERING AND COLLIMATION EFFICIENCY

The approach used in section 4 and 5 which allows to fit collimator locations in a given optic and to choose between different optics do not allow to compute the efficiency of a system. True scattering in matter in both primary and secondary collimators is needed. The complexity of a two-stage collimation system implies to use numerical methods. Even the simple case of scattering near the edge of a block of matter cannot be treated analytically. In this section, we discuss only elastic interactions. Inelastic interactions are discussed in Section 8.

Elastic scattering must be coupled to multiturn tracking in the ring. Elastic scattering near the edge of a media was treated exhaustively for the first time, to our knowledge, by Andy van Ginneken [14]. Our own code K2 [15] was inspired by his ELSIM program. The K2 code is made of a scattering module, does tracking between collimators in a beam line section described with the MAD format, does an amplitude analysis and closes a turn if the particle was not absorbed. To ensure an approximately realistic distribution of impacts on the primary collimator, the proton is circulated inside the primary aperture using linear motion superimposed with a variable transverse drift speed until it touches a collimator. We gave some emphasis to fast algorithms, to allow for the large statistics needed to compute high collimation efficiencies.

Halo drift

Halo protons become unstable through transient resonant states or experience chaotic motion. The detailed mechanism of losses might depend strongly on operational conditions of the machine. An average case is used for collimator studies. We use a smooth variable transverse drift speed v_d. We verified that the calculated collimation efficiency do not vary strongly over a quit large range v_d with a two-stage collimation system, while it is obviously not the case with a single stage system.

Tracking in collimator

While in Section 3 we considered multiple coulomb scattering to show the importance of edge scattering, nuclear scattering of protons on both nuclei and the nucleons inside the nuclei is of similar importance. This is shown by computing a weighted ratio of average scattering angles (mcs and elastic scattering on individual nucleons, and using the data of Table 4) in a Cu target as

$$r = \frac{\theta_{pp,elastic}}{\theta_{mcs}(1\lambda_{abs})} \frac{\sigma_{pp}^{Cu}}{\sigma_{inel}^{Cu}} = 0.5 \qquad (12)$$

We only briefly describe how we parametrise nuclear elastic processes. In this report, the soft momentum dependence of some parameters is neither shown or discussed. This will be the object of a more exhausive document [16]. Nuclear elastic processes can to a very good degree of precision be described by an optical model. The incident wave diffracts on a grey object of density decreasing transversely with a Gaussian law. The angular distribution of the distribution is the Fourier transform of the density of the target, i.e. it is also Gaussian. Its standard deviation $\sigma(\theta)$ is related to the effective radius R_{eff} of the proton-target compound. The Lorentz invariant $t = (p\theta)^2$ is usually used and the angular distribution is written

$$\frac{d\sigma}{dt} = \sigma_{el} b e^{-bt}. \qquad (13)$$

The parameter b is related to R_{eff} with

$$R_{eff} \approx 0.4 b^{1/2} \quad [\mathrm{fermi}, (\mathrm{Gev/c^2})^2] \qquad (14)$$

and σ_{el} is the elastic cross-section .

A proton can scatter both on nuclei (noted N) and on nucleons (noted n) inside the nucleus. Proton and neutrons are treated identically. In addition to elastic scattering , the incident proton do diffractive dissociation on nucleons.

Proton-nucleon elastic scattering

Proton-nucleon (pn) elastic scattering has been much studied [17],[18]. For our purpose, the approximate differential cross-section (13) is adequately precise, accounting for most of the cross-section . From data at 20 Gev/c [19] and at 175 Gev [20], we deduce that pp elastic scattering is not visibly modified when occuring inside a nucleus. In particuliar, no trace of double elastic scattering is observed. The equivalent number of free scatterers, as measured by [19] can be modelled with a simple geometrical model, considering that only the nucleons located near the equator in a plane perpendicular to the incoming proton contributes to the cross-section . The dependence of the cross-section on the atomic mass A is fixed by adjusting the thickness of the contributing layer. We get a number of indivual scatterers per nucleus

$$n_{pn} = 1.56 A^{1/3}. \qquad (15)$$

The pn elastic cross-section is then $\sigma_{pn}(A) = n_{pn}\sigma_{pp,el}$. In the TeV range (LAB frame), $\sigma_{pp,el} \approx 8.5$ mb and $b \approx 13$ GeV^{-2}.

Single diffractive dissociation

The single diffractive dissociation process is close to elastic scattering but the excitation of one of the nucleons, to a mass M larger than the nucleon mass m_n is done at the expense of a relative momentum loss $\delta_p = -\Delta p/p$ of the nucleon staying intact. The case of the incident proton staying intact is of interest here. The other case is treated like an inelastic interaction (see Section 8). The variables δ_p and

M are related by (at low-order approximation)

$$\delta_p \approx \frac{M^2}{s} \approx \frac{M^2}{2m_n p} \tag{16}$$

with s the centre of mass energy squared and m_n the nucleon mass. The double differential cross-section can be approximated by [17]

$$\frac{d^2\sigma}{d\delta_p\, dt} = \frac{a_d\, b_d}{\delta_p} e^{-b_d t} \tag{17}$$

We use $b_d = (7/12) b_{pp,el}$, while $a_d \approx 0.7 mb$ [17]. The mass range is $M \epsilon [M_o, (0.15s)^{1/2}]$. We use the approximation $M_o \approx m_n \approx 1\ \mathrm{GeV/c^2}$. With (16), we compute a momentum range $\delta_p \epsilon [M_o/(2p), 0.15]$. The integral cross-section is $\sigma_{d,pn} = n_{pn} a_d \ln(0.15s) = n_{pn} a_d \ln(0.3p)$.

Proton-nucleus scattering

Total proton-nucleus (pN) cross-section are reported in [7]. They are almost constant in the few hundred GeV/c momentum range. Elastic pN (or coherent) cross-sections are found at the same source, while the differential elastic cross-section are found in [20] at 175 GeV/c. Some of these values are given in Table 4. Non measured values (W) are interpolated with $\mathrm{A}^{1/3}$ or $\mathrm{A}^{2/3}$ laws, which fit well the data [20], [16]. A slight momentum dependence is given to the data in Table 4. It is related to the pn scattering , which has a impact on the total cross-section . We consider that the coherent cross-section cannot rise significantly at high energy for the nucleus to be already a black absorber below 1 TeV/c. The formula (13) is adequate to describe the data, except for very heavy nuclei where secondary and tertiary diffraction peaks are visible in data [20]. This is explained by the blackness of the high-A nuclei up to their edge. But even for lead ($A = 82$), the relative integral of the second peak is only 5% of the elastic scattering cross-section , while the heaviest target to be considered in practice woud be tungsten ($A = 74$). Numerical values can be found in Table 4.

Algorithm for multiple coulomb scattering

In the neighbourhood of the edge of a collimator jaw, multiple coulomb scattering , which is a quasi continuous scattering process needs a special treatment. The obvious method of doing small steps is precise but time consuming. The complete m.c.s. formalism shows that using the correlation factor $\rho_{\theta\Delta} = \sqrt{3}/2$ between the angle and the transverse offset (both following Gaussian distributions of variances (3)), an arbitrarily large step can be made without biasing the result. The actual step is computed as the distance at which the transverse offset $\Delta = 4\Delta^o_{mcs}$ coincides with the edge of the jaw. This procedure, even if it requires to solve a 3rd-order equation at each step is very fast. When the impact parameter is large enough, the jaw is traversed in one step, if other interactions do not occur [16].

The large angle tail of Coulomb, or Rutherford, scattering is treated as a discrete interaction. The cross-section is the integral of the differential cross-section above $\theta \geq 4\theta^o_{mcs}$ [16].

Tracking from collimator to collimator

The protons are transported by standard linear transfer matrices [21]. Drift spaces, bending magnets and quadrupoles are considered. To allow the use of linear transfer matrix elements in the relative momentum deviation δ_p , a cut-off is made at $\delta_p < 1\%$. Those protons scattered beyond that momentum are treated like inelastic collisions (Section8).

Check of ring aperture and collimator efficiency

Doing an aperture control all along the ring is very time consuming. Step tracking and a detailed and coherent model of misalignments (magnetic and mechanic) and closed orbit defaults would be needed. While this kind of analysis is under work, up to now we checked the combined amplitude of the proton at the end of the cleaning section. Above a specified amplitude (in general close to the effective geometrical aperture of the ring), the proton is considered to have touched the vacuum chamber and the tracking is stopped. Below this cut-off amplitude, at each turn the amplitude is recorded in a so-called survival plot (see Section 7 and Figure 5 for an example), which gives the relative number of proton surviving a given amplitude F_s. Then, off-line, the betatronic phase-space plots are analysed. A lower limit of the longitudinal dilution of the losses is given by the approximative formula

$$F_d \approx 1/2\pi\beta \tag{18}$$

and by using for β the smallest of β_x and β_z near the aperture limitation. This formula is valid if the dilution in phase is almost homogeneous (checked with the phase-space plot). Then the efficiency of the system, for a given aperture limitation, is

$$\eta_{ring} = F_s(A_{ring})\ F_d \tag{19}$$

Closing a machine turn

A proton surviving the aperture control is transported in one step to the beginning of the cleaning section, with a linear transfer matrix. The sole non-linear effect introduced in K2 is some tune smearing of adjustable range. The actual tune is drawn randomly following a truncated Gaussian distribution at each turn.

7 USING K2 FOR LHC COLLIMATION

A preliminary calculation of the efficiency of the LHC cleaning insertion (see Section 5) was made with the K2 code. The primary collimators were made of 200 mm long Aluminium jaws while the secondary collimator jaw are made of Copper and 500 mm long. The survival plot at injection energy (Figure 5) indicate that the effective edge of the secondary halo is close to the amplitude $A_{sec} = 8$, a value slightly better than the geometrical edge computed

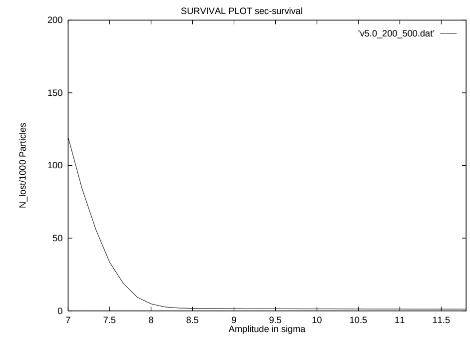

Figure 5: The survival plot in LHC at injection with the cleaning insertion described above, see text. In abscissa, the radial betatronic amplitude A_r. In ordinate, the function $F_s(A_r)$, normalised to 1000 events touching a primary colimator. See text.

Table 6: Expected efficiency of the betatronic cleaning insertion.

p [Tev/c]	F_s -	F_d [m^{-1}]	η [m^{-1}]	η_{DS} [m^{-1}]	m
.45	$2\,10^{-3}$	$5\,10^{-3}$	10^{-5}	10^{-5}	≈ 40
7	$4\,10^{-4}$	$5\,10^{-3}$	$2\,10^{-6}$	10^{-5}	≈ 330

by DJ (Section 5). The relative flux of protons F_s above $A_{sec} = 8.4$ is given in Table 6. The longitudinal dilution F_d of these protons along the ring is computed with (18) using $\beta = \beta_{min,arc} \approx 30$ m.

Efficiency margin in the ring

The margin factor m in Table 6 is either

$$m = \frac{\Delta n_q}{f N_p \eta} \text{ or } m = \frac{\dot{n}_q}{\dot{N}_{loss}\eta} \tag{20}$$

Comparing (20) to (1) indicates that an effective length of dilution of the halo after collimation can be defined by $L_{eff} = \eta^{-1}$.

Another efficiency factor , η_{DS}, is related to losses in the dispersion suppressor which is adjacent to the collimation system. Protons issued from diffraction dissociation and lower momentum particles (mostly neutrals ones) are swept out by the bending magnets and are lost locally. The effect is minimised by the presence of the warm bending magnets of the so-called dog-leg structure of the collimation insertion [23] but cannot be avoided completely. It limits locally the efficiency at top energy.

The margin factor is computed with the largest of η and η_{DS}.

An earlier simulation (LHC V4.2) was compared to a simulation with the STRUCT code [24]. Both calculations agree to better than a factor three for η.

The margins look comfortably large but high values are needed. It must be remembered that beam losses are partly of erratic nature. A spicky time structure can strongly lower the margin temporarily. The ring aperture is also dependent of the operation. Lowering the aperture of the ring by one normalised unit near A_{sec} drops the margin by nearly one order of magnitude.

7.1 Halo rates upstream of experiments

Residual halo rates near experiments are estimated by integrating the fraction of the protons which escape the cleaning area and are captured by the aperture limitation upstream or at an experiment. We consider first the case of a so-called Roman pot, i.e. an abrupt change of the pipe aperture made of two half-planes, separated by $\pm n_{pot}$ r.m.s beam sizes. Protons of amplitude $A = A_{ring} \approx 30$ must be inside a phase window $\Delta\mu = \pm\cos^{-1}(n_{pot}/A_{ring})$ to touch the pot. Protons of amplitude $A < n_{pot}$ never touch the pot. With an amplitude distribution $dN/dA \sim \; const$ above $A_{sec} \approx 10$ (see Section 7), it follows that out of the fraction F_s of the protons surviving the collimation system, the subfraction $F_{pot} = 0.5\Delta\mu/2\pi \approx 0.33$ touches the pot, with $n_{pot} \approx 15$. The overall rate with nominal LHC parameters shall therefore be (see Section 2)

$$\dot{n}_{pot} = F_{pot} F_s \dot{N}_{loss} = 3\,10^5 \text{ ps}^{-1} \, . \tag{21}$$

Near experiments installed in a low-beta insertions, both $\beta_x(s)$ and $\beta_z(s)$ grow to very large values. We can use $F_{low-beta} \approx 1$ and therefore (21) becomes $\dot{n}_{low-beta} \approx 10^6$ ps^{-1}. These rates are comparable to beam-gas losses at the same locations. Their impact in terms of muon backgrounds have been carefully computed [22].

8 INELASTIC INTERACTIONS IN DISPERSION SUPPRESSORS NEAR COLLISION POINTS

Downstream of collision points, most of secondary particles issued from inelastic interactions are lost in the adjacent triplet of quadrupoles and in the beam separation magnets [25], but the forward protons of diffractive dissociation will be lost where the dispersion grows, i.e. after entering the dispersion suppressor. Their impact can be estimated in a simple way. It is shown in [26] that in a section with a vacuum pipe of fixed radius, the rate of diffractive losses per unit length along the pipe is $\dot{n} = \mathcal{L}\, a_d\, D'/D$, with $\mathcal{L} = 10^{34}$ cm^{-2}s^{-1}, $a_d = 0.7$ mb, $D(s)$ the local dispersion and $D' = dD/ds$. In the high luminosity insertions of LHC, $(D'/D)_{max} \approx 0.07$ and therefore $\dot{n}_{max} = 5\,10^5$ m^{-1} s^{-1} . With a steady quench level at $\dot{n}_{max} = 8\,10^6$ m^{-1} s^{-1} , the margin factor is $m \approx 16$ and is reduced to $m \approx 6$ with the ultimate luminosity $\mathcal{L} = 2.5\,10^{34}$cm^{-2}s^{-1} . There is little chance for the luminosity to grow erratically above its design value. The margin factor is therefore adequate. A small degradation of the margin must be expected if magnet misalignments and closed orbit effects are taken into account.

9 EXPERIMENTAL WORK

In order to validate the K2 code an experiment was made in April 1997 at the SPS accelerator. A 120 GeV proton

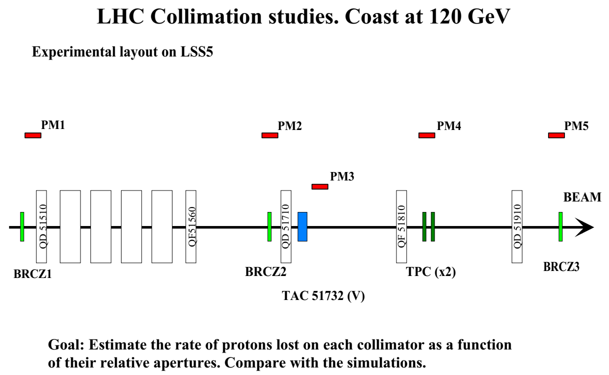

Figure 6: The experimental layout of the SPS collimation experiment at 120 GeV/c.

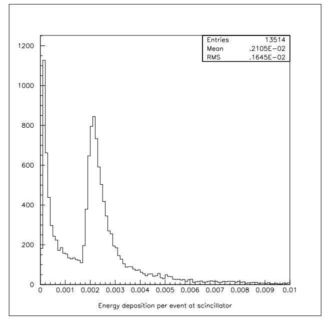

Figure 7: The analog spectrum in the scintillator as simulated with GEANT.

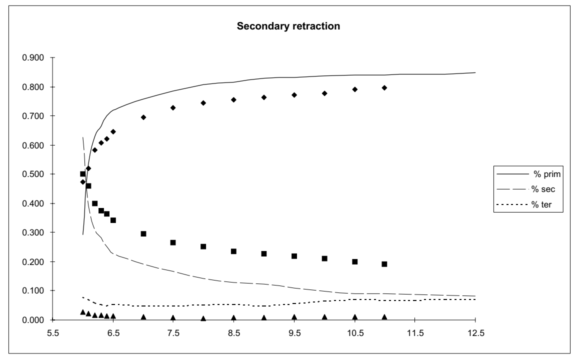

Figure 8: The raw relative rates measured at the collimators . Diamonds and upper curve : PRIM, squares and medium curve : SEC, triangles and lower curve : TER. Points are raw measurements (for some corrections see text). The curves are the result of multi-turn tracking and scattering in jaws made withe K2 code. The wavy structures on the curves are of statistical nature. The data analysis is preliminary.

beam was made to coast. Its intensity was $N_p \approx 10^{12}$p. The beam was debunched and made to slowly diffuse transversely by injecting some wideband noise in the kHz range through a damper. The noise level was adjusted to set the loss rate to $\dot{n}_{loss} \approx 5\ 10^8$ps^{-1}. Three horizontal collimators , called BRCZ1, 2 and 3 in Figure 6, were installed in a weakly radioactive straight section . They are made of two opposite 250 mm long Aluminium jaws. The phase advance between the collimators was $\mu_{1-2} = 90°$ and $\mu_{1-3} = 200°$. The length and the material were chosen to get collision rates of the same order of magnitude in the three collimators . A system aiming at highest efficiency (thicker secondary jaws) would have made the rate at the tertiary collimator too low for reasonable conditions of measurements. A vertical collimator , made of two $4\ \lambda_{abs}$ jaws (stainless steel), was installed at $\mu_{1-v} = 90°$ to keep under control the large amplitude scattered protons.

9.1 Detection of interactions

The most immediate observable which is proportional to the collision rate in a collimator is the rate of inelastic interactions. The detection of elastic collisions would require to install telescopes in the vacuum chamber and would be affected by a large background because of the thick target. Inelastic interactions, on the other hand develop a shower of which low energy particles escape at large angle.

A detailed simulation with the code GEANT [27] allowed to compute the energy deposition in scintillation counters (surface 35 cm^2, thickness 1 cm) placed near the collimators . To avoid the saturation of the photomultipliers, the counters were placed 90 cm above the beam line. The rate right above the collimator is small and grows with the distance when moving downstream. A broad maximum is reached at a distance of 65 cm downstream of the centre of the collimator . Installed at that location the counters are almost insensitive to a position error and the simulated yield is $Y_{pm} \approx 3\ 10^{-3}$, with a maximum rate in operation $\dot{n}_{pm} = Y_{pm}\dot{n}_{loss} \approx 3\ 10^5$counts s^{-1}.

One sample of the analog spectrum to be recorded at the counters is shown in Figure 7. Minimum ionising particles traversing the scintilator populate the second peak. Very low energy electrons and photons converted to photoelectrons populate the first peak. To best control the calibration a threshold for counting was fixed near the lower edge of the second peak. The counters were calibrated in a high energy tertiary muon beam of the SPS fixed target beams.

9.2 The measurements and their simulation.

The principle of the measurements is to set all the collimators at their respective transverse position n_i, measured in normalised units. We use the notation n_1 for the primary collimator (PRIM), n_2 for the secondary collimator (SEC), n_3 for the tertiray collimator (TER) and n_v for the vertical collimator (VERT). The nominal positions are $n_1 = 6$, $n_2 = 7, n_3 = 10$ and $n_v = 8$. At the horizontal collimators , $\Delta n_i = 1$ is equivalent to 0.8 mm. We recorded the rates of the four counters, varying n_2 (SEC retraction) by steps $\delta n = 0.5$ in the range $n \ \epsilon\ [6, 11]$.

The origin of the n_i scales is found by removing all the jaws except one. Then, its opposite jaw is pushed towards the beam by small steps, until a spike of losses indicates that

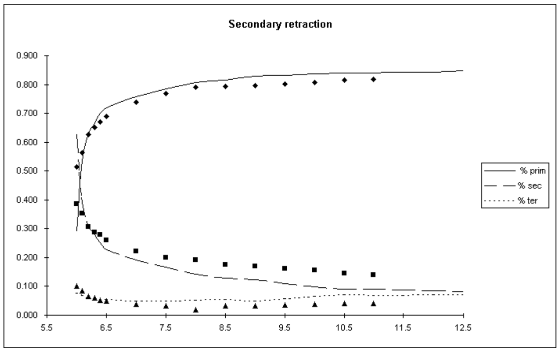

Figure 9: The adjuted relative rates measured at the collimators . The data are adjusted to the simulation (curves) by leaving free two parameters, see text. The data analysis is preliminary.

the mobile jaw is more inside the aperture than the fixed one. The losses are monitored and displayed continuously with a time integration of $\approx$ 10ms to allow this measurement. The procedure is repeated for all the collimators . The closed orbit (CO) at the collimator is the average of the two positions when the spike occurs. We estimate the CO error to $\sigma(n) \approx 0.5$.

The proportionality between the normalised an the real position is given by the computed beta functions, with an error likely to be smaller than 5%. The raw data are presented in Figure 8. We ran K2 for every set of n_i positions. Many small effects on the data are taken into account. A non exhaustive list includes the variation of the GEANT yields Y_{pm} with the distance between two opposite jaws or with the impact parameter distribution changing with different relative retractions. The absolute loss rate during the data acquisition time of one set of positions (≈ 10 s) cannot be measured with adequate precision. It would rely on the beam current transformer, which shall have a resolution of at least $\dot{I}/I \approx 10^{-4}$ to be useful. The data are therefore presented as fractions of unity. No relative factors between collimators were introduced, and only the data relative to the three BRCZ (which are identical) are compared. The agreement in both shape and amplitude of the data at the primary and the secondary collimators is quite good. The tertiary rate on the other hand is quite below the simulation.

To evaluate the importance of the discrepancy, we let a cross-calibration coefficient to vary between the three rates, to fit better to the K2 simulation. In Figure 9, the SEC data are multiplied by $f_{SEC} \approx 0.7$ and the TER data by $f_{TER} \approx 3$. More work is needed to determine if the discrepancy observed with the tertiary data is of experimental nature or related to the K2 algorithms (while we have a preference for the first hypothesis).

If the present results are not fully satisfactory from a physics point of view, on the other hand they are quite good in view of the design of a collimator system. The measured rates at the tertiary collimator being smaller than the predicted ones, the last ones shall be used to compute the expected efficiency of the collimator system

10 MOMENTUM COLLIMATION

Momentum collimation is not discussed here, but its need at LHC is established (see section 2). The formalism to design an insertion exists [8], and a case study is going on, using a updated version of the DJ code [10].

11 REFERENCES

[1] L.Burnod and J.B. Jeanneret , CERN SL/91-39(EA), LHC Note167,1991.
[2] J.B.Jeanneret et al,CERN LHC project report 44,1996.
[3] A.van Ginneken,CASIM,Fermilab TN 309,1978.
[4] R.D.McCarty,NBS Tech.Notes 1029 and 1972.
[5] L.Burnod et al.,CERN/SL/90-01(EA),LHC Note 117,1990.
[6] N.Catalan Lasheras and J.B.Jeanneret, CERN LHC project Note 101,1997.
[7] Review of Particle Properties,Phys.Rev. D45,1992.
[8] T.Trenkler and J.B.Jeanneret, Particle Accelerators, 50,287(1995) and the bibliography therein.
[9] D.I.Kaltchev et al.,EPAC96,Barcelona,June 1996 and CERN LHC Proj.Rep.37,1997..
[10] D.I. Kaltchev et al.,PAC97,Vancouver,June 1997 and CERN LHC Proj.Rep.134,1997.
[11] Design of the Large Hadron Collider,CERN 91-03, 1991
[12] A.Corona et al.,ACM Trans. on Math.Soft.13,p262,1987.
[13] T. Risselada,CERN SL/Note 95-67(AP),1995.
[14] A.van Ginneken,Phys.Rev.D37,p.3292,1988.
[15] T.Trenkler,J.B.Jeanneret,CERN SL/Note94-105(AP),1994.
[16] to appear in N.Catalan Lasheras,Ph.D.,1998.
[17] K.Goulianos,Physics Report 101,No3,p.169,1983.
[18] G. Matthiae,Rep.Prog.Phys,57,p743,1994.
[19] C.Belletini et al.,Nucl.Phys.79,p.609,1966.
[20] A.Schiz et al.,Phys.Rev.D21,p.3010,1980.
[21] K.L.Brown et al.,CERN 80-04,1980.
[22] Workshop on LHC backgrounds,K.Potter ed.,CERN,1996.
[23] The Large Hadron Collider,CERN/AC/95-05(LHC),1995.
[24] A.I.Drozhdin and N.V.Mokhov,PAC97,Vancouver,1997.
[25] N. N.Mokhov and J.B.Strait,PAC97,Vancouver,1997.
[26] J.B.Jeanneret,CERN/SL/92-44(EA),LHC Note 211,1992.
[27] GEANT,Application Software Group,CERN,March 1995.

Beam Collimation at Tevatron, TESLA and Muon Colliders

A. I. Drozhdin and N. V. Mokhov[1]
Fermilab, P.O. Box 500, Batavia, IL 60510 USA

Abstract

High performance of a collider is achievable only with a dedicated beam cleaning system embedded in the lattice. The system prevents quenching of superconducting magnets, decreases backgrounds in the detectors and protects accelerator components, the environment and personnel against irradiation. Realistic Monte-Carlo simulations are described for design of efficient beam collimation systems for hadron, electron and muon colliders. Tevatron, TESLA and high and low energy muon colliders are taken as the representatives of their classes.

1 INTRODUCTION

Creation of beam halo is unavoidable in any collider. Beam-beam collisions at the interaction points (IPs), interaction of beam with residual gas, the diffusion of particles out of the beam-core due to various non-linear phenomena, as well as various hardware and software errors, all result in emittance growth and eventually in beam loss in the lattice [1, 2, 3]. This causes irradiation of conventional and superconducting (SC) components of the machine, an increase of background rates in the detectors, possible radiation damage, quenching, overheating of equipment and even total destruction of some units. A very reliable multi-component beam collimation system is the main way to control beam loss. It is mandatory at any SC accelerator and provides [2, 3, 4, 5]:

- reduction of beam loss in the vicinity of IPs to sustain favorable experimental conditions;
- minimization of radiation impact on personnel and the environment by localizing beam loss in predetermined regions and using appropriate shielding in these regions;
- protection of accelerator components against irradiation caused by operational beam loss and enhancement of reliability of the machine;
- prevention of quenching of SC magnets and protection of other machine components from unpredictable abort and injection kicker prefires/misfires and unsynchronized aborts.

Depending on particle type, beam energy and intensity, machine and detector parameters and performance objectives, the requirements to the collimators vary but the systems have much in common. This paper describes the current approach to the efficient collimation at hadron, electron and muon colliders, using the Tevatron, TESLA and high and low energy muon colliders as the representatives of their classes. In all cases, the system consists of a set of primary and secondary collimators, designed on the basis of detailed Monte-Carlo simulations of the source term, particle tracking through the lattice, showers at the beam loss spots with thermal and stress analyses and optimizational studies of the protective measures.

[1] Work supported by the U. S. Department of Energy under contract No. DE-AC02-76CH03000

2 TEVATRON

2.1 Scraping Beam Halo

In the early Tevatron days the first collimation system was designed [1] on the basis of the MARS-STRUCT [6, 7] full-scale simulations of beam loss formation in the machine. The optimized system consisted of a set of collimators each about 1 m. When it was installed in the Tevatron it immediately made it possible to raise the efficiency of the fast resonant extraction system and the intensity of the extracted 800 GeV proton beam by a factor of 5. The data on beam loss rates and on their dependence on the collimator jaw positions were in excellent agreement with the MARS-STRUCT predictions.

We have since refined the idea of a primary-secondary collimator set and shown that this is the only way to use such a system in the TeV region with a length of a primary collimator going down to a fraction of a radiation length. The whole system should consist then of a primary *thin scattering target*, followed immediately by *a scraper* with a few *secondary collimators* at the appropriate locations in the lattice [2, 3, 5]. The purpose of a thin target is to increase the amplitude of the betatron oscillations of the halo particles and thus to increase their impact parameter on the scraper face on the next turns. This results in a significant decrease of the outscattered proton yield and total beam loss in the accelerator, avoids scraper jaws overheating and mitigates requirements on scraper alignment. Besides that, the scraper efficiency becomes almost independent of accelerator tuning, there is only one significant but totally controllable restriction of the accelerator aperture and only the scraper region needs heavy shielding and probably a dogleg structure. The method would give an order of magnitude in beam loss reduction at multi-TeV machines, but even at the Tevatron we have achieved a noticeable effect. The existing scraper at AØ was replaced with a new one with two 2.5 mm thick L-shaped tungsten targets with 0.3 mm offset relative to the beam surface on either end of the scraper (to eliminate the misalignment problem). This resulted in the reduction of the beam loss rate upstream of both collider detectors [8].

2.2 Beam Collimation for Tevatron Run II

A new sophisticated beam collimation system has been designed for the Tevatron Run II (Fig. 1). It consists of a set of primary and secondary collimators both for nominal momentum and off-momentum halo interception. L-shaped primary collimators shave the proton and antiproton beams as shown in Fig. 2. The proton halo phase space at the corresponding secondary collimator is shown in Fig. 3. Ellipses

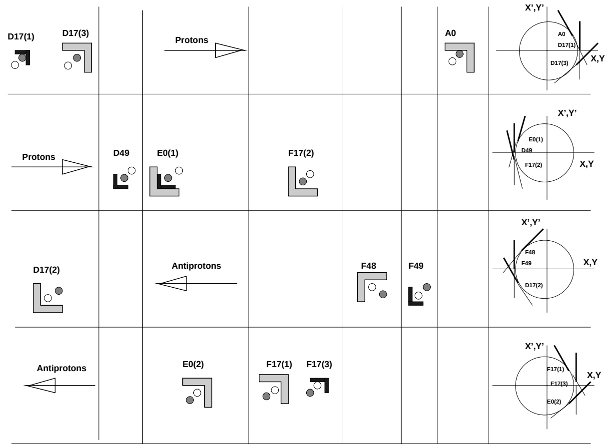

Figure 1: Tevatron Run II collimators.

represent a 6σ beam envelope. A vertical line shows the location of the collimator jaw. After the first interaction with a primary collimator, large amplitude particles are intercepted by the secondary collimators at the first turn. Some fraction survives and will interact with the secondary collimators on the next turns. Particles with amplitudes $<6\sigma$ are not intercepted by the secondary collimators and survive for another 20-30 turns until their angular divergence (and therteby the amplitude later) increases in the next interactions with a primary collimator. Thus, the halo occupies the 6σ envelope with a negligible number of particles outside (see Figs. 4-5).

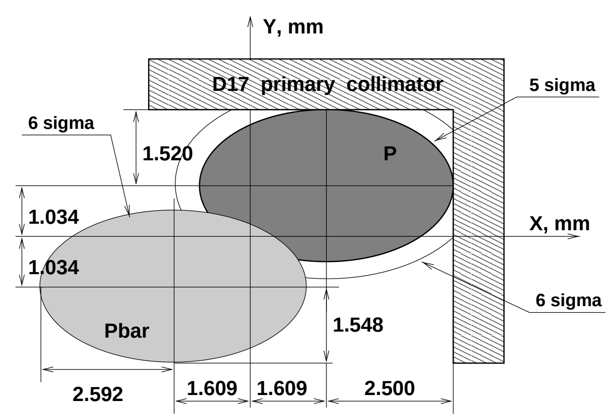

Figure 2: Proton beam primary collimator D17(1)

Beam loss distributions in the Tevatron are presented in Figs. 6-7 for proton and antiproton directions. Antiproton collimators intercept $6\times10^6\ \overline{p}/s$ in the proposed system, that is five times lower than the proton scraping rate and results in about five times lower accelerator-related background in DØ and BØ. Beam loss rates in the IRs are 35% lower if one puts the secondary collimators at 5.5σ, but one needs to verify that such a 0.5σ offset is reliable and stable.

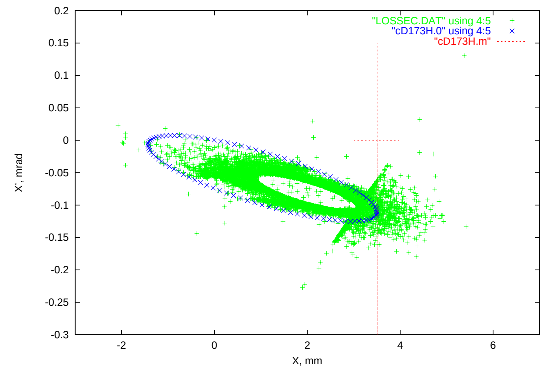

Figure 3: Horizontal phase space at secondary collimator D17(3).

2.3 *DØ and CDF Forward Proton Detectors*

At SC hadron colliders the mutual effect of the radiation environment produced by the accelerator and experiments is one of the key issues in interaction region and detector developments [9, 10]. The overall Tevatron and DØ and CDF detector performances are strongly dependent on details of such an interface. Efforts were made at Fermilab to optimize the DØ and BØ regions with proposed forward detectors in place for the Run II era.

Two new forward detectors have been recently proposed as new sub-detectors of the DØ and CDF collider detectors for the Tevatron Run II (see, e. g., [11]). These detectors

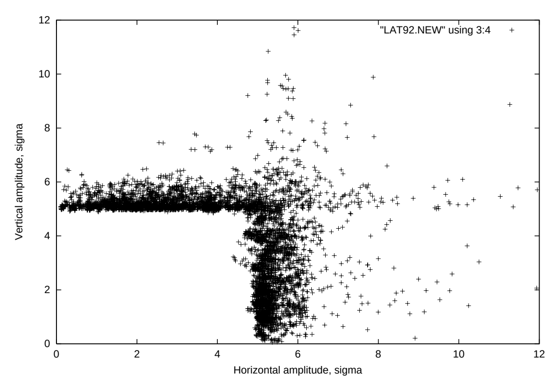

Figure 4: Proton beam halo in the Tevatron aperture.

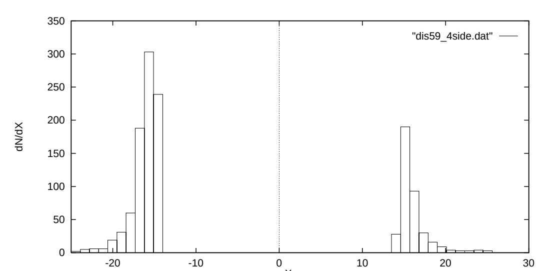

Figure 5: Proton beam halo distribution at DØ quadrupole spectrometer Roman pots positioned at 8σ.

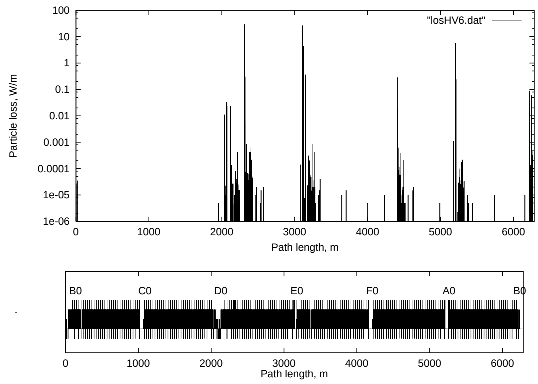

Figure 6: Beam loss distributions in the Tevatron for proton direction.

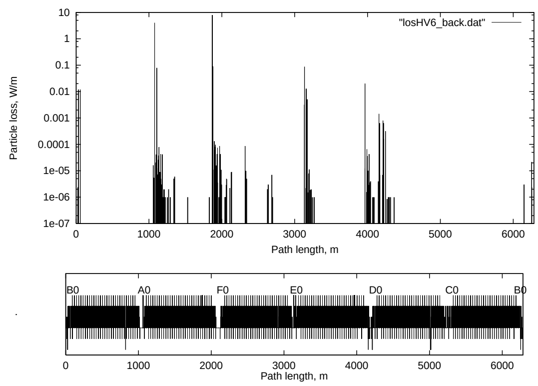

Figure 7: Beam loss distributions in the Tevatron for antiproton direction.

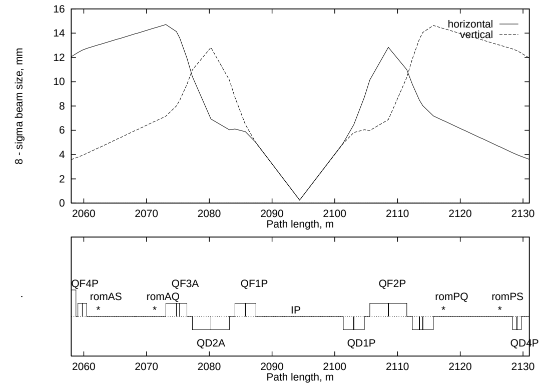

Figure 8: 8σ proton beam envelopes in DØ . Roman pot locations are shown as romAS, romAQ, romPQ and romPS.

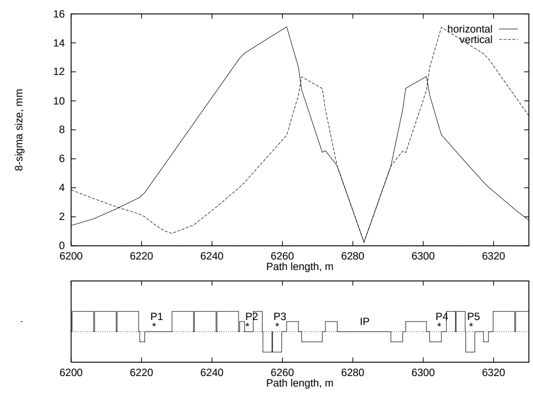

Figure 9: 8σ proton beam envelopes in BØ . Roman pot locations are shown as P1–P5.

use the Tevatron magnets along with points measured on the track of the scattered proton to determine the proton momentum and angle. They consist of quadrupole spectrometers which tag outgoing protons or antiprotons with a minimum t and a dipole spectrometer which detects particles with a minimum Δp (see Fig. 8-9). The DØ FPD includes four Roman pot units (with four pots each) placed in the DØ straight section and two single units in the C48 location. The four units are upstream and downstream of the separators with 'A' referring to the outgoing antiproton side and 'P' to the outgoing proton side. Each unit consists of four square $2{\times}2$ cm^2 detectors placed in horizontal and vertical planes on each side of the beam. The C48 units are placed on inside the orbit of the beam. The Roman pot positions are adjustable in the x or y directions and can be moved according to the beam halo conditions in the Tevatron.

Calculations of both DØ and CDF forward detector acceptances were done via tracking of particles ejected from the IP with various momenta and angles for several configurations. The calculated values are quite acceptable and naturally go down with the Roman pots at larger distancies from the beam axis.

Realistic simulations of beam loss formation in DØ and BØ with beam collimation system and forward proton detectors in place followed by full simulations of induced hadronic and electromagnetic cascades were performed with the MARS-STRUCT code system [6, 7]. It turns out that the accelerator related background in the collider detectors originates from beam halo loss in the Tevatron and FPD components within $\pm$50 m of the IPs. The limiting apertures are the β_{max}-region and the Roman pots placed at 8σ (DØ) and 10σ (BØ).

Some halo particles can pass through the Roman pot detectors several times inducing excessive hit rates in the pots themself and in the main BØ and DØ detectors. Calculations show that beam loss and hit rates are decreased by a factor of two by moving the Roman pots at DØ from $8\sigma_x$ to $9\sigma_x$. The price one pays is decreased FPD acceptance. Therefore, the Roman pot positions will be chosen as a compromise between the main detector background and the FPD acceptance.

Typical results for charged particle fluxes in the Tevatron tunnel and in the DØ forward muon system are shown in Fig. 10. A ratio of hit rate in the forward muon chambers with FPD to that without FPD is calculated to be 4.5 for pots at 8σ and 1.5 for pots at 9σ, implying a total increase in background rates of at most 15% and 5%, respectively. The situation is rather similar for the central detector.

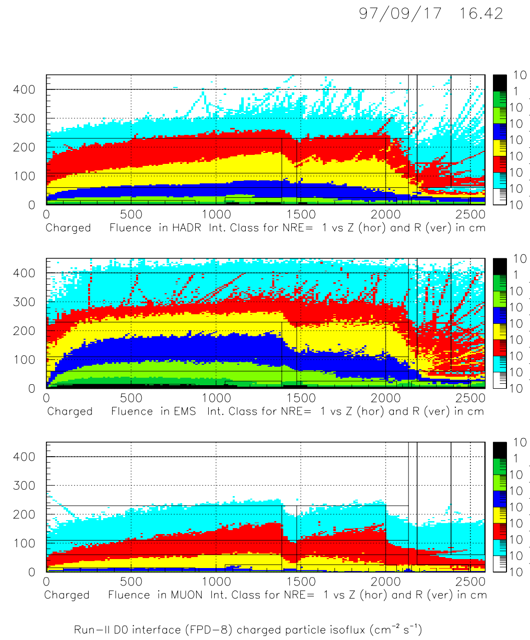

Figure 10: Particle flux distributions in the DØ region for charged hadrons, electromagnetic showers, and muons.

2.4 Proton Beam Removal from the Tevatron

Another implementation of the Tevatron collimation system is proton beam removal. This implies aborting the proton beam before deceleration while leaving antiproton beam for recycling. There are two main restrictions to the fast high intensity beam removal using an internal collimator: SC magnet quenches caused by the secondary particles from the collimator and target-collimator overheating. The quench level of the Tevatron magnets at 1 TeV is about 3×10^8 p/m/s which corresponds to $\sim$ 50 W/m.

With the Main Injector, the EØ straight section will be free of the magnets used for beam injection into the Tevatron. With the last 15 m of the EØ straight section reserved for the SC RF, the first 35 m can be successfully arranged for proton beam removal (Fig. 11).

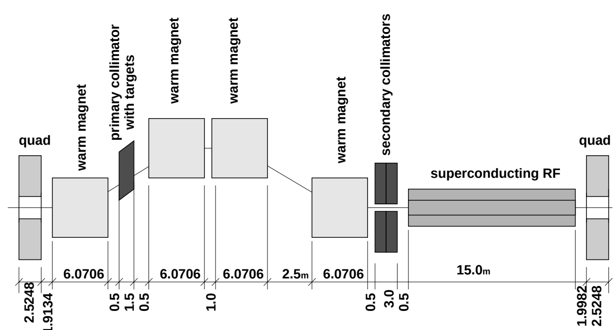

Figure 11: Dog-leg system for proton beam removal at the EØ straight section.

The purpose of collimation at beam removal is to protect the SC magnets downstream of the straight section. Two 2.5 mm thick targets are attached to both ends of the collimator with a 0.3 mm target-collimator offset. They are used as primary collimators. The collimator-target assembly is positioned at 7σ and is the limiting aperture in the accelerator. This system is in principal an example of a two-stage collimation system, but primary and secondary collimators are at the same location. This makes it possible to concentrate both sources of particle loss in the same dog-leg system.

Four warm bump-magnets are used to protect the Tevatron magnets against neutrals and low-energy charged particles from the primary collimator. Two 1.5 m long L-shape secondary collimators placed at 9 σ downstream of the dog-leg at the entrance to the cold region intercept most of these particles. Such a system tremendously decreases particle loss downstream of the EØ straight section by intercepting most of low energy particles emitted from the primary collimator. Tevatron closed orbit correctors are used to move the beam towards the target. Monte-Carlo simulations [12] show that the total proton intensity of 10^{13} ppp can be removed from the Tevatron without magnet quenches in 100 seconds using the EØ collimators. The maximum temperature rise in the target-collimator will be about $40°C$ for a spill duration $\geq$ 1 second.

3 TESLA

At the TESLA e^+e^- linear collider (2×10^{14} particles per second at E=250 GeV), the loss of a small fraction of the beam along the lattice can have a drastic effect on the machine and detector components performance and survival. The collimation system [13] is intended to localize the beam loss in a special section of the beam line. The peculiarity of an electron-positron linear collider collimation system is that halo must be cleaned out during one pass of the beam through the collimation system. In addition to this, the detector must be protected from synchrotron radiation emitted by the core of the beam and halo. Because of that, the system should consist of a large number of longitudinally distributed collimators. The philosophy of the TESLA beam collimation system is to use large aperture quadrupoles and collimate the beam at the largest amplitudes in order to minimize muon background produced by the collimators.

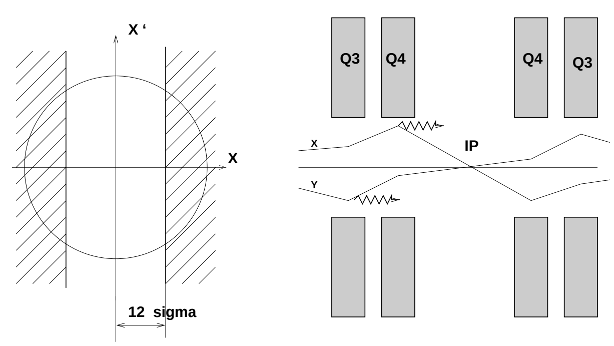

Figure 12: Principle of the TESLA collimation system.

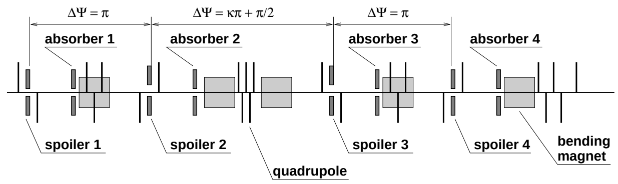

Figure 13: Schematic view of the TESLA beam collimation system.

The beam collimation system design is driven by the requirement that synchrotron radiation generated in the doublet upstream of the IP should pass freely through the aperture of the final focus (FF) quad to the opposite side (Fig. 12). This means a collimation of the "sine-like" trajectories (with respect to IP) at 12σ in the x- and 48σ in the y-planes. The system consists of four frame shape titanium spoilers and four copper absorbers. The spoilers are located at $8\sigma_x$ and $32\sigma_y$ and at 2% of the momentum deviation in a region with large horizontal and vertical β-functions and maximum dispersion (Fig. 13).

The first two spoilers are placed at a phase advance of π between them to intercept the "sine-like" trajectories. The second pair of the spoilers is placed at a $\pi/2$ phase advance downstream of the first pair and intercepts the "cosine-like" trajectories. Collimation of both phases becomes necessary because of the magnets inserted between the collimation section and the FF. The off-momentum trajectories which are purely sine-like at the IP, can thus be (fully or partially) cosine-like at the entrance to the collimation section. Such a collimation system eliminates beam loss in the detector and decreases the synchrotron radiation emitted by halo in the last doublet by a factor of 3×10^5.

This system intercepts the particles with a momentum deviation close to the equilibrium, but large momentum deviation particles spoil the picture. To improve that, the second stage of collimation is embedded into the high-β region of the FF $\sim$200 m upstream of the IP (Fig. 14). This is situated $k\pi$ in phase advance from the last doublet, that is suitable for the "sine-like" trajectory collimation in both horizontal and vertical planes. Electron and synchrotron radiation loss distributions in the TESLA beam line are shown in Fig. 15-16 without and with halo collimation.

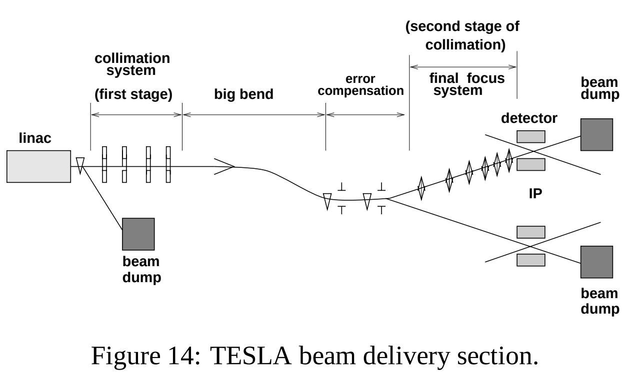

Figure 14: TESLA beam delivery section.

The second stage of halo collimation gives additional safety in suppressing the background from large amplitude particles which can escape from the first stage or can be produced by beam-gas interactions between the collimation section and the FF. It is independent of the phase advance between the first stage and the IP. This gives a possibility for future modifications of different parts of the beam delivery section without influence on the collimation system efficiency.

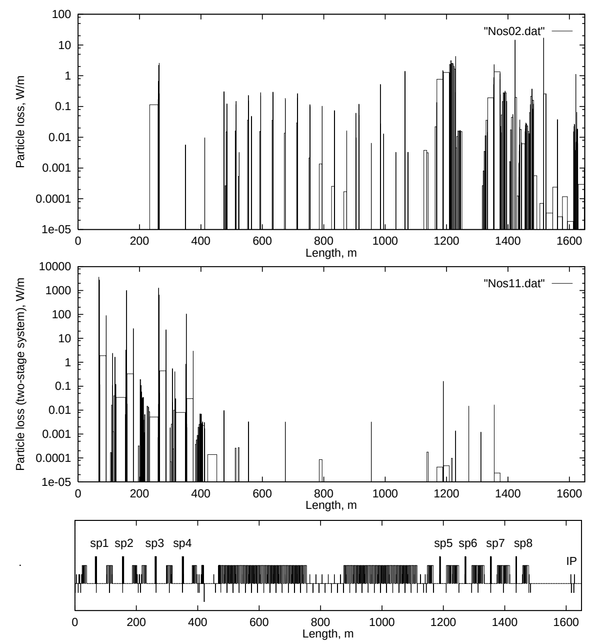

Figure 15: Beam loss in the TESLA beam line without and with halo collimation.

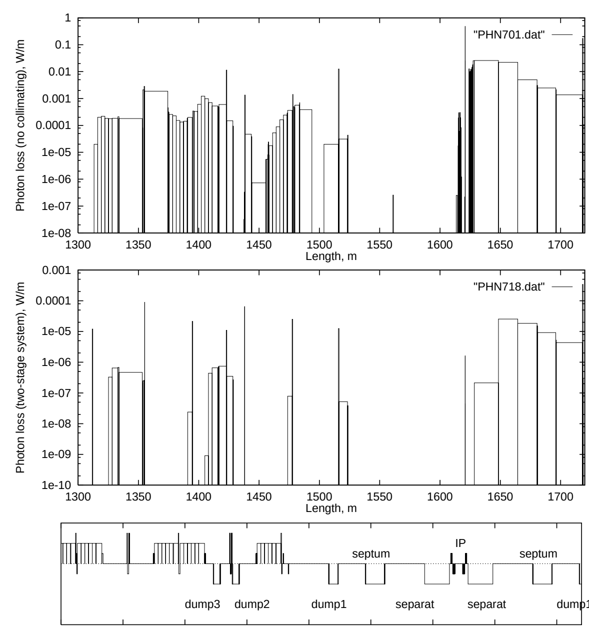

Figure 16: Synchrotron radiation loss in the TESLA beam line without and with halo collimation.

4 MUON COLLIDER

High background rates in the detectors are one of the most serious problems on the road towards a high-luminosity $\mu^+\mu^-$collider [14, 15]. It was shown at an early stage [16] that detector backgrounds originating from beam halo can exceed those from decays in the vicinity of the interaction point (IP). Only with a dedicated beam cleaning system far enough from the IP can one mitigate this problem [17]. Muons injected with large momentum errors or betatron oscillations will be lost within the first few turns. After that, with active scraping, the beam halo generated through beam-gas scattering, resonances and beam-beam interactions at the IP reaches equilibrium and beam losses remain constant throughout the rest of the cycle. Two beam cleaning schemes are possible: beam halo extraction with an electrostatic deflector and standard collimation.

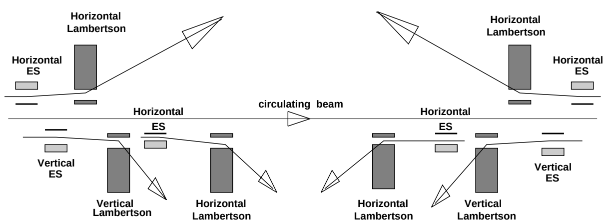

Figure 17: Schematic view of a $\mu^+\mu^-$collider beam halo extraction.

4.1 Beam Halo Extraction

A 3-m long electrostatic deflector separates muons with amplitudes larger than 3σ and deflects them into a 3-m long Lambertson magnet, which extracts these downwards through a deflection of 17 mrad (Fig. 17-18). A vertical septum magnet is used in the vertical scraping section instead of the Lambertson to keep the direction of the extracted beam down. The shaving process lasts for the first few turns. To achieve practical distances and design apertures for the separator/Lambertson combinations and minimize muon interactions with the electrostatic deflector wires, the β-functions must reach a kilometer in the 2-TeV case, but

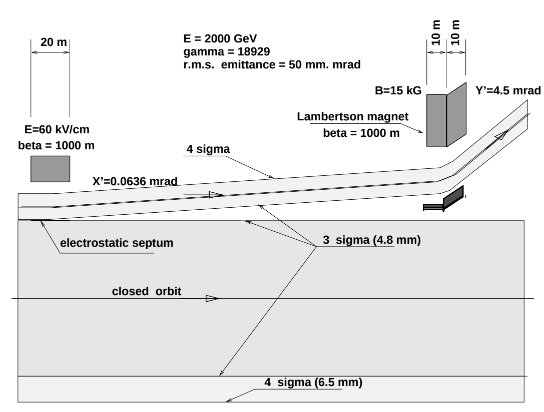

Figure 18: Extraction of muon halo.

only 100 m at 50 GeV. The complete system consists of a vertical scraping section and two horizontal ones for positive and negative momentum scraping (the design is symmetric about the center, so scraping is identical for both μ^+ and μ^-). The halo is always extracted down into the ground downstream of the utility section (US).

In the length between one high-β region to the next, halo muons are sufficiently separated from the circulating beam to be cleanly extracted by a Lambertson magnet. Extracting large-amplitude and off-momentum muons dramatically decreases beam loss in the IR. Calculations show that 83% of the halo is extracted from the collider over the first few turns. About 30% of the beam halo passes through the electrostatic deflector wires. These muons loose on average 0.6% of their energy and are lost at the limiting apertures along the collider, mostly in the first 70 m after the US (see Fig. 19). About 4% of the halo muons just get an angular (amplitude) kick without noticeable momentum loss and are lost in the IR resulting in detector background. Assuming the interception of 1% of the circulating beam in the beam cleaning process, 8×10^8 muons are lost in the final focus quadrupoles (just a few meters from the IP) over the first few turns after injection. After that, the scraping system becomes very efficient as beam halos are regenerated by beam-gas and beam-beam scattering, ground motion and resonances.

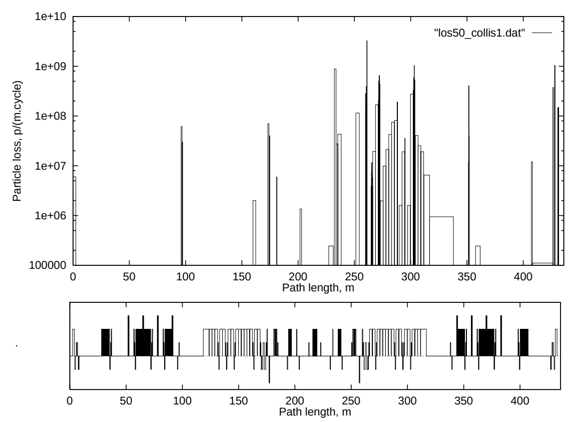

Figure 19: 50 GeV muon beam loss distributions for the beam halo extraction. 1% of the beam intensity is intercepted.

4.2 Beam Halo Collimation

An alternative scheme is to collimate the halo using a solid absorber (Fig. 20). Our studies [17] showed that no absorber, ordinary or magnetized, will suffice for beam cleaning at 2 TeV; in fact the disturbed muons are often lost in the IR. At 50 GeV, on the other hand, collimating muon halos with a 5-m long steel absorber (Fig. 20) in a simple compact US does an excellent job. Muons loose a significant fraction of their energy in such an absorber (8% on average) and have broad angular and spatial distributions.

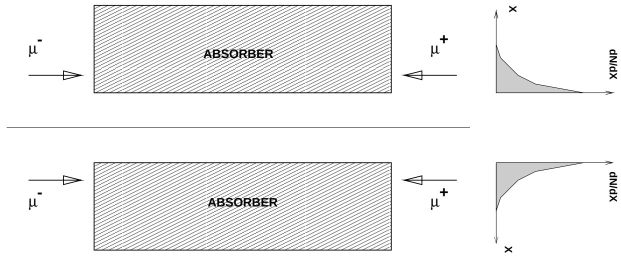

Figure 20: Scraping muon beam halo with a 5-m steel absorber.

Therefore, almost all of these muons are lost in the first 50-100 m downstream of the absorber as shown in Fig. 21, with only 0.07% of the scraped muons reaching the low-β quadrupoles in the IR. This is 60 times better than with the halo extraction scheme at 50 GeV. At the same time, the peak beam loss in SC magnets downstream of the US is six times higher compared to the halo extraction (Fig. 21). Without halo scraping, a full 1% of the beam is lost in the IR, i.e., the collimation system reduces beam loss in the IR by almost a factor of 1500. One percent of the steady-state beam loss on the collimators results in a total of 1.4×10^7 muons lost in the low-β quadrupoles during the cycle. The collimators could, in fact, be placed in the matching sections on either side of the IP leaving the US for injection and extraction and reducing the overall accelerator circumference.

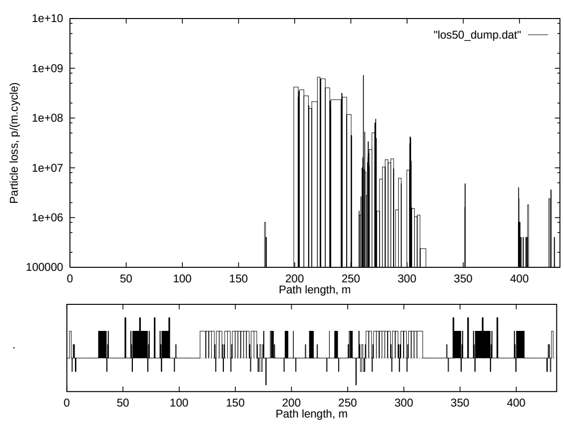

Figure 21: 50 GeV muon beam loss distributions for the beam halo collimation with the internal absorber. 1% of the beam intensity is intercepted.

5 CONCLUSIONS

Beam losses in hadron, electron and muon colliders can be reliably controlled with a dedicated multi-component collimation system. Beam induced deleterious effects on the machine and detector components and on their performance are significantly mitigated via careful optimization and design of the beam collimation system parameters.

6 REFERENCES

[1] A. I. Drozhdin, M. Harrison and N. V. Mokhov, 'Study of Beam Losses During Fast Extraction of 800 GeV Protons from the Tevatron', Fermilab FN-418, 1985.

[2] M. Maslov, N. Mokhov and I. Yazynin, 'The SSC Beam Scraper System', SSCL-484, 1991.

[3] A. I. Drozhdin, N. V. Mokhov, R. Soundranayagam and J. Tompkins, 'Toward Design of the Collider Beam Collimation System', SSCL-Preprint-555, 1994.

[4] A. I. Drozhdin and N. V. Mokhov, 'Optimisation of the LHC Beam Cleaning System with Respect to Beam Losses in the High-Luminosity Insertions', LHC Project Report 148, 1997; IEEE 1997 Particle Accelerator Conference, Vancouver, BC, Canada, May 1997.

[5] A. I. Drozhdin and N. V. Mokhov, 'Beam Loss Handling at Tevatron: Simulations and Implementations', IEEE 1997 Particle Accelerator Conference, Vancouver, BC, Canada, May 1997.

[6] N. V. Mokhov, 'The MARS Code System User's Guide, Version 13(95)', Fermilab–FN–628 (1995).

[7] I. Baishev, A. Drozhdin and N. Mokhov, 'STRUCT Program User's Reference Manual', SSCL–MAN–0034 (1994).

[8] J. Butler, D. Denisov, T. Diehl, A. Drozhdin, N. Mokhov and D. Wood, 'Reduction of Tevatron and Main Ring Induced Backgrounds in the DØ Detector', Fermilab–FN–629, 1995.

[9] N. V. Mokhov, 'Accelerator/Experiment Interface at Hadron Colliders: Energy Deposition in the IR Components and Machine Related Background to Detectors', Fermilab-Pub-94/085, 1994.

[10] A. I. Drozhdin, M. Huhtinen and N. V. Mokhov, 'Accelerator Related Background in the CMS Detector at LHC', Nucl. Instruments and Methods in Physics Research, **A381**, pp. 531-544, 1996.

[11] A. Brandt, A. Drozhdin, N. Mokhov et al., 'Proposal for Forward Proton Detector at DØ ', Fermilab, October 1996.

[12] A.I. Drozhdin and N.V. Mokhov, 'Beam Loss Handling at Tevatron: Simulations and Implementations', Presented at the 1997 Particle Accelerator Conference, Vancouver, BC, May 1997.

[13] R. Brinkmann, A. Drozhdin, D. Schulte, M. Seidel, 'The TESLA Beam Collimation System', DESY TESLA 95-25, December 1995.

[14] $\mu^+\mu^-$ *Collider: A Feasibility Study*, The $\mu^+\mu^-$ Collider Collaboration, BNL–52503; Fermilab–Conf–96/092; LBNL–38946, July 1996.

[15] N. V. Mokhov, Nucl. Phys. B, **51A**, 210-218 (1996).

[16] G. W. Foster and N. V. Mokhov, in *AIP Conference Proceedings* **352**, *Sausalito, November 1994*, pp. 178–190; also Fermilab–Conf–95/037 (1995).

[17] A. I. Drozhdin, C. C. Johnstone and N. V. Mokhov, '2×2 TeV $\mu^+\mu^-$ Collider Beam Collimation System', Workshop on Muon Colliders, Orcas Island, WA, May 1997.

A PROPOSED TEVATRON COLLIMATION SYSTEM FOR COLLIDER RUN II

M. Church, Fermilab*, PO Box 500 Batavia, IL, 60510

Abstract

The hardware, software, and procedures used for beam halo scraping in the Tevatron at the beginning of a colliding beam store must be improved for Run II in order to reduce losses at B0 and D0 to a level the Collider experiments can tolerate. In addition, during Run 1b the typical scraping procedure took about 20 minutes at the beginning of each store -- sometimes much longer if there was an emittance blowup during acceleration, incorrect tunes, large orbit distortion, or some other anomalous condition. This paper describes a new, automated Tevatron beam collimation system which is currently being built. This system is intended to scrape the beam halo at the beginning of each store quickly and in a systematic manner.

1 LAYOUT AND PRINCIPLE OF OPERATION

In Collider Run II a two stage collimation system, already pioneered at SPS and HERA [1,2], will be used. A primary collimator (target), made from a movable, thin heavy metal piece, 5-10 mm thick, acts to scatter the particles in the beam halo. Secondary collimators, consisting of 1.5m long stainless steel absorbers, are located at suitable phase advances downstream of the target to intercept the scattered particles. The target and the secondary collimators are L-shaped and can intercept particles with both large horizontal and large vertical amplitudes. The target is moved to within about 5σ of the beam centroid. The scattered particles are efficiently intercepted by secondary collimators moved to about 8σ from the beam centroid. The current design [3] has the proton target located at D17(1) and three secondary collimators located at D17(3), D48, and A0(1). The antiproton target is located at A0(2) with three secondary collimators at F48, D48, and D17(2). The collimator at D48 is used for both proton and antiproton halo scraping. The choice of position of these collimators is dictated by the available space in the ring, the helix separation, the beta functions, and the phase advances from target to secondary collimator. In addition, there will be three collimators located at E0 to be used for removing the proton beam at the end of the store. These three collimators can also be used for beam halo scraping, and will use the same controls architecture. Calculations to optimize the locations of the collimators have been done using the STRUCT [4] and MARS [5] codes.

2 CONTROLS

Figure 1 is a block diagram of the controls system for a single collimator. Each collimator station will be controlled by an MVME162 processor running VXWORKS in a VME crate located in a nearby service building. Primary collimators will have a single motor for vertical motion and a single motor for horizontal motion. Secondary collimators will have two motors in each dimension to control upstream and downstream positions independently. The stepping motors (200 steps/turn) will be geared so that the collimator can be moved at a maximum speed of ~2.5cm in 10 seconds, which is approximately the distance from the full out position to the beam axis. This gearing will yield a minimum step size of 12μm, which is never larger than about 1/20th of the beam sigma. Position readback is provided by LVDT's (Linear Variable Differential Transformers) -- 4 per secondary collimator and 2 per target. Limit switches will protect hardware from damage. Local fast feedback for the motion control, operating at 720 Hz in the CPU, will be provided by 4 standard TEV loss monitors. These are gas filled ionization chambers, and there will be 2 upstream and 2 downstream of each collimator for redundancy. Stepping motors, loss monitors, and LVDT's will be interfaced to the CPU via 3 IP's (Industrial Packs), and cabling will be handled by a Fermilab-designed daughter board. Communication with ACNET (Accelerator Controls Network) will be via Ethernet. Up to 4 systems can be installed in a single VME crate.

3 MATERIALS CONSIDERATIONS

For normal operations (beam halo scraping) the energy deposition in the collimators and targets is very small and does not cause any damage or overheating in the absorbers. However, in an accident scenario, where the entire beam (10^{13} protons) is dumped into a collimator on a single turn, the instantaneous energy density is very high and is capable of damaging some materials. In particular, experience with the Fermilab Antiproton Source production target [6] has shown that tungsten can be damaged by shock wave effects at energy densities as low as 200 J/g. In addition, tungsten collimators installed in the proton ring at DESY were found to have scoring on

*Operated by Universities Research Association, Inc. under contract with the U.S Department of Energy.

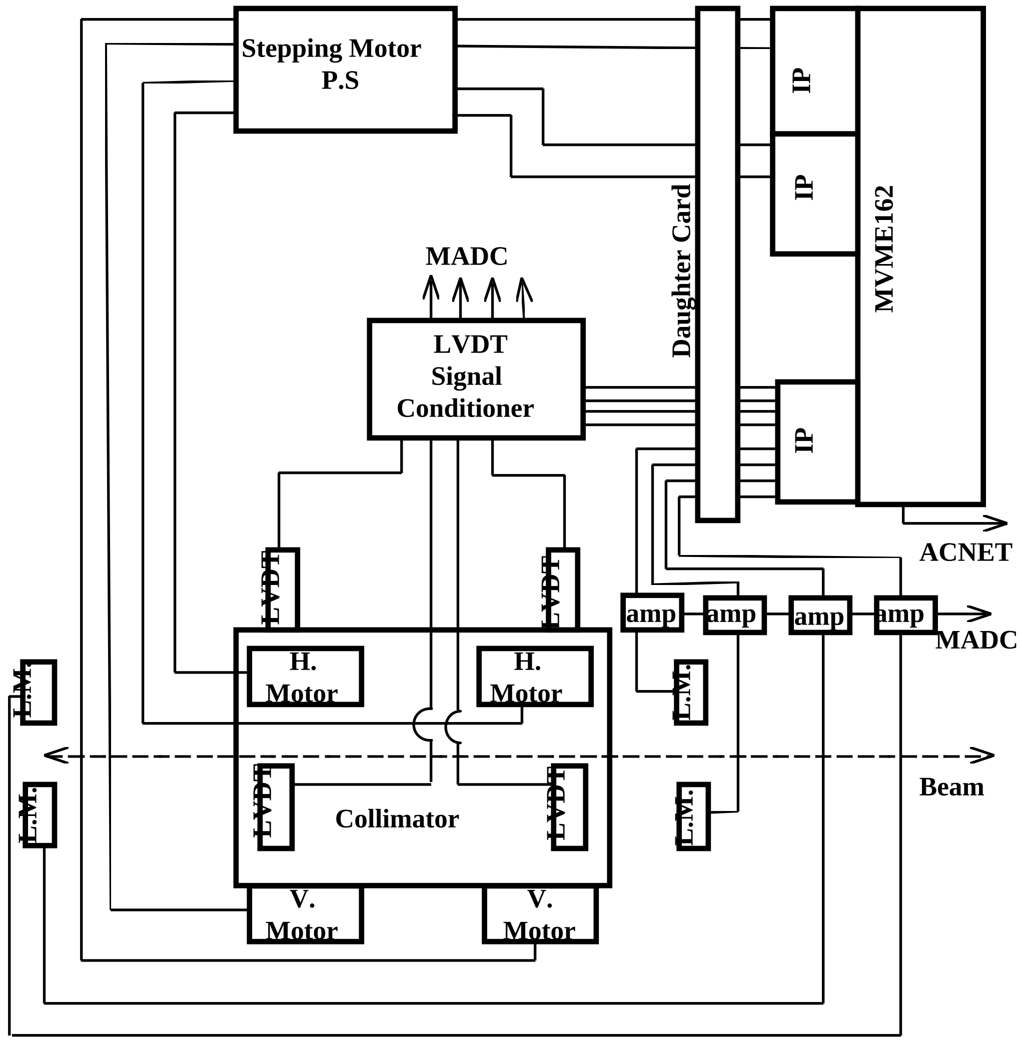

Figure 1: Block diagram of controls for one collimator station

the absorber faces after extended operation. This makes tungsten an unsuitable choice for the Tevatron collimation system targets. In the Antiproton Source production target copper and nickel have been shown to hold up well after repeated energy depositions of over 600 J/g. With a density of 8.9 - 9.0 g/cm^3, these materials are reasonable choices for a primary target. One would like to choice the most dense material available for the primary targets in a collimation system and still avoid damage. For the secondary collimators, a less dense material is more suitable -- if the absorber is too dense, the particles are scattered out of the absorber before being absorbed. Stainless steel appears to be an adequate choice for the secondary collimators, and is probably about as robust as copper and nickel in resisting damage under conditions of large instantaneous energy depositions.

4 TENTATIVE SCRAPING ALGORITHM

Each collimator is controlled locally by its own front-end with feedback from local loss monitors and position sensors (LVDT's). The beam halo scraping procedure will be initiated and sequenced by a console application program, which can download critical parameters to each collimation station, initiate scraping, and wait for completion. A two step procedure is probably adequate. First, all the collimators are simultaneously requested to move in to a position near the beam (about 10 σ). This is done under protection from the local loss monitors. Then each collimator is moved one at a time to its final position near the beam. This is also done under protection from the local loss monitors, and the final positions are determined by the loss rates from the local loss monitors. This second step can be repeated if the losses at B0 and D0 are still too high. Fine tuning of this algorithm will necessarily be done under real operating conditions. It is envisioned that the entire beam halo scraping procedure can be completed in 2-3 minutes.

5 STATUS AND PLANS

The new controls system is designed, and a prototype system is currently being assembled for testing in the lab using an old collimator stand. Calculation of optimum collimator location has gone through several iterations, and the current plan is thought to be final. Front-end code and the application program (user interface) are yet to be written. The schedule calls for the installation of the three collimators at E0 before the next Tevatron startup, and installation of the remaining collimators before the start of the next Collider running period

6 REFERENCES

[1] M. Seidel, "The Proton Collimation System of HERA", DESY 94-103 (1994)

[2] P.J. Bryant and E. Klein, "The Design of Betatron and Momentum Collimation Systems", SL/92-40 (1992)

[3] A.I. Drozhdin and N.V. Mokhov, this Workshop Proceedings

[4] I.S. Baishev, A.I. Drozhdin, and N.V. Mokhov, "STRUCT Program User's Reference Manual", SSC-MAN-00034 (1994)

[5] N.V. Mokhov, "The MARS Code System User's Guide, Version 13(95)", Fermilab-FN-628 (1995)

[6] S. O'Day, K. Anderson, and F. Bieniosek, "New Target Results from the Antiproton Source", Proceedings of the 1993 Particle Accelerator Conference, Washington D.C.: p3096-3098 (1993)

A Study of Betatron and Momentum Collimators in RHIC

D. Trbojevic, A.J. Stevens, and M. Harrison
Brookhaven National Laboratory, Upton, NY, 11973, USA

Abstract

Two separate accelerator rings in the Relativistic Heavy Ion Collider (RHIC) will provide collisions between equal and unequal heavy ion species up to the gold ions, including the two polarized proton beams. There are six interaction points with two regions with β^*=1-2 m occupied by the large detectors PHENIX and STAR. The transverse and longitudinal emittances of the gold ions are expected to double in size between one to two hours due to intra-beam scattering which may lead to transverse beam loss. Primary betatron collimators are positioned in the ring where the betatron functions have large values to allow efficient removal of particles with large betatron amplitudes. In this report we investigated distributions and losses coming from the outscattered particles from the primary collimators, as well as the best positions for the secondary momentum and betatron collimators. Additional studies of the detector background due to beam halo and other details about the collimation in RHIC are reported elsewhere (ref. [1] and [2]), while more information about the momentum collimation was previously reported in ref. [10].

1 INTRODUCTION

Collisions of equal or different heavy-ions occur at six interaction regions (IR). Two IR are designed to be at a lower β^*=1-2 m to provide luminosity of the order of $\mathcal{L}$=$10^{27} cm^{-2} s^{-1}$ for gold on gold collisions. Two large detectors, STAR and PHENIX, are located at the high luminosity regions. The strong focusing triplet quadrupoles at opposite sides of interaction points (IP) are the limiting apertures due to the large betatron amplitude functions of the order of $\beta \sim$ 1500 m.

Table 1: MAJOR RHIC PARAMETERS

Kinetic energy, Au	10.8 - 100 GeV/u
Kinetic energy, p	28.3 - 250 GeV/u
Number of Bunches	60
Circumference	3833.845 m
Number of IP	6
Betatron Tunes	28.19/29.18
γ_t	22.89
Max Dipole Field	3.45 T
Max quad gradient	71.2 T/m
Arc magnet coil ID	80 mm
Triplet coil ID	130 mm

The major RHIC parameters are presented in table 1. The six dimensional emittance of the heavy ion beams is expected to double in size due to intra-beam scattering between one to two hours. Particle amplitudes can also grow due to other effects like beam gas interaction, beam diffusion due to the nonlinear beam dynamics etc. The amplitude growth could result in a beam loss at limiting apertures, like the triplet magnets close to the large detectors, which results in a significant background. A limiting aperture of the collimator can reduce the background. The primary betatron collimator has to be able to remove particles with large amplitudes. As reported earlier [1] the background flux ϕ in a detector can be written as:

$$\phi = N \cdot (1-\epsilon) \cdot P \cdot F, \quad (\text{hits}\, \text{cm}^{-2}\text{s}^{-1}) \qquad (1)$$

where *N* is the number of particles per unit time on the collimator, (1-ϵ) is the collimator inefficiency, *P* is the fraction of the outscattered ions interacting in the "local" triplet magnets upstream of the detector, while *F* is the secondary particle fluence per locally interacting particle. This report studied the distribution of scattered particles from the primary collimators and their propagation throughout the RHIC accelerators - an estimation of the factor *P* in the above equation. More information about evaluations of the collimator efficiency (*factor* (1-ϵ)) and the hadron cascade calculation factors (*factor F*) is reported in [1]. The first part of the report (section 3) is about the initial conditions: particle's distributions at the primary collimators which are input for the tracking studies. In the second part (section 4), particle distributions of the survived outscattered particles around the rings in both transverse and longitudinal phase spaces are shown. In the next part of the report (sections 6 and 7) distributions of the lost particles around the ring are shown. The optimum location for the secondary betatron and momentum collimator are reported.

2 PRIMARY COLLIMATORS

Positions of the primary collimators in the two RHIC (*blue* and *yellow*) rings are set downstream of the large PHENIX detector at locations with high β value. The efficiency of the betatron collimator improves with higher values of the betatron amplitude function. The best possible locations in the RHIC lattice are about 5-6 m downstream of the high focusing quadrupoles where $\beta \sim$1100 m. An illustration of halo particles encountering a limited aperture of the primary collimator is shown in Fig. 2. The heavy ion beams in RHIC, as gold $^{+79}Au^{197}$, are expected to have a very fast emittance growth due to intra-beam-scattering (IBS) ($\sigma \simeq Z^4/\mathrm{A}^2$). Particles in the bunch exchange longitudinal and transverse momenta by Coulomb scattering. A transverse halo may be created by particles escaped from the *rf* bucket. The initial bunch area grows for almost one order of magnitude due to the IBS and the transverse emittance is expected to grow from the initial value at injection of ϵ=10 π mm mrad after few hours of store up to ϵ=40 π mm mrad. The halo growth in this study, as we already reported [1] is simplified by a diffusion process which was based on measurements in the SPS [6] and [7]. The amplitude growth *A* is presented [1] as:

$$\delta A = 2.45 \cdot \sigma \cdot e^{(\frac{A}{\sigma}-4)}, \qquad (2)$$

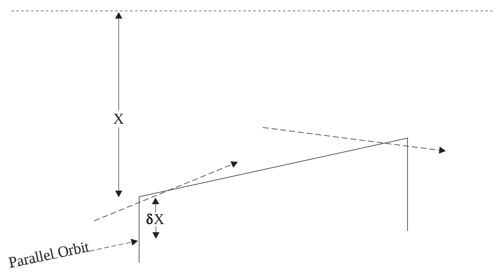

Figure 1: Illustration of halo particles encountering a limiting aperture collimator. Optimal collimation is achieved for orbits parallel to the face of the collimator.

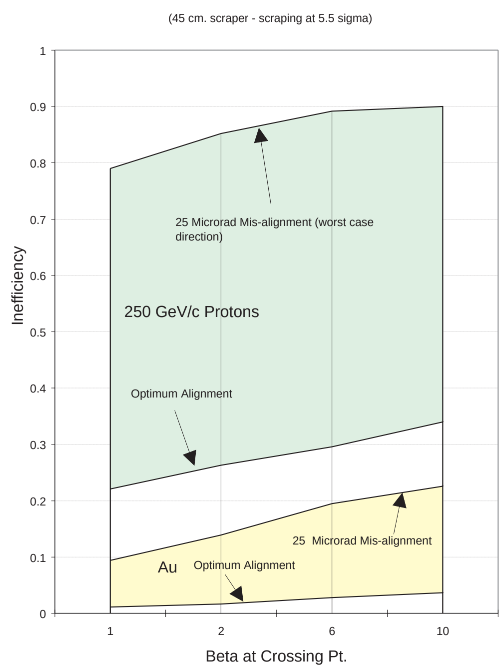

Figure 2: Results for a single pass scraping Inefficiencies

where $\sigma = \sqrt{\epsilon/6\pi\,\beta\gamma}$, the normalized emittance is labeled as ϵ, and $\gamma\beta$ are the relativistic factors. The dynamical aperture of RHIC in the gold ion store was previously [3] estimated to be at the beginning of the store 8 σ while at the end of the 10 hours store 5 σ. The amplitude growth presented above assumed [1] the dynamical aperture of 4σ. The upstream edge of the collimator is set at 5.5 σ with a slope which corresponds to the betatron function slope. Particles which reach the front edge of the collimator are transported through the 0.45 m long collimator by a computer code *ELSHIM* written by Van Ginneken [4]- [5]. The collimator material is assumed to be nickel-copper compound. The emittance of the heavy-ions (gold) is assumed to be 40 π mm mrad, and 20 π mm mrad for the proton beam. A single pass scraping inefficiency as a function of alignment for the gold ions and protons is shown in Fig. 3.

3 INITIAL CONDITIONS

The initial particle distributions are created by particle's orbits which emerge from the collimator without having inelastically interacted with the collimator. Fig. 4 represents the initial distribution of outscattered gold ions in the horizontal phase space at the primary collimator. The angle of the scattered ions is very narrow. Fig. 5 represents the initial outscattered particle distribution in the vertical phase space at the primary collimator. The momentum distribution of the scattered particles from the collimator shows (see Fig. 6) that a large number of particles have momentum offsets much larger than the projected RHIC bucket size at storage $\sigma_p \pm 0.2\%$. A distribution in the horizontal phase space of the outscattered protons from the primary collimators is quite different with respect to already presented gold ion distributions. The major difference are significant number of the outscattered protons with opposite-positive angle of the primary collimator (see Fig. 7). Figures 7 and 8 present the initial proton distributions in x-x' and y-y' phase space, respectively.

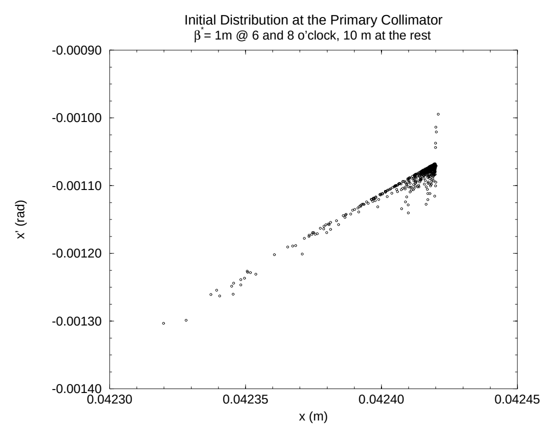

Figure 3: Initial distribution in x-x' phase space of gold ions outscattered from the primary collimator

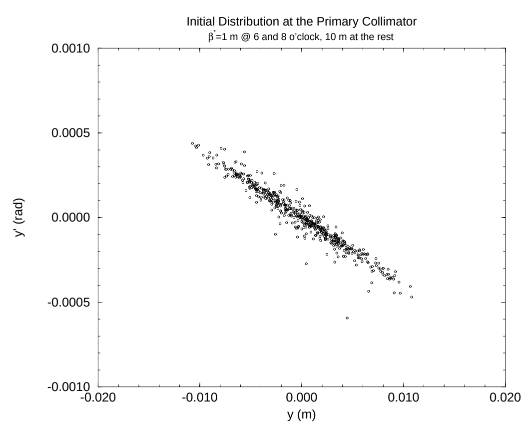

Figure 4: Initial distribution in y-y' phase space of gold ions outscattered from the primary collimator.

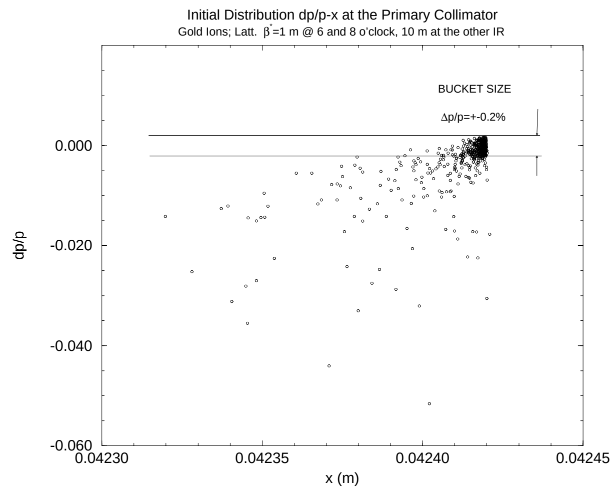

Figure 5: Initial momentum distribution of gold ions scattered from the primary collimator versus horizontal position.

4 PHASE SPACE DISTRIBUTION OF THE SCATTERED PARTICLES AROUND THE RINGS

The initial particle distribution is used as input for the tracking program TEAPOT [8]. The tracking was performed with the systematic and random multipoles within the quadrupoles and dipoles obtained from the measurement data, at the top energy of 100 GeV/nucleon for gold or 250 GeV for protons and for 256 turns. The misalignment and roll errors were obtained from the surveying data. The rms values for misalignment of the arc quadrupoles were Δx,y $\simeq$ 0.5 mm and $\Delta\theta$=0.5 mrad, while from the measurements of the triplet quadrupoles the roll and misalignment errors for the rms values were $\Delta\theta$=0.5 mrad and Δx,y=0.5 mm.

4.1 Longitudinal Phase Space

During tracking the RF voltage was included and the longitudinal motion of the surviving particles was monitored. Particles with momentum offsets within the bucket size limit executed synchrotron oscillations. Particles projections in the longitudinal phase space show in Fig. 9 that only particles within the bucket survive. Only few particles, which survived all 256 turns, finished almost one synchrotron oscillation. This is in accordance to the value used in tracking (synchrotron frequency used in the TEAPOT f=300 Hz) of $\simeq$260 turns for the full synchrotron oscillation. (It should be noted that the correct gold ion beam storage synchrotron frequency in RHIC is 326 Hz).

4.2 Transverse Phase Space Distribution

The transverse positions of the scattered particles on the first turn show that most of the particles with large momentum offsets are lost around the first bending elements. Particles outscattered from the primary collimator could continue to make few or more turns around the accelerator. Their distributions in the horizontal phase space at a location $\simeq$30 m downstream of the primary collimator is presented in Fig. 10.

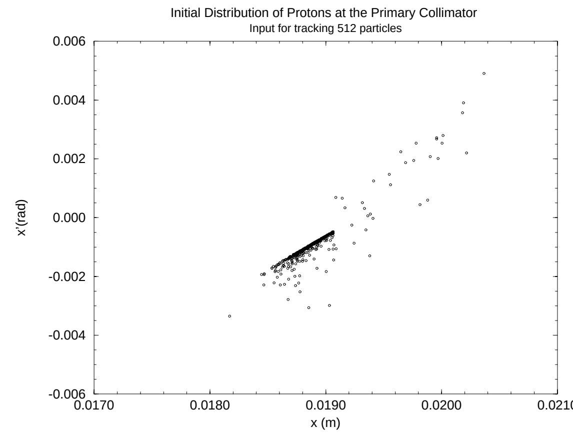

Figure 6: Initial distribution in x-x' phase space of protons outscattered from the primary collimator

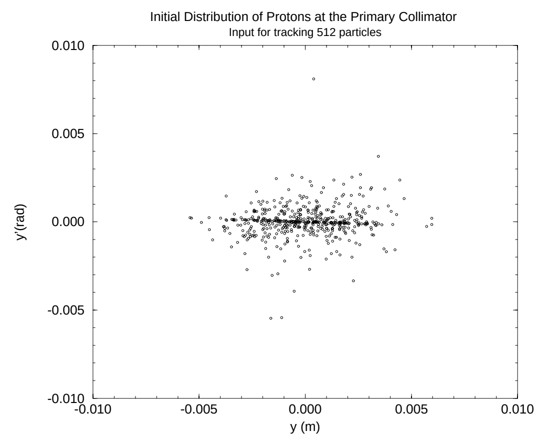

Figure 7: Initial distribution of protons in y-y' phase space outscattered from the primary collimator

5 THE SECONDARY COLLIMATORS

Particles outscattered from the primary collimators could not only increase the beam halo due their large amplitudes but they can create secondary showers towards detectors due to their interaction with the walls of the limited apertures of the upstream triplet quadrupole magnets. The function of secondary collimators is to reduce the beam halo around experiments further. If the primary collimator jaws were set at 5.5 σ from the central axis it is preferable to have the secondary collimators retracted at 6.5 σ at least one σ further than the primary one. The secondary collimators in RHIC would have to fulfill their purpose for both outscattered particles heavy ions (gold ions) as well as the protons. As it is easy to see from Fig. 7 the large number of

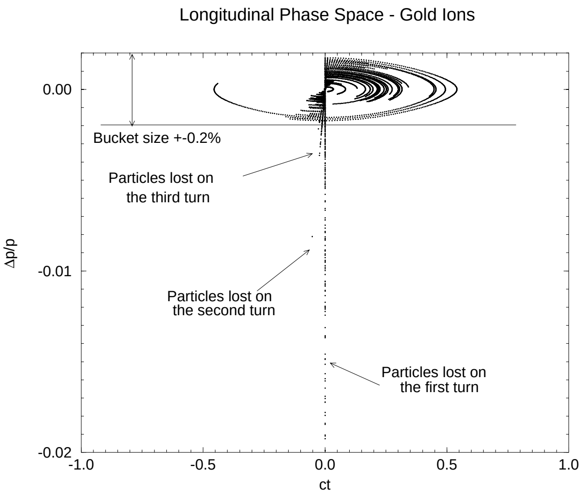

Figure 8: Longitudinal tracking

outscattered protons from the primary collimator have positive slope of the horizontal betatron function. To remove these particles, the preferable phase differences between the secondary betatron collimators and the primary ones, are [9] $\Delta\phi \simeq 15 - 30^o$ or $\Delta\phi \simeq 185 - 210^o$. The heavy ions, as it is presented for the gold ions in Figures 4 and 5, interact with the collimator's jaws differently. The preferable phase differences between the secondary and the primary betatron collimators which remove the largest amount of both outscattered protons and gold ions from the primary betatron collimators, are: $\Delta\phi \simeq 150 - 165^o$ or $\Delta\phi \simeq 330 - 345^o$. We determined the optimum positions for the secondary collimators by studying the outscattered parti-

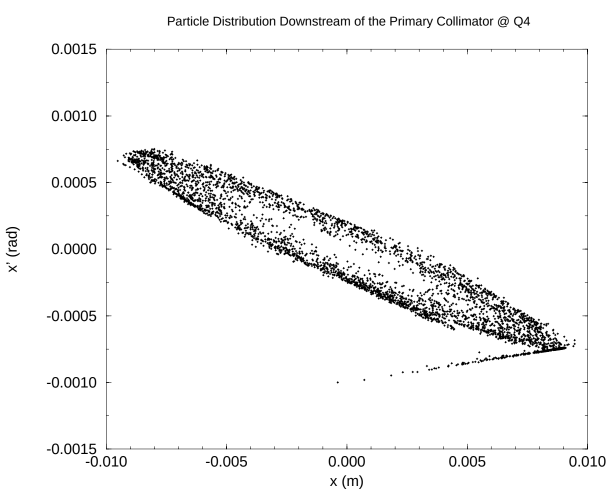

Figure 9: The outscattered particle's distribution in the x-x' phase space.

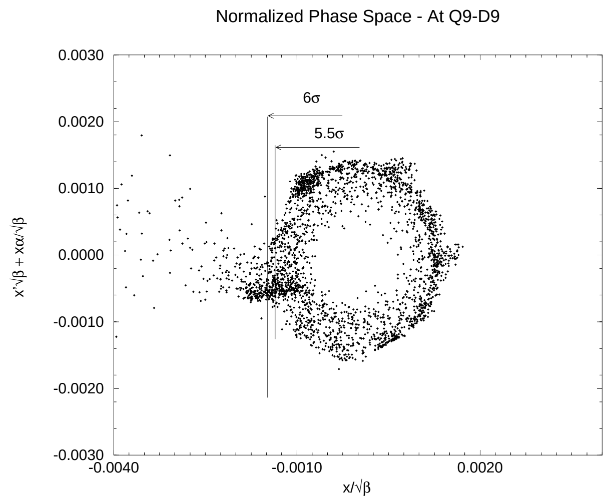

Figure 10: Optimum position of the secondary collimator

cles' phase space distributions around the ring. We studied all three: x-x', y-y', and x-dp phase space distributions. As we already emphasized, the beam halo in the gold ion store is created by the IBS, when the high momenta particles escape the *rf* bucket. A previous study [10] has shown preferable positions in the RHIC lattice for the "momentum scrapers". We will show that our most preferable positions for the secondary betatron collimators coincide with the most desirable positions of the "momentum scrapers". Particle distribution in the horizontal betatron space is shown in the normalized phase space. The normalized phase space is defined by the Floquet' transformation [11] as:

$$\xi = \frac{x}{\sqrt{\beta}} \quad and \quad \chi = x'\sqrt{\beta} + \frac{x\alpha}{\sqrt{\beta}}, \tag{3}$$

where the β and α are the Courant-Snyder functions, while x and x' are the offset and the slope of the horizontal position. The best positions (*Q9-D9 in the RHIC lattice*) for the secondary collimators are shown in Fig. 11. These positions (*Q9-D9 in the RHIC lattice*) were previously [10] selected due to the large value of the dispersion function ($D_x \simeq 1.5$ m @ Q9-D9 drift). The large amplitude of the particles at this position is a combination of two terms:

$$\sigma \;=\; \sqrt{\sigma_{twiss}^2 \;+\; \left(D_x \frac{dp}{p}\right)^2}. \tag{4}$$

The horizontal phase difference at the chosen location between the primary and the secondary collimator is 165^o.

5.1 *Particles' momenta at the secondary scraper*

Fig. 12 represents projections of the particles positions at the possible secondary collimator but in a different space. The horizontal axis represents particles' momenta, while the vertical axis is chosen for their horizontal positions.

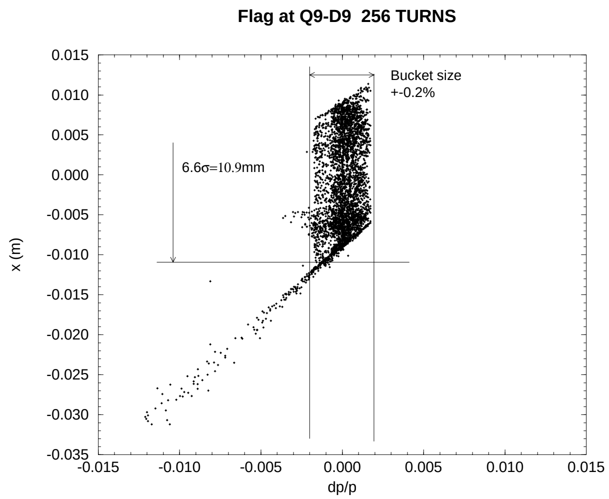

Figure 11: Horizontal positions of gold ions scattered from primary collimator at the secondary collimator with respect to their momenta.

This plot clearly shows the additional advantage of having the secondary scraper at this location. When the secondary scraper is set to a horizontal offset larger than 7σ, particles out of the bucket are eliminated. this location.

6 BEAM LOSS LOCATIONS IN THE RING

The RHIC lattice functions were transferred from the RHIC data base directly to the program TEAPOT. The aperture size of every element was present during the tracking. When a specific particle reaches the aperture limitation its tracking stops and the "loss" location, three coordinates, and an identification of particle are recorded. At the large detectors where the $\beta^* = 1$ m the strong focusing quadrupoles (as shown in Fig. 12) have their effective apertures reduced, due to the large values of the β functions. The losses of the outscattered particles from the primary collimator occur at these quadrupoles. The lost particles are presented on a logarithmic scale. Fig. 12 also shows losses at a set of magnets downstream of the primary collimator which are mostly due to the large momentum offset particles. The largest number of lost particles is at the strong focusing quadrupoles.

6.1 Secondary Collimator Retraction Scan

The efficiency of the secondary collimators was studied with the fixed position of the primary collimators at 5.5 σ. The tracking was performed as a function of the secondary collimator position. Fig. 13 shows number of lost particles at four selected locations with respect to the position of the secondary collimator obtained by tracking. Almost all outscattered particles from the primary collimator are lost during the 256 turns. When the secondary collimator jaws are fully retracted a large number of the outscatters will be lost again at the primary collimator. Particles which

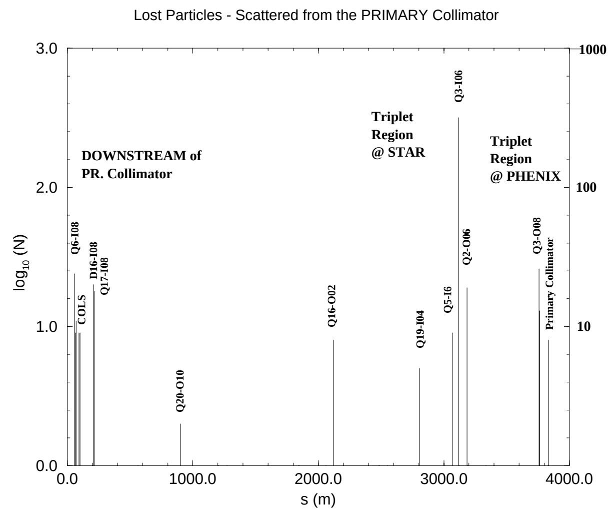

Figure 12: Losses around the ring from the primary collimator. The sample tracked consisted of 512 outscattered ions.

reached again the primary collimator were not transported through the collimator material by the *ELSHIM* code; they are assumed to be lost. When a retraction of the secondary collimator reached 11 σ the number of lost particles at both collimators became equal. A number of the lost particles at Q2 triplet quadrupole was dramatically lowered when the jaws of the secondary collimator reached 6.5 σ. The presented secondary collimator scan was obtained from the study of the *blue* ring, while the losses presented in Fig. 12 are obtained in the *yellow* ring.

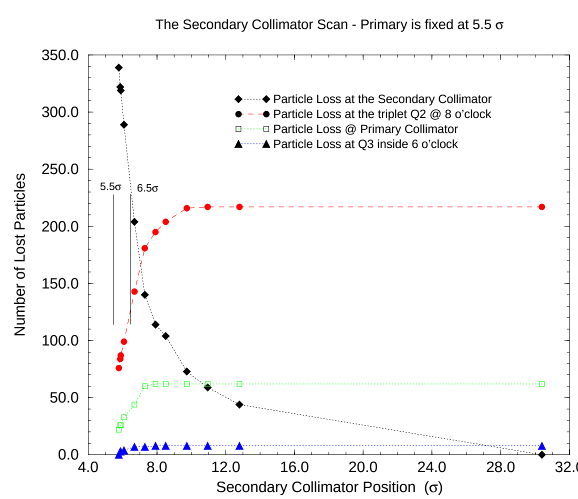

Figure 13: Distribution of losses during the secondary collimator scan.

7 CONCLUSIONS

The primary collimators in RHIC are important for many reasons:

- To remove the beam halo and reduce the background noise for the detectors.
- As a very good tool for beam diagnostics [9]: acceptance measurements, transverse particle distribution of the beam, frequency analysis of the beam loss rate, etc.

A combination of the primary and secondary betatron collimators can be used to remove not only the scattered particles from the primary collimator but also to remove particles out of the buckets. The secondary betatron collimators are effective only if the betatron phase difference between the two scraping stages is correctly chosen. Efficient momentum collimation [10] had already been reported at the same location, as it is the optimum position of the secondary betatron collimator (found in this study). It would be possible to create *macro buckets* with the use of the RHIC 28 MHz cavities to trap the particles outside of the buckets and scrape them [10]. The secondary collimator position determined in this study removes particles with large momentum offsets scattered from the primary collimator. It should be noted that losses from the primary collimators will still be the same in the same intersection region between the primary and secondary collimators. The spray at the triplets with the high values of β functions exists although it is significantly reduced.

8 REFERENCES

[1] A. J. Stevens, P.A. Thompson, and D. Trbojevic, *"Simulation of Detector Background Due to Beam Halo in RHIC"*, Internal Report Brookhaven National Laboratory, AD/RHIC/RD-117, October 1997, p.13.

[2] D. Trbojevic, A. J. Stevens, M.A. Harrison, F. Dell, and S. Peggs, *"A Study of Betatron and Momentum Collimators in RHIC"*, PAC97, Vancouver, Canada, May 1997, to be published.

[3] Jie Wei ,*"Magnet Quality and Collider Performance Prediction"*, Internal Note: RHIC/AP/117 (1996).

[4] A.Van Ginneken, *"Elastic scattering in thick targets and edge scattering"*, Physical Review D, Vol. 37, number 11, 1 June 1988, pp.3292-3307.

[5] A.Van Gineken, *"ELSHIM, Program to simulate Elastic Processes of Heavy Ions"*, BNL-47618, AD/RHIC-100, Informal Report, May 1992.

[6] L. Burnod and J.B. Jeanneret, *"Transverse Drift Speed Measurements of the Halo in a Hadron Collider"*, Proceedings of the Workshop on Advanced Beam Instrumentation, KEK, p. 375 (1988).

[7] W. Fischer, M. Giovannozzi and F. Schmidt, *"Dynamic aperture experiment at a synchrotron"*, Phys. Rev. E, Vol. 55, Number 3, p. 3507 (1997).

[8] L.Schachinger and R. Talman, *"A Thin Element Accelerator Program for Optics and Tracking"*, SSC Central Design Group, Internal Report SSC-52 (1985).

[9] M. Seidel, *"The Proton Collimation System of HERA"*, Dissertation, DESY 94-103, June 1994, Hamburg 1994.

[10] S. Peggs and G.F. Dell, *"Momentum Collimation at Q9"*, Report-no:RHIC/AP/78, November 1995.

[11] E.D. Courant and H.S. Snyder, *"Theory of the Alternating Gradient Synchrotron"*, Ann. Phys. **3**, 1 (1958).

COLLIMATION ISSUES FOR THE PEP-II B-FACTORY*

M. Sullivan
Stanford Linear Accelerator Center, Stanford University, Stanford, CA 94039 USA

Abstract

This note describes how beam collimation affects detector backgrounds at the collision point for the PEP-II B-factory, a joint effort of three laboratories: LBNL, LLNL, and SLAC. Beam collimation controls the transverse size as well as the maximum allowed energy spread of the beam. The location of synchrotron radiation masks is determined by the transverse size of the beam in that the masks must prevent radiation generated by beam particles located at large transverse beam positions from directly striking the detector beam pipe. Collimation of the energy spread of the beam is important in the control of backgrounds produced by beam particles that strike a gas molecule (lost beam particles).

I describe some preliminary information from background studies during the first months of commissioning the high energy ring of the PEP-II B-factory and present some model predictions for synchrotron radiation backgrounds when collimators are not present.

1 INTRODUCTION

PEP-II, a high-luminosity B-factory located at the Stanford Linear Accelerator Center (SLAC) is a high current (1-2 A) asymmetric-energy e^+e^- storage ring accelerator that operates at a center-of-mass energy equal to the mass of the Upsilon (4S) resonance (10.58 GeV).[1,2] The high beam currents are achieved by storing a large number of bunches (about 1600) into each beam. The energy asymmetry imparts a boost to the nearly stationary B mesons formed from the decay of the 4S resonance and allows precision vertex tracking detectors to look for a difference between the decay profiles of the matter and antimatter B mesons, thereby observing a violation of CP.

The PEP-II design has a low-energy beam (LEB) of 3.1 GeV and a high-energy beam (HEB) of 9 GeV. The beams collide head-on and are separated by a horizontal bending magnet located between 0.2 m and 0.7 m on either side of the interaction point (IP). The separation of the beams continues as they travel through QD1, a vertically focusing quadrupole. The QD1 magnets are essentially centered on the HEB orbit which places the LEB off-axis in these magnets. The large offset of the LEB orbit in QD1 bends the LEB further away from the HEB producing enough separation to allow QF2, a horizontally focusing magnet located between 2.8 m and 3.4 m from the IP, to be a septum quadrupole. QF2 is the second half of the final focus doublet for the LEB (QD1 is the other half). The HEB travels through a field free region in QF2; QD4 and QF5 (centered at 4.45 m and 6.2 m and 1.5 m long) are the main final focusing magnets for this beam. Figure 1 shows a layout of the interaction region of PEP-II. The B1 magnets and the QD1 magnets are made from permanent magnet material; both of these magnets are inside the solenoidal field of the detector.[3]

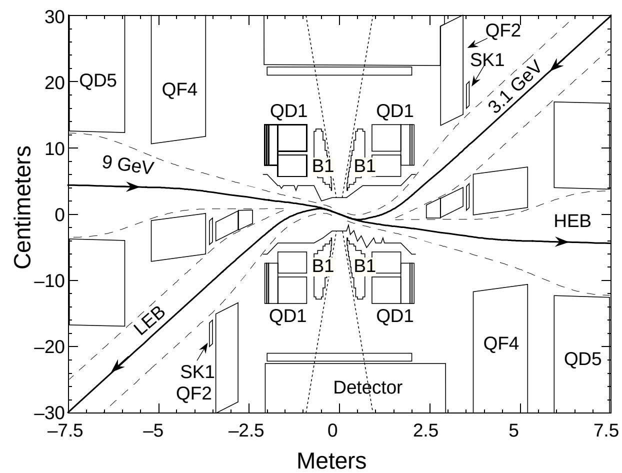

Figure 1. Layout of the interaction region of the PEP-II B-factory. The vertical scale is highly exaggerated. The detector for PEP-II is offset in z by 37 cm in the direction of the HEB.

2 DETECTOR BACKGROUNDS

The detector in a B-factory must be protected from two main beam-related backgrounds, synchrotron radiation and beam-gas bremsstrahlung. These backgrounds are controlled through the use of masks located near the detector or just upstream of the detector. I make a distinction between masks and collimators as follows. Masks are beam aperture limiting devices that are generally used near or just upstream of the collision point to block or absorb specific backgrounds. Collimators are aperture limiting devices that are designed to limit the overall range of the beam particles. They limit the maximum transverse size of the beam and the maximum energy spread of the beam particles. Usually, collimators are located farther from the collision point since they concentrate on screening out particles that can travel several times around a ring before escaping and striking the beam pipe.

*Work supported by U.S. Department of Energy, under contract number DE-AC03-76SF00515.

2.1 *Synchrotron radiation masking*

The beam separation scheme of the PEP-II design generates strong bending radiation just upstream of the collision point. This radiation must be blocked from striking the detector beam pipe. The radiation generated by the beams as they go through the powerful B1 magnets does not strike any of the upstream masks or beam pipes. However, the radiation produced by the LEB as it travels through the QD1 magnet must be intercepted by masks before the radiation can strike the detector beam pipe.

The QD4 magnet is placed about 14 mm off-axis from the HEB orbit. The bending of the HEB by the off-axis QD4 redirects the radiation produced by beam particles at large transverse orbits (many beam sigmas) as they go through QF5 from striking the inside surfaces of the masks near the IP. The beam pipe of the detector is a thin tube of beryllium and is very transparent to x-rays. Just outside of the Be beam tube is a silicon vertex detector that is sensitive to x-rays; the vertex detector is concerned about occupancy as well as radiation damage. Figures 2 and 3 show the bend radiation fans for the LEB and the HEB near the collision point.

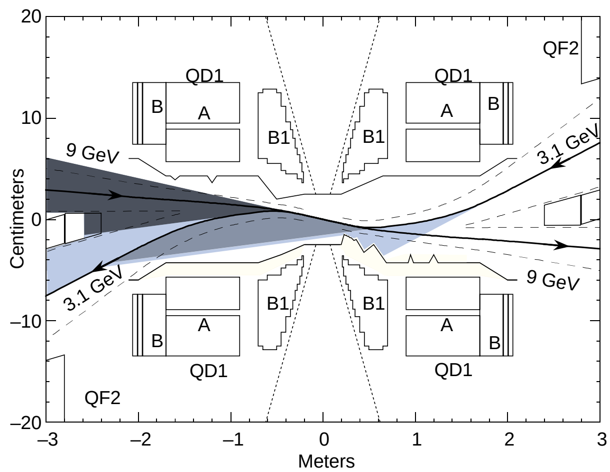

Figure 2. The bend radiation fans generated by the LEB as it travels through the interaction region. The shading of the fans is a measure of the intensity of the radiation. The darker the shading the more intense the radiation.

In addition to blocking the upstream bend radiation, the masks also prevent the radiation produced by beam particles out at large transverse distances from striking the beam pipe. The primary source of synchrotron radiation background for PEP-II is from photons that strike close enough to the tip of the masks to scatter through the tip and strike the detector beam pipe. Nevertheless, the photon rate from large transverse beam particles (out in the beam tails) can be quite high if the particle density is high enough. There is a great deal of uncertainty about the particle density in these beam tails. The density depends on several not fully understood mechanisms that can push particles out into the tails. The beam-beam

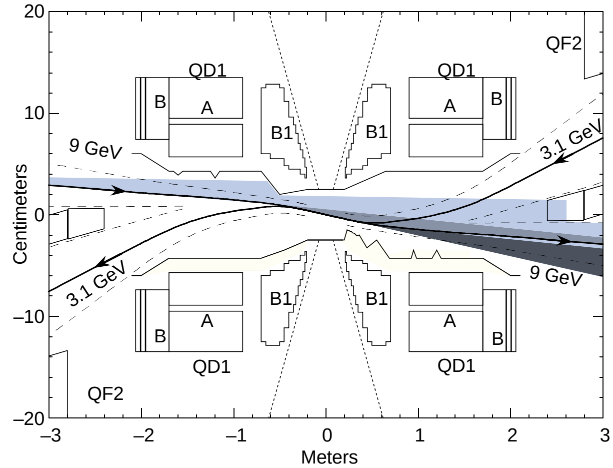

Figure 3. The bend radiation fans generated by the HEB as it travels through the interaction region. The more intense radiation fans have a darker shading. The very intense radiation fans produced in the B1 magnets does not strike any nearby surfaces and is absorbed in a dump that is about 15 m away.

collision is one such mechanism and another is gas-scattered beam particles that are still inside the energy and/or dynamic aperture of the accelerator. The exact parameters that determine the distribution of the beam tails are very accelerator specific. A study of the beam tails in the CERN LEP accelerator has been made and the results are in rough agreement with the tail distributions used in the B-factory design.[4] For synchrotron radiation background studies, the PEP-II design models the beam-tail distribution as another, lower amplitude, gaussian with a larger beam sigma than the nominal beam gaussian distribution. This second gaussian has a particle density at the 10σ limit that determines a beam life-time of about one hour assuming there is a physical aperture at the 10σ limit.[5] Figure 4 shows the beam tail distributions used in the calculation of detector backgrounds from synchrotron radiation. The backgrounds are calculated using the maximum emittance allowed by the accelerator design for each beam. This emittance is also used to calculate the beam-stay-clear (BSC) for each beam. The maximum total emittance used for the LEB is 100 nm-rad and for the HEB is 50 nm-rad.

2.2 *Lost beam particles*

Beam particles can scatter off of gas molecules in the vacuum chamber in two ways: beam-gas-bremsstrahlung (BGB) and coulomb scattering. In BGB, the beam particle loses energy and emits a photon with the photon energy and the scattered beam particle energy nearly adding up to the original beam energy. In coulomb scattering, the beam particle scatters elastically off of the gas molecule changing the trajectory of the particle but leaving the particle energy intact. In BGB, the photon energy spectrum falls off as 1/k so the scattering rate is highest

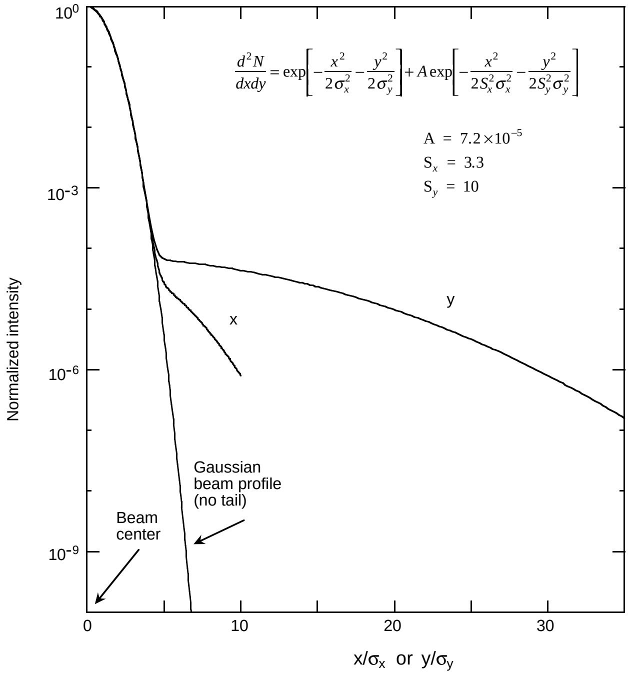

Figure 4. The beam tail distribution used in the calculation of the synchrotron radiation backgrounds for the BaBar detector in PEP-II. The model assumes the tails are cut off at 10σ in x and 35σ in y.

for the lowest energy photons. Since photons travel in straight lines, only those interactions sufficiently close to the detector have a photon as part of the background source. The off-energy beam particles can travel through some portion of the magnetic lattice of the machine before striking the beam pipe near the detector and generating electromagnetic showers that produce backgrounds in the detector. In the PEP-II design, an energy loss of at least 2% is needed before the lost particle will strike the beam pipe near the detector. For coulomb scattered lost particles a minimum scattering angle of 0.33 mrad is needed before the particle has a chance of striking near the detector beam pipe.

Masks are installed upstream of the detector (from 10 m to 60 m) to clip off lost particles before they can strike the beam pipe near the detector. These masks are placed as close to the beam as possible (right up to the BSC) and hence the effectiveness of these masks is determined by the transverse size of the beam.

3 BEAM COLLIMATION

The background studies for the PEP-II B-factory assume that there are no particles beyond the 10σ limit in transverse dimensions as well as in energy. In the vertical dimension, the 10σ value is computed when the beam is fully coupled (half of the total emittance is in the vertical dimension). With the nominal coupling of 3%, this corresponds to about 35σ. This extra room accounts for the ring dynamic aperture needed for the injected beam since the vertically injected pulse enters the ring at about 8 fully coupled beam sigmas or 28 nominal beam sigmas.

3.1 Beam particles beyond 10σ

If there is no beam collimation then the particles in the beam tails extend out either to the limits of the dynamic aperture or until a physical aperture is encountered. The physical aperture of the beam pipe near the IP in the PEP-II B-factory is designed with a BSC of 15σ plus an additional 2 mm for closed orbit distortion. However, the beam lines in the rest of the two-ring accelerator have a fairly large physical aperture (generally > 35σ_x uncoupled and 30σ_y fully coupled except in the injection region). Therefore, without collimation, the interaction region is one of the few tight spots in the accelerator. In addition, the beta functions are larger in the interaction region than anywhere else in the ring for both beams. This makes it much more likely for off-energy particles to escape in this region and strike a local beam pipe thereby generating backgrounds in the detector.

3.2 Synchrotron radiation from particles beyond 10σ

The synchrotron radiation masking design has been optimized with the assumption that there are no beam particles beyond 10σ in x and 35σ in y. Table 1 summarizes the change in background rate in the detector for cases in which there are beam particles beyond the design limits.

Table 1. Summary of the effect on backgrounds from synchrotron radiation when beam particles exist beyond the design values of 10σ_x and 35σ_y.

Case	Photons/collision > 4 keV that strike the detector beam pipe	Ratio to nominal	Primary source
Design	10	1	mask tips
11σ_x, 39σ_y	10	1	mask tips
12σ_x, 42σ_y	10	1	mask tips
13σ_x, 46σ_y	370	37	HEB direct
14σ_x, 49σ_y	4200	420	HEB direct
15σ_x, 53σ_y	15400	1540	HEB direct

The photon rates shown in Table 1 depend exclusively on the assumed particle density in the high sigma regions. For this study, I take a conservative approach and assume that the beam life-time is determined by the particle density at the edge of the distribution. Therefore the beam-tail particle density remains constant at the beam edge. This is done by broadening the beam-tail sigma while holding the beam-tail amplitude constant.

3.3 Lost beam particles beyond 10σ

Lost particle simulations used to study backgrounds in electron storage rings have not studied lost beam particles that survive for more than one turn and, in most cases, only lost beam particles produced just upstream of the detector have been analyzed. The PEP-II design included lost particle production as far upstream as one sixth the circumference of the ring (about 370 m). As stated earlier, lost particle background studies found that a beam particle had to lose at least 2% of the beam energy before the particle would be able to strike the beam pipe near the detector. The 10σ energy aperture for PEP-II is 0.6%. If no beam particles are allowed to be outside the 10σ energy cut either through the use of collimators or because of the dynamic aperture of the accelerator, then only those lost particles produced just upstream of the detector can contribute to background calculations. However, if the dynamic aperture is large enough to include particles with a large energy deviation and no collimation has been installed, then beam particles can have a significantly increased energy distribution. Particles out at the high sigma energy values may be stable enough to go around the accelerator several times before getting lost. If this is the case, the interaction region is one of the more likely places for these particles to finally strike a beam pipe.

The PEP-II HEB was first commissioned last June 1997 and was further commissioned last September and October. Lost particle backgrounds were measured in the interaction region and the rates were significantly higher than expected. Some preliminary tests were made to discover the source of this background by turning off sections of pumping around the ring. It was found that the entire ring was contributing at some level to the observed background. The ring dynamic aperture was found to be reasonable (the accelerator matches the model quite well) and no collimators were as yet installed. The lack of energy collimation allows beam particles to populate the energy space out to the edge of the dynamic aperture. It can take several turns for these particles to be finally lost with the odds being high the particle will be lost in the interaction region. This coming January 1998 an energy collimator will be installed and it is hoped that this will make a significant difference in the background level measured in the interaction region.

4 SUMMARY

Collimation of the PEP-II B-factory stored beams is an important aspect of the overall design of the control of detector backgrounds. The masking of the detector beam pipe from upstream synchrotron radiation sources depends on the maximum transverse size of the beam. The masks are positioned so as to shield the detector beam pipe from radiation generated both by upstream bend magnets and by large transverse beam particles as they travel through the final focusing quadrupoles. Beam particles that are beyond the design cutoff can increase backgrounds in the detector by as much as a factor of a thousand.

Lost beam particles (especially beam-gas bremsstrahlung) produce a tail of off-energy particles that will go out to the limit of the dynamic aperture of the accelerator in energy space. This limit can be much larger than the 10σ limit assumed in background models. The off-energy particles near the aperture limit are not necessarily accounted for in background models since these particles can travel around the ring several times before they are lost. The class of particles that do get lost this way are likely to leave the machine in the places where physical apertures are close to the beam orbit. This is usually in one of two places: the injection region where physical apertures are close to the beam and in the interaction region where the large beta functions push the beam out to near the physical aperture.

Beam collimation helps control detector backgrounds by cutting off the long non-gaussian beam tails in energy and in the transverse beam dimensions. Good collimation produces a better understood beam profile in transverse space and in energy space which, in turn, makes the accelerator more amenable to modeling and computer simulations leading to a more accurate understanding of the dynamics of the accelerator.

5 ACKNOWLEDGMENTS

I would like to thank the organizers, Nikolai Mokhov and Dick Carrigan for inviting me to the symposium. I found the conference very interesting and pleasant. The experience greatly helped to clarify my own thinking about collimation and detector backgrounds.

6 REFERENCES

[1] "PEP-II an Asymmetric *B* Factory," Conceptual Design Report, CALT-68-1869, LBL-PUB-5379, SLAC-418, UCRL-ID-114055, UC-IIRPA-93-01, June 1993.

[2] M. Sullivan, *et al.*, "Interaction Region Design at the PEP-II *B* Factory," European Particle Accelerator Conference, p. 460 (1996).

[3] M. Sullivan, *et al.*, "Results from a Prototype Permanent Magnet Dipole-quadrupole Hybrid for the PEP-II B-factory," Proceedings of the Particle Accelerator Conference, held in Vancouver, B.C. (1997).

[4] I. Reichel, *et al.*, "Observation and Simulation of Beam Tails in LEP," Proceedings of the Particle Accelerator Conference, held in Vancouver, B.C. (1997)

[5] M. Sands, "The physics of Electron Storage Rings, an Introduction," SLAC-121 (1970).

IV. BEAM EXTRACTION

Proton and Pb Ion Beam Extraction Experiments with Bent Crystals at the CERN-SPS

K. Elsener, W. Herr and J. Klem
CERN, Geneva, Switzerland

Abstract

Extraction of particle beams from the CERN-SPS using bent silicon crystals is described. A summary of the early results is given. Emphasis is on the recent experiments, in particular on the energy dependence of proton extraction at 14, 120 and 270 GeV. 'U-shaped' crystals of different thickness and with a different miscut angle have been compared at 120 GeV. Non-linear excitation of the beam was used in one experiment, with the aim to achieve larger impact parameters - the results show a particular behaviour in the tails of the beam. Finally, the first experimental result on extraction of a 22 TeV fully stripped Pb ion beam with a bent crystal is also described.

1 INTRODUCTION

Following the early experiments in Dubna and Protvino [1, 2], proton beam extraction experiments with bent silicon crystals started at CERN in 1992 in the framework of the RD22 experiment. The aim at that time was to proof that 10% extraction efficiency in such a scheme is feasible, and to investigate the possibility of a parasitic extraction with a bent crystal to a fixed target beauty physics experiment (LHB) at the LHC collider.

After LHB was abandoned in favour of a collider beauty physics experiment, the extraction studies with bent crystals were continued as machine development experiments. During five years, seven different silicon crystals have been used, three different beam energies (14, 120 and 270 GeV) were explored for protons and a fully stripped 22 TeV Pb ion beam was extracted for the first time with a bent crystal.

In all these experiments, the extracted beam was observed after a very short setting up period, and efficiencies of 10% and more were readily obtained. Due to the channeling effect, the extracted beam has a very small divergence in the deflection plane and a beam transport system could thus be matched for a fixed target facility. Extraction by means of a bent crystal, therefore, is a tool which is easy to use and can be applied at any high energy circular accelerator. This method allows parasitic fixed target operation in parallel with collider running, using halo particles otherwise lost in collimators.

The experimental technique and the early results from the CERN-SPS proton extraction experiments with bent crystals are described in a review paper [3] as well as in [4, 5, 6, 7, 8]. In this contribution to the International Symposium on Near Beam Physics, we concentrate on more recent results, such as the energy dependence of the extraction process, and present a number of as yet unpublished results obtained with protons.

Extraction of heavy ions with bent crystals has been proposed and theoretical estimates have been given [9], but no experiment has ever been performed. At the SPS, the fully stripped Pb ion beam at 270 GeV per charge, i.e. 22 TeV, could be used for a short test. Again, extracted beam was readily observed at intensities corresponding to roughly 10% extraction efficiency. The Pb ion results are reported in section 7.

2 EXPERIMENT

For a detailed description of the extraction experiment at the CERN-SPS, the reader is referred to [3]. The methods of beam excitation, the mounting, bending, installation and pre-alignment of the crystals with the help of laser light reflection, as well as the different detector systems used to observe the extracted beam are described there in detail. Figs. 1 and 2 show a schematic view of the most important parts of the system.

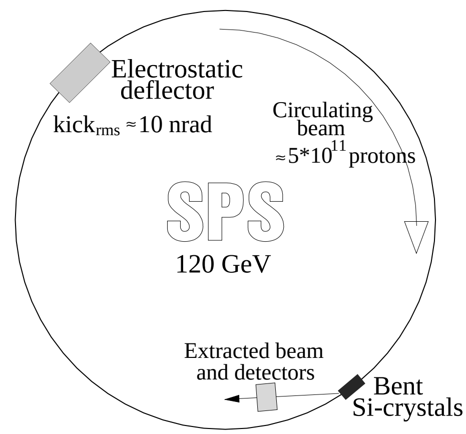

Figure 1: Extraction experiments as performed at the SPS. The typical kick strength at 120 GeV as produced by noise on the electrostatic deflector (damper plates) is indicated. The detectors are shown in more detail in Fig. 2.

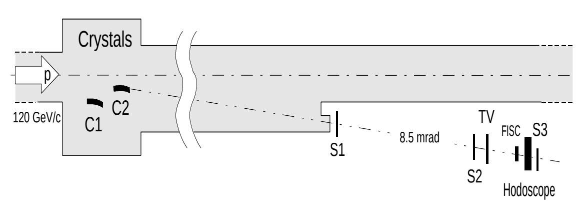

Figure 2: Schematic top view of the experiment at the SPS. Two crystals can be used to extract beam through a thin window to a set of detectors. For more details, see text and [3].

Two crystals can be used alternately to extract particles from the beam halo towards the inside of the accelerator, by an angle of 8.5 mrad. (It was found very useful to have two crystal positions available - this allowed to compare two different crystals in exactly the same beam conditions - see e.g. section 5). Three scintillators in coincidence (S1, S2, S3) are used to measure the extracted beam rate during angular scans. 'TV' indicates a luminescent screen viewed by a CCD camera. The scintillator hodoscope allows to measure horizontal and vertical profiles with a 1 mm resolution, while the FISC (FInger SCintillator) gives the horizontal profile with 0.2 mm resolution. For detailed measurements of extracted beam profiles, and to determine the (background subtracted) extracted beam intensity, the hodoscope was used in all proton runs. In the Pb ion run, only S1-S2-S3 and the digitised profiles from the luminescent screen were available (see section 7).

The evaluation of the horizontal and vertical profiles gives two accurate, independent measurements of the extracted beam intensity, and good agreement was found. Together with the measurement of the circulating beam by BCT's (beam current transformer), a direct and precise measurement of the extraction efficiency can thus be obtained. We define the efficiency of the extraction process as the ratio of the number of extracted particles I_{extr} to the number of particles lost from the circulating beam I_{lost}, i.e. we make the assumption that all particles are lost due to the presence of the crystal:

$$\epsilon_{extr} = \frac{I_{extr}}{I_{lost}} \tag{1}$$

The extraction efficiencies reported here can therefore not be compared to the ones obtained by the Fermilab experiment, where a reduction in a background counting rate rather than the extracted beam intensity is used to determine the efficiency, as reported in [10].

In a typical extraction experiment, the SPS beam is brought into coast at the desired energy, and is scraped with vertical collimators to an intensity of some 5*10^{11} circulating protons. The crystal is placed at e.g. 10 mm distance from the centre of the beam, and diffusion is created by a white noise voltage on a pair of electrostatic plates (dampers). Once particles start reaching the crystal, angular scans using the goniometer are performed with the crystal in order to find optimal alignment. Finally, for the best angular setting, i.e. the highest extracted beam intensity observed, and after the waiting time needed to reach a true 'steady state', the extraction efficiency is determined as described above.

3 SUMMARY OF EARLIER EXPERIMENTAL RESULTS

Initial experiments at CERN were conducted using 3 cm long (110) silicon crystals, bent in so-called 'bridge-type' bending devices. Results are reported in [3, 6, 8]. While in the diffusion mode high extraction efficiencies of 10% were readily obtained, the angular scans were found to be very broad and the extracted beam profiles showed strange double-peaks. This was traced back to the bending device used: the 'bridge- type' bender, while attractive for its simplicity, bends a crystal both in the wanted (channeling and extraction) plane, but also in the unwanted opposite plane - this is referred to as the 'anticlastic' bending.

A remedy to this problem was found to be the so-called 'U-shaped' crystals (cf. Fig. 3), developed at ESRF Grenoble, for which the anticlastic bending is minimal. Initial results showed similar extraction efficiencies, and - as expected - the double peaks in the profiles disappeared [3, 7].

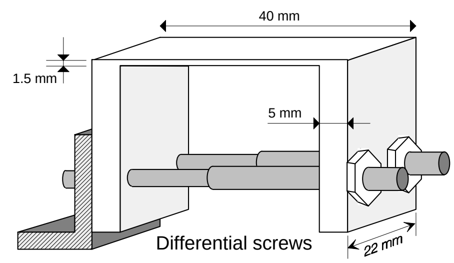

Figure 3: Drawing of a U-shaped crystal with two differential screws used to bend it to the desired angle of 8.5 mrad.

At this point, an important issue was the question of single or multi-pass extraction: when a proton impinges on the crystal with a small impact angle (cf. Fig. 4), it has a high probability to be channeled and extracted. In the alignment scan of the crystal with respect to the beam, such first-pass extraction should show as a narrow peak (typically 30 μrad at 120 GeV). On the other hand, if a proton hits the crystal with a very small impact parameter, it might find itself in an imperfect crystalline region and can not be channeled . It will, however, undergo small angle multiple scattering, continue to circulate in the accelerator and hit the crystal at a later turn, now with larger impact parameter. Wide angular scans as shown below are indirect evidence of such multi-pass extraction.

The first direct experimental proof of the existence (and dominance) of this multi-pass extraction effect was provided at the CERN-SPS and is reported in [4, 5]. In these papers, high efficiency extraction of 120 GeV protons is reported using a crystal covered with a 30 μm thick amorphous layer. First pass extraction is thus prevented, and all protons observed in the extracted beam must stem from multi-pass processes.

At this stage of the experiment, and when comparing the measurements with simulations [11, 12], a number of outstanding questions remained to be answered experimentally: (a) dependence on machine parameters (beam energy, tune, beta function), (b) dependence on crystal parameters (thickness, surface quality, miscut angle). In particular, a reasonable agreement between measurement and simulation could only be obtained if a rather bad crystalline surface or a large (negative) miscut angle of the crystalline planes with respect to the surface is assumed.

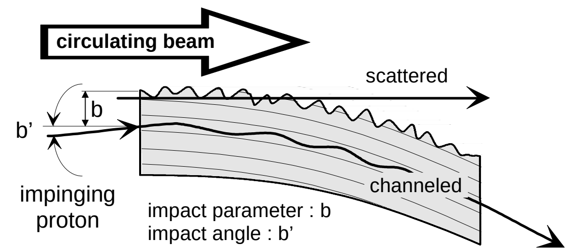

Figure 4: Impact parameter and angle with respect to the crystal surface and the crystalline planes used for channeling and extraction. The surface imperfections are largely exaggerated.

Concerning the quality of the surface, it should be noted that measurements at ESRF using grazing incidence X-ray reflection, thus probing the first few μm, indicate a perfect crystalline lattice at the surface. The roughness of the surface, after polishing it using the standard techniques for X-ray mirrors, is estimated to about 2-3 nanometres. However, some scratches (visible in microscopic pictures and estimated to be about 1 μm deep) have been introduced, e.g. during the installation of the crystals in the accelerator.

Other parameters not fully under control in the experiments concern the details of the beam distribution at the crystal, i.e. very far away from the core of the stored proton beam. This is apparent, for example, from the fact that experimental extraction efficiencies varied slightly from run to run, or from the observation of instabilities in the extracted beam intensities - all of these effects are obviously not accounted for in the simulations.

Given the resources and time available, only a few of the open questions concerning crystals and beam properties could finally be addressed, as is shown in the following.

4 ENERGY DEPENDENCE OF PROTON BEAM EXTRACTION

Among the proton beam parameters which could be changed at the SPS without major modifications, one is the energy of the circulating beam. While 120 GeV has been traditionally the energy to carry out experiments with coasting beam (the SPS is a very linear machine at this energy), beam could also be used in coast at 270 GeV and 14 GeV, the latter being the injection energy. The beam lifetime is of course much worse at this low energy due to the rest gas in the SPS (10^{-7} torr). Under such conditions, the value of I_{lost}, used to calculate the extraction efficiency (cf. eq. 1) had to be corrected by comparing the measured beam lifetimes with and without the presence of the crystal.

The investigation of the energy dependence is crucial for the possible modelling of parasitic beam extraction with a bent crystal at a higher energy machine. While the channeling and beam deflection effects in bent crystals are now well understood [13], the complex interaction between accelerator and crystal,

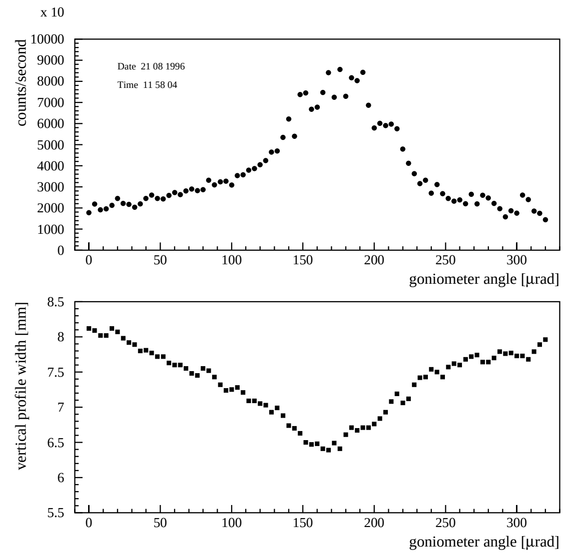

Figure 5: Measured angular scan (top) and vertical profile width during the scan (bottom) for proton beam extraction at 14 GeV.

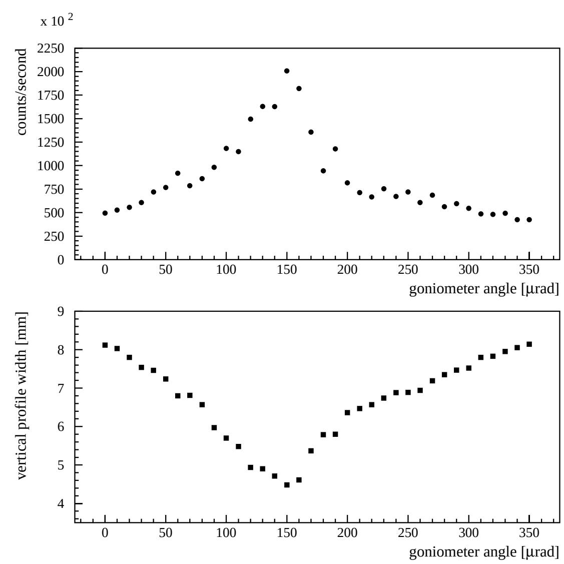

Figure 6: As Fig. 5, but for 270 GeV proton extraction.

demonstrated by the importance of the multi-pass processes, needs more detailed studies. Therefore, not only the peak extraction efficiencies at a given momentum were compared to simulations, but also the extracted beam profile width was studied. Finally, the behaviour of the vertical beam width (not governed by channeling, but rather by multiple scattering and multi-passes) is investigated during angular scans at the three energies. The results obtained are

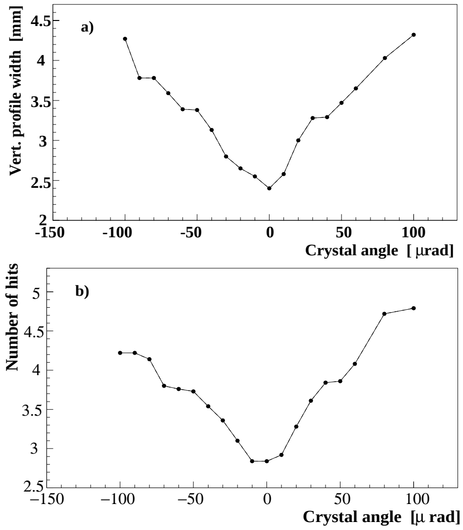

Figure 7: Simulated vertical profile width during an angular scan at 120 GeV (top) and the number of passes (before extraction) through the crystal, as found in the simulation.

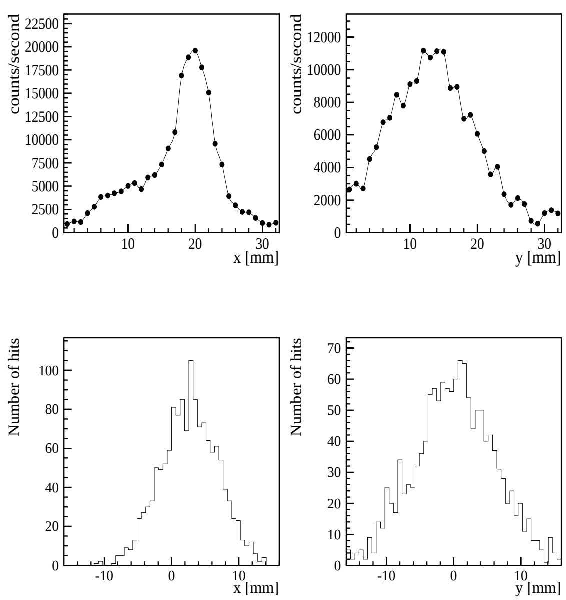

Figure 8: Measured (top) and simulated (bottom) extracted beam profiles, as seen by the hodoscope, for the case of 14 GeV proton beam extraction. The off-set from zero in the measured position is due to the positioning of the detectors, which is not taken into account in the simulations.

described in [11, 14, 15] and are summarised here.

In Figs. 5 and 6, typical angular scans for 14 and 270 GeV proton extraction and the change of the vertical profile width during the scan are shown. Far away from the optimal alignment, more passes (thus more multiple scattering) are required to increase the probability for channeling and extraction. At the peak of the angular scan, two or three passes are sufficient - thus the vertical profile is blown up more at angles far from the best alignment. A similar behaviour is observed at 120 GeV [3]. For the case of 120 GeV, the simulation shown in Fig. 7 confirms the interpretation as discussed here: in the simulation, the number of passes can be recorded. As shown in the lower part of Fig. 7, this number is smallest for the best aligned crystal.

While the horizontal size of the extracted beam profiles is dominated by multiple scattering in the vacuum window and detectors upstream of the hodoscope (cf. Fig. 2), the vertical size is also given by the multi-pass processes in the crystal. It is therefore reassuring to see that the simulation reproduces the measured profiles very well for the three beam energies. For the extreme cases of 14 and 270 GeV, this is shown in Figs. 8 and 9, respectively.

An absolute prediction of the extraction efficiency proved to be very difficult, as it strongly depends on some parameters that are less well known, e.g. the width of the inefficient layer on the crystal and the exact distribution of impact parameter and angle. The prediction can vary by up to a factor of two, depending on the assumptions [11, 12]. In the experimental results, these uncertainties are reflected by scattering of the measured extraction efficiencies from run to run, i.e. depending on the beam conditions.

To minimise this variation in the comparison between experiment and simulations, we proceeded as follows: for the experimental result, the highest measured efficiency at every beam energy is given. The simulation is normalised to the experimental result at 120 GeV. The energy dependence of the extraction efficiency obtained in this way is given in Table. 1.

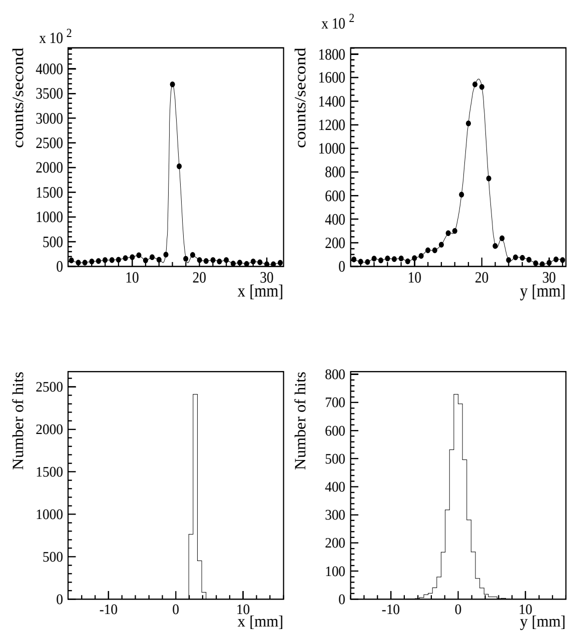

Figure 9: As Fig. 8, but for 270 GeV proton extraction.

Table 1: Measured and simulated extraction efficiencies at three different beam energies. The simulated efficiencies, marked with an asterisk, are normalised to match the experimental value at 120 GeV.

SPS beam energy [GeV]	Extraction efficiency [%]	Simulated extr. efficiency [%]
14	0.55 ± 0.3	0.48*
120	15.4 ± 2.2	15.4*
270	18.6 ± 2.7	18.0*

5 EXTRACTION WITH DIFFERENT CRYSTALS

Given a persistent discrepancy between measured and simulated extraction efficiency, and given the strong suppression of first-pass extraction in our experiments (indicated by wide angular scans), two different crystal types were used for a few short experiments.

First, a thicker crystal of the U-shaped type was tested at 120 GeV. Here, the hope was to be able to extract more beam, i.e. those protons which were initially scattered and would eventually end up at impact parameters larger than the crystal thickness of 1.5 mm. To this end, a 3.5 mm thick crystal was used, with the same length (4 cm) and width (2 cm). This was the thickest crystal in our standard geometry (cf. Fig 3) which is safely below the elastic limit for bending. A horizontal beam profile, measured with the FISC counter with its enhanced resolution, is shown in Fig. 10 .

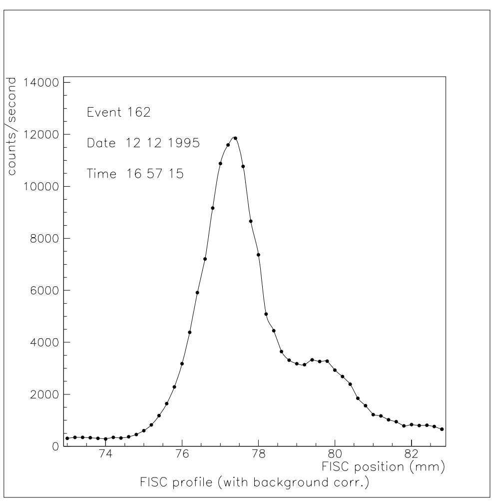

Figure 10: Horizontal profile of the extracted beam measured with the FISC during extraction with a 3.5 mm thick U-shaped crystal. Note the better resolution of the FISC compared to the hodoscope.

There is a clear shoulder on the side opposite to the circulating beam, a somewhat different feature compared to the 1.5 mm thick crystal (see e.g. Fig. 9). However, the measured extraction efficiencies were around 12%, not higher than with the thinner crystal [11], in agreement with the expectation from simulations.

Second, a 1.5 mm thick crystal with a definite positive miscut angle of about 1 mrad was used. Here, the idea was to make sure that no inefficient surface layer be created by the fact that in the first micron or two of the crystal protons are lost due to the fact that the 110 planes point outwards, i.e. leave the crystal surface before the full length of the bend is reached (see Fig. 4). Again, the results were not encouraging, the standard crystal and the one with a deliberate miscut giving the same extraction efficiency.

6 BEAM EXCITATION WITH NONLINEARITIES AND TUNE MODULATION

One of the challenges of the extraction experiments with bent crystals is the possibly damaged surface layer on the crystal. In the diffusion method used for most of our experiments, impact parameters larger than a few microns are very difficult to obtain. On the other hand, the so-called 'kick-mode' does not allow detailed studies due to the very high instantaneous rates in the detector system ([3, 8]). Therefore, a few dedicated tests were performed during which particles were driven out into the halo by non-linearities in connection with tune modulation.

Non-linearities were introduced in the SPS with the extraction sextupoles. At the same time, tune modulation was created by changing the current in a particular quadrupole (this element is used for slow extraction spills in standard SPS operation). Tune modulation together with the nonlinearities causes high diffusion speeds in the tail of the beam, which should give much larger impact parameters at the crystal than the damper noise excitation. However, the behaviour of the protons in the beam tail is not well known and it is very difficult to simulate this experiment.

In these experiments, the tune modulation depth and crystal position were varied and several angular scans were made. The current in the sextupoles was 140 A. The tune modulation was created by a function generator. The frequency of the modulation was 9 Hz and the amplitude was between 100 mV and 400 mV (peak-to-peak 200 mV – 800 mV). This method has been developed earlier and was used extensively for dynamic aperture studies at the SPS (F. Schmidt and W. Fischer [16]).

During standard beam extraction experiments, i.e. when the beam is excited with white noise on the damper plates, one rather wide peak is observed in the angular scans. With nonlinear excitation, the angular scans often have more than one peak. Moreover, in some cases we saw very narrow peaks in the angular scans, indicating a more important first-pass contribution to the extraction process. Also, partially overlapping peaks have been observed. Three selected angular scans are shown in Fig. 11.

Another observation was that the vertical profile of the extracted beam had sometimes a double-peak (Fig. 12).

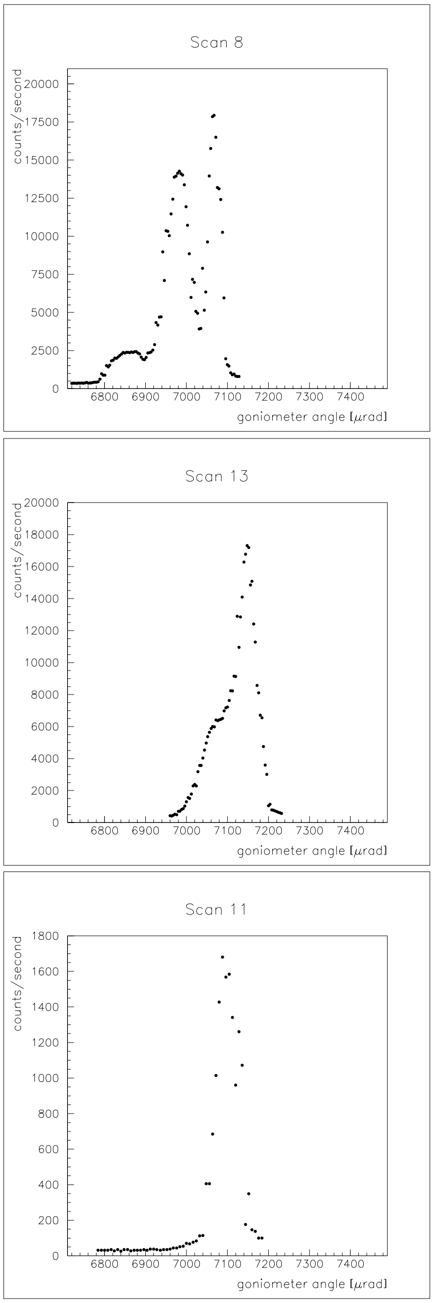

Figure 11: Angular scans when the SPS beam was excited with non-linearities. The beam excitation is unchanged in the three examples, however, the distance of the crystal to the closed orbit was 26, 27.8 and 28.9 mm (top to bottom).

The structure in the angular scan as well as these double peaks seem to indicate a very interesting beam behaviour at large distances from the core of the beam.

In order to verify that the multi-peak angular scans are indeed due to the non-linearities, a comparison was made - on a later occasion - in a dedicated experiment between non-linear excitation and diffusion by small angular kicks (i.e. noise on damper plates). The crystal was left fixed at one position during this test, here at 26.9 mm from the beam.

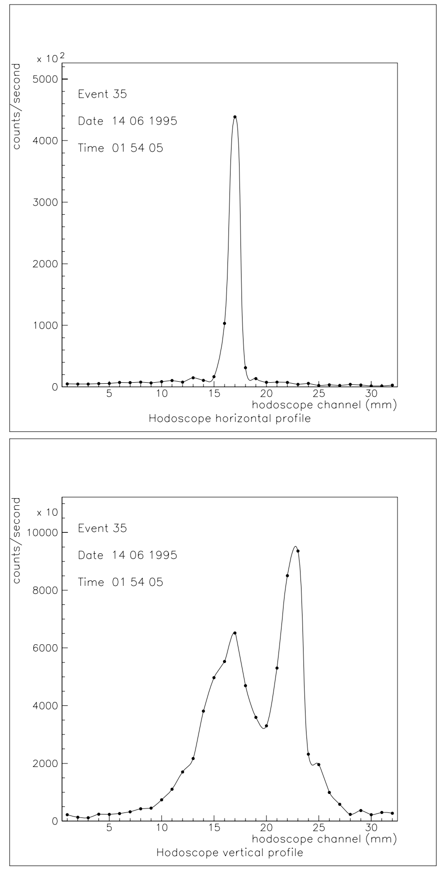

Figure 12: Hodoscope profiles when the SPS beam was excited with non-linearities and tune modulation.

The comparison of the two angular scans observed is shown in Fig. 13. Clearly, the particular shape and width of the angular scans and beam profiles (Figs. 11 and 12). has to be attributed to the nonlinear beam excitation. Moreover, this method of creating high diffusion speed in the tails is found to very sensitive to all machine parameters and thus not easily reproducible from run to run - thus the difference between the angular scans shown in Fig. 13 and 11.

The narrow peaks in the angular distributions (some with FWHM less than 40 μrad) indicated the presence of first or second pass extraction. It was thus tempting to establish an extraction efficiency with the crystal aligned on such a peak. It should, however, be noted that during all the measurements using non-linearities, strong beam losses all around the SPS machine were observed independently of the presence of the crystal. Under such circumstances, it seemed not advisable to try and deduce an extraction efficiency from the observed extracted beam intensities.

In summary, these very preliminary results seem to indicate that a bent crystal used as extraction device can also serve as a valuable beam diagnostics tool, due to its strong angular selectivity. However, as word of caution it should be mentioned that multiple scattering in the crystal and multi-pass extraction can dilute the initial phase space of the

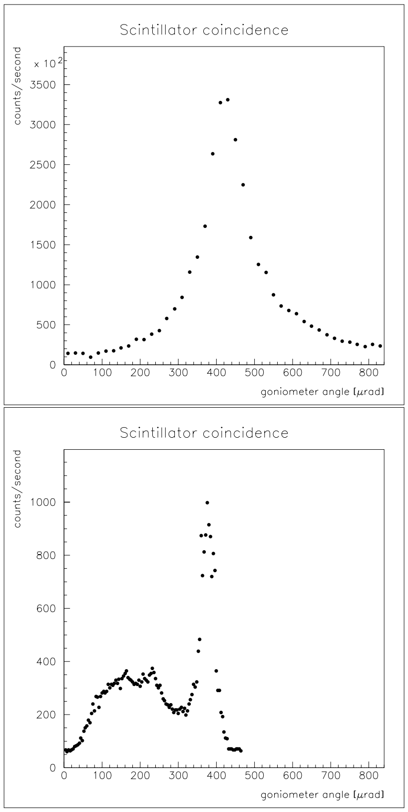

Figure 13: Angular scans measured with white noise (top, step size 20μrad) and with nonlinear beam excitation (bottom, step size 4μrad), shown on the same angular scale.

protons hitting the crystal.

7 EXTRACTION OF A 22 TEV PB ION BEAM

The experimental procedure for the Pb ion extraction experiment at the SPS is similar to the one used for extraction of protons [17, 18]. Here, a stored beam of Pb^{82+} ions is used at 270 GeV/c per charge, and hence the momentum is 22 TeV/c. Ions diffusing out to the crystal located in the halo (about 10 mm from the beam centre) can channel and thus be deflected and extracted, provided the impact angle lies within the critical angle.

The coincidence of the three scintillation counters (cf. Fig 2) is used to count extracted particles, and the luminescent screen allows the real-time observation of the extracted beam. The gain of these detectors was reduced with respect to the proton experiments, thus allowing the suppression of a part of the interaction products stemming from the crystal and surrounding material. Angular scans were taken at different times during the experiment to study the reproducibility. An example is shown in Fig. 14. After the background in such scans of 20 to 25 % is subtracted, the full-width-half-maximum (FWHM) of the scan in Fig. 14 is around 50 μrad, significantly narrower than the ones measured for protons between 14 and 270 GeV/c [14, 15]. One may speculate whether these narrower angular scans are due to a suppressed contribution of multi-pass extraction to the total extracted rate. Profiles of the extracted beam were measured with the luminescent screen and a CCD camera, and could be digitised and stored. Here, the background of light particles (stemming from nuclear interactions) is completely suppressed in the profiles due to the strongly reduced gain. The results can be seen in Fig. 15. The profiles are similar to the ones obtained with the scintillator hodoscope for protons [3, 14]. The vertical beam profile is always found to be wider due to the effects of multiple Coulomb scattering (MCS) and multiple passes through the crystal before extraction. The width of the horizontal profile is given by the critical angle for channeling, while MCS in the material downstream of the crystal contributes equally to the width of both profiles. The number of extracted ions is determined from a threefold coincidence of scintillation counters S1*S2*S3 and the background estimated from the

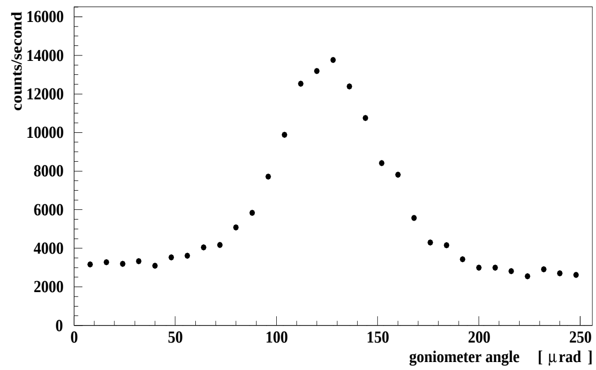

Figure 14: Angular scan for extracted Pb ions from a stored SPS beam, 270 GeV/c per charge (22 TeV/c).

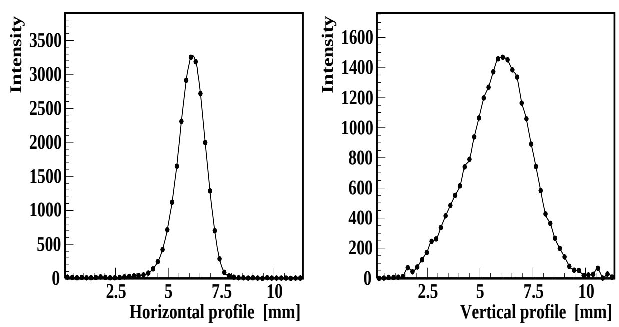

Figure 15: Horizontal and vertical profiles of the extracted Pb ion beam for optimum alignment of the crystal (i.e. at the peak in Fig. 14).

measured angular scans (cf. Fig. 14) is subtracted. The number of particles lost from the beam is determined from the beam intensity measured with a beam-current-transformer (BCT) at 19.2 s intervals. This is equivalent to measuring the beam lifetime. For the calculation of the efficiency we use rather conservative values and estimate a relative error on the efficiencies of approximately 35 - 40 %. This error is larger than reported for protons [3] and is governed by uncertainties on the beam lifetime as well as on the background subtraction. The results of our efficiency estimates are given in Table 2 for four different excitation levels, i.e. different beam lifetimes. For the first four measurements in Table 2 the standard U-shaped crystal (cf. Fig. 3) was positioned at a distance of about 10 mm from the closed orbit. For the last measurement a second U-shaped crystal was used at a larger distance of approximately 20 mm from the orbit. Significant differences were not observed between the two types of crystals. Compared with the measured efficiency from proton extraction at 270 GeV/c, which was about 18% (see above), the efficiencies for lead are about a factor two smaller and the spread of the measured efficiencies is slightly larger. A possible dependence of the efficiency on the beam lifetime (i.e. the diffusion speed) cannot be proven nor excluded.

Table 2: Extraction efficiencies for Pb ions at 22 TeV/c.

Circ. beam intensity (10^7 ions)	Beam lifetime (hrs)	Extraction efficiency (%)
13.0	2.2	4.0±1.5
10.0	0.3	10.0±3.5
6.7	1.2	9.0±3.0
5.0	0.04	11.0±4.0
5.0	0.23	5.0±2.0

8 SUMMARY AND CONCLUSION

At the CERN-SPS accelerator, a long and fruitful series of extraction tests using bent silicon crystals has been performed. Much has been learned concerning the bending and installation of the crystals as well as on many details of the extraction mechanism leading to the observed extracted beams. Recently, protons have been extracted at three different beam energies, 14, 120 and 270 GeV, and the results are compared to simulations. Also, a first experiment to extract ultra relativistic Pb ions with a bent crystal has been performed. All the experience gained during the past five years indicates that the technique is 'ripe' and that a parasitic extraction scheme for a fixed target facility at e.g. the LHC could be designed, if such a facility was requested in a new physics proposal. The extraction efficiency to be expected should be well above the 10% initially obtained at the SPS, and the multi-pass mechanism should help to avoid any sensitivity to the (as yet unknown) impact parameter distribution at the future colliders.

9 REFERENCES

[1] V.V. Avdeichikov et al., JINR Comm. 1-84, Dubna (1984), and Fermilab 80/45.

[2] A.A. Asseev et al., Nucl. Instr. Meth. **A334**, 283 (1993).

[3] K. Elsener *et al.*, Nucl.Instr.Meth. **B119**, 215 (1996).

[4] X. Altuna *et al.*, Phys.Lett. **B357**, 671 (1995).

[5] B. Dehning et al., 1995 IEEE Particle Accelerator Conference, Dallas, 1995.

[6] H. Akbari et al., Phys. Lett. **B313**, 491 (1993).

[7] H. Akbari et al., 4th European Particle Accelerator conference, London, 1994.

[8] S. Weisz et al., 1993 IEEE Particle Accelerator Conference, Washington DC, 1993.

[9] A.D. Kovalenko, A.M. Taratin, E.N. Tsyganov, Preprint JINR E1-92-8, and A.D. Kovalenko et al., JINR Rap. Comm. No.4 (72)-1995.

[10] T. Murphy *et al.*, Nucl.Instr.Meth. **B119**, 231 (1996), A. Asseev et al., FERMILAB-PUB-97/300-E, and T. Murphy et al., contribution to these proceedings.

[11] J. Klem, PhD thesis, Helsinki University of Technology, 1997 (unpublished)

[12] W. Herr, J. Klem, G.Vuagnin, in preparation.

[13] C. Biino et al., Phys. Lett. **B403**, 163 (1997), and U. Mikkelsen, PhD thesis, University of Aarhus (1997, unpublished.

[14] G. Arduini *et al.*, Proc. Part. Acc. Conference 1997, Vancouver, May 1997.

[15] G. Arduini et al., CERN SL report (1997), submitted to Phys. Lett. B.

[16] W. Fischer et al., Phys. Rev. **E55**, 3507 (1997), and CERN SL/95-96 and W. Fischer, PhD thesis, Hamburg University, Germany, and CERN SL/96-10 (AP).

[17] G. Arduini et al., CERN-SL/97-36(AP), IEEE Particle Accelerator Conference, Vancouver, 1997

[18] G. Arduini et al., CERN-SL/97-43(DI), and Phys. Rev. Lett. **79**, No. 20, 1997, in print.

RESULTS FROM BENT CRYSTAL EXTRACTION AT THE FERMILAB TEVATRON

C. T. Murphy and R. A. Carrigan, Jr.†, Fermilab, Box 500, Batavia, Il 60510, USA

Abstract

A recent experiment at the Tevatron has tested the feasibility and efficiency of extracting a low-intensity beam from the halo of a superconducting collider using channeling in a bent silicon crystal. The experiment, Fermilab E853, was motivated by the possibility of applying crystal extraction to trans-TeV accelerators like the LHC. Luminosity-driven channeling extraction was observed for the first time using the 900 GeV circulating proton beam at the Tevatron. The extraction efficiency was found to be about 30%. A 150 kHz beam was obtained during luminosity-driven extraction with a tolerable background rate at the collider experiments. A 900 kHz beam was obtained when background limits were doubled. This is the highest energy at which channeling has been observed.

1 INTRODUCTION

By the early nineties protons had already been extracted with bent crystals from the circulating beams at Dubna, Serpukhov, and the SPS at CERN. Fermilab E853 extended these experiments by seeking to obtain significant parasitically-extracted beam at 900 GeV in a superconducting accelerator. With 10^{12} protons circulating, the goals of E853 were to extract 10^6 proton/s and show that; 1) the luminosity lifetime was not seriously shortened; 2) the crystal could be aligned to the beam quickly; 3) no intolerable backgrounds were created at the collider experiments; 4) diffusion created by some kind of perturbation could create halo with an adequate step size, or jump, to clear the edge region of the crystal (called the "septum"); and 5) measure the extraction efficiency in the diffusion mode. E853 also investigated the relative contributions of first-turn extraction and "multi-pass" extraction, the latter resulting from particles which encountered the crystal on the first turn but were not channeled, and then returned to be channeled on some successive turn.

The original motivation for this experiment was to test a proposal that a beam of 10^8 protons/s could be extracted from the SSC for a fixed target B-Physics experiment. The new equipment for this experiment was funded by the SSC. Despite the demise of the SSC, the experiment remained of interest as a step towards possible applications at both LHC and Fermilab.

The following sections discuss the experiment, extraction observations in the kick mode, multi-pass extraction, diffusion measurements, the efficiency, and summarize the results.

2 THE EXPERIMENT

2.1 Beam line

E853 took place in the C0 straight section of the Tevatron, the normal location of the proton abort line. The abort line consists of a magnetic dogleg that provides a 4 mrad horizontal kick so the abort line can clear the magnets at the downstream end of the long straight section. The middle bend in the dogleg consists of a series of Lambertson magnets. A series of four vertical kicker magnets are used to abort the beam into the field-free region of the Lambertsons. During collider runs, the abort line is not used at 900 GeV, so one of the kicker magnets was replaced by a bent crystal for E853.

A sketch of the beam line geometry of the Tevatron Collider crystal extraction system is shown in Fig. 1. Protons in the halo of the beam distribution which intercept the bent crystal with the correct angle were deflected by 640 μrad upward into the field-free hole in the Lambertsons (see inset, Fig. 1). Protons in the field-free region travel straight into the Tevatron abort line toward the extracted beam detectors.

The crystal was mounted at the upstream end of a 1 m beam pipe with articulating bellows at the ends. Two precision motors (x, y) at each end of the pipe allowed for the alignment of the crystal with four degrees of freedom. The most critical parameter was the alignment of the vertical angle of the crystal with the beam angle, which had to be done to within 10 μrad to match the critical angle of the crystal with the beam angle. Therefore, motors were selected such that the least step in angle changes was 2.5 μrad.

Fig. 2 shows the core of the beam with respect to the crystal. Schematically, beam was "pumped" from the outer edge of the core of the beam into the horizontal halo by some mechanism, where it eventually intercepted the crystal on some turn following the appropriate number of betatron oscillations. Two methods were used to pump the outer edge of the beam into the crystal. In the first method, called "kick mode," a single proton bunch was given a single angular kick which gave a maximum deflection of 0.5 mm at the crystal. In the "diffusion mode" the experiment operated parasitically with p-pbar collider physics experiments. The principal source of pumping was elastic p-par collisions at the two collision points.

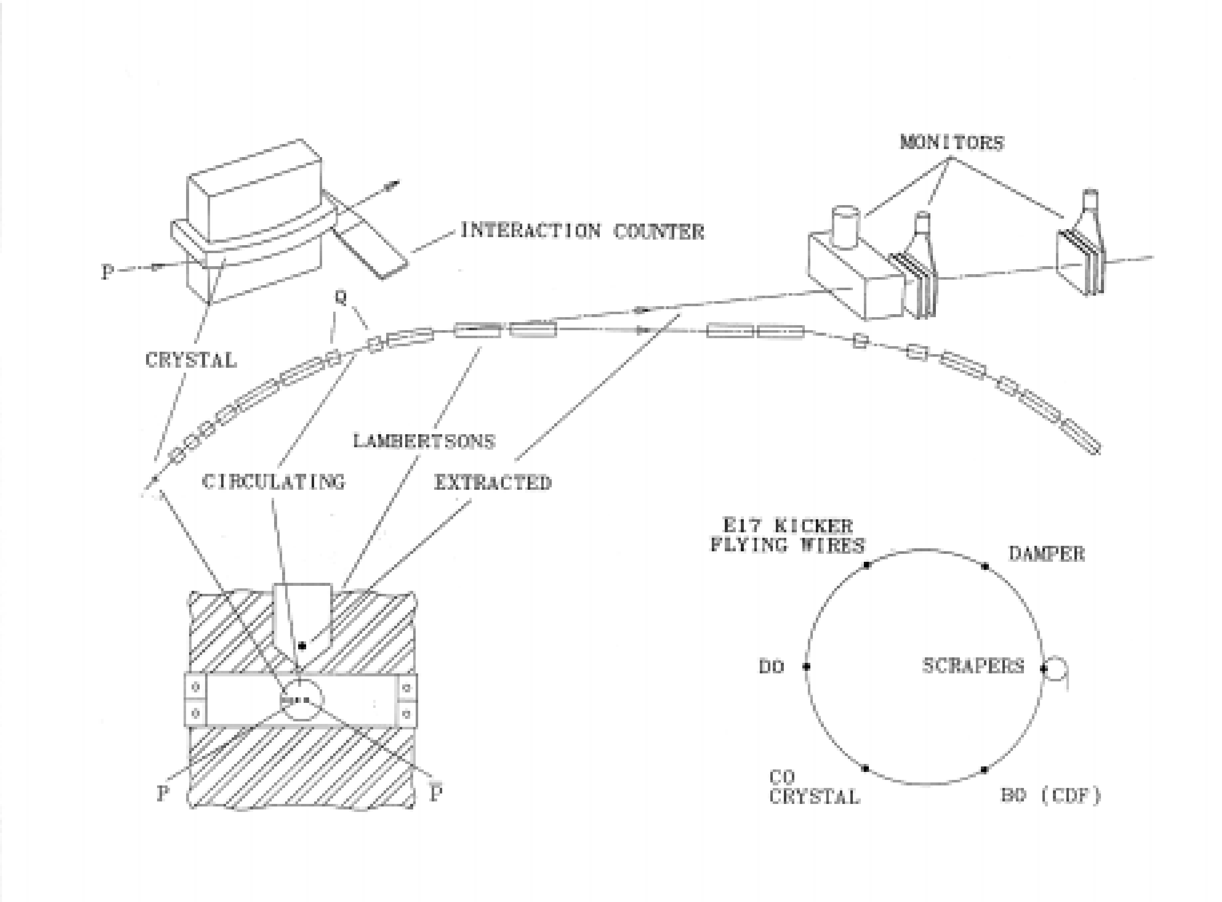

Figure 1: Schematic of the channeling apparatus. The bent crystal deflects protons up through the quadrupoles into the field-free region of the Lambertson magnets. The protons are detected with a system of scintillators in two air gaps separated by 40 m. The inset shows the location of the crystal extraction system, the fast kicker, and the collider experiments at B0 (CDF) and D0.

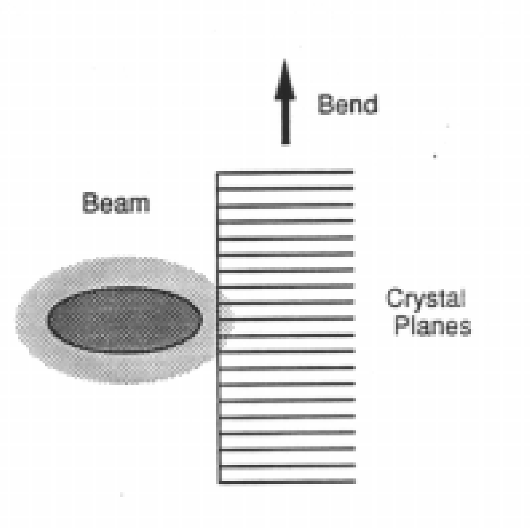

Figure 2: View of the circulating beam looking upstream at the bent crystal. The ellipse represents the halo of the beam schematically. The crystal was bent upwards 640 µrad and was on the outside of the ring. The parallel lines represent the crystal planes.

2.2 Instrumentation

In the extracted particle line (see Fig. 1) there were two air gaps separated by 40 m in which there were six scintillators and four silicon strip planes to count the extracted beam and measure its trajectory precisely (in order to prove that it was channeled beam, not just scattered background). These detectors were removed from the beam line remotely when they were not in use.

Two more scintillators were placed near the crystal outside the circulating beam vacuum tube at 90^{o}. These counters were referred to as "interaction counters" since they monitored inelastic nuclear collisions in the crystal. The signals from the interaction counters were proportional to the beam incident on the crystal.

The beam was also monitored with a CCD camera imagining a fluorescent flag in the first air gap. The camera signal was digitized and stored by a computer as well as broadcast in real-time over the Fermilab video distribution system. A standard Tevatron segmented wire ionization chamber (SWIC) also monitored the *x* and *y* distribution in the second air gap. Further details about the experiment are given in Murphy et al. [1]. and Ramachandran's thesis [2].

2.3 Crystal and bender

A silicon single crystal with dimensions 39mm x 3mm x 9mm was used. Details concerning the crystal quality and characterization are given in Baublis et al. [3]. The crystal was oriented so that the (111) plane was the bend plane. The planar critical angle for channeling at 900 GeV is 6 µrad compared to a vertical divergence of the unperturbed beam in the accelerator at the crystal of $\sigma_V = 11.5$ µrad.

An important quality of the crystal is the flatness of the edge facing the circulating beam (see Fig. 2). Particles intercepting this surface with small impact parameters were bent upward by only part of the total bend angle if they left the crystal because of the non-flatness of the surface. Interferometric studies of this surface indicated that it was flat to within 0.3 µm. This flatness was fully adequate for kick mode, in which the "step size" into the crystal was distributed between zero and 500 µm. In diffusion mode, in which initial step sizes of fractions of a micron were expected, the relevant comparison is with the increase in the betatron amplitude of a particle which had been multiple scattered by, for example, 10% of the length of the crystal. This increase in amplitude was distributed between zero and roughly 10 µm, large compared to the 0.3 µm flatness.

The bending jig was a four-point bender, adjusted by a spring-loaded screw. The bend angle was set by adjusting the screw while measuring the bend angle using conventional optical techniques. The angles of reflection of light reflected from the two flat ends of the crystal which extended beyond the bending jig were measured; the difference was the bend angle. This technique was accurate to about 30 µrad. A subsequent measurement of the bend angle by an interferometric technique gave a bend angle of 642±5 µrad.

The radius of curvature of the central region of the crystal was 3125 cm, so that P/R was 0.3 GeV/cm. The standard plot [4] of centripetal dechanneling loss vs. P/R, gave a bending dechanneling loss of 12%.

3 EXTRACTION OBSERVATIONS IN KICK MODE

During the runs in which extraction was first observed, the Tevatron typically operated at 900 GeV with six equally spaced bunches of protons (there were no antiprotons), each with an initial intensity of 10^{11}. The normalized emittance (1 σ) of the circulating proton beam was 3.33 π/p mm•mrad. This resulted in a beam at the crystal with $\sigma_x = 0.6$ mm, $\sigma_y = 0.32$ mm, $\sigma_{x'} = 6.2$ µrad, and $\sigma_{y'} = 11.5$ µrad, where x and y refer to horizontal and vertical, respectively. The horizontal and vertical tunes of the machine were 20.585 and 20.574, respectively.

In kick mode, one of the six proton bunches was given an angular kick using a Tevatron injection kicker with a pulse length of 3 µs (1/6 of a turn). This kick gave a maximum deflection of 0.5 mm at the crystal. The purpose of this mode was to move a fraction of the beam deep into the crystal, well past the (possibly misaligned) imperfect edge of the crystal facing the beam. In this

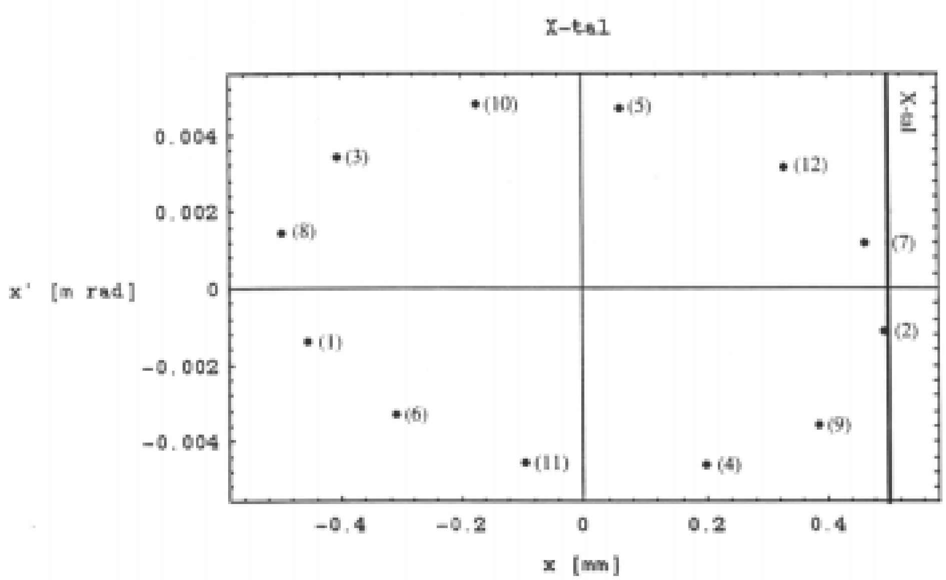

Figure 3: Horizontal beam position and angle on successive turns after a kick. The size of these quantities depends on the magnitude of the kick. Most of the extraction occurs on turns when the beam is near the crystal face, as in turns 2 and 7.

mode, there was substantial channeling on the first pass in which the kicked beam encountered the crystal.

Because of the accelerator phase advance between the kicker magnet and the crystal, on the first turn following a kick, the beam moved away from the crystal (as illustrated in Fig. 3). On turn 2, and again on turn 7, the beam was at maximum amplitude towards the crystal. To first order, sizable extraction was expected on turn 2. Extraction on later turns was anticipated only to the extent that the beam that was not channeled on turn 2, but multiple scattered to a different vertical angle, and then returned to encounter the crystal with the correct angle.

In the first successful E853 observation of crystal-extracted beam, the crystal edge was placed 4.5 mm from the beam centerline, equivalent to 8 standard deviations of the unperturbed horizontal beam size. The beam density was so rare at this distance that no beam was observed to interact with the crystal on the first few kicks. However, after a few hundred turns following each kick, the beam had grown, as non-linearities in the machine gradually spread the beam to fill most of the phase space mapped out by the betatron oscillation shown in Fig. 3. After about 7 kicks, the beam had grown by a factor of 3 in the horizontal plane (and a factor 2.5 in the vertical plane, owing to the strong vertical/horizontal coupling in the Tevatron), in both size and divergence. Thereafter, an equilibrium state persisted in which the crystal edge defined the beam size, and about 2.4×10^9 protons/kick (~ 3% of the total bunch intensity) were lost from the machine on each kick.

In this equilibrium state situation, the vertical angle of the crystal was varied in 10 μrad steps to try to bring the crystal plane into alignment with the beam direction. The pulse heights of various counters in the two air gaps, whose voltages had been decreased several hundred volts so that they were operating in a "calorimeter mode," were recorded during a 1200 ns gate matching the second turn of the selected bunch.

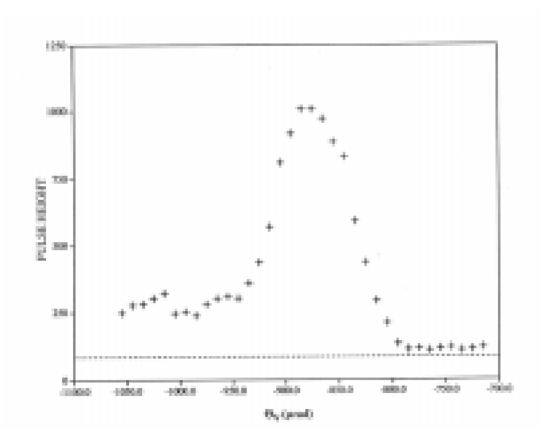

Figure 4: Pulse height in an air gap 2 counter vs vertical angle of the crystal with respect to an arbitrary angle. The dotted line shows the pedestal in the ADC unit with no kick.

A plot of pulse height of a counter in air gap 2 vs. crystal angle is shown in Fig. 4. A clear peak with a width (σ) of 35 μrad is seen. The width of this distribution is due to the convolution of the critical angle for channeling (6 μrad) and the beam angular divergence (20 μrad after the growth noted above).

A picture of the CCD camera image of the fluorescent screen at the peak of the above distribution is shown in Fig. 5. In the central bright spot, the CCD is heavily saturated, so the apparent beam size is much bigger than the true beam σ. The most interesting feature of this image is the narrow "comet tail" descending downward from the central spot. This corresponds to protons which were not bent through the full 640 μrad of the full crystal. This tail could be the result of some combination of several effects. Particles which entered the crystal with a small impact parameter could exit the face of the crystal facing the beam (mentioned above) either because their horizontal angles were directed toward that face or because they were within the "septum width" (irregular region) of that face. Centrifugal dechanneling could occur anywhere in the bent part of the crystal, and dechanneling resulting from multiple scattering could also occur anywhere in the crystal. In fact, the tail extends further downward, but it was cut off by the V-shaped aperture of the field-free hole in the Lambertsons (see Fig. 1).

Information on the beam width at the air gaps was obtained from the CCD camera and thin finger counters. The vertical beam width was $\sigma_V = 0.25$ mm after correcting for the height of the finger counter, compared with an expected width of 0.23 mm. σ_X ranged from 1-2.8 mm. The measurement with the best resolution was based on the CCD camera measurement of the tail. This gave $\sigma_X = 1.3$ mm.

4 MULTI-PASS EXTRACTION

It was mentioned above that contributions to extraction would be observed on turns following turn 2, resulting from multiple scattering of beam not channeled

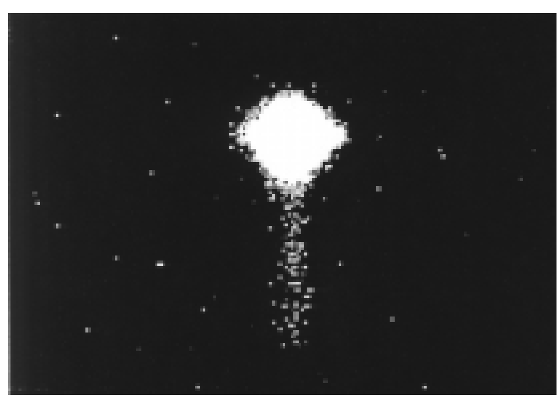

Figure 5: CCD camera of fluorescent screen in the first air gap. The width of the tail (see text) is 3 mm.

in turn 2. Fig. 6 shows what was actually observed on later turns following one particular kick. There are ~ 20% fluctuations from kick to kick. In Fig. 6 these are also compared to an elementary Monte Carlo simulation.

The Monte Carlo [5] takes into account the following effects. An ensemble of particles with Gaussian distributions of positions and angles consistent with the measured values is generated and given a kick. On the second turn, protons in the outer 0.5 µm portion of the distribution encounter the crystal. Those protons within the critical angle are counted as channeled.

The protons outside the critical angle are given an angle change in accordance with a Gaussian distribution with the width of the rms multiple scattering angle for a particle remaining inside the crystal for the full crystal length (11 µrad). This scattering can be seen in the upper right hand box of Fig. 7. These multiple scattered protons are assumed to remain within the aperture of the Tevatron, for the rms scattering angle is within the acceptance of the Tevatron. They are propagated through another turn using the linear transfer functions for the Tevatron and tested again for acceptance within the critical angle. The process is repeated for particles not within the critical angle. Any proton incident on the crystal is given a 9% chance on each pass of having an inelastic nuclear interaction in the crystal and is considered lost on some aperture if a nuclear interaction occurs.

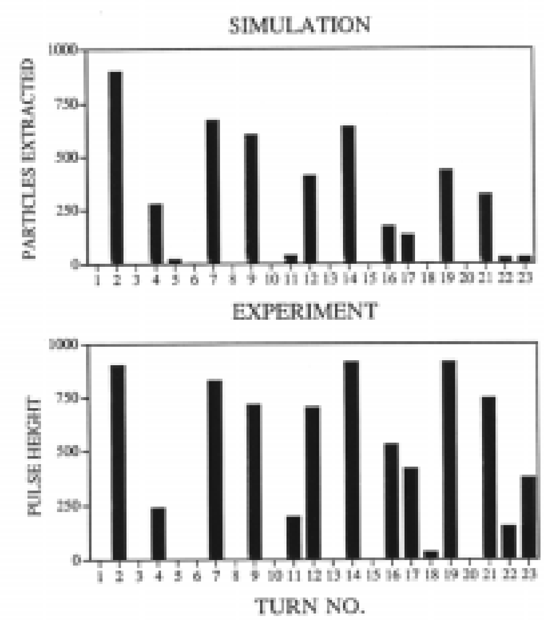

Figure 6: Extraction rate as a function of the turn number from the computer simulation and from the pulse height in a scintillator following a particular kick, renormalized to the simulation result for turn 2. Pulse heights of less than 30 units are indistinguishable from the noise. There are 10% fluctuations in the relative pulse heights from kick to kick. Agreement between the observations and the simulation is good in the early turns but extraction persists during later turns longer than the simulation predicts.

The qualitative agreement between the observations and the simulation on the first 7 turns is thus understood. The minor peaks at turn 4 and 5 are the result of the tail of the protons multiple scattered on turn 2 arriving at the crystal with an angle within the critical angle, even though the un-scattered beam is not close to the crystal. On turn 7 the beam again comes very close to the crystal (see Fig. 3) leading to a large amount of extraction.

There is qualitative, but not quantitative, agreement between the predictions and observations in Fig. 6, in two senses. First, most of the turns predicted to have only a small extraction rate (11, 16, 22, 23) are observed to have a factor two or more of the predicted rate. Second, at ~ 20 turns the simulation indicates that the maximum extraction rate should be ~ 50% of that of turn 2, while the data shows extraction on turns with large extraction rates still equal to that on turn 2. The difference is even more pronounced after ~ 80 turns (not shown), when the observed extraction rate is still ~ 50% of turn 2, but the simulation rate is ~ 2%. These disagreements are not surprising, given the simplistic nature of the simulation.

It is possible that the continuing large extraction rate after 20 turns is a result of non-linearities (not included in the simulation) and fluctuations in the orbit at the micron level. Fermilab has not investigated fluctuations at that level. Other factors not included in the simulation are dechanneling effects, the possibility that a particle incident on the crystal leaves through the crystal side which faces the beam, and vertical-horizontal coupling.

Longer term effects were observed using the CCD camera which was videotaped continuously during study sessions. At the peak of the angular scan the bright flash on the screen (see Fig. 5) persisted for approximately 30 ms. Following that, occasional weak flashes occurred at random time intervals and at the same spatial position as the major portion of the extracted beam. These weak extractions appeared as late as 20 s after the beam had been kicked. The cause for beam to be moved onto the crystal so long after the kick is not understood.

5 DIFFUSION MEASUREMENTS

Extraction rates for diffusion were measured under three conditions: extraction diffusion driven by natural diffusion during proton-only stores, RF noise-driven diffusion during a proton-only store, and luminosity-driven extraction during proton-antiproton stores.

In a typical proton-only store, 10^{11} protons were circulating in six bunches. The extraction rate was 200 kHz. Higher rates could have been achieved by moving the crystal closer to the beam, but with only six bunches, a rate of 287 kHz corresponded to extracting on average one proton per bunch, and the counters could not count more than one particle per bunch.

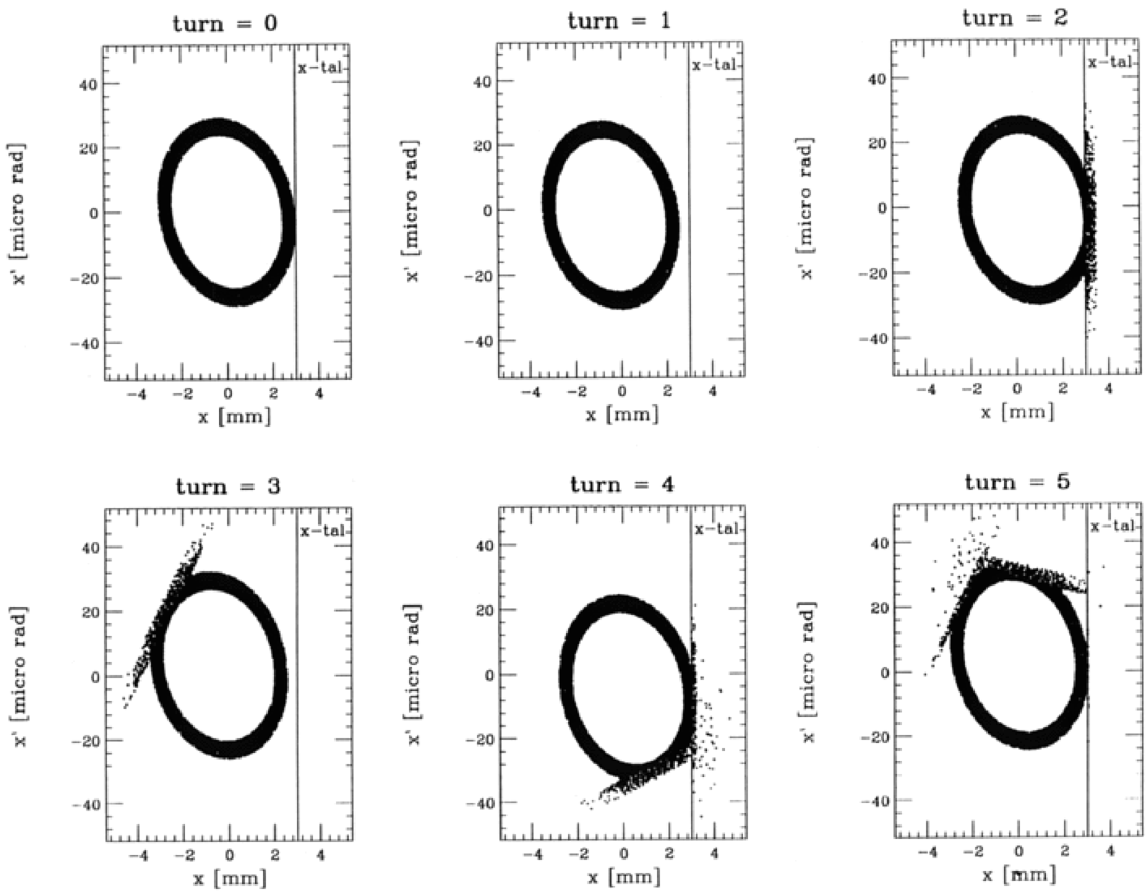

Figure 7: Horizontal phase space distributions as a function of turn number after a kick. The first pass through the crystal multiple scatters the protons which were not within the half angle for channeling (see spread in upper right corner). These multiple-scattered protons come back in later turns with different angles, and some of them are extracted. The hole in the distribution results from suppressing the core of the beam, which will never intercept the crystal.

To mitigate this limitation, a special proton-only store was arranged with 10^{11} protons circulating in 84 bunches. Additional diffusion was induced by transverse RF horizontal noise using an electrical damper, creating an rms diffusion rate at the crystal of 0.023 µm per turn. The extraction rate achieved was greater than 450 kHz.

In the luminosity-driven stores, typically 10^{12} protons were circulating in six bunches. The maximum extraction rate achieved was 150 kHz. In this mode the limitation was the impact of particles scattered from the crystal in creating additional backgrounds for the operating collider experiments. Although the CDF experiment was not affected, the D0 "lost protons" monitor reached the conservative limit set by that experiment at an extraction rate between 50 and 150 kHz.

This limitation was removed during a special store with 36 proton bunches and 3 antiproton bunches during which D0 was not taking data. There were $3x10^{12}$ protons circulating, and an extraction rate of 900 kHz was achieved. The D0 lost proton monitor exceeded its upper limit by a factor of two.

During that same store, the extraction rate was also studied as a function of luminosity. Only 6 of the 36 proton bunches were colliding with antiprotons. Colliding and non-colliding proton bunches were observed during the same counting interval. The extracted beam rate increased by factors of 4 to 8 for proton bunches that were colliding with antiprotons.

6 EFFICIENCY

Another purpose of this experiment was to measure the extraction efficiency. Efficiencies up to 15.5% were measured in a recent CERN 120 GeV experiment [6]. "Efficiency" in this context is defined in two ways. One practical definition, which we call the "extraction efficiency," is the extraction rate divided by the increase in the total circulating beam loss rate after the crystal was inserted. This definition was used by CERN.

The major contribution to lowering this efficiency was from protons which interacted inelastically with the crystal (8.8% of an interaction length) on one of their several passes through the crystal. A second contribution was from protons which dechanneled after being bent through approximately 50 to 350 mrad. A third contribution was from protons which were fully channeled but left the crystal through the beam-side surface because they had a large negative horizontal angle, called hereafter the "surface loss" contribution.

While the numerator was straight-forward to measure, determining the change in the total loss rate from the accelerator was difficult. The variation with time of the loss rate before the crystal was inserted, resulting from various instabilities in the accelerator, usually exceeded the difference between the crystal out and in loss rates. No measurements of this efficiency were possible.

A second way to measure the efficiency is to compare the number of protons that interact with the crystal when its vertical angle is not aligned to the beam with the number that interact when it is correctly aligned for maximum channeling. Fewer interactions were observed when the crystal was well aligned with the beam because the channeled protons did not come close to nucle [7]. We call this the "channeling efficiency" and define it as the difference between the aligned and unaligned interaction monitor rate, divided by the unaligned rate.

The "surface loss" mentioned above does not lower this efficiency, and the dechanneling losses contribute only partially (once a proton has dechanneled after channeling through part of the crystal, it has less than 8.8% probability of a nuclear interaction). Thus we expect this efficiency to be slightly higher than the extraction efficiency (by a factor of about 1.13 in a simple model).

In operation, the interaction counter rates were sensitive to fluctuations arising from such effects as small horizontal fluctuations of the circulating beam. Some of the effects could change in an unpredictable way in the time it took to do a typical Θ_V scan. To mitigate this time dependence, the best measurements were obtained by moving the crystal quickly back and forth from an aligned to a very unaligned vertical angle. An example of such data from a luminosity-driven store is shown in Fig. 8 (top). These data were taken within minutes after the Θ_V scan shown in Fig. 8 (bottom). No time-dependence in the data was discernable.

In two stores in which the extraction was luminosity driven, the channeling efficiencies were 28±8% (Fig. 8) and 35±11%. During the 84-bunch proton-only fill, the efficiency was 32±9%. The errors in these efficiencies are derived from the rms scatter of the many data points about their average value. The simulation [8] predicted an extraction efficiency of 35% for a realistic crystal.

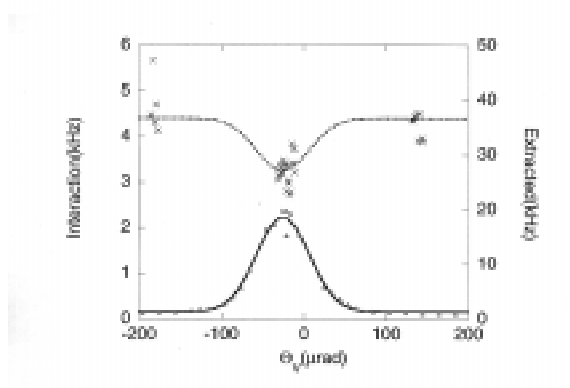

Figure 8: The lower data set (right ordinate) is the counting rate in a coincidence between scintillators in the two air gaps as the vertical angle of the crystal was varied. The solid curve is a fit to a Gaussian plus a flat background. The upper data set (left ordinate) is the counting rate in the interaction monitor at three different vertical angles. The dotted curve is a Gaussian of the same width and central value as the solid curve.

The same simulation program correctly predicted the efficiency measured at 120 GeV at CERN [9].

7 SUMMARY

This experiment has observed luminosity-driven crystal extraction and demonstrated crystal extraction in a superconducting accelerator for the first time. At 900 GeV E853 was the highest energy channeling experiment ever carried out. No heat load on the Tevatron cryogenics from the interactions in the crystal was observed. The extraction efficiency has been measured and found to be significantly higher than at lower energies, but consistent with a simulation incorporating multiple-pass extraction.

A parasitic extraction rate of 150 kHz has been achieved without impact on the collider experiments. A six-fold increase in this extraction rate will occur when the Tevatron changes from 6 bunches to 36 bunches, and additional increases could be realized if additional collimators are installed and the D0 "lost proton" limit can be increased.

Crystal extraction efficiencies are high enough to make this technique an interesting candidate for several applications. One such possibility is using a crystal as an active primary collimator [10]. The use of crystals to extract protons to generate neutrino beams has also been investigated [9]. A continuous 1 TeV proton beam of order 1 MHz could be extracted from the upgraded Tevatron collider into the fixed target areas with no significant impact on collider detector operation [12]. This might be quite useful as a test beam for LHC detectors. One report [13] has suggested that an experiment operating in such a beam could produce 10^7 charm candidates a year. A proposal for a B physics experiment using such a system was considered for the

LHC at CERN. The proposal was rejected because of uncertainties about channeling extraction on a TeV-scale superconducting collider. With the completion of this experiment these concerns should now be significantly reduced.

8 ACKNOWLEDGMENTS

We acknowledge important help received from the Fermilab Accelerator, Computing, and Research Divisions in carrying out this experiment. We thank the SSC Laboratory for financial support. This work was supported by the U. S. Department of Energy.

†The other members of the E853 collaboration are S. Baker (ANL), D. Chen and A. McManus (AT&T), S. Ramachandran (BACG), D. Cline, J. Rhoades, and J. Rosenzweig (UCLA), G. Jackson and N. Mokhov (FNAL), A. Asseev and V. Biryukov (IHEP), A. Taratin (JINR), A. Bogacz (JNAF), V. Golovatyuk (Lecce), J. A. Ellison (New Mexico), A. Khanzadeev, T. Prokofieva, V. Samsonov, and G. Solodov (PNPI), E. Tsyganov (Southwestern Medical Center), B. Newberger (Texas), H.-J. Shih (Affiliated Computer Services), W. Gabella (Vanderbilt), and B. Cox (Virginia).

REFERENCES

[1] T. Murphy, et al, Nucl. Instr. and Methods **B119**, 231 (1996).
[2] S. Ramachandran, PhD thesis, UCLA (1997).
[3] V.V. Baublis, et al., Nucl. Instr. and Methods **B119**, 308 (1996).
[4] R. Carrigan in "Relativistic Channeling," eds. R. Carrigan and J. Ellison (Plenum Press, New York, 1987) p. 347 or "Crystal Channeling and Its Application at High Energy Accelerators," V.M. Biryukov, Y.A. Chesnokov, and V.I. Kotov (Springer, Berlin), 1997.
[5] S.A. Bogacz, D.B. Cline, and S. Ramachandran, Nucl. Instr. And Meth. **B111**, 224 (1966).
[6] X. Altuna et al., Phys. Lett. **B357**, 671 (1995)): K. Elsener et al., Nucl. Instrum.and Methods **B119**, 215 (1996).
[7] R.A. Carrigan, Jr., et al., Nucl. Phys. **B163**, 1 (1980).
[8] V. Biryukov, Phys. Rev. **E52**, 6818 (1995).
[9] V. Biryukov, Nucl. Instrum. and Methods **B117**, 463 (1996)
[10] M. Maslov, N. Mokhov, and L. Yazynin, SSCL-484 (1991).
[11] R.A. Carrigan, Jr., Nucl. Instrum. and Methods **B119**, 239 [1996].
[12] R.A. Carrigan, Jr., Fermilab TM-1978 (1996).
[13] D. Christian in "Heavy Quarks at Fixed Target," B. Cox, ed. (Frascati Physics Series), 421 (1994).

Near Beam Physics at IHEP: I. Near Beam Methods of Particle Extraction

A. A. Asseev
Institute for High Energy Physics, Protvino, Moscow region, 142284 Russia

Abstract

Systematic investigations of beam dynamics have made it possible to study the accelerator possibilities for particle extraction. Besides the established methods of extraction new techniques were realized thus providing particle beams for experimental facilities where it is not possible to extract charged particles by the classic methods.

1 INTRODUCTION

Investigations have been carried out at the IHEP 70–GeV proton synchrotron (A–70) with the aim of studying features of beam dynamics during acceleration and extraction. The data obtained were used for the development of new methods of particle extraction which allowed one, without interference with current experiments, to extract beams for new experimental setups.

The new experiments run simultaneously with the existing ones. This significantly improves the efficiency of the accelerator use for physics research due to the increase of the number of simultaneously working setups (by 1.3–1.5 times). This has also increased the duration of beam extraction by $\sim$ 2 times. Realization of the new methods of extraction allowed one to extend significantly the experimental program of the Institute.

2 NON–RESONANT SLOW EXTRACTION

The IHEP program of physics research was supplemented with a number of new experiments which required beams of accelerated protons of intermediate intensity ($10^7 \div 10^{11}$ particles per cycle, ppc). The experimenters placed high demands on the beam parameters. The existing resonant slow extraction system [1] cannot provide the required time structure of the extracted beam in the range of intensities shown.

The main target of our investigations was the extraction of a beam of protons deflected into the aperture of the septum magnets of the slow extraction system by scattering from internal targets. This mechanism of betatron amplitude increase does not introduce non–linear distortions in beam dynamics and provides uniform extraction of particles with a relatively small momentum spread.

A new quality of extracted beam was achieved due to the use of a thin target of carbon material [2]. The beam time structure modulation is decreased by an order of magnitude. An extraction level of $\sim$7–10% was reached. Simultaneous extraction of 70 GeV protons was achieved for any of the experimental setups SPHINX (channel 21), Tagged Neutrino Facility (TNF, channel 23), FODS–2 and SWD (channel 22) and secondary particles ($K^{\pm}$, $\pi^{\pm}$, e^{-}, etc.) of energies 10–60 GeV for 3–4 experimental setups (channels 2, 14, 4, 6, 18, 5N). The duration of the extracted spill can reach 2 s of ~ 10 s of the magnetic cycle.

2.1 Principle of Extraction

There are four different processes (see, for example [3]) which take place when a proton hits a target. They are absorption, elastic scattering, multiple Coulomb scattering and ionization energy loss. Absorption of protons leading to production of secondary particles is the main mechanism of beam intensity decrease during the interaction with an internal target on the flat top of the magnetic cycle. The contribution of elastic nuclear scattering is generally included with inelastic interactions since elastic scattering forces particles to leave the vacuum chamber aperture. As was shown in [4], part of the protons from elastic scattering remain in the region of stable motion for a long time. These particles can also be extracted. Multiple Coulomb scattering and ionization energy loss both change the amplitude and phase of betatron oscillations. Ionization energy losses also shifts the closed orbit of the protons. The sum of these processes causes a blow up and a radial shift of the whole proton beam. It throws particles into septum magnet apertures where they are extracted from the accelerator.

We will show how a target influences the beam dynamics in the accelerator. Only the processes of multiple Coulomb scattering and ionization energy loss are taken into consideration. Elastic nuclear scattering produces an increase of the amplitude of betatron oscillations which deflects particles into the aperture of the first magnetic deflector and consequently kicks them from the accelerator even after a single intersection of a target. Estimates of the significance of such processes are given in [4].

2.2 Effect of multiple Coulomb scattering

Let us imagine that on a phase plane (see fig. 1) normalized for round trajectories (circle 1) a point with coordinates $x_1, \beta x'_1$. Let Θ be the angle of scattering at a certain intersection of a target by a particle and R_0 be its amplitude. Scattering brings the point ($x_1, \beta x'_1$) to the point ($x_1, \beta x'_2$) that is away from the first one by $\beta\Theta$ (β is the β–function of the accelerator).

As a result, we get a new phase region for the scattered particle (circle 2) which reflects its motion with a new amplitude R. From the geometric relations one can see:

$$R^2 = R_0^2 + (\beta \cdot \Theta)^2 + 2\beta^2 \cdot x'_1 \cdot \Theta, \quad (1)$$

After averaging for all the scattering angles one can get an expression for the new amplitude of the particle:

$$< R^2 >=< R_0^2 > + < (\beta \cdot \Theta)^2 >, \quad (2)$$

As it follows from the analogous approach, the particle of amplitude R_0 on a phase plane will have an amplitude after

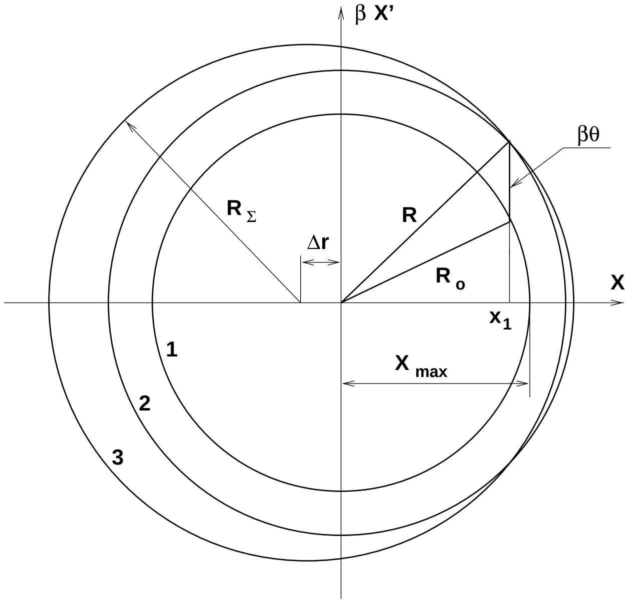

Figure 1: The effect of beam scattering by a target on a phase plane.

n intersections:

$$< R_n^2 >=< R_0^2 > +n < (\beta \cdot \Theta)^2 >, \tag{3}$$

It is seen from (2) that the mean square growth of the betatron amplitude of a particle ΔA_t at the target azimuth after a certain intersection equals:

$$< \Delta A_t >= (< \Delta R_t^2 >)^{1/2} = \beta_t \cdot \Phi, \tag{4}$$

where β_t is the value of the β–function at the target azimuth. The projection of a mean–square scattering angle of a particle on the appropriate direction is expressed by [5]:

$$\Phi = \sqrt{< \Theta^2 >} = \frac{E_s}{p\beta_v c}\sqrt{\frac{D_t}{L_R}} \cdot (1+\epsilon). \tag{5}$$

Here $E_s = 15$ MeV, p is the particle momentum, β_v and c are the relativity factor and speed of light, respectively; D_t, L_R are the thickness of a target along the beam and the radiation length of the material, and ϵ is a correction factor.

One needs to emphasize that if the scattering occurs at the point $X = X_{max}$ (see fig. 1) we have growth of the betatron amplitude of the particle that is determined by the second term of the expression (2), independent of the sign of the scattering angle Θ. This effect of betatron amplitude growth (which is stronger than the effect of orbit displacement due to ionization losses) allowed us to do slow extraction of protons from the accelerator for new experiments.

The dependence for the particle amplitude after interacting with the scattering target is (at the target azimuth):

$$A_{rt}^2 = A_{0rt}^2 + (\beta_t \cdot \Phi)^2, \tag{6}$$

where A_{0rt} is the initial amplitude of the particle. Simple transformations show that the expression for the particle amplitude at the azimuth of the first deflector will be similar:

$$A_{rd}^2 = \left(\frac{\beta_d}{\beta_t}\right) A_{0rt}^2 + \beta_d \cdot \beta_t \cdot \Phi^2, \tag{7}$$

and its growth due to scattering into a target:

$$\Delta A_d = (< \Delta R_d^2 >)^{1/2} = (\beta_d \cdot \beta_t)^{1/2} \cdot \Phi, \tag{8}$$

where β_d is the β–function of the accelerator at the deflector azimuth.

Deflection of a particle into the first deflector aperture occurs when, after some “last” pass through the target, the growth of its amplitude satisfies the condition:

$$|(< \Delta R_d^2 >)^{1/2}| > D_d,$$

where D_d is the thickness of the first septum in the deflector system. This assumes that the septum is placed at the edge of the undisturbed beam envelope.

2.3 *Influence of ionization energy losses*

As we can see both from (2) and fig. 1, the change of a particle’s angle during its motion in the accelerator is transformed into growth of its amplitude. Analogously, a change of momentum by Δp is transformed into a change of the position of a particle due to displacement of the closed orbit in the horizontal plane. After intersecting a target, the energy loss for a particle is expressed by the formula [5]:

$$\Delta E = -\left(\frac{1}{\rho} \cdot \frac{dE}{dx}\right) \cdot D_t[MeV], \tag{9}$$

where $(1/\rho \cdot dE/dx)$ is the specific ionization energy loss in the target material and D_t is the target thickness. A relative change of the proton momentum for a single intersection of the target $\Delta p/p_0$ leads to a displacement of its orbit to the inside at the target and deflector azimuth of Δr (see fig.1). This is expressed by:

$$\Delta r_{t,d} = -\psi_{t,d} \cdot \frac{\Delta p}{p_0}; \tag{10}$$

where $\psi_{t,d}$ is the dispersion function at the target or deflector azimuth and p_0 is the initial momentum of the particle.

If $\psi_t' \sim 0$ (which is valid for the case of A–70),the growth of the betatron amplitude is $\Delta A_r = |\Delta r_t|$. If a target is outside of the beam, the maximum of the particle displacement will be after half a period (or any odd number of semiperiods) of horizontal betatron oscillations. At the first deflector azimuth the maximum of the particle displacement will be:

$$\Delta r_{dmax} = -\left[\psi_d \frac{\Delta p}{p_0} + \left(\frac{\beta_d}{\beta_t}\right)^{1/2} \cdot \psi_t \frac{\Delta p}{p_0}\right] \approx -2\psi_d \frac{\Delta p}{p_0}; \tag{11}$$

This effect can also be used for extraction of particles from the accelerator if the following condition holds:

$$|\Delta r_{dmax}| > D_d, \tag{12}$$

It is important to note that the scattering target needs to be carefully chosen for this case. That is, its mechanical, thermal and nuclear characteristics, as well as the thickness of the target along the beam must be considered. The phase advance of the target placement along the orbit relative to the first deflector is also important. According to calculations in [6] use of the effect allows one to obtain highly efficient ($\varepsilon = 97\%$) slow extraction from the proton storage ring of the Moscow Meson Factory of the Institute of Nuclear Research.

2.4 *Joint influence of scattering and energy loss*

Taking account of the above effects, the amplitude of the horizontal oscillation of particles at the deflector azimuth are given by the formula:

$$A_{rd\Sigma} = A_{rd} + \left(\frac{\beta_d}{\beta_t}\right)^{1/2} \cdot \psi_t \cdot \frac{\Delta_p}{p_0}, \qquad (13)$$

where A_{rd} is the amplitude of the betatron oscillations of the particle (7).

Fig.1 (circle 3) gives a visual impression of the growth of the amplitude of the betatron oscillations and the displacement of the closed orbit due to multiple scattering and ionization energy loss after interaction with a target.

The final expression for the amplitude of the particle oscillations at the first deflector azimuth after a single interaction with a target is:

$$A_{rd\Sigma} = \left[\frac{\beta_d}{\beta_t} \cdot \left(A_{0rt} + \psi_t \cdot \frac{\Delta p}{p_0}\right)^2 + \beta_d \cdot \beta_t \cdot \Phi^2\right]^{1/2}; \qquad (14)$$

The resulting growth of the amplitude after n interactions is important for nonresonant slow extraction. The growth is expressed by the formula:

$$\Delta A_{rd\Sigma} \sim \left[n(\beta_d \cdot \beta_t)\Phi^2 + 2n\left(\frac{\beta_d}{\beta_t}\right) A_{0rt} \cdot \psi_t \frac{\Delta p}{p_0}\right]^{1/2}; \qquad (15)$$

The maximum displacement of a particle at the first deflector azimuth is:

$$\Delta r_{dmax\Sigma} = \Delta A_{rd\Sigma} \pm n \cdot \psi_d \cdot \frac{\Delta p}{p_0}. \qquad (16)$$

The last term of expression (16) has a "+" or "−" sign depending on the coordinate of the septum magnet (inside or outside of the closed orbit). For example, for ED–106, which is placed inside, the growth is added to $\Delta A_{rd\Sigma}$ while for the SM–18 which is placed outside, oppositely, the growth is subtracted.

2.5 *Experimental results*

During the investigations it was desirable to study a principle possibility for extraction of a beam of intensity $\sim 10^{10}$ ppc that is necessary for a new experiment. Earlier, when NRSE (non-resonant slow extraction) of protons was made towards channel 22 such an intensity was not obtained. The next stage of the research was to obtain the maximum intensity that it is possible to reach when all deflectors of the slow extraction system of A–70 were used.

Two schemes were used for beam extraction. The first one, where beam extraction is done by a series of magnetic deflectors (septum magnets) with gradually increasing septum thicknesses which were installed in straight sections (SS) 18, 20, 22, 26, has already been used at IHEP for many years [1, 7]. The first deflector of the scheme which is responsible for the extraction efficiency is the septum magnet SM–18 with a "mechanical" thickness of the septum of ~ 0.5 mm [8].

The second scheme has, in addition to the septum magnet arrangement of the first one, a first element that is an electrostatic deflector (ED). The septum is installed at ED–106 to separate the circulating and extracted beam. It consists of 0.1 mm diameter W–Re alloy wires which are placed down the deflector length at 2 mm intervals. This provides an electric field distribution without "pits" influencing the beam circulation. The dimension of the gap between the anode and cathode of the deflector is 20 mm and the length of the deflector is 3 m [9].

Beam extraction by scheme 1 (with SM–18). NRSE was done in series with high intensity resonant slow extraction (RSE) which used the first half of the flat top of the magnetic cycle and in parallel with generation of secondaries by internal targets for experimental setups for beam lines 2, 4, 5N. After tuning the septum and the magnets, the extracted intensity was optimized by using beam bumps to displace the beam towards septums SM–18, 20. Those bumps were formed with currents in additional windings on magnetic blocks 15, 21 and 16, 22. With a current of ~ 95A in the 15-21 bump, the extracted intensity was optimized with bump 16–22. It was programmed in such a way that the change of the gap between the circulating beam and the septums at SM–18, 20 was compensated due to absorption of particles by the target . Simultaneously, the displacement of the extracted particles was decreased due to energy losses in the target. The current of bump 16–22 was increased linearly in time by ≈ 30A. That is in agreement with the ramp of bumps steering beam on to internal targets and makes the above gaps constant during the extraction period. The corresponding dependence of extracted intensity on the current of bump 16–22 at the end of extraction is shown in fig. 2 (curve 1).

It is seen that an extracted intensity of $\sim 10^{10}$ ppc is reached. After the target of the Tagged Neutrino Facility (TNF) there are $\sim 10^6$ K–mesons (curve 2). This flux was enough to start physics research for the new program.

Beam extraction by scheme 2 (with ED–106). For this case proton extraction continues for the duration of the accelerated beam interaction with the internal targets (≥ 1.7s). Scattered particles are thrown into the ED–106 aperture, then further into SM–18 (with a current reduced by 20%) and extracted towards channel 23 along the well-known trajectory through the septum magnets of the SS–

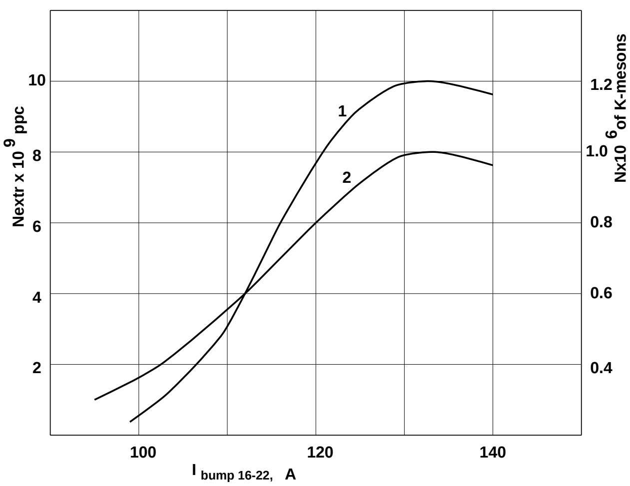

Figure 2: Dependence of beam intensity in channel 23 on the current of bump 16–22 at the end of extraction: 1 is for protons extracted from A–70; 2 is for K–mesons after a target of the TNF setup.

20, 22, 26 chain. The full scheme for extraction is shown in fig. 3 where the beam orbit distortion in the region of ED–106, septum–magnets and targets (T_1, T_2) is presented with curve $1, 1'$ while the trajectory of the extracted beam is shown with curve $2, 2'$.

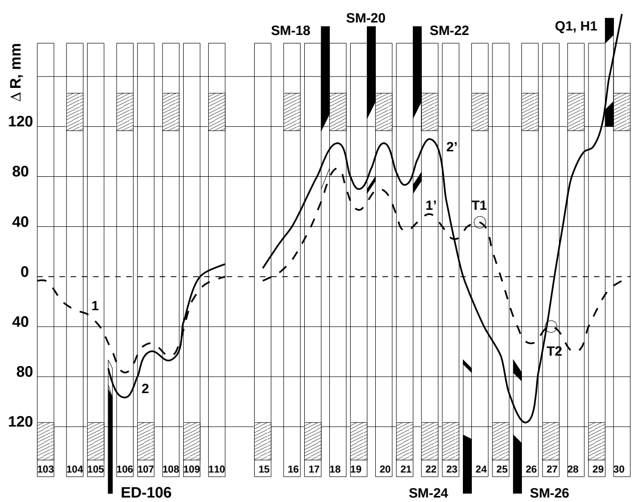

Figure 3: Full proton extraction scheme: ED–106, SM–18, 20, 22, 26 are the electrostatic and magnet deflectors of the extraction system; Q_1, H_1 are first elements of the beam transport system, SM–24 is the septum magnet of the fast ejection system, T_1, T_2 are internal targets of channels 2(14) and 4, respectively. Other targets are beyond the extraction region and are not shown.

At this experiment an extracted beam intensity of $\geq 5 \cdot 10^{10}$ ppc was obtained and at the TNF $\sim 5 \cdot 10^6$ K–mesons was achieved. The order of magnitude of the cross section for K–mesons in this extraction scheme agrees well with the results of the previous experiment.

After obtaining practically full duration for extraction and an intensity for the proton beam high enough to start the research program, the factor which determines the statistical efficiency of a new experiment is the quality of the extracted beam.

Beam quality is obtained by using a “thin” carbon target [2] to form a particle distribution in the beam which permits the beam steering system, with a limited range of frequencies, to minimize ripples in the extracted beam intensity. As a result, there are no high frequencies in the extracted beams (for example, at the frequency of the beam revolution $\sim 200KHz$). At the same time low frequencies (from one to hundreds of Hz) which are in the regulation region for the beam steering systems are significantly suppressed. The level of the ripple is not higher than $\pm(7-12)\%$ of the amplitude of the appropriate signal.

2.6 *Evaluation of the extraction efficiency*

The extraction efficiency for NRSE was evaluated by taking account of the intensity of the primary beam that interacted inelastically with internal targets, the number of particles scattered by targets as well as the intensity measured in the channel. All these data are summarized in the accompanying table.

Table 1: Distribution of accelerated intensity($\times 10^{11}$ppc)

I_Σ	Intensity for internal targets				ΔI	ΔI
A–70	ΔI_{24}	ΔI_{27}	ΔI_{35}	ΔI_Σ	NRSE	EXTR
24.0	11.0	10.0	1.0	22.0	2.0	$\geq 0.5^{*)}$

$^{*)}$Limit of measurements due to saturation of the ionization chamber that was used.

Explanation of the table:

$I_{\Sigma A-70}$ is the accelerator intensity; ΔI_i is the intensity of the beam interacting with targets (i is the magnetic block number where the respective target is placed); $\Delta I_{NRSE}, \Delta I_{EXTR}$ are intensities of particles scattered by targets and extracted, respectively.

The extraction efficiency was evaluated as follows:

$$\varepsilon = \frac{\Delta I_{EXTR}}{\Delta I_{NRSE}} \geq \frac{5 \cdot 10^{10}}{2 \cdot 10^{11}} \geq 25\%.$$

The error of the reported value is not more than 10%. This value of efficiency was obtained for the NRSE mode at the IHEP accelerator for the first time. It is expected that with nominal current for SM-18 an extraction intensity of $\geq 10^{11}$ ppc can be obtained. With the high quality of the extracted beam time structure this meets the requirements of the new research program for physics facilities in channels 21, 22, 23.

The results of numerical estimates of the particle step size in to the aperture due to deflection from scattering by the Be target ($D_t = 3.0$ cm) of channel 2(14) after 1, 4 and 6 intersections, respectively are given in table 2. The additional data necessary for evaluation are (see, for example, [2]):

- Energy loss of particle for a single pass through the target, $\Delta E = 10.86$ MeV,

- $\Delta p/p_0 = -1.55 \cdot 10^{-4}$,
- $\Phi = 0.061$ mrad,
- $A_{0rt} = 5$ mm.

Analysis of the data of table 2 allows one to explain the difference of extracted intensities for the two cases mentioned above (see sections 1.5.1 and 1.5.2).

We have, at extraction through the SM–18, a particle step size after a single target pass of $\Delta r_{dmax\Sigma} = 2.36$ mm. After 4 and 6 passes $\Delta r_{dmax\Sigma}$ is 3.94 and 4.40 mm. Figures 4 and 6 illustrate the behavior. After a number of passes through the target a particle undergoes elastic scattering which results in kicking it into the deflector aperture with a high level of probability[4]. For extraction through SM–18, taking into account the septum thickness of 0.5 mm we see that the real step size of particles in the aperture of a septum magnet is 1.86–3.90 mm.

Table 2: The step size of particles into apertures of ED–106 and SM–18.

Parameters		Block 24	ED – 106	SM – 18
$\lvert\varphi_r\rvert$, m		6.42	5.18	5.29
β_r, m		41.22	26.81	28.0
$\psi_{\Delta p}$, m		3.20	2.48	2.51
ΔA_d, mm (8)	1		2.03	2.07
	4		4.06	4.14
	6		4.97	5.07
$\lvert\Delta r_{t,d}\rvert$, mm (10)	1	0.50	0.38	0.39
	4	2.00	1.52	1.56
	6	3.00	2.28	2.34
$\Delta A_{rd\Sigma}$, mm (15)	1		2.69	2.75
	4		5.38	5.50
	6		6.59	6.74
$\Delta r_{dmax\Sigma}$, mm (16)	1		3.07	2.36
	4		6.90	3.94
	6		8.87	4.40

Considering septum magnet alignment errors, orbit instabilities, beam divergence, and the decrease of intensity of the beam undergoing a scattering, one can see that the possibility of extraction of a high intensity beam through the SM–18 is limited.

In the case of extraction of a beam through ED–106 we have $\Delta r_{dmax\Sigma}$ = 3.07, 6.90, and 8.87 mm for 1, 4 and 6 intersections of a target, respectively. This means that if ED–106 is powerful enough to deflect a beam over the SM–18 septum only, the gap between circulating and extracted beams at the SM–18 azimuth will be $\sim 2.7 \div 8.5$ mm counting the closed orbit displacement to the inside. (We disregard the thickness of the septum of ED–106 here.) Obviously, this means there will be a decrease of particle losses on the septum of SM–18. As a result there will be an increase of the intensity of the extracted beam.

Based on the above estimates the increase of the effective gap between the circulating and extracted beams by 1.5–2 times due to the use of an electrostatic deflector have led to an increase of the extraction intensity by almost an order of magnitude. For scheme 1 this amounts to $\leq 10^{10}$ at extraction while for scheme 2 it results in $\geq 5 \cdot 10^{10}$ ppc extracted towards the setup TNF.

Conclusion. Use of an electrostatic deflector as the first element of the extraction system in the nonresonant slow extraction mode allowed one to reduce particle losses on the septums. Even with the current for SM–18 reduced by 20% from the nominal current one obtains extracted beam intensities of $\geq 5 \cdot 10^{10}$ ppc. Evaluations show that it is possible to extract $\geq 10^{11}$ ppc and also maintain high quality time structure for the extracted beams.

Nonresonant slow extraction is the only method at A–70 so far to extract high quality proton beams of the intensity $\sim 10^{11}$ ppc in parallel with extraction of secondaries for other experiments. Extraction of particle beams of such intensity, long duration and high quality time structure as well as stability of other parameters has not yet succeeded with other well–established methods.

3 EXTRACTION BY BENT CRYSTALS

The effect of particle channeling in bent crystals which has been used at IHEP for extraction of beams for physics experiments [10] has broaded the possibilities for beam extraction from charged particle accelerators. Bent crystals help to solve the problem of beam extraction under circumstances when the traditional well known methods can not be used. An example is lack of adequate space in the accelerator. This extraction method does not require installation of expensive equipment such as the septum magnets and their power supplies required for resonant slow extraction. It can be employed simultaneously with particle extraction by other methods thus increasing the efficiency of accelerator use.

At IHEP crystal extraction was used to deflect the proton beam toward two channels: to channel 14 for the PROZA setup [11,12] and channel 4D for the WES setup [13]. In the first case the 70 GeV beam was used to check an indication of the possible discovery of the previously unknown phenomenon of "scaling asymmetry" [14]. The availability of a beam in channel 4 (for a search for charmed particles) broadens possibilities for both the WES setup and the setups for GAMS and ISTRA that will be spaced along the beam. The possibility of extraction of negatively charged particles with energies of 20-40 GeV in these directions from internal targets has been maintained. A reveiw of the possibility of extraction of proton beams by bent crystals is given below.

3.1 Extraction of protons towards the PROZA setup

As was shown in [11, 12], extraction of protons of 70 GeV energy from A–70 towards the existing channel is possible if the crystal deflector is placed at a certain accelerator azimuth and there is a closed orbit bump to make a displacement of the beam onto the crystal. Since the upstream part of channel 14 which joins to the accelerator is common with channel 2 the region of SS-25 is satisfactory for the crystal location.

In our case a Si crystal with a (111) orientation and dimensions 65x15x0.6 mm^3 was used. Because of the geometry of the vacuum chamber, the crystal was placed about 1 m downstream from the beginning of block 25. The working coordinate and bend angle of the crystal are respectively ~ 60 mm and 80 mrad. For these conditions extracted protons get to the channel 2(14) axis and are transported to the experimental setups without appreciable loss.

The bend radius of the crystal installed in block 25 is 0.8 m. It is known (see, for example [15]) that with the increase of crystal curvature the particle capture efficiency into the channeling mode is decreased. Crystal curvature can be reduced by placing it in block 24 ($\sim$ 0.5 m from the end upstream). In this case the necessary bend angle becomes $\sim$ 60mrad. In addition less amplitude for the closed orbit bump will be needed.

The main complication for carrying out this method of proton extraction was the requirement to retain the possibility of simultaneous operation with the PROZA setup of other physics setups in channels 4, 18, 5N et al. The method of beam steering discussed in [11] gives such a possibility during the extraction period (by 2 s on the flat top of a magnetic cycle).

In fig. 4 a scheme is shown which illustrates the possibility of bent crystal extraction of accelerated protons simultaneously with extraction of secondary particles from the internal target placed in magnetic block 27. Curve 1–1 is the closed orbit bump which is formed for displacement of the beam on to the crystal of magnetic block 25 (CR_{25}). Curve 2–2 presents the bump for displacement of a beam simultaneously on to the internal targets of channels 2 (T_1) and 4 (T_2) where the working coordinates have a different polarity with respect to the central orbit.

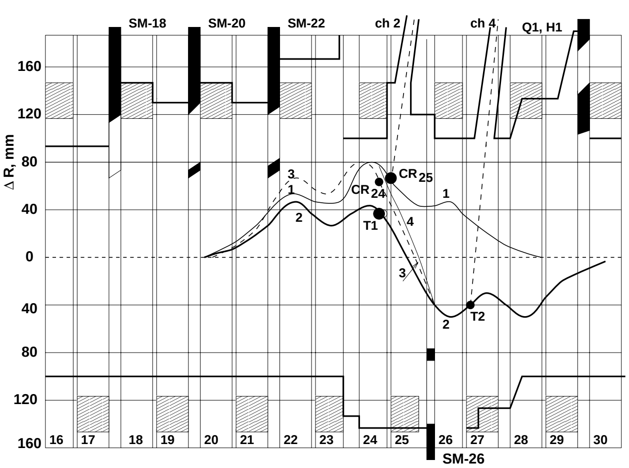

Figure 4: Scheme for simultaneous extraction of protons and secondary particles from the accelerator. The dotted lines are trajectories of the extracted secondary beams.

For simultaneous extraction of accelerated protons by CR_{25} towards channel 2 and secondary particles from the target T_2 into channel 4 the bump should have the form which is shown by curve 1–4–2. Curve 3–3–2 shows the necessary closed orbit bump for the case using a crystal at block 24 (CR_{24}) instead of CR_{25}. The smaller bend angle needed at CR_{24} will allow the experimenters to get more extracted particles.

3.2 *Extraction of protons towards the WES setup*

To extract to the existing layout of channel 4 a crystal is to be placed in the radially defocusing block 27 (between the points 75 and 77 [16]) at a distance 6.55 m from its beginning downstream with a bend angle ~(83–89) mrad. Some of the conditions that must be met are:

- the working region of the crystal deflector is to be in the zone of positive coordinates from the central orbit (as distinct from targets of block 27 generating secondaries on coordinates $r < 0$),
- a local distortion of the closed orbit is to be formed by two bumps since the existing bump does not permit steering the beam onto the crystal at a postition more distant than the target coordinate.

The edge of the beam envelope at the azimuth of the crystal installation corresponds to $r \sim 53$ mm. In calculations the working coordinate of the crystal was taken as $r_{CR} = +50$ mm.

Several variants for local distortion of the closed orbit to steer accelerated beam on to the crystal are presented in fig. 5. The main bump of channel 4 which is formed by magnetic blocks 24 and 30 of A–70 is used together with bumps to be formed with the help of blocks 23, 29(curve 1–1), 25, 31 (curve 2–2) or 26, 32 (curve 3–3). The shaded line shows the crystal (CR) installation in block 27 of the accelerator.

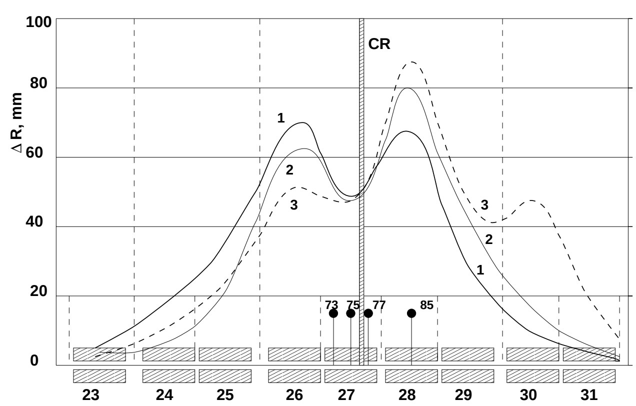

Figure 5: Local distortions of the orbit for steering beam on to the crystal made by bump 24–30 together with bumps 23–29, 25–31 or 26–32.

It is seen that by selecting an appropriate combination of bumps for beam steering, one can change the entry angle of a beam on the crystal over a wide zone thus providing the best conditions for capturing particles into the channeling mode. Such steering schemes allow one to significantly weaken the requirements for mutual alignment of the

Table 3: Coordinate variations for a beam at the crystal azimuth

Additional distortion of the field,%	Bump 24–30 only		Bump 24–30, 3% together with					
			23–29		25–31		26–32	
	r, mm	r',mrad	r, mm	r',mrad	r, mm	r',mrad	r, mm	r',mrad
1.0			42.34	-0.03	42.61	0.418	41.94	0.840
2.0			49.25	-0.203	49.82	0.605	48.78	1.419
3.0			56.00	-0.381	56.89	0.761	56.26	1.912
4.0	47.19	0.222						

beam and crystal as well as to simplify the construction of the goniometer. Data for the angle displacement of a beam at the azimuth of a crystal for different combinations and strengths of the bumps are given in table 3.

It is seen from the table that the angular range of beam displacements relative to the crystal at steering is ~ 1.6 mrad. It is more than the full angular divergence of particles in the beam at maximum energy. The choice of the optimum bend angle of a crystal for extraction towards channel 4D is illustrated by fig. 6 where the dependence of the extracted beam parameters ΔR and $\Delta R'$ at the exit of the accelerator (in SS–28) is shown as a function of the bend angle of a crystal Θ. ω in fig. 6 is an angle region of the crystal bend that deflects channeled particles into the channel 4D acceptance.

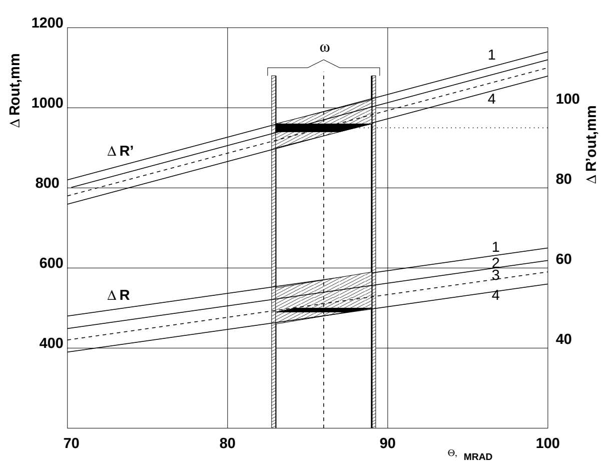

Figure 6: Beam parameters as a function of the crystal bend angle at the exit of the accelerator (middle of the SS–28).

3.3 *Experimental results*

Extraction towards the PROZA setup. The first results for this case are presented in [10]: $\sim 4 \cdot 10^6$ of protons were deflected into the channel when $\sim 10^{11}$ ppc interacted with the crystal. The extraction efficiency was $\sim 4 \cdot 10^{-5}$. This low value (in comparison to [15], for example) was explained by several factors:

- the great length and curvature of the crystal,
- the dynamics of beam steering on to the crystal which was set at a fixed coordinate and had a fixed angle relative to the closed orbit during extraction,
- the dynamics of the beam for multipass interactions with the crystal where most of the particles scattered by the crystal were not captured into channeling later and gave no contribution to the extraction efficiency on following turns.

Further investigations and tuning of the extraction conditions raised the extraction efficiency to $\sim 1.5 \cdot 10^{-4}$ [12].

Interesting dependencies which characterize the efficiency of crystal proton extraction are shown in fig. 7. Curves 1 and 2 show the dependence of the particle count registered in the channel as a function of primary beam intensity interacting with a crystal for two cases: when the bump of the closed orbit is formed with the help of a current in additional windings of the four even blocks and when two even and two odd blocks are used to form the necessary bump. The difference corresponds to angle displacements of beam and crystal before steering. Curves 3 and 4 of fig. 7 present the dependence of extraction efficiency corresponding to curves 1 and 2.

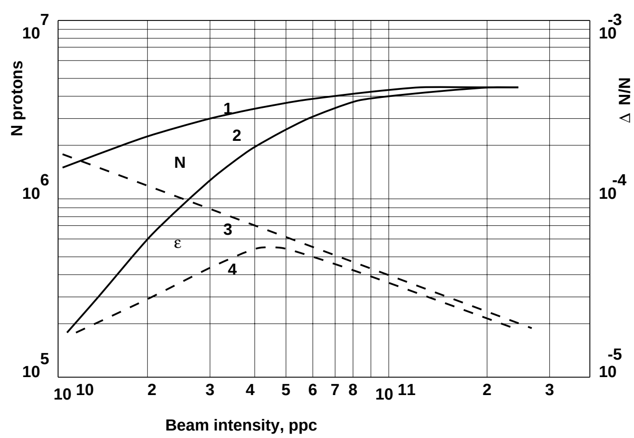

Figure 7: Number of particles in the channel and efficiency of proton extraction as a function of primary beam intensity interacting with a crystal in two modes: a) with a bump of four even blocks, b) with a bump of even and odd blocks.

It is seen that by using two pair of even blocks for forming the bump an efficiency of $\sim 1.5 \cdot 10^{-4}$ is obtained at a crystal interaction rate of $\sim 10^{10}$ of the primary protons. The efficiency decreases if the crystal is moved further in to the beam but the extraction intensity increases by ~ 3 times and reaches $\sim 4.5 \cdot 10^6$ protons.

The important feature of crystal use for beam extraction is simultaneous operation with other experiments (in particular, with extraction of secondary particles). Investigations show that the influence on the extracted proton intensity of the target T_2 (see fig. 4) and other targets placed outside the crystal region for generating secondaries is very weak. This means independent tuning and apparatus calibration can be done with high precision. The quality of the beams extracted simultaneously in different directions for different (4–5) experiments is kept high enough (see, for example, [12]). The duration of extraction can be as long as the flat top of the magnetic cycle, that is –2 s.

Scattering by a thin target. As is shown in [12] for direct steering of the beam on to a crystal an extraction efficiency of $\sim 1.5 \cdot 10^{-4}$ is reached and the intensity of the extracted beam is $\sim 4.5 \cdot 10^{6}$ ppc. The extracted intensity does not increase with an increasing number of accelerated particles interacting with the crystal beyond of 10^{11} ppc. However the extraction efficiency increases significantly when the accelerated protons are pre-scattered by a thin internal target [2] installed upstream of the crystal. The number of particles in the channel is doubled by this and reaches 10^{7} ppc.

The idea of the method is shown in fig. 8 (see, for example, [17]) where two cases are illustrated:

- direct steering of the accelerated beam on to the crystal (phase ellipses of the r–plane are marked as 1 and 1′),
- preliminary steering of the beam on to the target (phase ellipses are 2 and 2′) so that the crystal is struck by particles with large amplitudes.

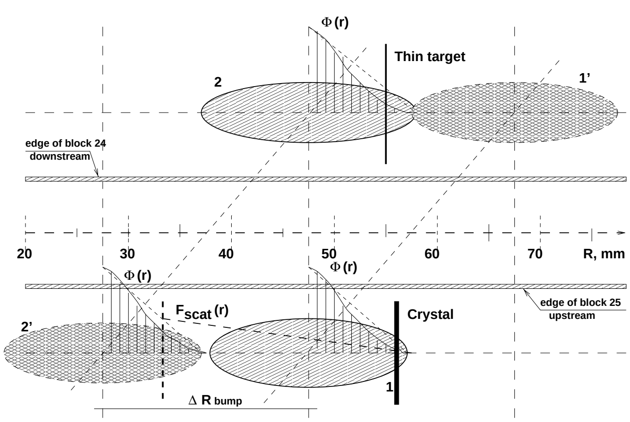

Figure 8: Geometry of the experiment for scattering particles with a thin target before extraction by a bent crystal.

Phase ellipses are shown for the accelerator magnet blocks 24 and 25 where the target and crystal are installed. The functions $\Phi(r)$ for the beam particle distribution are normalized to 10^{12} protons. The positions of the crystal and thin target are also shown in fig. 8.

A similar experiment was done at A–70 when 50 GeV protons were extracted towards the SIGMA setup (channel 2). The results and some analysis are presented in [18]. An estimate of the extraction efficiency obtained without taking into account the fraction of the particles that underwent nuclear inelastic scattering with targets gave a value of $\sim 0.7\%$ [17]. It turned out to be ~ 3 times lower.

Computer simulation of the particle dynamics for particles which undergo a pre-scattering by a thin target before hitting the crystal showed that this case is similar to the variant of placing a crystal at azimuths where the β function of A–70 has a maximum. The orientation of the crystal relative to the beam x_0' is kept stable during the entire extraction time. However in this case certain values of x_0' depend on the amplitude of the betatron oscillations of particles interacting with the crystal. The maximum of the extraction efficiency reaches $\sim 2\%$. A correct accounting of the number of particles which remain after inelastic interactions with the internal targets and hit the crystal gives a result close to this [19].

To recapitulate, the efficiency of particle extraction by a bent crystal for the case where the emittance of a beam is much more than the crystal acceptance (as it is at A–70) does not exceed a few percent. One can expect an increase of the extraction efficiency with an increase of the energy and the corresponding decrease of the size of the accelerated proton beam. This has been demonstrated by experiments at the SPS [20] and the Tevatron [21].

Extraction towards the WES setup. Channel 4D where the WES setup is installed was designed for transporting negative particle beams with energies 20–40 GeV generated by internal targets. As for PROZA, it was not possible to extract 70 GeV protons from A–70 with traditional techniques. In addition, reconstruction of the upstream part of the channel would have been required. The difficulties of beam line reconstruction and production of expensive new equipment were avoided by use of a bent crystal. The possibility of extracting negatively charged particles from internal targets towards the channel was also retained.

When $\sim 10^{11}$ ppc were steered on to the crystal the extracted proton beam intensity reached a level of 10^{7} particles. This resulted in an extraction efficiency of $\sim 10^{-4}$ [22].

The dimensions of the extracted beam are shown in fig. 9 and have half widths of 14 mm and 6 mm in the horizontal and vertical planes, respectively. These parameters for the extracted beam meet all the requirements of the new experiment planned for the WES setup.

Extraction of the accelerated proton beam to the WES setup demostrated once more the expedience of using bent crystals. Notwithstanding the low extraction efficiency obtained in the first experiments the intensity of the beam in the channel is enough for execution of the planned research program.

One needs to point out also that the fraction of the accelerated beam interacting with a crystal gives particle loss rates in the accelerator which are much less compared with losses for operation of other extraction systems. So, in this case we have no significant radiation loads on the accelerator equipment. Further development of beam extraction towards channel 4 with a bent crystal permits simultaneous operation of it with the other 4–5 experimental setups. With

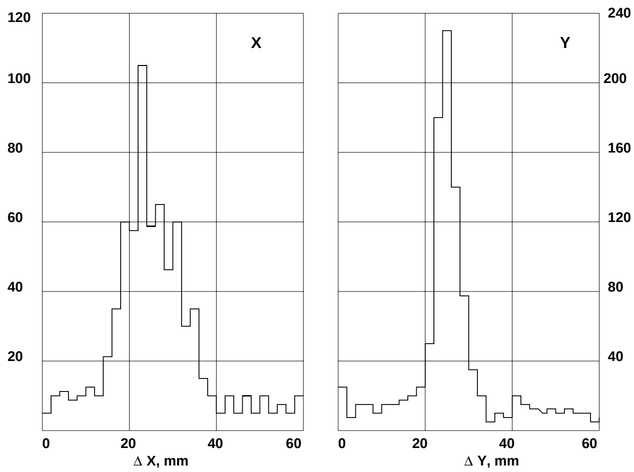

Figure 9: Profiles of the proton beam at the WES setup.

the maximum energy proton beam in channel 4 experimental possibilities are extended both for the WES setup and for the physics setups GAMS, ISTRA,MIS JINR wich are placed along the beam line.

3.4 Perspectives on using crystals at IHEP

Development of the IHEP experimental program through the creation of new physics facilities requires extension of the potential at the existing accelerator for apparatus preparation and operation with particle beams of different types, polarities, and energies. The fullest and most effective use of the A–70 accelerated beam will be obtained if in addition to the existing classic facilities bent crystals will be broadly used for beam extraction. Because of the simplicity of their application, crystals are used in different regimes of accelerator operations and physics experiments. The expedience of the practical applications of crystals at the IHEP accelerator has been demonstrated by the proton extraction arrangements towards the setups PROZA (channel 14), SIGMA (channel 2B) and WES (channel 4D) that are reported above. A sequence of successful experiments was also carried out using bent crystals (see, for example, [23]) in particle beam lines for dividing and forming the 70 GeV proton beams.

Analysis of the existing experimental base at A–70 taking in to account its transformation to new tasks has shown that there are a number of places where bent crystals can be placed to extend the possibilities of the accelerator complex. The most significant of them (some of which are already in use) are marked in fig. 10 with dark circles.

As was noted above, for direct extraction by a bent crystal the beam extraction efficiency is of the order of $\sim 10^{-4}$. This means that to get $\sim 10^6$ particles at an experiment one need to steer $\sim 10^{10}$ particles of accelerated beam on to the crystal. This is two orders of magnitude less than the intensity that must be steered on to internal targets to generate secondary particle beams. At A–70 an intensity of $\sim 10^{10}$ ppc is obtained from the halo that surrounds the central core of the accelerated beam (see, for example, [24]).

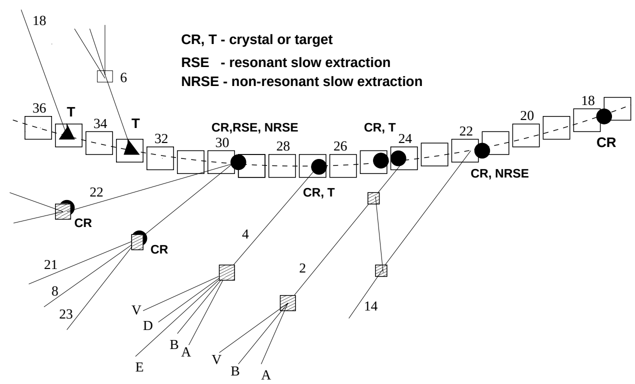

Figure 10: Zones for potential use of bent crystals for extraction of protons from A–70.

These particles can be extracted easily to form a beam with the required parameters for high efficiency fast extraction towards the Neutrino Detector.

Use of bent crystals also provides a significant decrease of the radiation loads which otherwise shorten the life of the accelerator equipment. This factor will have a particularly high significance after the A–70 reconstruction when A–70 will be operating with an intensity significantly higher than the current one. Under these conditions use of crystals for extraction of accelerated protons together with the restriction of intensity for internal targets will promote extended operation of the accelerating complex without failure of physics equipment due to over-irradiation.

Conclusion. Experience has been obtained for the first time at IHEP using the new technique of extraction of maximum energy protons with bent crystals for physics experiments. This experience, obtained over a long period (~ 8 years), allows one to reach conclusions about crystal extraction reliability, high stability of beam parameters, compatibility with other activities, and methods of particle extraction. The simplicity of application of bent crystals supports the expedience of their use for beam extraction both at the IHEP accelerator and accelerators of higher energies.

It should be pointed out that the efficiency values obtained in our regimes include the full extraction efficiency which depends of the efficiency of particles capture in to the channeling mode, the dechanneling processes that are a function of a crystal length and bending radius as well as the geometric matching of the crystal acceptance and output emittance from the accelerator vacuum chamber. Further development is planned of a program to increase the extraction efficiency by use of crystals of different materials and thicknesses as well as the use of crystals in combined modes with other beam extraction techniques.

4 CRYSTAL-AIDED NONRESONANT SLOW EXTRACTION

A bent Si crystal placed in front of the first septum-magnet of the existing slow extraction system of the IHEP accelerator has allowed up to $3 \cdot 10^8$ additional protons to be extracted for physics experiments. These protons which represent about 10-30% of the beam intensity extracted towards channel 22 without a bent crystal were otherwise lost on the septum in the non-resonant slow extraction mode. The use of an unbent crystal as an amorphous target results in a decrease of the extracted beam intensity.

Nonresonant slow extraction of protons [7, 25] has made it possible to carry out experiments with hadron beams for the experimental setups FODS–2 and SWD at extracted beam intensities in the range $10^6 \div 10^9$ ppc. However to make experiments possible with electron beams higher intensity extracted proton beams are desirable.

It turned out that the number of extracted particles can be increased by placing a bent Si crystal in the SS–18 upstream of the first extracting septum magnet SM–18. Compared to direct beam extraction (see, for example, [11]), this mode demonstrates the existence of other techniques for using bent crystals to extract beams from high energy accelerators for physics experiments.

4.1 Scheme for deflecting beam over a septum

The initial part of the extraction system is shown in fig. 11.

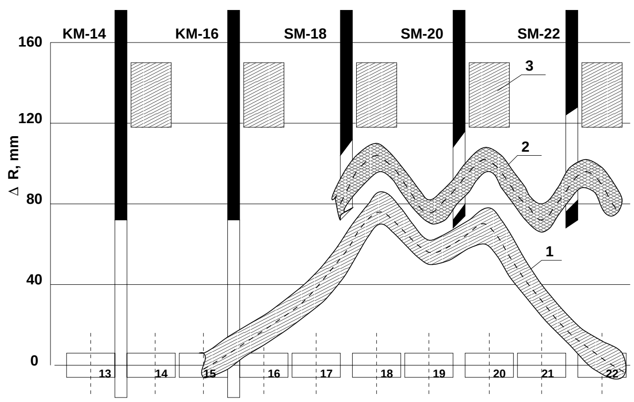

Figure 11: Initial part of the extraction scheme. 1 is the circulating beam before extraction; 2 is the region occupied by extracted beam; 3 are non–linear zones in the gap of the magnets; KM–14,16, SM–18,20,22 are the kicker– and septum–magnets of the fast and slow extraction systems, respectively; 13–22 are the blocks of the accelerator.

The required deflection of the circulating beam towards the septum-magnets is made by a local distortion of the closed orbit [26]. The region occupied by the beam inside the vacuum chamber and septum-magnet apertures at extraction is marked by 2. A part of the beam is lost on the septum of SM–18 due to its finite thickness, while some particles are lost at the edges of other septum magnet apertures. It was possible to diminish these losses by employing a bent Si crystal. The 3 cm long crystal cut along the (110) plane was bent by 2.5 mrad. It was placed in SS–18 at a distance about 40 cm upstream of the first septum magnet. The thickness and width of the crystal are 2 mm and 15 mm, respectively. The bending device for the crystal is similar to the "Serpukhov type" bender [27].

The layout of the septum magnet and the bent crystal in SS–18 is shown in fig. 12 where the aperture of the SM–18 (1), the crystal (2) with its moving mechanism (CR) and the region of non–linear field of magnet 18 (3) are marked.

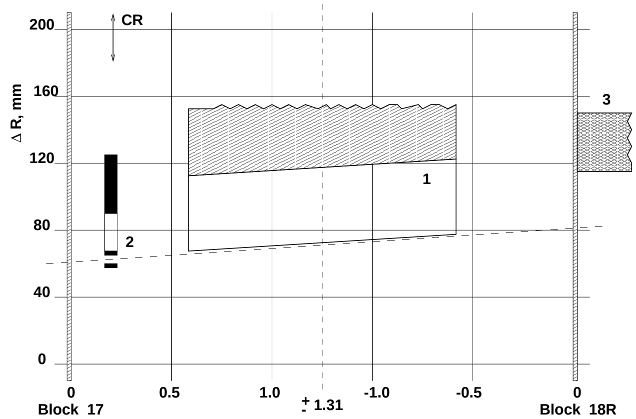

Figure 12: Layout of the septum magnet and bent crystal in SS–18. The crystal position is seen inside and outside of the septum edge, respectively. The hatched vertical lines mark the exit and entry edges of the accelerator magnets; the broken line indicates the beam envelope at injection.

If the entry face of the crystal is perpendicular to the circulating beam, this setup would allow particles that would otherwise hit the septum to be captured into channeling and receive a radial displacement at the septum:

$$\Delta R_{CR} = L \cdot \Theta_{CR} \approx 1\text{mm},$$

where L is a distance from the crystal to the septum-magnet along the closed orbit and Θ_{CR} is the crystal bending angle.

Since the septum is ~ 0.5 mm thick, this displacement is enough to allow particles incident parallel to the septum and channeled by the crystal to be deflected into the SM–18 aperture. In our case the crystal was fixed with an angle to the central orbit of ~ 4 mrad, so that no particles could be channeled from the entry end of the crystal (the so called "end-face capture mechanism"). The main mechanism responsible for capture of particles into channeling in our experiment must then be the "volume capture mechanism" discovered in 1982 [28].

4.2 Experimental results

Fig. 13 shows the dependence of the number of particles extracted towards beam line 22 [25] as a function of the radial position of the bent crystal from the center of the accelerator vacuum chamber for various levels of extracted beam intensity (curves 1, 2 and 3, respectively).

It is seen that when the crystal is moved towards the chamber center the intensity of the extracted beam grows up to a certain maximum. The intensity increase at this maximum reaches $\sim 3 \cdot 10^8$ protons which represents $\sim 30\%$ when extracting $\sim 9 \cdot 10^8$ ppc or $\sim 10\%$ when the extracted beam intensity was $\sim 3 \cdot 10^9$ ppc, respectively.

In order to be convinced that this result is due to channeling and not to simple scattering of particles by the crystal acting as an amorphous target, analogous measurements

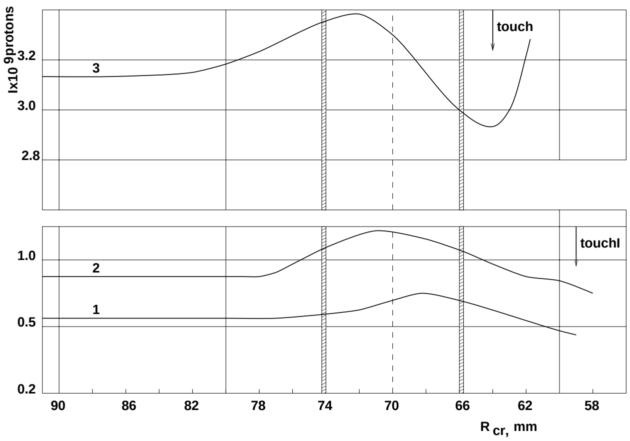

Figure 13: Dependence of intensity extracted into channel 22 versus radial coordinate of the bent crystal from the central orbit. Radial coordinates of the entry and exit ends of the septum are shown with vertical hatched lines.

were taken with an unbent crystal placed at the same radial positions in the accelerator. The results are shown in fig. 14.

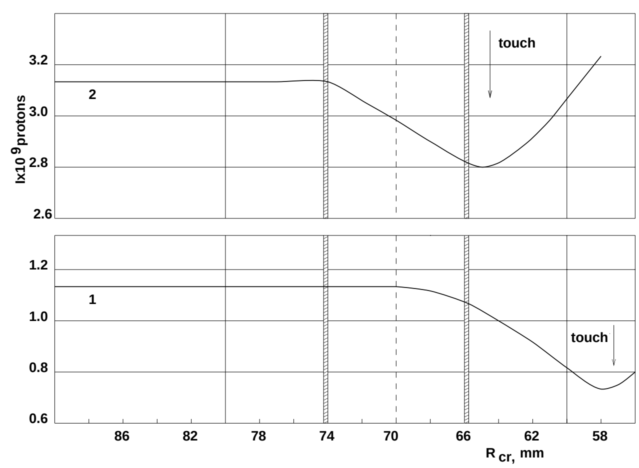

Figure 14: Dependence of intensity extracted into channel 22 versus radial coordinate of an unbent crystal placed in front of the SM–18. Curves 1, 2 correspond to different levels of extracted intensity.

There is an essential difference between the curves in figs. 13 and 14. In the case of the bent crystal (see fig. 13), the intensity increase is already seen at a radial coordinate of ~ 80 mm, that is ~ 14 mm inside the septum–magnet aperture. The unbent crystal (see fig. 14) does not give rise to any intensity increase but rather a loss of particles which interact with it when it is inside the entry end aperture of SM–18 (the entry and exit ends of the septum are shown with vertical hatched lines). Losses increase as the crystal is moved towards the entry end coordinate of the septum. Further motion of the crystal across the septum into the accelerator chamber results in an additional loss of particles (in both figs. 13 and 14). When the crystal touches the dense part of the beam (the positions shown with arrows) which has not yet been scattered by internal targets, one can see some increase of extracted intensity. But in this case a significant shortening (by 1.5–2 times) of the spill was observed for secondary particle beams generated by those targets for other experiments.

4.3 Discussion of results

Beam extraction mechanism. Capture of particles into channeling occurs when the particle trajectories are tangential to the crystallographic planes of a crystal. Two mechanisms of capture are known [29]: end-face and volume capture, i.e. when particle trajectories are tangential to the crystallographic planes at the entry face or in the depth of the crystal, respectively. In the first case, the number of particles channeled depends on the ratio of the critical channeling angle to the divergence of the incident beam, ψ_c/Θ; while in the second case it depends on the capture probability $W(R)$, where R is the crystal bend radius.

The phenomenon of proton capture into channeling in the depth of a bent crystal has been demonstrated experimentally at 1 GeV [28] and 8.4 GeV [30]. The existence of volume capture at 70 GeV has been shown in [31] where data for proton capture probability into the channeling regime are presented as a function of the crystal bend radius. Here the data from [31] is used to explain the results of the experiment.

One can understand the behavior in figs. 13 and 14 with the help of fig. 15 where the phase-space diagram of the circulating unperturbed beam and the beam deflected into the SM–18 aperture (zones 1 and 2, respectively) are shown. The region of possible loss of particles with various angles in front of the septum (3) is shown in fig. 15, along with the crystal transmission (4), the calculated acceptance of the extraction channel including septum magnets with their apertures (5) as well as the phase–space region (6) for particles having undergone scattering in the upstream targets.

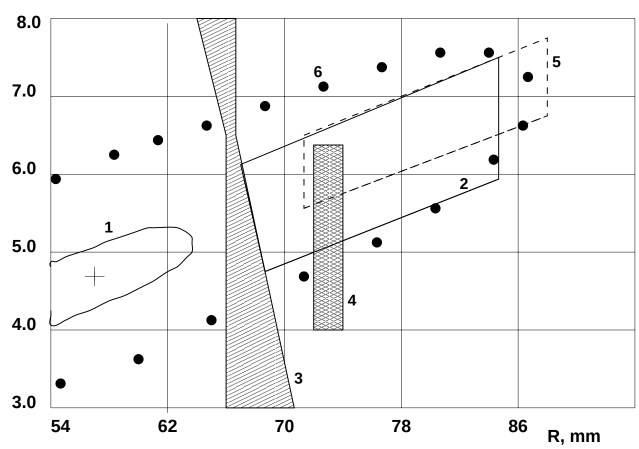

Figure 15: Phase–space illustration of crystal-aided nonresonant extraction.

The growth of the extracted beam intensity that begins when the crystal is at the coordinate ~ 80 mm (see fig. 13) is due to transmission of particles of small divergence by the crystal into the acceptance of the extraction channel (zone 5 of fig. 15). The maximum intensity reached at the crystal coordinates ~70–72 mm is due to extraction of a portion of the beam which is deflected into the SM–18 aperture instead of hitting a wall of the septum or lost somewhere in the ring.

The decrease in intensity on moving the crystal towards the entry end of the SM–18 can be explained by proton losses on the septum after undergoing multiple Coulomb scattering in the crystal acting as an amorphous target.

If the crystal goes deeper into the beam in front of the septum, protons that are captured into channeling can deflect into the septum magnet aperture only on later turns after receiving a noticeable growth of betatron amplitude and when the phase is favorable. At the "high" level of extracted intensity (curve 3 of fig. 13) some increase is seen when the crystal touches the dense part of the beam (marked with an arrow). In this case the crystal acts as an additional target which interferes with beam steering and shortens the extraction spill by 30–50%.

At a "low" extracted intensity (curves 1, 2 of fig. 13), when the dense part of a beam has been moved away from the septum by a decrease in bump strength, the crystal touches the beam at a larger distance from the septum (marked with an arrow on curve 2). The decrease of the intensity in this case can be due to particles being lost because of the crystal acting as a target in which the particles undergo multiple interactions. The growth of the betatron amplitude of particles captured into channeling turns out not to be enough to reach the acceptance region of the extraction channel.

The characteristics of the curves in fig. 14 for the case of an unbent crystal can easily be understood from consideration of the dynamics of particles undergoing interactions with an ordinary target. The scattering of a beam in the target has no influence on the extraction intensity because of the small scattering angles involved until the target comes into the shadow zone in front of the septum. At this point the losses increase because scattered particles hit the septum. This results in a decrease in extracted intensity. Some intensity growth only appears when the crystal is closer to the circulating beam than the septum and a dense part of the beam touches it. However since the spill of other secondary beams is shortened in this case by 1.5–2 times, this arrangement is of no practical use.

4.4 Numerical estimates

We can estimate the order of magnitude for the intensity which can be extracted using a bent crystal placed in front of the first septum magnet in our scheme. The beam intensity on to each ordinary target is estimated to be 10^{12} ppc. It is known (see, for example, [7]) that for simultaneous operation of a few internal targets 70–75% of the beam particles have inelastic nuclear interactions with the targets or are lost on the accelerator chamber walls. The rest of the particles undergo multiple Coulomb scattering and loose energy by ionization and nuclear elastic scattering. They continue their motion in the accelerator with a noticeable growth of betatron amplitude. Eventually, we obtain the radial distribution of particles at the point of the crystal location shown in fig. 16.

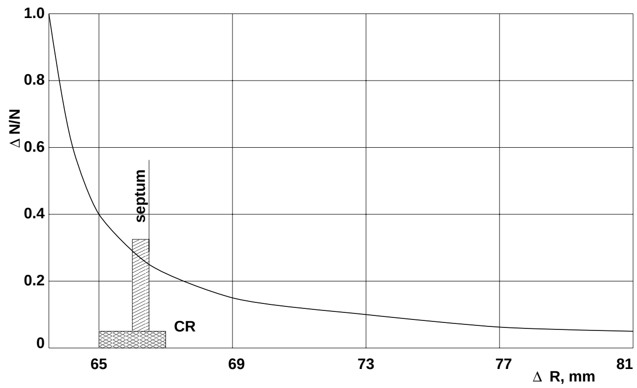

Figure 16: Radial distribution of particles scattered by internal targets in the SM–18 region.

One can determine that for $\sim 3 \cdot 10^{11}$ particles under this curve about $1.2{\cdot}10^{10}$ protons hit the crystal at the coordinate corresponding to a maximum of the extracted beam intensity. The probability of volume capture according to [31] where the energy of particles as well as the radius of crystal curvature are taken into account is about 1% for our case.

As a result with the help of a bent crystal in our scheme one can extract an additional contribution of about $1.2 \cdot 10^8$ particles per 10^{12} protons interacting with each internal target. To obtain the full additional extracted intensity observed in our experiment, one has to take into account that from 3 to 5 targets operate simultaneously and interact with a total intensity of up to $2.5 \cdot 10^{12}$ primary protons during every accelerator cycle [7].

Conclusion. A bent crystal placed in front of the first septum magnet of the IHEP accelerator slow extraction system has made it possible to extract up to an additional $3 \cdot 10^8$ protons toward channel 22 which would otherwise be lost on the septa. Protons were extracted in parallel with operation of several internal targets generating secondary beams for other experiments. Depending on the extraction regime, the relative increase of the extracted proton beam intensity was 10–30%. Particles were captured into channeling in the crystal by the volume capture mechanism.

The advantages of volume capture compared to end-face capture are: [31]:

- no precise alignment of the crystal is necessary,
- the effect of particle deflection by the crystal is less sensitive to beam instabilities,
- changes of crystal bend angle due to heating by the beam are less critical.

Moreover, for a beam of large divergence volume capture can be more effective than end-face capture.

This method of extraction can be used in future experiments for channels 22, 23. The extracted beam intensity can be further increased by introducing a goniometer to optimize the angle between the crystal and beam in relation to its position with respect to the septum magnet.

5 SHADOW TARGETING

5.1 Internal targets

To carry out methodical research which don't need high intensity beams, such as physics apparatus callibration before a run for gathering statistics, some internal targets are operated in the "shadow" mode at IHEP. In this mode targets for which there is no possibility for a local distortion of the closed orbit interact with particles with large betatron oscillations produced by scatterings from other internal targets. Those other targets do use displaced beam and are considered as the "main targets" in the current run of the accelerator.

The possibility of such operation of internal targets allows one to improve the efficiency of the accelerated beam use due to the increase of the number of physics facilities working simultaneously. The positions of the targets working in the "shadow" mode are arranged so that they can interact with protons scattered by the main targets. The integral distribution function of the accelerated beam intensity for the IHEP proton synchrotron $F(x)$ has the functional form [24]:

$$F_1(x) = e^{-x^2/\sigma^2}, \tag{17}$$

and

$$F_2(x) \approx A(P) \cdot \frac{P}{x^2}; \tag{18}$$

where x is the distance from the center of the beam, P is the residual gas pressure, and σ is the dispersion. The function $F_1(x)$ describes the distribution of the dense part of the accelerated beam and $F_2(x)$ – the distribution of particles at the level of $\leq 1\%$ of intensity (the so-called beam halo). The existence of the halo is explained by processes of single scattering of particles in the residual gas by angles which do not result in particle losses on the A–70 vacuum chamber walls. It has been shown experimentally [24] that at a beam intensity of $\sim 4.4 \cdot 10^{12}$ ppc and a "normal" vacuum $(4.5 \cdot 10^{-7}$ tor) about $(4-5) \cdot 10^8$ particles are contained in the region at distances $\geq\ 22 - 24$ mm from the beam center. The interaction of the accelerated beam with targets gives an analogous effect where the betatron amplitudes of the circulating protons interacting with a target grow due to multiple Coulomb scattering in the target material. Three to five percent of the particles reach values of the betatron amplitudes of 20–30 mm [32]. Calculations indicate that single (and several pass) scattering processes occuring in the residual gas lead to amplitude growth of 40–50 mm. This means that a point target (with a diameter of 3 mm as compared to an amplitude 30–50 mm) placed at the edge of the dense part of a beam with an intensity $\sim 10^{11}$ protons [33] is able to generate secondary beams simultaneously with the "main" targets. These secondary beams are of acceptable quality and can be used by other setups. They typically have intensities ($\geq 10^5$ ppc) with beam quality comparable to beams from the main targets.

At IHEP a target for the positive particle channel 6 works in the "shadow" permanently. Periodically (after operation with bumps) the targets T_{35} and T_{45} of the setups GIPERON and CHARM, respectively, go in "shadow". Shadow operation of targets partially influences the efficiency of the main targets. It may lead to a decrease of intensity of the beam extracted towards a channel of the main user and even to some deterioration of the beam structure. It has been found experimentally that to reduce the influence of "shadow" targets their location should be 20–25 mm from the densest part of the beam interacting with the main targets.

It should be noted that "shadow" target operation further reduces particle loss along the accelerator perimeter due to the target localization. (A target is effectively a "narrow" place in the accelerator vacuum chamber). Scraping a beam to increase the fast ejection efficiency or to reduce the radiation background [24,34] is also possible in the "shadow" regime.

5.2 Efficiency of internal targets

One of the main characteristics of secondary particle extraction from an accelerator is the efficiency of accelerated proton interaction with the internal targets. The efficiency is considered to be the share of the accelerated beam that made nuclear interactions (including elastic scattering) directly in the target [32].

According to [35,36] the efficiency of an internal target of a proton synchrotron is expressed by the formula:

$$F = 2\sum_{s=1}^{\infty}\left[\lambda_s \cdot J_1(\lambda_s) \cdot (1+\lambda_s^2 \cdot Y)\right]^{-1}, \tag{19}$$

where Y is a universal parameter defined as follows:

$$Y = \frac{1}{4} \cdot \frac{<\Theta_1^2>}{\Theta_0^2}, \tag{20}$$

where $<\Theta_1^2>$ is the mean square scattering angle in the the target and Θ_0^2 is the square of a minimum scattering angle that is large enough to hit the vaccum chamber wall. The behavior of $F = F(Y)$ is shown in fig. 17.

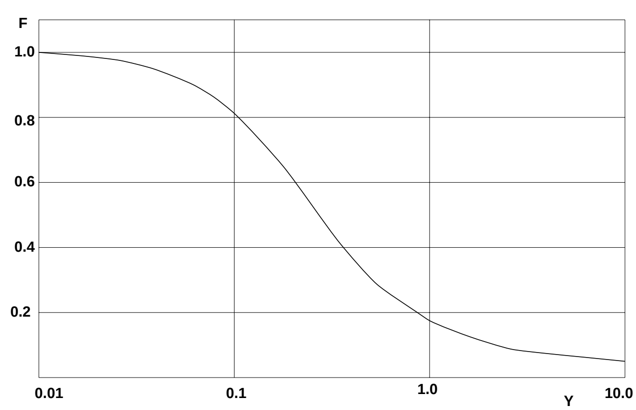

Figure 17: Behavior of the target efficiency $F = F(Y)$.

In the case of the IHEP proton synchrotron the universal parameter is expressed by the formula:

$$Y = 0.492 \cdot 10^{-6} \cdot \frac{|\phi_t|^2}{A_0^2} \cdot \frac{L_N}{L_R}, \tag{21}$$

where $|\phi_t|$ is a module of the Floquet function at the azimuth of the target and A_0 is the free semi-aperture of the vacuum chamber.

Substituting here the data for the Al target installed in the radially focusing magnetic block we have $Y = 0.026$. The value of the efficiency of the internal target $\sim 97\%$ corresponds to this figure. It is in agreement with experimental results obtained for operation of a single beam steering system with no restrictions of aperture in the accelerator vacuum chamber [32].

In the case of simultaneous operation of three targets the value of the universal parameter Y appeared in the region of $0.212 \div 0.104$ due to the change of A_0. The effective semi-aperture of the vacuum chamber at the extraction region decreases in this case by 2–2.5 cm due to the installation of the septum magnets for the slow extraction system and the lenses for resonant beam excitation. The efficiency value of $\sim 60 \div 82\%$ corresponds to the definition of Y. In the case of "shadow" operation for target positions choosen for a reasonable intensity in a channel for low level operations a value of $A_0 \sim 15$ mm is possible. The efficiency of the main targets can be lowered by 50% in this case.

6 REFERENCES

[1] K.P.Myznikov et al., IHEP 70-51, Serpukhov, 1970.

[2] Yu.M.Ado, A.A.Asseev et al., IHEP 88–9, Serpukhov, 1988.

[3] H. G. Hereward, J. Ranft, W. Richter, CERN 65–1, Geneva, 1965.

[4] Yu.M.Ado, A.A.Asseev et al., IHEP 85–23, Serpukhov, 1985.

[5] A.N.Kalinovsky, N.V.Mokhov, Yu.P.Nikitin, Propagation of high energy particles through the matter, Moscow, Energoatomizdat, 1985.

[6] N.D.Malitsky, Yu.P.Severgin, I.A.Shukeylo et al., Proceedings of the XI All-Union Part. accel.conf., Dubna, 1989, v.2, p.170.

[7] A.A.Asseev et al., J. of Techn. Phys. N9, v.60(1990)70, Leningrad.

[8] Yu.M.Ado, E.A.Ludmirsky, IHEP 87-30, Serpukhov, 1987.

[9] A.G.Afonin et al., Proceed. of the XII All-Union Conference on charged part. accel., Dubna, 1992, v.1, p.371.

[10] A.A.Asseev, M.D.Bavizhev et al., IHEP 89–57, Serpukhov, 1989.

[11] A.A.Asseev et al., Nucl. Instr. & Methods A309(1991)1.

[12] A.A.Asseev et al., Nucl. Instr. & Methods A330(1993)39.

[13] A.A.Asseev et al., Proceed of the XV Part. accel. conf., Protvino, 1996, v.2, p 299.

[14] V.D.Apokin et al., Phys. Lett. B243(1990)461.

[15] R.A.Carrigan, Nucl. Instr. & Methods B33(1988)42.

[16] E.D.Tarasov et al., ITEP $N^o 242$, Moscow, 1964.

[17] A.A.Asseev et al., Nucl. Instr. & Methods A324(1993)31.

[18] A.A.Asseev et al., Nucl. Instr. & Methods A334(1993)283.

[19] A.A. Asseev et al., Proceed. of the 5–th European part. accel. conf., Barcelona, 1996, v.3, p.2412.

[20] X. Altuna et al., CERN SL/95–41(DI), Geneva, 1995.

[21] C.T.Murphy,...A.A. Asseev et al., Nucl. Instr. & Methods B119(1996)231.

[22] A.A.Asseev et al., Proceed. of the XV Part. accel. conf., Protvino, 1996, Abstracts, p. 78.

[23] M.D.Bavizhev et al., Proceed. of XI All-Union Conference on charged part. accel., Dubna, 1989, v.2, p.285.

[24] A.A.Asseev et al., IHEP 79–91, Serpukhov, 1979.

[25] A.A.Asseev et al., Proceed. of the 3–d European part. accel. conf., Berlin, 1992, v.2, p. 1486.

[26] A.A.Asseev et al., IHEP 91–17, Protvino, 1991.

[27] N.A.Galyaev et al., IHEP 89–191, Serpukhov, 1989.

[28] V.A.Andreev et al., Letters to JETP, N9, v.6(1982)340.

[29] N.A.Galyaev et al., Proceed. of the IEEE part. accel. conf., San Francisco, 1991, v.1, p.192.

[30] N.K.Bulgakov et al., Communications of JINR N1–83–725, Dubna, 1983.

[31] N.A.Galyaev et al., IHEP 90–147, Protvino, 1990.

[32] V.I.Gridasov et al., IHEP 73–78, Serpukhov, 1973.

[33] A.A.Asseev et al., IHEP 77–65, Serpukhov, 1977.

[34] A.A.Asseev et al., IHEP 80–104, Serpukhov, 1980.

[35] E.D.Courant, BNL, EDC–46, 1962.

[36] L.I.Sokolov, ITEP $N^o 942$, Moscow, 1972.

Simulation of Crystal Extraction Experiments

Valery Biryukov
IHEP Protvino, 142284 Moscow Region, Russia
E-mail: biryukov@mx.ihep.su

Abstract

We discuss the simulation methods and results for the crystal extraction experiments performed recently at the high energy accelerators. Possible future applications of the crystal channeling technique are considered.

1 INTRODUCTION

Crystal extraction experiments have greatly progressed in recent years, spanning over two decades in energy and more than two decades in the crystal bending angle[1, 2, 3]. The theory of crystal extraction is essentially based on Monte Carlo simulations, as the extraction process includes multiple passes through the crystal, and turns in the accelerator, of the beam particles. Even more importantly, tracking of a particle through a bent crystal lattice requires not only a calculation of a particle dynamics in this nonlinear field, but also a generation of random events of scattering on the crystal electrons and nuclei.

To track particles through the curved crystal lattices in simulation we apply the approach with a continuous potential introduced by Lindhard. In this approach one considers collisions of the incoming particle with the atomic strings or planes instead of with separate atoms, if the particle is sufficiently aligned with respect to the crystallographic axis or plane. The typical step size along the crystal length in simulation is about 1 micron, as defined by the particle dynamics in crystal channel. By every step the probabilities of scattering events on electrons and nuclei are computed depending on their local densities which are functions of coordinates. This ensures correct orientational dependence of all the processes in crystal material. Further details on the simulation code may be found in Refs.[4, 5].

Leaving aside the details of channeling physics, it may be useful to mention that accelerator physicist will find many familiar things there:

- Channeled particle oscillates in a transverse nonlinear field of a crystal channel, which is the same thing as the "*betatronic oscillations*" in accelerator, but on a much different scale (the wavelength is 0.1 mm at 1 TeV in silicon crystal). The number of oscillations per crystal length can be several thousand in practice. The concepts of beam emittance, or particle action have analogs in crystal channeling.

- The crystal nuclei arranged in crystallographic planes represent the "*vacuum chamber walls*". Any particle approached the nuclei is rapidly lost from channeling state. Notice a different scale again: the "vacuum chamber" size is $\sim$2 Å.

- The well-channeled particles are confined far from nuclei (from "aperture"). They are lost then only due to scattering on electrons. This is analog to "*scattering on residual gas*". This may result in a gradual increase of the particle amplitude or just a catastrophic loss in a single scattering event.

- Like the real accelerator lattice may suffer from *errors of alignment*, the lattice of real crystal may have dislocations too, causing an extra diffusion of particle amplitude or (more likely) a catastrophic loss.

- Accelerators tend to use low temperature, superconducting magnets. Interestingly, the crystals cooled to *cryogenic temperatures* are more efficient, too.

2 THE SPS EXPERIMENTS

A detailed account for the crystal extraction experiments made at the CERN SPS can be found in this volume[2]. Before these SPS studies, the theoretical comparisons [6] with extraction experiments [7, 8] were restricted by analytical estimates only, which gave the right order of magnitude. The computer simulations considered idealized models only and predicted the extraction efficiencies always in the order of 90–99% (e.g. [6]) while real experiments handled much smaller efficiencies, in the order of 0.01 % [7, 8].

The considered-below theoretical work has been the first and rather detailed comparison between the realistic calculation from the first principles (computer simulation) and the experiment. The simulation was performed [9] with parameters matching those of the SPS experiment. Over 10^5 protons have been tracked both in the crystal and in the accelerator for many subsequent passes and turns until they were lost either at the aperture or in interaction with crystal nuclei.

In the simulation, different assumptions about quality of the crystal surface were applied: one was an ideal surface, whereas the other one assumed near-surface irregularities (a 'septum width') of a few μm due to a miscut angle (between the Si(110) planes and the crystal face) 200 μrad, surface nonflatness 1 μm, plus 1 μm thick amorphous layer superposed. Two options were considered. The *first*, with impact parameter below 1 μm and surface parameters as described above, excludes the possibility of channeling in the first pass through the crystal. This is compared to the *second* option, in which the crystal surface is assumed perfect, i.e., with a zero septum width.

Table 1 shows the expected extraction efficiencies for both options from the first simulation run and the measured lower limit of extraction efficiency as presented at the 19-th meeting on "SPS Crystal Extraction" [10] held at CERN.

Though the efficiency comparison, theory to measurements, was not possible at that time, from the analysis of the simulation results one could see that the perfect-surface simulation predicted narrow high peaks for the angular scans (30 μrad FWHM) and extracted-beam profiles,

Table 1: SPS crystal extraction efficiencies from the early runs, Monte Carlo and experiment

Option	Monte Carlo	Experiment
Poor surface	15%	lower limit of 2-3%
Ideal surface	40%	only known

which have not been observed. The imperfect-surface option, however, is approximately consistent with the experimental observations: wide (about 200 μrad FWHM) angular scan and sophisticated profiles of the extracted beam (dependent on the crystal alignment).

The efficiency was measured in the SPS experiment with that first tested crystal to be 10$\pm$1.7%. The detailed simulations have shown that efficiency should be a function of the vertical coordinate of the beam w.r.t. the crystal (for its given shape), and be from 12 to 18% at peak, with imperfect-surface option.

The simulation studies for a new crystal with another geometry ("U-shaped") were performed prior to the measurements. The model followed the parameters and design of this crystal, with the same SPS setting. Again the two options, an imperfect or perfect edge, have been studied.

Figure 1 shows the angular scan (as narrow as 70 μrad FWHM) of the efficiency simulated for the U-shaped crystal with edge imperfections; a comparison to the measurements shows a good agreement. The peak efficiency, 19.5$\pm$0.7%, was expected to be just slightly increased with the new crystal. For an ideal crystal and a parallel incident beam, the simulation predicted a peak efficiency of $\sim$50% and a very narrow angular scan (25 μrad FWHM).

Another SPS experiment employed a crystal with an amorphous layer at the edge to suppress the channeling in the first passage of the protons [2]. The extraction efficiency with this crystal was indeed of the same order of magnitude as found without an amorphous layer, thus confirming the theoretical prediction [9] that the first-pass channeling is suppressed in the SPS crystals.

In order to understand some overestimate of the peak efficiency in the model, we made a more detailed simulation [11]. Overestimate of the channeling efficiency might mean an underestimate of the scattering and/or losses in the multipasses in crystal. It is clear that the parameters influencing crystal extraction are not defined perfectly; there are several unknowns in the model, such as the impact parameters and quality of the crystal edge.

In the subsequent simulations the realistic details of the crystal design, such as the "legs of U" (the scattering here was missed previously) were introduced. The window for the extracted protons was $\pm$30 μrad ($\pm$2 θ_c) from the extraction line, in order to match the experimental procedure (earlier, all protons bent at >8.0 mrad were accepted).

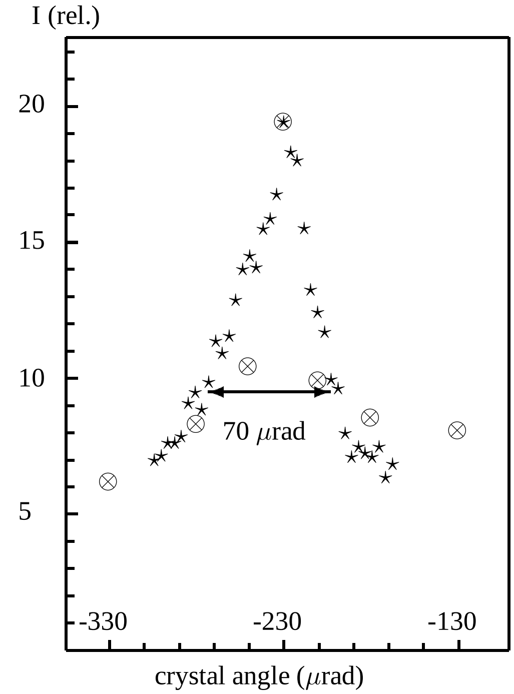

Figure 1: The angular scan of extraction with a U-shaped crystal. Prediction ($\otimes$) and measurement ($\star$).

Table 2 shows the computed peak efficiency as a function of the septum width t (modelled as an amorphous layer) of the U-shaped crystal. The dependence on t is rather weak; this agrees with the experiment where the 30-μm amorphous layer did not affect the efficiency.

These simulations have been repeated with the energies of 14 and 270 GeV, where new measurements have been done at the SPS. The results are shown in Table 3.

Table 2: The peak efficiency F (%) for different septum widths t (μm). The statistical error is 0.6 %.

t (μm)	1	20	50	100	200
F (%)	13.9	12.4	12.9	10.9	8.2

The length of the Si crystal used in the experiment is optimal to bend the 120 GeV proton beam by 8.5 mrad with a *single* pass. The efficiency of the *multi*-pass extraction is defined by the processes of channeling, scattering, and nuclear interaction in the crystal, which depend essentially on the crystal length L. As the scattering is added, it is qualitatively obvious that the optimal length is reduced as compared to bending with a single pass.

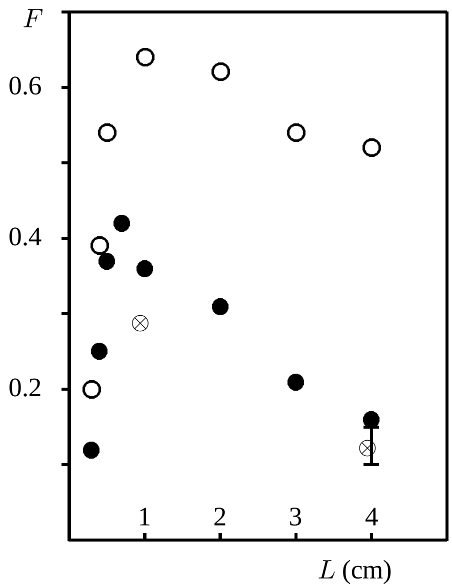

Figure 2: The SPS extraction efficiency vs crystal length. For a perfect surface (o) and septum width t=1 μm (•). The ⊗ are for the U-shaped design and t=20 μm. Also shown is the measured range of efficiencies, 10–15% for the 4-cm U-shaped crystal.

The optimization with the simulations was made with the assumption of a uniform crystal curvature, Fig. 2. For a perfect surface there is almost no dependence for $L \geq 1$ cm in the range studied, but for an imperfect surface there is an important dependence. A new optimum around $L \simeq 0.7$ cm almost doubles the efficiency as compared to that for the 3 cm crystal. Figure 2 shows also two points from a simulation with a U-shaped design and t=20 μm. The shorter crystal had 1-mm "legs" and 8-mm bent part (10 mm in total), and has shown an efficiency near 30 %.

3 THE TEVATRON EXPERIMENT

The Tevatron extraction experiment has provided another check of theory at a substantially higher energy of 900 GeV. A detailed report of predictions for this experiment from the Monte Carlo simulations was published in Ref. [5], and the experimental data can be found in this volume [3].

In our computer model we have investigated three options: a crystal with ideal surface, one with a septum width (amorphous layer) of t=1 μm, and one with t=50 μm. The crystal bending shape and other details were as used later in the experiment. Figure 3 from Ref.pre3 shows that there is little difference between the three options; the peak efficiency is about 35-40%, and the angular scan FWHM is 50-55 μrad. This insensitivity to the crystal surface quality is due to the set-up different from that used in other experiments; as a result, the starting divergence of incident protons at the crystal was not small and hence less sensitive to edge scattering.

The measured peak efficiency was about 30%. This value, together with the measured angular scan, is superimposed in Figure 3 on the theoretical expectation, showing a rather good agreement.

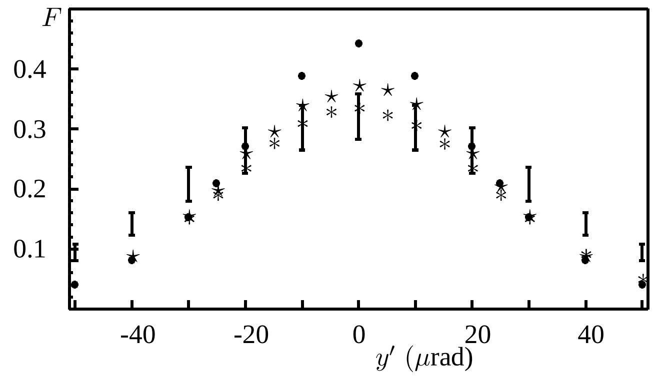

Figure 3: Vertical angular scan of the overall efficiency for the perfect horizontal alignment, x'=0. Ideal crystal (•); imperfect crystal: ($\star$) with t=1 μm, ($*$) is the same with t=50 μm. Also shown is the measured peak efficiency and angular scan.

The efficiency of extraction can again be increased with the use of a shorter crystal. Fig. 4 shows the extraction efficiency dependence on the crystal length L, for uniform bending of crystal. The efficiency is maximal, near 70 %, in the length range from 0.4 to 1.0 cm.

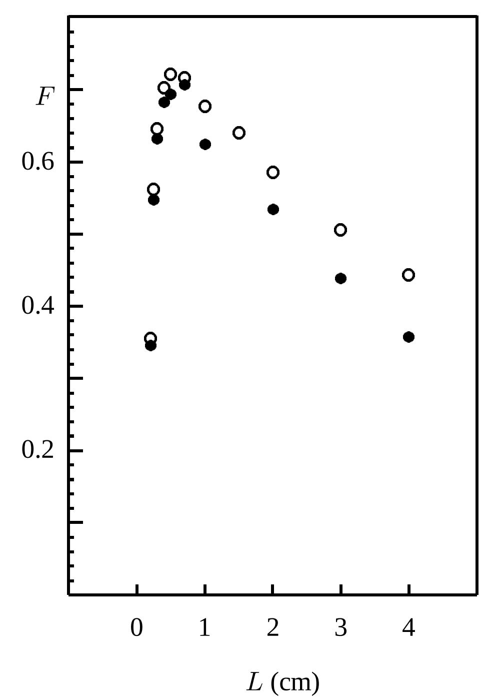

Figure 4: Efficiency as a function of L for the ideal (o) and imperfect (•), t=1 μm, crystals.

4 ANALYTICAL THEORY OF MULTIPASS CRYSTAL EXTRACTION

An analytical theory of multipass crystal extraction would be highly helpful in understanding the experimental results. Below we describe a simple theory for the extraction efficiency [12].

Suppose that a beam with divergence σ, Gaussian distribution, is aligned to the crystal planes. Then as many as

$$(2\theta_c/\sqrt{2\pi}\sigma)(\pi x_c/2d_p) \tag{1}$$

particles get channeled in the initial straight part of the crystal. Here θ_c stands for the critical angle of channeling, d_p the interplanar spacing, $x_c \approx d_p/2 - a_{TF}$ the critical distance, a_{TF} being the Thomas-Fermi screening distance.

We shall first consider the case where particles first come to the crystal with nearly zero divergence, due to very small impact parameters. We assume then that any particle always crosses the full crystal length; that pass 1 is like through an amorphous matter but any further pass is like through a crystalline matter; that there are no aperture restrictions; and that the particles interact only with the crystal not a holder. After some turns in the accelerator ring, the scattered particles come to the crystal with rms divergence as defined by scattering in the first pass:

$$\sigma_1 = (E_s/pv)(L/L_R)^{1/2}, \tag{2}$$

where E_s=13.6 MeV, L is the crystal length, L_R the radiation length, pv the particle momentum times velocity.

After k passes the divergence is $\sigma_k = k^{1/2}\sigma_1$. The number of particles lost in nuclear interactions is $1-\exp(-kL/L_N)$ after k passes; L_N is the interaction length. In what follows we shall first assume that the crystal extraction efficiency is substantially smaller than 100 % (which has actually been the case so far), i.e. the circulating particles are removed from the ring predominantly through the nuclear interactions, not through channeling.

That pulled together, we obtain the multipass channeling efficiency by summation over k passes, from 1 to infinity:

$$F_C = \left(\frac{\pi}{2}\right)^{1/2} \frac{\theta_c x_c}{\sigma_1 d_p} \times \Sigma(L/L_N) \tag{3}$$

where

$$\Sigma(L/L_N) = \Sigma_{k=1}^{\infty} k^{-1/2}\exp(-kL/L_N) \tag{4}$$

may be called a "multiplicity factor" as it just tells how much the single-pass efficiency is amplified in multipasses.

A fraction $1-T$ of channeled particles is to be lost along the bent crystal due to scattering processes and centripetal effects. Then the multipass extraction efficiency is

$$F_E = F_C \times T = \left(\frac{\pi}{2}\right)^{1/2} \frac{\theta_c x_c}{\sigma_1 d_p} \times \Sigma(L/L_N) \times T \tag{5}$$

We shall use an analytical approximation (as used also in [13]) for silicon

$$T = (1-p/3R)^2 \exp\left(-\frac{L}{L_d(1-p/3R)^2}\right), \tag{6}$$

where p is in GeV/c, and R is in cm; L_d is dechanneling length for a straight crystal. The first factor in T describes a centripetal dechanneling. E.g., at pv/R=0.75 GeV/cm (which is close to the highest values used in extraction) our approximation gives $(1-p/3R)^2$=0.563 whereas Forster et al.[14] measured 0.568±0.027. We shall use the theoretical formula for L_d [11]. The sum (4) can be approximated as

$$\Sigma(L/L_N) \simeq (\pi L_N/L)^{1/2} - 1.5 \tag{7}$$

Let us check the theory, first against the CERN SPS data [15] where the crystal extraction efficiency was measured at 14, 120, and 270 GeV (Table 1).

Table 3: Extraction efficiencies (%) from the SPS experiment, theory, and detailed simulations.

pv(GeV)	SPS	Theory	Monte Carlo
14	0.55±0.30	0.30	0.35±0.07
120	15.1±1.2	13.5	13.9±0.6
270	18.6±2.7	17.6	17.8±0.6

The Tevatron extraction experiment at 900 GeV provides another check. Here a slight modification of the formulas is needed to account for the non-zero starting divergence, namely σ_0=11.5 μrad (rms). This results in the change in Eq.(4):

$$\Sigma(L/L_N) = \Sigma_{k=1}^{\infty}(k + \sigma_0^2/\sigma_1^2)^{-1/2}\exp(-kL/L_N) \tag{8}$$

Since in this experiment Si(111) planes were used, consisting of narrow (1/4 weight) and wide (3/4 weight) channels, this is to be taken into account in Eq.(5). Eq.(5) then gives an extraction efficiency of 40.8 %. However, a minor correction to the theoretical value is discussed below.

As the extraction efficiency is getting high, our earlier assumption that the nuclear interactions dominate over the crystal channeling may need correction. To take into account the fact that the circulating particles are efficiently removed from the ring by a crystal extraction as well, one would require a *recurrent* procedure of summation: instead of ΣF_k one has to sum ΣF_k^*, where F_k^*=$F_k(1-F_{k-1}^*)$. This "recurrent" correction doesn't affect our earlier SPS calculation at 14 GeV and makes ~1% drop to the efficiencies at 120 and 270 GeV listed in Table 1. For Tevatron this correction constitutes −6.7%, converting 40.8% into 34.1%, more into line with the measurement.

To see the dependence of extraction efficiency on the microscopic properties of the crystal material and on the particle energy, let us use the well-known theoretical expressions for θ_c=$(4\pi N d_p Z e^2 a_{TF}/pv)^{1/2}$, radiation length L_R=137/$[4Z(Z+1)r_e^2 N\ln(183Z^{-1/3})]$, and E_s=$2\sqrt{2\times 137}m_e c^2$, where N is the number of atoms per unit volume of crystal. The multipass extraction efficiency is then

$$F_E = \frac{\pi}{4}\left(\frac{x_c^2 a_{TF}}{L(Z+1)d_p r_e\ln(183Z^{-1/3})}\right)^{1/2} \tag{9}$$

$$\times \left(\frac{pv}{m_e c^2}\right)^{1/2} T\Sigma(L/L_N)$$

here m_e is the electron mass, r_e the classical electron radius. Despite of the simplifications done, this equation still predicts the SPS efficiency of 15.7% at 120 GeV which is within the experimental error limits.

Figure 5 shows the $F_E(L)$ dependence for extraction at the 120-GeV SPS, 900-GeV Tevatron, and 7-TeV Large Hadron Collider (where 0.7 mrad deflection angle is assumed); in all the cases the crystal bent part was 0.75 of the full length. One can see that the analytical dependences $F_E(L)$ are very close to those obtained earlier in Monte Carlo simulations [16]. The same maxima at the same optimal lengths are predicted.

Formula (5) predicts a high efficiency of multipass extraction at a multi-TeV LHC, about 45 %, with the optimal length of Si(110) crystal being 6±1 cm.

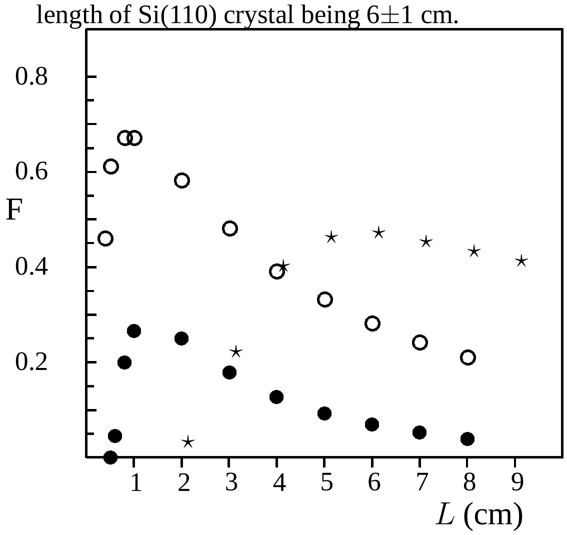

Figure 5: The extraction efficiency, Eq.(5), as a function of the crystal length L; for the SPS (•), Tevatron (o), and Large Hadron Collider (⋆).

5 IHEP EXPERIMENT

The pioneering crystal extraction experiments at Protvino IHEP 70-GeV accelerator were made [8] before any computer simulations of this kind. This is why we prefer to mention a new IHEP experiment planned for November 1997 where one could make predictions in advance.

This experiment employs a very short (7 mm along the beam) silicon crystal bent a small angle of 1.75 mrad. Figure 6 shows the angular scan of the extraction efficiency as seen in Monte Carlo simulations. The peak efficiency is rather modest, about 20%, because of a big effective divergence of the protons at crystal w.r.t. the crystal planes (part of it is due to the crystal design, another part is due to the beam phase space geometry).

As the experiment would also investigate a co-existence of crystal extraction with simultaneous work of two internal targets, this option was simulated as well. We have seen practically no influence on the crystal efficiency from a very

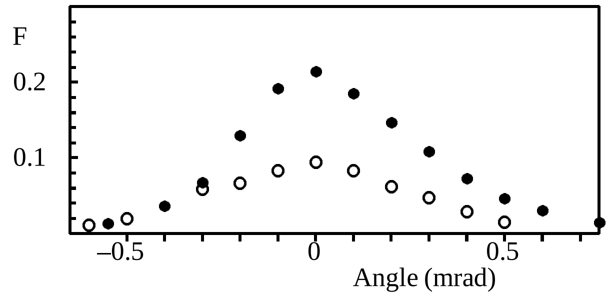

Figure 6: The angular scan of the extraction efficiency as seen in Monte Carlo simulations for 70-GeV IHEP experiment. Crystal without targets (•), and with Be target (o).

thin carbon target, whereas a 3-cm long beryllium target could decrease the extraction efficiency (defined as the ratio of protons extracted to protons lost in nuclear interactions in the crystal) up to factor of two. Figure 6 shows the angular scan in this case also.

6 FUTURE APPLICATIONS

The progress in crystal extraction studies at CERN and Fermilab has been stimulated by the prospects of application of this technique for extraction of a parasitic beam from a large hadron collider for a fixed target physics. Such an extraction is quite feasible from the standpoint of channeling physics. The theory and simulations predict the extraction efficiency of about 50% even under the most conservative assumptions on the crystal design and edge quality.

Another discussed option is extraction from the Tevatron [13] with required minimal angle of 16.4 mrad. In our simulations of this option with use of the same set-up as in the E853 experiment, the efficiency is expected to be 6.3±0.7% with Si crystal of ∼12 cm length even if the first-pass channeling is fully suppressed. However, if channeling in the first encounter is efficient (good crystal edge), the efficiency becomes as high as 23% with the use of optimal 5-cm long Ge(110) crystal. Notice, that this figure—over 20% efficiency of bending at 16.4 mrad by a Ge(110) crystal—is already demonstrated experimentally at CERN with a 200 GeV beam [17]!

One very interesting option is a crystal use in the beam collimation systems. A principle problem for an amorphous collimator is the edge scattering causing a leak of particles incident closer than ∼1 μm to the collimator edge. Furthermore, if collimator of length L is misaligned by an angle θ, the inefficient edge thickness is increased by $L\theta$; therefore, an amorphous collimator should be aligned with accuracy of order $\theta \ll 1\ \mu\text{m}/L \simeq 2\ \mu$rad (for L=450 mm[18])! Compare this with critical angles for crystals—order of 20 μrad at 100 GeV and order of 2 μrad at 7 TeV. Of course, it is much easier to align crystals than huge collimators.

An edge leak doesn't exist in crystalline material for channeled particles. The simplest idea is to put a bent crystal in front and at the edge of a heavy collimator. A large fraction of incident particles is bent by the crystal some small angle of 0.1-0.3 mrad toward the depth of the collimator, and hence fully absorbed (this idea has something common with the idea of a magnetized collimator[18]). The collimator has only to deal with the remaining particles, unchanneled in crystal. According to our Monte Carlo simulations, the efficiency of bending of a parallel beam is about 90% for a 1-TeV beam and 2-cm long Si(110) crystal bent 0.2 mrad, and for a 7-TeV beam and 5-cm long Si(110) crystal bent 0.1 mrad. Notice, that the experimentally demonstrated record of bending efficiency at CERN is already 60% for 2 mrad bending angle at the energy of 0.45 TeV [17]! Hence, under the optimal conditions the inefficiency the collimation system can be reduced by factor of 10. If it were a two-stage collimation system, and both stages equipped by bent crystals, the inefficiency of the whole system would be reduced by factor of 100. Notice that this simplest idea doesn't affect the optics of the collimation design. One could take the existing collimation system and just add crystals to improve its efficiency. More advanced idea would be to separate a bent crystal from a heavy collimator, and to optimize its position w.r.t. the collimator. This idea has been discussed and simulated in Ref.[19].

7 ACKNOWLEDGEMENTS

The author is much indebted to Dick Carrigan, Nikolai Mokhov, and Thornton Murphy for kind hospitality and support during the author's stay at Fermilab.

8 REFERENCES

[1] Asseev A.A., et al., these Proceedings
[2] Elsener K., et al., these Proceedings
[3] Murphy C.T., et al., these Proceedings
[4] Biryukov V., *Phys. Rev. E* **51** (1995), 3522; **52** (1995), 2045; *Phys. Rev. Lett.*, **74**, 2471 (1995)
[5] Biryukov V., *Phys. Rev. E* **52** (1995), 6818
[6] Biryukov V.M. *Nucl. Instr. and Meth. B* **53** 202 (1991). Taratin A.M. et al. *Nucl. Instr. and Meth. B* **58** 103 (1991)
[7] Avdeichikov V.V. et al. JINR Commun. **1** (1984), 3
[8] Asseev A.A., et al., *Nucl. Instr. and Meth. A* **309** (1991), 1
[9] Biryukov V.M. SL/Note 93–78 (AP), CERN, 1993
[10] Minutes of the 19th Meeting on Crystal Extraction from the SPS. SL/BT/Min/CE/93-19. CERN (1993)
[11] Biryukov V., Chesnokov Yu. and Kotov V., *Crystal Channeling and its Application at High Energy Accelerators*. (Springer, Berlin: 1997)
[12] Biryukov V., and Murphy C.T., Fermilab TM-2026 (1997)
[13] Carrigan R.A., Jr., Fermilab TM-1978 (1996)
[14] Forster J.S. et al., *Nucl. Phys. B* **318** (1989), 301
[15] Arduini G., et al., contributed to PAC 97 (Vancouver, 1997)
[16] Biryukov V., *Nucl. Instr. and Meth. B* **117** (1996), 463
[17] C.Biino et al., CERN-SL/97-05(EA), and Phys.Lett. B
[18] LHC Design Report, CERN 93-03 (1993)
[19] Maslov M., Mokhov N. and Yazynin I., SSCL-484 (1991)

V. BEAM DIAGNOSTICS AND INSTRUMENTATION

Fast Beam Loss Monitors at Tevatron

Vladimir Shiltsev
Fermi National Accelerator Laboratory
P.O. Box 500, Batavia, Illinois 60510

Abstract

The article is devoted to results of fine time structure of particle losses in Tevatron with use of fast beam loss monitors (BLM) based on PIN-diodes. An ultimate goal of the new BLMs is to distinguish losses of protons and antiprotons from neighbor bunches with 132 ns bunch spacing in the Tevatron collider upgrade. The devices studied fit well to the goal as they can recognize even seven times closer – 18.9 ns – spaced bunches' losses in the Tevatron fixed target operation regime. We have measured main characteristics of the BLM as well as studied the proton losses over 10 decades of time scale – from dozen of minutes to dozen of nanoseconds. Power spectral density of the losses is compared with spectra of the proton beam motion.

1 INTRODUCTION

The Tevatron collider upgrade follows several approaches to get higher luminosity. Improvement of the injection chain with Main Injector ring, an increase of the antiproton production rate and antiproton recycling in the Recycler ring,etc, all will valuably increase a number of bunches and bunch population, and the colliding proton and antiproton beam intensities as a whole [1, 2].

Besides general expectation of higher beam losses with higher beam intensities due to beam-gas collisions and intrabeam scattering, several issues arise caused by beam-beam forces at two interaction points (IPs, at B0 and D0 low-beta regions) and additional $2 \times (N_b - 1) \sim$ 200-300 parasitic crossings of proton and antiproton bunches. The design value of the total tune shift for antiprotons (pbars) is about maximum experimentally observed value for proton colliders $\xi \approx 0.025$. Thus, as the tune spread of the same value, one may expect an increase of the particle losses due to crossing of higher order lattice resonances.

Then, in order to achieve sufficient beam-beam separation outside IPs, a crossing angle of about 200 microradian between proton and antiproton orbits at the main interaction points is proposed. The crossing angle leads to synchrobetatron coupling, additional resonances, beam blow-up, particle losses and luminosity degradation [3].

Another beam-beam induced effect is the betatron tunes variation along the bunch train (composition of the "head-on" and long-range electromagnetic interaction and due to unequal proton bunch intensities) and $x - y$ coupling due to skew component of the beam-beam kick [2]. The maximum bunch-to-bunch spread $\Delta\nu_{max}$ of the vertical and horizontal tunes is estimated to be about 0.003 during the Tevatron Run II and about 0.01 in TEV33. Thus, the lifetime becomes dependent on the bunch position, e.g. the most severe effects and, therefore, higher losses, are expected for the bunches near the abort gap and injection gaps in the beams (so called PACKMAN effect). As several ways to avoid the effect are under consideration (see, e.g. [4]), there is a need in a beam loss monitor which can distinguish particles lost from different bunches even when the bunch spacing is 132 ns. Such monitors could be also considered as an ideal candidate for loss diagnostics in future multi-bunch machines, like 100 TeV proton-proton supercollider "Pipetron", where the bunch spacing is of the order of hundred nanoseconds [5].

The present Tevatron loss monitor system [6] relies on 216 Argon filled glass sealed coaxial ionization chambers. Most are positioned adjacent to each superconducting quadrupole. Linear dynamic range of the ionization chamber is about 10^4 (usable of about 10^5). There was no need in a bunch-by-bunch loss monitoring at the time of the system installation and the integration time constant was selected to match known properties of the beam-induced quench of the Tevatron superconducting dipoles, and is equal to 60 ms.

About 10^6 times faster PIN-diode BLMs and the first results of their application at the Tevatron are described in this article.

2 OPERATION, TEST AND CALIBRATION OF PIN DIODE BLM

The PIN diode is essentially a p^+nn^+ semiconductor structure (usually silicon based). Details of its operation can be found elsewhere [7]. The most important feature for the purpose of particle detection is enlarged depletion region (region of Si bulk without free carriers, electrons or holes, in PIN diode it is n region, also referred as I-layer), which can be as large as 300 μm in Hamamatsu S2662-02 PIN photo-diode used in our studies. Minimum ionization particles (MIPs) come through the depletion region leaving products of ionization behind, about 25,000 electrons and holes over 300 μm. Therefore, MIPS lose energy – 3.6 eV is required to create an electron-hole pair – with a rate of $dE/dx = 3.7\,MeV/cm$. Thicker depletion layer is beneficial because of more pairs born, and smaller capacity which is proportional to *(diode area/depletion layer width)*. Now, if the reverse voltage applied, then the electric field prevents the pairs recombination and separate charges effectively, and one sees current impulse. Charge collection time decreases with increased depletion voltage and is limited by velocity saturation at high fields, e.g. at extreme, in 300 μm thick detectors with about 300 V reverse bias, electrons are collected within about 8 ns, and holes within about 25 ns. We operate the PIN diode with 25 V bias, and the BLM output pulse width was τ=56 ns at 10% amplitude – see Fig.1.

The beam loss monitors using PIN diodes were developed in DESY [8]. In our studies we used essentially the same type of BLMs by BERGOZ Precision Beam Instrumentation [9] which made the monitors smaller by using surface mounted components – the size of the monitor is 69×34×18 mm.

The monitor consists of two reverse biased PIN-diodes

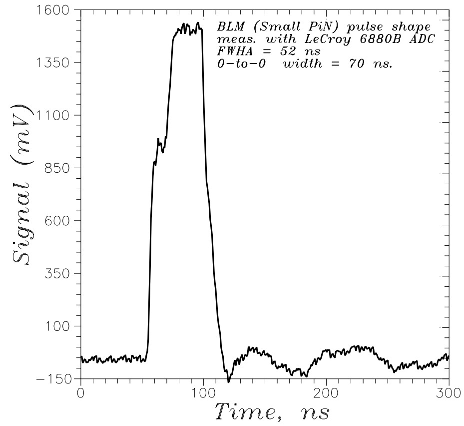

Figure 1: The output signal of the BLM with 7.34 mm^2 BPW34 PIN-diode from Siemens.

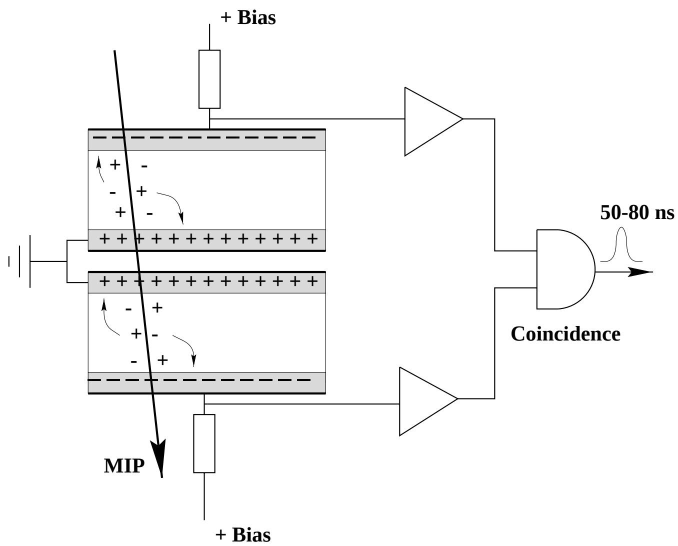

Figure 2: Scheme of the PIN-BLM operation.

mounted face-to-face. Charged particles which cross both diodes produce signals in both diodes. To reduce the electronic noise [1] and low-energy photon background only a coincidence signal from the two diodes is used – see the BLM layout in Fig.2. For example, a single diode spurious count rate is some kHz, while the coincidence scheme output gives less than 1 Hz. Further reduction to 0.1–0.01 Hz can be made by adjusting the discriminator threshold. Therefore, taking into account about 50ns pulse width, we get the dynamical range of the monitor of $2 \cdot 10^8 - 2 \cdot 10^9$.

The monitor with Siemens BPW34 PIN-diode of 7.34 mm^2 area was calibrated at DESY with respect to the BLM with previously measured efficiency of $\varepsilon_0 = 0.35 \pm 0.02$ [10]. The same Ru-106 β-source with about 300 μCi activity was used for both probes. The DESY BLM covered 2π solid angle and gave 105.2±37.2 counts per 10 seconds while the PIN diode in BERGOZ BLM covered only 1.27 srad of solid angle being about 2.4 mm from the source and produced 26.0±7.9 counts per 10 seconds. Therefore, the efficiency of the BERGOZ BLM can be estimated as $\varepsilon_1 = \varepsilon_0 \times (1.2 \pm 0.56)$, i.e. the same as ε_0 within the error of measurements, although the latter was large.

Two BLMs equipped, one with two 7.34 mm^2 BPW34 diodes from Siemens and another with $7.5\times20 = 150$ mm^2 S2662-02 photodiodes from Hamamatsu were used in our experiments at Tevatron. The electronic circuits are the same in both cases. The larger area BLM signal has a slightly different pulse shape, about 10% larger pulse width, and about 1.5-2 times larger amplitude than the smaller area PIN diode monitor (2.5-3 V on 50 Ω load with respect to 1.5-2 V). Besides +24V for reversed biasing of the diodes, the BLM requires $\pm$5V power supplies for electronics.

Initial tests with Sr-90 0.5 MeV β source and with Ru-106 3.5 MeV β source have shown that in order to get well detectable count rate, the source activity has to be several dozens of μCi. While the energy of the β particles is in the MeV range, the 0.2 mm thick copper cover over the PIN-diode causes about 10 times reduction in the count rate. For high energy particles (hundreds GeV protons) the cover does not matter. Extremely high radiation resistance of the PIN diode BLMs – they are reported to survive well irradiation of $2{\cdot}10^8$ rad [11] – makes them very useful for accelerator applications.

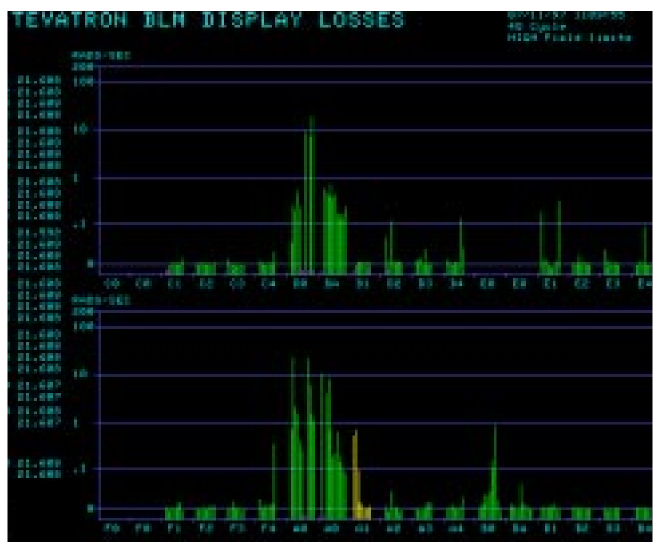

Figure 3: Radiation levels around the Tevatron ring measured with ionization chambers (courtesy of the Tevatron control room).

3 PIN-BLMS AT TEVATRON

Particle loss studies with the PIN-BLMs were carried out from March to June 1997 when the Tevatron worked for fixed target experiments. Injection of about $2.5{\cdot}10^{13}$ protons from the Main Ring took place at 150 GeV. The accelerator operated with some 1000 bunches at 800 GeV. Minimum bunch spacing was about 18.9 ns which is 7 times less than for TEV33 upgrade regime. The rms bunch length in Tevatron is about 1-2 ns – very small with respect to the PIN-diode pulse width. Therefore, if two or more particles,

[1] mainly produced by the diode dark current, its capacitance, and by transistors in the first amplification circuit

simultaneously lost from the same bunch, cross the diode area then one can see only one BLM count. It yields in maximum possible counting rate of about 159×47.7kHz=7.6 MHz with 132ns bunch spacing (i.e. one particle lost and detected from each of maximum 159 bunches at every turn, the revolution frequency of 47.7 kHz); and $1/\tau \simeq$12-16 MHz for 18.9ns spacing (one count per turn from every 3-4 bunches).

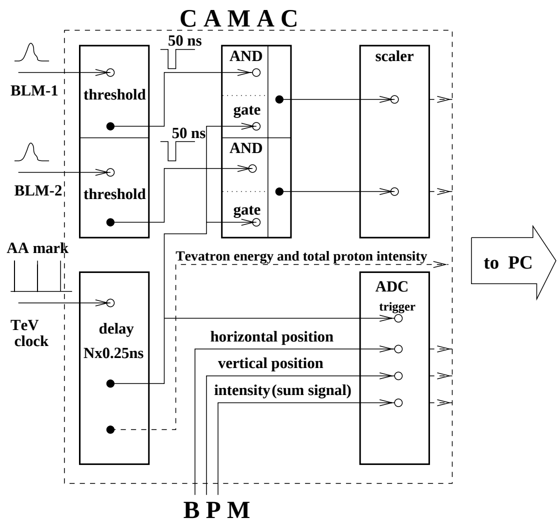

Figure 4: Scheme of the data acquisition used in the beam loss studies.

For our studies we attached two BLMs immediately to the vacuum chamber of the Tevatron near the end of the Sector F0, at the F11 magnet. Nearby located ionization chamber gives the radiation level there to be about D =0.0005-0.0012 rad/sec – one of the lowest values along the Tevatron. The radiation level distribution in the Tevatron during the fixed target regime is shown in Fig.3. Having the dose D one can estimate the flux of MIPs Φ accordingly to formula:

$$\Phi = D/\big(dE/dx\big), \tag{1}$$

or $\Phi \approx (1.25 - 3) \cdot 10^4\, 1/cm^2/s$ for $dE/dx = 2.5\, MeV/(g/cm^2)$. [2] For a monitor with 1.5 cm^2 area of the PIN diode, and efficiency of 0.35, one gets the BLM count rate of $\dot{N} = 6 - 16$ kHz. In fact we observed up to 6 times larger rates, probably because of a) continuously improving beam intensity, b) ionization chambers are installed not so close to the vacuum chamber and shielded by the magnet iron that reduces the flux:

$$\Phi \propto \frac{1}{r} exp(-d/\lambda) \tag{2}$$

where r is radius from the beam orbit, d is the metal thickness, and $\lambda \sim 15$ cm is the interaction length in iron.

About 40 m long coaxial cables from the Tevatron RF equipment room to the tunnel are used to supply the BLMs with ±5V and +25V, and for transmitting outputs of the BLMs and nearby located strip-line BPM to a data acquisition system.

[2] here we used an definition 1 rad/sec=6.24·10^7 MeV/g/s

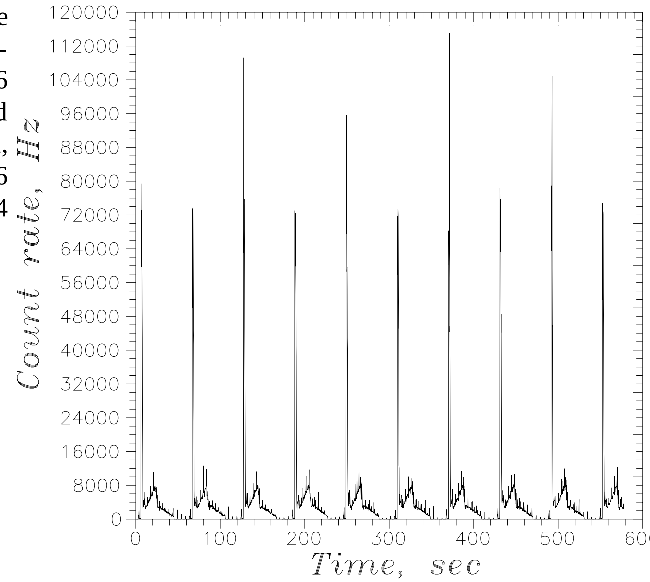

Figure 5: The BLM count rate over several cycles of acceleration in Tevatron.

3.1 Data acquisition

Scheme of the CAMAC-based data acquisition system is shown in Fig.4. Analog signals from the two PIN-BLMs (+1.5–2.5 V) go to LeCroy 2323A gate generator which works as a discriminator with variable thresholds and forms two NIM level outputs of 50 ns each. These signals go to the second LeCroy 2323A which produces the outputs as long as the external gate signal is asserted. The gate signal is synchronized with the Tevatron 7.57 MHz RF clock provided by Beam Clock/Timer module 279. Its duration is variable from 50 ns to 21 μs (the Tevatron revolution period), and its delay with respect to AA synchronization mark is controlled by computer with a minimum step of 1/4 ns. If the signals pass the gate, then they are counted by LeCroy 2551 scaler.

Other information we used is the proton energy (proportional to the Tevatron dipole current) and total proton intensity – these numbers are available in digital form with use of MDAT receiver module 169. ADC QD 808 triggered by the same gate signal as for BLMs, is used for digitizing analogous signals from the BPM: horizontal orbit position, vertical orbit position and sum signal proportional to the beam current. Analog electronics of the strip-line BPM occupies a separate VME crate and has a 5 MHz frequency band.

All information channels from the CAMAC crate are available in a personal IBM PC/AT 386 computer through C1000 crate-controller and a parallel PC-CAMAC interface card.

4 RESULTS

4.1 Longer time scales

Fig.5 presents the PIN-BLM count rate in Tevatron over a 10 minute time scale. The gate width 1s full revolution turn,

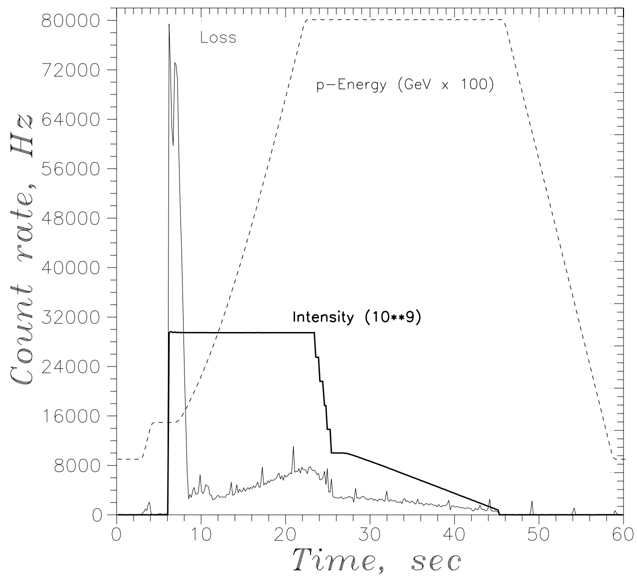

Figure 6: The BLM count rate (thin line), proton beam intensity (thick solid line) and proton energy (dashed line) over one cycle of acceleration in Tevatron.

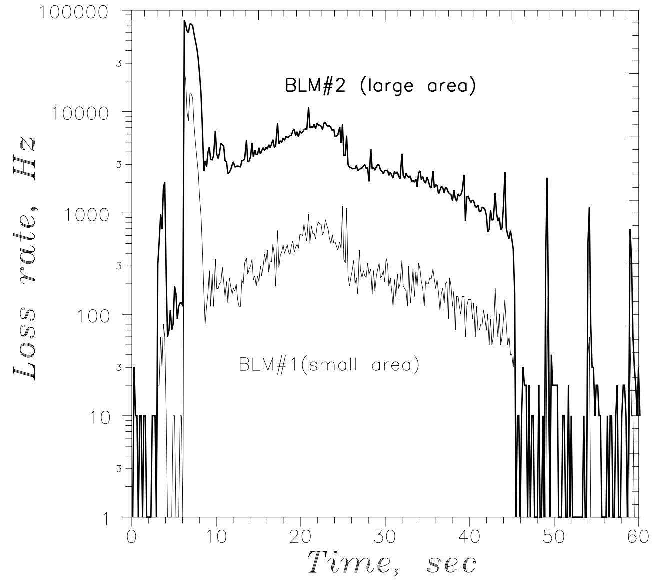

Figure 7: Count rates during the cycle of acceleration from two BLMs with different PIN-photodiode areas.

i.e. losses from all bunches are taken into account. The loss rate is averaged over regular 100 ms intervals. The rate is almost periodic with a period of 60 sec – the Tevatron fixed target cycle period. Fig.6 shows the first of the cycles in Fig. 5 in more detail over 60 seconds. Proton energy (calculated via the SC dipole current) and intensity are presented by dashed line and thick solid line, correspondingly. About $2.8{\cdot}10^{13}$ are injected from the Main Ring at 150 GeV (at 6 sec in Fig.6) then they are accelerated to 800 GeV within 15 sec (over so called ”parabola” – as the energy changes quadratically in time) without substantial change in the beam intensity. After reaching the top energy, the beam is extracted in five steps of fast extraction to one third of initial intensity, and then slow extraction takes place over 20 sec. After finishing the extraction, the current in the dipoles goes down and the cycle repeats.

The BLM count rate is very high over the first few seconds after injection, probably caused by imperfections like non-flat kicker pulse top, remaining betatron oscillations after injection, etc. It is then somehow stabilized at the beginning of the ”parabola” and grows with the energy because each lost proton give birth to a number of secondary particles which still can ionize the PIN-diode depletion region bulk. That number is approximately proportional to the incident proton energy. During the slow extraction, the count rate decreases as the total proton current goes down. Over all the cycle, one can see some dozen of smaller and sharp peaks in the loss rate with a period of about 4 sec, which is equal to the Main Ring injection period. These peaks can be explained by injection losses in the MR which is located in the same tunnel over the Tevatron magnets.

In Fig.7 we compare count rates from two BLMs: one with large area PIN-diode and another with smaller one. One can see that they show the same temporal behavior and are different only in scale. At top energy, the monitor calibration constants are 49 counts of BLM#1 per 10^9 lost protons and 513 counts of the BLM#2 per 10^9 lost protons. The difference factor of about 10.5 is twice smaller than the ratio of the diode areas 20.4$= 150\,mm^2\,/7.34\,mm^2$ – probably because the probes are not located in the same point. Instead, one of them (larger area BLM#2) is set on the top of the vacuum chamber, while the other one (smaller area BLM#1) is attached to the outer side. Due to non-zero dispersion and collimators, the losses are not supposed to be equal over the azimuth, although the issue needs further experimental studies.

Next Fig.8 demonstrates dependence of the BLM count rate on the bias voltage. The reverse bias was set to be equal to 24V, 20V, 16V, 12V, 8V, 4V and 3V at seven consequent cycles. The beam intensity is almost the same for all cycles. One can see that the count rate varies slowly if bias goes down from 24V to 16V, but drops significantly if the voltage is 8V and less.

Looking in more detail (another factor of 1/10 in time) one can observe the time structure of losses during fast extraction as is shown in Fig.9 (thick line - for loss rate, thin line - for the horizontal orbit). The horizontal orbit is measured by the BPM in a frequency band of 300 Hz and its maximum deflection in Fig.9 corresponds to approximately 1 mm movement. In this measurements only, the BLM signals are transformed from positive 60-ns pulses to negative NIM pulses 10 μs long, which are further integrated by an amplifier with 100 Hz bandwidth and sent to the same ADC as used for the BLM signals. The beam position is disturbed five times by extraction kicks, and, correspondingly, there are five peaks in the BLM signal. Aside from periods of strong beam disturbances, no regular structure is seen in losses which look like a noise.

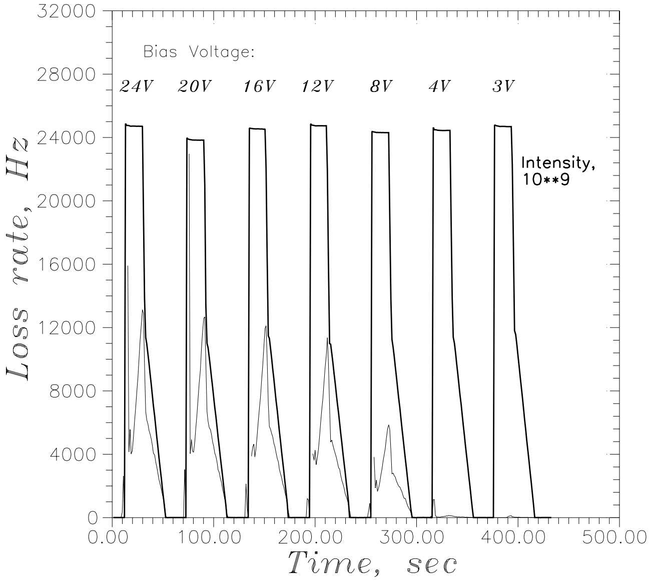

Figure 8: The PIN-BLM count rate with different reverse bias voltages. The proton intensity (thick line) is about the same over seven cycles.

It is clearly seen in the power spectral densities of the loss and BLM signals measured during the "parabola" (acceleration) – see Fig.10. The orbit spectrum demonstrates many peaks at 4.5Hz, 7Hz, 9.5Hz, while the only not-well recognizable peak at about 9.5Hz is seen in the loss spectrum. Broad and continuous spectrum is a specific feature of noisy processes. Note, that during the the fixed target of operation Tevatron, the beam is very unstable. It does not live for a long time under the same condition, its losses are higher and not stationary. In the collider regime with hours of stable operation, one may expect more stationary and, generally speaking, smaller losses which now can carry information about routine beam orbit disturbances. This information can be used for their identifications via analysis of the peaks in the spectra as it is done at HERA [12, 13].

4.2 One-turn and one-bunch time scales

Now we consider how the PIN-BLM count rate varies over the whole bunch train of the Tevatron. Fig.11 shows the count rate measured during the first few seconds after the injection vs time delay with respect to the gap. The step in the delay time is 132 ns – every 7th RF bucket – and as it is supposed to be a bunch spacing in TEV33, we counted the time in Fig.11 as "bunch number" N from 0 to 159, although the real number of bunches in Tevatron is about 1000 in the fixed target regime.

The procedure of the measurement is as following: first, the BLM signals are counted by scaler only if a) the beam energy is in the interval from 150 GeV to 225 GeV, i.e. during the first few seconds after the injection; b) the counts appear at the time interval of 64+64=128 ns starting the chosen delay $N \times 132$ ns with respect to the AA synchronization mark. The scaler counts over 20 turns of the Tevatron (0.42 ms), then the computer saves the number of the counts in the memory, gets the ADC reading of the BPM sum signal proportional to the proton charge (ADC is triggered by the same synchronization signal as the scaler gate), saves it too, and changes the synchronization from N to $N+1$, etc. The data are averaged over many cycles of the Tevatron (for the particular data presented in Fig.11, the number of cycles is 434 – about 7 hours of integration).

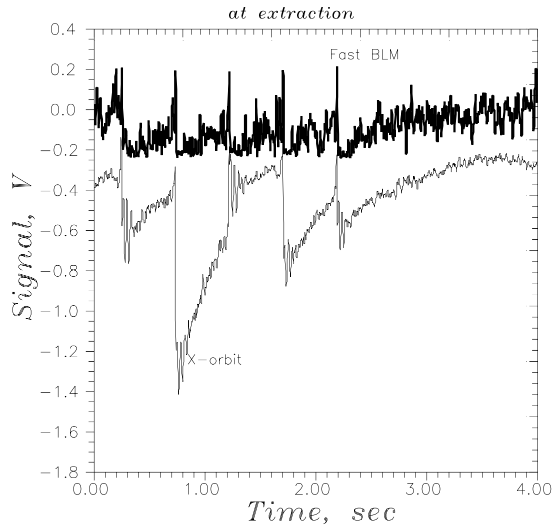

Figure 9: 4-sec time record of the horizontal orbit signal from BPM and the BLM output integrated with $\tau = 1/f_0 = 1/300$Hz=3.3 ms (thick solid line) during fast extraction from Tevatron.

In the same Figure one can see the proton intensity (thin line) which clearly demonstrates that there is about 2 μs long abort gap in the beam, and there are twelve batches (84 bunches in each) with smaller ~ 100 ns long gaps in between them. These short gaps are not seen as a full 100% drop in the intensity plot because of the limited frequency band of the BPM electronics and the ADC module electronics. The proton intensity does not vary too much over the beam, while the count rate varies significantly. First of all there is a huge increase of losses near the abort gap (although there are no losses during the gap time). Then, the count rate emphasize small inter-batch gaps, decreases with N and has additional broad peak at $N = 40 - 60$. Initially there was the idea that the smooth decrease of the count rate is an artifact of the measurements because the loss rate rapidly goes down after injection and we make one cycle of the measurements over rather long interval of 159×0.42 ms= 67 ms. Therefore, the losses at $N = 159$ always must be the smallest, while the count rate at $N = 1$ (beginning of the measurements' cycle) will be the biggest one. This consideration was not confirmed – e.g. in Fig.12 we present the count rate over the beam at injection but the synchronization is shifted on 130 "bunches" (and the abort gap takes place now at $N = 134$). One can see that still losses are larger near the gap, but there is no continuous de-

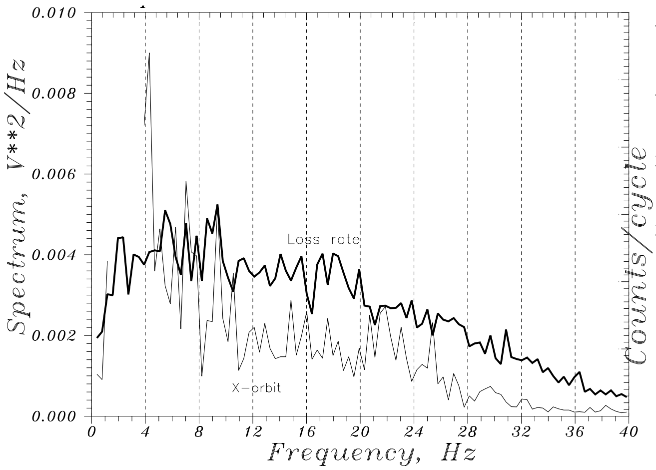

Figure 10: Power spectral densities (a.u.) of the BLM signal (thick solid line) and the horizontal orbit signal (thin line) measured during acceleration of protons from 225 GeV to 800 GeV (at "parabola").

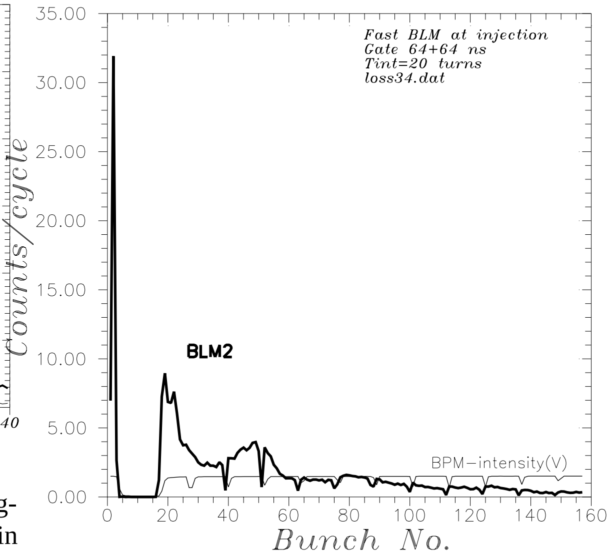

Figure 11: Distribution of losses over the proton beam at the injection energy. Thin line shows the proton intensity.

crease of loss rate with N. In opposite, one half of the beam $N = 70 - 130$ loses about twice particles then the other $N = 1 - 70$. Note, that data presented in Fig.11 and Fig.12 are obtained at different times when the operation conditions were not the same, e.g. injected beam intensities were about $1.6 \cdot 10^{13}$ and $2.4 \cdot 10^{13}$, correspondingly.

The beam loss rate at the "parabola" (Fig.13) looks very similar to the injection one – compare with Fig.11. Distribution of losses over the beam at the top energy is very different (see Fig.14): first, the count rate is much less than at the injection and "parabola", then, there are three huge peaks corresponding to moments of fast extraction (see thick line in Fig.14). Proton losses at slow extraction are distributed almost uniformly over the beam (see thin line in Fig.14), and they are proportional to the intensity as it is presented in Fig.15.

Next step of our studies is to measure loss distribution in more detail. We performed a scan of a 800 ns long part of the Tevatron beam with 2 ns step starting from "bunch" $N = 47$ in Fig.11, 13-15 ($N = 31$ in Fig.12). Counting of pulses took place over the whole acceleration cycle of the Tevatron. The result is presented in Fig.16. The most remarkable feature in this Figure is the gap between two batches. One can see that the gap width is approximately 130 ns although the edges of the gap are smeared because of the gate width of 50+50=100 ns. Several regions of enhanced losses (around 4170 ns, 4410 ns, 4530 ns and 4850 ns) are due to larger losses at the fast extraction (see below). Small periodic variation of the count rate corresponds to 18.9 ns bunch spacing. This modulation depth of these 18.9 ns variation is rather small because the gate width (the dead time of the PIN-BLM plus the gate width for the scaler) is about five times the bunch spacing.

The bunch structure of the proton losses at injection is clearly seen in Fig.17 where we made the scan with 100 ns gate over 100 ns starting with "bunch" #57 (see Fig.11) and with a step of 1 ns. To obtain low statistical noises with about 70,000 counts in every bin we performed integration over 5881 cycles of the Tevatron (more than 4 days of operation). The value presented in Fig.15 is an average over these cycles. Now the bunch-to-bunch modulation with period of some 19 ns is clearly seen. As noted above, the modulation can not be deeper because of the limited gate width. Indeed, assume that the lost particles come from 1-2 ns long bunches, then the factual picture of the losses $f(t)$ looks as it shown in the bottom plot of Fig.18. The BLM and the scaler gate serve as an effective window for integration $W(t)$ (presented by marked line in Fig.18) about 100 ns long, and the measured loss signal $Loss(t)$ is essentially convolution of the input signal and the window:

$$Loss(t) \propto \int_{-\infty}^{+\infty} W(t') \cdot f(t'-t)dt \qquad (3)$$

The resulting output is shown by dashed line which looks much like the experimentally measured data (upper solid line in Fig.18, the same as in Fig.17). For 132 ns bunch spacing in TEV33 we expect the bunch structure will be seen with full 100% deep modulation.

If we compare the losses which take place for the same bunches during the acceleration process (at "parabola) from 225 GeV to 800 GeV, then we get the picture shown in Fig.19. Although the count rate is many times smaller and the statistical error is larger than at the injection, the bunches are clearly seen again. Finally, the losses of same bunches at the top energy of 800 GeV are presented in Fig.20. The loss distribution looks different to what is shown in Figs.17,19, because of five peaks in the count rate. We found that these peaks are due to five steps of fast extraction. They always appear at the same moment of time because the extraction and the scaler gating are both synchronized to the same Tevatron clock. Locations of these

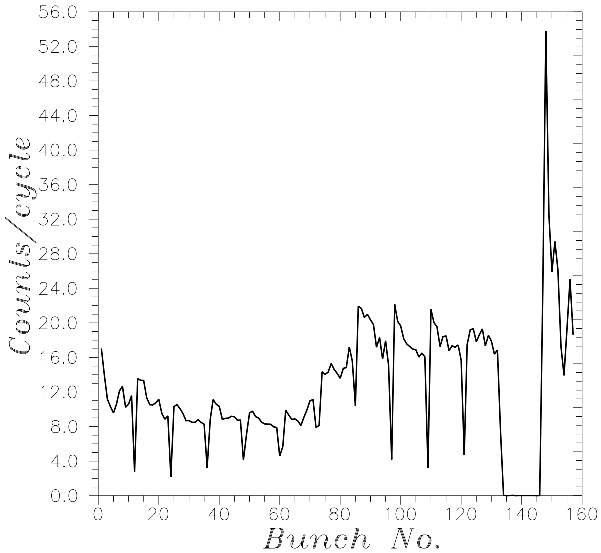

Figure 12: Distribution of losses over the proton beam at injection. Synchronization is changed from what presented in Fig.11.

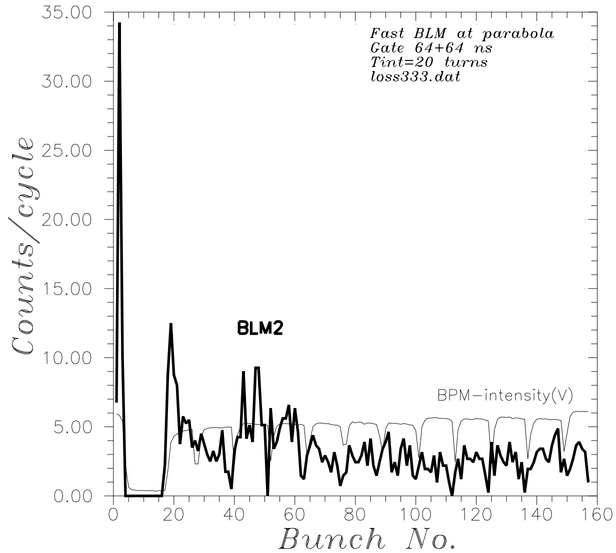

Figure 13: Distribution of losses over the proton beam during acceleration (at "parabola").

peaks depend on the number of the time scan steps (e.g. 400 in Figs. 19, 20 and 100 in Fig.17) while the positions of the bunches are always the same.

5 CONCLUSION

We studied the structure of the proton losses in the Tevatron during fixed target operation with use of very fast Beam Loss Monitors based on PIN photodiodes. The BLM are very useful as they have huge dynamical range of more than 10^8: from 0.1 Hz to few tens of MHz. Being very resistive to radiation, the PIN-BLMs are found very useful for accelerator applications. They allowed us to investigate the losses at the time scales from ten minutes to tens of nanoseconds, to observe the loss distribution over the whole Tevatron acceleration cycle, over one turn, one batch of bunches, and over few bunches.

These probes can be very useful for the Run II and TEV33 upgrades of the Tevatron collider. They can detect losses from different proton and antiproton bunches with minimum bunch spacing of 132 ns. The theory predicts that the losses will vary from bunch-to-bunch due to different bunch dynamics, therefore, the PIN-BLMs will provide the information needed for the beam control. For routine operation at Run II and TEV33, several probes can be installed in addition to an existing (much slower) loss monitoring system at the locations upstream and downstream of the collimators (that allows us to separate losses of protons and antiprotons, as it's done for electrons and positrons at LEP [14]), and at several other important locations.

Acknowledgments

I am indebted to Jim Zagel and Marvin Olson for their practical help at the early stage of the studies and during installation of the probes at the Tevatron tunnel. I also acknowledge technical assistance of Rupe Crouch and Sasha Moibenko in developing the data acquisition system for the experiment. My sincerely gratitude to Kay Wittenburg (DESY) and Julien Bergoz (BERGOZ Co.) for some useful hints concerning the BLM operation, and Fernando Ridoutt (DESY) for cooperation in the probes calibration. Very useful discussions on the scheme and the results of these studies were held with Nikolai Mokhov, Sasha Drozhdin, Pat Colestock, Oleg Krivosheev, Mike Martens and Alan Hahn. I would like to thank Marvin Olson, Jim Zagel, Pat Smith and Stan Pruss for reading the manuscript and useful correction, and Dave Finley and John Marriner for their interest in this work and steady support.

6 REFERENCES

[1] J.P.Marriner, "The Fermilab Proton-Antiproton Collider Upgrades", FERMILAB-Conf-96/391 (1996); S.D.Holmes, *et.al*, FNAL-TM-1920 (1995).

[2] P.Bagley,*et. al*, "Summary of the TEV33 Working Group", FERMILAB-Conf-96/392 (1996).

[3] V.Shiltsev, "On Crossing Angle at TEV33", FERMILAB-FN-653 (1997).

[4] V.Shiltsev, D.Finley, "Electron Compression" of the Beam-Beam Footprint in Tevatron", FNAL-TM-2008 (1997).

[5] D.Neuffer, "Discussion of Parameters, Lattices and Beam Stability for the MegaCollider", FERMILAB-TM-1964 (1995);
G.W.Foster, E.Malamud, "Low-Cost Hadron Collider at Fermilab: A Discussion Paper", FERMILAB-TM-1976 (1996).

[6] R.Shafer, *et.al*, "The Tevatron Beam Position and Beam Loss Monitoring System", *Proc. 12th Int. Conf. On High-Energy Accel.*, Fermilab (1986), p.609.

[7] E.Bleufler, R.O.Haxby, eds., "Methods of Experimental Physics: Vol.2, Electronic Methods", Part A, Academic

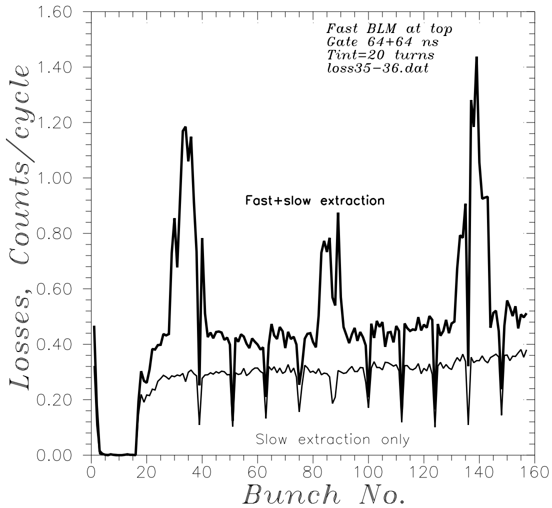

Figure 14: Distribution of proton losses over the Tevatron revolution period at 800 GeV. Thick line – the fast and slow extraction; thin line – slow extraction only.

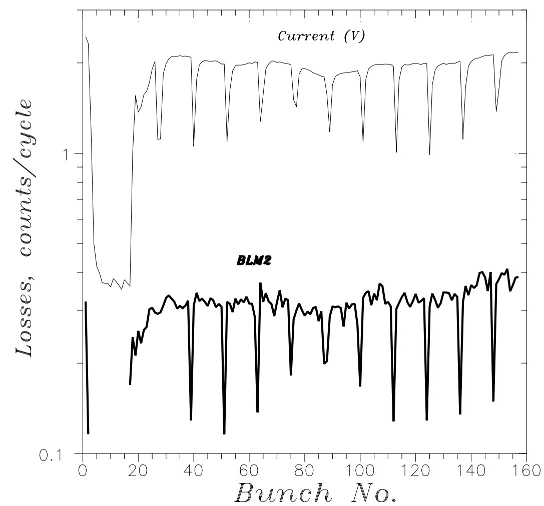

Figure 15: Distribution of proton losses over the Tevatron revolution period during slow extraction at 800 GeV. Thin line is for proton intensity.

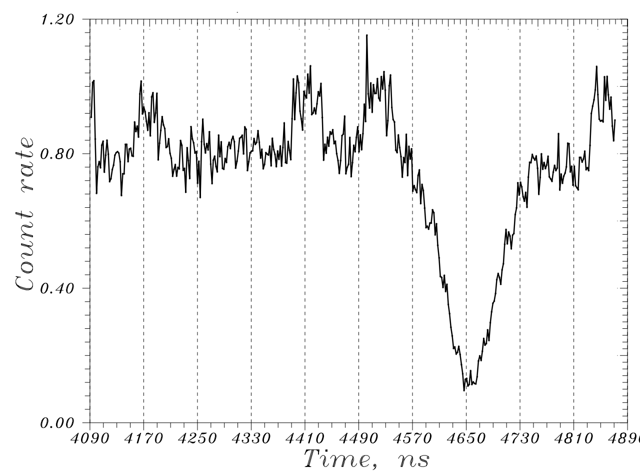

Figure 16: Losses of particular 0.8 μs long part of the proton beam, integrated over the whole cycle of acceleration.

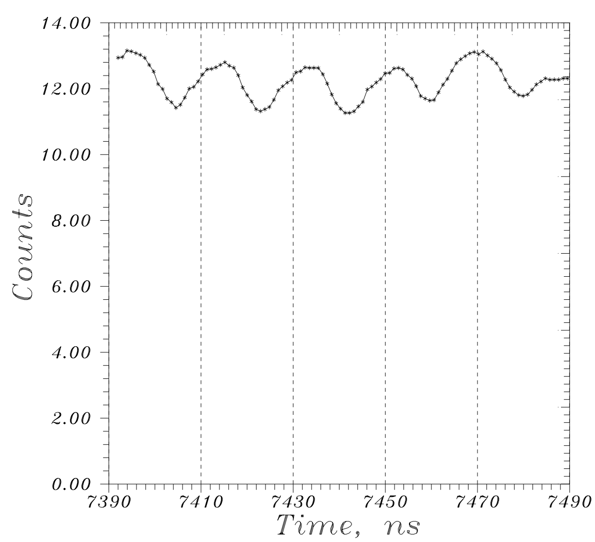

Figure 17: Proton losses of several bunches at injection.

Press, New York (1975);
G.Charpak, F.Sauli, "High-Resolution Electronic Particle Detectors", in *Experimental Techniques in High Energy Physics*, T.Ferbel, ed., Addison-Wisley Publishing (1987).

[8] K.Wittenburg, "Strachlverlustdetectoren fur den HERA Protonen-Ring", DESY-HERA 89-23 (1989); see also the same author in *Nucl. Instr. Meth. A270* (1988), p.56; *Proc. 1st DIPAC*, CERN (1993), p.11; *Nucl. Instr. Meth. A345* (1994), p.226.

[9] "Beam Loss Monitor. User's Manual", BERGOZ Precision Beam Instrumentation (1996).

[10] F.Ridoutt, "Das Ansprechvermogen Des PIN-Strahlustmonitors", DESY PKTR-Note-91 (1993).

[11] K.Werhheim, K.Wittenburg, "Radiation Resistance of Beam Loss Monitors", Internal Report DESY M-94-08 (1994).

[12] M.Zeidel, "The Proton Collimation System of HERA", PhD Thesis, DESY 94-103 (1994); see also the same author DESY-HERA 93-04 (1993); and K.-H.Mess, M.Zeidel, "Collimators as Diagnostic Tools in the Proton Machine of HERA", *Nucl. Instr. Meth. A351* (1994), p.279.

[13] V.Shiltsev, *et al.* "Measurements of Ground Motion and Orbit Motion at HERA", DESY HERA 95-06 (1995).

[14] H.Burkhard, *et. al*, "Beam Tails in LEP", *Proc. 1996 EPAC*, Barcelona, p.1152; and I.Reichel, H.Burkhardt, G.Roy, "Observation and Simulation of Beam Tails in LEP", *Proc. 1997 PAC*, Vancouver.

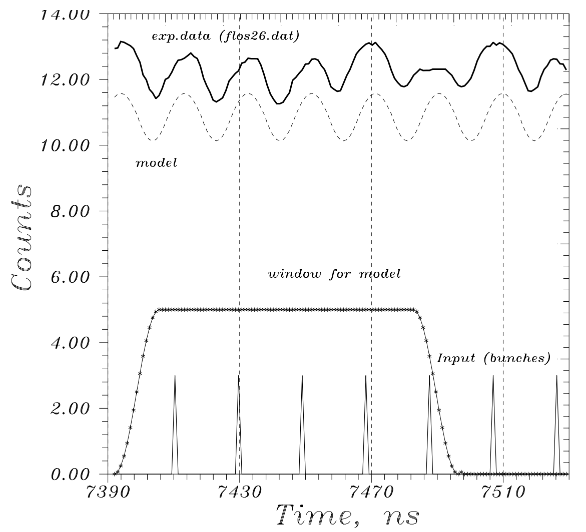

Figure 18: The same as in Fig.17 (top solid line) with results of the count rate modeling (see text).

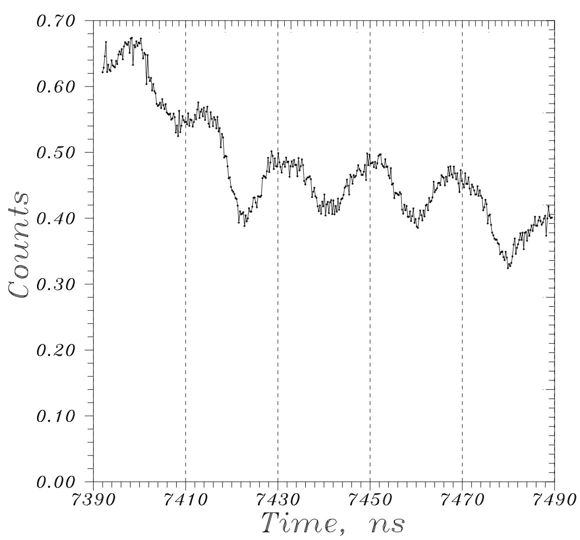

Figure 19: Proton losses of the same bunches as in Fig.17 during acceleration (at "parabola").

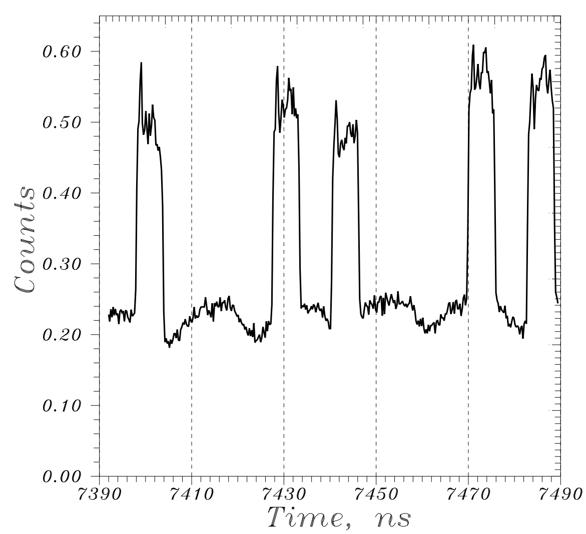

Figure 20: Proton losses of the same bunches as in Fig.17 at the top energy of 800 GeV.

VIBRATIONAL ANALYSIS OF TEVATRON QUADRUPOLES

C. D. Moore, Fermilab, Batavia , Illinois, USA

1 INTRODUCTION

There is motion of the beam in the Tevatron on various time scales from years (slow motion of the tunnel) to tenths of milliseconds (betatron tune motion). This paper will discuss a very restricted frequency range from a few Hertz to a few tens of Hertz. The assumption behind the analysis presented here is that the beam motion is due to transverse motion of Tevatron quadrupoles.

The introduction of the low beta insertions in the Tevatron has necessitated the installation of remote monitoring sensors on the quadrupoles since the quadrupoles are strong and are located in regions where the beta functions are large [1] as shown in Fig. 1. In general the magnet and support structures are mirror symmetric around the interaction points.

Motion of the beam due to a certain magnitude quadrupole motion is proportional to the product of the square root of the beta function and the strength of the quad. Table 1 shows the maximum amplitude in millimeters that would be measured on a Beam Position Monitor in the arcs for a one millimeter displacement of a low beta quadrupole at D0 [2].

The importance of this monitoring effort was brought to the fore during the rolled quad episode during the last collider run when we did not have this remote monitoring capability. Water levels and inclinometers have been installed on some of the quadrupoles in the interaction regions (Fig. 2) and have been used, for example, to indicate an ice ball forming on a quadrupole inside the CDF detector [3] and physical displacement of a quadrupole during the installation of shielding [4]. These are important examples however we shall restrict our discussion to motion on shorter time scales.

Fourier analysis of the inclinometer signals indicated a plethora of frequencies as shown in Fig. 3. This discovery of the spikes in the frequency spectrum started this analysis which attempts to correlate the spatial pattern of several differing frequencies of beam motion as measured by the Tevatron Beam Position Monitors (BPMs) with observed motion of the Tevatron quadrupoles (mainly low beta quadrupoles).

2 MAGNET VIBRATION SPECTRA

We enlisted the help of several experts from Argonne National Laboratory [5] to make a systematic study of the vibrational spectra of the ground, the tunnel floor, and quadrupoles (mainly low beta quadrupoles). Fig. 4 gives an overview of the site detailing where the motion studies took place.

A non low beta quadrupole spectrum is shown in Fig. 5 for various reasons, one of which is that it is so instructive. The location was at A3 which is physically close to the Central Helium Liquefier plant (CHL) which has two types of compressors which have fundamental frequencies of 4.6 and 8.5 Hz. We observe sharp lines in the ground and in the magnet at the fundamental and up to the fifth (third) harmonic for the Helium (Nitrogen) compressor. The ground motion is greater than the magnet up to the 19 Hz region where we observe a well known [6] stand resonance. A particular reason for mentioning the 4.6 Hz signal is that we use this signal as our "standard candle", i.e. this is our frequency calibration check at the different geographical locations.

Many sets of data were taken as shown in Fig. 4 and we will present three sets that are illustrative and that happen to agree with the analysis presented below. Fig. 6 shows the vertical frequency spectra measured on one of the Q3 quadrupoles in D0. The interesting portion of this spectrum is in the 20 to 25 Hz region and we shall discuss the relationship of this spectrum to the observed BPM spectrum in the following section. Fig. 7 shows the vertical frequency of the two Q3 style quadrupoles in the B0 interaction region. Of interest here is the slight offset in frequency of the two peaks near 18.5 Hz, we shall see this phenomena in the next Fig. and our interpretation is that the peaks are due to a support structure resonance and the mechanical assemblage, although theoretically mirror symmetric, is slightly different on either side of the collision point. The support structures are different at B0 and D0, and we shall discuss the structure at D0 in more detail below, however the slight differences are apparent at both B0 and D0.

To bring out the difference between ground motion and "stand" resonant effect an analogous plot to the one shown in Fig. 5 is given in Fig. 8 which shows the A4Q3 vertical spectra along with the concrete floor at the position of the magnet and we can see several of the ground motion spikes in the concrete and the magnet along with the broader peak at 18.2 Hz in the magnet spectra. So in the low beta quad vibration spectrum we can also see ground motion spikes and "stand" resonances. We expect the ground motion spikes to be the same for all magnets in a region but the possibility exist for slight differences in the mirror symmetric magnets on either side of the interaction regions.

An example of a horizontal spectrum is shown in Fig. 9 which has the same data plotted linearly and semilogarithmically, in the semilog plot we can see the 4.6 Hz, but the linear plot is much cleaner in pointing out the broad strong 13.5 Hz peak and the small differences from one side of the interaction region to the other.

3 BPM SPECTRA

A set of BPM spectra was taken in 1/6 of the Tevatron centered about the D0 interaction region. Twenty one spectra were taken in both the horizontal and vertical planes. Representative spectra in the horizontal and vertical plane are shown in Figs. 10 and 11. In the vertical case the distinctive pattern between 20 and 25 Hz is one of the most striking features of the vertical spectra and the similarity to the shape in Fig. 6 will be used to choose which quad to use in our modeling.

The signal above background was tabulated for the different frequencies and is given in tables 2 and 3, where the units are in millivolts and 1 millivolt corresponds to an rms motion of 83 microns. Also the displacements that would correspond to a 1 mm displacement of a low beta quadrupole are shown for several quads.

4 ANSYS CALCULATION

After measuring the frequency spectrum on the quadrupoles and noticing that not all the frequencies corresponded to floor vibrations due to external sources (CHL) or internal sources (water flow, air conditioning, ...), we asked for an ANSYS study [5] of the D0 girder and magnet assemblage. There were approximations made in the modeling and as noted above in the discussion about Fig. 9 there are slight experimental differences between symmetric magnets on either side of the interaction point, nonetheless the study pointed out that there were low lying resonances to be expected. First we will show two calculations that would indicate measurable frequencies when the magnets were measured but would not imply a large excitation to the beam. Fig. 12 implies a similar horizontal motion to a Q3 and a Q4 quadrupole but these are opposite polarity quadrupoles and the effect on the beam is less than one would expect from measuring the power spectral density on the Q3 and the Q4. Next we show in Fig. 13 a case where again a measurement on a quad could be misleading since there is almost no net motion of the magnetic center of the quad.

Fig. 14 gives an example where the contributions of a Q3 and a Q4 would add, and Fig. 9 shows that we had a signal on the C4 side at this frequency, but unfortunately the C4Q4 did not have a signal. The essential conclusion from the study is not the exact frequencies since fairly rough approximations were made but rather the fact that we should expect a number of low lying resonant frequencies.

5 ANALYSIS

It is the main thesis of this paper that a correlation can be made between the spatial pattern (more precisely the betatron phase pattern) of BPM signals at different frequencies and the observed vibration spectrum of quadrupoles (mainly low beta). We have not attempted an absolute prediction of BPM magnitudes since we did not take the quad vibration data at the same time as the BPM data and it was observed that the vibration magnitude could change drastically in the course of a day, although the order of magnitude is occasionally reasonable. The other point to be made is that due to the magnitude of the beta functions there is almost no betatron phase difference between the elements of the triplet (remember that the betatron phase goes like the integral of the inverse of the beta function). Also there is almost exactly a 180 degree phase advance in going through the interaction point, so one can not even pick out the side of the interaction region let alone a particular quad from the spatial pattern of the magnitude (we have no sign information) of the BPM frequency response. As mentioned above in the section on the ANSYS analysis, the fact that one measures a vibrational component on a magnet is no guarantee that there will be an effect on the beam. Having made these caveats, we are going to nevertheless compare the spatial pattern of the frequency components of the BPM spectra to the pattern of the magnitudes that one would expect from the vibration of a single quad at one of the measured vibrational frequencies. Figs. 15 shows the distribution of the 18.5 Hz component of the vertical BPM signal along with the magnitude of the signal expected from the motion of one of the B0 Q3 quadrupoles (refer to Fig. 7). Fig. 16 shows the 21.5 Hz vertical case (refer to Fig. 6). Our horizontal example is given in Fig. 17 (refer to Fig. 9).

These plots present clear evidence for beam motion arising from motion of the quadrupoles in the low beta regions of the accelerators. The cause of the motion is due to external vibrations (CHL for example), internal vibrations associated with the air handling equipment (and other causes), and low order "stand" resonances. The frequency spectrum of the losses during collider operation (C:LOSTP) is dominated by a low frequency component at .3 Hz which corresponds to the Main Ring cycle, however there have been periods of time in which higher frequencies in the ten to twenty Hertz region have been observed, Fig. 18.

6 ACKNOWLEDGEMENTS

The author would like to thank the following people for help in obtaining the data presented here, John Seraphin, Rich Janes, Hengjie Ma, and Todd Johnson.

REFERENCES

[1] Norman Gelfand, private communication
[2] Jim Holt, private communication
[3] Tevatron log book, ED42, page 234
[4] C. Moore, T. Johnson, J. Holt, "Observation of C4Q4 Motion", Fermilab internal note EXP-189
[5] J. Jendrzejczyk, R. K. Smith
[6] H. Pfeffer, private communication
[7] Bruce Hoffman, private communication

	C4Q2	C4Q3	C4Q4	D1Q4	D1Q3	D1Q2
Vertical	15	38	12	10	21	23
Horizontal	12	11	5	6	19	7

Table 1.
Maximum displacement in the arcs for a 1 mm quad displacement

	STATION #	NUY	4.5 Hz	10.5 Hz	17.5 Hz	18.5 Hz	21.5 HZ	24 HZ	ABS(B0Q3D)	ABSF(D1Q3)	ABS(D0Q4F)
0	33.000	15.269	0.0000	0.0000	0.043000	0.033000	0.17000	0.17000	13.000	4.8000	6.3300
1	35.000	15.452	0.0000	0.070000	0.10000	0.065000	0.27000	0.28000	27.400	6.6000	6.9100
2	37.000	15.637	0.020000	0.040000	0.14000	0.10000	0.36000	0.40000	34.700	10.000	11.800
3	39.000	15.824	0.0000	0.0000	0.0000	0.0000	0.0000	0.0000	0.0000	1.3000	2.4000
4	43.000	16.009	0.0000	0.11000	0.050000	0.050000	0.35000	0.38000	34.700	9.0000	9.8900
5	45.000	16.229	0.10000	0.090000	0.10000	0.050000	0.28000	0.27000	17.800	5.8000	7.2600
6	47.000	16.420	0.0000	0.040000	0.060000	0.058000	0.21000	0.21000	28.200	6.3000	6.3000
7	48.000	16.690	0.0000	0.0000	0.0000	0.0000	0.0000	0.0000	5.0000	1.6000	2.0900
8	49.000	16.880	0.0000	0.0000	0.0000	0.0000	0.0000	0.0000	19.500	3.6000	2.8500
9	50.000	16.889	0.0000	0.0000	0.0000	0.0000	0.060000	0.085000	20.100	4.0000	3.2500
10	51.000	17.375	0.0000	0.0000	0.0000	0.0000	0.20000	0.30000	15.800	2.8000	4.6000
11	11.000	17.383	0.0000	0.060000	0.077000	0.027000	0.22000	0.18000	40.900	5.1000	8.4000
12	12.000	17.400	0.0000	0.0000	0.0000	0.0000	0.0000	0.0000	19.800	0.67000	1.7500
13	14.000	17.790	0.0000	0.0000	0.0000	0.0000	0.65000	0.63000	10.700	10.700	13.300
14	16.000	17.888	0.0000	0.0000	0.0000	0.020000	0.13000	0.13000	16.300	1.7000	2.9000
15	18.000	18.071	0.0000	0.0000	0.080000	0.070000	0.29000	0.21000	37.700	8.7000	9.5000
16	21.000	18.255	0.0000	0.0000	0.0000	0.0000	0.25000	0.25000	15.300	8.7000	10.500
17	23.000	18.440	0.0000	0.0000	0.0000	0.040000	0.20000	0.20000	25.600	1.8000	1.1800
18	25.000	18.627	0.0000	0.060000	0.0000	0.030000	0.40000	0.27000	35.600	10.100	11.450
19	27.000	18.811	0.0000	0.0000	0.0000	0.0000	0.16000	0.14000	2.4300	6.2000	7.8000
20	29.000	18.997	0.0000	0.0000	0.0000	0.0000	0.0000	0.0000	33.600	5.2000	5.2000

Table 2.
Vertical BPM signal above background for BPMs around D0

Station #	NUX	13.5 Hz	17.5 Hz	D0Q4F	ABS(D0Q4F)	D0Q3F	ABS(D0Q3F)
32.000	15.235	0.16000	0.39000	3.2000	3.2000	-12.600	12.600
34.000	15.420	0.37000	0.60000	5.1000	5.1000	-18.300	18.300
36.000	15.607	0.043000	0.0000	0.92000	0.92000	-2.0000	2.0000
38.000	15.786	0.12000	0.36000	-4.3000	4.3000	16.500	16.500
42.000	15.973	0.19000	0.37000	-4.2800	4.2800	14.800	14.800
44.000	16.160	0.0000	0.11000	0.95000	0.95000	-4.7000	4.7000
46.000	16.259	0.70000	1.3700	5.9000	5.9000	-22.800	22.800
48.000	16.658	0.0000	0.0000	-0.97000	0.97000	5.1000	5.1000
49.000	16.671	0.20000	0.77000	-3.3000	3.3000	15.700	15.700
50.000	16.679	0.0000	0.10000	-1.8000	1.8000	8.6000	8.6000
51.000	17.165	0.0000	0.0000	2.4000	2.4000	-6.3000	6.3000
11.000	17.177	0.090000	0.26000	2.2000	2.2000	-6.1000	6.1000
12.000	17.440	0.084000	0.10000	-1.2000	1.2000	4.4000	4.4000
13.000	17.635	0.090000	0.0000	-3.6500	3.6500	11.800	11.800
15.000	17.805	0.13000	0.42000	2.2000	2.2000	-9.0000	9.0000
17.000	18.047	0.24000	0.20000	4.8000	4.8000	-16.600	16.600
19.000	18.229	0.040000	0.35000	-0.16000	0.16000	1.9000	1.9000
22.000	18.415	0.14000	0.35000	-4.8000	4.8000	18.000	18.000
24.000	18.605	0.20000	0.0000	-3.6000	3.6000	12.200	12.200
26.000	18.783	0.10000	0.31000	2.0500	2.0500	-8.6000	8.6000
28.000	18.972	0.10000	0.18000	5.3200	5.3200	-19.200	19.200

Table 3.
Horizontal BPM signal above background for BPMs around D0

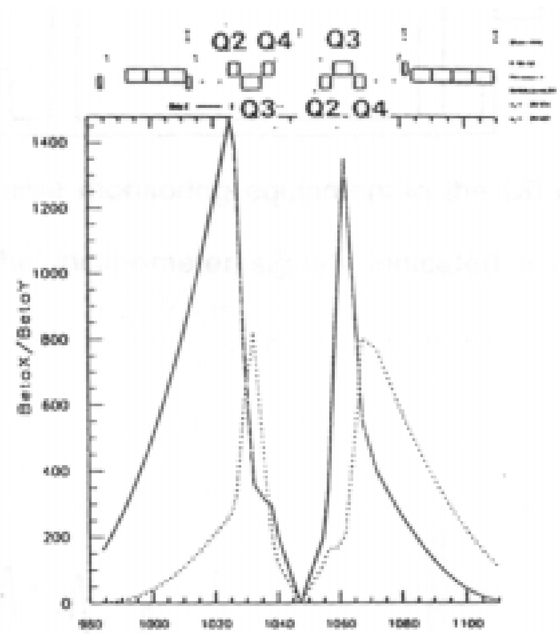

Fig. 1 Lattice Beta functions in the D0 interaction region

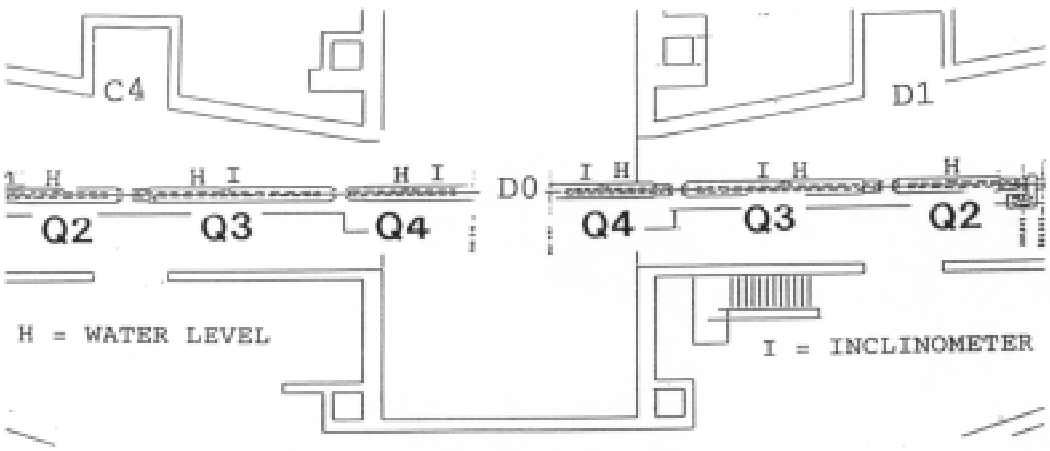

Fig. 2 Layout of remote monitoring equipment in the D0 interaction region

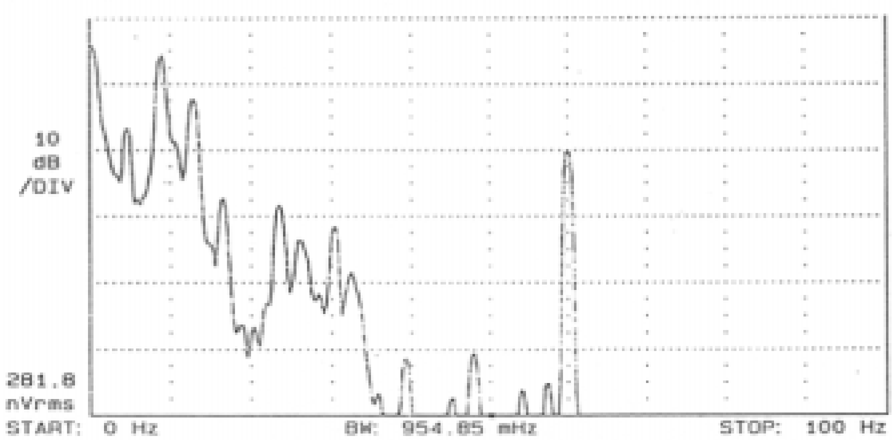

Fig. 3 Fourier spectrum of the D1Q3 inclinometer (roll)

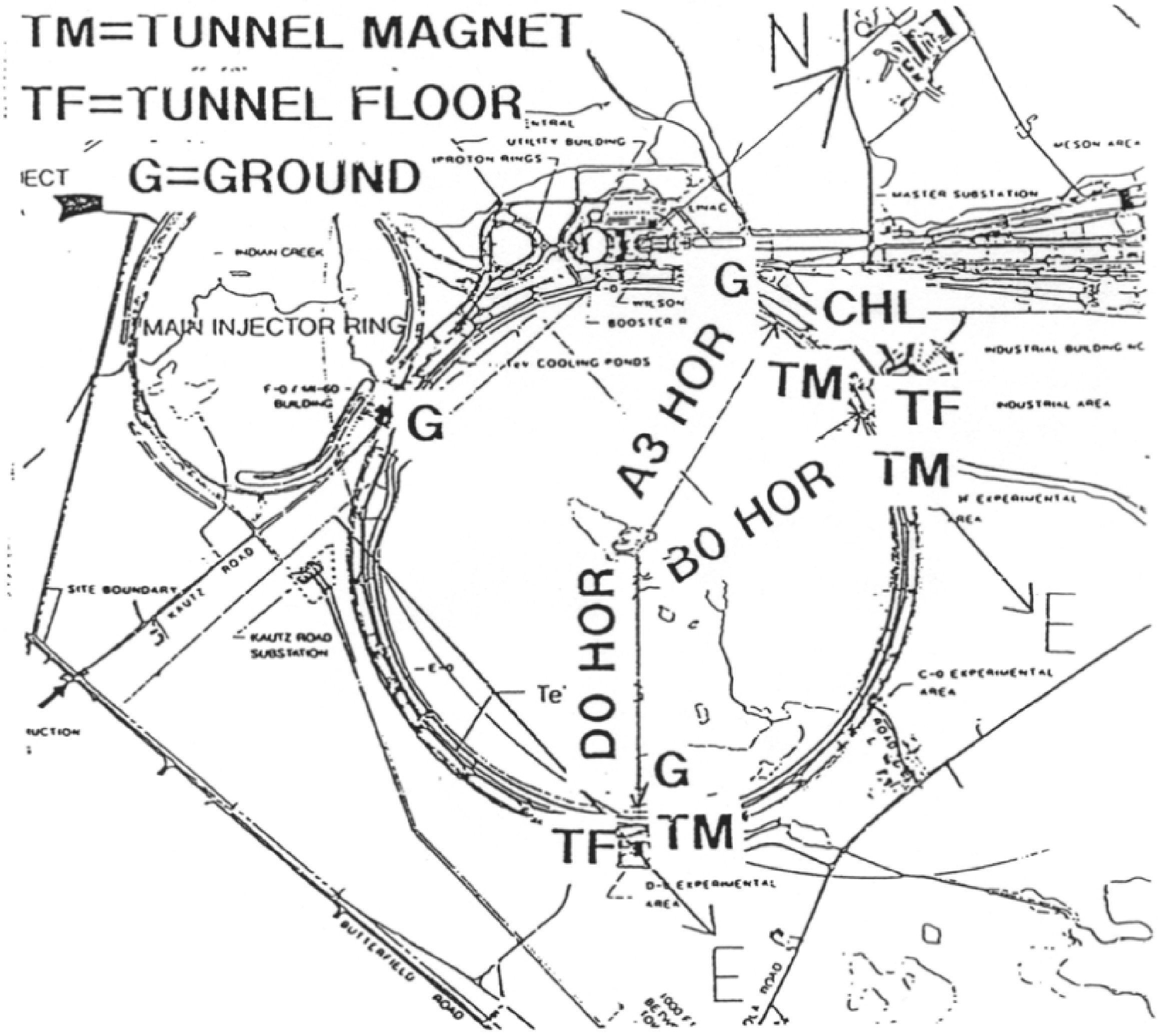

Fig. 4 Location of the vibration analysis studies

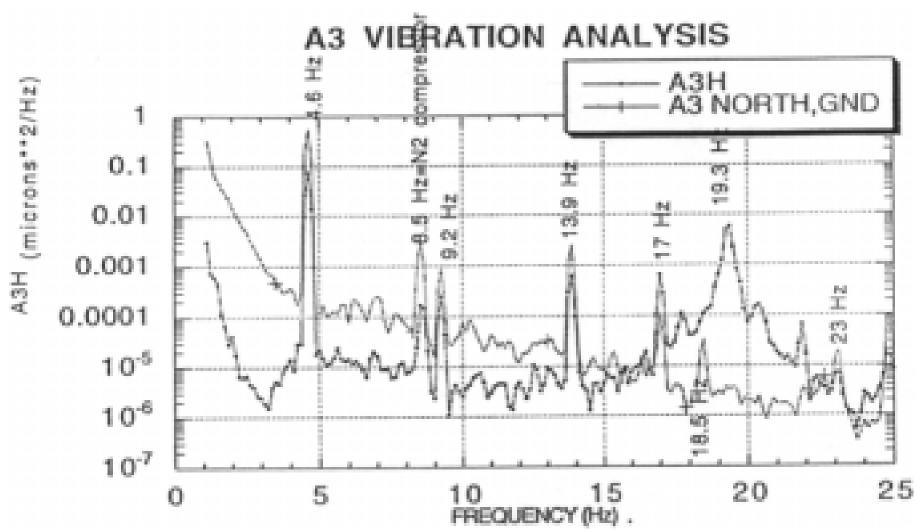

Fig. 5 Frequency spectra of the A35 Tevatron Quad and the ground nearby

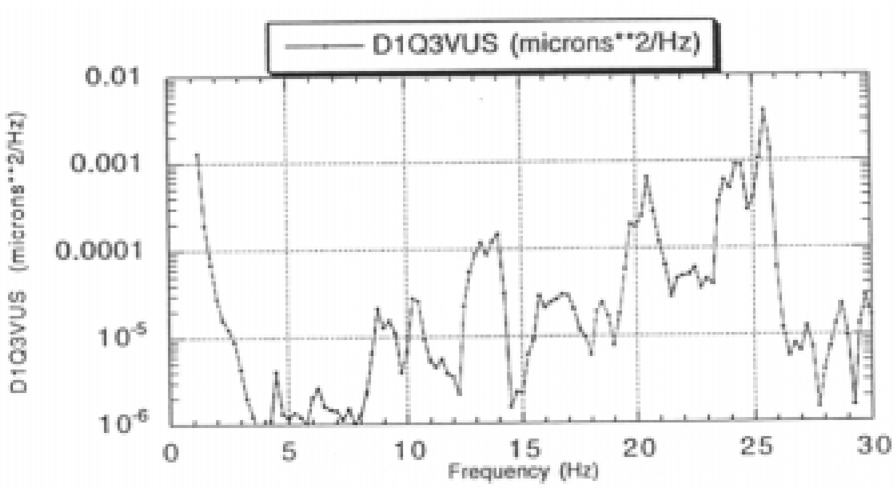

Fig. 6 Vertical frequency spectrum of the D1Q3 quadrupole in the D0 interaction region

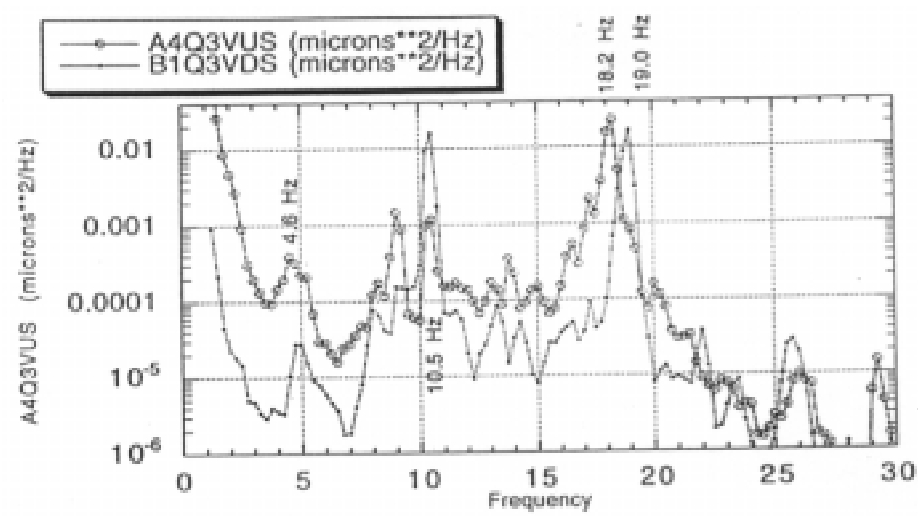

Fig. 7 Vertical frequency spectra of the Q3 quadrupoles in the B0 interaction region

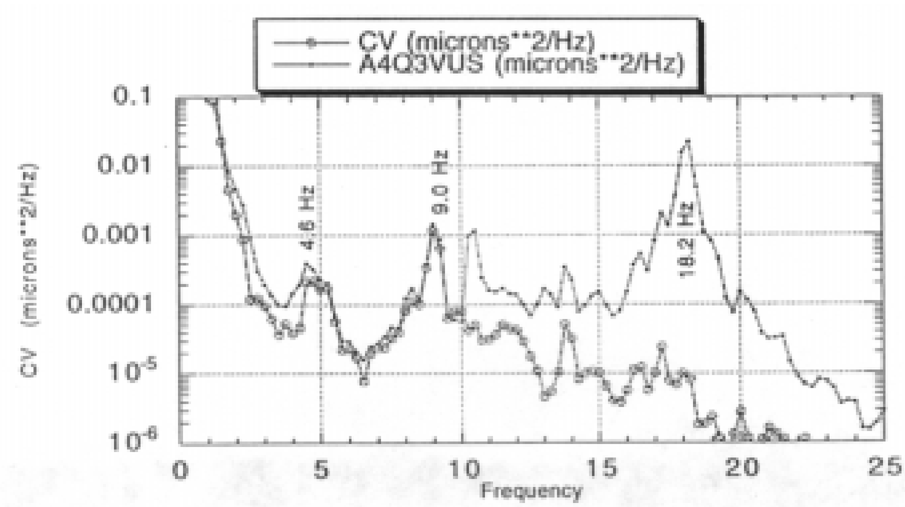

Fig. 8 Comparison of the frequency spectra of Q3 magnet and the nearby floor

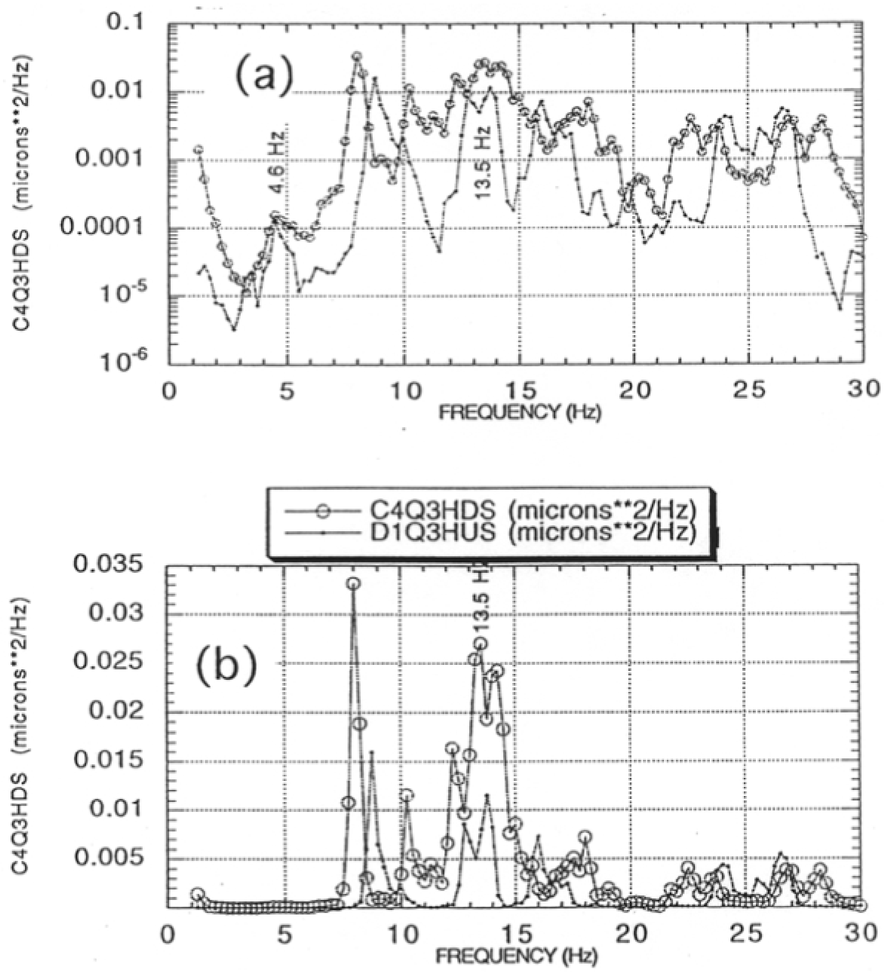

Fig. 9 Horizontal frequency spectra of the Q3 magnets at D0

a. semilog plot b. Linear plot

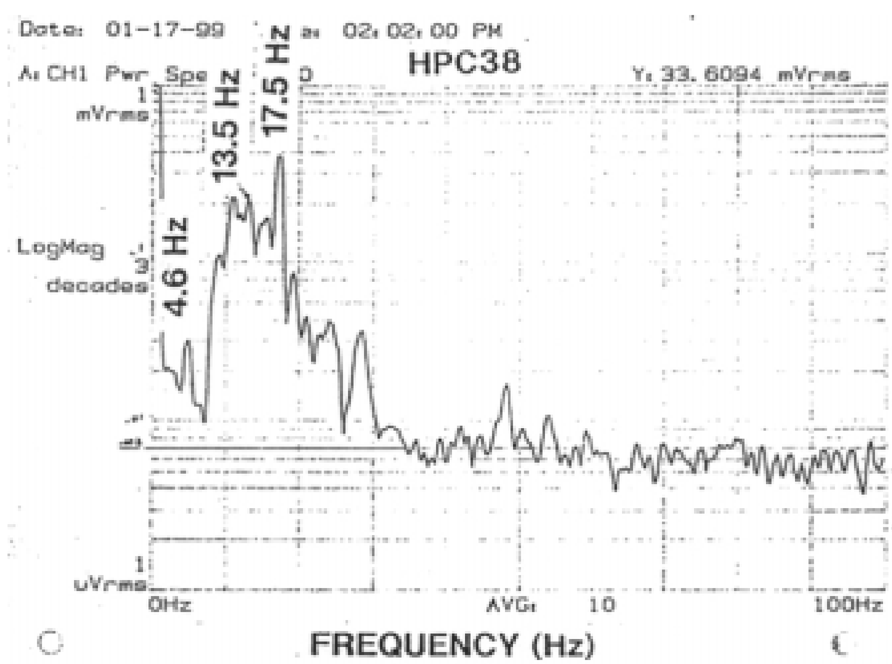

Fig. 10 Frequency spectrum of the horizontal Tevatron BPM at station C38

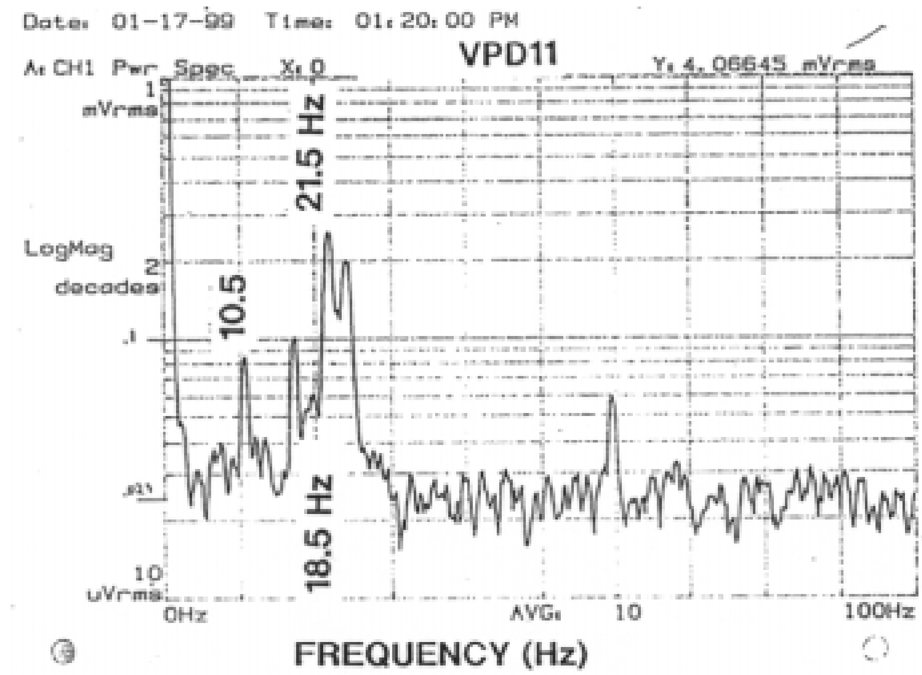

Fig. 11 Frequency spectrum of the vertical Tevatron BPM at station D11

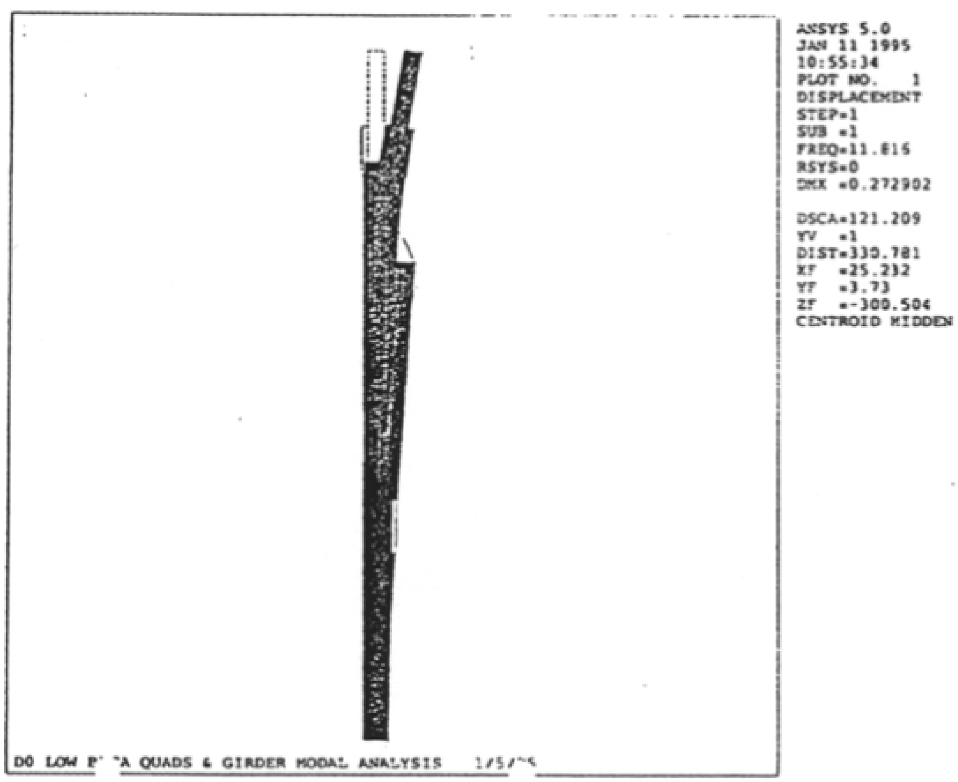

Fig. 12 ANSYS simulation of one mode of the D0 girder and magnet system

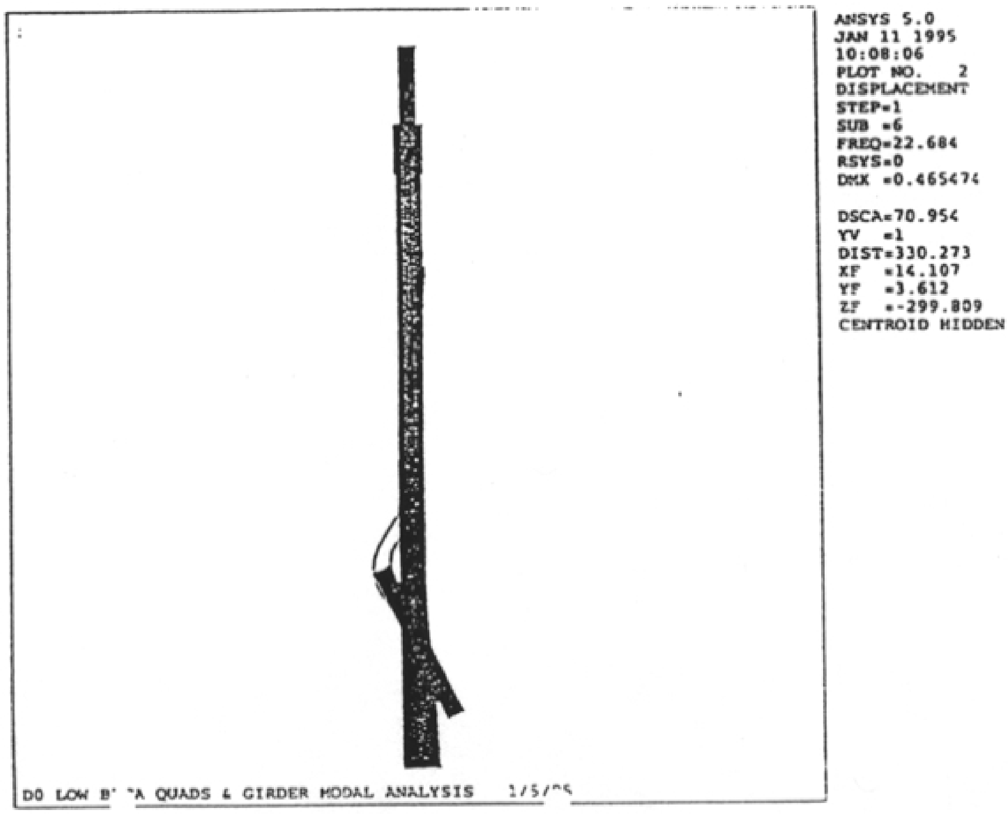

Fig. 13 ANSYS simulation of one mode of the D0 girder and magnet system

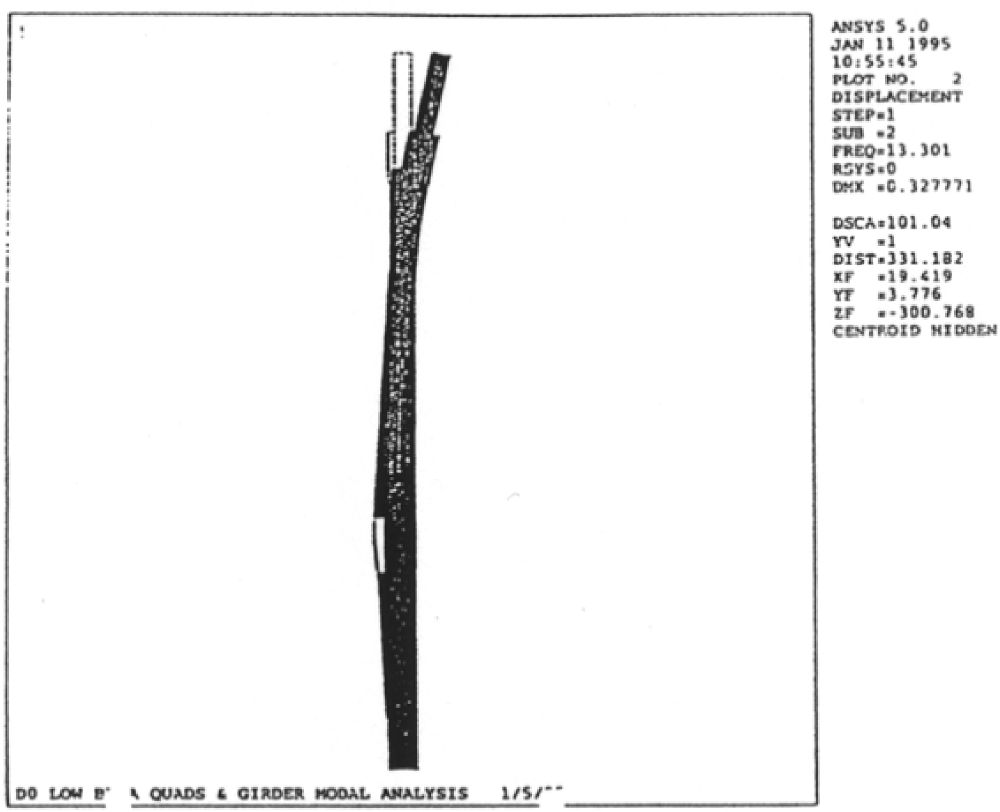

Fig. 14 ANSYS simulation of one mode of the D0 girder and magnet system

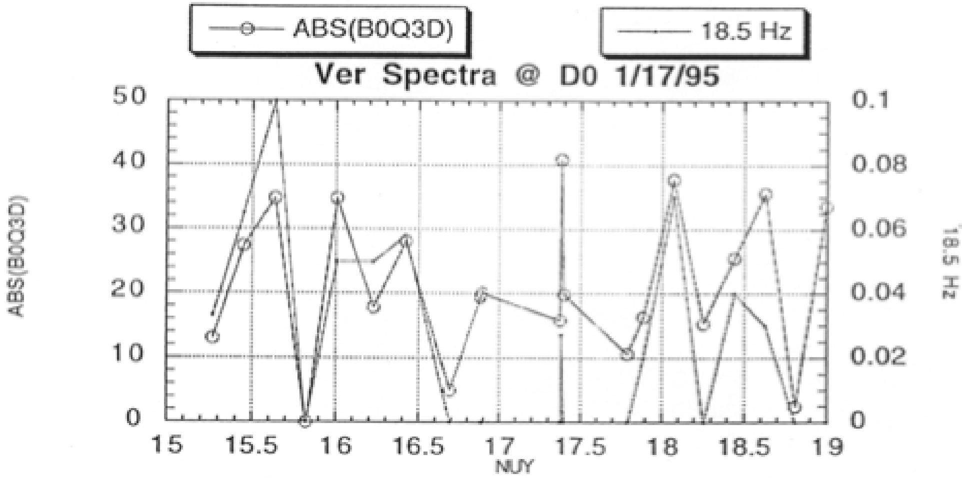

Fig. 15 BPM spectrum as a function of normalized betatron phase compared to the relative pattern expected from the motion of the downstream Q3 quadrupole at B0

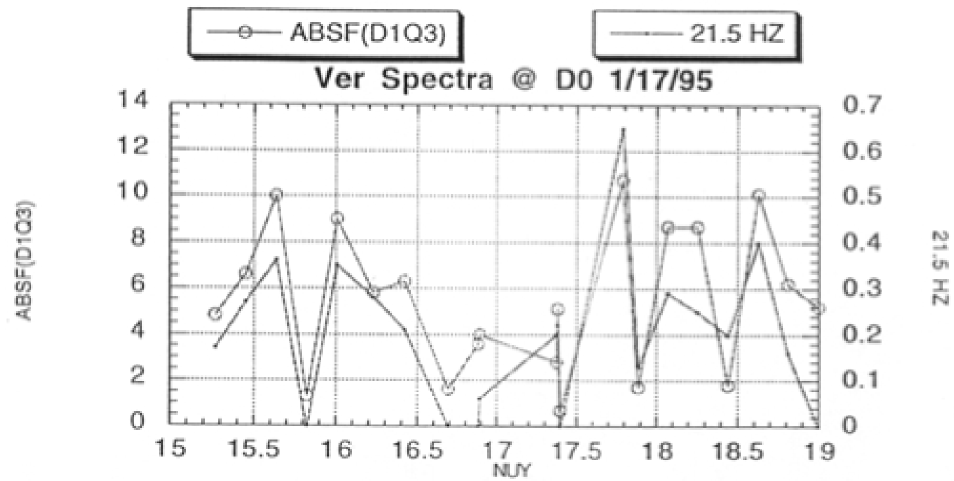

Fig. 16 BPM spectrum as a function of normalized betatron phase compared to the relative pattern expected from the motion of the downstream Q3 quadrupole at D0

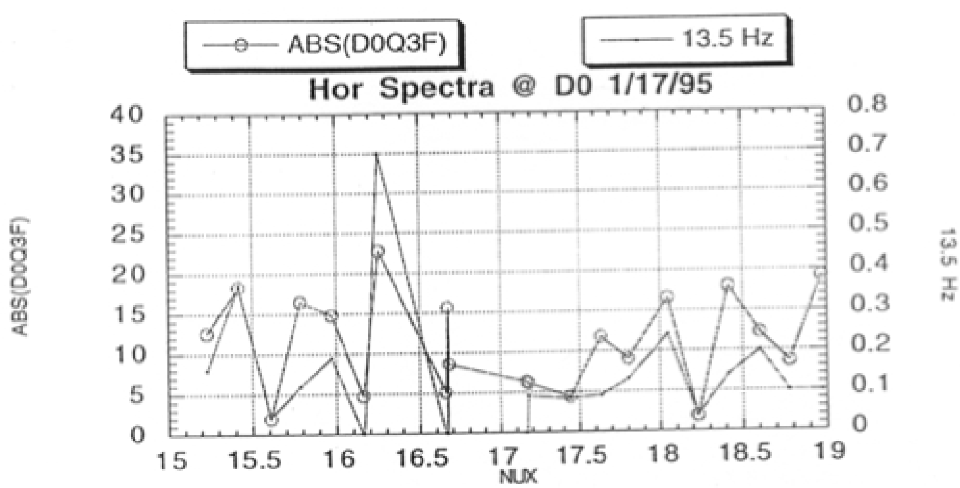

Fig. 17 Horizontal BPM spectrum as a function of normalized betatron phase compared to the relative pattern expected from the motion of the downstream Q3 quadrupole at D0

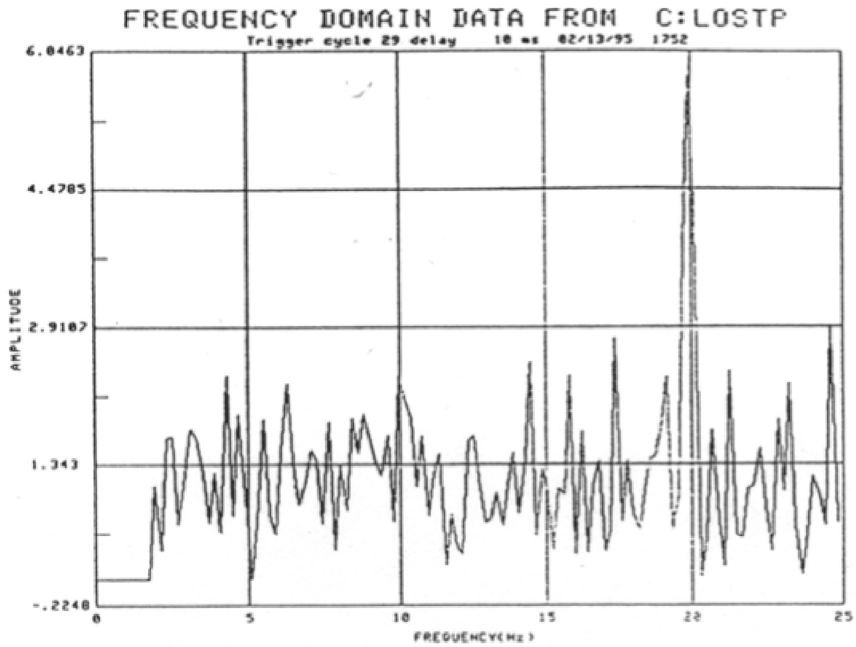

Fig. 18 Proton loss spectrum at B0 with a low frequency cut off at 2 Hz

Seismic Measurements at Fermilab Site for Future Collider Projects

B. Baklakov, T. Bolshakov, A. Chupyra, A. Erokhin, P. Lebedev, V. Parkhomchuk, Sh. Singatulin
Budker Institute of Nuclear Physics, Novosibirsk, Russia, 630090
V.Shiltsev
Fermi National Accelerator Laboratory, Batavia, IL 60510, USA

Abstract

Ground motion can cause significant beam emittance growth and orbit oscillations in large hadron colliders due to a vibration of numerous focusing magnets. Larger accelerator ring circumference leads to smaller revolution frequency and, e.g. for Very Large Hadron Collider(VLHC) 50-150 Hz vibrations are of particular interest as they are resonant with the beam betatron frequency . Seismic measurements at an existing large accelerator under operation can help to estimate the vibrations generated by the technical systems in future machines. Comparison of noisy and quiet microseismic conditions might be useful for proper choice of technical solutions for future colliders. This article presents results of wide-band seismic measurements at the Fermilab site, namely, in the tunnel of the Tevatron and on the surface nearby.

1 INTRODUCTION

Leading accelerator laboratories mount serious efforts in alignment and vibration studies concerning the stability of future accelerator facilities such as photon and meson factories, future linear colliders, and hadron supercolliders [1, 2, 3, 4, 5, 6]. There are several future collider projects under consideration at Fermi National Accelerator Laboratory, including muon collider, linear collider and Very Large Hadron Collider(VLHC). On-site data on seismic vibration are of interest for all of them.

Besides concerns about orbit or trajectory stability, operation of large hadron colliders is a potential subject of transverse emittance growth due to fast (turn-to-turn) dipole angular kicks $\delta\theta$ produced by fast motion of quadrupoles. The emittance growth rate is equal to [3]:

$$d\epsilon_N/dt = (1/2)\gamma N_q f_0^2 \overline{\beta} S_{\delta\theta}(\Delta\nu f_0)$$

or, for a white seismic noise with rms value of magnet vibrations σ_q

$$d\epsilon_N/dt \simeq (1/2) f_0 \gamma \overline{\beta} N_q (\sigma_q/F)^2, \qquad (1)$$

where f_0 is the revolution frequency, $\Delta\nu$ is a fractional part of tune, $S_{\delta\theta}$ is the power spectrum density of kick at a quadrupole $\delta\theta = \sigma_q/F$, F is the focusing length of quadrupole, N_q is a total number of quadrupole focusing magnets, $\overline{\beta}$ is the mean beta-function. The requirement of $d\epsilon_N/dt < \epsilon_N/\tau_L$, where τ_L is the luminosity lifetime, sets a limit on the turn-by-turn jitter amplitude which looks extremely tough – of the order of the atomic size.

Table 1 shows main parameters of three hadron collider projects and their tolerances on low frequency vibrations [7]. The comparison of the emittance growth tolerance σ_q with the results of measurements worldwide (see Section 5 below) shows that for all these colliders the effect may have severe consequences.

Last two raws present necessary precision of quad-to-quad alignment in order to keep rms closed orbit distortion within 5 mm over the ring, and the estimated frequency of realignment of the most of focusing magnet.

Table 1: Stability of Hadron Colliders

Parameter	LHC	SSC	VLHC
Energy E, TeV	7	20	50
Circumference C, km	26.7	87.1	550
Emittance ϵ_N, μm	4	1	1
L-lifetime τ_L, hrs	10	20	5
$\Delta\nu f_0$, Hz	3100	760	90-230
Quads jitter σ_q, nm	0.15	0.1	0.1
Measured jitter, nm	0.01-0.1	0.2	0.1-50
5mm COD align., μm	100	60	30
Realign. time, days	$\sim$200	$\sim$45	$\sim$5

In this article we discuss vibration measurements at Fermilab.

2 SEISMIC PROBES AND DATA ACQUISITION SYSTEM

The data acquisition system used in our measurements were based on IBM PC Pentium 200 computer and two seismic stations [8]. Each station consists of a set of probes and data acquisition module (DAS Module). Backbone of our seismic instrumentation is modified geophone of SM3-KV type (made by collaboration of Special Design Bureau of Institute of Earth Physics (Moscow) and Budker INP, Novosibirsk). The SM3-KV seismometer is a single pendulum velocity-meter to measure (by choice, one of) vertical or horizontal vibration component in the frequency range from 0.05 up to 120 Hz. Main parameters of SM3-KV are:

sensitivity	0.5 $V \cdot s/\mu m$
working frequency band	0.05-120 Hz
electronic noise-	
at 1Hz	10^{-7} $\mu m^2/Hz$
at 100 Hz	10^{-15} $\mu m^2/Hz$
noise amplitude at frequency	
more than 1 Hz	$1.5 \cdot 10^{-4}$ cm
more than 100 Hz	$1.5 \cdot 10^{-7}$ cm
mass	$\simeq$ 8 kg
dimensions	$24 \times 17 \times 14.5$ cm^3
working temperature	-10...45^{o}C

SM3-KV probes and supplemental piezoaccelerometers of 731A model by WILCOXON Research (USA) [1] were found suitable for the task of vibration amplitude measurements for the VLHC [9].

The seismic probes are connected to the stations by short 5 m long cables. Maximum 8 analog signals can be processed by DAS Module of each station. The stations can be installed at a relatively large distance because they are connected to the PC operation board by a single RF cable up to 300 m long. Usually we fed each station with 24V and about 1.2 A of DC power through additional coaxial cable. By a command from the PC we can change gain and low-pass filters of the DAS Module amplifiers and sampling frequency. To suppress a frequency "aliasing" usual for FFT, we use analog 4th order Butterworth low-pass filters with 3dB frequency of 2, 20, 200 and 2000 Hz. Gain can be changed from 1 to 30. Sample frequencies varies from 2 Hz to 700-900 Hz .

The software to process data delivered to the PC operation board is written on C++ for Windows'95. It provides access to DAS Module sample frequency, filter and gain for each channel. It also allows to view probe signals, calculate and display spectra on the PC monitor on-line and/or store it on the PC hard disk.

For any pair of stationary random processes $x(t)$ and $y(t)$, the correlation spectrum $S_{xy}(f)$ is defined as a limit $T \to \infty$ of following equation:

$$S_{xy} = \frac{2}{T} \int_0^T x(t) e^{i\omega t} dt \int_0^T y(t) e^{-i\omega t} dt \qquad (2)$$

where T is time of measurement, $\omega = 2\pi f$ is frequency. If $y(t) = x(t)$, then the value of $S_{xx}(f)$ is called Power Spectral Density(PSD) of signal $x(t)$. Normalized correlation spectrum (which we quote everywhere below) is equal to

$$C_{xy}(f) = \frac{< S_{xy} >}{\sqrt{< S_{xx} >< S_{yy} >}} \qquad (3)$$

where $< \, .. \, >$ means an averaging over series of measurements.

By the definition, $C_{xy}(f)$ is a complex function. Modulus of the correlation $|C(f)_{xy}|$ is the coherence of two signals at frequency f. It is always positive and less or equal to 1 – for example, if $C_{xy}(f) = 0$ then the Fourier components of signals have no connection to each other, i.e. the phase difference between them varies in time.

During our measurements we used 1024-point FFT of data from 16 channels of both stations to calculate the PSDs and correlation spectra matrix $C_{xy}(f)$. To reduce statistical errors in the spectra estimate we averaged the spectra up to several hundred times.

As an example of the setup arrangement Fig. 1 shows the scheme of measurements in the Tevatron tunnel. Here, "SM3" are the SM3-KV probes (V-vertical and H-horizontal), "piezo" is the piezoaccelerometer, "BPM" and "BLM" are beam position monitor and beam loss monitor, respectively.

[1] frequency band from 1-450 Hz, are named as very low noise probes, although work well under comparatively noisy conditions only

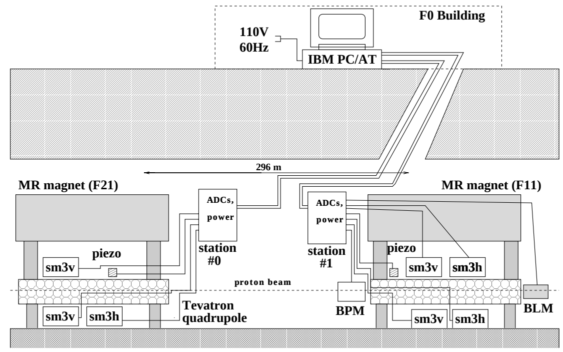

Figure 1: Scheme of measurements in the Main Ring tunnel. Tevatron ring is located under the Main Ring magnets.

3 ON SURFACE MEASUREMENTS AT E4

Initial measurements and test of seismic equipment have been carried out on the surface at E4 location (building E4R, South-West corner of the Main Ring) near the Tevatron RF building. Fig. 2 presents variation of the maximum amplitude of the ground vertical velocity versus time which is presented in units of days (e.g. 19.0 means midnight of 19 September 1997). The record had been done with 5 Hz sampling frequency and 2 Hz low-pass filter. One can see significant increase of the signal around 7 a.m. (or 19.3 in our time units) due construction activities at Fermilab Main Injector and traffic noise and operation of technological equipment within few miles from the point of measurements. The night time amplitude is approximately 5-6 times less than that at working time.

Next Fig. 3 demonstrates record of two signals of SM3-KV geophones placed at the distance of 32 m at night of 17th of September 1997. Both signals are practically the same, and 5-7 seconds period oscillations are clearly seen. It is well known that this "7 seconds hum" of "microseismic waves" with some dozens km wavelength is produced at the nearest coasts and can be detected almost everywhere on the Earth, see e.g. [1]. The coherence spectra of these two signals is presented in Fig. 4. The coherence is equal to 1 in a frequency range from 0.1 up to 1 Hz, that says about identity of the signals.

Fig. 5 shows the power spectrum density of vertical vibrations. Again, the "microseismic waves" demonstrate themselves as a broad peak near 0.2 Hz.

At the working day time (7 a.m.-5 p.m.), human activity significantly increases the vibration amplitudes in frequency range of 2-100 Hz. Fig. 6 shows the vertical SM3-KV signal at working time – compare with Fig. 3. Now the signal has high frequency components and looks like a white random noise. Consequently, the microseismic peak is not seen neither in the data record nor in the spectrum.

Fig. 7 presents the coherence of vertical vibration at distances of 0 m and 62 m measured at E4R site. As seen, the

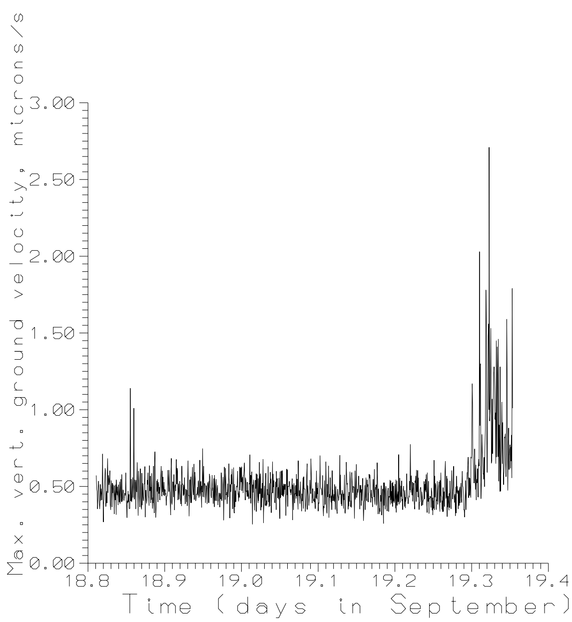

Figure 2: Maximum vertical ground velocity at E4R building recorded from 7:30 p.m. of Thursday, 18 September 1997 till 8:30 a.m. 19 September 1997.

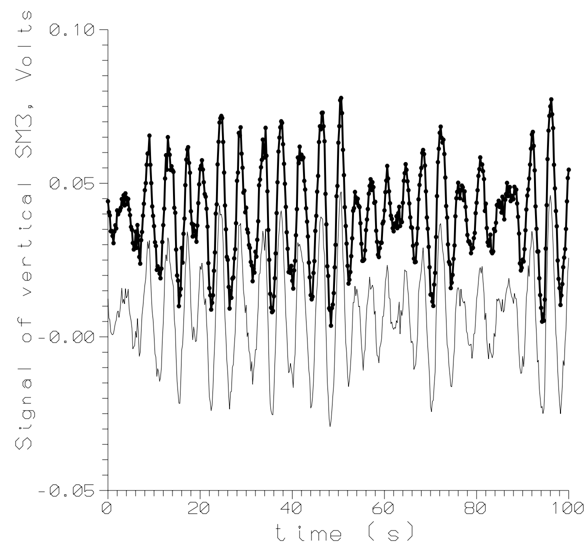

Figure 3: Signals from two vertical SM3-KV geophones distanced by 32m. Measured at night of 17-18 September 1997 at E4R building.

correlation between two vertical SM3-KV is very close to 1 in frequency range from 0.1 up to 100 Hz when the probes are placed side by side. At the distance of 62 m the coherence is near 1 only at microseismic and around 0.8 Hz peaks, then it rapidly falls to 0 at 50-100 Hz. For comparison, at the same Figure we present Tevatron tunnel coherence measurement where two SM3-KV probes were placed at the distance of 296 m. In that case the coherence is practically equal to zero for all frequencies higher than 0.1 Hz, except some sharp peaks due to technical noise (rotating parts of machines, etc.).

Besides technological noise frequencies, the coherence tends to decrease very fast with increase of a distance between probes. Therefore, widely used model of plane waves for calculating of the impact of the vibration on accelerators is not fully adequate to reality. Multiple uncorrelated sources of seismic noise generated around an accelerator have to be taken into account too.

Fig. 8 presents the distribution of the displacement amplitudes of ground vibrations at E4R. We divided many hours long record of the ground motion signal on 10 s intervals and calculated maximum amplitude of displacement in each interval (by means of integration of the velocity signal). The distribution of those maximum amplitudes is practically flat up to the 0.2- 0.3 microns, then it rapidly decreases for vertical signals and somewhat slower for horizontal vibrations. Both distributions are far from the Gaussian and look more power law like. [2]. One can fit the probability of the displacement at the E4R building by the function:

[2] Generally speaking, power law distributions are indicators of fractal arrays and natural in geophysics (e.g. for earthquakes) – a lot of examples can be found in Ref.[10]

$$dW/dx = \frac{\alpha-1}{\alpha a_{min}} \quad for \quad x < a_{min}$$

and

$$dW/dx = \frac{\alpha-1}{\alpha a_{min}} \cdot (a_{min}/x)^{\alpha} \quad for \quad x > a_{min}. \quad (4)$$

For horizontal amplitude in Fig. 8 we have $a_{min} = 0.3\mu$m and $\alpha \simeq 3$. Corresponding probability that over 10 s interval the displacement will occur with amplitude more than $x > a_{min}$ is equal to :

$$W = \frac{1}{\alpha}(\frac{a_{min}}{x})^{\alpha-1} \quad (5)$$

For example, predicted probability of the horizontal displacement to be larger than 10 micron is equal to $3 \cdot 10^{-4}$, or, equivalently, it will take place once every 10 hours.

Such a distribution can be very useful for determination of parameters of the feedback system to control the closed orbit in accelerators. These distributions can help to estimate probability of very large relative displacements of the magnets. Using only r.m.s. values without knowledge of the distribution one can not predict these large amplitude events. Extrapolation of the Eq.(5) beyond range of our measurements, give us that the vibration amplitude of about 1 mm within period of 10 s may happen in Fermilab every 3.5 years – that does not seem ridiculous.

4 MEASUREMENTS IN THE TEVATRON TUNNEL

The vibration measurements in the Tevatron tunnel have been done at Sectors F11 (near the Tevatron RF cavities) and F21. Computer was located on the surface in the

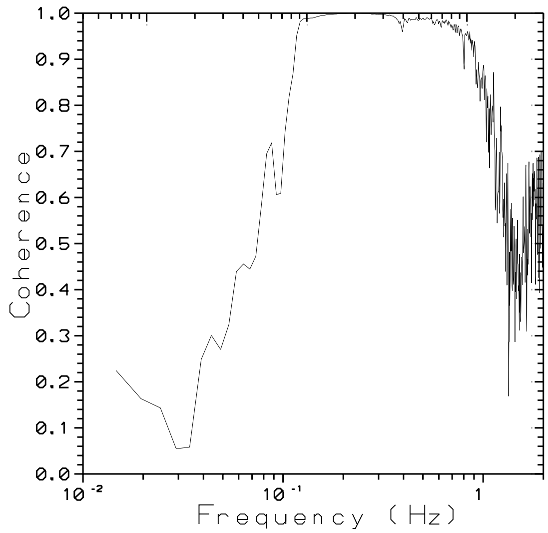

Figure 4: Coherence of vertical ground motion at distance 32 m. Night time of 09/17/97 at E4R building.

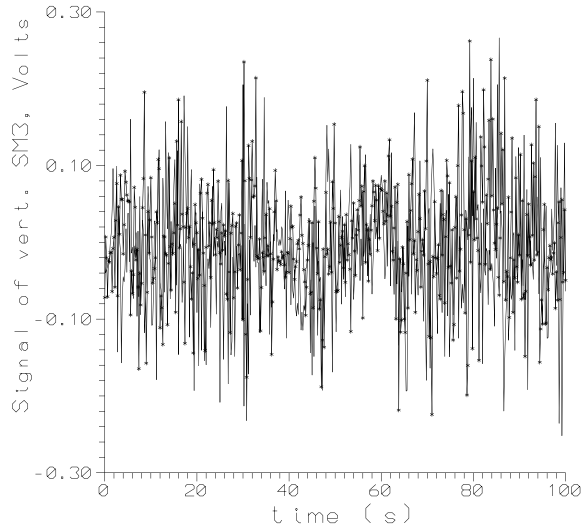

Figure 6: Signal of SM3KV at working time

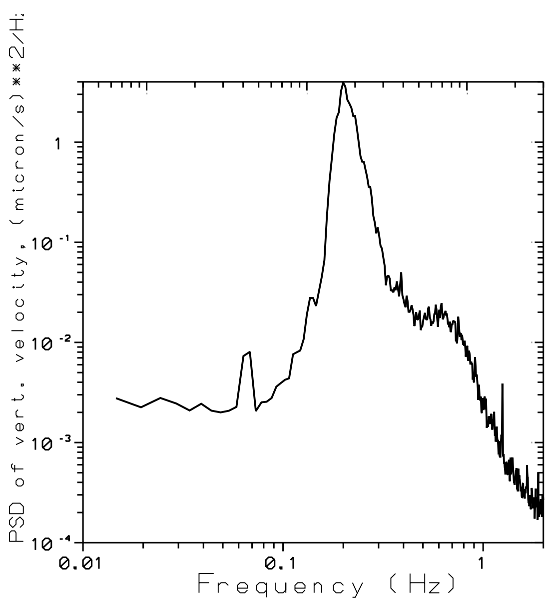

Figure 5: Power spectral density of vertical ground motion at night time.

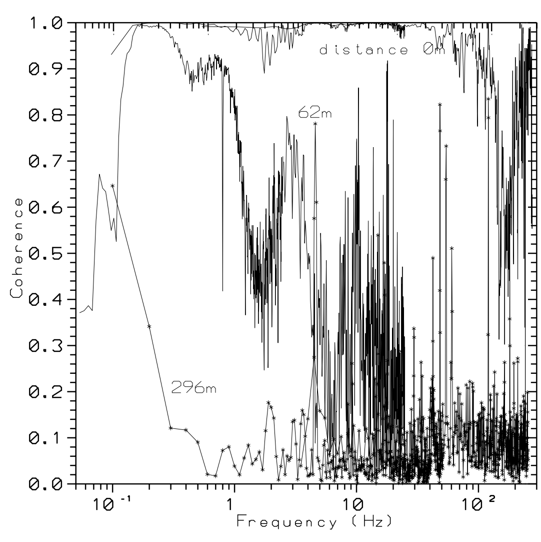

Figure 7: Coherence of vertical ground motion signals measured by probes 0 m and 64 m apart in E4R, and 296 m apart in the Tevatron tunnel.

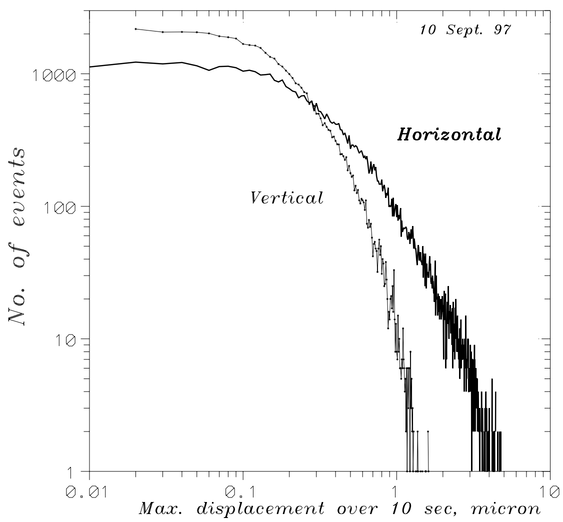

Figure 8: Distribution of maximum ground displacements over 10 s interval.

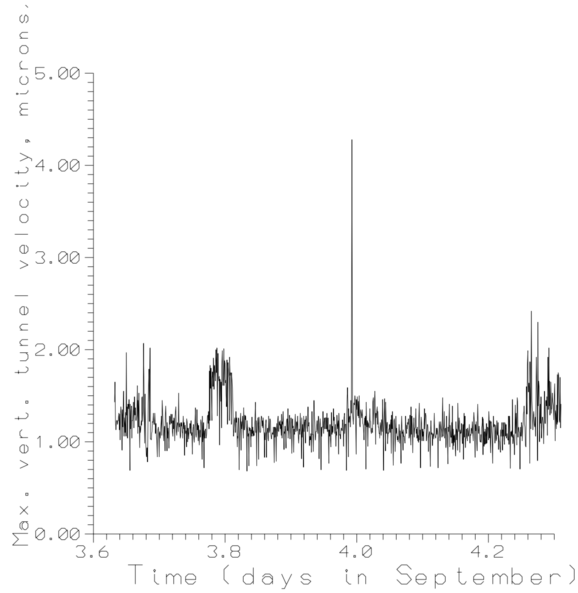

Figure 9: Vibration amplitudes in the tunnel of Tevatron over 16 hours starting 3:30 pm September 3, 1997. The Main Ring and the Tevatron ring are under operation.

F0 building. Seven SM3-KV probes (four vertical and three horizontal) and two vertical piezoaccelerometers were used. The layout of experiment is shown in Fig. 1.

Station 0 is placed at a distance 296 m from station 1. The station 0 digitizes the signals from one vertical and one horizontal SM3-KV probes on the floor of the tunnel at F21, and from vertically oriented piezoaccelerometer and vertical and horizontal SM3-KVs on the Tevatron quadrupole magnet.

The station 1 digitizes the signals from four SM3-KV geophones (vertical and horizontal on the quadrupole magnet at F11 and vertical and horizontal on the tunnel floor nearby), one piezoaccelerometer placed on the same magnet, and additionally from a beam position monitor (BPM) and a beam loss monitor (BLM).

Ambient technological noise at the Tevatron tunnel concludes in little day-night variation of the maximum amplitude – see Fig. 9 measured from 3:30 pm September 3, 1997 until about 7:30 am next day, and compare it to similar Fig. 6 for E4R site.

PSDs of the F11 magnet and on the tunnel floor are compared in Fig. 10. They are almost the same at frequencies of 5–20 Hz. At frequencies below 5 Hz and above 20 Hz, the magnet spectrum is 1-2 orders of the floor spectrum. For comparison, the PSD measured on the surface at the E4 site at night time is also shown in Fig. 10. One can see, that again, below 5 Hz and above 20 Hz the power of vibrations at the tunnel is higher than on the surface at night. Supposedly, at high frequencies the amplitude is higher due to the technical equipments under operation inside the tunnel (water and helium pipes, power cables, magnets themselves, etc.). At frequencies around 1 Hz and lower the main contribution is possible due to strong mechanical distortions of the magnets during the Main Ring cycle (about 3 s) and the Tevatron acceleration cycle (about 60 s in fixed target oper-

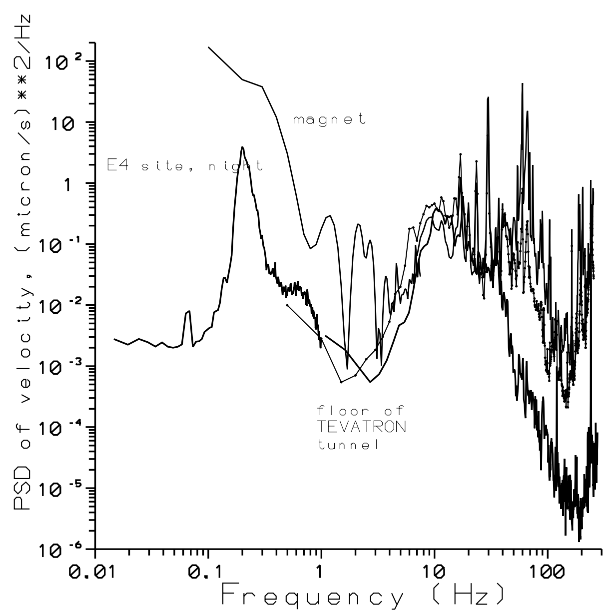

Figure 10: Power spectral densities of vertical vibrations of the Tevatron quadrupole magnet (upper curve), the tunnel floor (middle line with marks) and on the surface at E4 (lower curve).

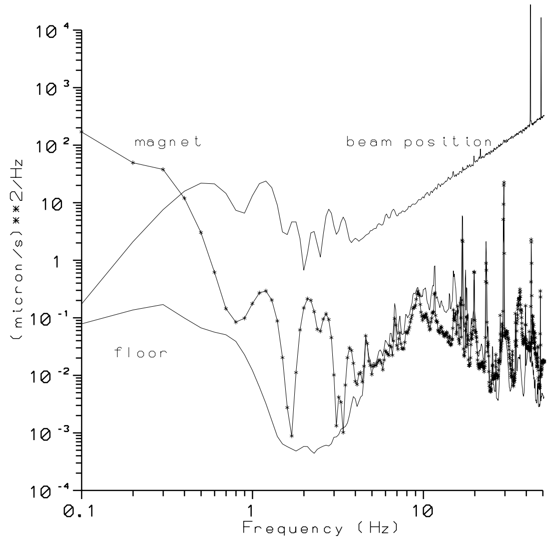

Figure 11: Spectra of the Tevatron beam orbit vibrations, tunnel floor motion and the Tevatron quadrupole vibrations at F11.

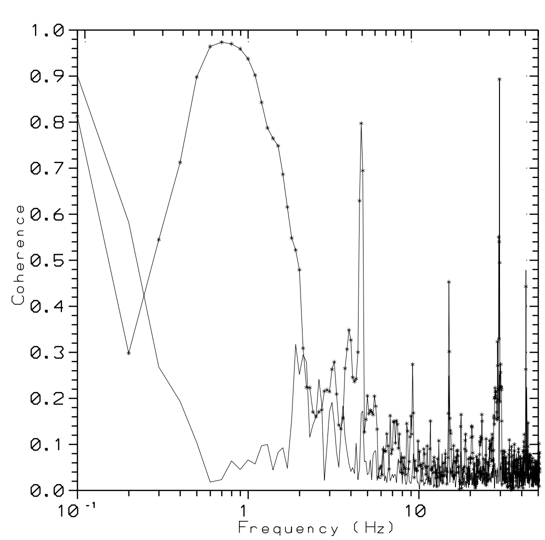

Figure 12: Coherence between signals of the vertical Tevatron beam orbit motion and the F11 magnet vibrations (marked line) and between the orbit and the tunnel floor.

ation).

Simultaneously measured spectra of the vertical orbit velocity [3], the F11 magnet and the tunnel floor velocities are compared in Fig. 11. The coherences between the beam orbit and the magnet and between the beam orbit and the tunnel floor motion are presented in Fig. 12. One can see that the orbit correlates well with the floor only at low frequency 0.1 Hz, while some excessive but small coherence exists at 2-4 Hz. On the other hand, the beam orbit correlates very well with the quadrupole magnet motion at frequencies of 0.2-2 Hz. One of possible origin of such coherence may be related to 3 s accelerating cycle of the main Main Ring which mechanically affects closely located Tevatron magnets and produce impact on the Tevatron beam via straw magnetic fields at harmonics of 1/3 Hz.

The closed orbit distortion is caused by the displacements of all magnetic elements along the circumference of Tevatron. The strong coherence between the magnet and beam vibrations means that there is a common source of vibration along the whole accelerator ring. For example, several remarkable peaks in the orbit-magnet coherence occur at 4.6 Hz, 9.2 Hz, 13.8 Hz, etc., at the Fermilab site specific frequencies caused by Central Helium Liquefier plant operation [11].

5 DISCUSSION AND CONCLUSION

The results of measurements allow us to make following conclusions for the VLHC:

1.The amplitude of vibration at frequencies of 50-200 Hz performs large variation in time due to man-made activity. Neither location at the Fermilab site satisfies the tolerance of 0.1 nm (Table 1) at the day time. But at night time vibrations outside the Tevatron tunnel becomes less than required by the VLHC.

We have to remark that accelerators are relatively 'noisy'. For example, Fig. 13 from Ref.[7] compares the PSDs of velocity $S_v(f) = S_x(f)(2\pi f)^2$ for the "New Low Noise Model" [12] – a minimum of geophysical observations worldwide – and data from accelerator facilities of HERA [5], UNK [6], VEPP-3 [13], KEK [14], SSC [15], CERN [16], FNAL [11], APS [17], and SLAC[18].

That comparison tells us that if during the design and construction of the VLHC some proper attention is paid to decrease the level of technical vibration, than it will be possible to obtain vibrations by 10-100 times lower that at the Fermilab site now. For that, it is necessary to place potential sources of vibrations as far as possible from the accelerator ring or/and to dump vibrations at their origin. From these point of view it seems very useful to have a seismic monitoring system at the VLHC site.

2.Thorough investigations of a spatial characteristics of the fast ground motion have shown that above 1-4 Hz the correlation significantly drops at dozens of meters of the distance between points. Therefore, the displacements of different magnetic elements of the accelerator (which will be spaced by hundreds of meters) can be regarded as uncorrelated except characteristic frequencies of technical devices producing the vibrations along the whole ring (electric power, water, Nitrogen and Helium systems etc.)

3. Careful engineering of mechanical supports, of vacuum, power and cooling systems should be an important part of R&D efforts to decrease the level of vibrations in the VLHC as well as in any other future collider.

6 ACKNOWLEDGMENTS

We acknowledge help of many people during preparing of the apparatus and the measurements in the Fermilab: Anatoly Medvedko, Frank Nezrick, Mark Averett, Dean

[3]calculated as the PSD of the BPM signal multiplied by ω^2

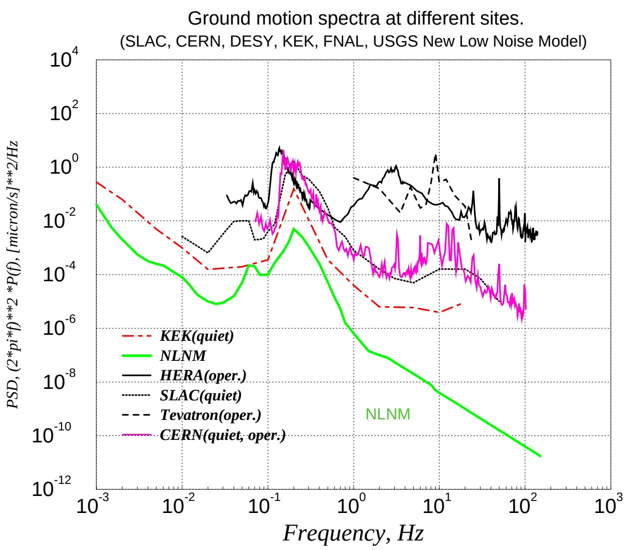

Figure 13: Ground motion spectra at different accelerator sites and New Low-Noise Model.

Still, Ken Koch, Rupe Crouch, Marv Olson and Jim Zagel. We are indebted to Chris Adolphsen(SLAC) and Jim Norem(ANL) for cooperation in providing us with two STS-2 seismometers. Numerous language corrections made by Natalia Maltseva after reading the manuscript are sincerely acknowledged.

We would also like to thank Dave Finley and Nikolay Dikansky for steady interest and support of this activity.

7 REFERENCES

[1] G.E. Fischer, in AIP Conf. Series No. 153, *Summer School on High Energy Part. Accel.*, Batavia (1984).

[2] D.Neuffer, FNAL TM-1964 (1996).

[3] V.Lebedev,et.al,*Part.Accel.*, v.44 (1994), p.147.

[4] V. Parkhomchuk,et.al,*Part. Accel.*, v.46 (1994), p.241.

[5] J.Rossbach, DESY 89-023 (1989).

[6] B.A.Baklakov,et.al, Preprint INP 91-15, Novosibirsk; *Proc. of 1991 IEEE PAC*, San-Francisco, p.3273; *Sov. Tech. Phys.*, v.38 (1993), p.894.

[7] V.Shiltsev, "Stability of Future Accelerators", *Proc. of 1996 EPAC*, Barcelona (1996).

[8] Seismic Measurements at Fermilab for Future Collider Projects (Design report) Novosibirsk March, 1997.

[9] V. Shiltsev, "Pipetron Beam Dynamics with Noise", FNAL TM-1987(1996).

[10] C.H.Scholz, B.Mandelbrot, eds., *Fractals in Geophysics*, Birkhauser (1989).

[11] C.Moore, "Vibrational Analysis of Tevatron Quadrupoles", *Proc. IV Int. Workshop on Accel. Alignment, Tsukuba, Japan*, KEK Proceeding 95-12 (1995), p.119.

[12] J.Peterson, USGS Open-File Report 93-322, Albuquerque, NM (1993).

[13] V.A.Lebedev, et.al, Preprint INP 92-39, Novosibirsk (1992).

[14] S.Takeda, M.Yoshioka, KEK-Preprint 95-209 (1996).

[15] V.D.Shiltsev, in AIP Conference Proceedings 326, pp.560-589 (1995).

[16] V.Jouravlev,et.al, CERN-SL/93-53 and CLIC-Note-217 (1993).

[17] V.D.Shiltsev,*Proc. 1995 IEEE PAC*, Dallas, p.2126.

[18] *Ground Motion: Theory and Measurements*, Appendix C of NLC ZDR, SLAC-R-0485 (1996).

[19] V.Shiltsev,et.al, DESY-HERA-95-06; *Proc. of 1995 IEEE PAC*, Dallas, p.2078, p.3424.

SYNCHROTRON RADIATION DAMAGE TEST OF INSULATING MATERIALS IN THE TRISTAN MR

H.Mitsui,R.Kumazawa,and T.Tanii
Toshiba Corporation
2-4 Suehiro-cho,Tsurumi-ku,Yokohama-shi,230 Japan
Y.Ohsawa,T.Ozaki,and K.Takayama
National Laboratory for High Energy Accelerator Research Organization(KEK)
1-1,Ohno,Tsukuba-shi,Ibaraki-ken,305 Japan

Abstract

An irradiation test of typical insulating materials for an accelerator magnet was carried out, using actual radiation in the TRISTAN MR(main ring) which is operated at a quite high level of radiation. Physical and chemical degradations of the insulating materials due to irradiation were systematically studied. The radiation degradation effects on insulating materials and combinations of these as well as the influence of insulation manufacturing process are discussed.

1 INTRODUCTION

TRISTAN is an e^+e^-colliding beam accelerator with the collision energy in a range of $\sqrt{S} \approx 60$ GeV. The MR was operated first in October 1986 at a beam energy of 25 GeV. Since then the beam energy has been increased step by step from 25 GeV to 30 GeV [1]. Thereafter the radiation damage on accelerator components had become increasingly serious [2].

Systematic studies of the radiation damage on electrical insulating materials used for particle accelerators are found in the literatures [3,4], meanwhile, the same kind tests were carried out in the TRISTAN MR several years ago[5]. However, radiation damage beyond 100 MGy is likely to occur in localized regions of existing machines. Therefore systematic tests on three types of EISs (electrical insulation systems) have been done on the synchrotron radiation damage up to 167 MGy by using the TRISTAN MR. Details of the study are dicussed in reference [6]. Here its highlights are presented.

2 SPECIMENS

Three types of EISs for a magnet coil, as shown in Table 1, were chosen as test specimens. Type A is the so-called vacuum-pressure-impregnation(VPI) insulation system which consists ofglass-cloth reinforced mica-paper tape impregnated with epoxy resin. Type B is a resin-rich insulation system which is manufactured in the atmosphere, by molding bismaleimide triazine(BT) resin preimpregnated glass-cloth, and by heat shrinkable tape. Type C is another resin-rich insulation system which is manufactured, by molding polyimide preimpregnated glass-cloth with an asphalt compound, after vacuum drying. Accordingly, type A and C were manufactured with the vacuum treatment.

TABLE 1 Insulation constitution of test specimens

Type	Material	Manufacturing process	Applied machine
A	Epoxy/mica/E glass	Vacuum-pressure-impregnation	TRISTAN main ring
B	BT resin/S glass	Heat shrinkable tape-molding	PS ring
C	Polyimide/T glass	Asphalt-compound under vacuum	None

E glass: Electric grade glass
S,T glass: Boron-free glass
BT resin : bismaleimide triazine resin

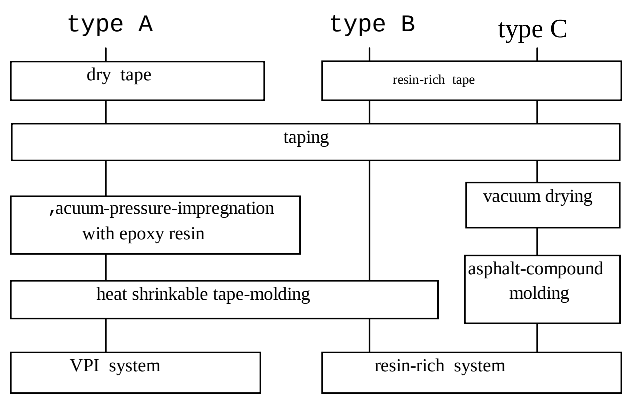

FIGURE 1 Insulation manufacturing processes of test specimens

Type B were manufactured without the vacuum treatment. Figure 1 shows the manufacturing processes of the test specimens.

For the purpose of detecting a change in their electrical properties such as tan, insulation resistance, and breakdown voltage(BDV), an aluminum bar with a cross-section of 6(mm)x25(mm) and a total length of 160(mm) was covered with each of these materials in the same manner as actual coils. To measure a change in their mechanical properties, on the other hand, samples were formed in a laminate by molding the tapes in the same manufacturing process as that of the bar coils. The plate sizes were 2 mm in thickness, 25 mm in width and 100 mm in length.

3 EXPERIMENTAL METHODS

3.1 Test bench

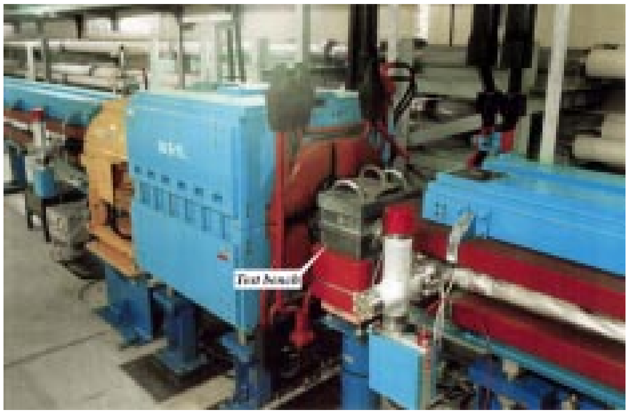

.

FIGURE.2 Location of test bench.

All of the test specimens were put in a radiation box located in the steering magnet where the dose rate was 37-65 kGy/h as shown in Figure 2. The dose has been calibrated with the thermo-luminescence dosimeter method[2], by employing a test beam with well monitored energy and current. The number of samples per test, material and dose was three, because of the limitation in irradiation space.

The samples taken out of the irradiation box at some fixed time period were subjected to the tests explained in the following. Measurements of insulation resistance and tan δ at high temperatures were made in order to study damage mechanism and recovery effects.

3.2 Electrical insulation tests

(1)Insulation resistance: The property was measured at 1 kV dc for a specimen as shown in Figure 3. The one minute value was used as the measurement value.

(2)Tan δ and capacitance: Tan δ and capacitance were measured at 50Hz by using a high voltage auto Schering bridge (Soken Electric Co., Ltd. type:DAC-HAS-3) for a specimen as shown in Figure 3.

(3)BDV: 50 Hz ac BDV was measured by the continuous

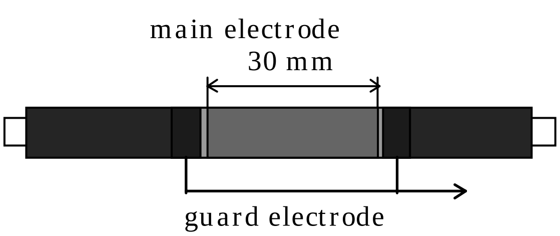

FIGURE 3 Test specimen for measuring insulation resistance and tan.

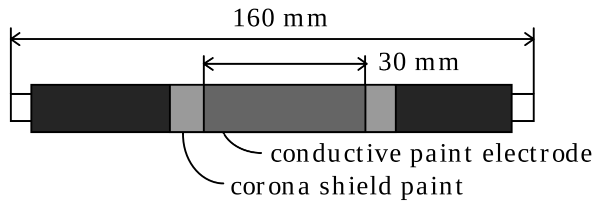

FIGURE 4 Test specimen for measuring BDV of bar coils.

voltage rising method in 0.5 kV/s for a specimen as shown in Figure 4.

3.3 Flexural tests

Flexural tests were carried out by using a universal materials testing machine(Instron Ltd. type:1186) on specimens with a thickness of about 2 mm. The span distance was 30 mm and the bending speed 0.5 mm/min in a three point bending method. Flexural strength and modulus were obtained.

3.4 FT-IR analysis

Fourier Transform Infrared Spectrometer (FT-IR) analysis was done by the KBr method for the powder obtained by filing the surfacial portion of samples, in order to survey the change in chemical composition.

3.5 SEM observation

Surface and cross-section of bar coils and laminates were observed by a scanning electron microscope(SEM).

3.6 Water content

Water content of the specimens were measured by the Karl Fischer's method.

4 TEST RESULTS AND DISCUSSIONS

4.1 Relationship between dose and electrical insulation properties

Figure 5 shows the relationship between dose and BDV. For all three samples, BDV decreases with the increase of dose. At 167 MGy, BDV is higher in the order of A, C and B. The fact that type A was higher than type B and C, may be due to the presence of mica. Comparing type B with type C in the samples without mica, type C is apparently superior to type B . This can be attributed to the existence of voids in the EISs. Type C is void-free because it was manufactured with vacuum treatment. On the contrary, type B includes voids, because of the manufacturing process without vacuum treatment. The oxidation tends more to develop in the void containing EISs than in the void-free ones.

Figure 6 shows the relationship between dose and Δ tan δ, where, Δ tan δ=(tan δ @3kV-tan δ @0.5kV). The parameter Δ tan δ is known to reflect partial discharges in

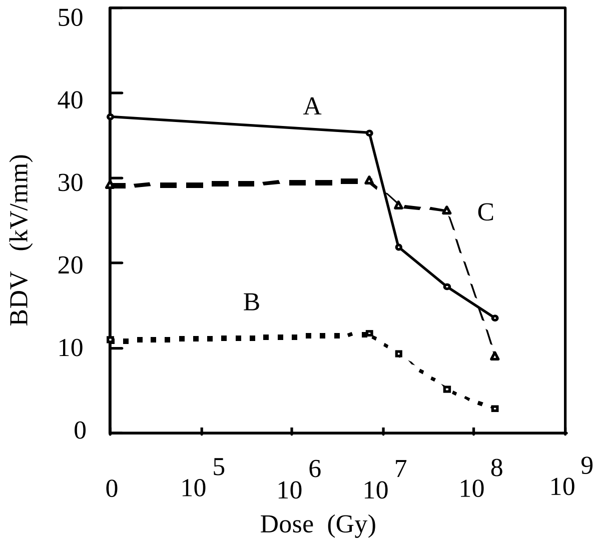

FIGURE 5 BDV of bar coils vs. dose.

a void, therefore it is reasonable to regard Δ tan δ as a measure of the amount of voids. The Δ tan δ increases at a smaller dose in type B than in type C. This suggests that gases evolved by radiation decomposition of the resin induce the delaminations of the insulating materials. The reduction in Δ tan δ at 167 MGy for type B could be due to a puncture of the insulation caused by the increase of pressure in the closed void and hence the void became open to the atmosphere resulting in a decrease in volume.

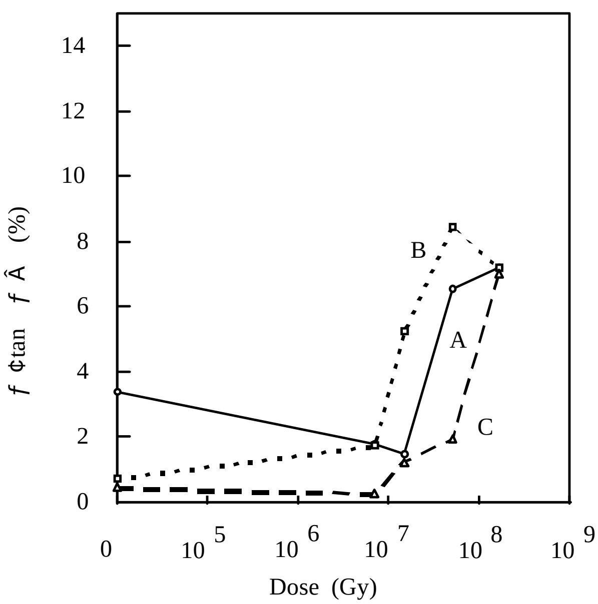

FIGURE 6 tan δ of bar coils vs. dose.

Figure 7 shows the relationship between dose and insulation resistance, as a function of measuring temperature for type B. Although the insulation resistance decreases with the increase of dose, it recovers up to the initial level above 100°C at 167 MGy. Figure 8 shows the relationship between dose and the water absorption content, in type B. The water absorption content increases with the increase of dose. The fact that the insulation resistance decreased with the increase of dose might be mainly due to the absorbed water. The reason why the insulation resistance recovered up to the initial level above 100°C at 167 MGy might be because the water should be released by heating, resulting in the recovery of insulation resistance, where voids might be opened at 167 MGy.

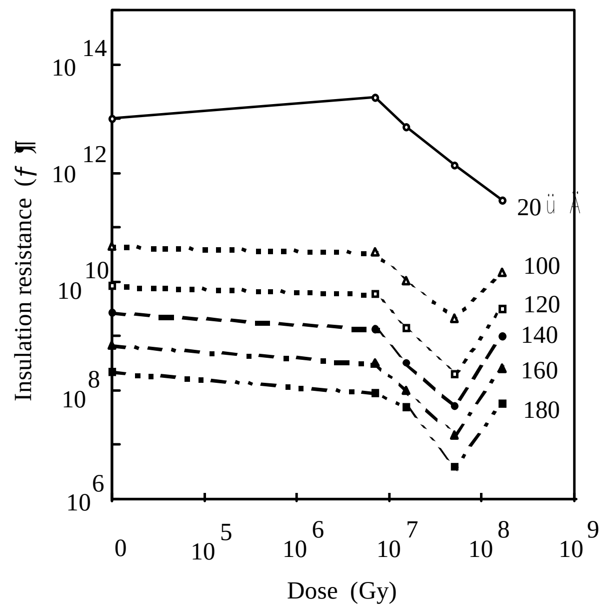

FIGURE 7 Insulation resistance vs. dose (type B).

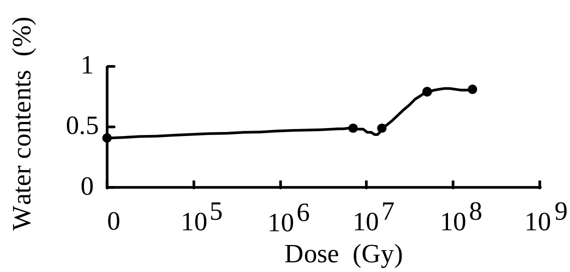

FIGURE 8 Water absorption contents vs. dose (type B).

Figure 9 shows the relationship between dose and insulation resistance. In type A, at temperatures above 120°C insulation resistance decreases with the increase of dose. In type A, it is supposed that most voids still were not opened to the atmosphere up to 167MGy due to mica as a barrier, and therefore the insulation resistance did not recover.

These phenomena, to recover the insulation characteristics at temperature above 100°C at 167 MGy, were also found in tan. Figure 10 shows the relation between dose and tan δ of type B. Tan δ increases at temperatures above 100°C, with the increase of dose, however, it de creases down to the unirradiated level after 167 MGy.

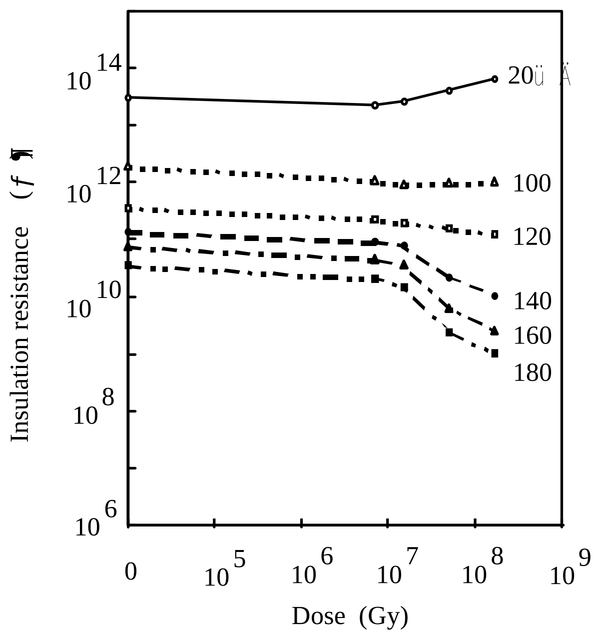

FIGURE 9 Insulation resistance vs. dose (type A).

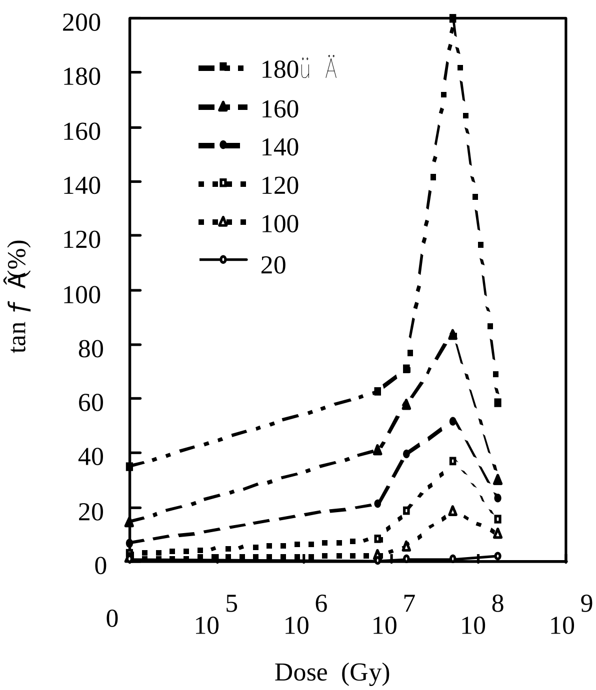

FIGURE 10 Tan δ of bar coils vs dose(type B).

In type A, such the recovery phenomena were not found, as shown in Figure 11. In type C, the same phenomena as in type B were also found both in the insulation resistance and tan. Both types B and C are reinforced with only glass-cloth without mica and it is supposed that voids in the resin progressively opened to the atmosphere once the insulation is delaminated.

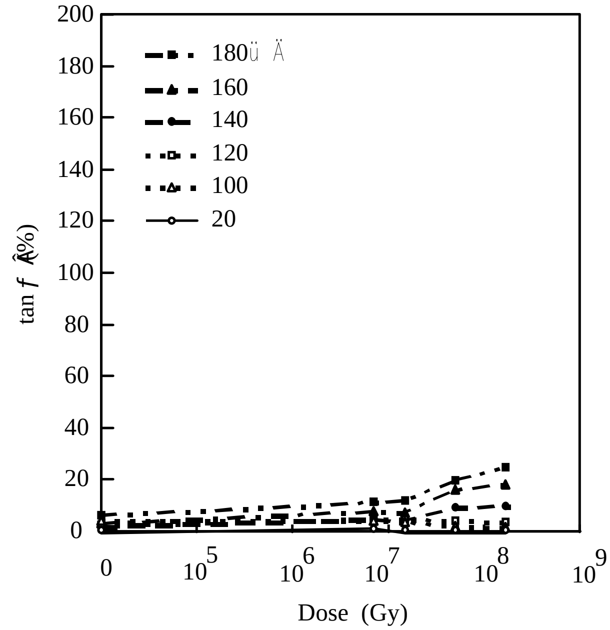

FIGURE 11 Tan δ of bar coils vs dose(type A).

4.2 Relationship between dose and properties

Figure 12 shows the relationship between dose and flexural strength. Flexural strength begins to decrease remarkably above about 4 MGy in type A and above about 15 MGy in type B. In type C, flexural strength decreases gradually up to about 15 MGy, then decreases more rapidly down to 167 MGy. The degradation starting dose and decreasing tendency of the flexural strength are differentiated by the combination of matrix resin and reinforcement. The flexural strength at 167 MGy is higher in insulation type C, then type B and is remarkably low in type A. The reason why type A was the weakest could be

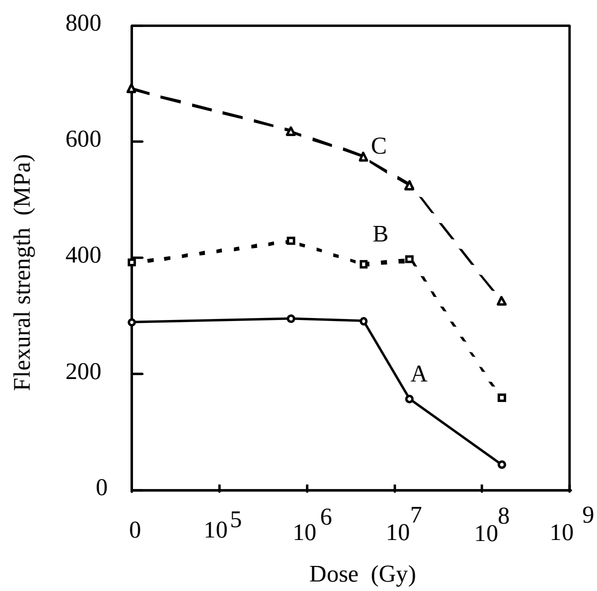

FIGURE 12 Flexural strength of laminates vs. dose.

the radiation degradation of the matrix resin, which induces the decrease of interfacial adhesive strength between the resin and the mica and glass-cloth reinforcements, in addition to the gas pressure effect as mentioned above.

Figure 13 shows the relationship between dose and the insulation thickness. As for type A, the insulation thickness increases sharply from 4 MGy, which is equal to the starting dose for the decrease in flexural strength. On the other hand, type B and C show little change in the insulation thickness.

Figure 14 shows the relationship between dose and the flexural modulus. Type A decreases the flexural modulus sharply from 4 MGy, which is equal to the starting dose for the decrease in flexural strength. On the other hand, type B and C show little change in the flexural modulus.

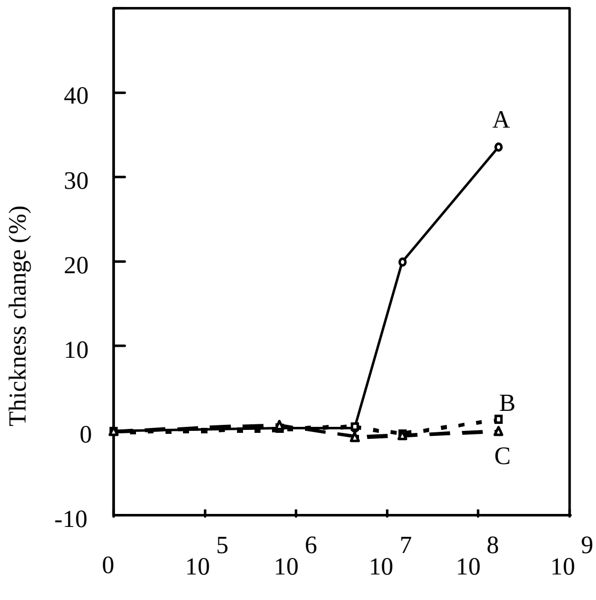

FIGURE 13 Thickness of laminates vs. dose.

4.3 Relationship between the morphology by SEM and electrical and mechanical properties

Figure 15 shows the cross-sectional views of coil insulations by SEM, for the unirradiated and 167 MGy irradiated specimens. In type A, less degradation is found in the mica layer, whereas the resin in the vicinity of glass-fibers is severely deteriorated. It is assumed that this is the reason why in type A, the BDV was relatively high, although the flexural strength was the lowest. In type B, voids are locally found even in the unirradiated specimens and, at 167 MGy, the resin around the glass fibers is whitened. This whitened part increased with the increase of the dose, as a result of the increase of voids. This fact agrees well with the tendency of Δ tan δ to increase. Moreover, voids stretch in the thickness direction, in type B. This might be the reason why, in type B, the BDV was the lowest, although there was no great swelling in the insulation. In type C, almost no voids were observed in unirradiated specimens. However, at 167 MGy, damage is

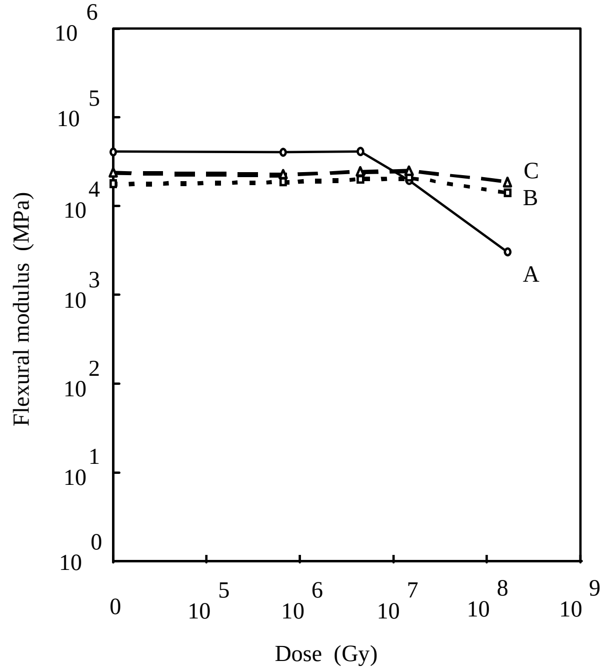

FIGURE 14 Flexural modulus of laminates vs. dose.

seen in the resin around the glass-fibers, like in type B, and voids are formed. This is supposed to be the reason why the BDV decreased remarkably at 167 MGy.

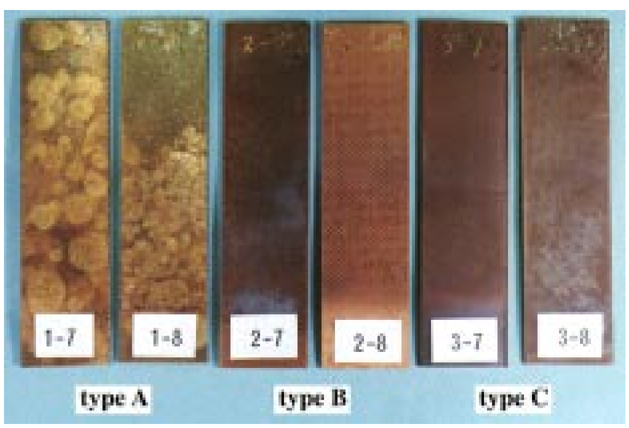

FIGURE 16 Appearance of laminates after 167 MGy irradiation

Figure 16 shows the appearance of the two flexural test samples after 167 MGy. Dotted swellings are observed in type A, however, no such swellings are observed in type B and C. The reason of such differences could be due to the ease by which gas evolved by irradiation to pass through the insulation. Further, the adhesive strength

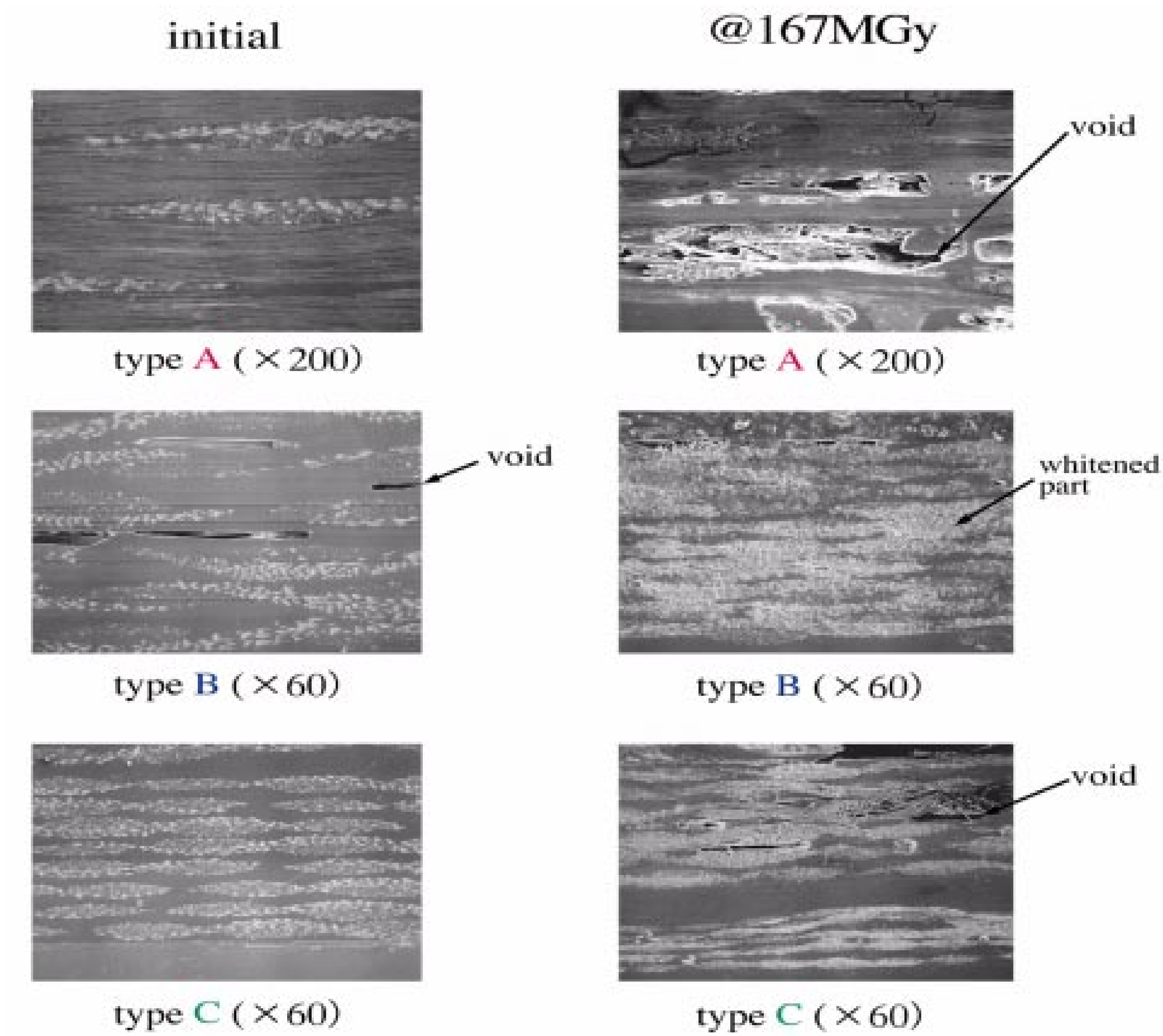

FIGURE 15 Cross-sectional photographs taken by a SEM

between the resin and the reinforcement is a dominant factor which can influence the radiation degradation of the insulation.

4.4 Comparison of degradation dose between electrical and mechanical properties

Experiments and operational experience support the fact that, with regards to the insulation degradation due to irradiation, the mechanical properties degrade in general faster than the electrical [7,8].

From this point of view, a comparison of the dose at start of the decrease in electrical and mechanical properties was made in this experiment.

Figure 17 shows the residual BDV and flexural strength as a function of dose. Only type C agrees well with the experience that the mechanical properties degrade faster than the electrical.. In type A, both properties start to decrease at almost the same dose. In type B, it is noticeable that the mechanical property starts to decrease at a larger dose than the electrical property. It might be said that the results of our test did not always support the past experience.

Table 2 shows the dose to reduce the initial property of the breakdown strength and the flexural strength to half. Such criteria are usually used for the life expectation of the insulation, and the dose is defined as an index for radiation resistance of the EISs, for example, as mentioned in the second edition of IEC 544-2 [8]. From this Table, the radiation resistance is superior in the order of C, B and A. This order might reflect the difference of the material constitutions and the manufacturing processes in EISs.

TABLE 2 Dose to reduce the initial property to half

Type	BDV	Flexural strength
A	33 MGy	19 MGy
B	46 MGy	110 MGy
C	110 MGy	130 MGy

4.5 FT-IR analysis

Figure 18 shows the relationship between dose and carbonyl absorbance which appeared in the region of 16501800 cm^{-1}. The characteristics of samples for carbonyl absorbance qualitatively coincides with that for Δ tan δ. The carbonyl compounds are originated from the

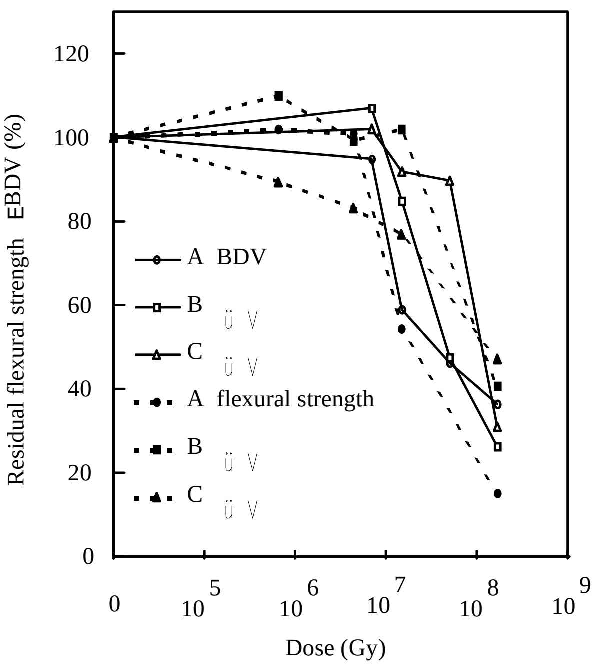

FIGURE 17 Residual BDV and flexural strength obtained from the results shown in Figure 5 and Figure 12.

oxidation reactions caused by radiation. With the advance of oxidation reactions, ketone, aldehyde, carboxylic acid, etc. are formed on the polymer molecules in resins, which are responsible for carbonyl absorbance. The aldehyde and carboxylic acid are the products from polymer chain scission by oxidation. These oxidation products increase the tan δ, and are liable to absorb water. Therefore, the water absorption of coil insulation increased with the increase of dose, and the decrease of electrical insulation properties are accordingly accelerated. Thus, the carbonyl absorbance is a good degradation index in the same insulation.

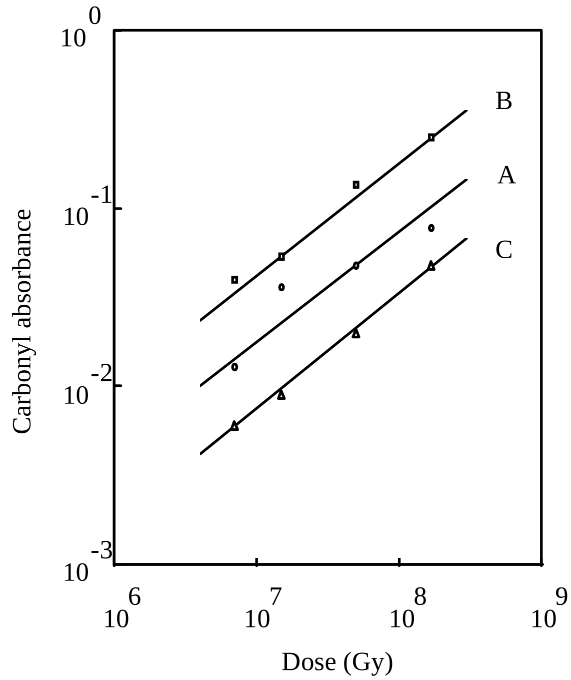

FIGURE 18 Carbonyl absorbance vs. dose.

5 CONCLUSIONS

From the irradiation tests of typical insulating materials for magnet coils, using actual radiation environment in the TRISTAN MR up to 167 MGy at the highest, the following conclusions can be drawn.

(1) The radiation degradation of EISs is caused by that the resin around the glass fibers is decomposed to produce gases, which make the voids in the resin matrix. The resin decomposition is mainly caused by the oxidation reactions.

(2) The radiation degradation is easy to occur in the EIS without vacuum treatment in the manufacturing process.

(3) The EIS including mica is higher in the dielectric strength and lower in the mechanical strength. It tends to swell and maintain a closed void system up to a larger dose, because mica acts as a barrier of degassing.

(4) The change in morphology observed by SEM are closely related to the electrical and mechanical properties.

(5) Carbonyl absorbance is a useful index of the oxidation degradation in resins caused by radiation.

As a concluding remark, studies of the manufacturing process as well as the insulating materials themselves are, indeed, important in order to develop the higher radiation-resistant EIS. In addition, since the measured absorbed dose of TRISTAN MR magnet coil exceeded 10MGy at the highest[9], the authors anticipate that some of the coils will reach to the end of life in the near future, based on the data presented here.

In addition, hereafter, neutron radiation damage on EISs will become important in accordance to the start of operation of large Hadron collider.

REFERENCESs

[1] Y.Kimura and H.Baba,Proc.the 6th Sym. on Accelerator Science and Technology, 15(Tokyo,1987).
[2] T.Momose, H.Hirayama, T.Ieiri, K.Takayama, Y.Ohsawa, K.Endo, H.Ishimaru, Y.Mizumachi, S.Takeda, T.Kawamoto, and K.Uchino, Proc. of the European Part. Accel. Conf., 1284(Rome,1988).
[3] P.Beynel, P.Maier, and H.Schönbacher, CERN 82-10(1982).
[4] G.Lipták, R.Schuler, P.Maier, H.Schönbacher, B.Haberthür, H.Müller, and W.Zeier, CERN85-02(1985)
[5] T.Ozaki, K.Takayama, Y.Ohsawa, T.Kubo, K.Endo, M.Hirano, T.Chugun, R.Kumazawa, and H.Mitsui, Proc. Part. Accel. Conf., 2015(1989)
[6] H.Mitsui, R.Kumazawa, T.Tanii, T.Chugun, Y.ohsawa, T.Ozaki, and K.Takayama, Particle Accelerators, Vol.52, pp.31-44(1996)
[7] IEEJ, Insulating Materials Irradiation Investigation Special Committee Report, Part I No.79(1967), (in Japanese).
[8] IEC 544-2 Second edition (1991).
[9] K.Endo and Y.Ohsawa, Radiation, 21, 2, 32 (1995) , (in Japanese).

Near Beam Physics at IHEP: II. Complementary Methods of Beam Control

A. A. Asseev
Institute for High Energy Physics, Protvino, Moscow region, 142284 Russia

Abstract

Results of investigations of beam interactions with accelerator elements and residual gas during acceleration and extraction are reviewed. Methods for shaping the beam before extraction are considered. Techniques for decreasing equipment irradiation are also discussed.

1 INTRODUCTION

Several factors have dictated the need for investigations of the accelerated beam transverse dimensions out to regions of normalized intensity densities less than a fraction of a percent. These investigations were needed to understand particle behavior at large distances from the beam center at the 70 GeV IHEP proton synchrotron (A–70). The factors are:

- the existence of particle losses during the accelerating cycle which could not be explained by the dynamics of a beam of normal dimensions [1,2];
- at fast ejection of a beam there are losses of particles on deflector septums before the ejection event. This shows the existence of particles beyond the limits of the distributions measured earlier [3].

Measurements of the horizontal dimensions of the beam [4] showed that during acceleration there are many particles whose betatron amplitudes are larger than the amplitudes of the dense part of the proton beam. This aggregate of particles of large amplitudes is the "halo" of the accelerated beam.

2 INVESTIGATION OF THE BEAM HALO IN THE ACCELERATOR

We consider the halo to be the aggregate of charged particles at a level of $\sim 10^{-2}$ of the full intensity which surrounds the core of the accelerated beam. The halo exists during the entire accelerating cycle and is self–preserved and self–revived. Halo particles are out of the dense part of a beam but in a region of betatron motion stability.

The factors which promote halo appearance are scattering of particles on nuclei (molecules) of the residual gas, effects of scattering inside the beam, influence of betatron resonances, etc.

2.1 Experimental results

The particle distributions in the halo at the end of acceleration for different residual gas pressures in the accelerator chamber [4] are given in fig. 1. Curve 1 corresponds to the residual gas pressure $\sim 4.5 \cdot 10^{-7}$, curve 4–to the pressure $\sim 2 \cdot 10^{-5}$ torr. Distributions corresponding to the residual gas pressure $\sim 10^{-6}$ and $\sim 3 \cdot 10^{-6}$ torr (curves 2 and 3, respectively) lie between curves 1 and 4.

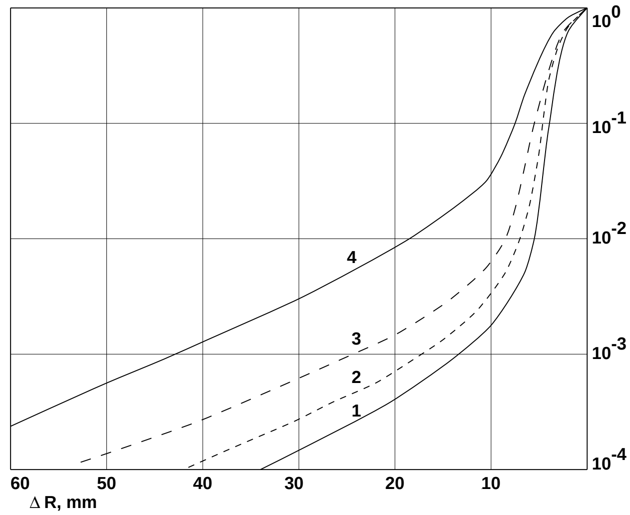

Figure 1: Horizontal beam size as a function of residual gas pressure.

It is seen that the beam size increases with the deterioration of the vacuum determined by the increase of the residual gas density.

To understand the halo generation mechanism it is useful to separate the contribution to the beam halo of particle scattering processes at different accelerator energies. The results of the calculations for particles of ~ 10 GeV to the increase of the halo of a 70 GeV beam are presented in fig. 2 [5]. Curve 1 is the distribution of particles in the "natural" beam, curve 2 is the distribution after the halo is removed at 10 GeV, curve 3 is the particle distribution in the dense part of the beam for the case of an ideal vacuum.

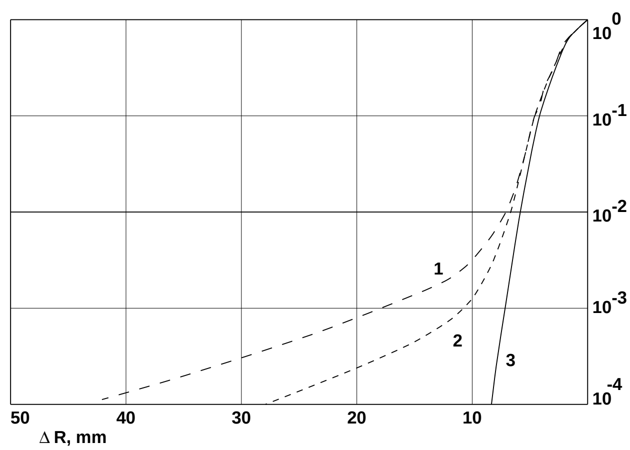

Figure 2: Distribution of particles at the end of acceleration for a pressure of $\sim 10^{-6}$ torr (calculation).

It is seen that scattering of protons by the residual gas in the energy region from 10 to 70 GeV gives an essential contribution to the beam halo. In other words, the halo is able to be self-generated.

The experimental dependence of the efficiency of beam halo interception at different energies is presented in fig. 3. The data correspond to the transition region of the distribution function. The vertical scale shows the relation of particle beam density from the transition region for the case for scraped halo and for the "natural" beam which was determined at maximum energy.

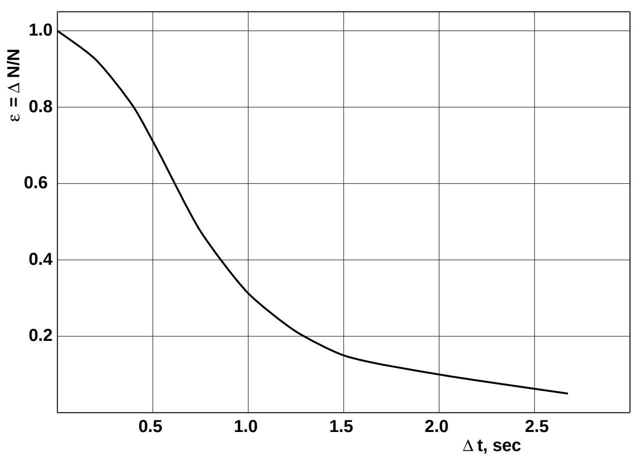

Figure 3: Efficiency of halo interception during acceleration.

It is seen that the beam halo grows during the whole accelerating cycle and, after being scraped during beam acceleration, it appears again. The intensity of halo particles at the end of the acceleration cycle depends on the time allowed for its development ($t_{max} \approx 2.7$ s).

From the analysis of the experimental data (including the errors of the experiment) one can conclude [5] that the main reason for halo appearance at A–70 is particle scattering on the residual gas. Scattering a beam on residual gas molecules (nuclei) leading to halo formation includes two processes:

- multiple Coulomb scattering by small angles, and
- single or several scatters that do not result in particle losses.

Large angle scattering processes leading to particle loss are not analyzed here.

As is shown in [5], the probability of getting large amplitude betatron oscillations by single scattering is much higher than the probability of multiple scattering. Both the initial intensity of the beam and the residual gas pressure in the accelerator chamber are responsible for halo formation. Our estimates were made for a residual gas pressure of $\sim 10^{-6}$ torr. They showed that the impact of other effects, including resonances, does not exceed 30%. Approximately 70% of the halo appeared in the energy interval from injection to 10 GeV and 30% at energies higher than 10 GeV.

2.2 Discussion of results

The integral distribution function $F(x)$ of the dense part of the proton beam (see fig. 1) at 70 GeV is approximated well by the function [4]:

$$F(x) \approx \exp(-x^2/\sigma^2), \qquad (1)$$

where x is the distance from the beam center and σ is the dispersion.

Theoretical analysis of the influence of the residual gas pressure on beam size including the effect of adiabatic damping of betatron oscillations from injection to the final energy showed that the integral distribtion function of the dense part of a proton beam $F_d(x,t)$ as a function of time t is expressed by:

$$F_d(x,t) = \exp(-x^2/\sigma^2(t)), \qquad (2)$$

where $\sigma(t)$ is expressed by:

$$\sigma(t) = \sigma_0^2 \frac{H_0}{H_t} + 4.1 \cdot 10^4 \frac{P}{H_t} \int_0^t \frac{\sqrt{(161)^2 + H_t^2}}{H_t^2} dt, \qquad (3)$$

here σ_0 is the initial value of $\sigma(t)$ in cm (at injection, in our case); H_0, H_t are initial and current values of magnetic field, oe; P is the residual gas pressure in μtorr, and t is the time in seconds.

As was pointed out, the existence of halo which affects the distribution function $F(x)$ at intensity levels $\leq 1\%$ can be explained by processes of single scattering by large angles (that have not yet led to a loss).

Theoretical analysis of this effect showed that the distribution function of particles in the beam halo has the form:

$$F_h(x) = A(P) \cdot \frac{P}{x^2}, \qquad (4)$$

where $A(P)$ is a coefficient depending of P, the residual gas pressure. At a pressure of $P \approx 10^{-5}$ torr $A(P) \approx 0.19$.

The experimental dependence of $A(P)$ for the pressure interval $4.5 \cdot 10^{-7} \div \sim 2 \cdot 10^{-5}$ torr is given in fig. 4(curve 1). The analytical form is expessed:

$$A(P) = -A_0 \cdot \ln\left(\frac{P}{P_0}\right), \qquad (5)$$

where $A_0 \approx 4.8 \cdot 10^{-2}$ and $P_0 = 10^{-3}$ torr. This dependence is shown in fig. 4 by curve 2. It is believed that the dependence (4) is true up to residual gas pressures of $\sim 10^{-8} \div 10^{-9}$ torr.

Analyzing expression (5), one notices that at $P = P_0$ $A(P) = 0$. Formally this can be interpreted as the disappearance of the halo. Actually it means that at this residual gas pressure particle scattering is so large that it is not possible to distinguish a core (dense part). The beam as a whole will be a halo which occupies all the vacuum chamber and will soon be lost on the vaccum chamber walls. Beam can not be accelerated at such a vacuum.

In fig. 5(curve 1) the distribution of particles in the maximum energy beam is presented. This data was taken with the help of internal targets and secondary particle monitors in the first run of 1997 when 90% of the corrugated vacuum

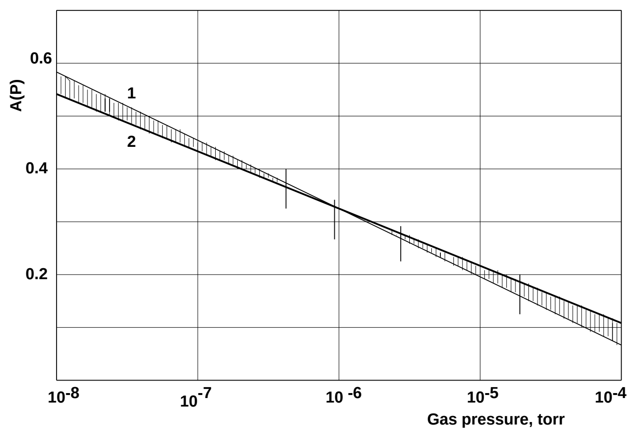

Figure 4: Dependence of $A(P)$ of expression (4) on the residual gas pressure.

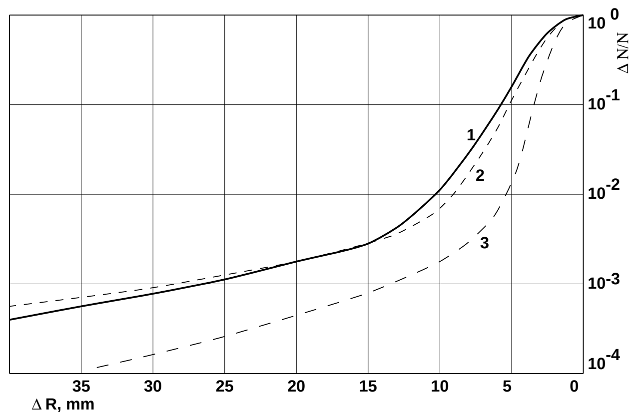

Figure 5: Distribution of particles in the beam with the new vacuum chamber.

chamber of A–70 was changed to a flat one. Curve 2 corresponds to earlier measurements at a vacuum of $\sim 3 \cdot 10^{-6}$ torr [4].

Two points are worth noting:

1. The beam halo extends out to coordinates ≥ 40 mm that agree well with previous measurements at a vacuum of $\sim 3 \cdot 10^{-6}$ torr;

2. The dense part of the beam is somewhat larger than it was earlier.

Possible explanations for these points are:

- The real vacuum in the A–70 chamber was $\approx 3 \cdot 10^{-6}$ torr. That could be because of considerable outgassing from walls of the new chamber. This was the reason for halo generation;

- ”Broadening” of the dense part of beam can be explained by a different composition of residual gas than for the earlier corrugated chamber and the existence of fractions that are heavier than nitrogen.

According to [5], the mean value of the nuclei charges of the residual gas of the corrugated vacuum chamber was Z=7 (Z=9 for nitrogen). Measurements show the necessity of investigating the new A–70 vacuum chamber both as regards the residual gas pressure and the partial composition of its components.

For comparison, the particle distribution taken earlier in the accelerated beam at a residual gas pressure of $\sim 4.5 \cdot 10^{-7}$ torr is shown by curve 3 in fig. 5 (see also curve 1 of fig. 1). It is clear that measures need to be taken to improve the vacuum in A–70.

3 INVESTIGATION OF PARTICLE LOSSES AND EQUIPMENT IRRADIATION

The first detailed analysis and characterization of beam losses in A–70 for actual conditions were given in [2] after several years of investigations. The importance of investigation of particle losses in the accelerator is obvious since particle losses irradiate equipment and shorten its working life. Beam losses also drive the growth of induced activity levels in equipment. The presence of induced activity complicates repair work. Maintaining accelerator operation readiness for longer times without failures due to overirradiation is a problem of control and limitation of beam losses. It is one of the most important problems for accelerator physicists.

3.1 Particle losses before startup of the booster

Invesigations show that at corresponding stages of the accelerator cycle there are particle losses defined by beam dynamics:

- at injection and in the beginning of acceleration,
- at the transition energy,
- at fast ejection of the protons,
- at resonant slow extraction,
- during internal targets operation,
- during scraping of unused beam.

As a rule, the losses occur over long time intervals from microseconds (for example, at fast ejection) to ≥ 1 s at slow extraction or internal target operation. They are distributed over the perimeter of the accelerator irradiating all of the equipment at different rates. The distribution of the losses depends on many factors including beam dynamics for a particular process, the existence of “narrow” apertures in the accelerator chamber, as well as beam intensity, extraction efficiency, etc.

The distribution of losses along the accelerator perimeter was invesigated with the the help of a Loss Measurement System (LMS) consisting of 120 scintillating detectors installed on all the blocks of A–70 and combined with corresponding electronics [6]. Pictures of the particle loss distribution at different stages of the accelerator cycle before the startup of the booster for an intensity level of $\leq 5 \cdot 10^{12}$ protons per cycle (ppc) are presented in details in paper [1]. As illustrations, two cases of loss distribution in the accelerator are shown: during the generation of secondary particles for physics experiments by internal targets and during residual beam scraping at the end of the accelerator cycle with a dumping target.

Losses during internal target operation. The distribution of particle losses around the perimeter of the accelerator during internal target operation is shown in fig. 6. The most complicated operating regime is shown: parallel targets operating in magnet blocks 24, 27 and 35 with beam sharing by bumps and targets in block 33 and SS–32 in the "shadow" mode (using beam scattered by other targets). The figure shows the behavior for the entire flat top of the magnetic cycle (~ 1.8 s). The summed intensity was $\sim 1.4 \cdot 10^{12}$ ppc.

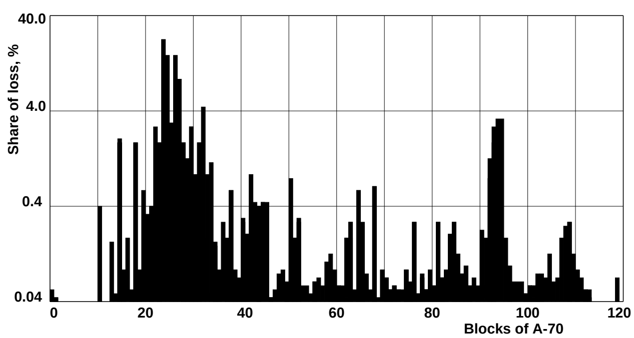

Figure 6: Distribution of particle losses around the perimeter of the accelerator during internal target operation.

Equipment installed in the region of the internal targets receives the maximum irradiation (straight sections 22–35). Particle losses also occur at SS–16, 18, 20 where the kicker magnet for fast ejection and septum magnets for slow extraction limit the vacuum chamber aperture. The existence of peak losses at blocks 94–97 is explained by particle losses at other "narrow" apertures such as the walls of the vacuum chamber of the octupole lens of SS–94.

Losses during dumping target operation [1,2]. The dumping target is a special target installed at SS–60 in the accelerator. The main task of the dumping target is to dump the beam that remains at the end of the accelerator cycle and localize its radiation in a region of the ring that is occupied with less valuable equipment. It is assumed that the intensity of the residual beam will not exceed $\sim 10^{11}$ ppc. The distribution of particle loss in the accelerator during dumping target operation is shown in fig. 7. The duration of the interaction of a beam with the target and the rate of irradiation of equipment depend on the residual beam intensity which can reach $\sim 5 \cdot 10^{12}$ ppc if fast ejection (FE) towards the neutrino channel is prohibited.

With the growth of residual beam intensity the LMS sum signal for the losses grows proportionally but the relative distribution is maintained. This demonstrates the stability of the loss dynamics for the residual particles. It is also seen from fig. 7 that there is no strong loss localization although the main deposit from the dumping target is in the 61–64 magnet blocks. The remaining losses are distributed mainly

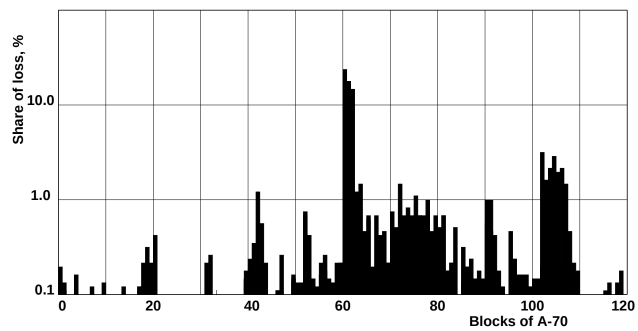

Figure 7: Distribution of particle losses during dumping target operation.

in the regions of blocks 43, 76, 93 and 104–107 of A–70.

It should be noted that beam losses occur during the whole accelerator run including the time for machine development. For accelerator studies all the intensity of the beam accelerated to its final energy is intercepted by the target. The beam losses during a run reach 15–20% of the full intensity [1].

3.2 *Particle losses at high intensity*

The beginning of A–70 high intensity operation ($\geq 10^{13}$ ppc) started at the end of 1985, or to be more precise, at the 5–th run when the beam injection scheme from the booster (A–1.5) was finally established. No peculiarities were noticed in beam loss dynamics during beam steering on internal targets and at resonant slow extraction operating with intensity of $\sim 5 \cdot 10^{11}$ ppc. However, differences appeared from preceeding runs in the loss dynamics and the equipment irradiation patterns for fast extraction (FE).

In fig. 8 the beam extraction scheme for A–70 is shown as well as the disposition of corresponding equipment. Trajectories of particles extracted at FE (curve 1) and at resonant slow extraction (RSE, curve 2) are shown. This scheme corresponds to the project variant of FE with equipment made at CERN: kicker magnet at SS-16 (KM–16) and septum magnets (SM–24, 26) installed in SS–24, 26, respectively [7]. RSE of a beam in this scheme is provided through SM–18, 20, 22, 26 (without current) and SM–28 [8], not shown.

Since the failure (at the end of 1983) of the SM–24 motion system, FE has been used for a few runs with SM–24 stationary at the position of the septum $R = -52$ mm. This operating regime turned out to be ineffective with a high rate of septum irradiation both at injection and acceleration because of a significant limitation of the accelerator acceptance. Therefore another approach was used: FE through the septum–magnets of the RSE system (curve 2 of fig. 8) [9]. A comparison shows that this regime is not equivalent to the original one reviewed in [7] for at least two reasons:

- The use at FE of four to five septum magnets instead of two leads to higher losses of the extracted beam;

- Forming the local distortion of the closed orbit necessary for beam displacement to septums of SM–18 and SM–20 increases circulating beam losses on the

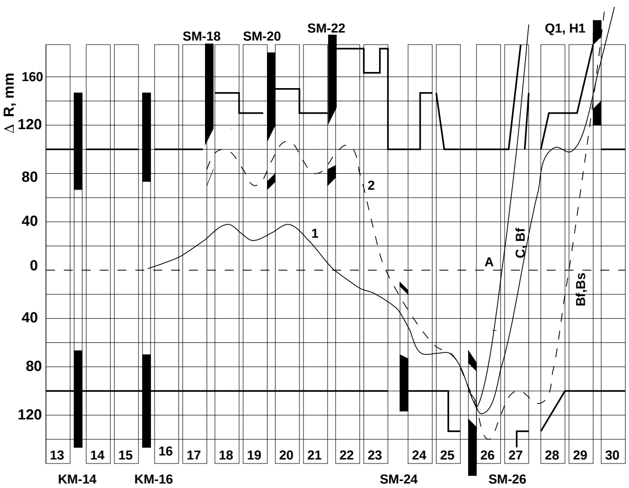

Figure 8: Proton extraction scheme from the IHEP accelerator: 1 is trajectory for FE; 2 is the trajectory for RSE. A,B,C are different extraction directions.

septums before extraction due to orbit instabilities, radiofrequency, etc.

Operation experience in the new regime shows that the efficiency of FE was at the level of 90% [10] (while for the original one [7] it was 98%).

The most reliable information concerning irradiation of equipment in this regime (distribution of beam losses in the accelerator at FE obtained with the help of the LMS [6]) is shown in fig. 9.

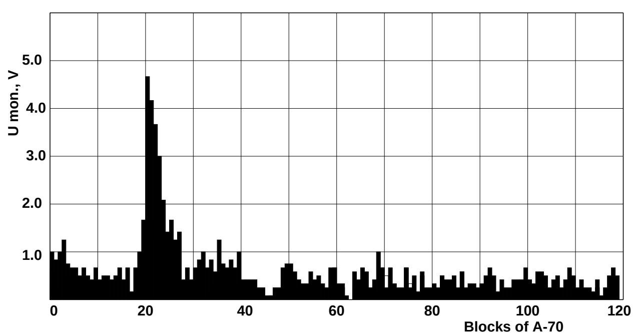

Figure 9: Distribution of particle losses at FE through the septum magnets of the RSE system.

The main losses come in the extraction region (blocks 18–30 of A–70). The largest losses are in the region of blocks 20–23 demonstrating the conclusion in [11] about the domination of losses on the septum SM–20.

For comparison, in fig. 10 particle loss distributions in the ring are shown for FE of 10^{13} ppc (fig. 10a) and at steering on to internal targets of $\sim 1.2 \cdot 10^{12}$ ppc (fig. 10b). The time interval for the loss measurements was 20 ms for FE, and 800 ms for internal target operation.

It is seen that the integrated losses $\int_0^{120} U_m dn$, where U_m is the value of monitor signal, V; and dn is number of A–70 blocks turned out to be very close for both cases. This confirms that:

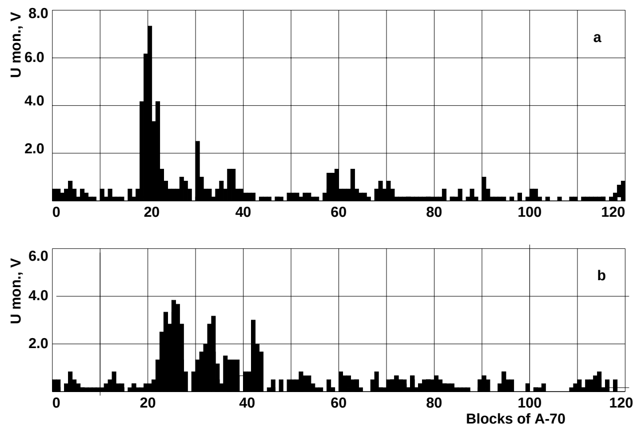

Figure 10: Distribution of beam losses in the accelerator: a) FE of $\sim 10^{13}$ ppc; b) for $\sim 1.2 \cdot 10^{12}$ ppc on the internal targets.

- The particle loss intensity at FE was not below the intensity interacting with internal targets, i.e. $1.2 \cdot 10^{12}$ ppc;
- The efficiency of FE in this case is not higher than 88%.

3.3 Irradiation of accelerator equipment

Before the start of booster operation. The parameters characterizing losses and the rate of equipment irradiation for different stages of the accelerating cycle are given in table 1. The main parameter of the table is the dose coefficient K_D that reflects the radiation load on the accelerator equipment at the particular stage for one lost proton. It was obtained on the basis of energy deposition data $\varepsilon(r, E)$ at the edge of vacuum chamber from protons lost around the perimeter of the accelerator [12] and results of direct measurements of radiation loads on the equipment [13].

The partly empirical coefficient K_D allows one to estimate the dose absorbed by equipment for a given sum of particle losses at a particular energy. Estimations of the equipment irradiation (in percent) at different stages of the accelerating cycle due to irradiation of equipment are presented in the table with the coefficient $D_{irr.}$.

Using scaling one can with the help of the beam loss monitors evaluate the dose absorbed by equipment in any region around the perimeter during any run. On the basis of these results we were able [11] to forecast the irradiation rate of equipment from accelerator intensity growth and the use of new beam extraction regimes as well as to make more systematic investigations of ways to reduce beam losses and equipment irradiation.

Using this method, some results of irradiation of blocks of the main magnet of A–70 for the period 1975–1990 were restored and put into the radiation loads data bank for the accelerator magnet system[13].

Working with high intensity. In the initial operation plans for of A–70 at high intensity ($\geq 10^{13}$ ppc) it was thought that the main part of the beam would be extracted

Table 1: Characteristics of equipment irradiation for losses at different stages of the accelerator cycle.

	Intensity of losses,ppc	Integral of losses,V	Dose coefficient K_D,rad/proton	Energy of particles	$D_{irr.}$
Injection		$4.5 \cdot 10^2$	$(0.8 - 1.8) \cdot 10^{-12}$	100 MeV	3–5%
"Stabilization" of intensity	$2.3 \cdot 10^{12}$	$2.4 \cdot 10^3$	$(0.73 - 1.04) \cdot 10^{-10}$	1 GeV	6–10%
FE	$2.1 \cdot 10^{12}$	$3.58 \cdot 10^2$	$(0.78 - 0.98) \cdot 10^{-12}$	67 GeV	$\sim 60\%$
RSE	$3 \cdot 10^{11}$	$2.2 \cdot 10^5$	$(1.2 - 1.8) \cdot 10^{-11}$	70 GeV	
Int. targets	$1.4 \cdot 10^{12}$	$1.35 \cdot 10^6$	$(0.96 - 1.35) \cdot 10^{-10}$	70 GeV	
Dumping target	$3 \cdot 10^{11}$	$8.55 \cdot 10^4$	$(2 - 2.6) \cdot 10^{-10}$	70 GeV	$\sim 25\%$

towards external setups and inside the accelerator there would be no regions with radiation loads and levels of induced radioactivity higher than the earlier case for intensities of $\leq 5 \cdot 10^{12}$ ppc [14]. The basis of this belief was that beam extraction would minimize losses and radiation loads on equipment inside the accelerator enclosures.

As at CERN [15], this proved not to be so. Because of the relatively low extraction efficiency and the "thick-target" nature of the particle losses on extraction elements the radiation loads as well as the levels of induced activity in the extraction region increased. Their absolute values (i.e. of the radiation loads as well as the levels of induced activity) turned out to be higher in this region than elsewhere on the perimeter of A–70. Evaluations showed that even if the extraction efficiency were larger the losses due to the higher beam intensity would still give the main contribution to equipment irradiation in this region.

At CERN they retreated from the initially specified irradiation levels and allowed the possibility of increasing induced activity in the 28 GeV PS accelerator by 3–4 times. After establishing stringent regulations with a corresponding analysis of the accelerator working conditions they concluded that it was possibille to increase the intensity by a factor of eight. A level of $3 \cdot 10^{12}$ protons/s corresponds to $6 \cdot 10^{19}$ protons per year or an average intensity of about $6.0 \cdot 10^{12}$ ppc [16]. For a short run with low losses the intensity limit of the CERN PS can be allowed to reach 10^{13} ppc.

For comparison this corresponds approximately to work at A–70 with $\sim 10^{14}$ ppc but with losses only 3–4 times higher than losses at acceleration and extraction of a beam of intensity $5 \cdot 10^{12}$ ppc. In order to reach the CERN level A–70 has to work with an average intensity of $\sim 3 \cdot 10^{13}$ ppc. The losses have to be lowered by a factor of two.

Considering the problems of radiation load growth [13] and the levels of induced activity on equipment at A–70 are more demanding at high intensity, we take into account only the proton loss effects which interact with accelerator elements, internal targets, extraction elements, absorbers, etc.

One can draw conclusions about the irradiation rate of septum magnets for beam extraction with a common trajectory (i.e. FE and RSE through the same septum magnets) from fig. 11 where data for SM–20 and SM–22 is presented:

- dose power of induced activity (curves 1 and 2);
- radiation loads on septum magnet insulation (curves $1'$ and $2'$.

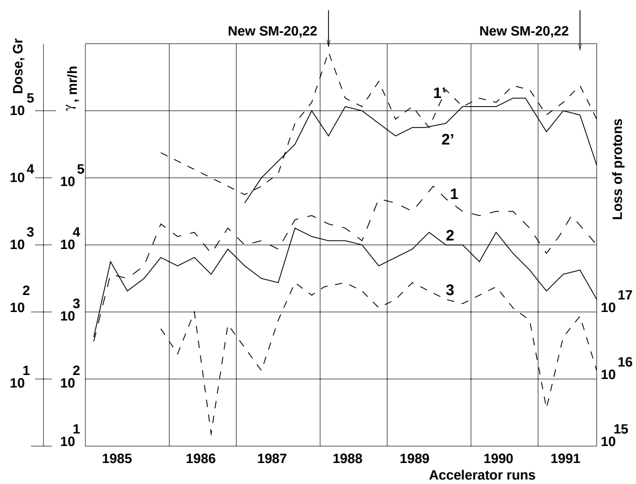

Figure 11: Results of radiation measurements on septum magnets: 1 is the induced activity and $1'$ is the radiation load on SM–20; 2 and $2'$ are the same for SM–22; 3 is the primary beam loss.

It is seen from fig. 11 that as a result of extracted beam intensity growth for FE the level of induced activity increases on both of the septum magnets but the absolute value of the induced activity on SM–20 is much higher. The growth of losses on SM–20 is confirmed by the data for radiation loads on septums SM–20 and SM–22 (curves $1'$ and $2'$) which directly depend on the value of the losses of the primary beam on the septa at extraction.

One has to point out a circumstance that had a direct connection to the data that is presented. Due to modernization, the new SM–20 and SM-22 were installed by the 2nd run of 1988. They failed in 1991 because of radiation damage and were changed again. The doses received by the septum magnets for this period were:
– for SM–20 $\sim 2.0 \cdot 10^6$ Grey ($\sim 2.0 \cdot 10^8$ rad);
– for SM–22 $\sim 1.2 \cdot 10^6$ Grey ($\sim 1.2 \cdot 10^8$ rad).

The "life time" of irradiated equipment is determined by the radiation resistance of the materials used for construction of A–70. For most of the insulating materials the limit of the dose value is about 10^6 Grey [17, 18]. As this dose is approached features of the materials change rapidly. This leads to failures of components and physics experiments.

Curve 3 in fig. 11 illustrates the change from run to run of the primary beam intensity lost on the septum magnets. The value of the lost intensity for any run is defined as the sum of particles hitting septums during both FE and RSE with account of their efficiencies. The figure illustrates the correlation between the primary beam losses, the radiation loads and the level of induced activity on SM–22 (curves 3, 2, $2'$). The weaker connection for SM–20 can be explained by the lower efficiency for FE that was used in the evaluation.

Results of radiation load measurement on the elements forming the trajectory of the extracted beam are presented in fig. 12. In the figure SM–18 is curve 1, SM–26 is curve 2, the lens and magnet of SS–30 is given by curve 3. SM–24 was out of use for beam extraction during 1985–1990. SM–24 has been in use (after investigations in 1990) since the first run of 1991. It is seen that for SM–18, SM–26 and elements of SS–30 the situation is similar to the situations for SM–20 and SM–22. That is, the radiation loads increase as a result of beam losses during high intensity extraction.

The character of the irradiation of SM–24 (curve 4) changed sharply in 1990 during investigations of FE through SM–24, SM–26. The irradiation increased much more in 1991 when it came into use for high intensity extraction.

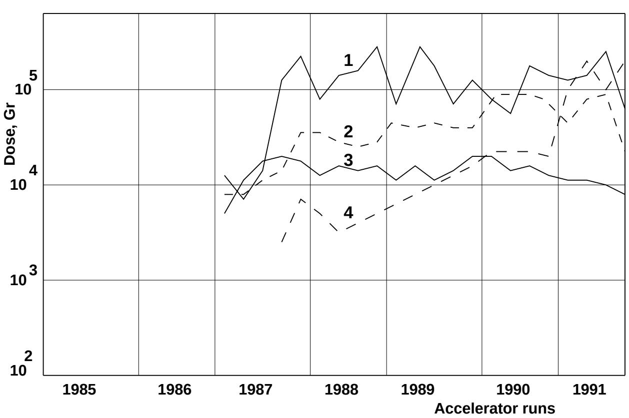

Figure 12: Radiation loads on elements of the beam extraction system.

It is seen from the data that compared to the “quiet” period (1987–1988) radiation loads on SM–24 in 1991 increased by two orders of magnitude. Their values reached the level of loads of the most irradiated septum magnets of the RSE system. This reflects the fact that the average efficiency of the FE system is as high as hoped for.

4 BEAM SCRAPING AND DUMPING

4.1 Beam scraping

The efficiency of a modern accelerator operation for physics experiments depends on correctly choosing a common extraction scheme and also the beam characteristics for the experiments. With the growth of intensity the problems of particle extraction are complicated because the associated increase of the beam dimensions leads to a decrease of efficiency both for FE and RSE.

The next experiment to be described [4] was done with the aim of investigating the possibility of beam collimation before FE. An internal target installed at SS–60 with a Cu core 4 cm thick along the beam was inserted 500 ms before FE in order to cut $\sim 5\%$ of the accelerated beam intensity. The result is presented in fig. 13 where the distribution of particles for the initial beam (curve 1) and for the cut one (curve 2) are shown.

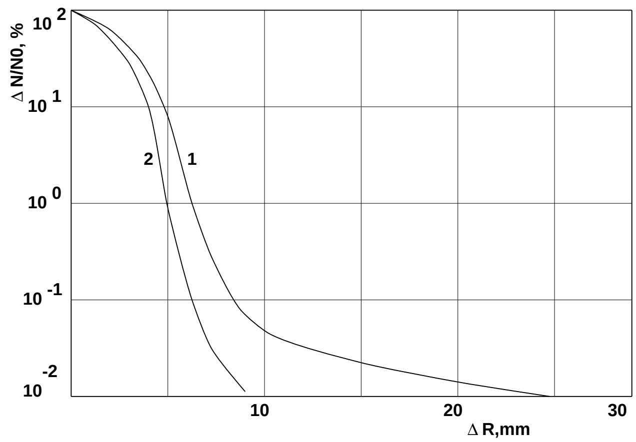

Figure 13: Radial half–size of a beam. 1 is for the initial beam; 2 is for the case where 5% of the beam is scraped.

It is seen that by this collimation technique one can form a beam where the main portion of the particles (by $\sim 5 \cdot 10^{-4}$ of the full intensity) lies within the beam half–size measured before scraping a few per cent of the beam.

FE of such a collimated beam was made towards the neutrino channel. The distribution of particle losses along the upstream part of the channel was compared with the loss distribution at extraction of the original beam. The result is presented in fig. 14 where the distribution of beam losses along the upstream part of the channel is shown in relative units. The ejection intensity was $\sim 1.5 \cdot 10^{12}$ ppc. It is seen that by this technique one can reduce losses in the channel on average by more than a factor of three.

4.2 Beam interception

Interception of proton beam losses is practically the only method to prolong the duration of the life of accelerator equipment. Interception is done in order to localize particle losses at a certain region of the accelerator thus providing minimum irradiation of the equipment in the remaining portion of the perimeter.

The IHEP system of beam interception [19] can guarantee beam loss localization over the energy span 1.5–70 GeV and for intensities up to $5 \cdot 10^{13}$ ppc. It also allows one to control the transverse dimensions of a high intensity beam before ejection by scraping particles with an absorber after

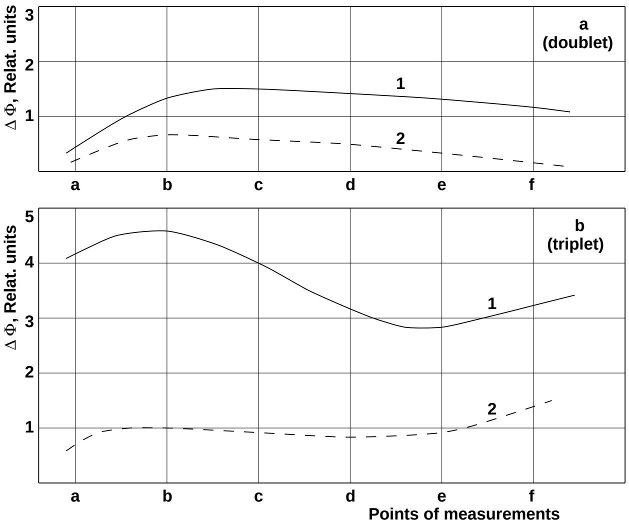

Figure 14: Distribution of losses along the upstream part of the neutrino channel. 1 is for the uncollimated beam; 2 is for the case where 5% of the beam has been scraped.

scattering them in the target.

Scheme for proton beam scraping. The beam scraping system is installed in SS–86 and consists of scattering targets, beam absorber and external shielding (see fig. 15).

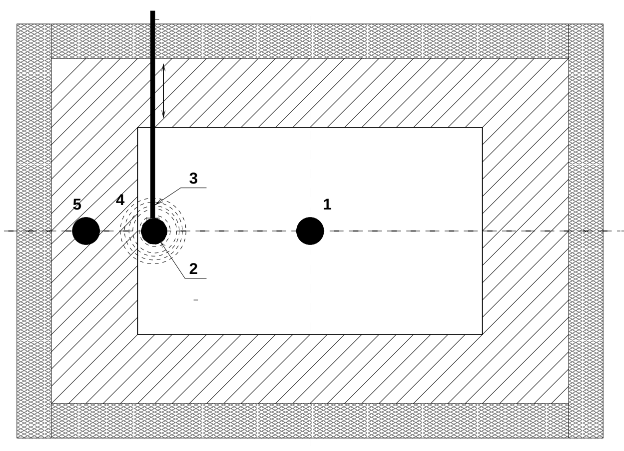

Figure 15: Disposition of beam, absorber and scattering target for the beam scraping and loss localization system. 1 is circulating beam; 2 is the beam displaced onto the scattering target; 3 is a target; 4 is the beam deflected onto the absorber after scattering by a target; 5 is the beam deflected on to the absorber by the kicker magnet.

The external shield around the absorber was designed for absorbtion of the dispersed radiation. The thickness from the top was defined by requirements for reducing the radiation to the level at which there was no need to reinforce the ground shield around the accelerator perimeter. The dimensions of the shield in the other directions were defined by the requirement that the induced activity dose on the surface of the shield not exceed 100 mrem/h.

The particle absorbers and scattering targets are outside of the beam envelope at injection. A local distortion of the orbit formed with the help of additional windings on the A–70 magnets is used for beam displacement towards the scattering targets. Interaction of beam with a target results in the increase of the betatron amplitude of the particles and deflects them on to an absorber. This mechanism removes part of the beam from the original distribution. In the case of full intensity interception, the beam is deflected on to the end face of an absorber by the FE kicker magnet [7]. Trajectories of the beam for full interception are presented in fig. 16.

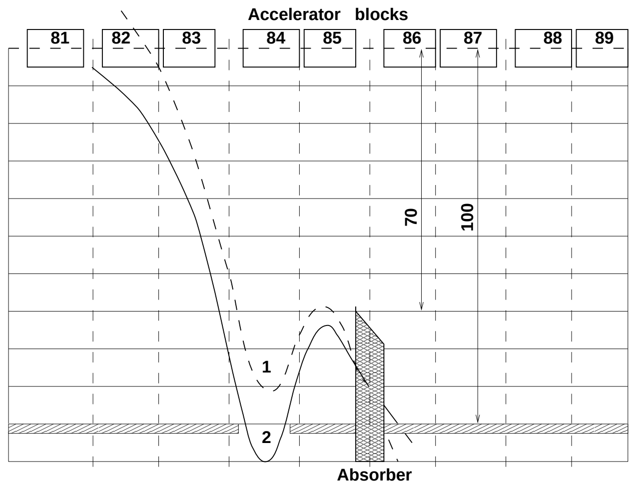

Figure 16: Trajectories of the beam in the region of the absorber (SS–86) for full interception. 1 and 2 illustrate the work of the bump with different kicker magnets.

Beam deflection on to the absorber by a scattering target. The processes leading to increases of the particle betatron amplitudes to be removed are well known (see, for example, [20]). The length of the target along the beam, the target material and the mutual layout of target and absorber were optimized based on calculations of the interactions of particles with targets.

A 3 mm long target of W was used as a scatterer for 70 GeV particles. A displacement of the target relative to the absorber of 2 mm is optimal from the point of view of growth of the particle step size deflected on to the absorber at scattering. The distribution of 70 GeV protons across the absorber after scattering by a target with the above parameters is given in fig. 17.

It is seen that the step size of the particle deflection at the absorber reachs 15 mm. The fraction of the inelastic interactions in the target is $\sim 8\%$. To get similar particle distributions on the absorber at other energies, targets of different thicknesses should be used. For example, to cut particles at transition energy (~ 10 GeV) one can use a W target with a thickness of $\sim 50 \mu m$. In this case the inelastic interactions will be $\sim 0.2\%$.

The speed of the beam displacement towards the scattering target is determined from the condition of scattering by the target of all protons that are to be cut. The accelerator beam steering systems that are on to steer beam on to the A–70 internal targets allow one to get the necessary speed

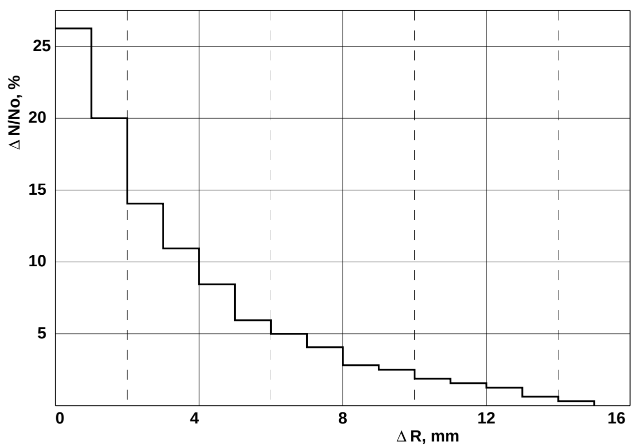

Figure 17: Distribution of proton beam density on the absorber after scattering by a 3 mm W target.

of beam displacement.

Beam interception efficiency. At SS–86 the length of the absorber is limited to 3 m. Calculations show that after interception the particle energy is about half of the accelerated proton energy after magnetic block 86 following the absorber. Particles of lower energy hit the walls of the vacuum chamber of this block. So, with account of block 86 at the region of losses localization, a share of energy E_1 of the secondary particles which is responsible for radiation loads on the remaining portion of the accelerator perimeter was defined. The relation of this value to the full energy of the intercepted beam is defined by the parameter $W = E_1/E$. In this case the value of the efficiency of the interception system for a known beam density distribution deflected on to the absorber is defined as:

$$\varepsilon = (E - E_1)/E \tag{6}$$

Values of the efficiency of the interception system for different regimes are given in table 2 for the distribution presented in fig. 17.

Table 2: Efficiency of the interception system.

	Deflected beam by targets			Deflected beam by KM–16
Beam energy, GeV	1.5	8.0	70.0	70.0
System efficiency, %	83	93	95	99.8

It is seen from the table that for the case of deflecting beam on to the absorber by KM–16 the scattering of particles from the edge of the absorber decreases significally and the efficiency of the system is close to 100%. A concern is the level of irradiation of block 86. Analysis shows that the fraction of energy lost in it is $\leq 1\%$ of the energy of the particles incident on absorber. This is acceptable for this mode of operation. It is also seen from the table that for the case of deflecting beam on to the absorber with the help of targets the system significally decreases the levels of equipment irradiation along the accelerator perimeter.

In summary, creating a sharp beam edge by removing a fraction of the particles with large betatron oscillation amplitudes allows one to improve the quality of extracted beams for physics experiments and gives the possibility of reducing radiation loads on equipment of these systems.

5 REFERENCES

[1] A.I.Akimtsev, A.A.Asseev, A.A.Zhuravlev, IHEP 83–20, Serpukhov, 1983.
[2] A.A.Asseev, A.A.Zhuravlev, IHEP 77–65, Serpukhov, 1977.
[3] V.I.Gridasov et al., IHEP 70–58, Serpukhov, 1970.
[4] A.A.Asseev et al., IHEP 79–91, Serpukhov, 1979.
[5] Yu.M.Ado, A.A.Asseev et al., Proceed. of the VIII All–Union conf. on part. accel., Dubna, 1983, v.1, p. 313.
[6] A.I.Akimtsev et al., IHEP 78–154, Serpukhov, 1978.
[7] A.A.Asseev et al., Proceed. of the III All–Union conf. on part. accel., M., Nauka, 1973, v. 2, p. 160.
[8] K.P.Myznikov et al., IHEP 70–51, Serpukhov, 1970.
[9] A.G.Afonin, V.I.Dianov, XII All–Union conf. on part. accel. Abstracts. M., ITEP, 1990, p. 197.
[10] A.A.Asseev, M.G.Dulimova, IHEP 90–154, Protvino, 1990.
[11] A.A.Asseev, V.E.Borodin, IHEP 92–147, Protvino, 1992.
[12] V.N.Lebedev, Proceed. of X Internat. conf. on part. accel., Serpukhov, 1977, v.2, p.400.
[13] A.A.Asseev, V.E.Borodin, IHEP 91–64, Protvino, 1991.
[14] A.G.Afonin et al., IHEP 86–3, Serpukhov, 1986.
[15] CERN/MPS/Int. DL/B 67–19, Geneva, 1967. The second stage improvement study.
[16] G. Azzoni, CERN/PS/OP 92–5, Geneva, 1992. Statistics of PS Operation 1991.
[17] M.H.Van de Voorde and C.Restat, CERN 72–7, Geneva, 1978.
[18] Radiation resistance of materials. Reference book under edition of V.B.Dubrovsky, ., Atomizdat, 1973.
[19] A.A.Asseev et al., IHEP 80–104, Serpukhov, 1980.
[20] A.A.Asseev et al., IHEP 96–17, Protvino, 1996.

LIST OF PARTICIPANTS

Mike Albrow (Fermilab)
Richard Andrews (Fermilab)
Saeed Assadi (Fermilab)
Alexey Asseev (IHEP)
Valeri Balbekov (Fermilab)
Chandra Bhat (Fermilab)
Michael Bieler (DESY)
Valery Biryukov (IHEP)
Andrew Brandt (Fermilab)
Charles Brown (Fermilab)
Guillermo Buitrago (aps-sociedad colombiana de fisica)
Richard Carrigan (Fermilab) - co-chair
Weiren Chou (Fermilab)
Michael Church (Fermilab)
Patrick Colestock (Fermilab)
Paul Czarapata (Fermilab)
Alexandr Drozhdin (Fermilab)
Klaus Ehret (DESY)
Konrad Elsener (CERN)
Peter Garbincius (Fermilab)
Wlodek Guryn (BNL)
Laszlo Gutay (Purdue Univ.)
Alan Hahn (Fermilab)
Carsten Hast (DESY)
James Holt (Fermilab)
Jean-Bernard Jeanneret (CERN)
Carol Johnstone (Fermilab)
Lawrence W. Jones (UMICH)
Daniel Kaplan (IIT)
Peter Kasper (Fermilab)
Alexei Khanzadeev (PNPI)
Tom Kobilarcik (Fermilab)
Oleg Krivosheev (Fermilab)
Simon Kwan (Fermilab)
Michael Martens (Fermilab)
Elliott McCrory (Fermilab)
Hisayasu Mitsui (Toshiba Corporation)
Nikolai Mokhov (Fermilab) - co-chair
Craig Moore (Fermilab)
C. Thornton Murphy (Fermilab)
David Neuffer (Fermilab)
Vassili Papavassiliou (New Mexico State Univ.)
Vasiliy Parkhomchuk (BINP)
Stanley Pruss (Fermilab)
Johannes Ranft (Univ. of Siegen)
Marion Richardson (Fermilab) - secretariat
Vladimir Samsonov (PNPI)
Alberto Santoro (Lafex/CBPF Rio)
Todd Satogata (BNL)
Cynthia Sazama (Fermilab) - secretariat
Walter Scandale (CERN)
Vladimir Shiltsev (Fermilab)
Sergei Striganov (Fermilab)
Linda Stutte (Fermilab)
Mike Sullivan (SLAC)
Ken Takayama (KEK)
Cyrus Taylor (Case-Western Reserve)
Dejan Trbojevic (BNL)
Stephan Tzenov (Fermilab)
Andreas Van Ginneken (Fermilab)
Weishi Wan (Fermilab)
Sebastian White (Fermilab)